PACIFIC EARTHQUAKE ENGINEERING RESEARCH CENTER

Effects of Connection Hysteretic Degradation on the Seismic Behavior of Steel Moment-Resisting Frames

Janise E. Rodgers

and

Stephen A. Mahin
University of California, Berkeley

PEER 2003/13
MARCH 2004

Effects of Connection Hysteretic Degradation on the Seismic Behavior of Steel Moment-Resisting Frames

Janise E. Rodgers

and

Stephen A. Mahin

Department of Civil and Environmental Engineering
University of California, Berkeley

PEER Report 2003/13
Pacific Earthquake Engineering Research Center
College of Engineering
University of California, Berkeley

March 2004

ABSTRACT

Fractures observed at the welded beam-column connections in steel moment-resisting frames after recent earthquakes have led structural engineers to investigate the hysteretic behavior of such connections. Extensive research was subsequently performed on connections, and much is now known about their behavior. However, the same cannot be said for the effects of this behavior on overall system response, particularly if degradation occurs in connection strength or stiffness. Some analytical studies have been performed, but experimental data are virtually nonexistent for systems with degrading connections. It is for this reason that the study presented herein was designed and carried out.

This study contains both experimental and analytical portions. The experimental portion consists of a series of 32 shaking table tests performed on a scale model test specimen. Idealized mechanical connections capable of mimicking different types of hysteretic behavior seen in real connections were used. Hysteretic behaviors considered were ductile bilinear, brittle fracture, ductile fracture, deformation softening (negative post-yield stiffness), and strength degradation. The ability of the connections to achieve the desired behavior was verified by experimental testing prior to their use in the shaking table test specimen. In some tests, a high-speed data acquisition system was used to capture highly transient phenomena associated with brittle fracture. Observed phenomena included propagation of elastic waves, changes in beam curvature, local moment redistribution, and excitation of member higher modes. These phenomena were found to have small impacts on the system response.

The data from the experimental portion of the study were used to develop a computer model of the structure for use in analytical studies that examined the effects of various degradation-related hysteretic parameters, earthquake excitations, and frame properties. Both experimental and analytical results show that the effects of connection hysteretic degradation on system behavior depend on several factors, including system location on the response spectrum, degradation type and severity, and earthquake excitation amplitude.

All types of hysteretic degradation causing substantial strength loss had adverse effects on the system behavior (including collapse) for short to intermediate length structure fundamental periods (relative to the predominant excitation period). Degradation did not have similarly adverse effects on structures with longer periods.

System-level effects of connection fracture were dependent on the severity of connection moment capacity reduction and the post-fracture tangent connection stiffness. Negative post-fracture and post-yield stiffnesses contributed significantly to large displacements and even collapse in some cases, exacerbating the effects of geometric nonlinearity.

ACKNOWLEDGMENTS

The support of the National Science Foundation, the sponsor of this research under grant CMS-9807069 is gratefully acknowledged.

This work was supported in part by the Pacific Earthquake Engineering Research Center through the Earthquake Engineering Research Centers Program of the National Science Foundation, under award number EEC-9701568.

Additionally, Janise Rodgers gratefully acknowledges the support of many people, chief among them husband Dane, parents Richard and Marilyn Redd, grandparents Cecil and Billie Marie Redd, and brothers and sisters in Christ at Shiloh Christian Fellowship and Veritas Fellowship.

CONTENTS

LIST OF FIGURES

LIST OF TABLES

1 Introduction

For a number of years, steel moment-resisting frames with welded beam-to-column connections were considered to be an excellent structural system for seismic resistance. Many buildings in regions of high seismicity utilized these steel moment frames, defined as “special moment-resisting frames” (SMRFs), in modern building codes for their primary lateral force-resisting systems. These moment frames were assigned the highest strength-reduction factor under the building codes in place when they were designed (such as the Uniform Building Code (International Conference of Building Officials, 1997)), a testament to the perception within the engineering practice that such systems, and hence their connections, were inherently very ductile.

All this changed in the aftermath of the 1994 Northridge, California, earthquake, as building inspectors and structural engineers discovered numerous fractures in welded moment connections in the Los Angeles area. In most of these connections, there was little or no evidence of yielding, indicating that the connections in reality had very little ductility. Many structures that at first appeared to have little damage were found upon more thorough inspection to have fractures in the connections. More fractures were found in buildings in Kobe, Japan, in the aftermath of the 1995 Hyogo-ken-Nambu earthquake, casting suspicion on Japanese moment-framed construction as well. The discovery of the fractures sparked considerable debate, and subsequently research, within the structural engineering community on both sides of the Pacific. Because of this, there are now two generally recognized eras of steel moment-frame design: pre-Northridge and post-Northridge.

The most immediate problems posed by the Northridge earthquake were first to assess the safety of buildings with fractured connections and then to determine the causes of the connection fractures. Other problems, such as how to determine the vulnerability of existing moment-frame construction in general to potential connection fractures, and how to design new moment connections that would not suffer brittle fracture, appeared shortly thereafter. Researchers throughout the U.S. and elsewhere began to work on these problems through both experimental and analytical studies. The vast majority of the experimental studies were performed at the component and subassemblage level, with the focus on the beam-to-column connection region. After an unprecedented number of beam-column connection tests in the years following Northridge, much has been learned about connection hysteretic behavior.

However, the larger questions of how connection behavior affects the global behavior of the structural system have yet to be answered conclusively. Many of the newer connections designed to avoid brittle fracture display some other form of hysteretic degradation. Thus, it is necessary to ask whether some of these more ductile forms of connection hysteretic degradation can cause undesirable or even dangerous system behavior, and, if so, under what circumstances.

Also, many of the buildings with brittle connection fractures caused by the Northridge earthquake suffered little damage otherwise. In addition, current design guidelines, such as FEMA 350 (FEMA, 2000), explicitly recognize that some brittle connection fractures may continue to occur in welded steel frames. It is therefore important to determine the effects of brittle fracture on response when looked at through the lens of global system performance.

1.1 PROBLEM DEFINITION

For the purpose of seismic response analysis, beam-to-column connections in steel moment-resisting frames are frequently characterized as having full hysteretic loops with an overall bilinear (or similar) shape. However, many connections exhibit more complex forms of hysteresis, including some form of deterioration during cyclic inelastic excursions. As such, the hysteretic loops are no longer full and may deteriorate during cycling into the elastic range. The type of deterioration varies from a sudden loss of capacity associated with fracture to a more gradual degradation of strength and stiffness, which may be accompanied by pinching of the overall hysteretic loop shape. The types of hysteretic behavior examined in this study are:

- *Ductile baseline*: No deterioration — stable, full hysteretic loops which are the ideal generally sought after by designers of moment-resisting connections;
- *Brittle fracture*: A connection fracture, usually in the beam flange-to-column connection region, where no yielding occurs prior to fracture. In the idealized connections used in this study, yielding is permitted to occur locally to provide ductile crack initiation;
- *Ductile fracture*: A connection fracture that occurs after significant yielding has taken place;

- *Deformation softening*: The presence of negative post-yield tangent stiffness in the connection hysteresis; and
- *Strength degradation*: The isotropic softening of the connection, where the yield strength reduces from cycle to cycle.

In this study, the effects of these five types of hysteretic behavior on SMRF system response will be assessed by examining their effects on global displacements and forces, connection rotations and moments, and other response quantities. As a result, the design of the experiment is based on capturing global behavior data for a structure with connections exhibiting one or more of the particular hysteretic behaviors defined above. A significant portion of the experimental problem involves the design of an appropriate test specimen that meets the design objectives and minimizes adverse factors such as dependence on particular details, scaling issues, and cost. The remainder of the experimental program involves the design and performance of the experiment itself, as well as examining and interpreting the data.

The overall questions posed in the introductory section can be answered much more efficiently by a combination of analytical simulations and experiments than by experiments alone, due to the very large number of cases that would need to be tested. Therefore, this investigation includes a significant analytical component as well. The analytical component involves the development and assessment of a mathematical model of the structure that is able to reliably represent the data collected in the experiments. This model is then used in computer simulations to further examine parameters that affect behavior. The use of simulations also allows consideration of parameters that would be difficult to examine experimentally without the construction of many test specimens, such as different member sizes for the beams and columns. The results of the analytical component of the investigation are synthesized with those from the experimental phase to draw more general conclusions than possible by experiment alone.

1.2 RESEARCH OBJECTIVES AND TASKS

The overall objective of the research program reported herein is to identify the effects that various types of connection hysteretic behavior have on the global seismic response of steel moment-frame systems. In particular, the effects of connection fracture versus other types of more ductile hysteretic degradation are investigated. One of the keys to understanding the effects of connection fractures on system response is gaining a clearer picture of what happens in the structure immediately following a fracture, and one of the objectives of this study is to gain insight into this area. Overall, the basic intent of the studies is to determine which types of hysteretic degradation cause particularly undesirable system behavior, and which, if any, cause relatively benign or even beneficial behavior, and under what circumstances.

Realization of these global objectives can be distilled into the following specific tasks:

- Design, construct, and verify by quasi-static testing an idealized mechanical connection that can faithfully and predictably reproduce the five types of hysteretic behavior defined above;
- Incorporate the mechanical connections into a small moment-frame specimen, and perform shaking table tests of the moment-frame specimen with various ground motion excitations;
- Determine from the data the effects of various types of hysteretic degradation under simple pulses, near-field ground motions, and long-duration subduction zone-type ground motions;
- Identify from the results any hysteretic behavior/ground motion combinations that produce undesirable system behavior;
- Use the data to develop and assess an analytical model considering both connection behavior and global behavior;
- Perform analytical parametric studies using the analytical model to further investigate the effects of specific hysteretic degradation parameters on global seismic response; and
- Identify future research needs.

1.3 SCOPE

This report covers the experimental and analytical studies of the effects of connection hysteretic degradation on system response. A review of pertinent literature, with an emphasis on analytical studies of systems with degrading connections, is presented in Chapter 2. The design of the test specimen is presented in Chapter 3, while the design and performance of the experiment itself is described in Chapter 4. Test results are presented in Chapters 5 and 6, with behavioral observations located in Chapter 5 and comparisons of behaviors observed in different tests presented in Chapter 6. The development of an analytical model for use in further studies is presented in Chapter 7. The design of and results from these analytical studies are then discussed in Chapter 8. Finally, conclusions obtained from both the experimental and analytical studies and recommendations for future work are presented in Chapter 9.

2 Literature Review

In the aftermath of the 1994 Northridge and 1995 Hyogo-ken Nambu earthquakes, inspections of steel moment-frame buildings uncovered various types of brittle fracture damage in the beam-to-column connections, ranging from small fractures visible only with sensitive electronic equipment to large visually apparent cracks extending from the beam flange-to-column weld through the beam or column flange. Since welded steel moment frames were expected to behave in a ductile manner, the fractures came as a shock to many engineers, who immediately called into question the safety of steel moment-frame construction in areas of high seismicity.

As a result, a number of investigators have performed analytical studies to assess the seismic safety and performance of steel moment-frame buildings, both damaged and undamaged, new and old (Astaneh-Asl et al., 1998; Bonowitz and Maison, 1998; Foutch and Shi, 1998; Gupta and Krawinkler, 2000; Lee and Foutch, 2000; Luco and Cornell, 1999; Mahin and Morishita, 1998; Maison and Kasai, 1997; Naeim et al., 1999; Nakashima et al., 2000; Rahnama and Krawinkler, 1993; SAC, 1995; Uetani and Tagawa, 2000). These studies range from specific case studies of instrumented buildings in the Los Angeles area subjected to Northridge ground motions to large Monte Carlo simulations using a variety of buildings and earthquake records.

Despite the variations in analytical methods, the conclusions drawn for SMRF structures of the type used in the U.S. tended to be similar: for collapse to occur, brittle fractures at the connections must be numerous and lateral displacement demands for an ideally ductile structure must be very large. These conditions generally occur only for very large near-field ground motions. For moderate ground motions, the effects of local fracture seem to be relatively benign. This result corroborates well with the Northridge damage (see Section 2.2): there were no collapses of steel moment-frame buildings, and many buildings with numerous connection fractures showed little other damage (though there were certainly some exceptions).

Nevertheless, the behavior of the pre-Northridge connections was inconsistent with the design assumptions, and this is troubling. Clearly, the presence of fractured connections in a building following an earthquake invalidates the engineering calculations used to obtain permits to construct and occupy the building. Even though no collapses due to connection fracture have occurred in recent earthquakes in the United States, this may have been simply because the necessary combination of ground motion, connection detail (or defect), and structural configuration did not occur for these earthquakes.

As will be discussed in Section 2.2, a small but significant number of welded steel moment-frame buildings collapsed during the 1995 Hyogo-ken Nambu earthquake. The analytical literature also suggests that there are some cases where connection fracture can cause adverse system behavior such as collapse, but that there are many cases where fracture has relatively little effect on overall system behavior. The wide variation in system behavior observed after recent earthquakes and predicted by analysis demonstrates that the effects of brittle fracture may be complex and dependent on a number of variables.

Brittle fracture is not the only connection hysteretic behavior that may have less-than-desirable effects on seismic system response. After pre-Northridge welded moment connections were found to be susceptible to brittle fracture, researchers began to develop new or modified connection designs which were more ductile. As these new connection designs were tested by the SAC Joint Venture and others (see FEMA-355D, FEMA, 2000), several other types of hysteretic degradation were identified as being of concern. These include negative post-yield stiffness and strength degradation, as well as fracture after significant yielding has occurred.

In light of these observations, it is important to investigate the effects of these other hysteretic behaviors, in addition to fracture, on the system response. Analytical studies have been performed to assess the impacts of these behaviors on system response, but as in the case of brittle fracture, experimental tests of system behavior are scarce. As more SMRFs with post-Northridge connections enter the built environment, experimental work on systems with these other types of connection hysteretic degradation will become even more important.

2.1 SCOPE

This chapter begins with a brief summary of damage to steel moment frames in recent earthquakes, with an emphasis on the Northridge earthquake due to the availability of data and the significant ramifications for U.S. practice. Next, analytical studies of steel moment-frame structures with degrading connection hysteretic behavior are discussed. Most of the analytical studies included a model with ductile, nondegrading connections for comparison purposes. For this reason, other studies of ductile baseline behavior are not included in this literature survey. The analytical studies discussed herein constitute the bulk of the current literature on the effects of connection degradation on system response. A brief summary of the results of selected recent connection tests is included to provide background information on the types of connection hysteretic behavior observed in connection details currently present in the field. Finally, the few experimental studies that have been performed on systems to date are discussed.

This literature survey is not intended to be a comprehensive treatment of the problems associated with welded steel moment frames, but is intended only to provide necessary background information for a portion of the problem discussed in this study. This study is focused on the effects of connection degradation on the system behavior *after* degradation begins, and does not focus on how or why the degradation occurs. A great deal of additional information on the problems of steel moment frames, much of it focused on why degradation occurs, is available in publications by the SAC Joint Venture and FEMA.

The SAC Joint Venture was formed after Northridge for the express purpose of solving the problems posed by the newly discovered brittle fracture tendencies of welded steel moment connections. SAC was comprised of the Structural Engineers Association of California (SEAOC), the Applied Technology Council (ATC), and the Consortium of Universities for Research in Earthquake Engineering (CUREe). SAC has published numerous documents on steel moment frames, a comprehensive listing of which can be found in the References and Bibliography section of FEMA 350 (FEMA, 2000). A brief but excellent summary of overall problems with steel moment frames and the findings of SAC are located in the FEMA 350 introduction. The reader is referred to the SAC publications for a comprehensive examination of welded steel moment-frame problems, as well as detailed background information.

2.2 SUMMARY OF DAMAGE TO STEEL MOMENT FRAMES IN PAST EARTHQUAKES

This section provides a brief overview of the damage to steel frames in recent earthquakes, with an emphasis on the 1994 Northridge earthquake. The intent of this section is to provide background information on the types and prevalence of fracture damage and the resulting effects on global behavior that were observed after recent earthquakes. These post-earthquake observations provided motivation for this research and were major considerations in the design of the experiment conducted in this study.

2.2.1 1994 Northridge Earthquake

The fractures that occurred during the Northridge earthquake were discovered after the initial reconnaissance and walk-through inspection efforts had been completed, and many engineers were under the impression that steel moment frames had performed well. Damage was first observed in buildings that were under construction, where the steel framing was still exposed (Bertero et al., 1994). In other cases, engineers noted that some buildings were disproportionately affected by small aftershocks.

Shortly thereafter, several steel-framed buildings were determined to be out of vertical alignment, which caused engineers to remove the interior nonstructural elements and fireproofing to look at the moment frames. In these buildings, inspectors and engineers found some beam-column connections with significant fracture damage, with little evidence of plastic deformation beforehand (Bertero et al., 1994). As word of the brittle fractures spread, more buildings were inspected, and the number of damaged buildings eventually climbed to over 150, mostly concentrated in the San Fernando Valley and west Los Angeles.

Much of this damage was discovered only after intrusive inspections (meaning fireproofing and interior finishes were removed) in buildings which had little residual drift or other visual indications of damage. This indicates that walk-through inspections of the type commonly used prior to the Northridge earthquake to assign red, yellow, and green building safety tags immediately following an earthquake were not a reliable method of determining whether steel moment frames suffered brittle fracture damage (for newer inspection requirements, see FEMA 352).

There were no collapses of SMRFs during the Northridge earthquake, and many buildings had little residual drift or nonstructural damage, though some of the more heavily damaged buildings had relatively large residual drifts and significant nonstructural damage (Bertero et al., 1994). The observed damage from the Northridge and Hyogo-ken Nambu earthquakes has been well documented both in summary reports by organizations such as the SAC Joint Venture (SAC, 1995, and FEMA-355E, FEMA, 2000) and in various reconnaissance reports (AIJ, 1995, Bertero et al., 1994, Bertero et al., 1995, Holmes and Somers ed., 1995, Youssef et al., 1994), so only a brief summary is provided here.

In the months following the Northridge earthquake, information on observed damage types and their prevalence was collected by Nabih Youssef and Associates using a lengthy survey form sent to engineers who had inspected damaged buildings. Damage types were classified according to the system shown in Figures 2-1 and 2-2. The reader is referred to the technical report SAC 95-06 (SAC, 1995) for a detailed description of particular damage types shown.

In the case of the Northridge earthquake, the fractures were confined to the beam-column connection region (SAC, 1995). The fractures nearly always initiated in or near the critical complete joint penetration weld used to connect the beam flange to the column flange. Most fractures were either in the weld itself or in the adjacent heat-affected zones (HAZ), and damage types W2, W3, W4, C2, and G3 were common. In many cases, the fracture completely separated the beam flange from the column. Some instances of shear tab fracture (type S3) were noted as well. In some cases, fractures initiating in the weld or the HAZ propagated into the column flanges and panel zone, but the more severe column damage types C3, P5, and P6 were less common.

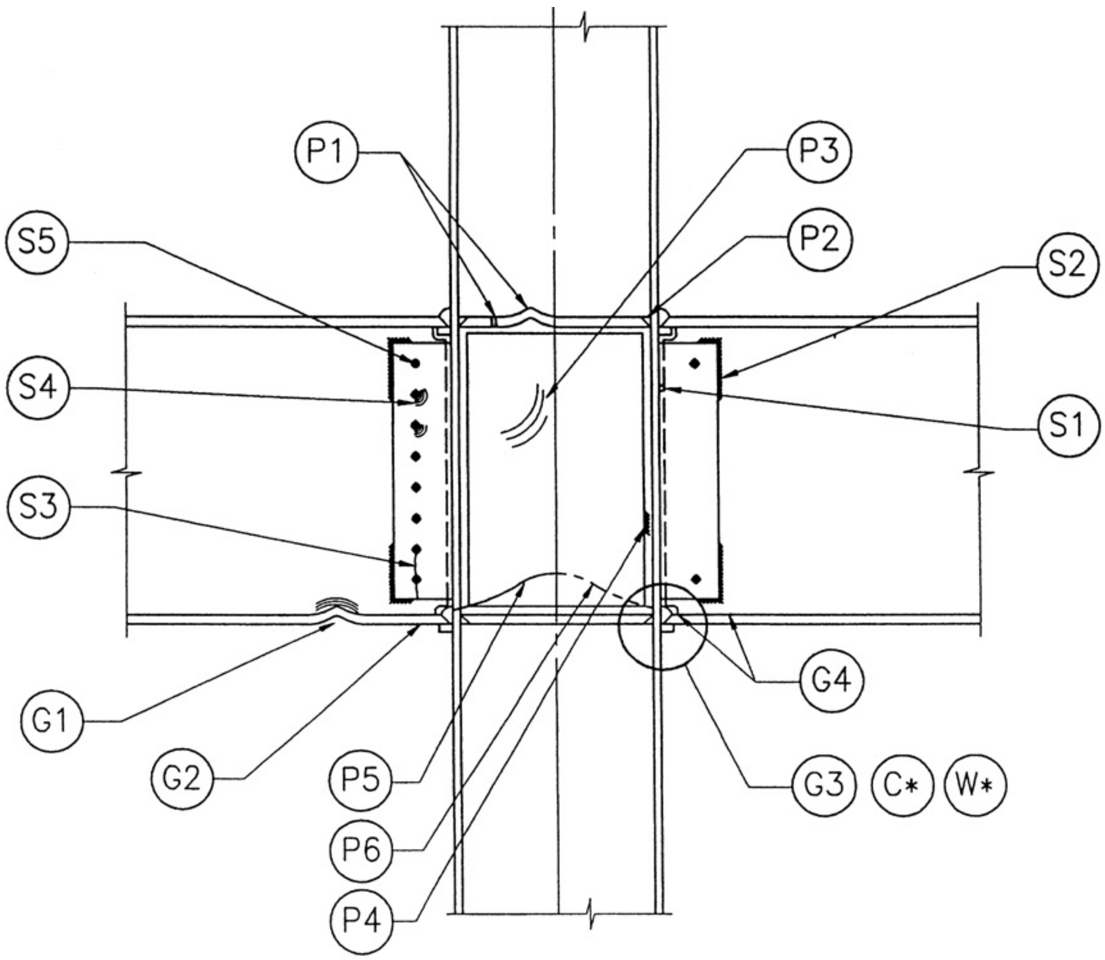

Figure 2-1. Typical pre-Northridge welded moment connection with damage types shown

Although complete fractures through the column were rare, situations were noted where fractures occurred in both the top and bottom beam flanges. Most observed fractures occurred at the bottom beam flange, with the ratio of observed bottom-to-top-flange damage at about 30:1. However, this figure may underestimate the true number of top flange fractures because the beam top flanges were more difficult to inspect than the bottom flanges, and consequently were not always inspected.

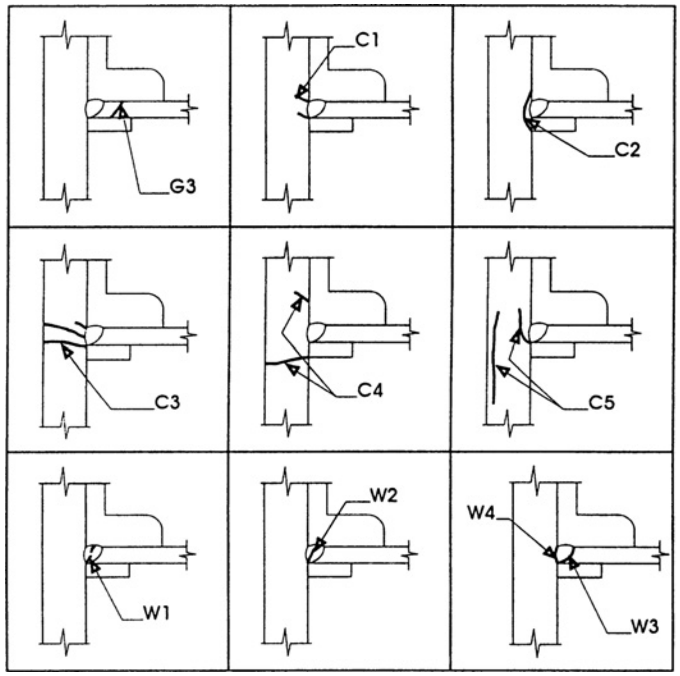

Figure 2-2. Detail of damage in vicinity of bottom beam flange-to-column weld

2.2.2 1995 Hyogo-ken Nambu Earthquake

Fractures were also observed in moment-frame buildings following the 1995 Hyogo-ken Nambu earthquake (AIJ Kinki Branch, 1995). Japanese moment-frame design and construction practice differs in several important respects from U.S. practice, and these differences (along with the many similarities) are discussed by Nakashima (Nakashima, Roeder, and Maruoka, 2000). These differences in design and practice are generally regarded as the major cause of the differences in the fracture-related damage observed after the Hyogo-ken Nambu and Northridge earthquakes, though there were some differences in ground motion characteristics. In particular, the most common beam-column connection used in newer buildings in Japan is the through-diaphragm detail, where girder flanges are welded to diaphragm plates that interrupt the column. Fractures in or near the welds connecting these diaphragms to the column could lead to a complete severing of the column and loss of axial load capacity.

In addition, many buildings in cities such as Kobe are tall and very narrow, so column demands due to overturning are high, making fractures in the columns more likely. Column fractures are believed to be an important contributor to the approximately 10% collapse rate of newer steel moment frames in Kobe (Nakashima et al., 1998). Complete column fractures were very rare in the U.S., however, and will not be considered as part of this study.

2.2.3 Other Recent U.S. Earthquakes

It is important to realize that earthquake-induced fracture damage was not limited to the Northridge and Hyogo-ken Nambu (Kobe) earthquakes. After the discovery of fractures in the aftermath of the Northridge earthquake brought the problems of the code-prescriptive pre-Northridge moment connection to light, a number of reports surfaced of similar fractures caused by other earthquakes, including the 1989 Loma Prieta and 1992 Landers, California, earthquakes (FEMA-355E; FEMA, 2000). In most of these cases, fracture damage was determined only after inspections conducted for business reasons (generally prepurchase) after the Northridge earthquake, when inspectors knew what to look for. The existence of Northridge-like fracture damage caused by other earthquakes serves to emphasize the widespread nature of the problems with WSMFs.

2.3 ANALYTICAL STUDIES OF STRUCTURES WITH DEGRADING CONNECTION HYSTERETIC BEHAVIOR

As mentioned previously, brittle fracture is not the only type of hysteretic degradation that may have adverse effects on system behavior. There are several other hysteretic behavior types that can occur in ductile connections and are cause for concern. In this section, analytical studies of the system behavior of buildings with the following connection hysteretic behaviors are examined:

- brittle fracture
- ductile fracture (defined as fracture after significant beam yielding occurs)
- deformation softening (negative post-yield stiffness)
- strength degradation

The focus of this section is on analytical predictions of the global behavior of systems with the above types of connection hysteretic degradation, though many of the studies themselves are more broadly focused. These analytical studies, along with the post-earthquake observations from the previous section, represent the bulk of current knowledge on the effects of connection degradation on global response, since experimental tests at the system level are virtually nonexistent.

The analytical studies are quite diverse in the types of buildings studied, the analytical techniques employed, and the types of connection hysteresis examined. For organizational purposes, the studies have been grouped into seven major types: (1) deterministic case studies and evaluations of Northridge-damaged buildings, (2) deterministic parametric studies, (3) probabilistic case studies and evaluations of Northridge-damaged buildings, (4) probabilistic parametric studies, (5) analyses of specific fracture-related phenomena, (6) comparisons of analytical and modeling techniques, and (7) analyses of the variation in nonlinear behavior with period.

The distinction between deterministic and probabilistic studies is necessary due to the very different assumptions of how fractures occur in these two types of analyses. In deterministic studies, connections are assumed to fracture at predetermined locations when a preset deformation (generally specified as connection rotation) is reached. The deterministic approach does not take into account the inherent variability in connection capacity and fails to capture the apparent randomness of observed fracture damage.

In the probabilistic approach, connection fractures are assumed to occur at deformation levels taken randomly from a distribution. This approach reintroduces the uncertainty in connection capacity and fracture location and thus gives a more accurate representation of observed behavior, but is more difficult to implement. No probabilistic methods have been applied to the occurrence of other types of hysteretic behavior, so the sections discussing probabilistic studies contain information only on fracture behavior.

There is some overlap between categories (1) through (4) and (6), since several types of analysis were often performed in one study. However, the intent of the discussion of the studies in categories (1) through (4) is to evaluate the effects of various hysteretic behavior types rather than analytical models. Category (6) was created because a discussion and evaluation of analytical modeling techniques is necessary background information for the analytical work presented in Chapters 7 and 8.

A comparison of key analysis parameters for the various studies of types (1)–(4) is shown in Table 2-1. The group of studies performed for the SAC Joint Venture Phase 1 Task 3.1 are shown as a unit because they were conducted with uniform modeling and analysis standards. Connection capacity distributions for the probabilistic studies are shown in Table 2-2.

Table 2-1. Comparison of analytical studies of structures with degrading connections

Study	Analysis Types	Buildings Studied	Model Parameters			Ground Motions	Acceptance Criteria
			Gravity Frames	P-Δ	Hysteresis Types		
Astaneh-Asl et al., 1998	Nonlinear dynamic	Damaged 4, 14, 27 story	?	?	BF (modeled post-fracture)	NR-NH, MKO	Collapse prevention (CP)*
Foutch and Shi, 1998	Nonlinear static and dynamic	Nine each 3, 6, 9 story, 27 total	?	?	DB, BF, SD plus pinching and combined behaviors	EC, LN, LP, MH, ML, NPS, NR-U, SF [CS, PD, U], TB, WH	CP*
Foutch and Yun, 2002	Nonlinear static and dynamic	SAC LA 9, 20 story 6 each	Yes, w/ simple connections	Yes	DB, BF	Selected SAC LA 2/50, EC, IV, MH, ML, NPS, NR-U, SF [CS, PD, U], TF	CP*
Lee and Foutch, 2000, 2002	Nonlinear static and dynamic	3 each SAC LA & Seattle 3, 9, 20 story	Yes	Yes	BF, simple connections	SAC LA and Seattle 50/50, 2/50	CP** (0.01 global, variable local), IO
Luco and Cornell, 1999, 2000	Nonlinear dynamic	SAC LA & Seattle 3, 9, 20 story	Yes	Yes, linear	BF, DF, capacities probabilistic	SAC LA and Seattle 10/50, 2/50 suites	Extreme drifts (>0.10), CP*
Mahin and Morishita, 1998	Nonlinear dynamic	SDOF systems	N/A	Yes	DB, BF, SD, DFS	Idealized pulses	Peak ductility demand
Maison and Bonowitz, 1999, 1998	Nonlinear dynamic	SAC LA 9 story	Yes	Yes, linear	BF, DF, capacities probabilistic	SAC LA 10/50, 2/50 suites	LS** (0.025) in rare events CP** (0.05) in very rare events
Maison and Kasai, 1997	Nonlinear dynamic	Damaged 13 story	Yes	Yes, linear	BF, DF, capacities probabilistic	EC, LN, NR-CP, NR-OX, NR-TZ, SF-PD, TB	CP*

Table 2-1. — *Continued*

Study	Analysis Types	Buildings Studied	Model Parameters			Ground Motions	Acceptance Criteria
			Gravity Frames	P-Δ	Hysteresis Types		
Naeim et al., 2000	Nonlinear static and dynamic	SAC LA, Seattle, Boston 3, 9, 20 story	Yes	Yes, linear	DB, SD	SAC LA, Seattle, Boston 10/50, 2/50 suites, LA 50/50 suite	CP*
Naeim et al., 1999	Nonlinear static and dynamic, linear dynamic	Damaged 8, 10, 16, 20 story	No, after evaluation	?	DB, Elastic	Site records: NR-EN, NR-HW, NR-SO, NR-TZ	UBC-97, FEMA-273 LS, CP
Rahnama and Krawinkler, 1993	Nonlinear dynamic	SDOF systems	N/A	Yes	SD, DFS, DB	CL, CO, EC, IV, LB, OL, PS, SF-CS, TF	Strength reduction factor, hysteretic energy
Phase 1 Studies, SAC, 1995	Linear and nonlinear static and dynamic	9 total with various conditions	Yes	Yes	BF, DB	SAC Phase 1 site-specific suites	Accurate reproduction of observed damage

* Collapse defined as numerical instability in the solution due to very large displacements

** Life safety limit (LS) or collapse defined by a particular story drift ratio, shown in parentheses

Hysteresis type abbreviations: DB: Ductile baseline, BF: Brittle fracture, DF: Ductile fracture, DFS: deformation softening, SD: Strength degrading.

Ground motion abbreviations: CL: Coyote Lake (1979), CO: Coalinga (1983), EC: El Centro (Imperial Valley 1940), LB: Long Beach (1933), LN: Landers-Lucerne (1992), LP: Loma Prieta unknown, IV: Imperial Valley (1979), MH: Morgan Hill (1984), ML: Mammoth Lakes (1980), MKO: Miyagi-ken-Oki (1978), NPS: North Palm Springs (1986), NR: Northridge 1994: [CP: Canoga Park, EN: Encino, HW: North Hollywood, NH: Newhall, OX: Oxnard Blvd., SO: Sherman Oaks, TZ: Tarzana, U: Unknown], OL: Olympia (W. Washington 1949), PS: Puget Sound (1965), SF: San Fernando 1971: [CS: Castiac (1971), PD: Pacoima Dam, U: Unknown], TB: Tabas (1978), TF: Taft (Kern County 1952), WH: Whittier Narrows (1987)

2.3.1 Deterministic Case Studies and Evaluations of Northridge-Damaged Buildings

After the Northridge earthquake, several studies were performed to determine the safety of damaged steel moment-frame buildings and to ascertain whether currently available analysis methods could predict the observed damage. The SAC Joint Venture provided funding, an analysis framework, and representative ground motions for a set of nine studies of Northridge-damaged welded steel moment-frame (WSMF) buildings under Phase 1, Task 3.1. [More studies were performed in

Phase 2 of the SAC project on hypothetical buildings in Los Angeles, Seattle, and Boston, and these are discussed in later sections.] Other studies with various funding sources were performed by Astaneh et al. and Naeim et al., though Naeim's study was primarily focused on the ability of available analytical tools to predict the Northridge damage.

The nine studies performed under SAC Task 3.1 are summarized together due to their similarities, though they were performed as nine individual investigations. The reader is referred to the SAC technical report 95-04 (SAC, 1995), and the summary by Deierlein in particular, for details. The major goals of these studies were to evaluate the ability of available analytical techniques to predict the observed damage, to investigate the safety of damaged structures, to determine the behavior of repaired structures, to determine connection rotation demands to be used in the development of testing guidelines, and to evaluate design methodologies.

The studies determined that the structures which had fractured beam-column connections would be unlikely to collapse in a future earthquake with ground motions similar to those they experienced during the Northridge earthquake. However, for severe ground motions such the Sylmar record, the safety of damaged structures was found to be questionable. Connection rotation demands were found to be extremely variable. Panel zone behavior was found to have a large effect on rotation demands in the adjacent beam plastic hinges.

Hart also investigated the sensitivity of the results to the amount of residual strength in the connections after fracture. He found that there is a negligible effect on peak base shear, roof displacement, and roof interstory drift when post-fracture capacity is reduced from 50% to 20% of the original moment capacity. Further reduction to 5% had relatively large effects. This indicates that the system behavior may not be sensitive to residual strength except below a certain threshold level. This is an interesting finding and should be confirmed by further analysis and testing because it may be period dependent, as results involving strength often are.

Astaneh et al. performed an analysis of three WSMF buildings (Astaneh-Asl et al., 1998) of various heights. This was a rapid study performed to determine the safety of WSMF buildings which had suffered fracture damage to the connections. At the time, there was a great deal of concern as to the remaining seismic capacity of the damaged buildings. The three buildings studied were 4-, 14-, and 27-stories tall, respectively.

The connections were modeled as though fracture had already occurred. It is unclear whether P-Δ effects or the contribution of gravity frames were included in the analysis. The Northridge-Newhall and Miyagi-ken-Oki ground motion records (both scaled to a PGA of 0.6 g) were used as the excitations. The study concluded that the damaged structures did not appear to be susceptible to collapse for the ground motions used, which is in agreement with the SAC Phase 1 studies.

2.3.2 Deterministic Parametric Studies

Foutch and Shi performed a large parametric study (Foutch and Shi, 1998) examining the effects of eight different hysteresis types, some of which are not examined in this study. Nonlinear static and dynamic analyses were performed on 3-, 6-, and 9-story buildings. Three periods and three Uniform Building Code strength reduction factors (R = 4, 6, and 8) were used for each building height, bringing the total of combinations studied to 27. Twelve recorded ground motions, which are shown in Table 2-1, were used for the time history analyses, which were conducted with a modified version of the computer program DRAIN-2DX (Powell, 1992) which allowed the use of asymmetric connection hysteretic models, including fracture (Foutch and Shi, 1996).

Foutch and Shi determined that hysteresis type had minimal effects on the global ductility demands of the structures for the R values used, which are quite large. For nonpinching hysteresis types, the ratio of global ductility of the degrading system to that of the corresponding EPP system was approximately 1.1, and was approximately 1.3 for pinched hysteresis types. Ductility demands were found to be much more dependent on R values and period than hysteretic type. This finding indicates that the displacement response may be much more sensitive to strength losses than to other effects of degradation.

Lee and Foutch performed a smaller, more focused parametric study (Lee and Foutch, 2002) on pre-Northridge moment-frame buildings with brittle connections. The study concentrated on determining the effects of building design and construction era on anticipated seismic performance of pre-Northridge moment-frame buildings. The building codes used for design of the study buildings were the 1973 (with and without drift limits), 1985, and 1994 versions of the Uniform Building Code. Brittle fracture and simple shear connection behavior were modeled explicitly, but deterministically. This study is classified as a deterministic study herein due to the way fracture is assumed to occur, even though the end results are presented in probabilistic format, and the SAC reliability procedure is used for portions of the process.

The ground motions used were the SAC Los Angeles 2% in 50 year (2/50) and 50% in 50 year (50/50) suites (Somerville, 1997), which correspond to the collapse prevention (CP) and immediate occupancy (IO) performance states in FEMA 350 (FEMA, 2000). The findings of the study indicate that there is a low to moderate confidence level (between 20% and 80%) that older steel moment frames with brittle connections will not collapse in a 2/50 event. The confidence level is very high, however, that such frames will not collapse in a 50/50 event. The confidence is low (between 5% and 30%) that these frames will be able to obtain the IO performance state for the 50/50 event. The conclusions regarding the CP performance state generally agree with those discussed in the previous section, since the 2/50 ground motions used in this study are similar in amplitude to the Sylmar motion used in some of the SAC Task 3.1 investigations which looked at “larger earthquakes.”

Naeim, Skliros, Reinhorn, and Sivaselvan performed a parametric study to examine the effects of hysteretic degradation on seismic demands (Naeim et al., 2000). The hysteretic types considered were bilinear, strength degrading, pinching, and stiffness degrading, where the stiffness degrading model only took into account reduction of the initial elastic stiffness. Negative post-yield stiffness and fracture were not considered. Three levels of degradation were considered for each hysteretic behavior (other than bilinear): nominal, moderate, and severe. The pre-Northridge SAC 3, 9, and 20 story buildings for Los Angeles, Seattle, and Boston were examined. Nonlinear dynamic analyses were performed using the SAC ground motion suites developed for each site (Somerville, 1997). Naeim et al. found that severe stiffness degradation and severe strength degradation had the most adverse effect on seismic demands, with severe pinching having less adverse effects. Several collapses were predicted due to LA 2/50 records for buildings with severe stiffness degradation, but no collapses were predicted for any of the other types of hysteretic behavior.

Mahin and Morishita performed a study of single-degree-of-freedom (SDOF) systems with several types of hysteretic behavior including ductile behavior (elasto-perfectly-plastic), strength degradation, deformation softening, and brittle fracture (Mahin and Morishita, 1998). Nonlinear dynamic analyses were performed using a variety of simple pulses for the excitations. In particular, different pulses were used to represent the fault-normal and fault-parallel components of a near-field ground motion, in order to gain insight into the effects of the different components on building response.

For pulses of equal displacement amplitude, the fault-parallel component produced greater ductility demands on fracturing systems than the fault-normal components in the constant amplified acceleration range (Figure 2-3) of the response spectrum. In other regions, and for other types of degradation, the fault-normal component caused larger ductility demands. Mahin and Morishita also determined that the deformation softening (negative post-yield stiffness) caused an increase in ductility demand particularly in the short-period range. Displacements tended to accumulate in one direction (sometimes called “ratcheting”). Results for strength-degrading systems showed that the displacement response was similar to that of the EPP system except in the short-period range where strength degradation caused modest increases in the response and thus the ductility demands.

Rahnama and Krawinkler conducted a study of SDOF systems, focusing on strength degradation and unloading and reloading stiffness degradation in the connection hysteresis (Rahnama and Krawinkler, 1993). P-Δ effects were also investigated by using hysteretic models with negative post-yield stiffness. Since this method was used, rather than direct incorporation of nonlinear geometry in the analysis, the results are directly applicable to systems which display negative post-yield stiffness for other reasons, such as those in this investigation.

Rahnama and Krawinkler determined that strength degradation and negative post-yield stiffness had the greatest adverse effects on the response of the SDOF systems under study. The effects of unloading and reloading stiffness were found to be small and negligible, respectively. The effects of strength degradation were found to be sensitive to the rate at which the degradation occurs, with severe strength degradation being much more problematic than moderate strength degradation. Negative post-yield stiffness was found to be very detrimental to system performance, since structures with this behavior have to be much stronger to be able to achieve the same ductility demand as systems without softening.

2.3.3 Probabilistic Case Studies and Evaluations of Northridge-Damaged Buildings

Maison and Bonowitz conducted several case study analyses of WSMF buildings that had been damaged during the Northridge earthquake. Maison and Kasai also conducted a similar analysis for an instrumented 13-story building. These studies took a probabilistic approach to defining when fracture was assumed to occur in the analytical model, in an attempt to replicate the apparently random locations of fractures observed in many Northridge-damaged buildings.

In Maison and Kasai's study of the 13-story WSMF (Maison and Kasai, 1997), they first correlated their analytical model to the response measured by the building's accelerometers and to the observed damage. This building was instrumented at the basement, sixth, and twelfth floor levels only, so drifts at each story were not available. Nonetheless, the instruments allowed the development of an analytical model with probabilistically defined connection plastic rotation capacities that matched the recorded damage reasonably well. After calibration, several studies were performed: (a) a damage prediction study using the El Centro and Northridge Canoga Park records, (b) repeat scenarios with pairs of recorded Northridge motions, (c) creation of frame and building vulnerability functions using an ensemble of near-field motions, and (d) multiple simulations with three connection types: brittle, "3%" semi-ductile (0.030 radian mean plastic rotation capacity), and perfectly ductile (EPP).

In study (b), Maison and Kasai found that the damaged building model was able to withstand another Northridge-intensity earthquake without collapse and without very many additional connection fractures. It was surmised that this result was due to the "weeding out" of the connections with low plastic rotation capacities during the first earthquake, but it is important to note that the connection model used in the study did not take cumulative plastic rotation demands into account. However, study (c) showed that larger near-field ground motions such as the Tabas, Iran, and Landers (Lucerne) records could cause collapse with no prior damage.

Study (d) provided the most interesting insight into how connection behavior affects system behavior. The connection plastic rotation capacities of the brittle and "3%" connections were selected in Monte Carlo fashion from probability distributions with the properties shown in Table 2-2 on page 22. Large near-field motions (1978 Tabas, Iran, and 1992 Landers (Lucerne)) were used for multiple simulations. These simulations were then compared with a deterministic analysis of the ductile case. Collapse occurred for the brittle connection cases for both records and for the “3%” connection cases for the Landers record. The ductile case did not suffer collapse. The key result of these analyses was that connection plastic rotation capacity governs the susceptibility to collapse for these large ground motions.

The first case study (Bonowitz and Maison, 1998) was presented in the context of the development of a probabilistic approach to modeling the occurrence of connection fracture. This study used the SAC Los Angeles nine-story building to compare the probabilistic approach of randomly assigning connection rotation capacities prior to fracture to a more conventional deterministic analysis with pre-set capacities. The computer program PC-ANSR (Maison, 1992) was used to perform nonlinear dynamic analyses. The results showed that the probabilistic approach was preferable for pre-Northridge WSMFs. The model was subsequently refined to provide better agreement with post-Northridge field observations and test data, and further description of the model is contained in the discussion of the second Maison and Bonowitz study below.

Maison and Bonowitz further developed their case study of the SAC Los Angeles nine-story building (Maison and Bonowitz, 1999), which is representative of existing mid-rise WSMF construction in the Los Angeles area. The study was done in a probabilistic manner, with the rotation capacities of fracturing connection elements assigned randomly from an empirical probability distribution. The top and bottom flange rotation capacities were chosen from normal probability distributions with values shown in Table 2-2. Interestingly, the model allows a very long finite time of one second for the fracture to occur and the capacity of the connection to drop off, though in reality fractures occur much more quickly than this. The effects of interior gravity frames and P-Δ were included in the model with a tree column assemblage and a P-Δ column, respectively. The ground motion excitations used were the SAC Los Angeles 10/50 and 2/50 suites of motions (Somerville, 1997).

For the model with fracturing connections, damage tended to concentrate in the lower stories for both the 10/50 and the 2/50 suites of records. Variability between ground motions was determined to be greater than variability between fracture patterns. For the ductile model, damage tended to concentrate in the upper stories for the 10/50 suite and in the lower stories for the 2/50 suite. The findings also indicate that the global behavior was rather insensitive to the spatial distribution of fracture occurrence. Maison and Bonowitz concluded that even a substantial level of fracture damage still results in a building with a “safe” response. However, the results show that there is only 50% confidence that the building will be life safe for such a safe response.

Table 2-2. Comparison of probability distributions of connection rotation capacities prior to fracture

Study	Top Flange		Bottom Flange	
	Mean (rad)	**Std. Dev (rad)**	**Mean (rad)**	**Std. Dev (rad)**
Maison and Bonowitz 1998	0.004	0.004	0.004	0.004
Maison and Kasai — “Brittle” Connections	0.008 W36 0.012 W33,W27	0.005	-0.003* W36 0.007 W33,W27	0.005
“3%” Connections	0.03	0.005	0.03	0.005
Maison and Bonowitz 1999	0.008	0.004	0.004	0.004
Luco and Cornell	0.015, 0.03, 0.045	?	0.015	?

* Allows fracture to occur often with no plastic rotation, at approximately 2/3 of beam yield moment

2.3.4 Probabilistically Based Parametric Studies

Luco and Cornell performed a large Monte Carlo simulation study into the effects of fracture on key system behavior parameters of steel moment frames. Part of this study is summarized in Luco and Cornell, 2000, with a more thorough treatment found in Luco and Cornell, 1999. Nonlinear dynamic analyses were performed on the SAC Phase II 3-, 9-, and 20-story buildings in both Los Angeles and Seattle, with both brittle and ductile connections. The brittle fracture model used was calibrated with experimental data and field observations, and was originally developed (Foutch and Shi, 1996) for a modified version of DRAIN-2DX. The spatial distribution of fracturing connections was set as a random variable, and the mean connection rotation capacity was varied in order to measure the effect of spatial distribution of fractures and of rotation capacity prior to fracture.

Comparisons were made between the model structures with different amounts of connection plastic rotation capacity, and between structures with bottom flange-only (BFO) fracture and those with both flanges (TBF) fracturing. Luco and Cornell found that the effects of connection fracture were dependent on the severity of ground motion, but did not address the particular features of the ground motions which caused some motions to be more severe than others.

Cornell and Luco found that fracture pattern (TBF vs. BFO) and plastic rotation had significant effects only for moderately severe ground motions. For the mild ground motions, neither fracture case had much effect on story drifts due to the low number of fractures. For the very severe motions (referred to as “rogue” by the authors), both fracture cases caused extreme story drifts (>10%) or collapse. In comparison, the ductile cases experienced relatively large story drifts with no collapses for these very severe motions.

For the moderately severe ground motions, TBF cases with small plastic rotation capacity showed substantially increased drift demands over the BFO cases. It was observed that if the interstory drifts in the ductile bilinear model reached 4% or 5%, then the fractures made the response worse, with the TBF case causing an adverse response more quickly. Both BFO and TBF cases with moderate to large plastic rotation capacities performed quite well, with less story drift than anticipated.

2.3.5 Analyses of Specific Fracture-Related Behaviors

Nakashima et al. performed an analytical study of static moment redistribution after the occurrence of fracture (Nakashima et al., 2000). For the case of a simple frame, the redistribution was obtained by performing a pushover analysis under displacement control, with the beam end moments explicitly calculated for the new state after each fracture using the three-moment equations. A simple portal model (with inflection points at column midheights assumed) of one story in a multistory frame was used to examine the redistribution within a story. Rigid-plastic hinges which lost all moment capacity after fracture (which occurred only after yielding), were used to represent the connections. Only beam bottom flange fracture was considered in this study.

Nakashima et al. determined that static moment redistribution, even for the simple models and loading used, involved a rather complicated sequence of loading, yielding, fracturing, and unloading as the system redistributed moments to obtain equilibrium. However, some notable patterns emerged, such as that fracture at one end of a beam causes unloading at the other end, and causes loading in the beam on the opposite side of the panel zone from the fracture. Sequential fractures triggered by redistribution were observed when all connections had small and/or similar plastic rotation capacity. Sufficient variation in plastic rotation capacity within a structure or large plastic rotation capacity prior to fracture made such triggered fractures unlikely, since there was a smaller chance that a connection would be on the verge of fracture, and the small additional moment from redistribution would push it over the edge. Since this study was performed statically, some behaviors may change for earthquake excitation.

Uetani and Tagawa examined the dynamic behavior of the beam and its associated connections after a fracture in one of the connections (Uetani and Tagawa, 2000). Two analytical models were used to predict this behavior — a finite element model with a large number of degrees of freedom, and a simplified analysis in which the element stiffness matrix for a fixed-fixed beam is replaced with the stiffness matrix for a fixed-pinned beam when a beam response quantity exceeds a critical value. The beam response quantities considered by Uetani and Tagawa are moment, rotation, and cumulative plastic rotation. This model does not include post-fracture residual strength, however, which can be significant if the fracture does not propagate into the web.

The finite element analysis showed that the fracture of the connection causes an oscillatory transient response which quickly decays to a steady state solution which is predicted by the simple model. Therefore, if the oscillations are not of interest, a simple model can accurately represent the connection hysteretic behavior. Both models show that beam-end rotation decreases sharply with fracture, while nodal rotation increases sharply, but the magnitude of the jump in nodal rotation is about one third that of the jump in beam-end rotation. The magnitude of the total change in rotation (change in connection rotation plus change in beam rotation) appears to be twice the pre-fracture rotation, but why this is the case is not apparent.

Uetani and Tagawa then used the simplified connection model in nonlinear dynamic analyses of a nine-story “fish-bone” frame subassemblage (meaning one column for the full height, with half-length beams on each side at each story). The frame, with fractures possible in the bottom flanges of the beams only, was subjected to the 1995 JMA Kobe, 1940 El Centro, and 1968 Hachinohe ground motions. The fracture criterion was varied, as was the amplitude of the ground motions, which were scaled to peak ground velocities of 80 cm/sec (~30 in./sec) and 120 cm/sec (~45 in./sec). Numerous fractures were observed, and interstory drift ratios of up to 6% occurred for the motions with velocity scaled to 120 cm/sec.

Overall, there was a great deal of variability in the story drifts, but some trends could be discerned. For instance, the frames with the lowest values of the fracture criterion tended to have higher drifts, but this was not always the case and this trend did not extend to the second- and third-lowest value of the fracture criterion. As expected, the 120 cm/sec motions caused more severe drifts than the 80 cm/sec motions. The concentration of drift in certain stories did not follow any particular trend except that drifts concentrated in either the second through fifth stories (more likely) or the fifth through eighth stories. Damage concentration seemed to be sensitive to both ground motion characteristics and fracture model. Uetani and Tagawa's results are similar to the apparently random damage distribution seen in other analytical studies in Sections 2.3.1–2.3.4 and observed after Northridge.

2.3.6 Evaluations of Analytical Modeling Techniques

Studies discussed in this category have the major objective of comparing and contrasting techniques used to model and analyze steel moment-frame structures with degrading hysteretic behavior. As a necessity, most of these studies also include discussions of how various analysis and modeling techniques fare for ductile connection behavior, so only one study concerned only with ductile behavior is discussed here. A simple tabular comparison of the major techniques and parameters employed by each study in question is presented in Table 2-3.

Table 2-3. Comparison of analytical and modeling techniques

Study	Analysis Types	Software used	Model Parameters				
			Hysteretic Models	Model Types	Panel Zones	P-Δ	Gravity Frames
Foutch and Yun, 2002	NS, ND, IDA	DRAIN-2DX	Trilinear w/strength degrad., Foutch and Shi BF, simple connection	Centerline, clear span w/panel zones, 2D	Linear and non-linear (scissors models)	Yes	Yes, w/ simple connections
Gupta and Krawinkler, 1999, 2000	NS, ND	DRAIN-2DX	DB, simple connection	Centerline, clear span w/panel zones, 2D	Nonlinear parallelogram model	Yes, elastic column	Yes, equivalent bay

Table 2-3. — *Continued*

Study	Analysis Types	Software used	Model Parameters				
			Hysteretic Models	Model Types	Panel Zones	P-Δ	Gravity Frames
Naeim et al., 1999	EL [UBC 97, FEMA 273], LD, NS, ND	DRAIN-3DX?	DB, Elastic	3D	Rigid and flexible	?	No, after evaluation
Phase 1 Studies, SAC, 1995	LD [RS, TH], NS, ND	ANSR-1, DRAIN-2DX, ETABS, FEAP-STRUC, IDARC, NODYN, SAP-90	Lumped and distributed plasticity DB, already-fractured BF	Centerline, clear span w/panel zones, 2D, 3D (elastic only)	Rigid and flexible, various models	Yes	Yes, w/various methods

Analysis type abbreviations: LS: linear static, LD: linear dynamic [RS: response spectrum, TH: time history], EL: equivalent linear code procedure, NS: nonlinear static, ND: nonlinear dynamic, IDA: incremental dynamic analysis

The studies summarized above are in general agreement about the types of modeling assumptions which should be made and the parameters which should be included in a reasonably accurate model. These include:

- use of clear span dimensions
- panel zone behavior, particularly if the structure being modeled has weak panel zones
- P-Δ effects
- fracturing connection hysteretic models if pre-Northridge connections exist
- inclusion of strength and stiffness contributions from gravity framing, particularly in cases where the limit state is collapse prevention

The SAC Phase I studies also recommend that other parameters should be included, such as the amount of strain hardening and composite beam action.

Overall, the analytical methods and modeling techniques studied were unable to predict fracture damage in specific locations, but the topic of specific damage prediction is outside the scope of this study. Nonlinear analysis methods were able to indicate the general locations of damage and predict global behavior moderately well, however, and this what is primarily of interest in this investigation. Nonlinear static “pushover” analyses were shown to be valuable for the prediction of P-Δ effects (Gupta and Krawinkler, 2000), but have serious limitations for taller structures where higher modes contribute significantly to the damage levels in the upper stories (SAC, 1995). Nonlinear dynamic analysis was seen by all of the studies in which it was evaluated to be the most reliable and accurate method when combined with an accurate model and appropriate ground motions.

2.3.7 Analyses of Variation in Nonlinear Behavior with Period

Newmark and colleagues, most notably Hall, studied response spectra and how the effects of material nonlinearity on structural behavior change as the period of the structure changes (Newmark and Hall, 1982). Though Newmark and Hall only considered ductile single-degree-of-freedom oscillators, the observations made on how the yield strength of these simple structures affects the dynamic response have implications for degrading systems as well. They observed that for some periods, the yield strength of the oscillators had large effects on the displacement, while for others the response did not seem to depend on strength at all.

Based on these observations, they developed a simple and elegant system for classifying the effects of strength on the response. Newmark and Hall had earlier postulated that elastic response spectra have a characteristic shape, and such spectra can be divided into several regions defined by constant acceleration, constant velocity, and constant displacement, as well as a transition region for very short periods. To convert these elastic spectra into inelastic spectra, they were divided into three period ranges that were based on the effects of strength on the response. These ranges were termed “short period,” “energy preserved,” and “displacement preserved,” and are shown in relation to the elastic regions for pseudo-acceleration spectra in Figure 2-3.

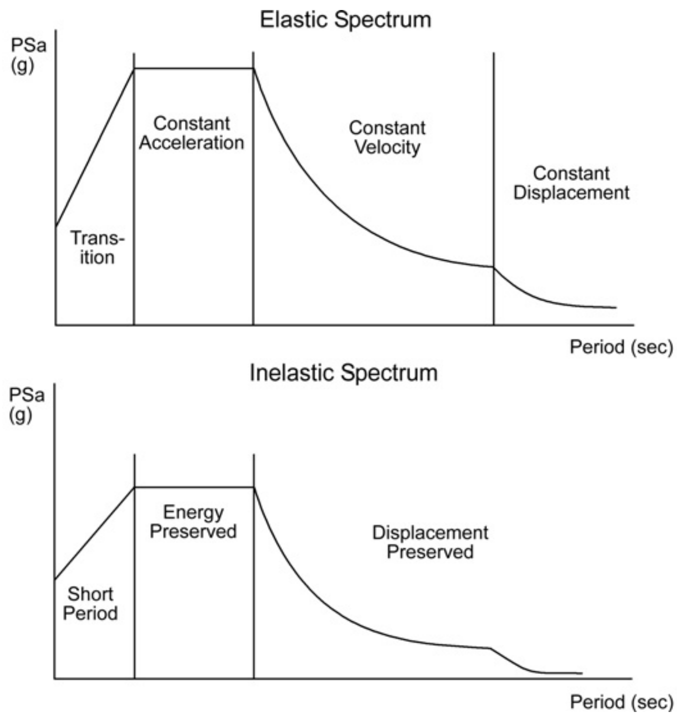

Figure 2-3. Newmark and Hall's response spectrum period ranges

In the short-period range, maximum displacements drastically increase as the structure becomes weaker. In the energy-preserved range, maximum displacements increase as strength decreases, but the amount of increase is limited to that which produces equal areas under the elastic and inelastic force-displacement curves. In the displacement-preserved range, the maximum displacements do not increase no matter how weak the structure becomes. The development of these spectral regions was intended provide a simple method of constructing spectra for design, but these regions are also useful in describing and interpreting behavior, and will be used in this capacity in this study.

2.3.8 Synthesis of Study Results

Considering the results of the studies of systems with fracturing connections, it appears that fractures can cause adverse system behavior, such as extreme drifts and collapse, in certain situations where a combination of small (or nonexistent) plastic rotation capacity and large ground motion occurs. In other cases, the effects of fracture seem to be relatively benign, though moderate drifts and some permanent offset can occur. The studies performed to date do not generally explore the reasons for these differences in system behavior beyond consideration of ground motion amplitude measures. Behavioral dependence on the spatial arrangement or number of fractures was explored by some investigators (Luco and Cornell, 1999), who found that fractures in the bottom flange only seem to have less effect than fractures in the top and bottom flanges for moderate ground motions.

Fewer analytical studies have been focused on more ductile forms of connection hysteretic degradation, such as deformation softening, ductile fracture, and strength degradation. In particular, the negative post-yield stiffness due to deformation softening has received relatively little attention in the analytical studies of degrading hysteretic behavior. Since the presence of negative post-yield stiffness has the potential to cause global instability, this particular type of hysteretic behavior deserves further study. Studies (such as Mahin and Morishita, 1998, and Rahnama and Krawinkler, 1993) indicate that negative post-yield stiffness can adversely impact system behavior.

In the few studies available, strength degradation was found to have small to moderate effects on behavior unless the degradation was severe. From Newmark and Hall's findings (Newmark and Hall, 1982), the effects of strength degradation should vary with structure period, though this topic has not been examined directly.

Investigators have only recently started to look into the possibility that ductile connections can exhibit types of degradation other than brittle fracture which may have serious ramifications for system behavior. More work is certainly needed in this area.

2.4 RECENT EXPERIMENTAL STUDIES OF CONNECTION HYSTERETIC BEHAVIOR

Following the Northridge earthquake in the U.S. and the Hyogo-ken Nambu earthquake in Japan, several series of beam-column connection tests were performed both to determine what caused the connection fractures and how to improve connection performance. Most of these tests were quasi-static, cyclic tests of full size bare-frame exterior connections. These tests provided a great deal of insight into the hysteretic behavior of connections with various geometries and details. During the course of these tests, researchers observed several other types of hysteretic degradation besides brittle fracture. These types of behavior included strength degradation, various types of stiffness degradation including negative post-yield stiffness, pinching, and ductile fracture.

The first tests of beam-column connections after Northridge were performed by Engelhardt and Sabol, who tested a limited series of 16 full-size specimens in the months following the earthquake (Engelhardt and Sabol, 1994). These were essentially emergency tests sponsored by AISC to help determine the reasons for the observed fractures and to determine the effectiveness of improved welding and certain connection reinforcements. Both pre-Northridge connections with improved welds and reinforced connections were tested. These tests produced two important results: (a) improved welding practice (i.e., workmanship and detailing) alone did not ensure good connection performance and (b) connection reinforcement was more effective at improving performance. Overall, perhaps the most important accomplishment of this series of tests was providing the first data that supported the effort to develop new connection geometries and refuted the idea that improved welding alone was a reliable way to prevent brittle fractures.

The many questions which persisted after the AISC tests were for the most part answered by the much larger number of connection tests conducted by the SAC Joint Venture and others. These results are summarized in FEMA-355D (FEMA, 2000), and the reader is referred to this document for detailed results, since only a very brief summary will be presented here.

On the question of whether pre-Northridge connections could be “fixed” by improved welding practice and materials, the answer was no. Several series of tests by Goel (Lee et al., 2000), Ricles (Ricles, et al., 2002), and others, plus finite element analyses, demonstrated that the complicated state of stress in the connection made it prone to fracture even with improvements to the weld details, notch-tough weld metal, and stringent quality control. These findings necessitated a massive shift in the types of connections used in practice, and ensured that the post-Northridge connections, which generally performed much better in the SAC tests, would now be utilized instead.

In both series of SAC tests, new post-Northridge connection details were able to provide much more ductile behavior. However, this ductile hysteretic behavior was generally not ideal, as strength and stiffness degradation and deformation softening (negative post-yield stiffness) were observed. Ductile fractures were also observed after significant inelastic behavior had taken place. The hysteretic behaviors which were predicted to have the most severe system behavior ramifications were negative post-yield stiffness, strength degradation and ductile fracture. One of the goals of this research is to determine the effects of these types of hysteretic degradation present in post-Northridge connections on the system behavior, and to evaluate these effects versus the effects of fractures in pre-Northridge connections.

In Japan, Nakashima performed a series of tests under the direction of AIJ's comprehensive testing program (AIJ, 1997). This series included some dynamic tests as well as quasi-static tests, and each dynamic test had a quasi-static counterpart for comparison purposes. One of the major results of this series was that dynamic loading did not appear to decrease the ductility or plastic rotation capacity of any of the specimens studied. Similar results were obtained by Uang et al., who tested much more brittle connections for the SAC Joint Venture (FEMA, 2000).

Upon closer inspection, however, it would be presumptuous to say that dynamic loading has negligible effect in all situations. Analyses and coupon tests performed by the SAC project indicated that strain rates expected due to earthquake loading were not high enough to affect the response of either very brittle weldments, which would fracture at very low strains anyway, or very ductile weldments, which have enough reserve toughness to overcome effects of expected strain rate. However, weldments of intermediate ductility could certainly be affected negatively by dynamic loading.

In the case of Nakashima's tests, it seems that the more brittle nature of the steel under higher strain rates may have been offset by the increase in temperature due to yielding in the numerous smaller cycles in the loading history preceding the large cycles. Since steel is less brittle at higher temperatures, the heat generated by yielding could act in a protective manner and reduce the chance of fracture. However, it is important to note that a real near-field ground motion could impose a high strain rate without many (or any) smaller cycles to "warm up" the steel by small amounts of yielding. Therefore, if weldments of intermediate ductility could survive an initial high strain rate, yielding might protect them from subsequent fracture.

2.5 EXPERIMENTAL STUDIES OF STRUCTURES WITH DEGRADING CONNECTION HYSTERETIC BEHAVIOR

Although many tests of beam-column connections have been performed, as summarized in the previous section, very few system-level tests of the behavior of steel moment frames have been performed. Thus, the experimental data needed to confirm the results of the analytical studies discussed in Section 2.3.6 are sorely lacking.

A few small-scale tests of steel frames with yielding panel zones were conducted in Japan by Hasegawa (Hasegawa, 2000), where small-scale wide flange and tube sections were used to represent structural members in frames loaded through collapse. Hasegawa's frames had standard connections without replaceable parts, so each frame could only be tested once, and only a few tests could be performed. Unfortunately, the paper documenting the results of the tests is published in Japanese, with only the abstract available in English.

Tests on steel moment-frame buildings with ductile connections have been performed by several investigators (Lee and Lu, 1989, Molina et al., 1999). Lee and Lu's tests were conducted prior to Northridge, and the investigators were probably not looking for deteriorating connection hysteretic behavior. Lee and Lu performed one quasi-static test on a 0.3-scale model of a six-story building frame. This model frame had moment frames in two dimensions, forming a space frame. The purpose of this test was to provide a comparison with two other tests: one of a concentrically braced frame (CBF)/moment-frame dual system and one of an eccentrically braced frame (EBF)/ moment-frame dual system. The moment-frame connections behaved in a ductile manner, and showed significant plastic deformation of the panel zones, which were quite weak. The hysteretic loops for the panel zone remained stable, though some degradation of initial stiffness was observed. No hysteretic plots for the full beam-column connection were available, unfortunately. The maximum roof drift was only 2%, due to limitations of the test setup, and maximum interstory drift was 2.5%. Interestingly, the moment frame proved to be more ductile than the CBF and EBF dual systems, both of which suffered fracture to either the braces (CBF) or shear link (EBF) after significant plastic deformation.

Molina used the pseudodynamic testing method to perform a full-scale test of a three-story steel moment-frame building with a composite concrete slab. The test specimen was designed in conformance to the European EC8 regulations, and the beam-column connections were of the post-

Northridge end-plate detail. No fractures were observed during the 2% drift quasi-static tests performed in both lateral directions as well as diagonally, or the pseudodynamic test. However, many bottom flange fractures were observed during a large amplitude (~ 5% interstory drift) quasi-static cycle performed after the seismic pseudodynamic test. The emphasis of the paper documenting this test seems to focus on the pseudodynamic testing method employed rather than the behavior of the moment-frame system.

Thus, no fully dynamic tests have been performed on steel moment-frame systems with fracturing or degrading connections. The ductile moment-frame tests that have been performed used specimens that were specifically designed to avoid connection fractures and other forms of deterioration, and may not have been designed in accordance with modern codes. Additionally, these specimens generally used smaller members which are less susceptible to fracture and had welds which were made in the shop. Connection hysteretic behavior and its effect on seismic response has not yet been considered explicitly in a dynamic test. Consequently, there is a great need for more experimental work in this area.

3 Test Specimen Design

To examine experimentally the effect of local connection behavior on system response, a simple reduced scale model of a moment-resisting steel frame will be tested on the earthquake simulator, or shaking table. This chapter initially describes the development of simplified mechanical connections intended to mimic certain generic forms of hysteretic behavior that might occur in real buildings. The design of a frame specimen incorporating these connections is subsequently described.

For the purposes of these tests it is not necessary to use connections that physically resemble those employed in real structures. Rather, efforts are directed herein at devising potential plastic hinge regions that exhibit predictable and repeatable flexural behavior. In particular, these efforts focus on developing mechanical connections that mimic stable ductile flexural behavior, fracture-critical behavior with either brittle or ductile crack initiation, kinematic softening behavior, and isotropic softening behavior.

Although realistic-appearing potential plastic hinge regions of various kinds could have been used, it was decided instead to use idealized mechanical connections located where inelastic behavior was expected to occur in the frame. Reasons for this decision include:

- Numerous tests involving different excitations and various distributions of connections with different hysteretic characteristics were desired for the testing program. Use of mechanical connections with readily replaceable components facilitates testing of many different specimens provided the specimen remains elastic outside of the potential plastic hinge regions.
- Connection hysteretic behavior does not depend on the numerous material, configuration, and other variables that influence the behavior of actual connection regions. As such, tests are expected to be representative of a general type of hysteretic behavior rather than of a specific connection detail.
- Simplified mechanical connections can be devised to reproduce the desired properties at a reduced scale. Phenomena such as fracture and local and lateral buckling do not lend themselves to reduced scale models, imposing undesirable limitations on the test program.
- Costs associated with reusable connections and with replaceable components can be reduced compared to more realistic models, regardless of scale.

Ultimately, a representative steel moment-resisting frame is needed to assess the effect of local hysteretic behavior on the global response. Thus, a multistory frame with one or more bays is desired. This geometry will allow assessment of the effects of local deterioration or fracture on the response of adjacent elements as well as on the structural system as a whole.

The first task addressed in this chapter is the development of simple, mechanical connections that provide predictable and repeatable behavior. Two options for this are presented in Sections 3.1 and 3.2. These sections summarize the work of van Dam and Mahin, and further details of the connection development process can be found in (van Dam, 2000). The design of a moment-resisting frame suitable for testing which incorporates the simple, mechanical connections of Section 3.2 is then described in Section 3.3.

3.1 BEAM-BASED CONNECTIONS

The initial attempt to devise a mechanical connection began with the idea of using flat bar-type coupons to replace the beam flanges. These flat bar coupons could then be notched to initiate fracture. By basing the notch sizes and geometry on work done in Japan on fracture initiation (Kuwamura and Yamamoto, 1997), uniaxial tensile tests of coupons with various notch configurations and sizes were performed. The results of these tests led to the selection of the notch geometry that was then used for the coupons in the first series of connection tests.

At this point, the proposed connection was fabricated from a specially designed small beam section (S4x7.7), as shown in Figure 3-1. Two options were considered for shear transfer in the web. In the first, the beam was cut all the way through at the desired potential plastic hinge location. A bolted shear tab connected the webs, allowing rotation. The second approach involved only cutting the flanges, and allowing the beam web itself to transfer shear. Rounded holes in the web at the end of the flange cut were used to prevent the initiation of fracture in the web. These two approaches are subsequently referred to as separated-web and notched-web, respectively.

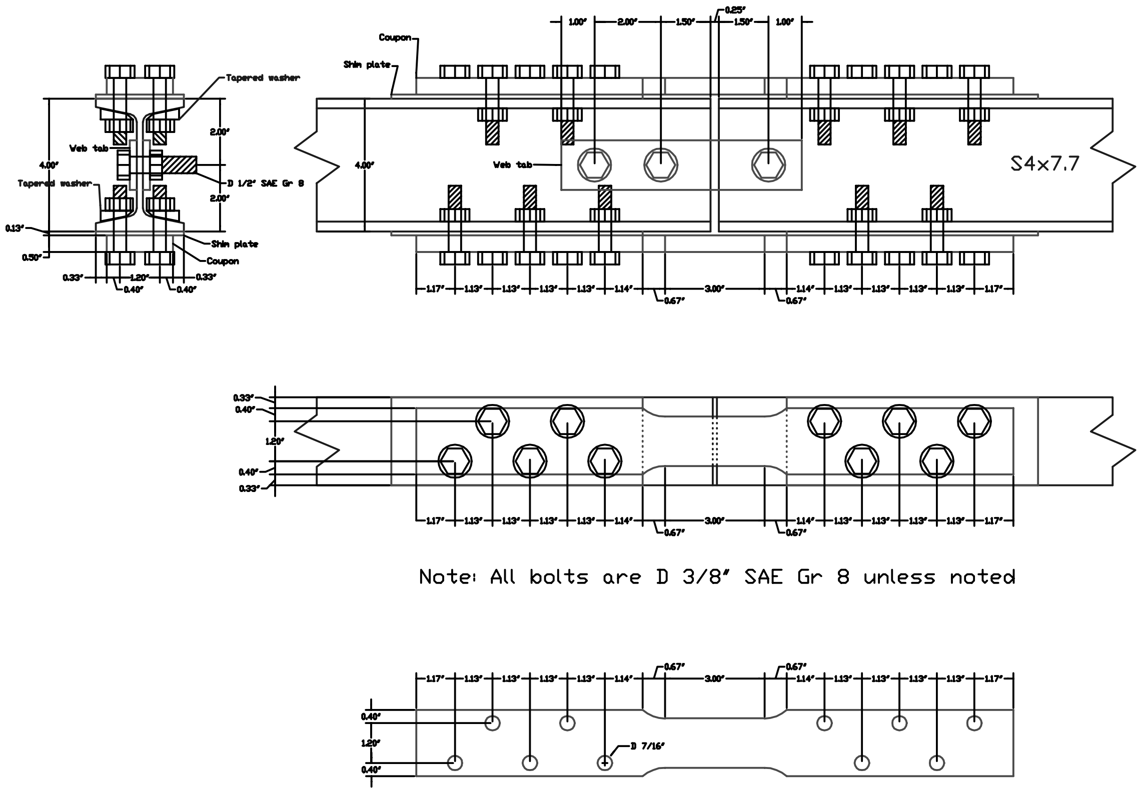

Figure 3-1. Beam-based connection and flat bar coupons

Both the notched-web and separated-web beam specimens had notched flat bar coupon "flanges" attached to the beam flanges (spanning the flange cuts) to provide moment resistance. The beam-based connection specimens were then tested statically in third-point bending, with the mechanical connection in the center constant-moment region. The behavior of the specimens was not as expected and fracture was not obtained. The state of stress in the flat bar coupons was not pure tension as in the uniaxial tension tests on which the notch selection was based, but instead mostly local bending. Fracture was not obtained, since the notches were oriented perpendicular to the direction needed for crack initiation. It was also determined that there was a high likelihood that portions of the beam and connection, in addition to the coupons, would suffer damage during testing. This would necessitate replacement of the whole beam between tests, increasing the time and cost and thus reducing the number of tests that could be performed.

3.2 CLEVIS-BASED CONNECTION

After the failure of the beam-based connections to achieve fracture, the decision was made to use a mechanical clevis as the base unit for the connections, and to use round bar coupons instead of flat ones. Using the clevis as the base unit turned out to be a much better idea, as the resulting connection satisfied all the design criteria and performed as intended during behavior verification tests.

3.2.1 Connection Design

The mechanical clevis functions as a base module that can accommodate different types and configurations of coupons. Coupon characteristics are chosen to mimic different types of beam-column connection behavior. In the clevis assembly, the coupons represent the "flanges" of the beam and their connection to the column, providing the moment-resisting mechanism. The coupons are inserted into holes in the end plates which are located above and below the clevis pin. The clevis pin represents the shear and axial load transfer mechanism provided by the web. Actual connections may also have webs that fracture or deteriorate. However, practicality and safety issues weighed against using web connections that could fail during tests. The clevis connection, which is shown in Figure 3-2, provided an economical and practical solution.

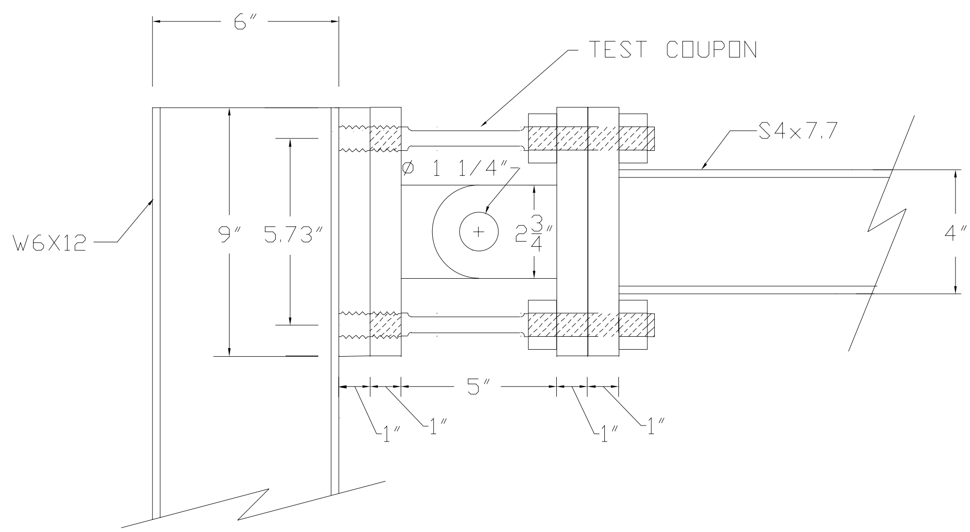

Figure 3-2. Clevis connection at column face

One side of the clevis was attached to the column and the other to the beam. As shown in Figure 3-2, the holes for the coupons in the clevis base plate are threaded on the column side, and unthreaded on the beam side. The coupons are secured on the beam side by nuts and washers, and several nut configurations are possible. By removing the nuts on the inside or the outside, the coupons can resist only tension or compression, respectively. The option to remove nuts allows for more variety in hysteretic shape than variations in coupon behavior would alone. Hysteretic loops with severe pinching on one or both sides can be obtained in this fashion.

3.2.2 Coupon Design

All coupons were made from round ¾″ ASTM A193 Gr. B7 steel all-thread bars. This steel was selected for its high yield strength and because it is less ductile than lower-strength steels, and therefore it fractures more readily. This steel proved to be quite ductile when unnotched, though, and thus was appropriate for use in the types of coupons that obtained their desired behavior through repeated cycles of buckling, as well as for coupons where stable, ductile behavior was required. The high yield strength was necessary because of the need to provide a "flange" force that was equivalent to the force in the real beam flange while maintaining a small cross section to facilitate buckling.

A smooth cross section was achieved by machining the center portion of the coupons down to the appropriate diameter. Obtaining strength and stiffness degradation with the round coupons was conceptually straightforward, since the buckling resistance of the coupons could be controlled quite easily using the slenderness ratio of the necked-down machined section.

One of the primary benefits of the round coupons over the flat coupons involved the ability to obtain fracture by using notches. A circumferential notch around a circular cross section provides significant triaxial constraint at the notch tip. The triaxial constraint helps by significantly delaying yielding, which makes obtaining a sufficiently brittle fracture (in connection moment-rotation terms) easier (Kuwamura and Yamamoto, 1997). Fracture in the elastic range or at the onset of yielding (brittle fracture) was still difficult to achieve, however, and required the testing of several different notch geometries before finding something that worked. Obtaining fracture after yielding (ductile fracture) was much easier, since the notch geometries that didn't provide brittle fracture provided ductile fracture instead.

Two different notch geometries, which are shown in Figure 3-3 and Figure 3-4, were used to obtain fracture before and after yielding. In both cases, the material at the tip of the notch yielded prior to fracture, but the degree of yielding was limited by the triaxial constraint and stress concentration caused by the notching. For the purposes of the experiments described in this report, brittle fracture is defined in the global sense — that is, the global stress-strain behavior of the coupon is essentially linear elastic up to the initiation of fracture (despite the very localized yielding that appears at the tip of the notch). Likewise, ductile fracture is defined as fracture occurring after the stress-strain behavior of the coupon has reached the yield plateau.

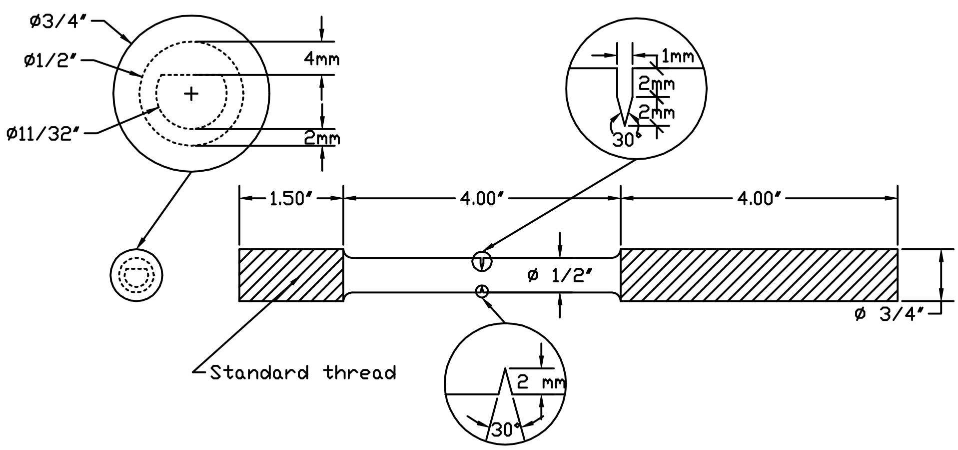

Figure 3-3. Notch geometry used to obtain brittle fracture

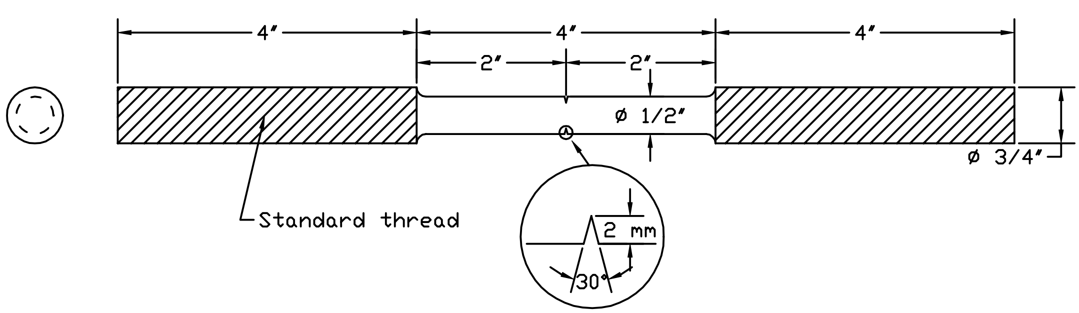

Figure 3-4. Notch geometry used to obtain ductile fracture

In order to obtain ductile baseline behavior, which is essentially bilinear, it was necessary to restrain the natural tendency of the necked-down section to buckle due to the reduction in the effective modulus of elasticity as the steel yields in compression. Buckling would inevitably lead to significant strength and stiffness degradation, both of which prevent the achievement of stable, ductile hysteretic behavior.

During the course of testing coupons with small slenderness ratios, it was determined that the desired behavior could not be achieved by reducing the slenderness ratio alone. Thus, the coupons were fitted with steel jackets to physically restrain buckling. These jackets were made from a steel pipe with a 7/8 inch inside diameter and a 1/8 inch wall thickness. Sections of the pipe long enough to cover the necked-down section of the coupon were cut in half lengthwise and then reconnected around the coupon using hose clamps. Since the coupon had limited space in which to buckle, this jacket limited cyclic deterioration due to buckling until very large deformations were imposed. Six types of coupons were used in the clevis connection test series, as shown in Figure 3-5.

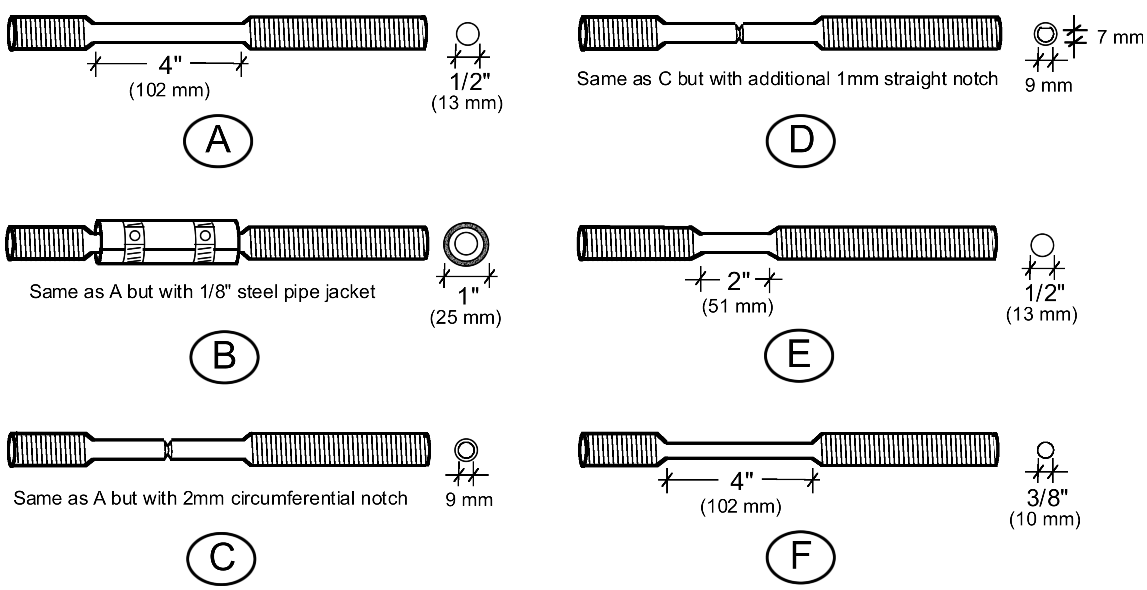

Figure 3-5. Round coupon types used in the second experimental series

3.2.3 Development of Connection Types

By selecting different types and numbers of coupons, as well as the nut configuration, a variety of hysteretic characteristics can be obtained. The coupons were arranged to create five different connection types, each corresponding to one of the five hysteretic behavior types defined in Section 1.1. Connection type and hysteretic behavior type are used interchangeably hereafter due to this one-to-one correspondence. Coupon composition, using the letter designations of Figure 3-5, and nut configuration are shown in Table 3-1 for each of the five connection types.

Table 3-1. Coupon composition and nut placement for connection behavior types

Connection Type	Top			Bottom		
	No. of Coupons	Coupon Type	Nuts placed on	No. of Coupons	Coupon Type	Nuts placed on
Ductile Baseline (DB)	1	B	2 sides	1	B	2 sides
Brittle Fracture (BF)	1	A	2 sides	1	D	2 sides
Ductile Fracture (DF)	1	A	2 sides	1	C	2 sides
Deformation Softening (DFS)	2	F	Inside	2	F	Inside
Strength Degradation (SD)	1	E	2 sides	1	E	2 sides

The coupons are interchangeable and replaceable, so one clevis assembly can be used to form any of the five connection types. In addition, since only the coupons are damaged during testing, the clevis base can be used as many times as necessary. The rest of the test specimen was designed to remain undamaged during testing as well. These design features make it possible to test a single frame specimen numerous times to assess experimentally the effects of various connection and ground motion characteristics.

3.2.4 Testing and Verification of Behavior

Tests of the connections indicated that the properties of the connections were quite consistent and reproducible (van Dam, 2000). These quasi-static, cyclic tests were performed on a test specimen consisting of a clevis connection and stub beam assemblage connected to a reaction frame, as shown in Figure 3-6.

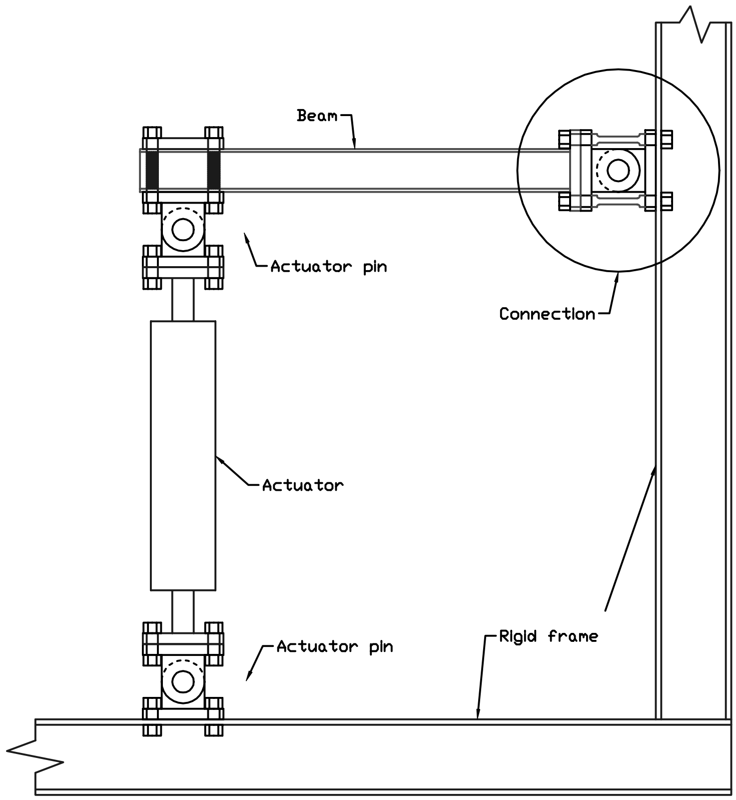

Figure 3-6. Test setup for clevis connection tests

The tests were conducted under displacement control, and two different loading histories were used, the first of which is shown in Figure 3-7 and is similar to the SAC multiple step loading protocol (Krawinkler et al. 2000). The second history was simply a large displacement (5 inches) cycle preceded by a few very small elastic cycles, which was meant to represent the effects of a near-field ground motion pulse. Following this initial cycle were several large cycles used to study post-fracture behavior. Moment-rotation results for the first loading history are shown in Figure 3-8 for all five connection behavior types. The moment-rotation relation for the second loading history is also shown for the ductile fracture (DF) type only.

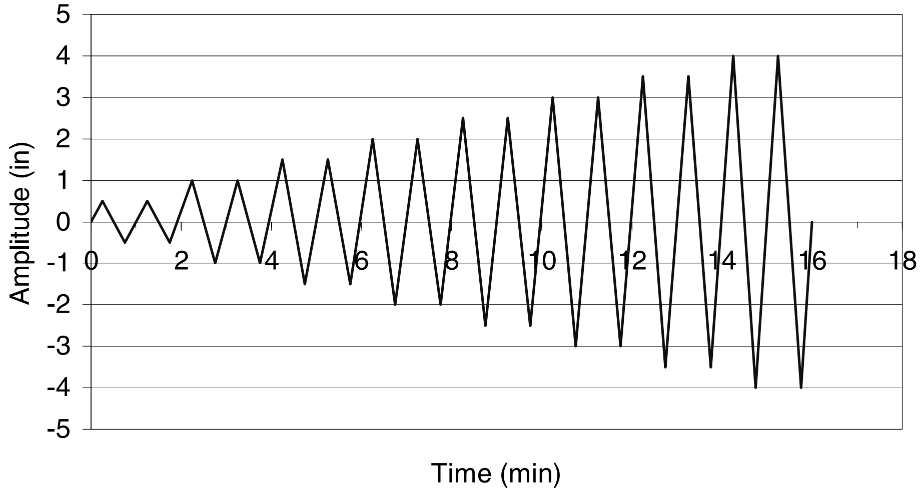

Figure 3-7. Displacement histories for clevis connection tests

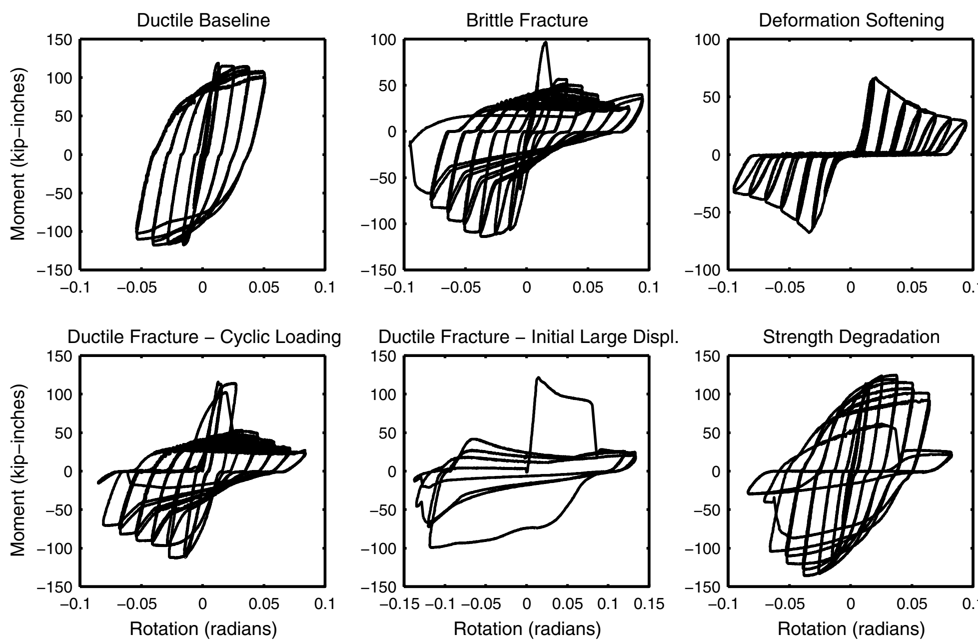

Figure 3-8. Typical moment-rotation results for various connection behaviors

3.3 FRAME DESIGN

In order to determine the effects of connection hysteretic behavior on the global behavior of steel moment-frame systems subjected to earthquake loading, the clevis-based mechanical connections developed in Section 3.2 were placed in a simple model frame which would then be tested dynamically on the shaking table.

The test frame was intended to be representative of part of the structural system of a low-rise building with large plan area. The design requirements for the frame model are shown below. The model frame specimen must

- be suitably sized and designed for unidirectional testing on UC Berkeley shaking table;
- be simple enough promote understanding of behaviors such as dynamic moment redistribution and fracture-related phenomena;
- remain elastic during testing, except at the connections;
- have a fundamental vibration period consistent when scaled with a full-sized two- or three-story prototype;
- be able to achieve large deformations (up to ~15% interstory drift) to allow study of behavior near collapse;
- minimize higher-mode contributions to facilitate the identification of potential high-frequency fracture-induced vibration phenomena;
- be economical to fabricate and erect; and
- be equipped with internal safety bracing and a catch system.

A two-story, two-bay moment frame was initially selected mainly because of the need for simplicity in order to understand the relationship between connection and system behavior. The pilot analytical study discussed in Section 3.3.2 indicated that little benefit would result from the second bay, and thus a single-bay system was selected for the tests. A period of 0.8 to 1.0 seconds was assumed representative of the prototype building height.

Due to the use of a clevis-based mechanical connection in each of the four beam-column joints, many different patterns of connection behavior were possible. For instance, all of the connections in the frame could fracture, or only those in one story could fracture, while those in the other story remained ductile.

3.3.1 Modeling and Similitude

The frame was designed to be tested dynamically using the shaking table at UC Berkeley's Richmond Field Station. This shaking table is 20 feet by 20 feet in plan, and has the properties listed in Table 4-1. A scale model which was representative of part of a building's moment-frame system was needed, and scale factors of two and three were initially considered. Three was eventually chosen as the scale factor so that a two-bay model, which was being considered at the time, could fit on the shaking table. Since unidirectional excitations were to be considered, the model chosen was two dimensional.

It is important to note that the prototype structure used in this experimental study is not a specific, real building. Instead, it is a generalized prototype representing this type of low-rise (2–4 story) construction, which is used in order to give more broadly applicable results. Due to this generalization, the only prototype properties of interest are the fundamental vibration period, the material, seismic weight, and the bay dimensions (span length and column height). A fundamental period of approximately one second was assumed. Story height was assumed to be half of the bay width.

The similitude relationship between the model and prototype for the shaking table tests is kept simple due to the difficulty in scaling many of the desired effects. An artificial mass simulation is used, and the pertinent scale factors are shown in Table 3-2. The scale factors S_x are defined as prototype quantity divided by model quantity. The prototype building's fundamental vibration period is about one second, so the corresponding model period is approximately 0.6 seconds. The material, ASTM A572 Grade 50 structural steel, is the same for both model and prototype. As seen in Table 3-2, this form of similitude preserves acceleration, stress, and strain in the model and prototype.

Table 3-2. Similitude relations and scale factors used

Quantity	Scale Factor	Value
Length	S_L	3
Time	$S_T = \sqrt{S_L}$	$\sqrt{3}$
Fundamental Vibration Period	$S_P = \sqrt{S_L}$	$\sqrt{3}$
Elastic Modulus	S_E	1
Acceleration	S_A	1
Mass	$S_M = S_L^2$	9
Strain	S_ε	1
Stress	S_σ	1
Force	$S_F = S_L^2$	9

3.3.2 Pilot Analytical Studies

A pilot study was performed using the OpenSEES analysis framework (McKenna, 2003). The main objectives of this study were to determine whether the test specimen should have one bay or two bays, to determine the necessary beam and column stiffnesses and strengths and assess instrumentation needs. Additional preliminary studies were performed as part of the experiment design and are discussed in Chapter 4.

The analytical models used were two simple two-dimensional (2D) planar frames with pinned supports, with one and two bays, respectively, which are shown in Figure 3-9. The beams and columns were modeled with nonlinear beam-column elements, though as soon as it was determined that stress levels were quite low, elastic materials were used to reduce the computation effort. The ductile baseline connections were modeled using zero-length rotational spring elements with simple bilinear moment-rotation relationships. The fracturing connections were modeled using a linear spring with a predetermined “vanishing value” which was placed in series with a bilinear spring. When the rotation reached the vanishing value, the linear spring would be deactivated, leaving only the bilinear spring. Though this was a crude model, it captured the drop in moment capacity due to fracture quite well and was computationally stable (i.e., there were few convergence problems).

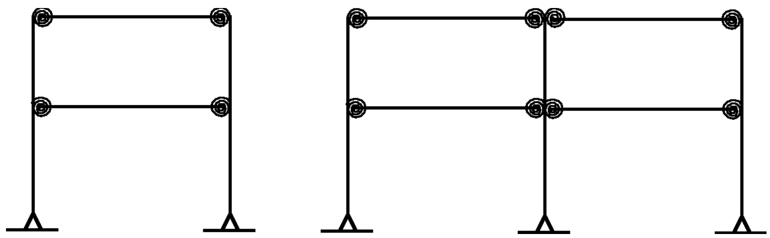

Figure 3-9. One- and two-bay analytical models used in preliminary study

The models were subjected to simple sine and cosine pulses of varying duration, and to numerous near-field and far-field earthquake ground motions. The sine and cosine pulses were used to study the effects of deterioration during simple ground motions and as idealizations of the pulse-like waveforms present in near-field ground motions.

The results of the study showed that fracture of one connection caused sudden changes in the moment and rotation time histories of connections in other parts of the frame. This effect was most pronounced at the other end of the beam with the fracturing connection, while it was small in the adjacent story and very small across the column in the adjacent bay. It should be noted here that differences in loading, model geometry, and connection behavior invalidate comparisons with Nakashima's study on static moment redistribution (Nakashima et al., 2000). Varying the column stiffness did not change the local effects of fracture across the column or in the adjacent story. Based on these results, a one-bay frame with two stories was found to be sufficient.

3.3.3 Member Selection and Detailing

The specimen, which is shown in Figures 3-10 and 3-12, has a main moment-resisting frame with four mechanical beam-column connections, and two outrigger frames. The added inertial mass is provided by four 2 kip concrete blocks stressed down to support beams. The outrigger frames (also referred to as perimeter frames) help to support the added inertial mass blocks and provide stability out of plane. These frames were designed as mechanisms with simple one-bolt pinned connections, and contribute a negligible amount of stiffness and strength in the in-plane direction. Lock nuts were used in the one-bolt pinned connections to ensure consistent bolt tightness throughout the test series.

The specimen was constructed of A572 Grade 50 rolled shapes: the columns from W6x12 sections, and the beams from S4x7.7 sections. Braces used for stability out of plane (in the direction perpendicular to the direction of excitation) were constructed of 5/8″ diameter rods. L3x3x1/4 angles were used to tie the mass support beams and perimeter frame beams together and create a diaphragm at each story. A complete set of specimen drawings is located in Appendix A.

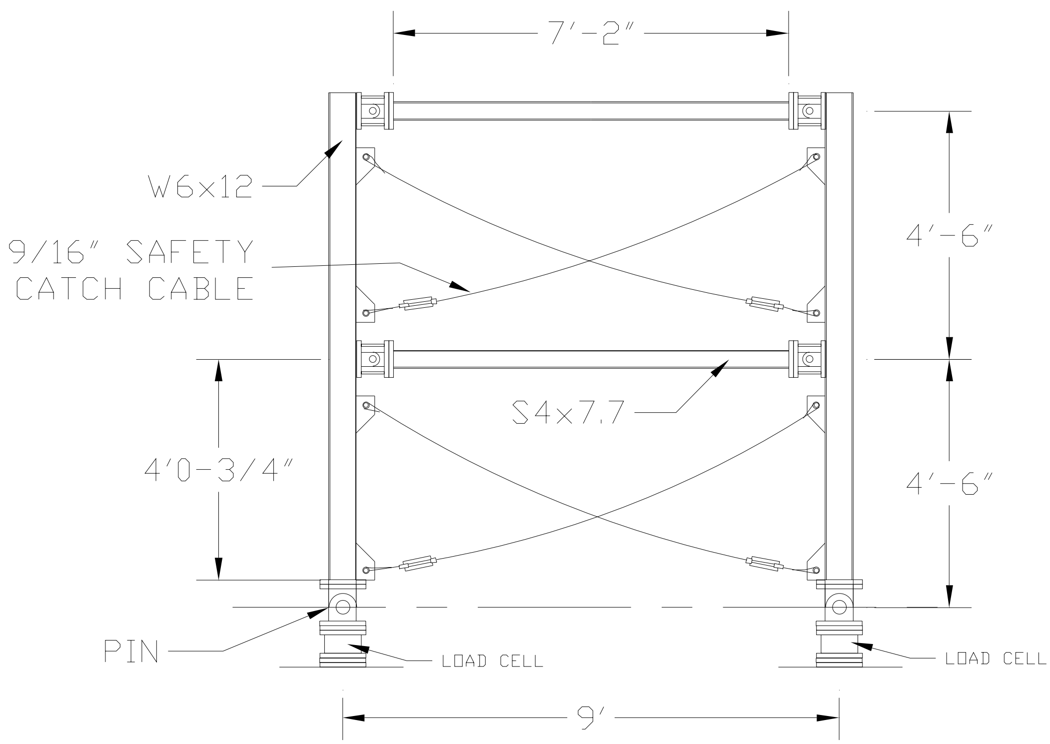

Figure 3-10. Main frame of test specimen

Approximate member sizes were selected based on strength requirements using capacity design concepts. Since the specimen needed to remain elastic except at the connections, the connection capacity determined the necessary main frame beam section modulus to provide elastic behavior with a factor of safety. The main frame column section was selected with significantly larger section modulus to satisfy strong-column, weak-girder requirements, to provide sufficient panel zone strength to prevent yielding without the use of doubler plates, to provide sufficient flange strength so continuity plates were not required, and to prevent yielding in the column. In addition, since the pilot study showed that column stiffness did not have a significant effect, a relatively stiff column was selected to minimize contributions of the second mode and permit consideration of a wide variety of connection types.

Perimeter beam sections selected were the same as those for the main frame for economic and constructability reasons. Perimeter column sections were selected based on in-plane stability requirements given their very long unbraced length (KL = 18 ft) and the fact that they were oriented in the weak axis direction, since their primary purpose was to brace the main frame out of plane.

Most of the main in-plane members have been given reference names and abbreviations which will be used in later chapters to refer to specific members in concise fashion. The member reference names and their abbreviations are listed in Table 3-3, along with a description of the member location. These locations are shown in a schematic of the frame (with abbreviations) in Figure 3-11. The north perimeter frame, which is not shown, is identical to the south perimeter frame except that the columns are PC3 and PC4 rather than PC1 and PC2. Also, the beams in this frame are not named since they are not instrumented.

Table 3-3. Abbreviations for member reference names

Member reference name	Abbreviation	Description of Location
Main Beam 1	MB1	Main frame, first story
Main Beam 2	MB2	Main frame, second story
Main Column 1	MC1	Main frame, East side
Main Column 2	MC2	Main frame, West side (closest to instrumentation frame)
Connection 1	C1	Connects east end of Main Beam 1 to Main Column 1
Connection 2	C2	Connects west end of Main Beam 1 to Main Column 2
Connection 3	C3	Connects east end of Main Beam 2 to Main Column 1
Connection 4	C4	Connects west end of Main Beam 2 to Main Column 2
Perimeter Beam 1	PB1	South outrigger frame, first story
Perimeter Beam 2	PB2	South outrigger frame, second story
Perimeter Column 1	PC1	South outrigger frame, East side
Perimeter Column 2	PC2	South outrigger frame, West side
Perimeter Column 3	PC3	North outrigger frame, East side
Perimeter Column 4	PC4	North outrigger frame, West side

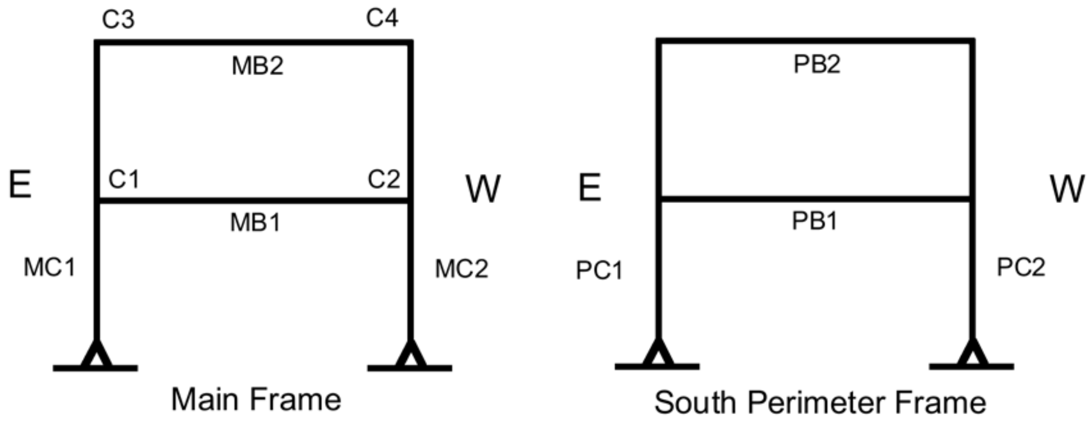

Figure 3-11. Member reference key

Because the intent of the tests was to assess behavior through collapse, the specimen was equipped with a system of internal cables, which were initially slack but were designed to engage at a predetermined interstory drift level to prevent the frame from completely collapsing. A come-along winch could be then be used with these cables to bring the frame back to a nearly vertical position after the test. The cables had turnbuckles installed along their length that could be tightened. When tightened the cables braced the frame laterally while the coupons were being changed, and provided fine adjustment of the plumbness of the frame.

Figure 3-12. Test specimen on shaking table

4 Experimental Program

In this chapter, the components of the experimental program will be examined. These components include the earthquake excitations, configurations and hysteretic behavior of connections, instrumentation scheme, and testing plan. A brief summary describing the execution of the testing plan and a discussion of errors and their effect on data interpretation are also included. The results from the tests are presented and discussed in Chapter 5 and comparisons between tests for response quantities of interest are made in Chapter 6.

4.1 PRELIMINARY ANALYTICAL STUDIES

Several preliminary analytical studies were performed, including response spectrum evaluations using potential pulse excitations and ground motion records, nonlinear static analyses of the frame considering few connection patterns, and linear and nonlinear dynamic analyses of the frame with many potential excitations and connection patterns. The static and dynamic analyses were performed using the OpenSEES analysis platform (McKenna, 2003). The objectives of the preliminary analytical studies were to select the earthquake excitations that would be used on the shaking table, determine connection configurations of interest for these excitations, and predict the response of the specimen with selected connection configurations to chosen excitations to help identify instrumentation needs. The results of these preliminary studies were combined with engineering judgment, and budgetary and time constraints to arrive at the final testing plan.

4.1.1 Selection of Earthquake Excitations

The earthquake excitations used in this study are of several types: simple pulses, near-field earthquake records, and far-field subduction zone earthquake records. Near-field motions (and likewise their pulse approximations) are of interest because of their high potential for causing structural damage, as demonstrated recently by the 1994 Northridge (Bertero et al., 1994) and the 1995 Hyogo-ken Nambu (Kobe) earthquakes (Bertero et al., 1995). Longer duration records are also of interest in order to study the cumulative effects of numerous cycles of strong shaking.

Simple pulses were examined first, in order to study the effects of hysteretic deterioration during smoothly varying excitations. Moreover, these pulses provide insight into the effects of near-field ground motions on seismic response. A simple excitation helps identify the effects of fracture and other forms of hysteretic deterioration. The value of such a simplification in representing near-fault excitations has been examined in several recent studies, (Krawinkler and Alavi, 1998, Makris and Chang, 2000). The pulses examined in this study were sine and cosine pulses; other shapes were examined in a prior analytical study (Mahin and Morishita, 1998).

A cosine acceleration pulse approximates the forward-and-back motion of the fault-normal component of many near-field accelerograms, while a sine acceleration pulse approximates the forward-and-stop motion of the fault-parallel component. A comparison of a cosine pulse with a near-fault record is shown in Figure 4-1. The acceleration, velocity, and displacement pulses used in this study are described by Equations 4-1 and 4-2 (as also done in Makris and Chang), which are written in terms of the pulse period T_p and velocity v_p.

$$\ddot{u}_g(t) = \omega_p v_p \cos(\omega_p t) \qquad 0 \le t \le T_p \qquad \text{(4-1a)}$$

$$\dot{u}_g(t) = v_p \sin(\omega_p t) \qquad 0 \le t \le T_p \qquad \text{(4-1b)}$$

$$u_g(t) = \frac{v_p}{\omega_p}(1 - \cos(\omega_p t)) \qquad 0 \le t \le T_p \qquad \text{(4-1c)}$$

$$\ddot{u}_g(t) = \frac{\omega_p v_p}{2}\sin(\omega_p t) \qquad 0 \le t \le T_p \qquad \text{(4-2a)}$$

$$\dot{u}_g(t) = \frac{v_p}{2}(1 - \cos(\omega_p t)) \qquad 0 \le t \le T_p \qquad \text{(4-2b)}$$

$$u_g(t) = \frac{v_p t}{2} - \left(\frac{v_p}{2\omega_p}\right)\sin(\omega_p t) \qquad 0 \le t \le T_p \qquad \text{(4-2c)}$$

The similitude relation used for the pulse excitations was a simple relationship between the pulse period T_p and the first-mode period of the test specimen T_n. The following pulses were chosen for use as shaking table excitations: one with a pulse period T_p = 0.6 seconds, approximately equal to T_n, and one with T_p = 1.2 seconds, approximately equal to twice T_n. These pulse periods were chosen to facilitate the examination of the effects of response spectrum position on behavior. As shown in Figure 4-2, a specimen with a period of about 0.6 to 0.7 seconds would be on the descending branch of the pseudo-acceleration response spectrum for the 0.6 second cosine pulse, while the structure would be on the ascending branch of the spectrum for the 1.2 second cosine pulse.

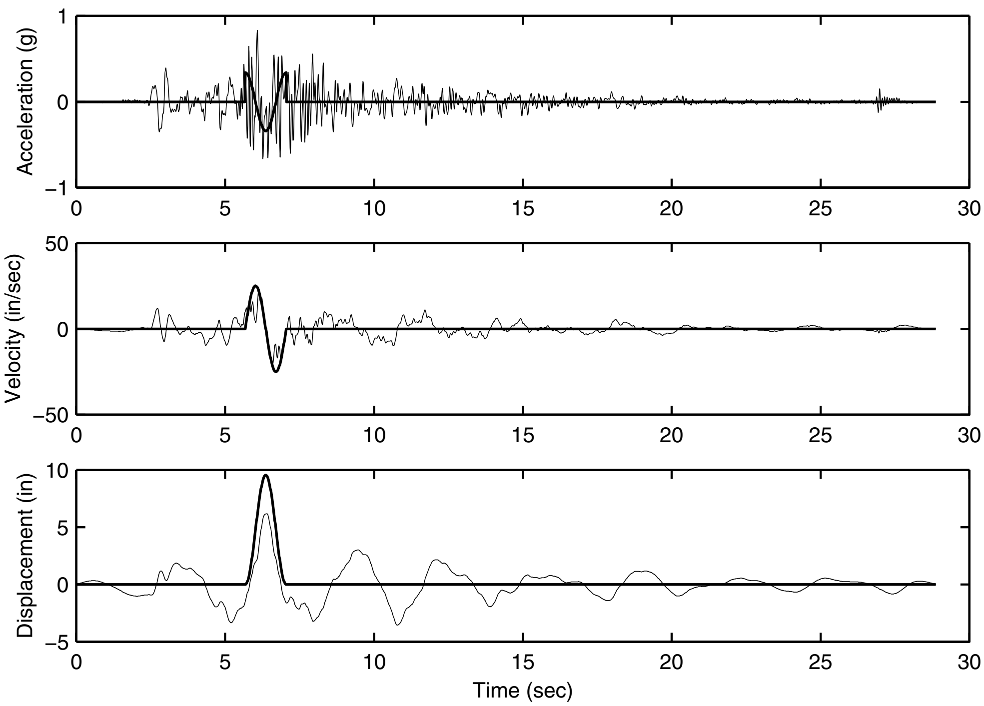

Figure 4-1. A 1.2 second cosine pulse compared with the SAC NF01 (Tabas) near-fault ground motion

Elastic response spectra for the sine and cosine pulses are compared in Figure 4-2 for the design period range, which is 0.5 to 0.7 seconds. These spectra show that the cosine pulses representing the fault-normal component have larger spectral values for both pulse periods than their sine counterparts. Also, the fault-normal component of a near-field ground motion is generally larger and thus more damaging to structures than the fault-parallel component (Somerville, 1998), making it of greater interest. For these reasons, cosine pulses were used in the shaking table study.

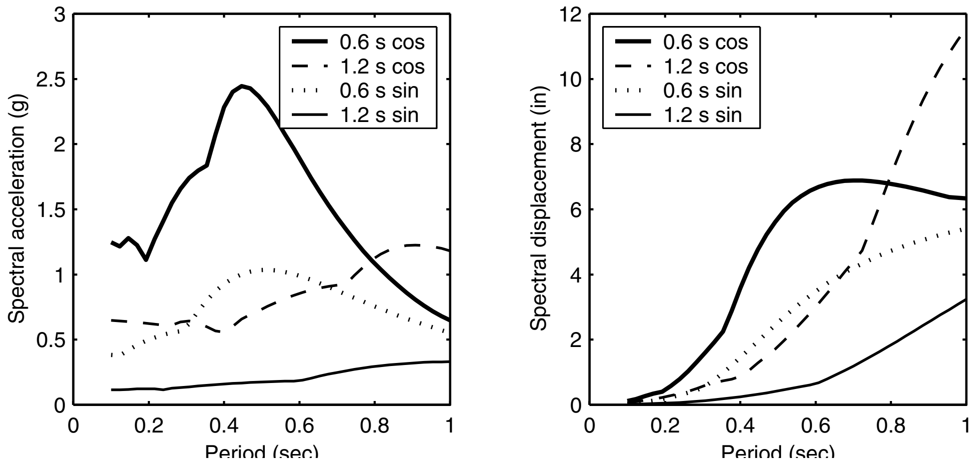

Figure 4-2. Comparison of elastic response spectra for sine and cosine pulses

The pulse amplitudes were limited by the capacity of the shaking table (see Table 4-1), particularly for velocity and displacement. The pulses all have a peak velocity of 25 in./sec, the shaking table maximum value, which would correspond to a peak ground velocity of 43 inches per second in the prototype structure. This is a reasonable value for near-field ground motions, and is similar to the value used in a recent analytical study of fracturing systems (Uetani and Tagawa, 2000).

Table 4-1. Shaking table constraints

Property	Specimen Design Value	Maximum for Bare Table
Maximum acceleration (g)	1.0	2.0
Maximum velocity (in./sec)	25	35
Maximum displacement (in)	+/- 5.0	+/- 5.0
Oil column frequency (Hz)	13	13
Degrees of freedom	1	6

The acceleration, velocity, and displacement time histories for the chosen pulses are shown in Figure 4-3, while their elastic response spectra are shown in Figure 4-4. The 0.6 second and 1.2 second cosine pulses are also subsequently referred to as JPULSE06 and JPULSE12, respectively.

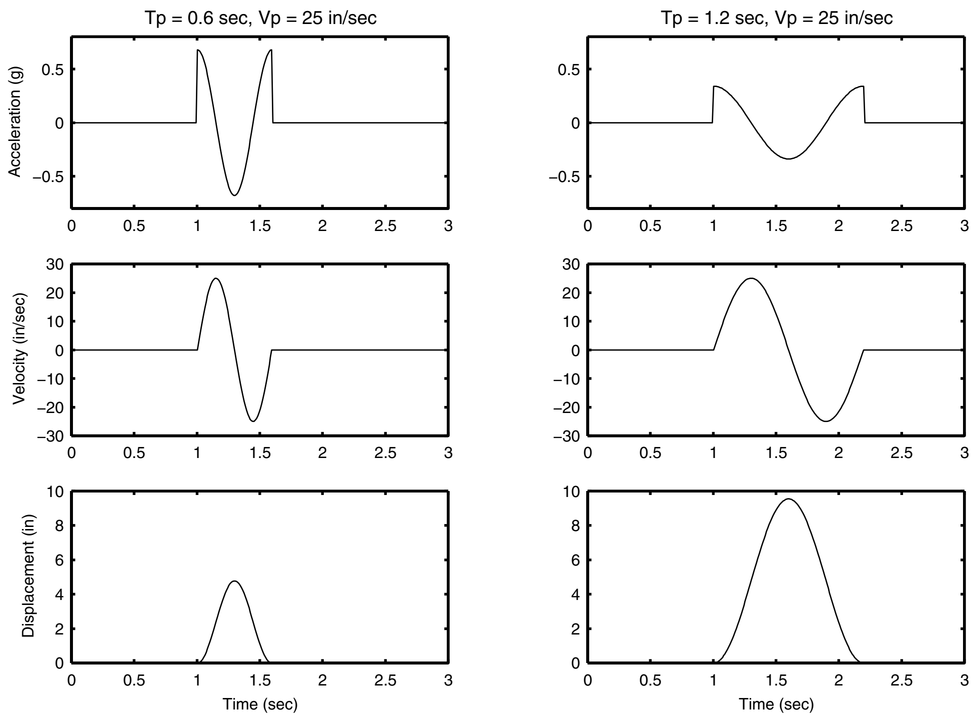

Figure 4-3. Acceleration, velocity, and displacement time histories of chosen cosine pulses

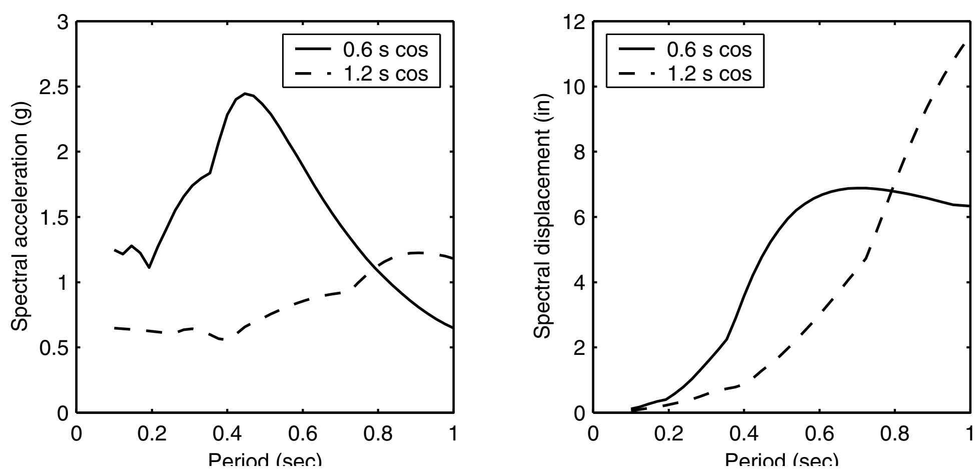

Figure 4-4. Elastic response spectra for chosen cosine pulses

Two types of earthquake ground motions were also considered: near-field motions and far-field, long-duration motions typical of subduction zone earthquakes. The motions used in the experiments were taken from the SAC near-fault and Seattle ground motion suites (Somerville, 1997). After scaling and performing minimal filtering of the records to fit the design values of the constraints of the shaking table shown in Table 4-1, records with sufficient displacement, velocity, and acceleration amplitudes were chosen for further examination. The records chosen included those derived from the following records: Tabas (NF01, NF02), Northridge Sylmar (NF15, NF16), and Kobe JMA (NF17, NF18) from the SAC near-fault suite, and Llolleo (SE17, SE18), Vina del Mar (SE19, SE20), and Valparaiso (SE29, SE30) from the SAC Seattle suite. The elastic and inelastic response spectra of these records were then examined using the computer program BiSpec (Hachem, 2000).

The choice of ground motions was based on the results of the inelastic response spectrum analyses and the preliminary analytical studies carried out using OpenSEES. Based on these studies, the NF01 and SE17 records were chosen. The NF01 motion was based on the 1978 Tabas, Iran record. The SE17 motion was based on the Llolleo record from the 1985 Chile earthquake. In both cases, the recorded ground motion accelerograms had been filtered and scaled to obtain spectra corresponding to the site conditions assumed for the SAC steel project (firm soil).

In order to comply with the similitude relations in Table 3-2, the time scales for the selected records were divided by $\sqrt{3}$ and the acceleration amplitudes left unchanged. Next, the amplitude scaling and filtering parameters were fine-tuned to achieve the best performance on the shaking table. Since the test specimen was quite light, it was possible to achieve additional acceleration and velocity above the design values shown in Table 4-1. The additional acceleration capacity was used to bring the velocities up to a higher level for the SE17 motion. This was possible because SE17 is not a near-field motion, and therefore large displacements are not present and the displacement limits did not govern.

In contrast, the scaling of the NF01 motion was controlled by the table's displacement limitations. Due to the fixed displacement capacity of the shaking table, an initial offset was employed to allow greater peak displacements since NF01's maximum displacements are not symmetric, as shown in Figure 4-5. The final scaled and filtered versions of the NF01 and SE17 motions used for the shaking table tests will hereafter be referred to as JNF01 and JSE17, respectively, to avoid confusion, since they differ from the SAC NF01 and SE17 records. The JNF01 and JSE17 motions along with their elastic response spectra are shown in Figures 4-5 to 4-8, and their properties are shown in Table 4-2. All motions and spectra are shown for model time scales. The properties of the selected pulse excitations and ground motions are listed in Table 4-2.

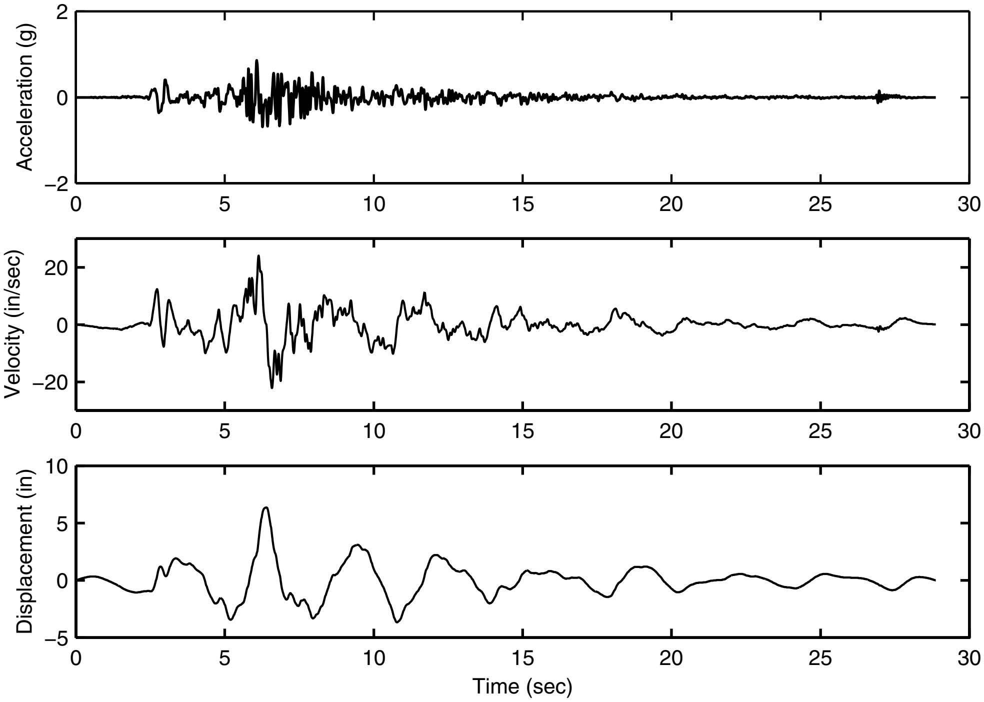

Figure 4-5. Acceleration, velocity, and displacement time histories for JNF01

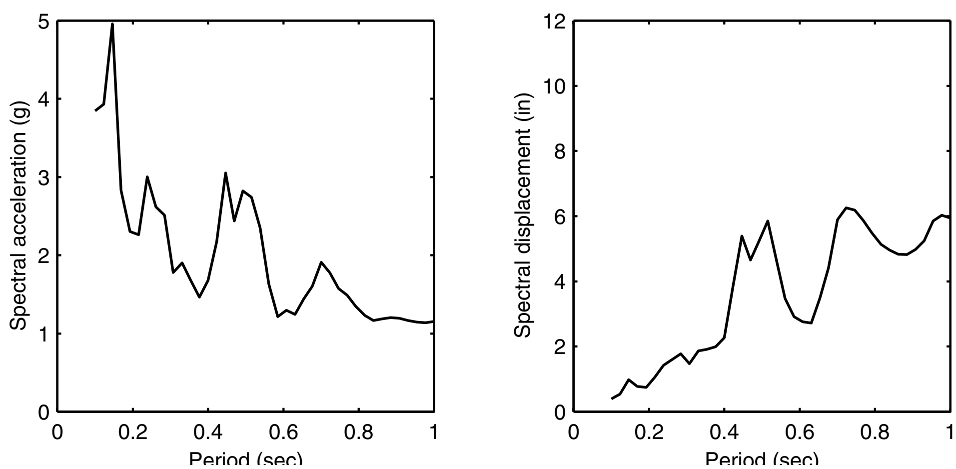

Figure 4-6. Elastic response spectra for JNF01

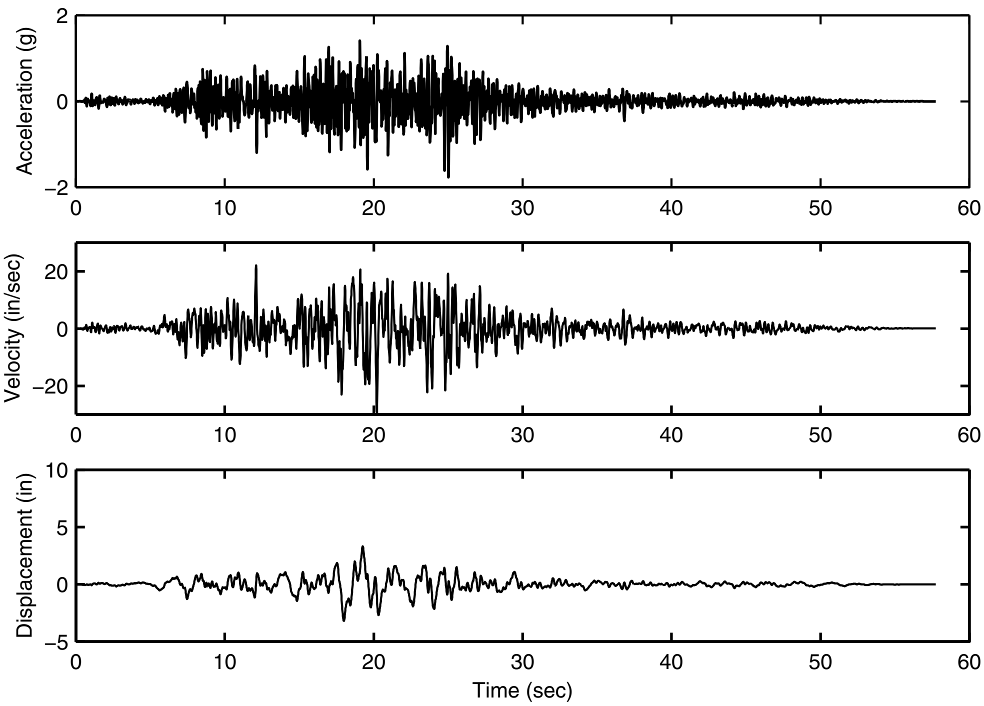

Figure 4-7. Acceleration, velocity, and displacement time histories for JSE17

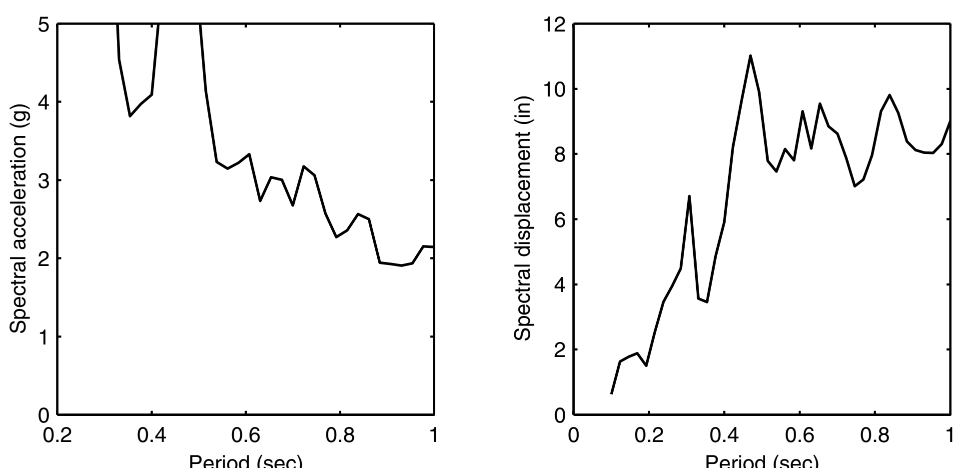

Figure 4-8. Elastic response spectra for JSE17

Table 4-2. Values of key parameters for earthquake excitations used in shaking table tests

Parameter	JPULSE06	JPULSE12	JNF01	JSE17
Peak ground acceleration (g)	0.678	0.339	0.836	1.77
Peak ground velocity (in./sec)	24.99	25.00	23.58	29.46
Peak ground displacement (in.)	4.77	9.55	6.36	3.32
Original digitization (sec)	0.01	0.01	0.02	0.025
Scaled digitization (sec)	0.01	0.01	0.01155	0.01443
Original duration (sec)	0.6	1.2	50	100
Scaled duration (sec)	0.6	1.2	28.875	57.72
Amplitude scale factor from original SAC motion	N/A	N/A	0.91	2.75
Full scale span setting	500	1000	954	685
Filter (low cut, low corner, high cut, high corner)	N/A	N/A	(0.25, 0.25, 12, 15)	(0.25, 0.3, 12, 15)
Time scale factor	1	1	$\sqrt{3}$	$\sqrt{3}$

4.1.2 Selection of Connection Patterns

With four of the clevis-based mechanical connections described in Section 3.2 placed in the frame (two in each story), many spatial arrangements of the different connection hysteretic types shown in Table 3-1 were possible. Of course, not all of the possible patterns were representative of a situation one might see in a real building, or that would have a significant impact on the system behavior. Time and budgetary constraints also dictated that only a limited number of patterns be examined. Nonlinear dynamic analyses and engineering judgment identified the patterns shown in Figure 4-9, where the circles represent connections exhibiting degrading behavior types (brittle fracture, ductile fracture, deformation softening, or strength degradation). At the ends of the beams without circles, the ductile baseline connection type with stable yielding hysteretic behavior was provided. It should be noted that all four beam ends have a clevis-based connection, regardless of whether a circle is present or not.

Also, patterns are hereafter distinguished by the connection type exhibiting degrading hysteretic behavior. For simplicity, only one type of hysteretic degradation is permitted in each configuration. For instance, if the two connections in the BP pattern with degrading behavior had the connection type brittle fracture, the pattern would be called “brittle fracture BP” or abbreviated as BF BP. For the case where all of the connections have hysteretic type ductile baseline, the pattern is simply called “ductile baseline” or abbreviated as DBC.

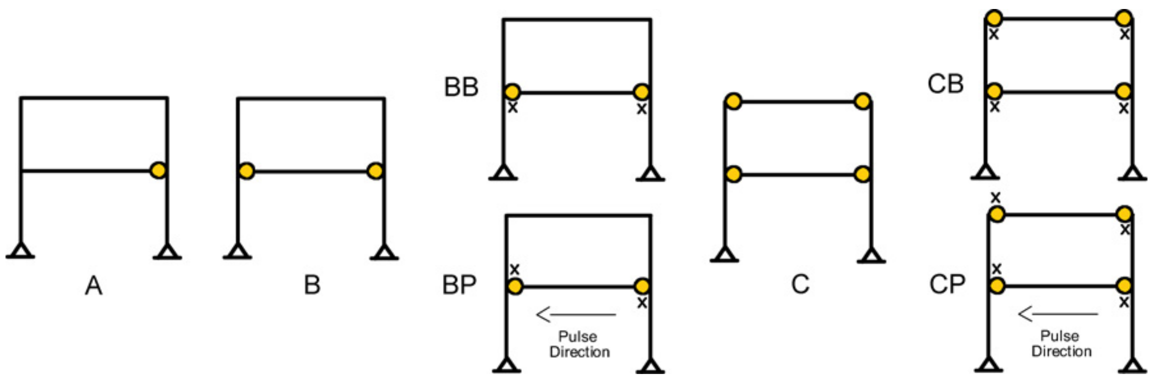

Figure 4-9. Connection patterns

Pairings of pattern and excitation are shown in the test matrix in Table 4-3 in Section 4.3, so only a brief qualitative description of the uses of and reasoning behind the above pattern selections are presented here. Pattern A was used for the sole purpose of examining the force redistribution and the effect of stress waves propagating through the structure after a fracture occurred at one end of the beam. Since the behavior immediately after the occurrence of a fracture was of interest (as opposed to the behavior beforehand), only the brittle fracture hysteretic type was investigated using pattern A. Pattern B was used to investigate the response of the system when all the connections at a particular story level suffered the same type of hysteretic degradation. Pattern C was used to examine the response of the system when all of the connections in the structure exhibited degrading behavior.

For the fracturing cases, two variations of the B and C patterns were used, which are shown above with an “x” representing the location of a potential fracture. The patterns on the bottom, called “BP and CP,” respectively, were used with the cosine pulse excitations only. They have notched coupons, with the potential to fracture, in all of the flanges of the degrading connections which are in tension when the structure moves in the direction of the pulse excitation (referred to hereafter as the positive direction). The purpose of the BP and CP patterns was to investigate the case in which all the flanges that can fracture do so nearly simultaneously during the pulse of a near-field ground motion.

In the patterns on the top, called “BB” and “CB,” fracture is only permitted in the bottom flanges. These patterns were used with the earthquake motions and with one of the cosine pulses for comparison purposes. The BB and CB patterns represent the type of fracture damage most commonly observed in the field during recent earthquakes, i.e., fractures occurring predominately in the bottom flanges of the beams (SAC, 1995).

4.2 INSTRUMENTATION

4.2.1 Data Acquisition Systems

The instrumentation for this experiment was challenging due to the necessity of capturing both global behavior data and very specific local data related to highly transient post-fracture behavior. Due to the extremely short time interval during which post-fracture stress-wave propagation can be observed, a high rate of data acquisition was necessary for some tests. In order to optimize the collection of high-quality global and local data, two separate test sequences were designed, and two data acquisition systems with different speeds were employed.

The first sequence, hereafter referred to as the main sequence, used the regular data acquisition system for the shaking table. A scan rate of 100 Hertz was used for this sequence. This sequence comprised the majority of the tests performed and focused on the system behavior of the structure when various types of hysteretic behavior were present at the connections. The number of channels for this sequence was 152, which included table channels, load cells, accelerometers, displacement transducers, and strain gages. A list of channels is located in Appendix B.

The second sequence, hereafter referred to as the wave-propagation sequence, used a special high-speed data acquisition system with a scan rate of 1 megaHertz. However, this system could only accommodate four channels, so the regular system was employed for the remaining channels. In order to measure the highly transient response at important locations, the test was repeated and the four high-speed channels were used to measure the response at key locations in turn. This sequence was comprised of a much smaller number of tests, and was focused on understanding the immediate post-fracture behavior of the structure.

4.2.2 Types and Placement of Instruments

Several types of instruments were used to measure the response of the specimen:

- Accelerometers
- Linear wire potentiometers
- Linear slider potentiometers
- Strain gages
- Load cells

Accelerometers were deployed in both the in-plane and out-of-plane directions, as well as at midspan of the main beams to measure the vertical response, as shown in Figures 4-11 and 4-12. These instruments were mounted on aluminum blocks which were attached with epoxy to the specimen. The accelerations of the shaking table were recorded by a separate set of accelerometers built integrally with the table.

Linear wire potentiometers, which were mounted off of the table on an instrument frame, were used to measure the global displacements of the specimen. Each potentiometer was connected by a flexible piano wire to the specimen as shown in Figures 4-11 and 4-12. A fairly large number of linear wire potentiometers were used to provide redundancy and to capture potential torsional or out-of-plane response. The ability to detect torsional and out-of-plane response was necessary, since the shaking table could cause low-level, unintended excitations both torsionally and out-of-plane even during a prescribed unidirectional test.

Linear slider potentiometers were used to measure the displacement above and below the connections and calculate the rotation. These were attached to the clevis base plates above and below the connection as shown in Figure 4-10. These instruments had a range of +/- 2 inches, which was necessary due to the large deformations expected. Since these potentiometers use an inflexible sliding rod and flexible wire rather than just a flexible wire, geometric corrections to the connection rotations are necessary at very large rotations.

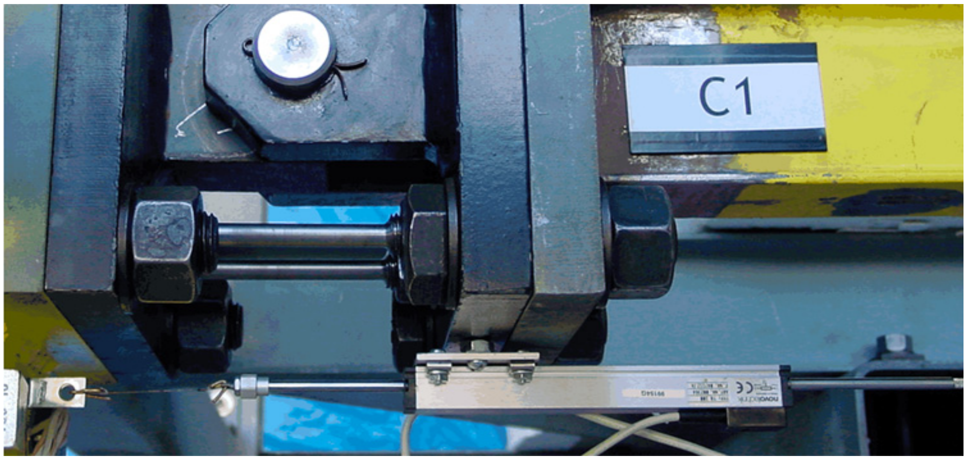

Figure 4-10. Linear slider potentiometer

Numerous strain gages were applied to the beams and columns of the main frame to measure strains, enable the calculation of curvatures and moments, and detect yielding. One perimeter column was instrumented in a like manner to the main frame columns to get an estimate of how much strain was present in the perimeter frames, and to detect yielding, though due to the negligible in-plane stiffness none was expected. Full instrumentation of the perimeter frames was not possible due to the limited number of data acquisition channels available, and was not a priority due to the low levels of stress expected in these frames. A listing of detailed locations of individual instruments is provided in Appendix B.

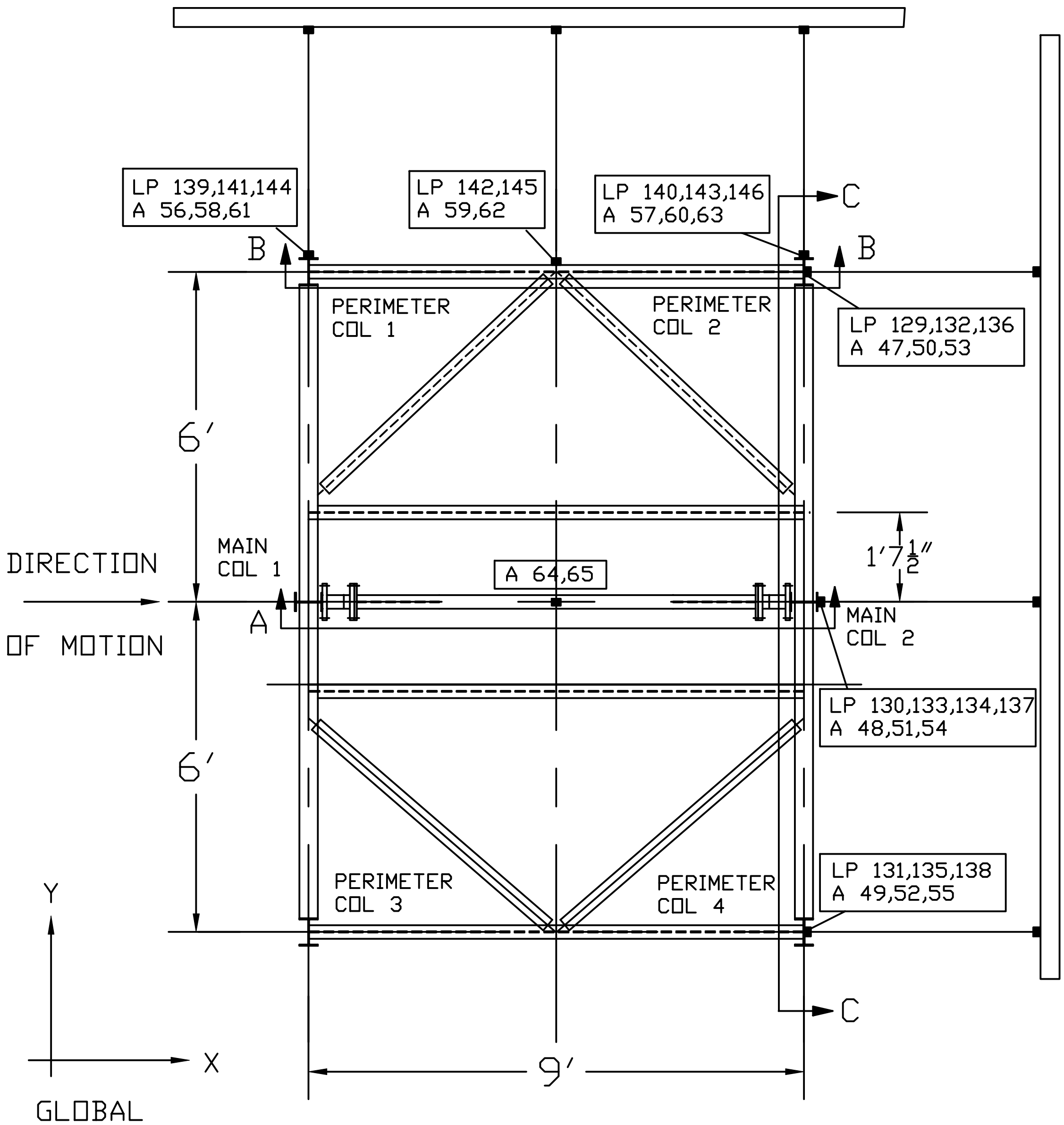

Figure 4-11. Plan view of instrumentation

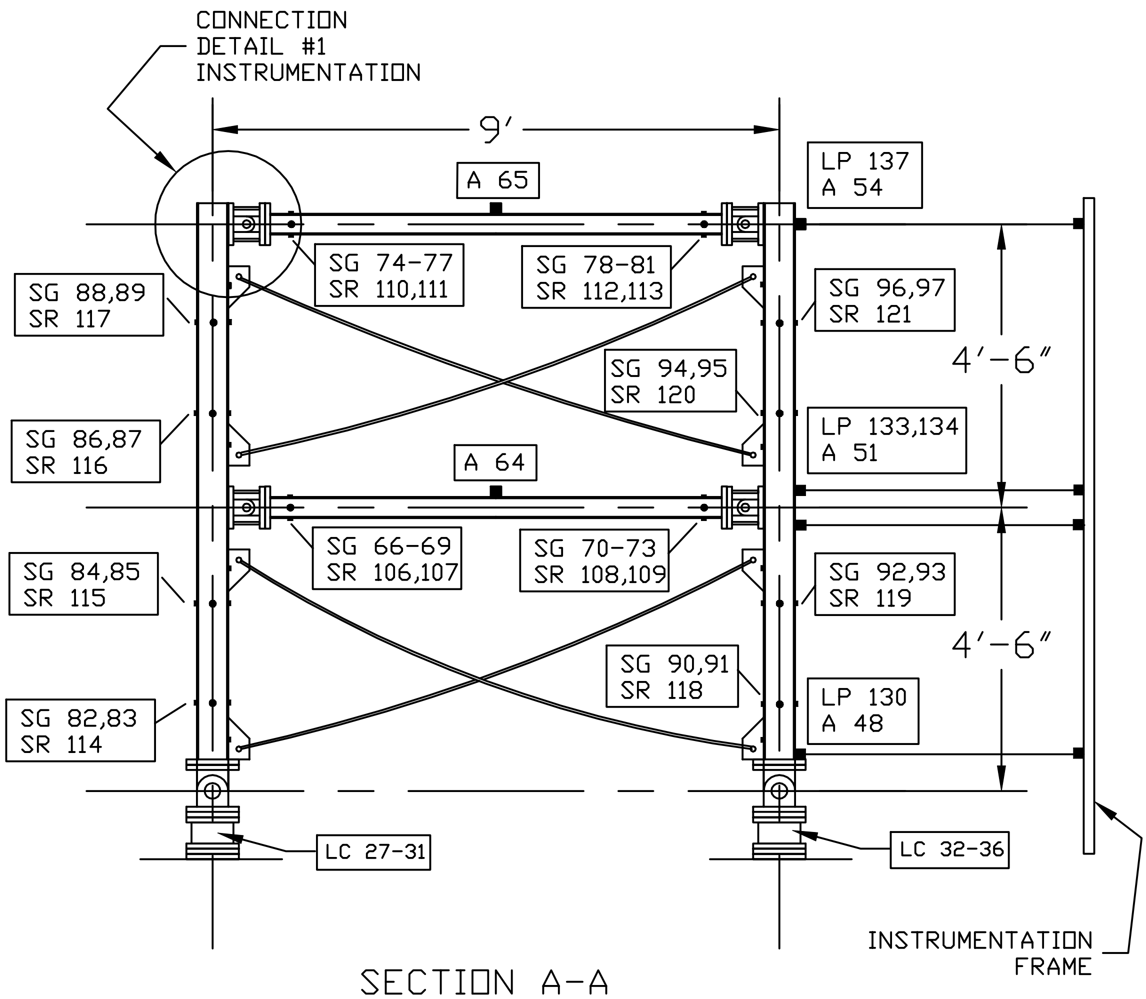

Figure 4-12. Elevation view of main frame instrumentation

4.3 TESTING PLAN AND EXECUTION

The shaking table tests in this study were organized into several phases. First, the four selected excitations were run on the empty table to establish the appropriate span settings on the table controller. The span setting proportionately scales the amplitude of the excitation signal sent to the table, and determines the maximum displacement of the actuators. After the span setting for each motion was determined, the specimen was placed on the table, secured, and instruments were connected to the data acquisition system and then calibrated.

After this, the actual testing phase began. A series consisting of several different test types was performed for each connection pattern/ground motion combination. A typical series consisted of two pullback free vibration tests, a “white noise” (random signal) test, and a high-level test using the appropriate excitation. The white noise test was performed at a very low peak acceleration level (~5% g) and thus functioned as a low-level test to check the instrumentation and data acquisition, as well as a means of determining vibration properties. The acceleration time history of a typical random signal used in the white noise tests is shown in Figure 4-13.

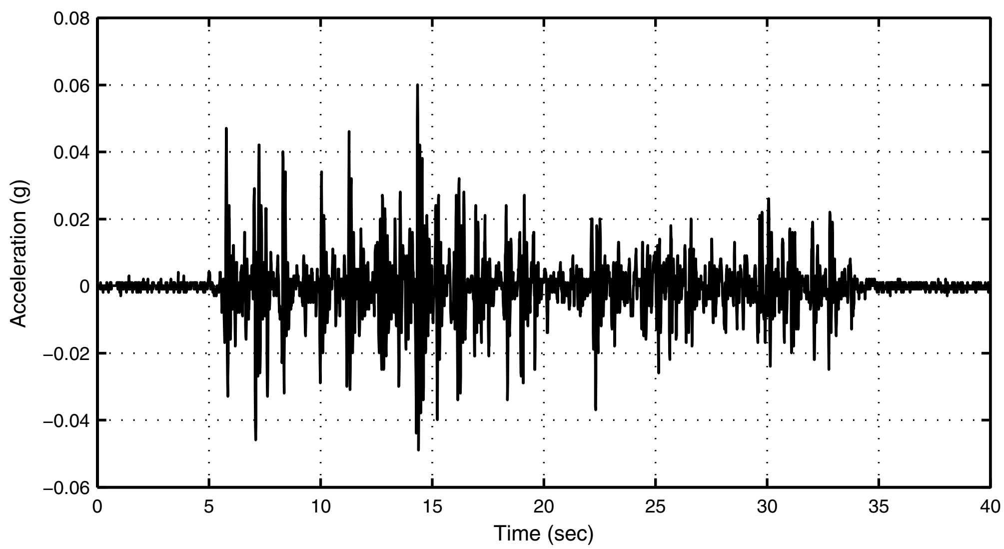

Figure 4-13. Acceleration time history for random signal used in white noise tests

A low-level test using the earthquake excitation was performed in the first series, but was omitted from the rest of the series once it was demonstrated that the data of interest could be obtained adequately from the random signal test. Also, if pullback tests had already been performed for a particular connection pattern, they were omitted in subsequent test series using that pattern. In these subsequent series the vibration properties were determined from the white noise test, and much time was saved by omitting the pullback tests.

A total of 32 high-level shaking table tests were conducted, in addition to low-level and random signal tests. The high-level tests performed can best be described by the use of the test matrix shown in Table 4-3. Amplitudes are shown as a percentage of the full-scale span settings.

Detailed information on each test such as span setting and filename is provided in Appendix C. The connection configuration patterns are shown in Figure 4-9, and the excitations are described in Section 4.1.1. In a few cases, multiple tests of the same connection pattern/ground motion combination were performed, and other quantities such as beam mass were varied.

Table 4-3. Test matrix

Excitation	Amplitude	Connection Configuration Pattern						
		A*	**B**	**BB***	**BP***	**C**	**CB***	**CP***
0.6 Second Cosine Pulse	100%		DFS		BF, DF	DB, DFS		BF, DF
	50%	BF			BF			
1.2 Second Cosine Pulse	100%		DFS		BF, DF	DB, DFS	BF	BF, DF
	75%							BF
	50%							BF
SAC NF01	100%		DFS	BF		DB, DFS	BF, DF	
SAC SE17	100%					DB, SD	BF	

where DB = Ductile baseline, BF = Brittle fracture, DF = Ductile fracture, DFS = deformation softening, SD = Strength degrading.

* Denotes connection pattern used for fracturing hysteretic behavior types only

The wave propagation sequence, which examined the local transient phenomena following a fracture, included six high-level tests. Brittle fracture patterns were used on all of the tests in this sequence, and the BF A/0.6 sec cosine pulse combination at 50% amplitude was used for the majority of the tests. This amplitude was chosen because the preliminary analytical study predicted it would barely cause fracture and would cause little or no yielding in the ductile connections.

The ultra high-speed data acquisition system discussed in Section 4.2.1 was utilized for this sequence. The channels for which high-speed data were taken varied by test and are shown in Table 4-4, but all were strain gages on either the first- or second-story beams in the main frame. High-speed data were also taken during two other normal tests to ensure that the triggering circuit on the high-speed data acquisition system was functioning correctly. Unfortunately, the high-speed data acquisition system failed during a test of the BF BP/0.6 sec cosine pulse combination and no high-speed data are available for that pattern.

Table 4-4. Tests with high-speed data collected

Name	Excitation	Amplitude	Pattern	Data Recorded at Gages	Supplemental Mass on Beam
Test A	0.6 sec cos pulse	50%	BF A	Top of MB1 (71, 101, 100, 67)	No
Test B	0.6 sec cos pulse	50%	BF A	Top/bottom at MB1 ends (71, 73, 67, 69)	No
Test C	0.6 sec cos pulse	50%	BF A	Top/bottom MB1, top MB2 (71, 73, 79, 75)	No
Test D	0.6 sec cos pulse	50%	BF A	Top/bottom at MB1, MB2 ends (71, 73, 79, 81)	No
Test E	0.6 sec cos pulse	50%	BF A	Top of MB1 (71, 101, 100, 67)	Yes
Test F	1.2 sec cos pulse	50%	BF CP	Top of MB1 (71, 101, 100, 67)	No
Test G	SAC SE17	100%	BF CB	Top of MB1 (71, 101, 100, 67)	No

Additional distributed mass was positioned along the first-story main beam for Test E to determine if the change of beam deflected shape after the fracture would excite the beam vertically. The additional mass was attached as shown in Figure 4-14, with a spacer between the mass and the beam, so as not to add stiffness to the beam.

Figure 4-14. Placement of additional distributed mass on MB1

The mass was added to the beam using three 100-pound lead weights at the quarter points of the beam. The equivalent uniform loading assuming centerline dimensions for this configuration of weights is 33.3 pounds per linear foot. By similitude, this amount is less than what would be expected from a typical concrete slab overlying the beam, but due to the beam size used, placing the amount of mass called for by similitude relations would have led to yielding of the beam under the vertical excitation expected at fracture, rendering all comparisons meaningless and compromising the assumptions used when studying the wave propagation in the beam.

4.4 ERROR SOURCES AND IMPACTS ON DATA INTERPRETATION

The amount of error in the data, both from aleatory variability, or randomness, and epistemic uncertainty, or uncertainty in scientific understanding, as well as from the occasional human mistake, is an important factor when interpreting the data. Since the following chapters are primarily concerned with data interpretation, the sources and extent of error in the data obtained from the tests described in the previous section will be presented here. Sources of error, primarily from the instrumentation, will be discussed in Section 4.4.1. Particular errors identified during the course of testing will be also be discussed and their impact on interpretation of the results will be estimated.

After these errors have been discussed, the overall error present in the experimental setup will be estimated by comparing the results from multiple tests of nominally identical connection configuration pattern/excitation pairings. Two tests of the BF BP pattern and four tests of the BF A pattern were performed with the 0.6 second cosine pulse excitation, and these case studies are examined in Sections 4.4.3 and 4.4.4, respectively. Combining the results of these case studies, estimates of the total error will be presented for various response quantities, and conclusions regarding the consideration of errors during data interpretation will be discussed in Section 4.4.5.

4.4.1 Sources of Error

During the course of the tests and in the data analysis afterward, errors from several sources were identified. Sources of local error within tests include instrument errors, noise, geometrical configuration of instruments under large deformations, unintended out-of-plane motions of the shaking table, and of course, human errors. These sources of error and their relative importance are discussed below.

4.4.1.1 Instrument and data acquisition system malfunctions

It is inevitable that some instruments and data acquisition (DAQ) components will malfunction during an experimental series of the length of the one discussed here. Thankfully, these malfunctions generally show up quite obviously in the data. Data with obvious instrument errors **were** not used in the generation of plots or summaries, and redundant instrumentation was relied on in these cases, which increases the errors slightly over the case where all instruments being averaged are functioning properly.

Before each high-level test, a low-level test was performed to check the data from the instrumentation and DAQ, and this low-level test allowed many instrument malfunctions to be identified and corrected quickly. Even so, occasional malfunctions occurred during the high-level tests in several types of instruments and components, including accelerometers, strain gages, slider potentiometers, adapters, and amplifiers. The malfunctions were of several different types, and each type of instrument was more prone to certain malfunctions than others.

Accelerometers malfunctioned by random glitches several times, with sudden large spikes over range. These over-range spikes are readily distinguishable from real spikes in acceleration, and data with over-range problems were removed from consideration. In these cases, the redundancy of the accelerometers both in plane and out of plane minimized any increase in error resulting from the removal of bad data from one accelerometer.

Several incidents of strain gages with wildly fluctuating values were observed, and several incidences of excessive noise were observed as well. Noise problems were usually due to loose strain gage-to-adapter connections which were easily fixed after identification in low-level tests and thus were not problematic in the high-level tests.

The noise level of the instrumentation and DAQ setup used was generally very low, and if noise is present in the data it is generally quite obvious when looking at the plots. No attempts were made to filter noise in this report, since substantial noise was rare and easily identifiable.

The slider potentiometers experienced occasional malfunctions of the connection of the wire extension and the target. The bottom slider potentiometer wires slid off of their targets during several tests, and the top slider potentiometer data was used alone to calculate connection rotations.

Using data from only one potentiometer increases the errors by approximately 2%, producing minimal impact on the quality of the results.

Malfunction of the analog-to-digital converter was the most likely culprit for the wild fluctuations and over-range problems of the strain gages and accelerometers. Apparently, an occasional bit was dropped at random for some channels in some tests, leading to large fluctuations in some data values. However, as stated previously, this type of malfunction is generally easy to identify so that the bad data can be removed from consideration. Malfunction of other DAQ components such as amplifiers was very rare in the high-level tests, and thus had very small effects on the results, since redundant instrumentation was available.

4.4.1.2 Errors caused by large deformations

Several instrument configurations had the possibility of introducing errors when the specimen underwent large deformations. The most significant of these was the rigid slider potentiometer arm used in measuring the relative displacements at the top and bottom of the connections. The error in the connection rotations caused by the angle between the slider potentiometer arm and the connecting wire at large deformations was found to be less than 2% for the angles observed in this study, the largest of which was approximately 18º. This is considered acceptable when compared to the variability between tests of the same configuration with the same ground motion. Also, this error canceled out when calculating rotations, and is only present when a single potentiometer's data were used for rotation calculations.

The other configuration, the out-of-plane linear wire potentiometers, was determined to have a maximum angle of about 13º from the perpendicular, which is within the small angle approximation. However, this 13º corresponds to an extra 2.2 inches of "displacement" out of plane at the top of the frame for an in-plane displacement of 18.5 inches. The actual maximum out of plane displacement for all cases was determined to be about 0.4 inches after the application of a simple geometric correction. Appendix D shows both uncorrected and corrected values in Tables D-4 and D-5, respectively. Corrected out-of-plane displacement data are used in data analysis and interpretation.

4.4.1.3 Errors caused by lack of true unidirectionality

Even though the test was unidirectional, out-of-plane excitations were generated by the shaking table. The maximum values of these excitations are summarized in Appendix D in Tables D-5 (displacements) and D-8 (accelerations). Before and after a few tests, the shaking table was observed to have minor control problems, and low-level spurious motions occurred with no excitation running at the time. These motions may have occurred during tests as well, and may have caused out-of-plane displacements and accelerations.

Out-of-plane table displacements were generally very small, with the maximum absolute value over all of the tests being less than 0.2 inches. With maximum in-plane table displacements of 10 inches, this amount of displacement is virtually negligible. The corrected out-of-plane relative displacements at the base, first-story, and second-story levels had maxima over all tests of about 0.4 inches. These displacements are also quite small, and it can be concluded that out-of-plane displacements were not large enough to affect the behavior of the frame in any significant way.

The table was also prone to some skew when it was traveling in the in-plane direction, causing differences in the in-plane table displacements at each of the three frame lines. These differences are summarized in Appendix D, Table D-2. The skew in the table led to some differences between the in-plane displacements at the second-story level of the two outrigger frames that were as large as 0.7 inches. [There were several instances of larger differences, but these were caused by engagement of the catch cables and will be discussed in Section 4.4.1.4.] In the cases where table skew occurred, a sudden “skew pulse” mimicking the shape of the excitation was observed at the time of the maxima in displacement differences. Notable tests where this occurred are the 0.6 second cosine pulse/ DFS B and 1.2 second cosine pulse/ DF BP tests. However, most in-plane displacement differences between frames were very small (less than 0.3 inches) compared to the overall maximum displacement.

Out-of-plane accelerations were more problematic, since the maximum out-of-plane table acceleration for all tests was 0.34 g. This value is about 25% of the maximum in-plane value for the particular test for which it was recorded, and thus indicates that spurious out-of-plane accelerations are not negligible compared to the in-plane values. Since these accelerations are out-of-plane and very short-lived, however, they have minimal effects on the specimen behavior.

4.4.1.4 Errors caused by lack of specimen diaphragm action

Since the bolted connections at the ends of the tube members connecting the perimeter frames and the main frame in the out-of-plane direction were not completely rigid, some differential movement between the frames occurred. This “slop” in the response became apparent in some of the in-plane displacement time histories, where the displacements were slightly different at the first and second-story levels of MC2, PC2, and PC4. The amount of differential movement is tabulated for each test in Table D-2, but it should be remembered that in some cases the differential movement was caused by skew motion of the shaking table, as discussed in the previous section. In most tests, the amount of differential motion from all sources was small (less than 0.3 inches).

However, in the cases when the catch cables engaged in a “hard” manner, larger differential motions (up to 1.75 inches in one case) occurred. These motions occurred at the time of the cable catch, and were observed in the 1.2 second cosine pulse BF CP, DF CP, and DFS C patterns, as the specimen was traveling quite fast in these tests when the catch cables engaged. The differential motions were probably occurred because it is practically impossible to loosen the catch cables so they will all engage at exactly the same time. Some cables are bound to engage slightly earlier than others, causing differences in displacement between the frames. When the impact of the catch on the frame is strong, larger displacement differences will tend to appear. Of course, at the point of cable engagement this difference does not matter, since the displacement behavior of the structure becomes compromised by the effects of the cables.

4.4.1.5 Human error

Human error is, of course, much more difficult to quantify. The slip present in some of the moment-rotation hysteretic loops can be attributed to a failure to fully or uniformly tighten the coupon bolts in some cases, but this is difficult to determine since the coupons invariably begin to slip a little when exposed to large deformations, even when they are initially very tight. Other sources of human error include forgetting to attach linear potentiometer wires and nonuniform loosening of the catch cables. The latter occurred in the DFS C/0.6 sec cosine pulse test, and as a result one cable engaged early, affecting the results. This early cable catch is accounted for in **the** result interpretation.

4.4.2 Definition of Terms and Normalized Global Response Quantities

Since behavioral data will be presented in tabular summary form, it is helpful to define some normalized response quantities which can be used for all of the cases. It is most useful for the purposes of this study to use normalized measures of global displacement, global force, and global dynamic properties to describe the behavior of the system. For simplicity, and because these normalized measures provide a good 'view' of the relative quality of the system behavior, only one measure each will be used for global displacement, global force, and global dynamic properties.

Interstory drift ratio (Θ_1) in the first story is used as a measure of the global displacement response. The percentage of maximum base shear remaining after degradation of the connections (λ_{Vb}), defined in Figure 4-15, is used as a measure of global forces. This term is defined such that a structure with no degradation in base shear capacity has λ_{Vb} = 100%. Finally, the percentage elongation of the first-mode period at the end of the test (λ_{T1}) is used to measure the change in the system's dynamic properties. If the structure has no period elongation, $\lambda_{T1} = 0$. These normalized quantities are calculated in decimal form as follows, and expressed in percent form in Tables 4-5 through 4-8:

Θ_1	mean displacement (for the 3 frames) at the first story minus mean displacement at the column base, divided by the story height
λ_{Vb}	base shear at end of base shear-Θ_1 hysteresis loop with most significant degradation divided by maximum base shear
λ_{T1}	First mode period after test (determined from free vibration after end of excitation) minus original first-mode period, divided by original first-mode period

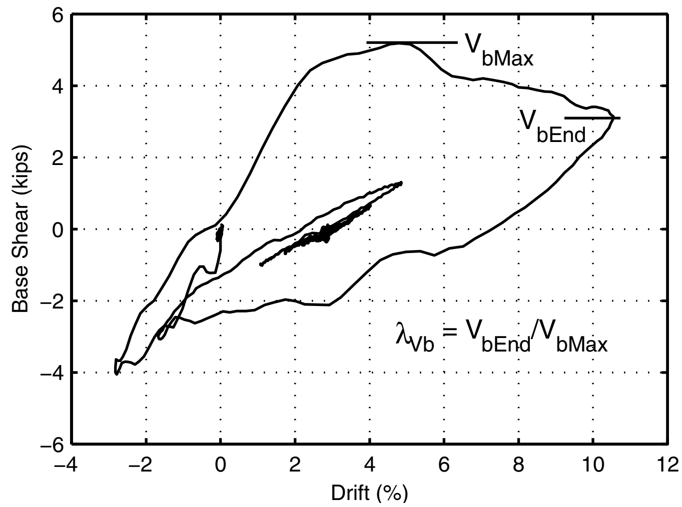

Figure 4-15. Definition of λ_{Vb}

The numerical comparisons between experimental results for different tests were obtained in most cases by using percent differences. Percent differences were calculated using Equation 4-3. In the case of small numerical values, however, small absolute differences sometimes led to very large percent differences. These cases are noted and absolute difference values, defined in Equation 4-4, are provided as necessary.

$$\%\ \text{difference} = \frac{\max(x_1, x_2) - \min(x_1, x_2)}{\min(x_1, x_2)} \cdot 100 \qquad (4\text{-}3)$$

$$\text{absolute difference} = \max(x_1, x_2) - \min(x_1, x_2) \qquad (4\text{-}4)$$

In some of the tests (involving the C patterns and cosine pulse excitations), the specimen experienced very large interstory drifts, to the point of engaging the system of safety catch cables. Drifts of more than 20% were not desirable due to concerns about safety and specimen reuse. The maximum drift level allowed by the catch cables was set at about 12%, and after confidence in the catch system was gained, the prescribed drift level was increased to approximately 16%. For the purposes of this study, the engagement of the safety catch cables to prevent the structure from going beyond the prescribed safe drift level is defined as *collapse*. This term is appropriate since judging by visual observations of the tests in which the catch cables engaged, the specimen generally would not have been able to maintain stability after experiencing such large drifts. Since the maximum drift level was increased, and the catch cables did not engage at precisely the same drift level for all tests with the same prescribed drift limit, the term collapse is used as a qualitative descriptor of behavior, not a specific numerical value.

4.4.3 Case Study of Two Repeated Full-Scale Brittle Fracture BP Pattern Tests

The brittle fracture BP pattern/0.6 second cosine pulse test was run twice, and the results are compared for these two tests to help determine the amount of variability inherent in the experimental setup. Percent differences are shown for in-plane displacement measures in Table 4-5, for other major global response quantities in Table 4-6, and for connection response quantities in Table 4-7.

The percent differences between the two BF BP tests (shown in boldface), named BF BP 1 and BF BP 2, provide an estimate of the amount of error in each response quantity due to the test setup and procedures. Similar quantities are calculated for the four repeated BF A tests discussed in the next section, and these two sets of results will be combined to arrive at the estimated error bounds for the experimental setup. In each table below, the benchmark BF BP differences are compared with differences between each BF BP case and the ductile baseline and ductile fracture cases.

Table 4-5. Percent differences in in-plane displacements and interstory drifts

Percent differences between		Maximum Relative Displacement			Residual Displacement		$\Theta_{1\ Max}$		$\Theta_{1\ Res}$	
		Base	**Story 1**	**Story 2**	**Story 1**	**Story 2**	**Story 1**	**Story 2**	**Story 1**	**Story 2**
BF BP 1	**BF BP 2**	**2.7**	**2.7**	**3.0**	**10.2**	**9.9**	**2.9**	**3.4**	**9.7**	**9.5**
BF BP 1	DB C	15.1	16.6	17.7	81.8	80.6	17.3	18.9	80.3	79.5
BF BP 2	DB C	12.0	13.5	14.2	64.9	64.4	14.0	15.0	64.3	64.0
Average of above 2		13.6	15.1	16.0	73.3	72.5	15.6	17.0	72.3	71.7
BF BP 1	DF BP	2.7**	0.8**	0.7**	3.5**	3.3**	0.7**	0.6**	3.3**	3.1**
BF BP 2	DF BP	0.0**	1.9**	2.3**	6.6**	6.4**	2.2**	2.7**	6.2**	6.2**
Average of above 2		1.4**	1.4**	1.5**	5.0**	4.8**	1.4**	1.7**	4.8**	4.6**

** Percent difference is less than or equal to that between BF BP 1 and BF BP 2

Table 4-6. Percent differences in major response quantities

Percent differences between		Max Relative Accel		Max Absolute Accel		Max Vb	Max OTM	λ_{Vb}	λ_{T1}
		Story 1	Story 2	Story 1	Story 2				
BF BP 1	**BF BP 2**	**14.4**	**11.0**	**34.5**	**2.5**	**2.0**	**0.2**	**17.3**	**17.1**
BF BP 1	DB C	2.3**	3.3**	0.0**	22.2	38.5	33.6	90.8	107
BF BP 2	DB C	11.9**	7.5**	34.5**	25.3	41.3	33.8	62.7	142
BF BP 1	DF BP	8.0**	5.1**	13.8**	1.2**	14.7	0.2**	11.7**	31.6
BF BP 2	DF BP	6.0**	5.6**	18.2**	3.8	16.9	0.1**	31.0	12.3**

** Percent difference is less than or equal to that between BF BP 1 and BF BP 2

Table 4-7. Percent differences in maximum values of connection response quantities

Percent differences between		Maximum θ_{conn}				Maximum M_{conn}			
		C1	C2	C3	C4	C1	C2	C3	C4
BF BP 1	**BF BP 2**	**10.4**	**7.5**	**9.1**	**3.8**	**1.1**	**2.0**	**4.7**	**1.9**
BF BP 1	DB C	43.0	37.3	33.0	31.3	27.1	36.7	4.9	5.4
BF BP 2	DB C	29.5	27.7	22.0	26.5	25.8	34.0	0.2**	7.4
BF BP 1	DF BP	0.4**	0.5**	0.1**	5.9	0.6**	5.6	2.0**	6.3
BF BP 2	DF BP	10.0**	7.0**	8.9**	2.0**	0.5**	3.6	6.8	8.4

** Percent difference is less than or equal to that between BF BP 1 and BF BP 2

Comparisons with the ductile baseline case show that the uncertainties in the test setup are generally smaller than the differences between behavior of the two hysteretic types. This indicates that the differences due to the connection hysteretic behavior are significant, since they are above the level determined by the two BF BP cases.

Comparisons with the ductile fracture case indicate another problem, which is that the ductile fractures may not have been very ductile after all. The relatively low scan rate of 100 Hz coupled with the rapidity of the fracture lead to few data points in the region of interest, as shown in Figure 5-18. This makes it very difficult to precisely determine the amount of pre-fracture plastic rotation. However, the velocity of the structure and the scan rate can be used to bound the possible amount of plastic rotation to a value much smaller than that seen in the large initial amplitude clevis connection tests (see Figure 3-8).

In almost all cases, the percent differences between the two BF BP cases are *larger* than between the BF BP and DF BP cases. All displacement and drift measures considered showed no *significant* difference (i.e., greater than the difference between BF BP cases) between ductile and brittle fracture hysteretic types. There are small differences in maximum base shear, but the percent differences in the moment for the fracturing connections show little to no increase for the ductile fracture case. Thus, the difference in base shear is not primarily due to a difference in hysteretic behavior in the fracturing connections. We can then conclude that for the response quantities of interest in this case study *there is not a significant difference in the behavior of the ductile fracture and brittle fracture connection types, and that the "ductile" fractures may not have been ductile at all.*

4.4.4 Case Study of Four Repeated Half-Scale Brittle Fracture A Pattern Tests

The wave propagation sequence performed using the 0.6 second cosine pulse at 50% amplitude with brittle fracture patterns provides another opportunity for making comparisons between repeated tests to help develop error bounds for the test setup. Four tests of the BF BP pattern were repeated, with the only significant changes being the gages where data were collected. The maximum percent and absolute differences between the four tests (Tests A–D) are shown in Table 4-8. Absolute differences are given due the very small numeric values of some of the response quantities (residual displacements in particular) where small absolute differences are masked by misleading large percent differences.

It is also a good idea to mention here that the coupons in the upper ductile baseline connections were not changed between tests in the interest of time, since little to no yielding occurred in each test. It can be shown from the percent differences in the connection response quantities shown in Table 4-8 that this practice did not significantly change the results and that it was therefore a rational cost-saving measure. The percent differences for these connection response quantities were less than those for the BF BP patterns, even though the absolute values were very small and were thus prone to large percent differences. The small absolute and percentage differences show the consistency of the connection-level results throughout the four tests.

As is apparent in Table 4-8, there were other cases which had very large percentage differences. This occurred for the residual displacements and residual interstory drift ratios, due to differences in small absolute values. However, the absolute differences in the displacement measures are very small and thus the large percent differences are misleading. In the case of the absolute accelerations in the first story, small values are not the problem and there is actually a sizeable difference of 0.12 g between the results. Since a similar difference was found for the previous case study on the BF BP patterns, it seems that there may simply be more variability in this acceleration value due to the higher modes, particularly the second mode.

Table 4-8. Percent differences between BF A pattern Tests A–D for major response quantities

Response quantity	Location	Percent Difference	Absolute Difference
Maximum relative displacement (in.)	Base	5.6	0.02
	Story 1	1.5	0.03
	Story 2	1.7	0.07
Residual displacement (in.)	Story 1	66.6	0.05
	Story 2	82.1	0.12
Maximum interstory drift ratio (%)	Story 1	1.6	0.06
	Story 2	2.1	0.07
Residual interstory drift ratio (%)	Story 1	120	0.14
	Story 2	101	0.12
Maximum relative acceleration (g)	Story 1	12.2	0.06
	Story 2	12.7	0.10
Maximum absolute acceleration (g)	Base	18.5	0.10
	Story 1	68.8	0.12
	Story 2	1.4	0.05
Maximum base shear (kips)		6.2	0.3
Maximum base overturning moment (kip-in.)		2.4	13
λ_{Vb} (%)		4.6	4.3
λ_{T1} (%)		28.3	4.9
Maximum connection rotation (rad)	C1	7.4	0.0017
	C2	6.3	0.0023
	C3	3.8	0.0007
	C4	5.9	0.0012

Table 4-8. — *Continued*

Response quantity	Location	Percent Difference	Absolute Difference
Maximum connection moment (kip-in.)	C1	2.5	3
	C2	4.5	5
	C3	6.8	7
	C4	2.3	3

4.4.5 Error Estimates and Impacts on Data Interpretation

It is plausible to assume based on the repeated BF BP and BF A pattern tests that the errors inherent in any of the high-level tests conducted are within the bounds shown in Table 4-9. Absolute error bounds are given for those quantities which may have small values (such as residual displacements) which lead to misleading large percent differences when the absolute differences are in fact small.

The uncertainty analysis of the two case studies resulted in several major findings which impact the interpretation of the data. Perhaps most important for subsequent data interpretation is the observation that the ductile fracture connections did not behave as anticipated. Based on the comparison of results of the 0.6 second cosine pulse tests discussed in Section 4.4.3, it can be reasonably concluded that the differences in most global and most local response quantities of interest for brittle and ductile fracture connection types are not significant with respect to the overall error present in the experimental setup. Additionally, there is a lack of evidence for plastic deformation in the moment-rotation hysteresis data for the ductile fracture cases. These data are relatively sparse in the neighborhood of the fracture, but not too sparse too detect significant amounts of plastic rotation.

These results lead to the conclusion that the ductile fracture was not very ductile, and little plastic deformation occurred, though it is impossible to determine the precise amount. Therefore, the data interpretation in Chapter 6 reflects this finding. The data for the ductile fracture patterns will still be distinguished from the data for the brittle fracture patterns by name, since the notches which initiate the fractures are physically different. However, the effects of the hysteretic type “ductile fracture” will not be presented as those of a distinct type of hysteretic behavior. Rather, when comparisons between hysteretic types are made, the term “fracture,” which encompasses both connection types, will be used instead.

Table 4-9. Estimated bounds on inherent system uncertainty by response quantity

Response Quantity	Amount of Error
Maximum relative in-plane displacements	< 5%
Residual in-plane displacements	< 10% or < 0.25 inch whichever is larger
Maximum in-plane interstory drift ratios	< 5%
Residual in-plane interstory drift ratios	< 10%
Maximum relative in-plane accelerations	< 15%
Maximum absolute in-plane accelerations	<20% or <0.2 g, whichever is larger
Maximum in-plane base shear	< 10%
Maximum in-plane base overturning moment	< 10%
Maximum connection moments	< 10%
Maximum connection rotations	< 10%
Maximum column moments	< 10% or < 1 kip-in, whichever is larger
Maximum column axial loads	< 5% or < 1 kip, whichever is larger
Maximum beam strains, high-speed data	< 8%
λ_{Vb}	< 20%
λ_{T1}	< 20%
Maximum in-plane table displacements	< 3%
Maximum out-of-plane table displacements	< 0.2 inch
Maximum in-plane table accelerations	< 0.3 g
Maximum out-of-plane table accelerations	< 0.3 g
Maximum relative out-of-plane displacements	< 0.4 inch

Another important finding was the relatively large uncertainty in the accelerations relative to most of the other response quantities. There are several contributions this uncertainty, such as the unintended motions of the shaking table, the contribution of higher modes, and the effects of fracture. Accelerations tend to be affected by these factors to a much greater degree than displacements. For the most part, the effects of spurious shaking table motions were confined to highly transient “spikes” in the accelerations and thus had little effect on the specimen’s overall behavior.

The effects of instrument errors on the quality of the data was small, since most errors of this type were readily detected and corrected. Most errors were obvious, and data with these errors were not considered during interpretation. On the whole, the sources of error involved in this test are manageable and generally detectable, and the data are therefore valid, with reasonable errors and test-to-test variability that are to be expected in experimental work of this type.

5 Experimental Results

The results of the shaking table tests are presented in this chapter. The tests were conducted in late May and early June of 2001. Elastic dynamic properties of the system are presented in Section 5.1. The results from the high-level shaking table tests are then presented in pictorial, tabular, and graphical format in Sections 5.2 through 5.5, with the focus on making general behavioral observations for each hysteretic behavior type. Detailed summaries of the data can be found in Appendix D.

5.1 SYSTEM CHARACTERIZATION

Several tests were performed in order to determine important dynamic characteristics of the test specimen. The mass, fundamental vibration period, and equivalent viscous damping ratio in the first mode were identified from these tests.

In order to establish the total as-built mass of the system accurately, a load cell was attached to the laboratory crane and the specimen was lifted up off its base. The total weight of the specimen was found to be 14.5 kips, which gives a mass of 0.0376 kip-s^2/inch.

The vibration properties of the structure in its fundamental mode were estimated using free vibration, or "pullback" and release tests. The shaking table platform was secured before the pullback tests were performed. Since this was a time-consuming operation, pullback tests were only performed the first time a certain configuration was tested.

The pullback tests were performed by attaching a cable apparatus to the top of the east side main column and to an attachment point on the floor of the lab. The cable was inclined at 23º. The cable apparatus was equipped with a turnbuckle which was used to tighten the cable, as well as a load cell to measure the applied force. By tightening the cable, the structure was "pulled back" to an initial displacement of approximately 1/2 inch. The specimen remained well within the elastic range during these tests. At the end of the cable apparatus near the specimen, a necked down threaded rod, or “dog-bone” connector was used to attach the cable to the specimen. When the cable had been tightened, the dog-bone was cut suddenly to release the specimen, and the resulting free vibration was recorded using the data acquisition system. A typical displacement response at the top of the frame is shown in Figure 5-1, with the reference position as the pulled back position.

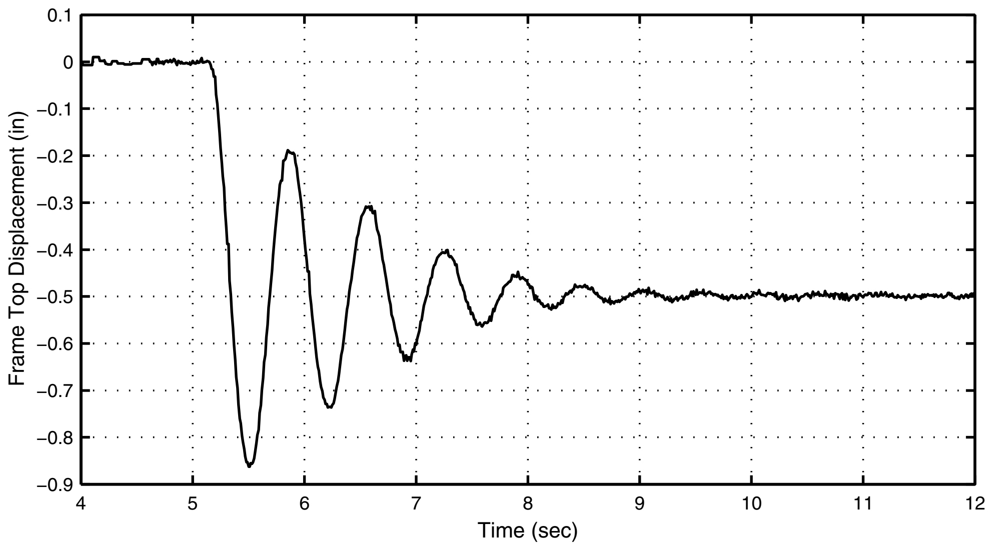

Figure 5-1. Typical displacement response at the top of the frame during a pullback test

The period and damping in the fundamental mode were then determined from the response time history using the logarithmic decrement method (such as in Chopra, 1995). Periods and damping ratios for each configuration are shown in Table 5-1. A measure of the flexibility of the system for each connection configuration was obtained from the deformation-force relationships generated by pulling the structure back for each free vibration test. The value of the displacement at the roof $u_2(x)$ for a unit roof load, which is the f_{22} flexibility coefficient, was found by normalizing the measured displacement by the applied force. The value of this flexibility coefficient for each of the configurations is also listed in Table 5-1 below.

Table 5-1. Specimen mean fundamental mode properties from pullback free vibration tests

Configuration	Flexibility (in./kip)	Period (sec)	Damping ratio (%)
Ductile baseline C	0.59	0.65	1.9
Deformation softening B	0.59	0.64	1.7
Deformation softening C	0.48	0.62	1.8

Table 5-1. — ***Continued***

Configuration	Flexibility (in./kip)	Period (sec)	Damping ratio (%)
Brittle fracture BP	0.59	0.67	1.7
Brittle fracture CP	0.59	0.63	1.7
Ductile fracture BP	0.63	0.64	1.7
Ductile fracture CP	0.59	0.62	1.8
Strength degrading C	0.53	0.64	2.2

Random signal, or white noise tests were also used to determine the vibration properties. The specimen was subjected to a low-level random signal (like that shown in Figure 4-13), which had a peak acceleration of approximately 0.05 g. The discrete fast Fourier transform (DFFT) algorithm in MATLAB (The Mathworks, Inc., 1999) was then used to determine the Fourier amplitude spectrum, from which the fundamental period and damping could be obtained using the half-power bandwidth method. The mean values of period and damping ratio in the fundamental mode, which were calculated using all tests of each configuration are shown in Table 5-2. Instances where only one test was performed for a particular configuration are noted with an asterisk.

Table 5-2. Specimen mean fundamental mode properties from white noise tests

Configuration	Period (sec)	Damping ratio (%)
Ductile baseline C	0.62	1.5
Deformation softening B	0.60	1.3
Deformation softening C	0.55	0.9
Brittle fracture A	0.66	1.6
Brittle fracture BP	0.63	1.6
Brittle fracture BB	0.60*	1.7*
Brittle fracture CP	0.61	1.4
Brittle fracture CB	0.64	1.7
Ductile fracture BP	0.59	1.4
Ductile fracture CP	0.61	1.7
Ductile fracture CB	0.56*	1.4*
Strength degrading C	0.57*	1.2*

*denotes that only a single value was available

In general, the vibration properties obtained from the free vibration and white noise tests were in agreement, though the white noise tests tended to predict lower damping ratios. The results from the white noise tests are less reliable than those from the free vibration tests, since the free vibration tests produced smooth displacement histories which facilitated the accurate calculation of vibration properties.

5.2 GENERAL OBSERVATIONS REGARDING GLOBAL AND MEMBER BEHAVIOR

The general behavior of the specimen when the connections have a particular type of hysteretic behavior is examined in the following subsections. Representative case studies are considered here, and more exhaustive summaries of the data are provided in Appendix D. Hysteretic behavior types are defined in Section 1.1, and have a one-to-one correspondence with the clevis-based connection types in Table 3-1. For simplicity, the case studies chosen for all hysteretic types except the ductile baseline and strength-degrading types are the B patterns with the 1.2 second cosine pulse excitation. The C pattern is used for the ductile baseline hysteretic type, since it is the only pattern possible. Since the strength-degrading hysteretic type was only tested with the C pattern and the JSE17 ground motion, that combination is used. In all of the study cases, the catch cables were not engaged and did not interfere in any way with the reported behavior of the specimen.

In addition to discussing the behavior of the case studied, selected global behavior measures for the other tests with the same hysteretic behavior type (but different patterns or excitations) are provided in tabular form with each case study. In each of these tables, the case study data are indicated by a boldface border. As a reminder, pattern definitions and excitations are found in Sections 4.1.2 and 4.1.1, respectively, and global behavior measures are defined in Section 4.4.2.

5.2.1 Ductile Baseline Hysteretic Behavior

The ductile baseline case provides a reference against which other behavior can be compared. As such, a careful observation of the behavior of this case is necessary. As discussed in the previous section, the case chosen for the study of ductile baseline hysteretic behavior is the 1.2 second cosine pulse case. The behavior will be examined in two parts: global, which includes the 3 global measures defined in Section 4.4.2, and local, which consists of the connection hysteretic behavior only for simplicity.

5.2.1.1 Global behavior

The global behavior of this case is characterized by one large displacement excursion followed by an oscillating response that quickly damps out, as shown in the interstory drift time history in Figure 5-3. Residual displacements are small, as is evident in the post-test photographs shown in Figure 5-2.

Figure 5-2. Residual displacement of specimen with ductile baseline connections after testing

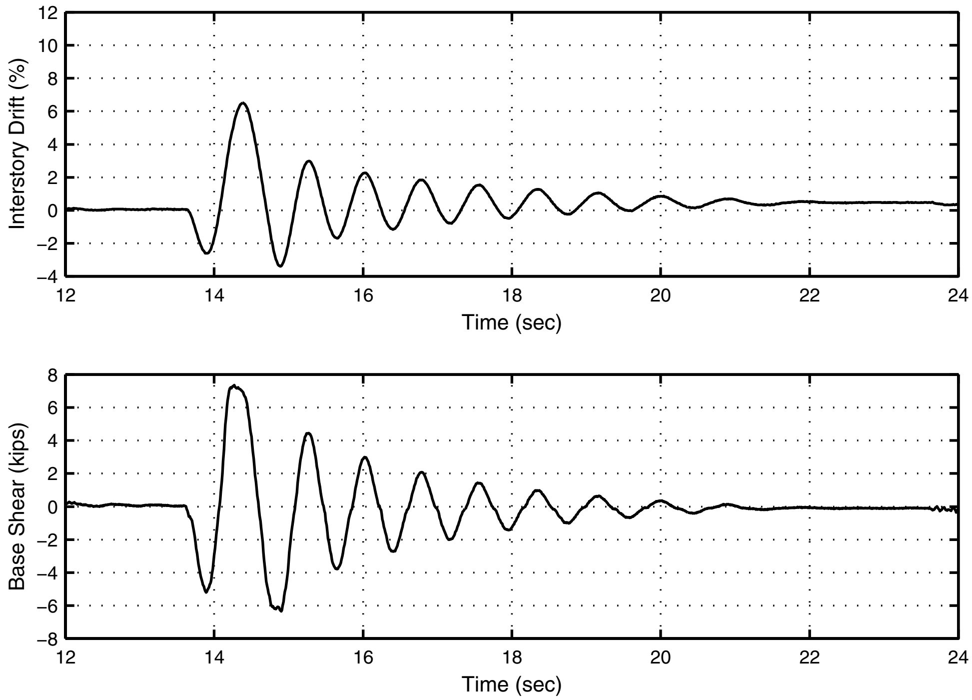

Figure 5-3. First-story interstory drift ratio and base shear time histories

The base shear in Figure 5-3 “flattens out” during the first positive and second negative excursions, indicating that plastic hinges are forming at the connections. The time history clearly indicates the two excursions where significant yielding (and some buckling of the compression coupons) takes place in the connections. As shown in Figure 5-4 and Table 5-3, some degradation in the maximum base shear is observed during the largest ductile cycle. Also, the period elongation is about 13%, indicating that the stiffness of the system is not greatly reduced. These values provide a baseline for comparing the other connection types.

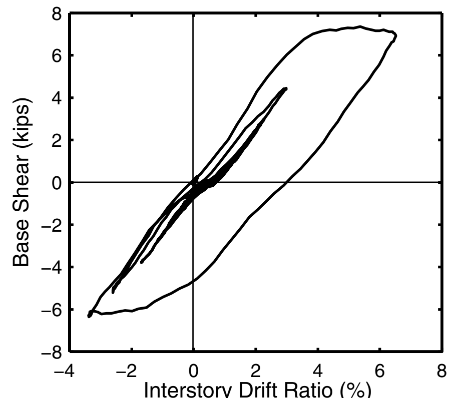

Figure 5-4. Base shear-interstory drift ratio hysteresis

The results are similar for JNF01. Some more drift and degradation in base shear and more period elongation were observed for the 0.6 second cosine pulse case. In the substantially longer duration JSE17 case, similar peak drift was observed but far greater deterioration occurred.

Table 5-3. Summary of global behavior measures for ductile baseline tests

Excitation	**Pattern**	$\Theta_{1\ \mathrm{Maximm}}$ **(%)**	$\Theta_{1\ \mathrm{Residual}}$ **(%)**	λ_{Vb} **(%)**	$\lambda_{T\,1}$ **(%)**
0.6 sec cosine pulse	C	8.6	3.8	82	17
1.2 sec cosine pulse	C	6.5	0.4	94	13
JNF01	C	4.9	0.9	92	15
JSE17	C	6.4	2.0	77	29

5.2.1.2 Local behavior

The most important observation regarding the local connection behavior for this case was that the connections behaved as expected. The before and after pictures in Figure 5-5 show that these connections behaved as intended — no severe buckling or damage to the coupon jackets is evident though the maximum drifts were large. A close-up of one of the coupons after testing is shown in Figure 5-6, and it is clear that the jackets on the coupons functioned properly and limited buckling. Limiting buckling is crucial to obtaining stable, ductile hysteretic behavior.

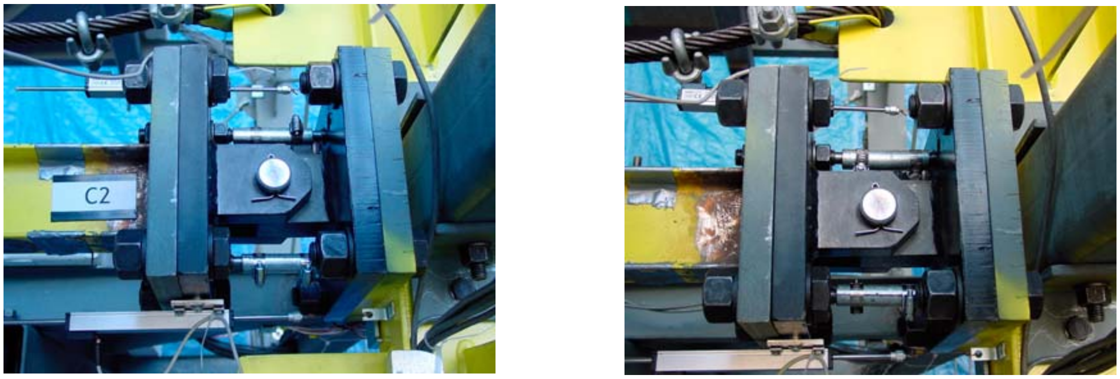

Figure 5-5. Ductile baseline connection C2 before (left) and after (right) testing

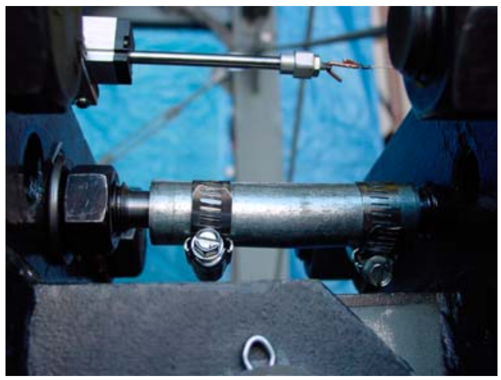

Figure 5-6. Close-up of buckled ductile baseline coupon after testing

As shown in Figure 5-7, the behavior of the ductile baseline connections was very similar to that observed in the quasi-static connection component tests. The hysteretic loops are full, and there is a relatively small amount of degradation of strength and stiffness. The loops are not bilinear, but are fairly close, particularly for the shaking table test study case. In both cases there is a change in slope similar to the Bauschinger effect. In the shaking table test, there is a single predominant plastic excursion in one direction and little residual permanent rotation. In addition, the hysteretic loops are slightly pinched as the force goes through zero due to slip in the connection between the coupons and the clevis.

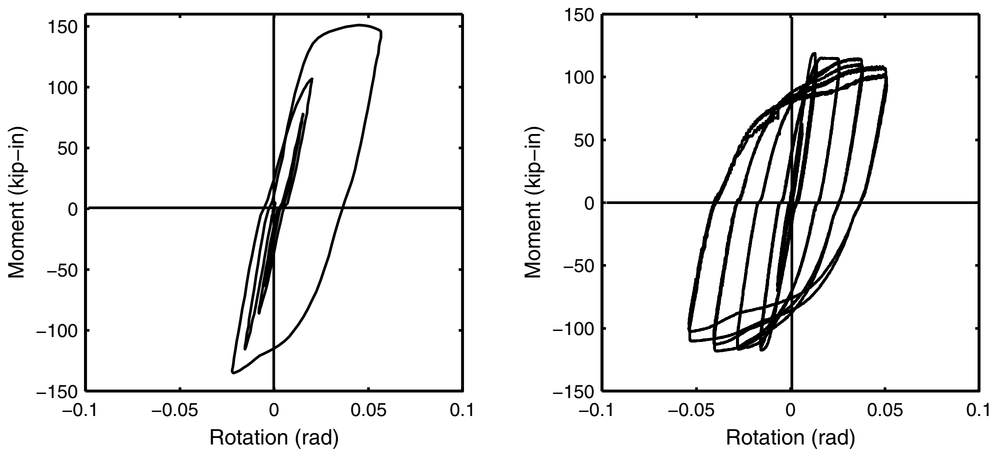

Figure 5-7. Comparison of connection hysteresis for shaking table test (left) and quasi-static test (right)

The post-degradation base shear ratio λ_{Vb} of the system is quite high, though not 100%. This does not satisfy the assumption of bilinear ductile behavior commonly used for analysis, but it comes close enough to satisfy *realistic* ductile behavior that might be expected in steel connections. The same can be said for period elongation, as the ideal bilinear assumption of no change in loading stiffness is unrealistic. Overall, the ductile baseline connections behaved in a stable ductile manner as expected.

5.2.2 Brittle Fracture

The case study selected for the brittle fracture hysteretic type is the BP pattern with the 1.2 second cosine pulse. In this pattern, the flanges which are in tension in the first story when the structure is moving in the positive direction are capable of fracture. In this case, both of the connections which were capable of fracture did in fact fracture virtually simultaneously during the specimen's first positive excursion (see Figure 5-9). Key response quantities for this case (highlighted by a boldface border), as well as other tests of brittle fracture patterns, are tabulated in Table 5-4.

5.2.2.1 Global behavior

The interstory drift time history, shown in Figure 5-9, is similar to that of the ductile baseline case: it is smooth and is characterized by a single large displacement excursion, followed by decaying oscillations. There is no sudden jump in the response when fracture occurs, as shown in the close-up of the large excursion in Figure 5-9. This is not an intuitive result—one might expect the sudden changes in system strength and stiffness caused by connection fracture to show up as a sudden change in the global displacement response.

The maximum interstory drift ratio of the specimen increased by 65% over the ductile baseline case, from 6.5% to 10.4%, however. The residual drifts also increased significantly, from virtually zero (0.4%) to 4.1%. The residual drifts were readily apparent visually, as shown in the post-test photos in Figure 5-8. However, as the time history in Figure 5-9 and the photos in Figure 5-8 show, structure remained stable and did not collapse.

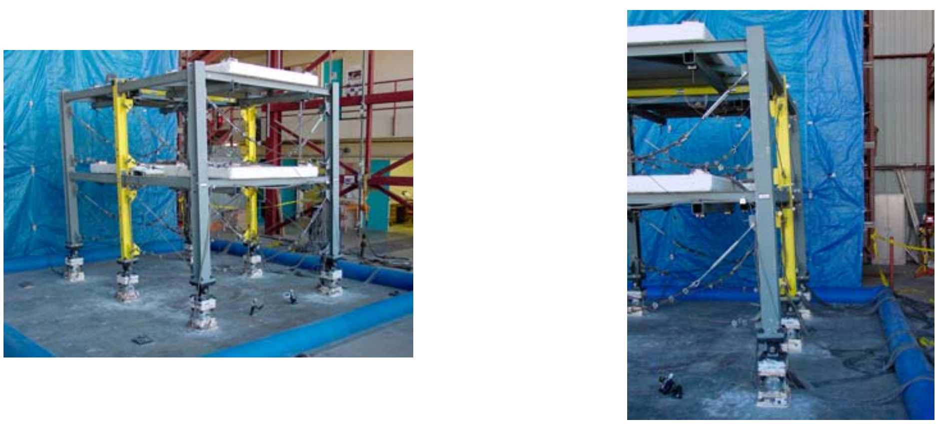

Figure 5-8. Residual displacement of specimen with brittle fracturing connections in the BP pattern after testing

In contrast to the smoothness of the displacement time history, the base shear time history in Figure 5-10 shows a clear discontinuity in the response at the time of fracture. This discontinuity is best described as a pause in the increase of base shear — the value increases at a greatly reduced rate for about 0.03 seconds. The base shear does not immediately decrease at fracture because the ductile connections in the top frame have not yet yielded and are able to provide additional capacity. After the initial pause due to fracture, the base shear increases until the ductile connections yield. Once this occurs, the base shear begins to decrease significantly.

The magnitude of the strength deterioration due to the fractures is indicated by a decrease of λ_{Vb} to 65% from the 94% observed for the ductile case. Similarly the period of the specimen also elongated by 36%, as opposed to 13% for the ductile case.

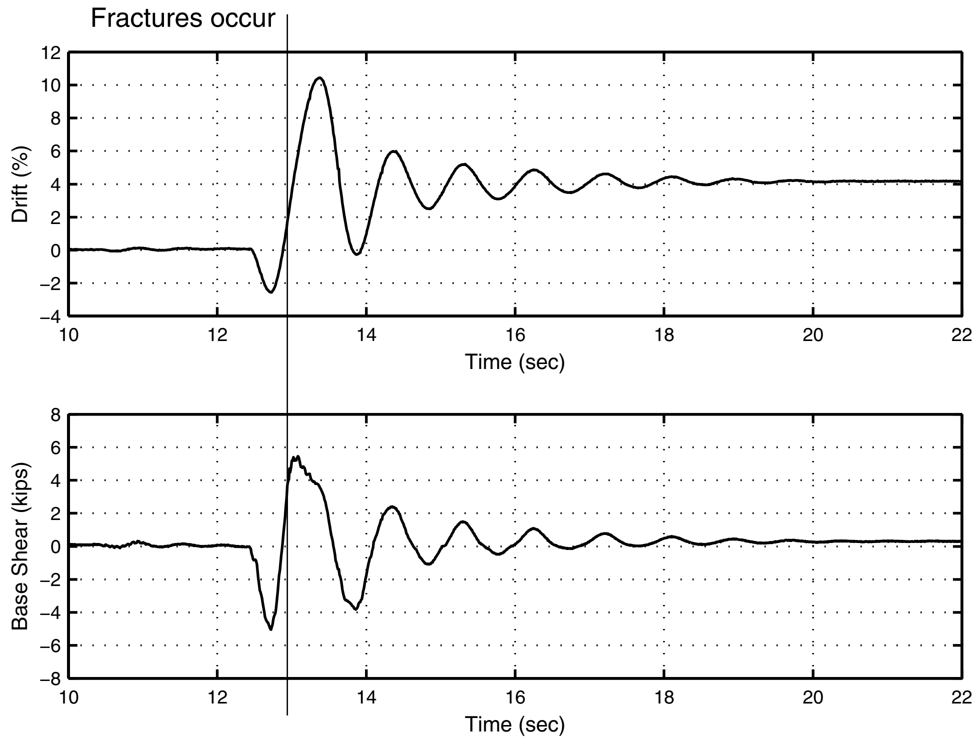

Figure 5-9. First-story interstory drift and base shear time histories

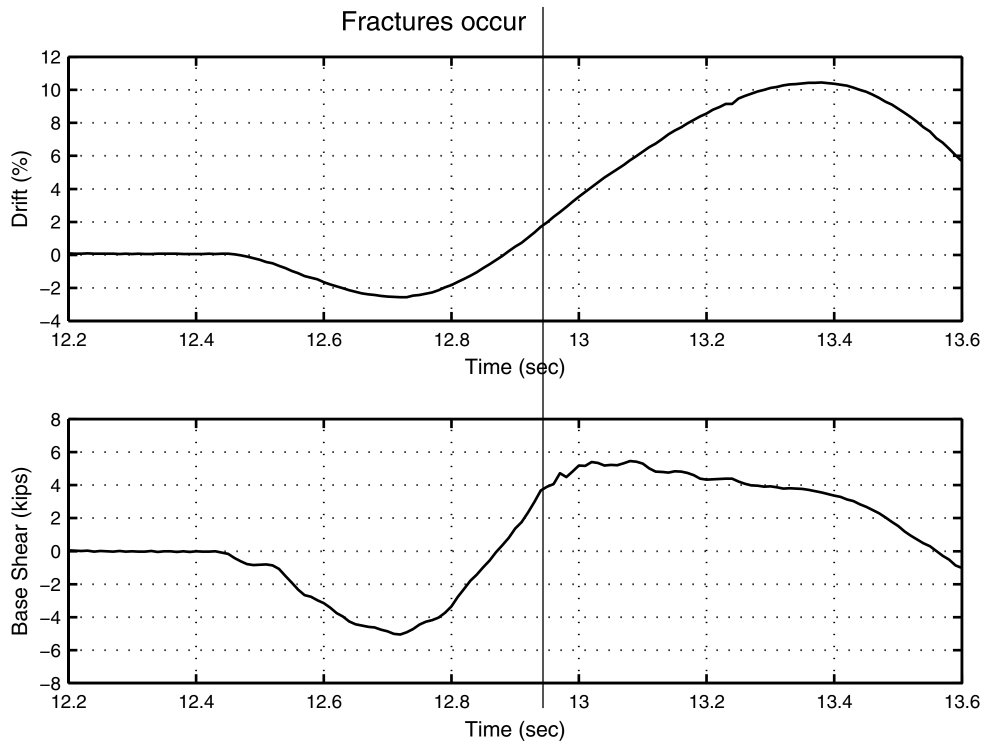

Figure 5-10. Close-up of interstory drift and base shear time histories

Table 5-4. Summary of global behavior measures for brittle fracture tests

Excitation	Pattern	Excitation Amplitude	$\Theta_{1\ \mathrm{Maximum}}$ (%)	$\Theta_{1\ \mathrm{Residual}}$ (%)	λ_{Vb} (%)	λ_{T1} (%)
0.6 sec cosine pulse	A	50%	3.8	0.3	93	17
	A	50%	3.9	0.2	97	19
	A	50%	3.8	0.1	95	22
	A	50%	3.9	0.2	94	22
	A	50%	3.9	0.2	97	14
	BP	50%	4.2	0.7	90	23
	BP Run 1	100%	10.0	6.9	43	35
	BP Run 2	100%	9.8	6.3	50	41
	CP	100%	12.7	11.7	9	n/a
1.2 sec cosine pulse	BP	100%	10.4	4.1	65	36
	CP	50%	2.7	0.2	80	22
	CP w/2 fracture	75%	12.5	11.9	28	50
	CP	100%	18.1	16.6	20	n/a
	CB	100%	10.0	3.5	57	52

Table 5-4. — *Continued*

Excitation	Pattern	Excitation Amplitude	Θ_1 Maximum (%)	Θ_1 Residual (%)	λ_{Vb} (%)	λ_{T1} (%)
JNF01	BB	100%	5.1	0.8	82	26
	CB	100%	4.8	0.4	72	41
JSE17	CB	100%	8.1	4.1	50	22

5.2.2.2 Local behavior

Figure 5-11 shows connection C2 (see Figure 3-11 for location) before and after fracture, and the residual plastic deformation in the connection is apparent. The fractured bottom coupon has “opened up,” as shown in the close-up view in Figure 5-12. The top coupon for this case was not constrained to prevent buckling and a significant buckle inward towards the clevis pin is evident. Inward buckling was observed in almost every test in this series, with very few exceptions. The coupons are predisposed to buckle inward because they are fixed at the ends to the clevis end plates, and these end plates rotate as the frame deforms, forcing the compression coupon to bend inward toward the clevis pin.

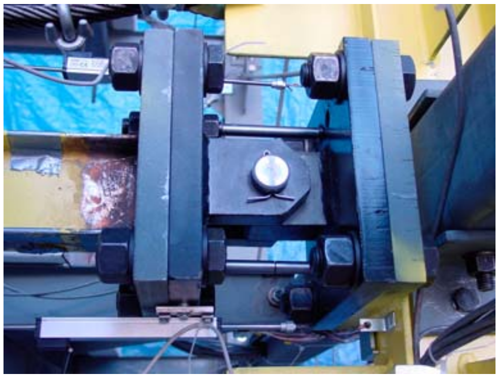

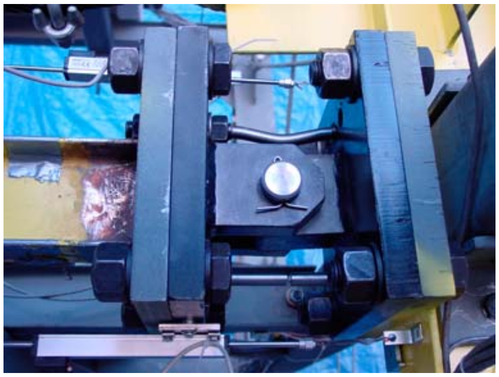

Figure 5-11. Brittle fracture connection C2 before (left) and after (right) testing

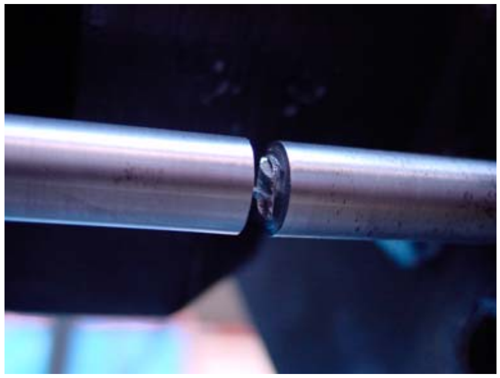

Figure 5-12. Close-up of fractured coupon after testing

As shown in Figure 5-13, the moment-rotation hysteretic behavior is similar for both the shaking table and the quasi-static tests. The maximum value for the moment prior to fracture was most probably not measured correctly for the shaking table tests due to the coarseness of the scan rate (100 Hz) compared with the rate of loading. This coarseness is indicated by the marked data points in Figure 5-13, and it is apparent that points are sparse during the rapid loading preceding fracture for the shaking table test. Since the peak of the hysteresis loop appears to have been "cut off," the maximum moment and the point of fracture most probably occur sometime between the two data points closest to the positive maximum. In contrast, the data from the quasi-static test are dense preceding the fracture, so the maximum pre-fracture moment could be measured accurately.

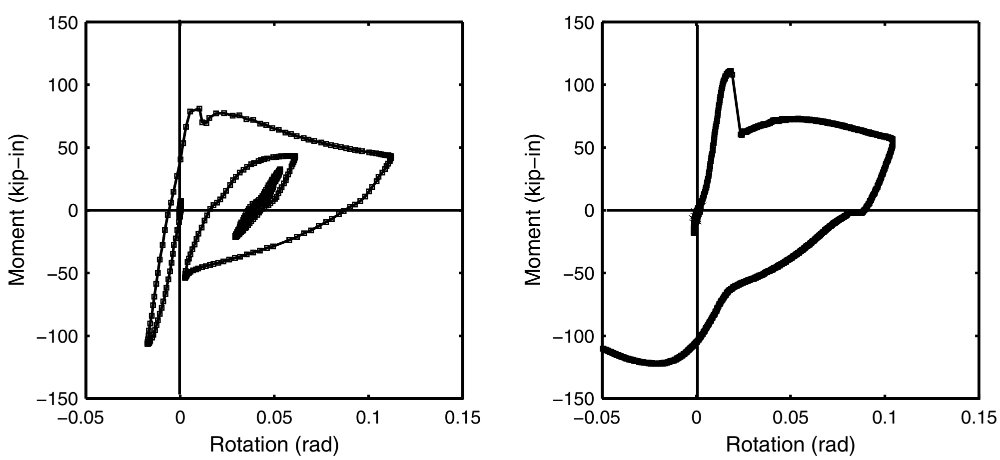

Figure 5-13. Comparison of connection hysteresis for shaking table test (left) and quasi-static test (right)

Though the hysteretic loops look very similar for the most part, the relatively low scan rate makes it difficult to show that the fracture was brittle. However, the high-speed strain data, which will be discussed in Section 5.4, show that no plateau in strain amplitude that would be characteristic of yielding occurred prior to fracture for any of the tests. Examination of the fractured test coupons also showed no evidence of yielding in the coupon body. It can therefore be concluded that there was little to no plastic rotation prior to fracture.

Also notable in Figure 5-13 is the presence of significant negative post-fracture stiffness in the hysteresis during the large excursion following fracture. In addition, the unloading and reloading stiffness are reduced after the large excursion in the shaking table test, with Bauschinger-like effects occurring during reloading in subsequent cycles.

5.2.3 Ductile Fracture

The pattern and excitation combination used for the ductile fracture study case was also the BP pattern and the 1.2 second cosine pulse. Both fracture-capable connections in the first story did actually fracture, and the fractures were simultaneous within the resolution of the data, which means that they were within 1/100 of a second of one another. Maximum values of key response quantities and residual values of displacement are listed in Table 5-5, with the study case highlighted by a thick outline.

5.2.3.1 Global behavior

The displacement response history shown in Figure 5-15 is similar to that of the brittle fracture case, but the maximum drift was only 9.3% as opposed to 10.4%. The drifts for the ductile fracture case were still larger than the ductile baseline case by 46%, however. The residual drift of 2.6% was in between those of the ductile baseline and brittle fracture cases, which were 0.4% and 4.1%, respectively. The specimen remained stable, and the residual drift, shown in Figure 5-14, is visibly smaller than that of the brittle fracture case.

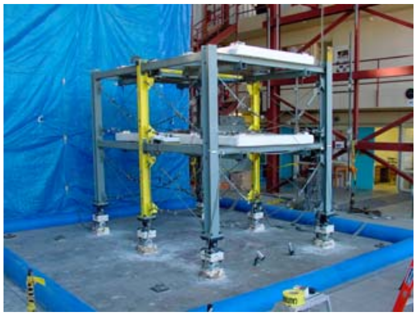 

Figure 5-14. Specimen with ductile fracturing connections in the BP pattern after testing

As shown in Figure 5-15, the fractures do not cause any sudden discontinuity in the global displacement response. However, the fractures do cause a discontinuity in the base shear response similar to that seen for brittle fracture. However, in contrast to the brittle fracture case the base shear does not increase as much after fracture. The close-up of the base shear time history in Figure 5-16 shows some transient high-frequency response after fracture that does not appear in the interstory drift time history.

The λ_{Vb} value of 70% is slightly higher than that for brittle fracture (65%), but still well below that of the ductile baseline case, indicating significant reduction in strength capacity of the specimen due to fracture. The period elongation is 41%, which is larger than the 36% seen for brittle fracture and approximately 3 times the 13% of the ductile case.

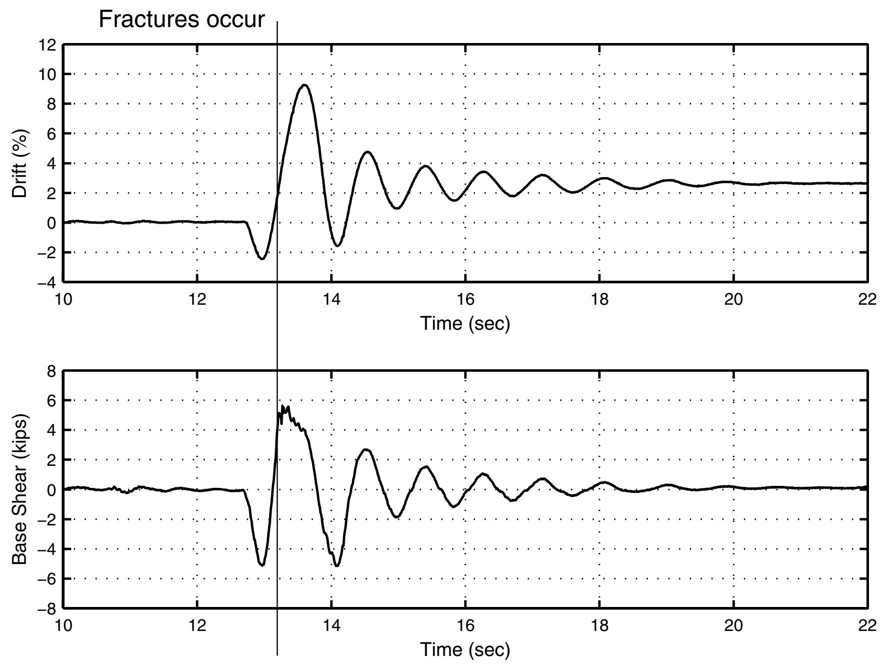

Figure 5-15. First-story interstory drift and base shear time histories

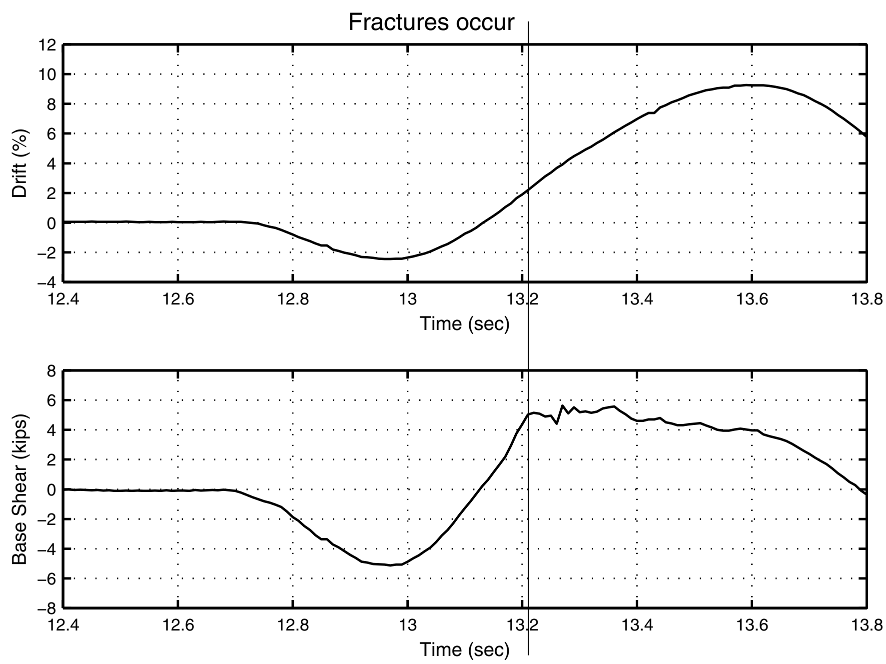

Figure 5-16. Close-up of interstory drift and base shear time histories

Table 5-5. Summary of global behavior measures for ductile fracture tests

Excitation	Pattern	Excitation Amplitude	Θ_1 Maximum	Θ_1 Residual	λ_{Vb}	λ_{T1}
			(%)	(%)	(%)	(%)
0.6 sec cosine pulse	BP	100%	10.0	6.7	38	46
	CP	100%	13.2	12.2	8	n/a
1.2 sec cosine pulse	BP	100%	9.3	2.6	70	41
	CP	100%	18.4	17.0	14	n/a
JNF01	CB	100%	5.0	0.7	72	51

5.2.3.2 Local behavior

As shown in Figure 5-17, the fractured top coupon has “opened up” and the bottom coupon, which was not restrained against buckling, shows a sizeable inward buckle. The connection shown in these photos is C1, because the after photo for C2 is not available. The behavior of these two connections is very similar, with only the position of the fracturing and buckling coupons (and therefore the signs of the moments) reversed. Connection hysteresis is shown for C2 in Figure 5-18, since it has the same sign as the quasi-static test, and thus makes for a more straightforward comparison.

Figure 5-17. Ductile fracture connection C1 before (left) and after (right) testing

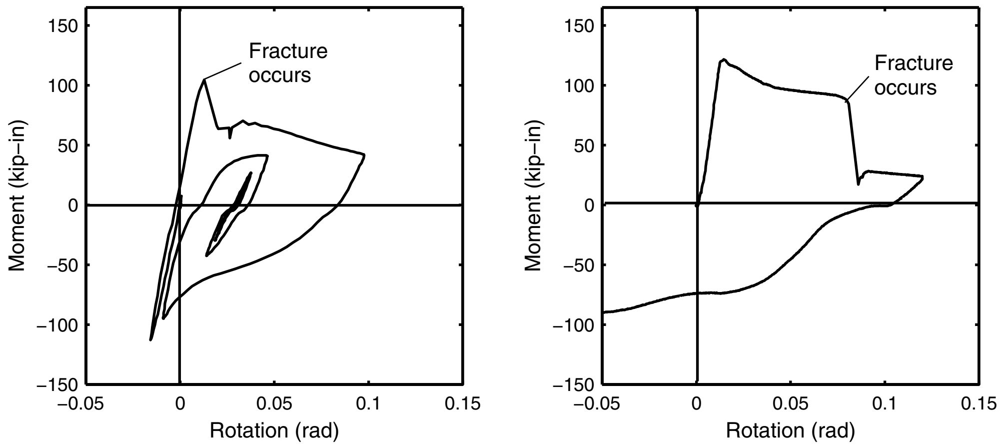

Figure 5-18. Comparison of connection hysteresis for shaking table test (left) and quasi-static test (right)

From the connection hysteretic loops in Figure 5-18, it is apparent that the connection was not as ductile prior to fracture as intended, or as the quasi-static tests indicated that it was. The moment-rotation relation from the large amplitude, pulse-like quasi-static test of the ductile fracture configuration showed a significant yield plateau, which was not present in the moment-rotation relation from the shaking table test with the 1.2 second cosine pulse excitation. Because of this, the ductile configuration clearly did not behave as intended — rather, it behaved in similar fashion to the brittle case.

It is not possible to determine with certainty the amount of yielding in the connection before fracture, since the scan rate is coarse and no high-speed data were taken. However, it can be shown through the error analysis discussed in Section 4.4.5 that the differences between ductile and brittle connection configurations are not significant when compared to the general level of error present in the tests. It is therefore plausible to assume that the "ductile" fracturing connections had little or no plastic rotation prior to fracture, similar to the brittle fracturing connections.

Degradations in stiffness similar to those seen in the brittle fracture case are also evident in Figure 5-18. These include significant negative post-yield stiffness during the single large excursion and reduced unloading and reloading stiffness in subsequent cycles. The increase in stiffness in the bottom left quadrant for the large shaking table test excursion indicates that either the two halves of the fractured coupons are bearing on each other, or the buckled coupons are straightening out in tension, both of which providing increased stiffness. The stiffening associated with bearing does not occur in any of the smaller, later cycles.

5.2.4 Deformation Softening Hysteretic Behavior

The B pattern was used for the deformation softening case study, along with the 1.2 second cosine pulse excitation. Deformation softening connections were placed in the first story, while the second-story connections were ductile baseline.

5.2.4.1 Global behavior

The interstory drift time history for this case, shown in Figure 5-20, has many of the same characteristics as the previous cases: a smooth response with a single large displacement excursion, followed by decaying free vibration oscillations. The maximum interstory drift ratio of 10.5% is about 65% larger than that of the ductile baseline case. This drift is about the same as that of the brittle fracture case and slightly larger than that of the ductile fracture case. However, the residual drifts of 2.8% are more similar to those of the ductile fracture case (2.6%). These residual drifts, as well as the stability of the frame after testing, are apparent in Figure 5-19.

Figure 5-19. Specimen with deformation softening connections in the B pattern after testing

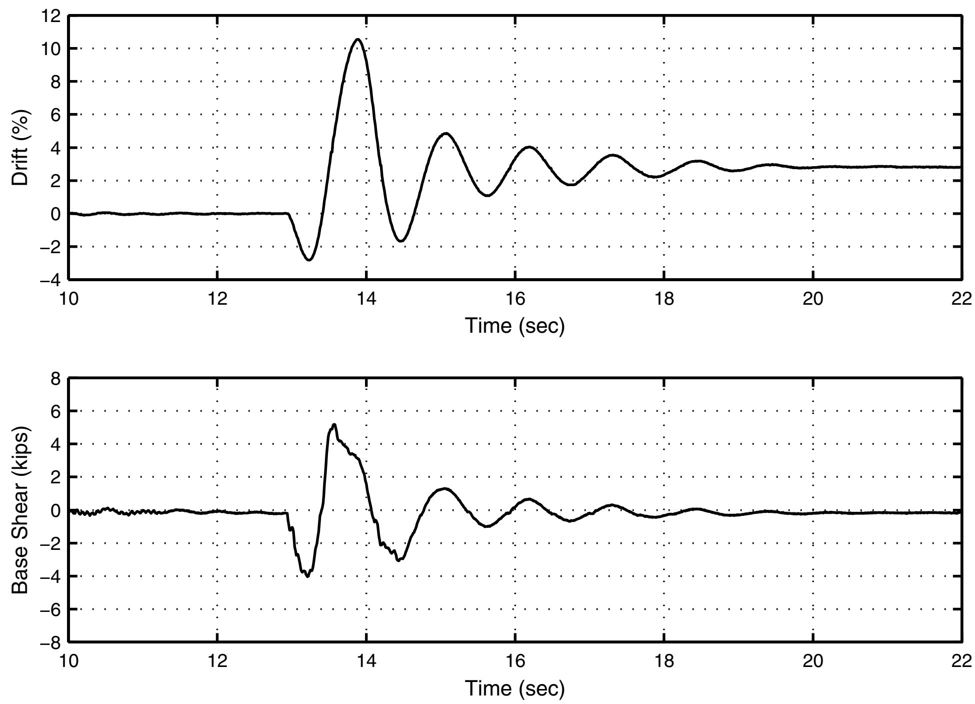

Figure 5-20. First-story interstory drift and base shear time histories

As shown in Figure 5-20, the interstory drift time history is smooth for this case, as expected, but the base shear time history is not. Degradation in the base shear occurs due to buckling of the coupons in the first story and yielding of the ductile baseline connection in the second story. The base shear time history also shows high-frequency response during the first second or so of the pulse, which may be due in part to the way the coupons were connected to the clevis.

Since the coupons had nuts placed only on the inside of the clevis end plates, they could take only compression. When placed in tension, the coupon simply slid through the holes and thus did not straighten out again after buckling. Since the coupon was threaded to allow the placement of the inside nut, the coupons might not slide smoothly and friction would be generated, allowing a small amount of tension capacity. This behavior during sliding may have affected the base shear time history to a small degree.

Significant buckling of the coupons was observed during two excursions, the first positive excursion and the second negative excursion. Interestingly, the base shear decreases during the yield period in the first positive excursion but increases during the second yield excursion. The increase in the base shear can be explained by the hysteretic behavior of the deformation softening connections, which is shown in Figure 5-23. These loops are extremely pinched (since the coupons cannot take tension), and the connection moments, and thus the base shear, can suddenly increase when the coupons begin to resist compression.

Table 5-6 shows the effects of the degradation in the first story connections, which are responsible for most of the degradation in system properties. The residual base shear ratio is 60%, indicating a significant reduction in strength has occurred, but the structure maintains some capacity due to the ductile baseline connections in the second story. The reduction in stiffness due to buckling of the coupons combined with the pinched hysteretic behavior causes a period elongation of 76%. This is substantially more elongation than that observed for any of the comparable study cases discussed in this chapter.

Table 5-6. Summary of global behavior measures for deformation softening tests

Excitation	Pattern	Excitation Amplitude	$\Theta_{1\ \mathrm{Maximum}}$ (%)	$\Theta_{1\ \mathrm{Residual}}$ (%)	λ_{Vb} (%)	λ_{T1} (%)
0.6 sec cosine pulse	B	100%	8.7	5.1	45	52
	C	100%	11.1	10.5	0	n/a
1.2 sec cosine pulse	B	100%	10.5	2.8	60	76
	C	100%	18.6	17.1	32	n/a
JNF01	C	100%	4.3	2.7	51	128

5.2.4.2 Local behavior

As shown in Figure 5-21, all of the coupons in the connection are buckled after testing. The previously noted nut placement did not allow the coupons to straighten out. This is apparent in the "after" picture at right in Figure 5-21, where the top coupons have shortened enough to pull the nut about a quarter inch away from the clevis end plate. The effects of this behavior are evident in the hysteretic loops shown in Figure 5-23, which shows large negative post-yield stiffness and severe pinching. In addition, the maximum moment is considerably smaller than what was seen for the other cases. This is due to the inability of the coupons to resist tension, which reduces the moment arm by half.

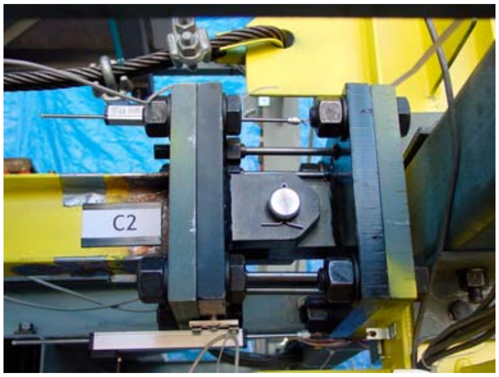

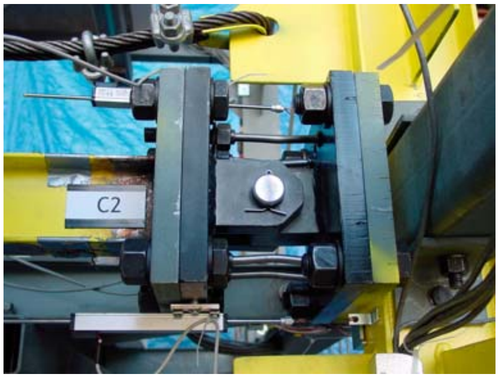

Figure 5-21. Deformation softening connection C2 before (left) and after (right) testing

Figure 5-22. Close-up of buckled coupon after testing

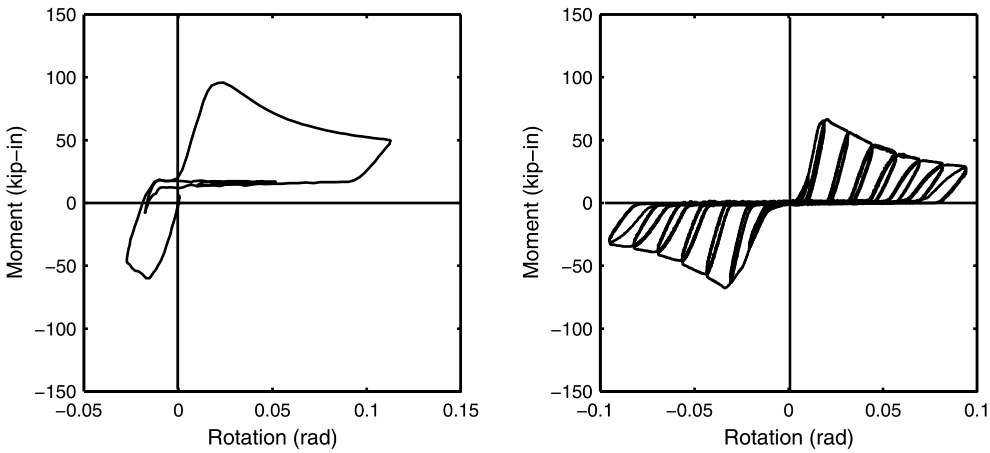

Figure 5-23. Comparison of connection hysteresis for shaking table test (left) and quasi-static test (right)

The moment-rotation behavior shown in Figure 5-23 indicates very good agreement between the shaking table and quasi-static test results. The connection behaved as intended for the shaking table loading, with the negative post-yield stiffness dominating the response during the pulse, and the pinching occurring during free vibration afterward.

5.2.5 Strength-Degrading Hysteretic Behavior

Since the strength-degrading pattern was only tested with one excitation/pattern combination, the case study is by necessity that case, which consists of the C pattern and the JSE17 (Llolleo-based) ground motion. Maximum values of key response quantities and residual values of displacement quantities are listed in Table 5-7.

5.2.5.1 Global behavior

The interstory drift time history in Figure 5-25 shows that there were many cycles of motion due to the long duration of the excitation. Many of these cycles had maximum drifts greater than 2%, and one large cycle at about 25 seconds caused the maximum drift of 6.8%. This single large cycle was responsible for most of the permanent deformation, and the remainder of the displacement response occurs as the specimen vibrates about the new equilibrium position. The residual drift, which is visually apparent in the post-test photos in Figure 5-24, is 2.7%.

Figure 5-24. Specimen with strength connections in the C pattern after testing

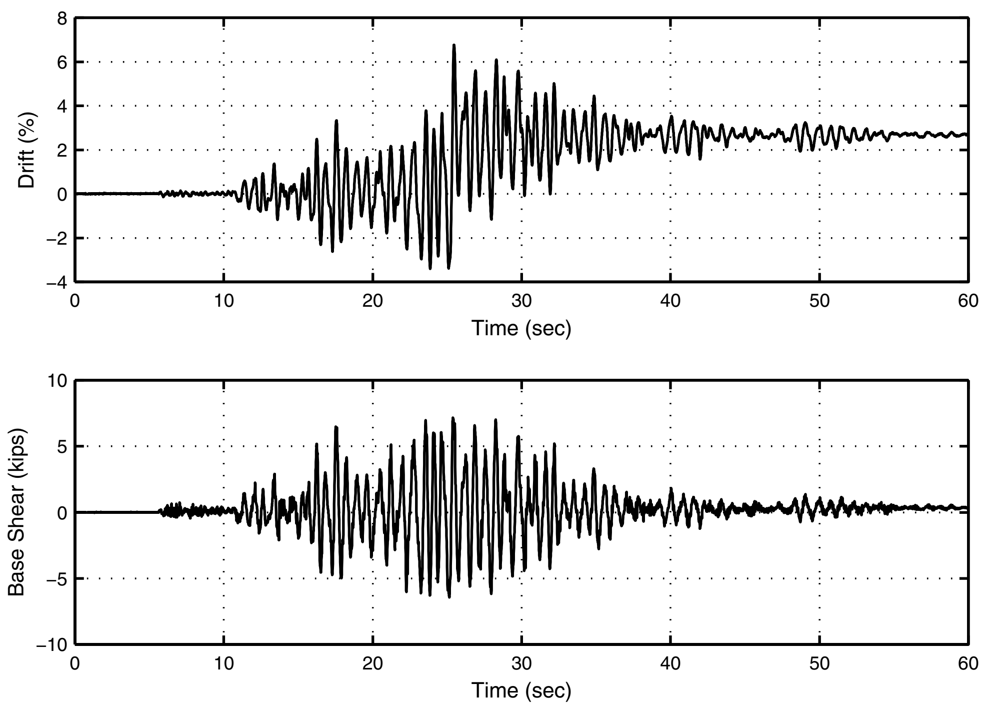

Figure 5-25. First-story interstory drift and base shear time histories

The base shear time history shows about seven cycles that are close to yielding, or have a small amount of yielding. The λ_{Vb} value of 78% indicates that the amount of strength degradation was virtually equal to the 77% experienced by the ductile baseline case for the same excitation (see Table 5-3). The 36% period elongation indicates that there was some stiffness deterioration over the course of the excitation, but again, this value is close to the 29% period elongation for the ductile case. Overall, a comparison of the ductile baseline values in Table 5-3 and the strength-degrading case values in Table 5-7 shows that the effects of the strength degradation were small. The actual amount of strength degradation which occurred will be discussed in the next section.

Table 5-7. Summary of global behavior measures for strength-degrading test

Excitation	**Pattern**	**Excitation Amplitude**	$\Theta_{1\ \mathrm{Maximum}}$ **(%)**	$\Theta_{1\ \mathrm{Residual}}$ **(%)**	λ_{Vb} **(%)**	λ_{T1} **(%)**
JSE17	C	100%	6.8	2.7	78	36

5.2.5.2 Local behavior

The strength-degrading connection configuration showed minor buckling of one of the coupons after testing, as shown in Figure 5-26. This behavior can be partly attributed to the short necked-down section of the coupon, to which the buckling was confined in this case. A close-up of a buckled coupon (from connection C1, at the other end of the beam) is shown in Figure 5-27. The coupons with the shorter necked-down sections behaved as intended during the test, and did not suffer the possible adverse behaviors of global buckling or fracture between the threads.

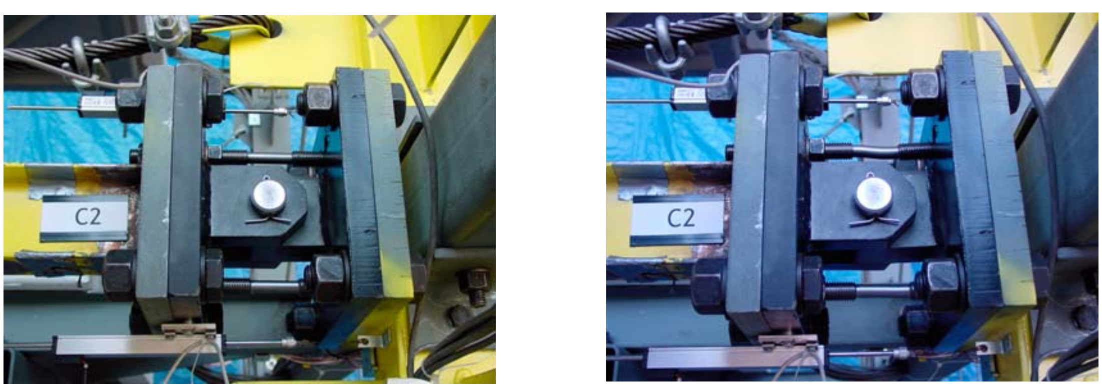

Figure 5-26. Strength-degrading connection C2 before (left) and after (right) testing

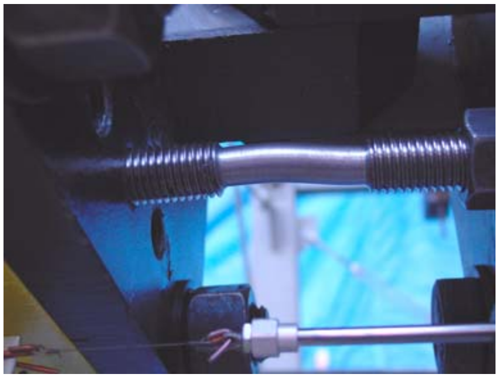

Figure 5-27. Close-up of buckled coupon in C1 after testing

As shown in Figure 5-28, there was only one large yield cycle during the shaking table test, and the corresponding amount of strength degradation was small. In contrast, the quasi-static test had many large yield cycles, and the strength degradation was much more severe. Thus, the connection did not achieve the amount of strength degradation intended. Both shaking table and quasi-static tests show Bauschinger-like behavior during reloading, as well as a small amount of slip when the force passes through zero.

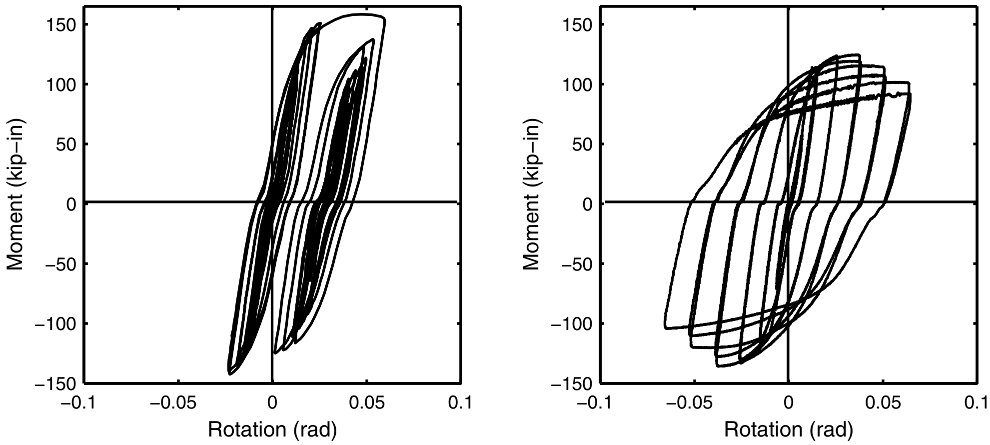

Figure 5-28. Comparison of connection hysteresis for shaking table test (left) and quasi-static test (right)

Overall, the strength-degrading connection behaved with less degradation than intended, and its behavior was similar to the ductile baseline case, albeit with small increases in deformation and degradation.

5.3 SUMMARIES OF GLOBAL AND MEMBER BEHAVIOR DATA FROM NORMAL-SPEED DATA ACQUISITION SYSTEM

Since many tests were conducted, tables are presented to summarize the large volume of data collected. Table 5-8 contains a summary of major global response quantities for each test conducted. Likewise, Table 5-9 contains a summary of major local response quantities. These summaries contain maximum (absolute) values of all response quantities and residual values of displacement measures for each test performed. Minimum values are zero in all cases because the specimen starts from rest, and all instruments were balanced prior to each test. The cases where the catch cables have engaged and affected the response are noted with an asterisk. Complete summary tables for all response quantities of interest are provided in Appendix D.

Table 5-8. Summary of data for major global response quantities

Excitation	**Pattern**	$\Theta_{1\,Max}$ **(%)**		$\Theta_{1\,Res}$ **(%)**		**Max Relative Acceleration (g)**		**Max** V_b	λ_{Vb}	λ_{T1}
		Story 1	Story 2	Story 1	Story 2	Story 1	Story 2	(kips)	(%)	(%)
0.6 sec cosine pulse	DB C	8.56	8.20	3.82	3.78	1.04	1.50	7.32	82	17
	BF BP 1	10.04	9.75	6.89	6.78	1.06	1.55	5.28	43	35
	BF BP 2	9.76	9.43	6.28	6.19	0.93	1.40	5.18	50	41
	DF BP	9.97	9.69	6.67	6.57	0.98	1.48	6.06	38	46
	DFS B	8.66	8.34	5.14	5.08	0.96	1.42	4.91	45	52
	BF CP *	12.70	12.41	11.70	11.53	0.93	1.54	5.51	9	n/a
	DF CP *	13.22	12.91	12.23	12.07	1.48	1.41	6.32	8	n/a
	DFS C *	11.09	10.87	10.50	10.35	0.96	1.32	3.96	0	n/a
	BF A A	3.84	3.58	0.26	0.24	0.51	0.84	5.62	93	17
	BF A B	3.88	3.63	0.21	0.22	0.49	0.85	5.29	97	19
	BF A C	3.82	3.57	0.12	0.12	0.46	0.91	5.59	95	22
	BF A D	3.88	3.64	0.17	0.20	0.45	0.81	5.62	94	22
	BF A E	3.92	3.65	0.23	0.21	0.44	0.85	5.44	97	14
	BF BP H	4.22	3.97	0.65	0.64	0.48	0.80	4.81	90	23

Table 5-8. — *Continued*

Excitation	Pattern	$\Theta_{1\,Max}$ (%)		$\Theta_{1\,Res}$ (%)		Max Relative Acceleration (g)		Max V_b	λ_{Vb}	$\lambda_{T\,1}$
		Story 1	Story 2	Story 1	Story 2	Story 1	Story 2	(kips)	(%)	(%)
1.2 sec cosine pulse	DB C	6.51	6.10	0.44	0.40	0.41	0.62	7.36	94	13
	BF BP	10.44	10.05	4.10	4.04	0.61	0.74	5.46	65	36
	DF BP	9.27	8.90	2.56	2.54	0.67	0.64	5.63	70	41
	DFS B	10.54	10.19	2.80	2.79	0.70	0.86	5.19	60	76
	BF CP 1 *	18.09	17.78	16.60	16.42	0.79	1.02	4.99	20	n/a
	BF CP 2	2.72	2.52	0.16	0.16	0.51	0.49	4.77	80	22
	BF CP 3	12.52	12.35	11.86	11.80	0.51	0.50	4.31	28	50
	BF CB	9.98	9.79	3.49	3.46	0.73	0.71	5.69	57	52
	DF CP *	18.37	18.24	16.96	16.78	0.92	1.08	5.63	14	n/a
	DFS C *	18.62	18.21	17.07	16.85	0.64	1.26	3.81	32	n/a
JNF01 (Tabas)	DB C	4.87	4.70	0.89	0.94	0.68	1.11	7.03	92	15
	BF BB	5.10	4.84	0.83	0.85	0.71	1.18	6.14	82	26
	BF CB	4.83	4.66	0.37	0.40	0.77	1.12	5.21	72	41
	DF CB	4.98	4.80	0.71	0.71	0.83	1.32	5.53	72	51
	DFS C	4.29	4.23	-2.68	-2.62	0.62	1.03	2.05	51	128
JSE17 (Llolleo)	DB C	6.37	6.20	1.98	2.03	1.90	2.48	6.62	77	29
	BF CB	8.13	8.12	-4.09	-4.07	1.85	2.18	5.21	50	22
	SD C	6.76	6.58	2.66	2.68	1.92	2.44	7.15	78	36

* Catch cables engaged — peak values compromised

Table 5-9. Summary of data for major local response quantities

Excitation	Pattern	Maximum θ_{conn} (rad)				Maximum M_{conn} (kip-in.)			
		C1	C2	C3	C4	C1	C2	C3	C4
0.6 sec cosine pulse	DB C	0.082	0.080	0.072	0.071	151.4	157.1	150.7	155.8
	BF BP 1	0.117**	0.110	0.096	0.093	119.1	114.9	143.6	147.9
	BF BP 2	0.106	0.103	0.088	0.090	120.4	117.2	150.4	145.1
	DF BP	0.116**	0.110	0.096	0.088	119.8	121.4	140.8	157.2
	DFS B	0.095	0.093**	0.077	0.079	78.4	83.5	140.9	133.6
	BF CP *	0.145	0.139	0.141	0.141	118.6	109.3	104.0	108.8
	DF CP *	0.151**	0.151	0.149	0.145	128.0	120.8	112.2	109.4
	DFS C *	0.126	0.123	0.122	0.124	84.8	84.0	74.7	80.9
	BF A A	0.023	0.039	0.020	0.020	136.0	114.8	114.0	130.7

Table 5-9. — *Continued*

Excitation	Pattern	Maximum θ_{conn} (rad)				Maximum M_{conn} (kip-in.)			
		C1	C2	C3	C4	C1	C2	C3	C4
	BF A AB	0.023	0.040	0.020	0.020	137.1	110.8	114.8	130.7
	BF A C	0.024	0.037	0.020	0.020	133.9	111.8	107.5	127.7
	BF A D	0.024	0.038	0.020	0.021	133.7	115.8	114.2	129.7
	BF A E	0.024	0.040	0.021	0.021	135.7	116.5	115.4	131.6
	BF BP H	0.041	0.036	0.025	0.025	109.1	98.2	101.7	129.3
1.2 sec cosine pulse	DB C	0.058	0.057	0.049	0.049	145.6	150.9	142.8	145.2
	BF BP	0.114	0.112	0.096	0.096	111.4	106.5	146.5	147.6
	DF BP	0.100	0.098	0.081	0.082	115.4	112.9	149.0	152.6
	DFS B	0.119	0.113	0.099	0.100	82.9	95.7	108.3	134.6
	BF CP 1 *	0.205	0.207**	0.207	0.208	109.4	108.6	105.8	105.4
	BF CP 2	0.022	0.023	0.012	0.015	105.1	100.1	79.7	94.6
	BF CP 3	0.143	0.142	0.141	0.136	90.6	82.0	73.0	85.0
	BF CB	0.099	0.113	0.093	0.108	127.9	103.5	98.8	90.5
	DF CP *	0.220	0.213	0.216	0.212	119.2	119.0	113.2	111.3
	DFS C *	0.220	0.219	0.216	0.215	78.8	81.5	62.4	74.5
JNF01 (Tabas)	DB C	0.045	0.036	0.030	0.034	132.8	153.4	105.0	125.0
	BF BB	0.040	0.052	0.033	0.034	130.2	113.7	115.4	133.6
	BF CB	0.035	0.054	0.032	0.044	137.4	113.7	161.9	104.4
	DF CB	0.040	0.053	0.034	0.048	121.2	128.2	177.9	112.7
	DFS C	0.045	0.045	0.041	0.040	80.0	79.9	58.3	75.8
JSE17 (Llolleo)	DB C	0.055	0.057	0.048	0.050	155.3	143.9	119.2	136.0
	BF CB	0.094	0.081	0.090	0.075	124.0	121.9	88.1	124.8
	SD C	0.061	0.060	0.054	0.047	151.0	158.3	122.4	171.0

* Catch cables engaged — peak rotation values compromised

** Data from one displacement transducer only due to malfunction of 2nd transducer

5.4 OBSERVATIONS OF LOCAL FRACTURE-INDUCED PHENOMENA

A fracture in the flange of a beam in a welded beam-column connection (or, in our case, in a coupon in the mechanical connection) results in a sudden change in connection properties. Because this change occurs virtually instantaneously, transient dynamic effects are produced in the members surrounding the connection. The results of the sequence of tests performed to study these local dynamic effects, previously referred to as the “wave propagation” sequence, are presented in this section. A listing of the tests performed in this sequence can be found in Table 4-4.

5.4.1 General Observations

The collection of data at a very high scan rate (1 MHz) allowed the capture of several extremely short-lived phenomena that occurred immediately following fracture. Fracture introduces a sudden change in stiffness and local forces. A subsequent redistribution of internal member forces and adjustment of inertial and viscous damping related forces are needed to maintain dynamic equilibrium. As a result, fracture may cause a number of dynamic phenomena associated with the change in member stiffness and the rapid change in local forces.

Four of these local fracture-induced phenomena were observed: change in the deflected shape of the beam, the presence and interaction of stress waves propagating away from the fracture, excitation of higher modes of vibration in the beam, and local redistribution of moments. These phenomena are described in detail in the following sections.

5.4.2 Change of Beam Deflected Shape

When fracture occurs at the beam-column connection at one end of a beam, the end conditions of the beam change suddenly. Since the beam is no longer restrained in the same way, its deflected shape changes, as noted by Nakashima (Nakashima et al., 2000). The change in deflected shape is illustrated schematically on a single-bay frame for simplicity in Figure 5-29, and the process is as follows:

1. As shown in (a), the frame undergoes lateral deformation Δ, and connection moments are $M_1 = M_{F1}$ and $M_2 = M_{F2}$, where M_{F1} and M_{F2} are moment values at the instant before fracture.
2. Fracture occurs at connection 1.
3. Either (b) or (c) occurs. In (b), connection 1 has no residual moment capacity after fracture ($M_1 = 0$), and $M_2 = M_{F2} + \Delta_{M2}$. In (c), connection 1 has residual moment capacity M_R after fracture, and $M_2 = M_{F2} + \Delta^*_{M2}$.

In general, Δ_{M2} in (b) is not the same as Δ^{*}_{M2} in (c). The more realistic scenario of the two is (c), since both beam-column tests and post-earthquake observations show that in most cases there is some post-fracture residual capacity due to the relative rarity of full top-to-bottom web fractures. Scenario (b) is often assumed for analysis purposes, particularly in Japanese studies (Nakashima et al., 2000, Uetani and Tagawa, 2000). In either case, the sign of Δ_{M2} is such that the total moment M_2 tends to reduce.

The beam end moments are reduced because the beam itself is elastic and the curvatures in the beam end regions are reduced due to the release of the restraint at one end. The beam is no longer forced into double curvature by its end restraints, and assumes a new deflected shape with reduced curvature-single curvature for (b), and something in between single and double curvature for (c).

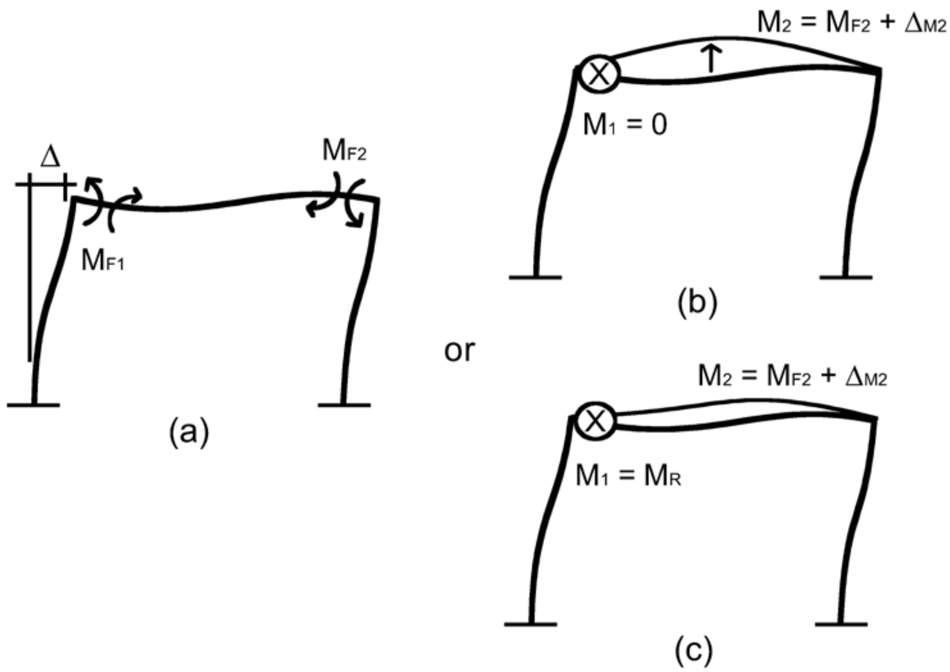

Figure 5-29. Deflected shape before and after fracture

The behavior presented in Figure 5-29 is borne out by experimental results from Test B. Curvature time histories at both ends of MB1 are shown in Figure 5-30, and it is clear that curvatures decrease suddenly at both ends following the fracture at the west end. The decrease in curvature is much larger at the end of the beam where fracture occurs than at the opposite end.

The curvatures were calculated at two sections, each 3/2*d* away from the respective ends of Main Beam 1 (MB1), where *d* is the beam depth. At these sections high-speed strain data were available at the extreme fibers of the beam, and a linear strain distribution was assumed for the curvature calculations, since the beam remained elastic.

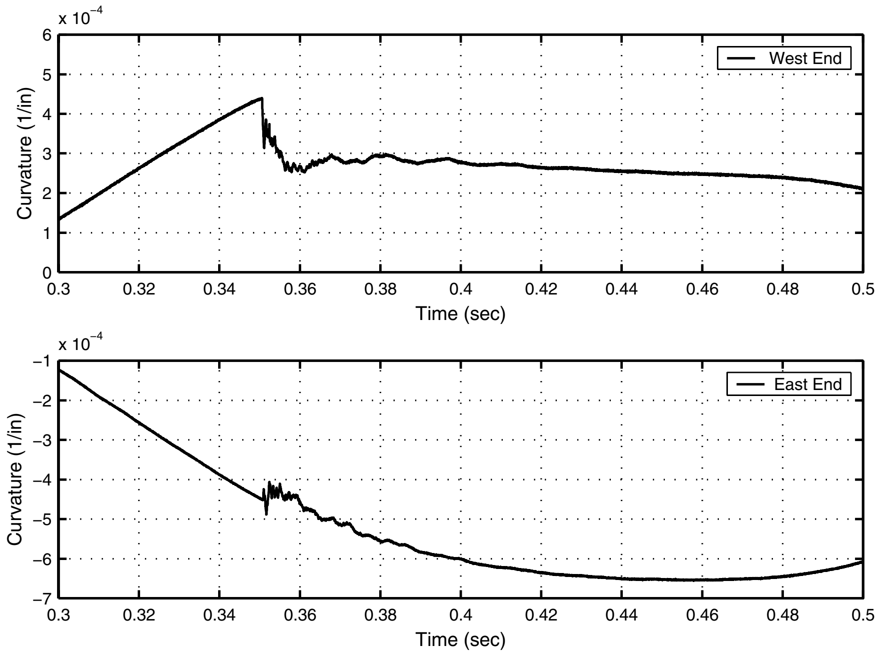

Figure 5-30. Curvature time histories at both ends of MB1, Test B

By equilibrium, decreases in beam end moments lead to corresponding decreases in the moments in the adjacent columns. Since the columns remain elastic, these moment decreases correspond to decreases in curvatures in the beam end regions.

5.4.3 Presence of Strain Spike and Propagating Waves

When a fracture occurs, strain energy absorbed by the connection is suddenly released. This has an effect similar to an impact loading, producing elastic waves which propagate away from the fracture surface (Kolsky, 1976). Some of these waves propagate from the fracture specimen into the air as sound waves, and this causes the characteristic loud “bang” heard in the lab when something fractures. Other waves propagate through the the specimen, reflecting off boundaries, interfering, and attenuating until they finally subside.

In the case of welded steel moment connections, a fracture in the vicinity of a beam flange-to-column weld or in the weld itself affects the beam in a manner similar to an impact on the end. Imagine hitting the end of one of the beam flanges with sledgehammer, and this gives a good picture of the impact-like effects of fracture.

According to wave propagation theory, the waves generated by an end impact of a thin rod will be longitudinal waves, and they will travel down the centroid of the rod (Graff, 1975). The situation is slightly more complicated if a prismatic beam is used instead of the rod, due to the effects of the geometry of the section. If the impact is eccentric or the beam is not rectangular, the situation is more complicated still, and the reflection pattern of the waves will be more complex. The reader is referred to appropriate texts (Graff, 1975, Clough and Penzien, 1993) for a discussion of wave propagation in rods and beams.

In this sequence of tests, the waves traveling in MB1 were captured by using strain gages located along the beam as as shown in Figure 5-31. High-speed data were also taken from gages on MB2 (second-story beam), located as shown in Figure 5-32. The four gages (limited by space on the high-speed board) used to take high-speed data and the fracture locations for each test are shown in Table 5-10.

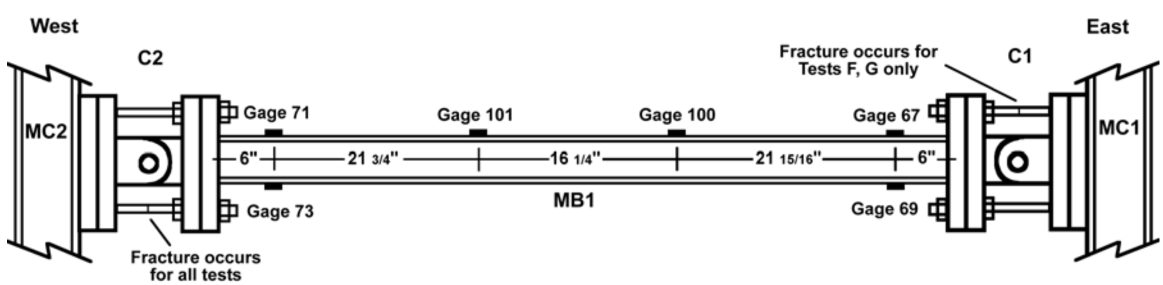

Figure 5-31. Elevation of MB1 with gage and fracture locations

Figure 5-32. Elevation of MB2 with gage locations

Table 5-10. Gages with high-speed data taken and fracture locations for high-speed tests

Test	Gages	Fracture Location(s)
A	71, 101, 100, 67	Bottom coupon, C2 (West end)
B	71, 73, 67, 69	“
C	71, 73, 79, 75	“
D	71, 73, 79, 81	“
E	71, 101, 100, 67	“
F	71, 101, 100, 67	Bottom coupon, C2 (West end) Top coupon, C1 (East end)
G	71, 101, 100, 67	Bottom coupon, C2 (West end) Top coupon, C1 (East end)

Plots such as Figure 5-33 were used to calculate the travel time of the wavefront, from which the wave velocity could be obtained. Observed wave velocities for each test with appropriately located gages are shown in Table 5-11.

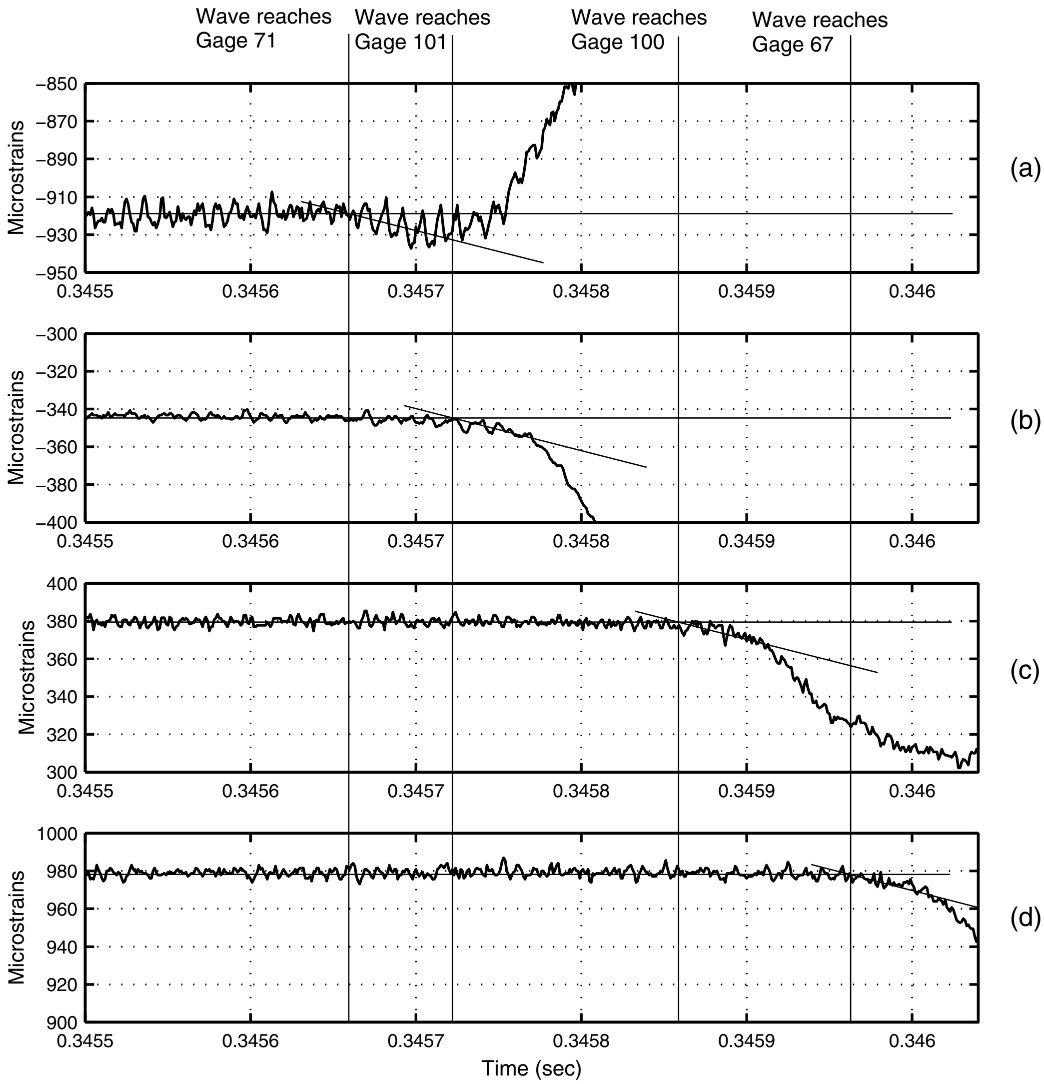

Figure 5-33. Test A elastic wave propagation along MB1: gages (a) 71, (b) 101, (c) 100, (d) 67

Table 5-11. Observed wave velocities

Test	Gages Used	V_{obs} (m/s)	% Difference from V_{long}
A	71, 101	9313	56.3
	71, 100	6651	11.6
	71, 67	6091	2.2
B	71, 67	6191	2.2
E	71, 101	6209	4.2
	71, 100	6318	6.0
	71, 67	5710	4.4

Table 5-11. — *Continued*

Test	Gages Used	V_{obs} (m/s)	% Difference from V_{long}
F (1st fracture)	71, 101	6985	17.2
	71, 100	6318	6.0
	71, 67	6301	5.7
(2nd fracture)	67, 100	5080	17.3
	67, 101	5494	8.5
	67, 71	5537	7.6
G	71, 101	7983	33.9
	71, 100	7433	24.7
	71, 67	6091	2.2

As shown in Table 5-11, the observed velocities V_{obs} of the first wave along the beam show agreement with the theoretical longitudinal wave velocity V_{long} for mild steel, which is 5960 m/s (Lide ed., 1992). It should be noted that the observations of wave travel times are less certain for the gage pairs 71, 101 and 67, 100, since these gages are closer together. With the exception of these cases, most of the observed velocities are within 10% of the theoretical velocity. It is thus reasonable to conclude that the waves observed in the beam are longitudinal waves (or p-waves) based both on this observation and the fact that longitudinal waves travel faster than other wave types, and thus are expected to arrive first.

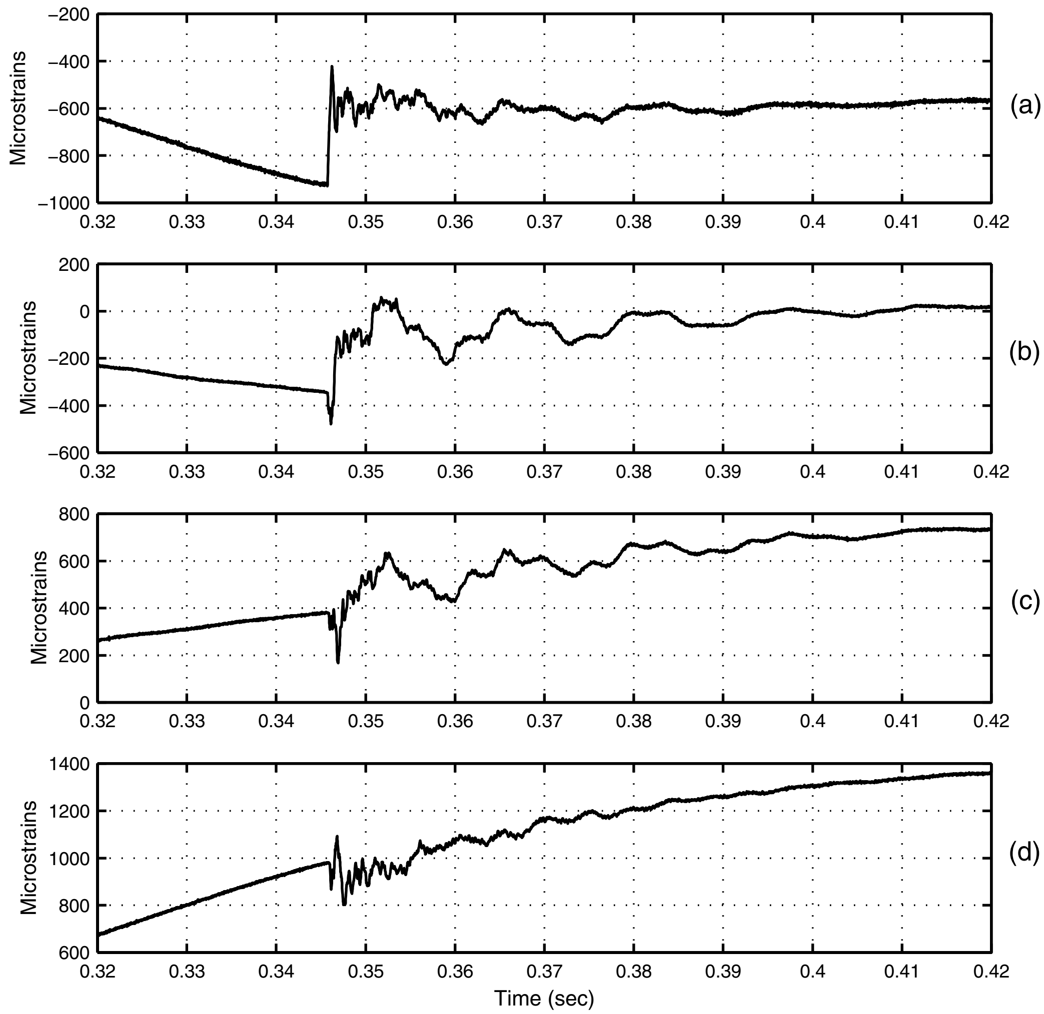

Figure 5-34. Post-fracture strains along top flange of MB1 at gages: (a) 71, (b) 101, (c) 100, (d) 67; Test A

If the fracture occurs at the west end of the beam (the left end in Figure 5-31), the waves generated by the fracture (mostly longitudinal waves) will travel down the beam toward the east end, so they will be moving from left to right in Figure 5-31. Likewise, if the fracture occurs at the east end of the beam, the waves will propagate in the opposite direction, toward the west end. In the case of Test A, there is only one fracture at the west end, and so the waves propagate toward the east end.

The shape of the wave front at different locations along the beam can be inferred from the strain time histories in Figure 5-34. The occurrence of the fracture is clearly indicated by the sudden, large discontinuity in the time history of the closest gage, shown in (a). A sudden change in strain also occurs due to the wave in the gages along the beam as shown in (b), (c), and (d), where the wave motion initially causes compression (or a reduction in tension). At the beam end opposite the fracture, the wave motion causes tension following the initial compression, as shown in (d). This creates what is defined as a “strain spike” — a very sudden increase and subsequent sudden decrease in the tensile strain time history.

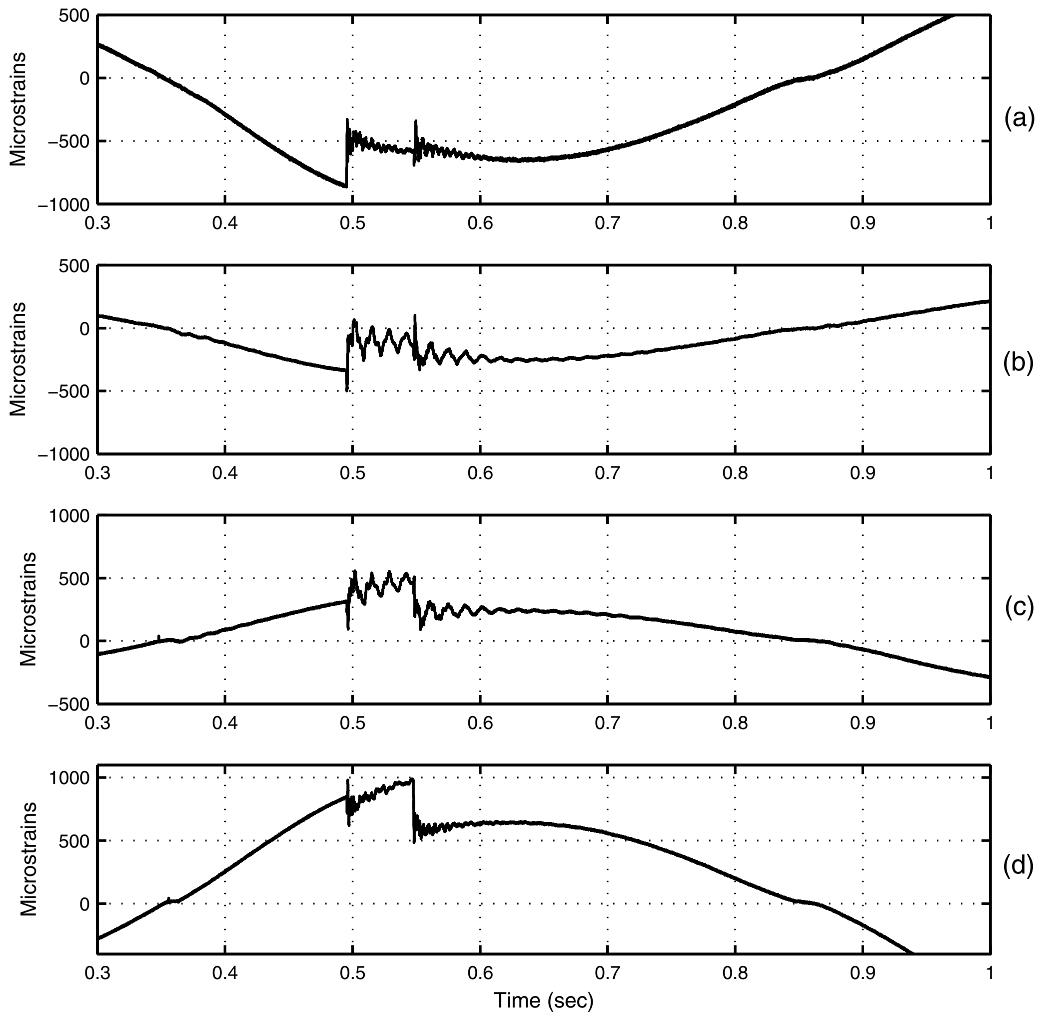

Figure 5-35. Strains along top flange of MB1 at gages: (a) 71, (b) 101, (c) 100, (d) 67; Test F

In the case of Test F, fracture occurs first at the west end of the beam, the waves propagate toward the east end, and again a strain spike is clearly visible in the time history of Figure 5-35(d). About 0.05 seconds later, the second fracture occurs, this time at the east end, and the waves propagate and cause another strain spike at the west end, although the amplitude is lower. Looking at the amplitudes of the tensile strain spike caused by the first fracture and the strain just before the second fracture, it is apparent that *the spike amplitude is close to that necessary to cause fracture*. Therefore, it is possible that a strain spike caused by propagating waves from a fracture at one end of the beam could trigger a fracture in the connection at the other end. Though the strain spike did not trigger a fracture in this case, Test F shows that the possibility exists.

Another concern raised by the existence of the strain spike is its strain rate, which is significantly higher than the strain rate induced by the excitation. Material testing has shown that the behavior of steel changes with large strain rates (Manjoine, 1944; Barsom, 1975); the yield strength increases and the toughness decreases, making fracture more likely. The calculated strain rates associated with the observed strain spikes are shown in Table 5-12. These rates, while significantly higher than the rates of 0.05 to 0.15 in./in./sec predicted in an analytical study by Harrigan (FEMA, 2000), are an order of magnitude less than the dynamic strain rates of 10 in./in./sec or greater (Barsom, 1975) which would significantly change the toughness of mild steel at room temperature. Thus, a strain spike would probably not be capable of generating a fracture by embrittling the steel.

Table 5-12. Strain rates associated with strain spike

Test	Average over spike (in./in./s)	Maximum in spike (in./in./s)
A	0.45	0.69
B	0.45	0.64
E	0.28	0.46
F	0.55	1.29
G	0.50	0.76

Clues to the causes of the strain spike can be found if the longitudinal and bending components of the section strain diagram are separated as shown in Figure 5-36. A linear strain profile across the section is assumed, since the beam remains elastic. Strain data from Test B are used to generate the bending and axial component time histories in Figure 5-37, since top and bottom flange values are available at both beam ends. The spike in the axial strain time history in Figure 5-37 (d) indicates that a portion of the strain spike is caused by propagating longitudinal waves generated by the fracture. This spike is not caused by the initial arrival of the longitudinal wave, but occurs shortly thereafter.

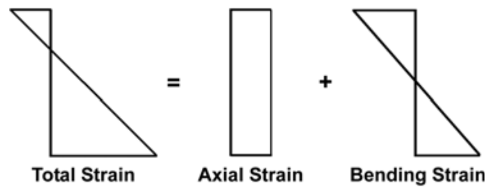

Figure 5-36. Separation of bending and longitudinal components of strain

However, there is also a spike in the bending strain time history in (b) at the same time, and it is approximately the same amplitude. This spike in the bending strain time history is most probably caused by either flexural waves or dynamic effects from the sudden change in beam curvature. Flexural waves, which travel more slowly than longitudinal waves, can be generated by eccentric impacts, such as that of a single flange fracture.

It appears at first that the bending and axial spikes are in opposite directions due to the sign convention used for bending strain (which is the same as for beam moment). However, they both cause an increase in tensile stress in the top flange at the east end of MB1, since the moment at the east end of MB1 is negative, placing the top flange in tension. Thus, the two spikes constructively reinforce each other, producing the larger spike that occurs in the unseparated time history.

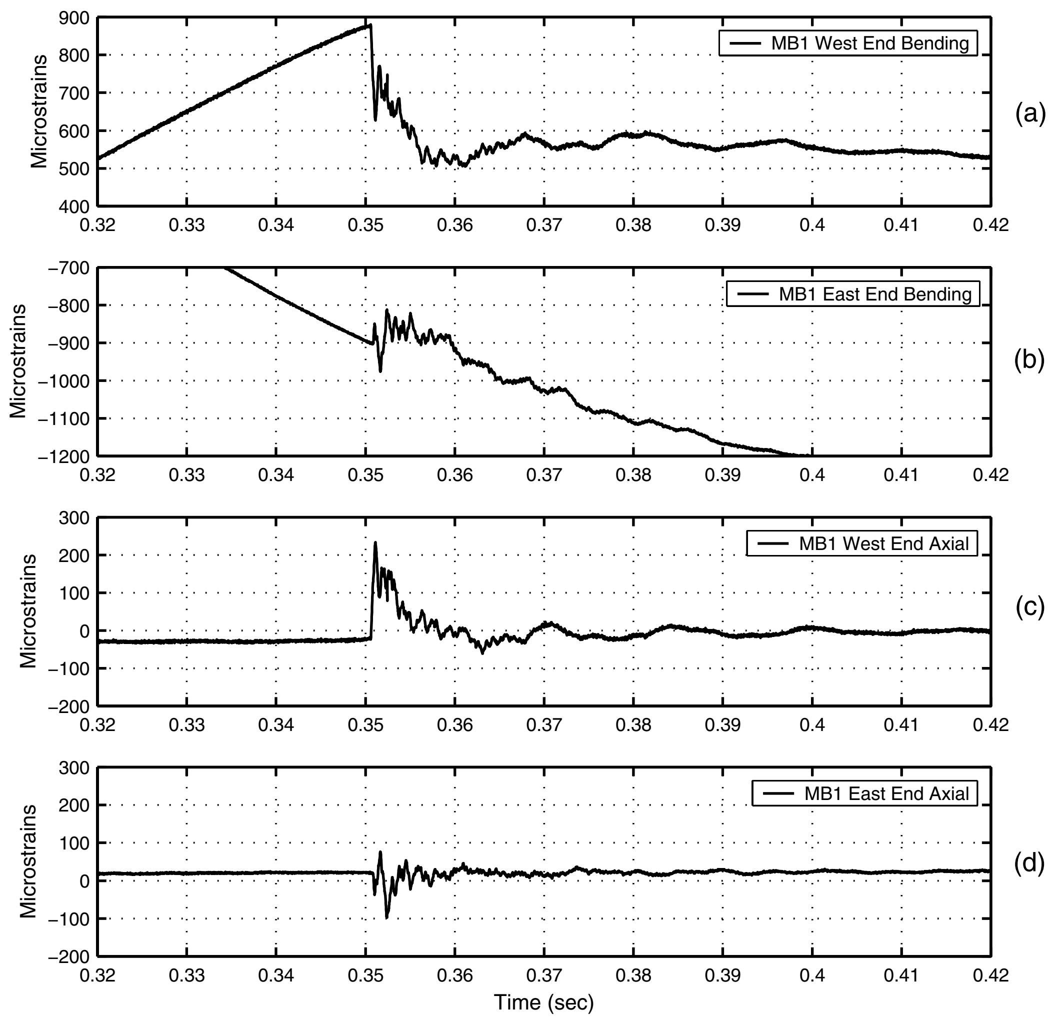

Figure 5-37. Close-up view of bending and axial strains at both ends of MB1, Test B

Propagating waves were also observed in MB2, although at very small amplitude. Separating the strain profile as before into the bending and axial strain components shown in Figure 5-38 gives a very small but still distinctive indication that longitudinal waves are propagating in MB2 due to the fracture in MB1. The wave arrival can be seen more clearly in the close-up of the curvature time history in Figure 5-39, as the response deviates from the tangent in a small but noticeable way.

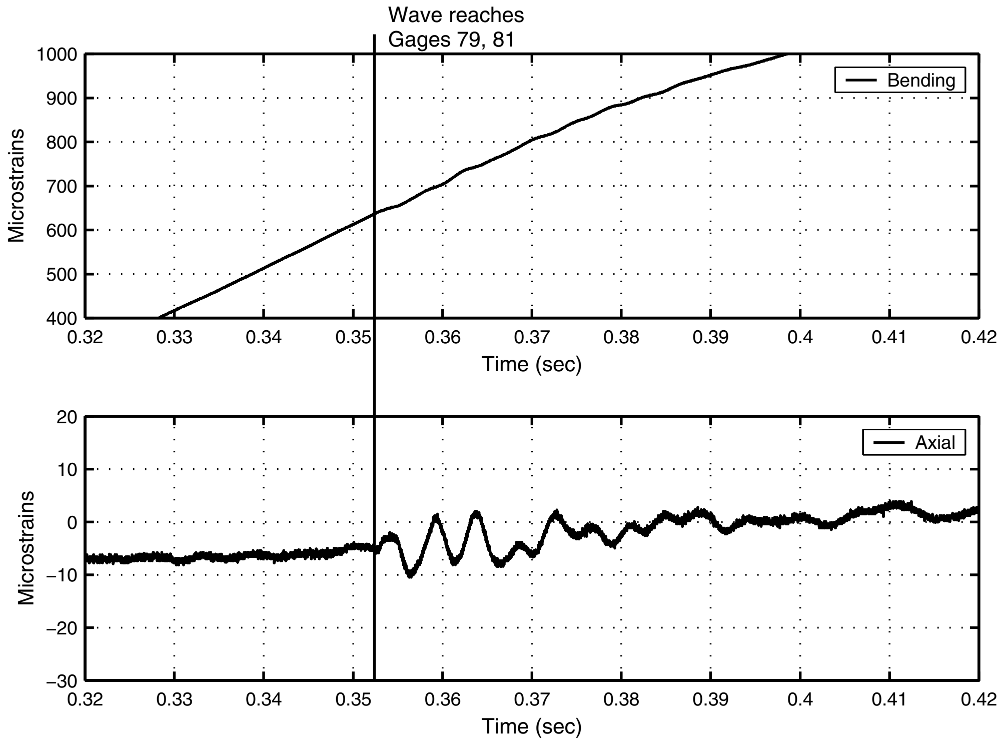

Figure 5-38. Close-up of bending and axial strains at west end of MB2, Test D

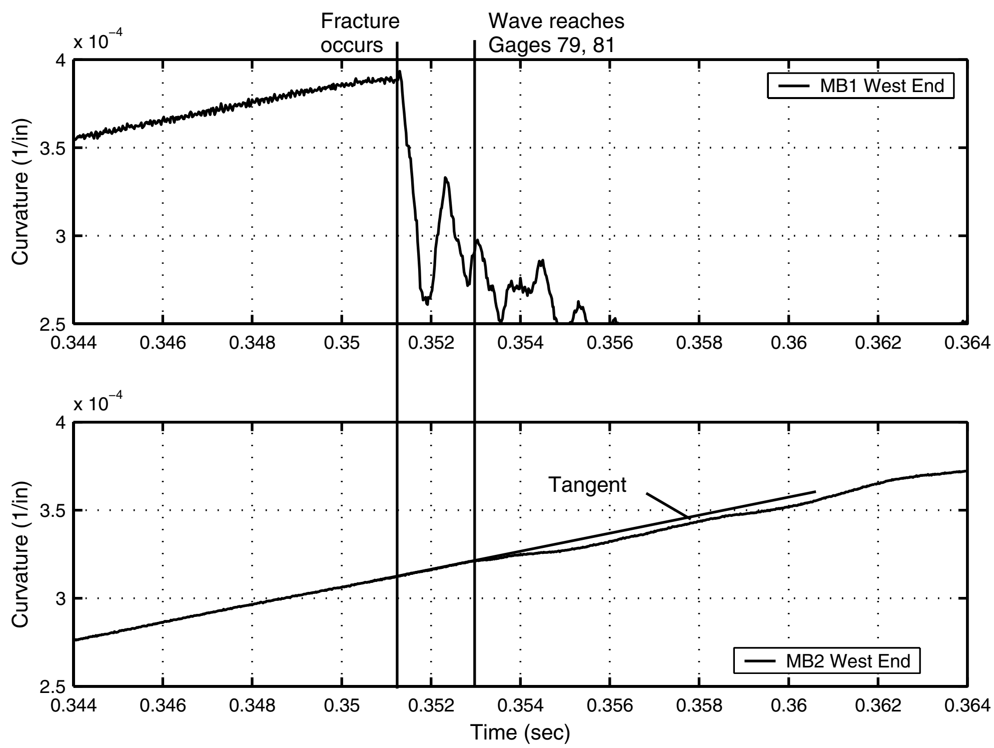

Figure 5-39. Curvature time histories, west ends of MB1 and MB2, Test D

5.4.4 Excitation of Higher Vibration Modes

When fracture occurs in one flange of a beam-column connection, the sudden change in moment has the same effect on the beam as an eccentric impact. This impact and the ensuing waves propagating excite higher modes. These higher-mode vibrations are more sensitive to the local distribution of stiffness, and especially mass, than the overall system level response to base excitation, and tend to damp out quickly.

Fourier amplitude plots of the response segment immediately following fracture (from gage 71) are shown for two frequency ranges of interest in Figures 5-40 and 5-41. The many well-separated peaks indicate that higher modes are excited by the fracture. Determining precisely which modes are excited requires finite element analysis, and is thus outside the scope of this chapter. The amount of energy dissipated through these higher modes, and whether it is significant to the overall structural response, are topics for future work.

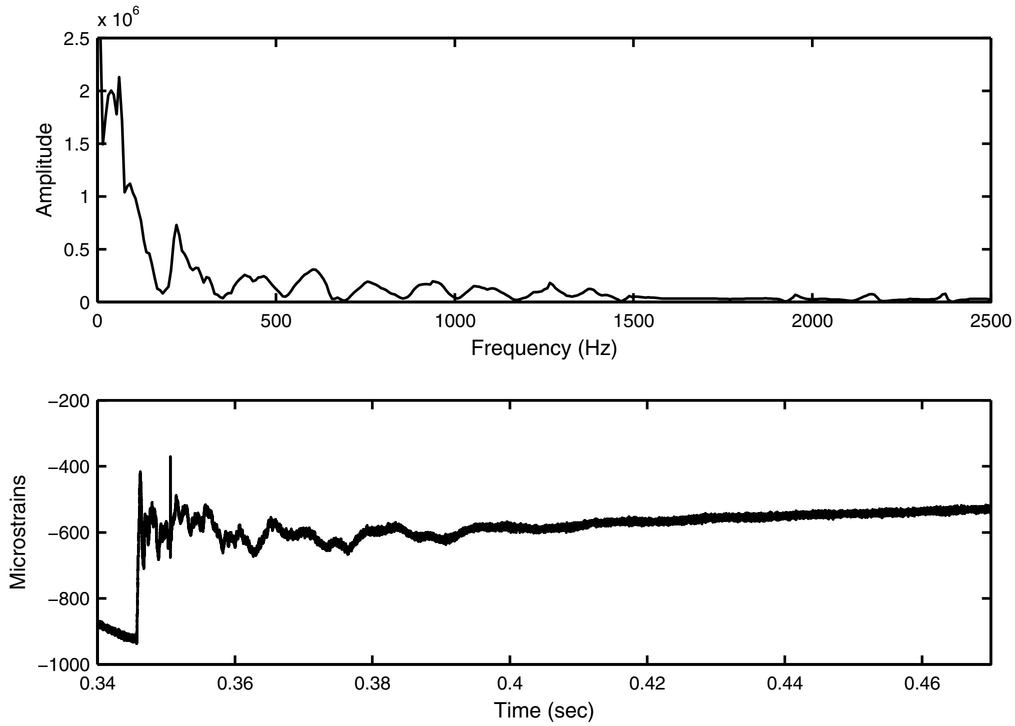

Figure 5-40. Fourier amplitude plot with section of time history obtained from Test A

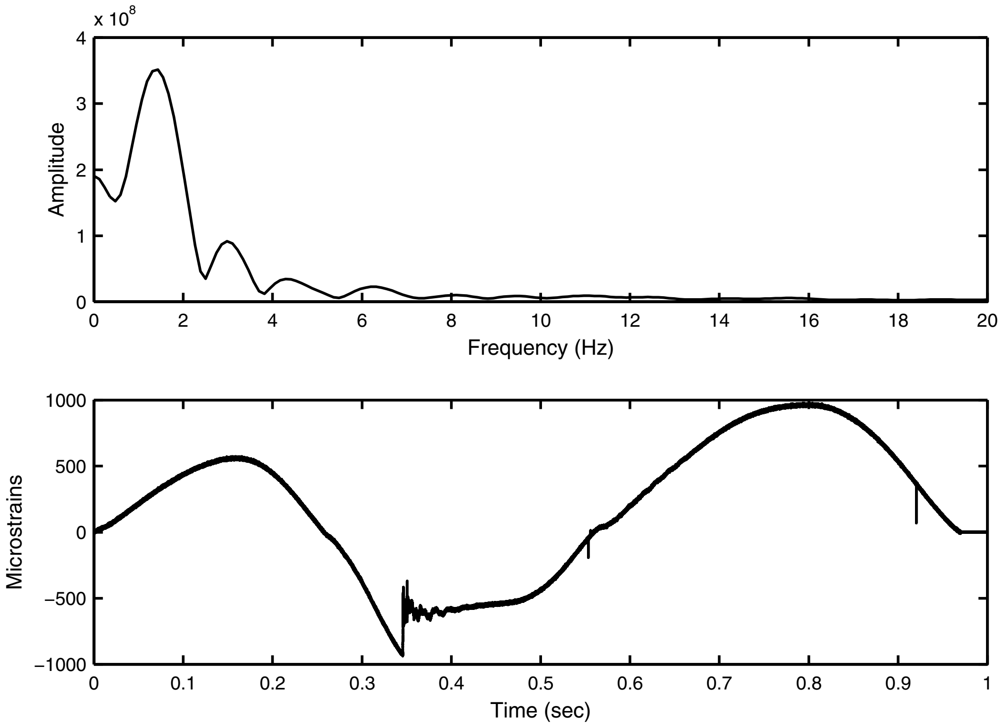

Figure 5-41. Fourier amplitude plot, frequencies less than 1 KHz, and time history

5.4.5 Local Area Moment Redistribution

When fracture occurs at one end of the beam, the moment capacity of the section where fracture occurs is drastically reduced. In the case of this experimental series, the reduction is generally 40–50%. The moment at the other end of the beam decreases as well, though the capacity is not reduced. The decrease in moment is due to the immediate post-fracture reduction in curvature at the end of the beam opposite the fracture, as shown in Figure 5-30. Since the beam remains elastic, the moment time history for the beam ends in Test B is simply this curvature time history multiplied by the section stiffness, which is the same at both ends.

The next question is what happens to the moments in the other members in the frame when fracture occurs. A close-up of the curvature time history for the west end of MB2 in Figure 5-39 shows a very slight decrease in curvature, and therefore moment, after the fracture occurs. No strain profile is available for the east end of MB2, but a lack of observable transient response in the single gage on the top flange indicates that any change in moment due to fracture is very small.

High-speed data are available only for the beams, so it is necessary to use normal-speed data for the columns, meaning that the highly transient oscillations will not be captured. The column strain time histories in Figure 5-42 show that the moment decreases suddenly in the column below the first floor fracturing connection C2. A decrease in the small moment above C2 also occurs, indicating that the whole joint region is unloading, as required by equilibrium if the beam end moment decreased. The moments at the second-story level, or top (below C4), and base (above the clevis) are virtually unchanged except for a small decrease at the top. This means that MC2 is unloading along its entire length, and thus straightening out.

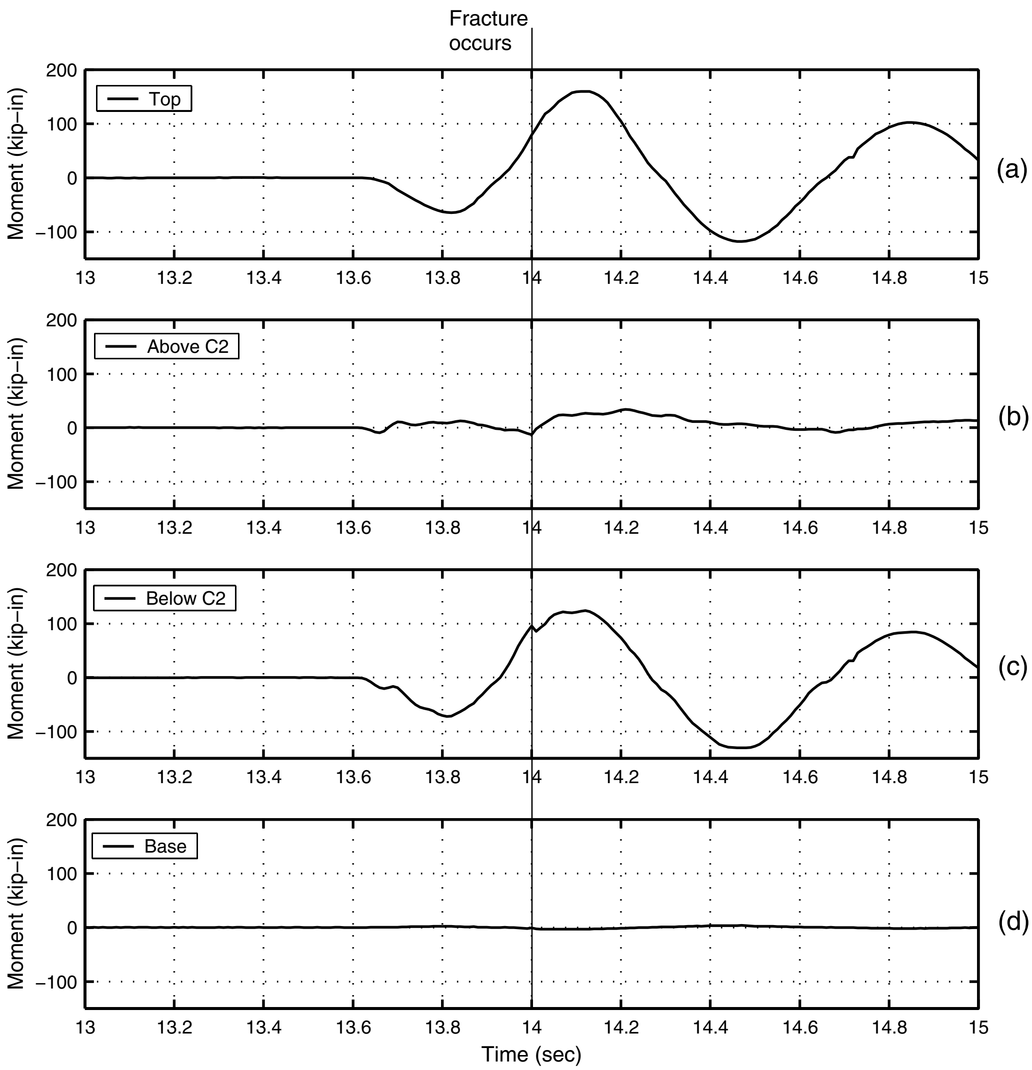

Figure 5-42. MC2 moments, BF A Test B, normal-speed data

The differential displacement of MC2 at C2 is shown in Figure 5-43, and it is difficult to determine if the connection is rotating clockwise due to the noise level in the data. However, it appears that this may be the case as there is a change in slope corresponding to the clockwise direction just after fracture, and then a "plateau" as the continuing deformation bends the column back again. It is a bit difficult to determine exactly what is happening, since the column is undergoing rigid body rotation in the positive direction as well.

On a lesser scale, a similar unloading is taking place in MC1. The east end of the beam near connection C1 is unloading, and by equilibrium the rest of the joint unloads as well. Thus, the whole column is unloading, as shown in Figure 5-44.

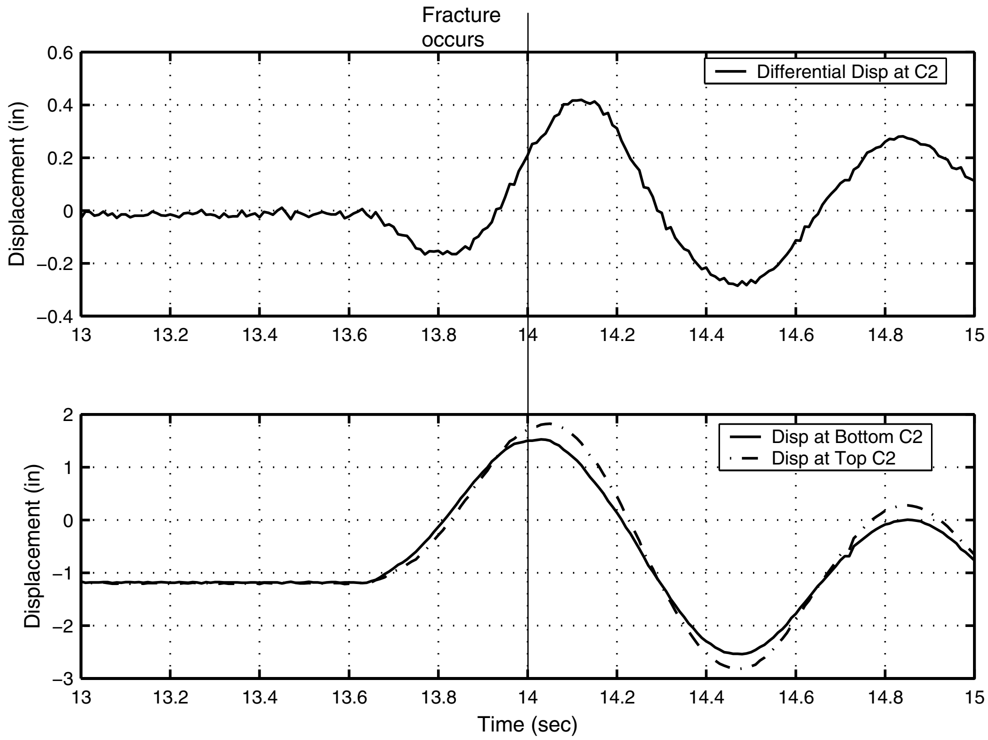

Figure 5-43. Differential displacement above and below C2 (MC2 first story), normal-speed data

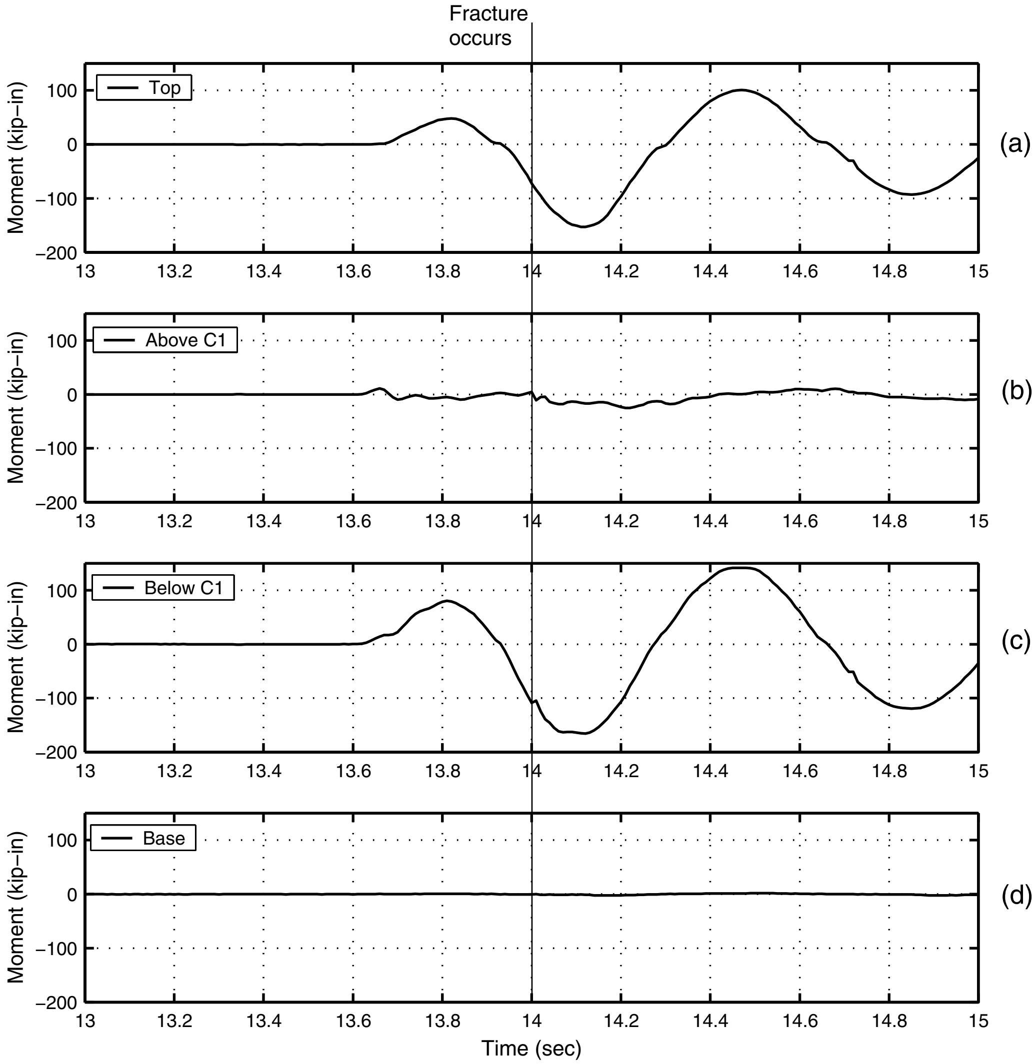

Figure 5-44. MC1 moments, BF A Test B, normal-speed data

The observations from the Test B time histories are combined into the conceptual moment diagram in Figure 5-45. This diagram shows the moments in the structure immediately before and after fracture occurs at Connection 2.

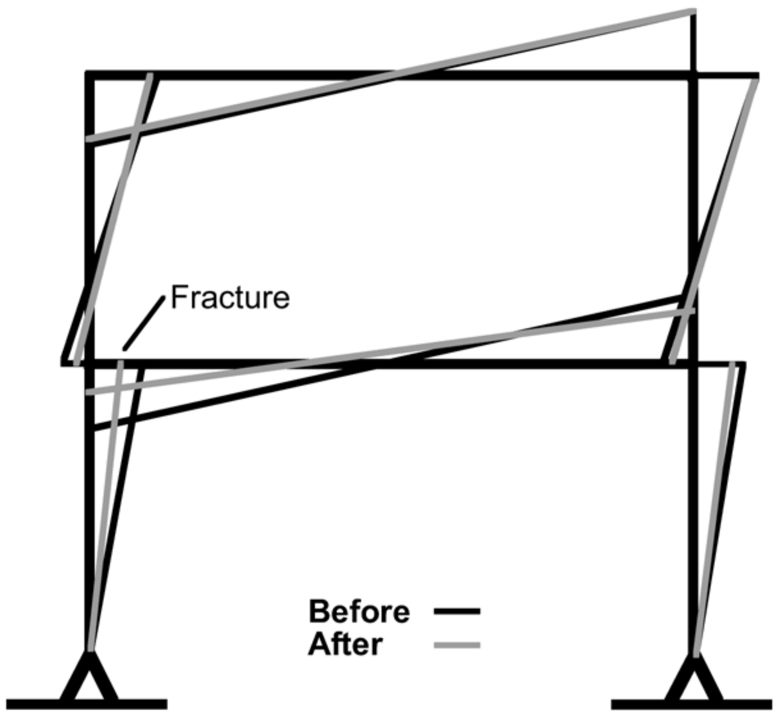

Figure 5-45. Conceptual moment diagram before and immediately after fracture, Test B

Since all of the members of the structure are unloading immediately after fracture, the term "moment redistribution" itself may be misleading. Moment redistribution *does not* mean that the same total amount of moment is present in the structure, and it is simply being moved around. What is meant by moment redistribution is the change in the shape of the moment diagram of the structure. It is important to state here that the equations of motion make no restriction on the value of global resisting forces. The moment resistance lost at fracture or during strength or stiffness degradation does not need to be "picked up" by other members to maintain equilibrium. The global-resisting forces can decrease, and the change can be accommodated by the other terms in the equation of motion.

5.5 SUMMARIES OF HIGH-SPEED LOCAL FRACTURE-RELATED DATA

In this section, tabular summaries of the high-speed data taken during the wave propagation sequence are presented. Maximum values of strain for all tests with high-speed data are listed in

Table 5-13, and maximum values of curvatures for tests where a strain profile at a section was available are shown in Table 5-14. Since data were not taken at all gages, those gages where high-speed data were not taken for a particular test are indicated by gray boxes. Excitation, amplitude, and other test particulars are listed in Table 4-4.

Table 5-13. Summary of maximum strain values

Gage Location and Channel Number	Test A	Test B	Test C	Test D	Test E	Test F	Test G
	(µstrains)	(µstrains)	(µstrains)	(µstrains)	(µstrains)	(µstrains)	(µstrains)
MB1 Top Flg W End (71)	977	942	940	1001	1004	872	1445
MB1 Bot Flg W End (73)		919	913	975			
MB1 Top Flg W Mid (101)	480				505	505	690
MB1 Top Flg E Mid (100)	767				805	558	759
MB1 Top Flg E End (67)	1392	1343			1357	991	1489
MB1 Bot Flg E End (69)		1284					
MB2 Top Flg W End (79)			1185	1180			
MB2 Bot Flg W End (81)				1189			
MB2 Top Flg E End (75)			1476				

Table 5-14. Summary of maximum curvature values

Section Location and Gage Channel Numbers	Test B	Test C	Test D
	(1/in.)	(1/in.)	(1/in.)
MB1 West End (71, 73)	4.65 E-4	4.63 E-4	4.93 E-4
MB1 East End (67, 69)	6.56 E-4		
MB2 West End (79, 81)			5.92 E-4

6 Comparisons of Data

In this chapter, detailed comparisons are made between the data obtained from the various shaking table tests. Summaries of these data and behavioral observations were presented in the previous chapter. In order to make comparisons, the tests are divided into comparison sets. The methodology for selecting the sets is discussed in Section 6.1. Graphical time history results are then presented by comparison sets in Section 6.2 for response quantities of interest, with the effects of hysteretic behavior type highlighted. Tabular comparisons of maximum values of key response quantities (see Appendix E) are discussed for each comparison set as well. Comparisons discussed in Sections 6.2.1 through 6.2.11 involve normal-speed data from the main sequence of shaking table tests. Comparisons involving both normal-speed and high-speed data from the wave propagation sequence are discussed in Section 6.2.12. Finally, the findings from the various comparisons are summarized in Section 6.3. This chapter contains comparisons between experimental data from different tests only; comparisons between experimental data and analytical models or theoretical predictions will be made in later chapters.

6.1 DESCRIPTION OF COMPARISON METHODS

In order to provide a straightforward method for determining the effects of various test variables on the structural behavior of the specimen, response quantities of interest were selected as the framework through which the comparisons between tests would be made. The effects of a particular test variable, such as connection hysteretic behavior type, are evaluated for each response quantity of interest. Since structural behavior can only be measured quantitatively by using response quantities, it is necessary to obtain the effects of test variables on structural behavior by synthesizing the effects of the test variables on the various response quantities of interest.

6.1.1 Definition and Organization of Comparison Sets

The organizational scheme selected to implement the above framework is that of the comparison set. A comparison set is a small group, or subset, of tests selected from the full set of tests, and comparisons are made between its members. The full set of tests was divided for several reasons:

- to minimize the number of variables present in any chosen subset
- to provide a rational way of organizing the comparisons
- to facilitate the identification of the effects of key variables

In the design of the experiment, several key test variables were identified. The comparison sets were selected to contain one key variable each. These key test variables are:

- hysteretic type
- spatial distribution of hysteretic type
- excitation
- amplitude of excitation
- period range/response spectrum region — i.e., short, energy preserved, displacement preserved
- additional distributed mass along beam for wave propagation tests

The comparison sets with their member tests are defined in Table 6-1. Multiple runs of the same test are indicated in parentheses under "Patterns" below.

Table 6-1. Comparison set definitions

Set	Key Variable	Pattern(s)	Excitation(s)*
1	Hysteretic type	DB, BF BP, DF BP, DFS B	1.2 sec cosine pulse
2	Hysteretic type	DB, BF CP, DF CP, DFS C	1.2 sec cosine pulse
3	Hysteretic type	DB, BF BP (1&2), DF BP, DFS B	0.6 sec cosine pulse
4	Hysteretic type	DB, BF CP, DF CP, DFS C	0.6 sec cosine pulse
5a	Hysteretic type	DB, BF CB, DF CB, DFS C	JNF01
5b	Spatial distrib. of hysteretic type	DB, BF BB, BF CB	JNF01
6	Hysteretic type	DB, BF CB, SD C	JSE17
7	Excitation	DB	0.6 sec cosine pulse, 1.2 sec cosine pulse, JNF01, JSE17
8	Excitation	BF CB	1.2 sec cosine pulse, JNF01

Table 6.1 — *Continued*

Set	Key Variable	Pattern(s)	Excitation(s)*
9	Response spectrum position	DB, BF BP, DF BP, DFS B	0.6 sec cosine pulse, 1.2 sec cosine pulse
10a	Spatial distrib. of hysteretic type	DB, BF BP, DF BP, BF CP, DF CP	0.6 sec cosine pulse
10b	Amplitude	BF BP	0.6 sec cosine pulse (50, 100% amp)
11a	Spatial distrib. of hysteretic type.	DB, BF BP, DF BP, BF CP, BF CB, DF CP	1.2 sec cosine pulse
11b	Amplitude	BF CP	1.2 sec cosine pulse (50,75,100% amp)
12a	Mass on beam	BF A (Tests A–E)	0.6 sec cosine pulse, 50% amplitude
12b	Spatial distrib. of hysteretic type	BF A (Tests A–E), BF BP	0.6 sec cosine pulse, 50% amplitude

* Excitations are 100% amplitude unless otherwise noted.

Comparison sets are also presented in matrix format in Table 6-2, where all tests performed are listed and the numbers of the comparison sets each test is a member of are noted. The number of tests performed for each excitation/pattern combination, if greater than one, is shown in brackets.

Table 6-2. Comparison set matrix

		Excitation and Amplitude						
		0.6 sec cosine pulse		1.2 second cosine pulse			JNF01	JSE17
		50%	100%	50%	75%	100%	100%	100%
Ductile Baseline	C		3, 4, 6, 9, 10a			1, 2, 6, 9, 11a	5a, 5b, 6	6, 7
Brittle Fracture	A	10b, 12a, 12b [5]						
	BB						5b	
	BP	10b, 12b	3, 9, 10a, 10b [2]			1, 9, 11a		
	CB					8, 11a	5a, 5b, 8	6
	CP		4, 10a	11b	11b*	2, 11a, b		
Ductile Fracture	BP		3, 9, 10a			1, 9, 11a		
	CB						5a	
	CP		4, 10a			2, 11a		

Table 6.2 — *Continued*

		Excitation and Amplitude						
		0.6 sec cosine pulse		1.2 second cosine pulse			JNF01	JSE17
		50%	100%	50%	75%	100%	100%	100%
Deformation Softening	B		3, 9			1, 9		
	C		4			2	5a	
Strength Degrading	C							6

* Connections C1 and C2 already fractured by 50% amplitude test

In the interests of space, time, and avoiding unnecessary redundancy, comparisons are not made for all response quantities for each comparison set. Only those quantities of interest for a particular comparison set are presented. The quantities presented for each set are shown in Table 6-3.

Table 6-3. Response quantities considered for each comparison set

Response Quantity	Comparison Set Number											
	1	2	3	4	5	6	7	8	9	10	11	12
Relative in-plane displacement	x	x	x	x	x	x	*	*		x	x	
Interstory drift ratio (Θ_1, Θ_2)	x	x	x	x	x	x	*	*		x	x	x
In-plane base shear	x	x	x	x	x	x	*					
Base shear-interstory drift hysteresis	x	x	x	x	x	x	x	x	x	x	x	x
λ_{Vb}	*	*	*	*	*	*	*	*		*	*	
λ_{T1}	*		*		*	*	*	*				
Absolute in-plane acceleration	x	x	x	x			*	*				
Relative in-plane acceleration	x						*					
Connection moment	x		x									
Connection rotation	x		x									
Connection moment-rotation hysteresis	x	x	x	x	x	x				x		
Column axial force	x											
Beam vertical accelerations												x
Beam strains, high-speed data												x

x Graphical comparisons

* Percent differences only

6.1.2 Effects of Other Variables in the Comparison Sets

In each comparison set (or subset), there is one key variable. The sets are defined in order to facilitate the detection and understanding of the effects of the key variable. However, in the case of some key variables, there is an associated variable or variables. These associated variables may also have effects on the system response quantities discussed in Section 6.2, and so it is important to identify them here.

In the case of Comparison Sets 1-5a and 6, where the effects of the key variable hysteretic type are examined, the connection strength (i.e., bending moment) at which nonlinear behavior begins varies with hysteretic type. This is because each hysteretic type is achieved by a unique configuration of a particular type (or types) of coupons in the clevis connection. These configurations do not all have the same yield or fracture strength, as shown in Table 6-4, though they have very similar initial stiffness, as shown in Section 5.1.

Table 6-4. Average moment quantities by hysteretic type

Hysteretic type	Max plastic M (k-in.)	Yield M (k-in.)	Fracture M (k-in.)	Min. Residual M (k-in.)	Max Residual M (k-in.)	Max M in comp (k-in.)
Ductile Baseline	145	127	--	--	--	--
Brittle Fracture	--	--	101	60	71	113
Ductile Fracture	--	--	108	62	70	115
Deformation Softening	81	81	--	--	--	--
Strength Degrading	160	128	--	--	--	--

During the connection design and testing process, it became apparent that it was not possible to obtain the same initial stiffness and yield or fracture strength for all the desired hysteretic behavior types. Thus, some variability in strength was allowed where necessary. The effects of strength on response quantities of interest will be examined and evaluated in an analytical parametric study, which is located in Chapter 8.

In Comparison Sets 7 and 8, which examine the effects of the key variable excitation, it is important to recall that the amplitudes of the excitations are scaled to the same peak velocity. Therefore, the peak acceleration and peak displacement are associated variables which may vary rather widely between excitations. These differences in excitation amplitude measures must be kept in mind when making comparisons of the effects of excitation on response quantities, particularly when the quantity is related to a particular excitation amplitude measure.

6.1.3 Comparison Measures

Two major ways of measuring the differences in the data between tests in a comparison set are employed in this chapter. The primary and most information-rich approach is graphical comparison. Time history or hysteretic data for all tests in a comparison set are plotted on a single graph, facilitating comparisons throughout the duration of the response. All comparison plots are located in the text of this chapter.

The second approach to comparison is a numerical one, using only the maximum and/or residual values from a time history. These point values are then compared between tests using percent differences, which were defined in Section 4.4.2. Tables of percent differences, organized by comparison set, are found in Appendix E and referenced in the text where appropriate.

For the sake of brevity, the global error bounds are not reported along with percent differences in the following sections. For instance, an x percent difference in maximum base shear will be reported as x% rather than x% +/- y% error. However, the reader should keep in mind that the values being compared can only be considered accurate to within the estimated global error bounds in Table 4-9.

6.2 COMPARISONS OF SELECTED RESPONSE QUANTITIES

In this section, the effects of key variables such as hysteretic degradation type on particular structural response quantities will be examined using the previously defined comparison sets. The comparisons are presented by set, and all of the response quantities of interest for a particular set will be discussed together. As previously noted, these response quantities of interest differ from set to set. The arrangement by sets facilitates understanding of specimen behavior by encouraging examination of the interrelation of response quantities.

6.2.1 Comparison Set 1 — B patterns, 1.2 Second Cosine Pulse

In Comparison Set 1, the key variable examined is the effect of hysteretic type. This set contains the ductile baseline case, BP brittle and ductile fracture patterns, and the deformation softening B pattern. The B and BP patterns have hysteretic degradation in the first-story connections only; the second-story connections are ductile baseline connections. The excitation for all tests is the 1.2 second cosine pulse at 100% amplitude.

All of these tests were introduced as case studies for their respective hysteretic types in Sections 5.2.1 to 5.2.4. The catch cables did not engage for any of the tests, so the response was unhindered. The percent differences for this set are found in Tables E-1 through E-3. In this case, the percent differences between the DF BP and BF BP patterns are larger than the global error bounds, so results will be discussed for each case individually.

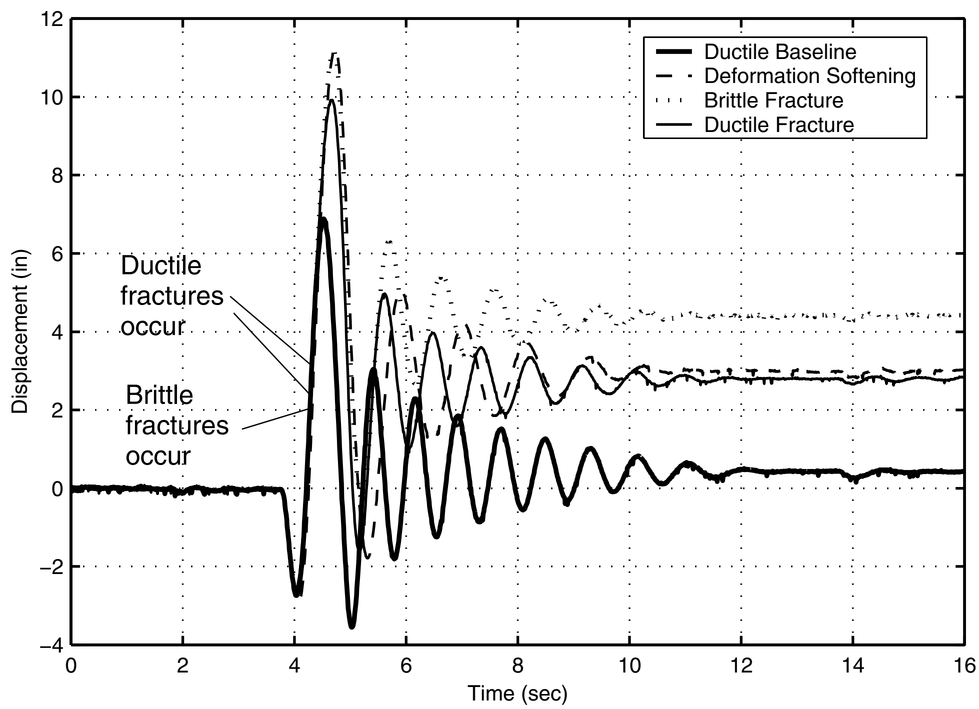

Figure 6-1. Comparison of relative displacements at top, B patterns, 1.2 sec cosine pulse

Relative displacements at the top of the frame are compared in Figure 6-1. All of the patterns with hysteretic degradation show significantly larger maximum and residual displacements than the ductile baseline case. The maximum relative displacements increase over the ductile case by 62%, 43%, and 63% for the brittle fracture, ductile fracture, and deformation softening cases, respectively. The brittle fracture case has the greatest increase in residual displacement (900%) over the ductile baseline case, followed by the deformation softening (580%) and ductile fracture (540%) cases. The increases in maximum displacement have similar absolute value to the increases in residual displacement, but the small numerical value of the residual displacement causes huge percent differences. For these two patterns, the percent difference in the maximum displacement and drift response was about 7%, while the difference in residual measures was about 48%, with the BF BP pattern having the greater response, as shown in the plots. The differences between the BF BP and DB patterns were about 50% for maximum values and 900% for residual values, due to the fact that the residual displacement for DB was almost zero.

The percent differences were much smaller between the degrading patterns themselves. The differences between the BF BP and DFS B patterns were not significant for maximum values and the BF BP residual values were about 47% larger. Conversely, the differences between the DF BP and DFS B patterns were not significant for residual values, and the DFS B maximum values were about 13% larger.

The portion of the response during the pulse is examined in Figures 6-2 and 6-3. Figure 6-2 shows that both fracture patterns have very similar responses to the ductile baseline case until about 4.4 seconds, when response for the fracture cases continues to increase, while the ductile baseline case peaks out. There is no sudden change in the displacement response due to the fractures, as the response remains smooth. The responses of the two fracture cases diverge shortly thereafter, as the brittle fracture case has a larger maximum response.

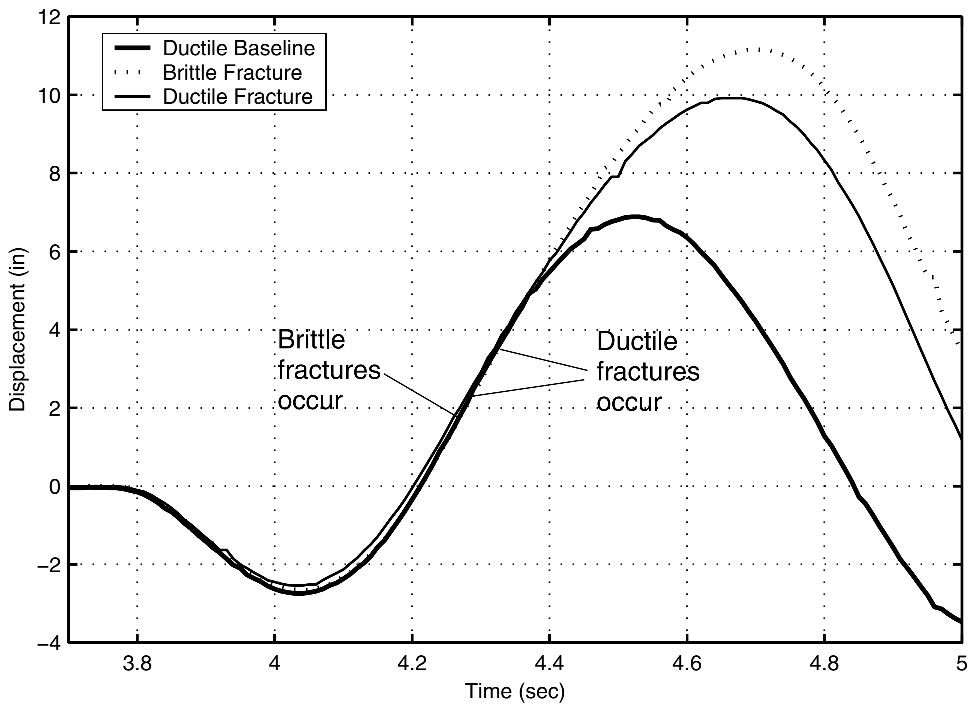

Figure 6-2. Close-up comparison of relative displacements at top, BP fracture and ductile baseline cases

Next, the deformation softening case is added in Figure 6-4. The response of this case begins to differ during the first negative excursion due to yielding in the first-story connections, as shown in Figures 6-10 and 6-14. This causes period elongation as well as a larger response. The response in the first positive excursion is the largest of any of the degrading patterns, going well beyond the ductile baseline case.

The trends for interstory drift are very similar to those for relative displacement. The portion of the response during the pulse is shown in Figures 6-4 and 6-5. The results are very similar for the first and second stories, indicating that the response for all of the cases is primarily first-mode.

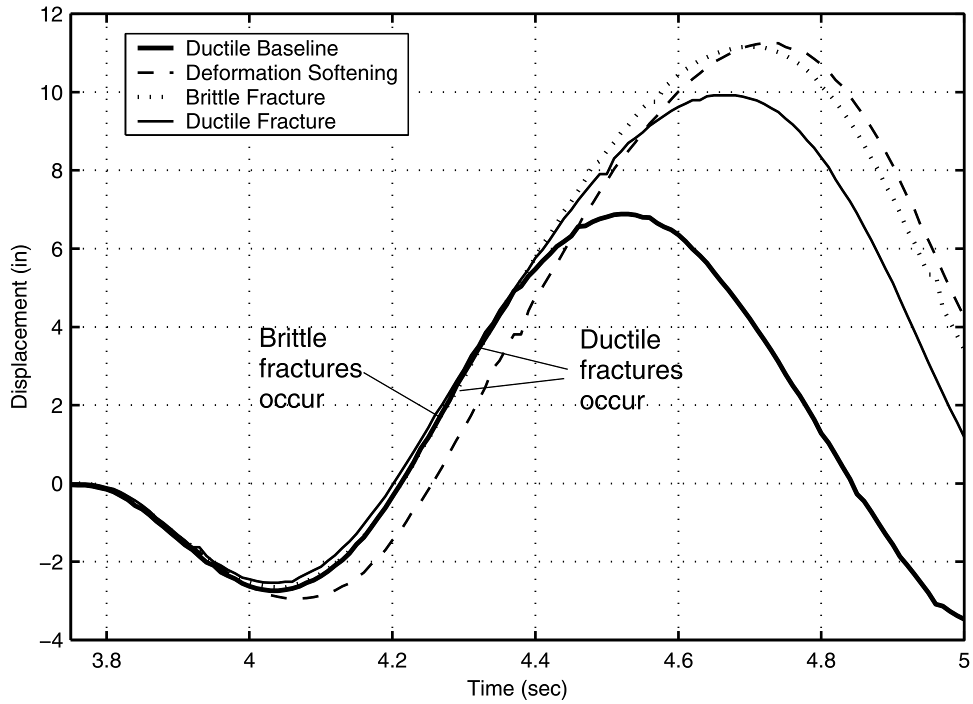

Figure 6-3. Close-up comparison of relative displacements at top, all B patterns

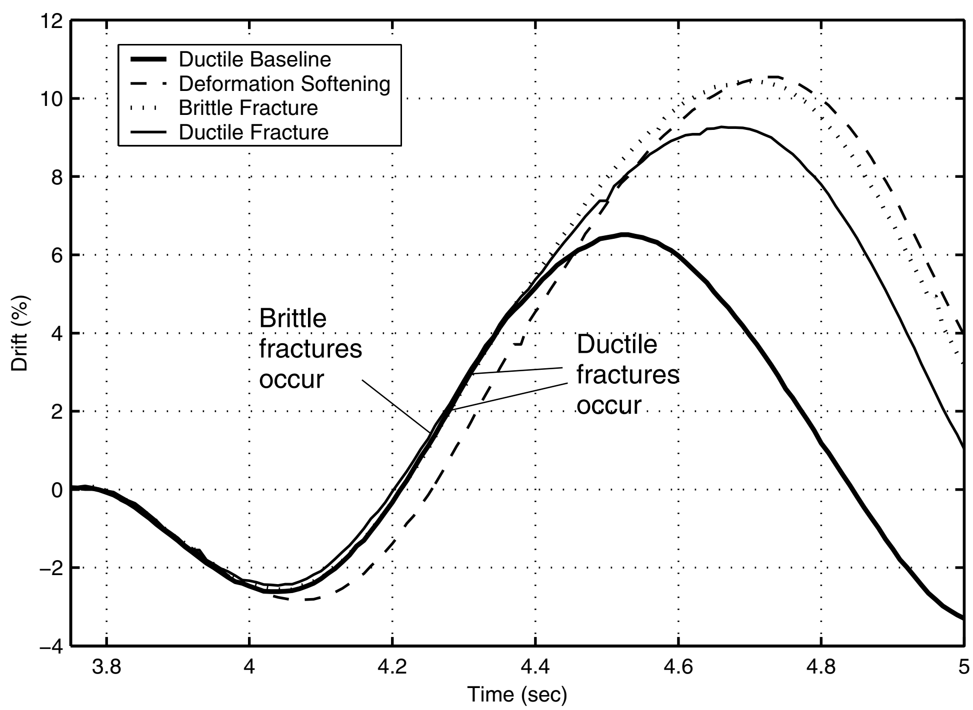

Figure 6-4. Comparison of first-story interstory drifts, B patterns, 1.2 sec cosine pulse

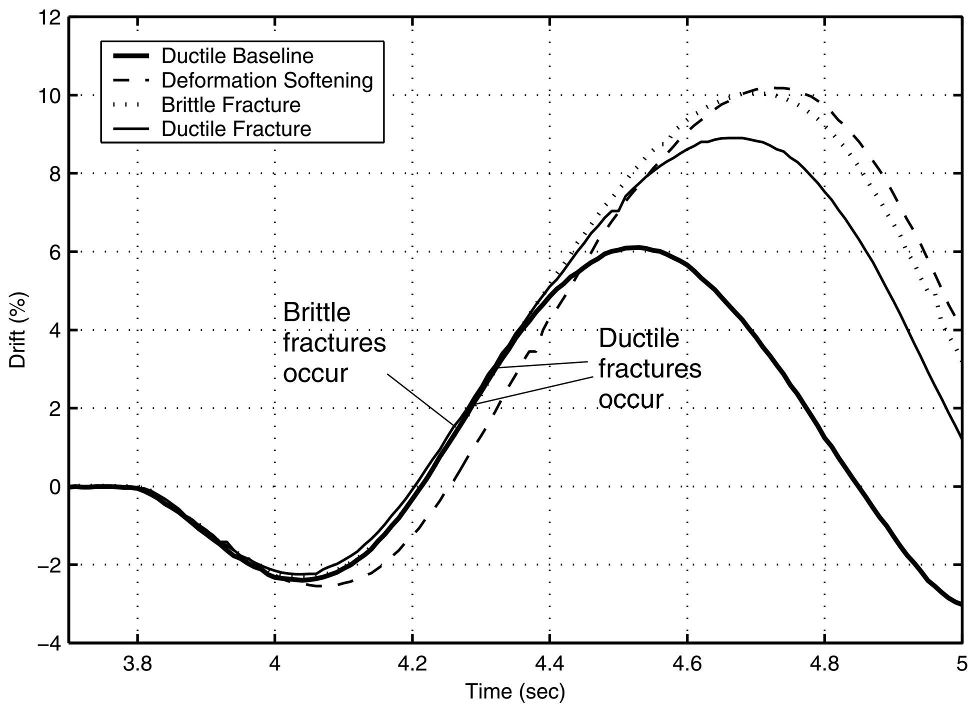

Figure 6-5. Comparison of second-story interstory drifts, B patterns, 1.2 sec cosine pulse

In contrast to the displacements, the effects of fracture and deformation softening on the base shear are sudden and immediate, as shown in Figures 6-6 and 6-7. The behavior of the degrading cases is similar, characterized by a short plateau followed by a steady decrease that persists until the specimen begins to unload. Some higher-mode effects are also visible in Figure 6-7 after degradation begins, particularly for the fracture patterns.

The previously mentioned yielding of the deformation softening case during the first negative excursion is evident in Figure 6-7. A small discontinuity as the base shear nears zero is also observable. This can be attributed to the severe pinching seen in the deformation softening connection hysteresis in Figure 6-10.

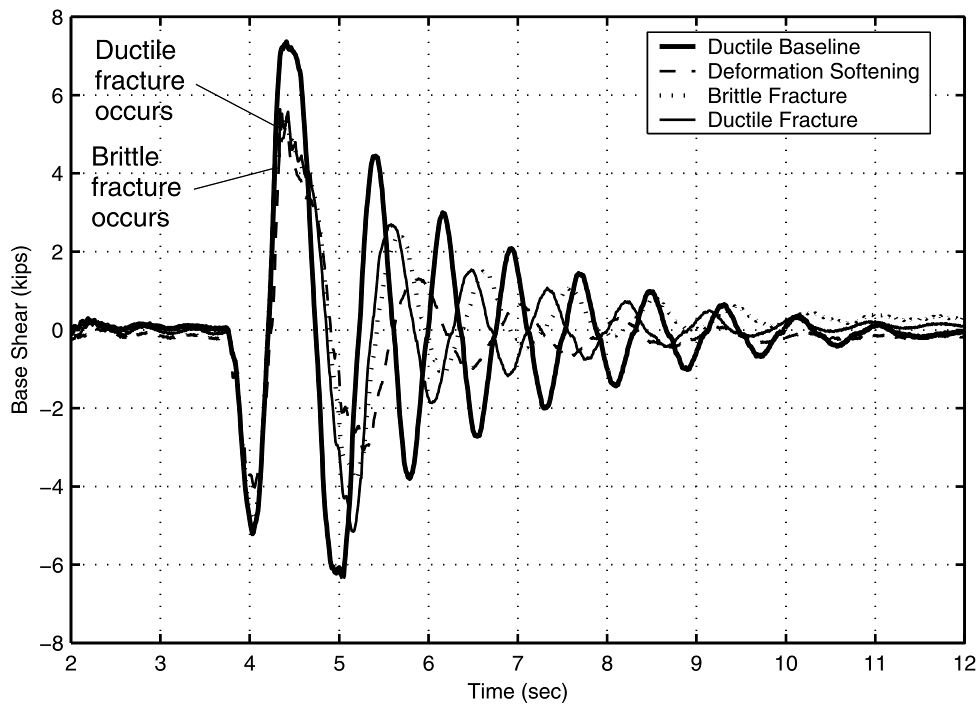

Figure 6-6. Comparison of base shear time histories, B patterns, 1.2 sec cosine pulse

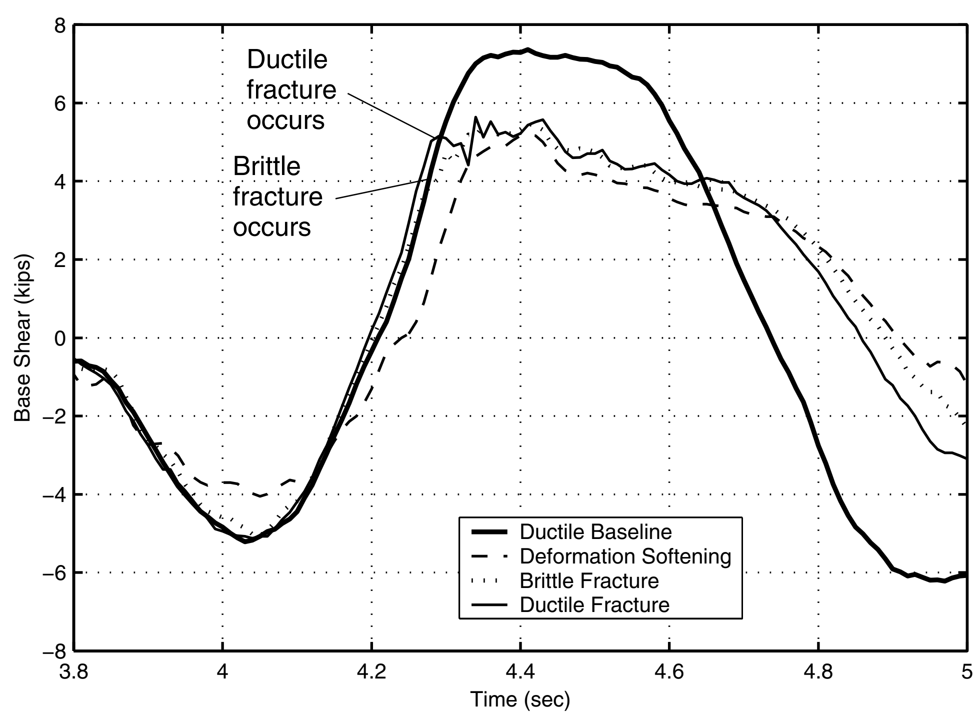

Figure 6-7. Close-up of base shear time histories, B patterns, 1.2 sec cosine pulse

The base shear and interstory drift time histories are next plotted together in Figure 6-8 to show system-level hysteresis. The effects of degradation are apparent: reduced strength and increases in displacement. The increase of displacements with strength loss may be indicative of the structure's position on the response spectrum, which is on the ascending branch where displacements are not preserved. The residual displacements are lower for the deformation softening case than either of the fracture patterns. This is most likely due to the lower unloading stiffness of the DFS B pattern, which allows it to "come back" farther when unloading, reducing the residual displacement as shown in Figure 6-10. The negative slope of the hysteresis curve for the degrading patterns indicates negative stiffness in the connections, P-Δ effects, or a combination of the two. At the level of drift the specimen is experiencing, P-Δ effects are expected.

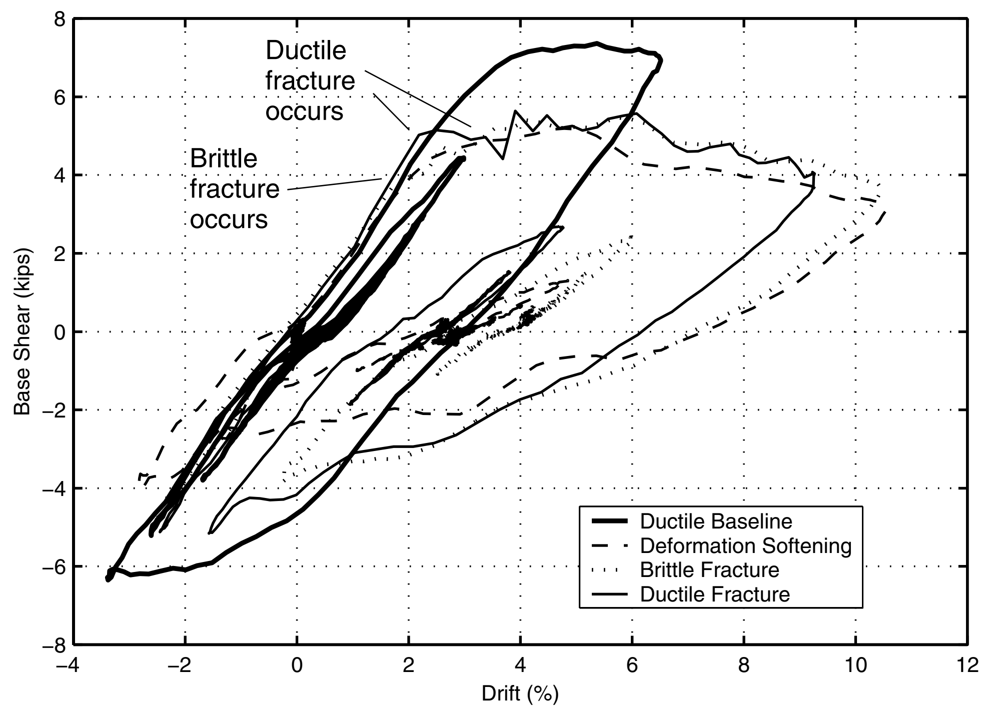

Figure 6-8. Comparison of base shear first-story drift hysteresis for 1.2 sec cosine pulse, B patterns

The nature of the decrease in base shear indicates that the connections are steadily losing strength after the initial fracture or yielding occurs. This is indeed the case, as shown in Figures 6-9 and 6-10. All of the degrading cases have negative post-yield or post-fracture stiffness, which causes a steady drop in the moment capacity. By equilibrium, this translates into a steady drop in base shear for the frame.

Figure 6-10 shows similar behavior for the ductile and brittle fracture patterns, though the brittle fracture pattern has larger maximum and residual rotations. In both cases, the unloading and reloading stiffnesses have been significantly reduced by the fracture and subsequent buckling of the compression coupon. This reduction is greater for the brittle fracture case, which is expected since the maximum rotations are about 15% larger. The residual displacements are also larger for the brittle case, even though the specimen was able to come back farther due to its reduced stiffness. Some pinching is also present for the fracture cases as the moment passes through zero.

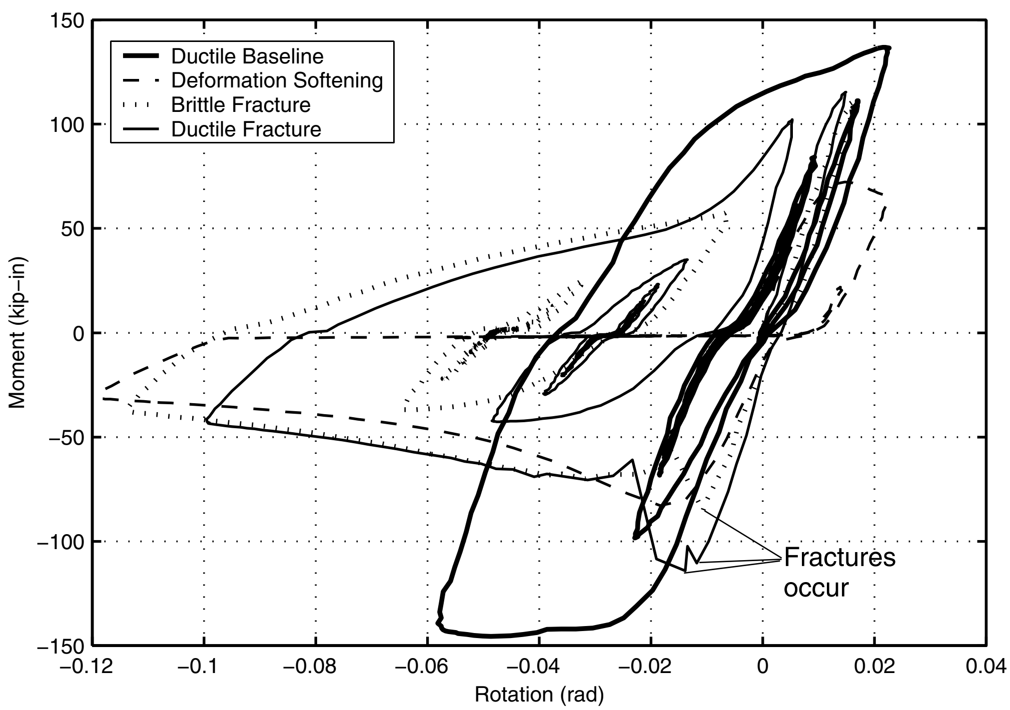

Figure 6-9. Comparison of C1 moment-rotation hysteresis, B patterns, 1.2 sec cosine pulse

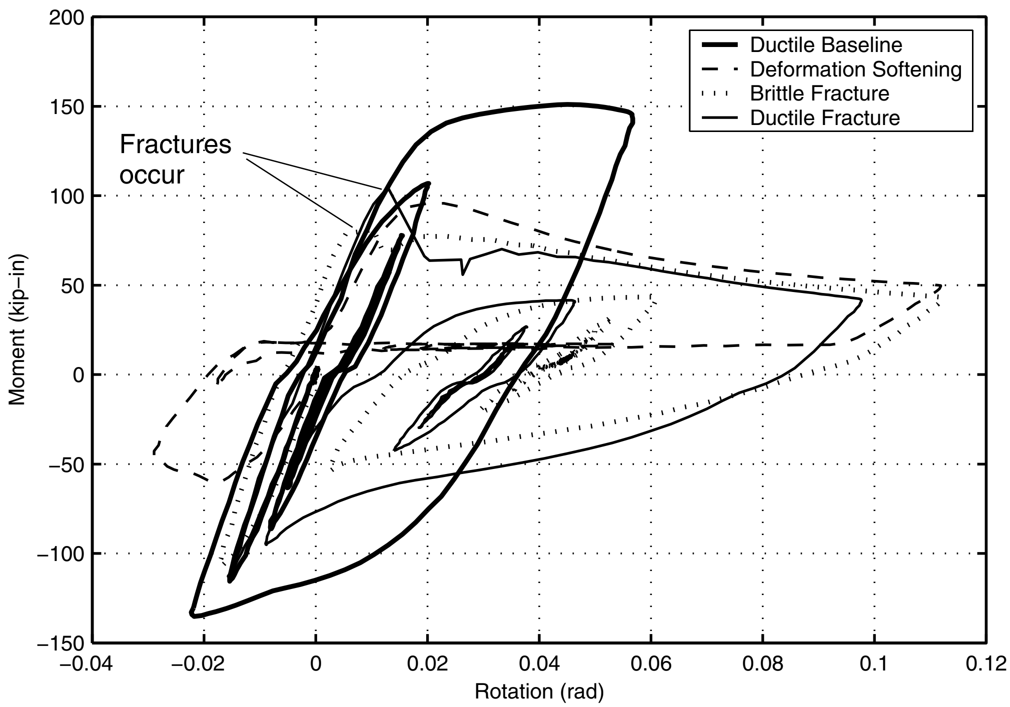

Figure 6-10. Comparison of C2 moment-rotation hysteresis, B patterns, 1.2 sec cosine pulse

There are some important similarities, as well as differences, in the response of the deformation softening pattern and the fracture cases. The most important similarity is that the post-yield stiffness for the deformation softening case is very close in slope to the post-fracture stiffness. The most readily apparent difference is the presence of severe pinching in the hysteresis of the deformation softening case, but this pinching was intended in the design, as discussed in Chapter 3. The yield strength of the deformation softening connections is also significantly lower than the fracture or yield strengths of the other patterns. This causes some plastic deformation to occur in the first negative excursion, as shown in Figure 6-12, while the other patterns remain elastic. Also, the deformation softening case has greater maximum rotation for C1 and similar maximum rotation for C2.

The moment and rotation time histories for C2 are shown in Figures 6-11 through 6-14, and these show similar behavior to the global displacements and forces except that the fractures are much more evident, particularly in the case of the rotations. In Figure 6-14, a change in the slope of the rotation curve at fracture is evident, as well as some discontinuities for the ductile fracture case.

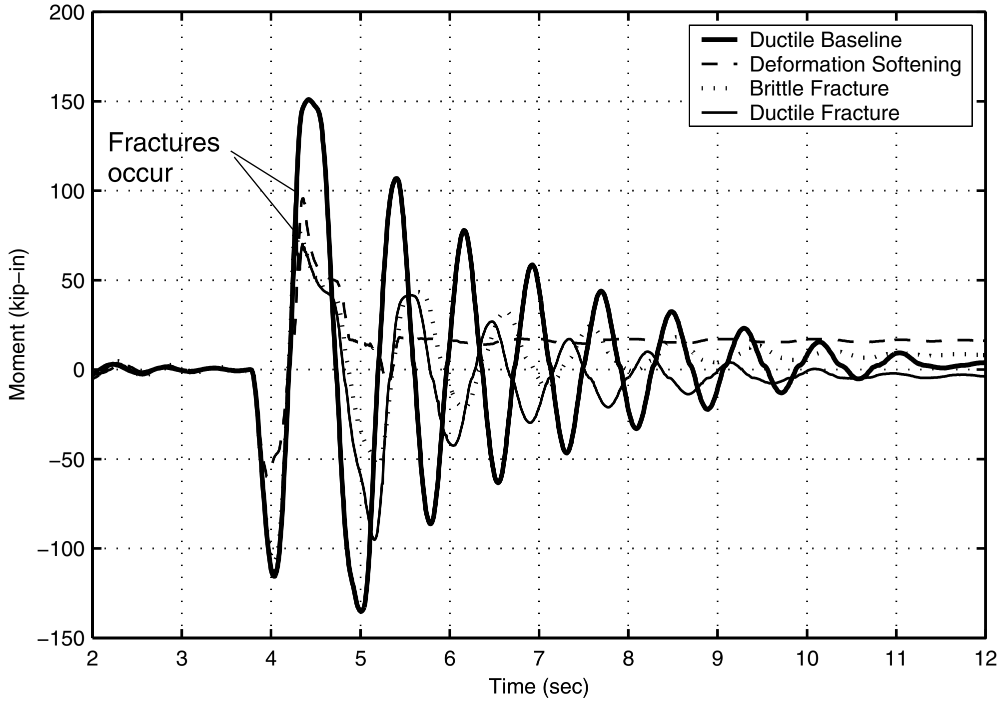

Figure 6-11. Comparison of C2 moments, B patterns, 1.2 sec cosine pulse

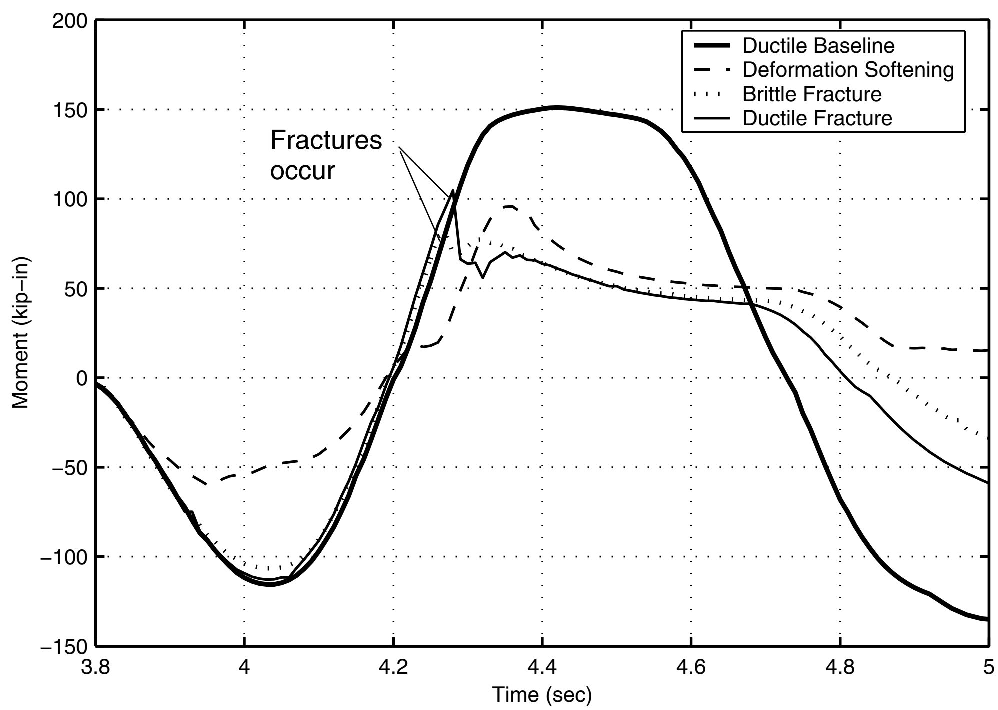

Figure 6-12. Close-up of C2 moments, B patterns, 1.2 sec cosine pulse

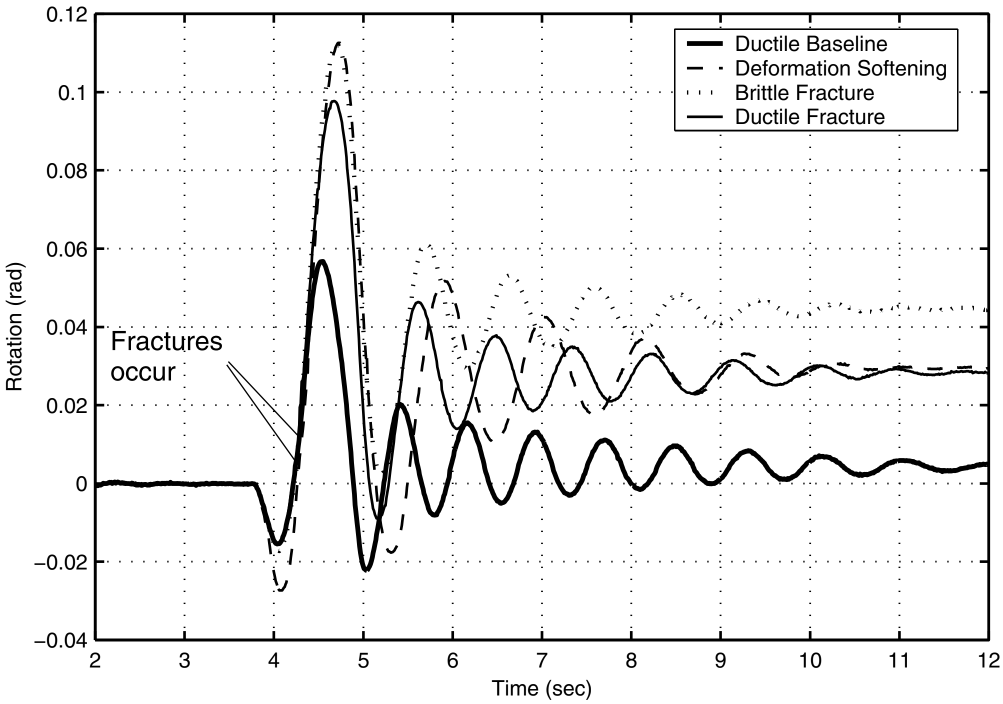

Figure 6-13. Comparison of C2 rotations, B patterns, 1.2 sec cosine pulse

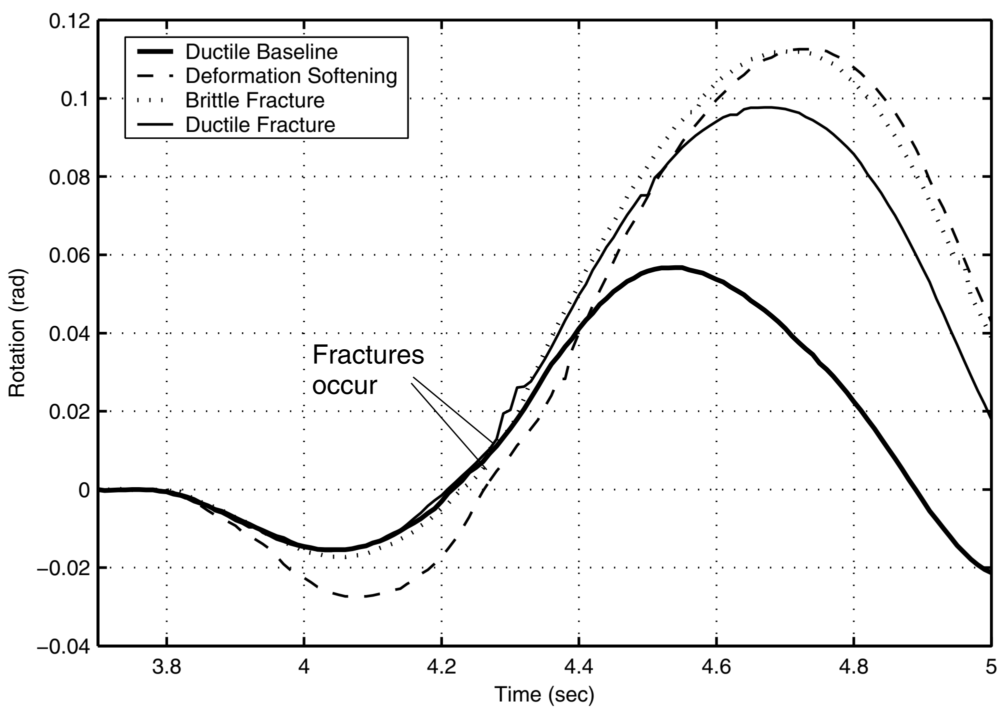

Figure 6-14. Close-up of C2 rotations, B patterns, 1.2 sec cosine pulse

Total accelerations at the top of the frame are shown in Figures 6-15 and 6-16. The effect of the fractures is a sudden discontinuity in the increase of acceleration. Some higher frequency vibrations are present in all of the time histories, indicating that the participation of higher modes is not confined to the fracturing case. The acceleration responses are similar for the fracture and deformation softening, though the fracture patterns have more high-frequency activity in the neighborhood of the fracture. All of the degrading patterns show a significant decrease in acceleration at the onset of degradation with respect to the ductile case. This is expected, since the total accelerations are related to global forces, and the global force capacity has been reduced substantially in these cases, as has been discussed previously.

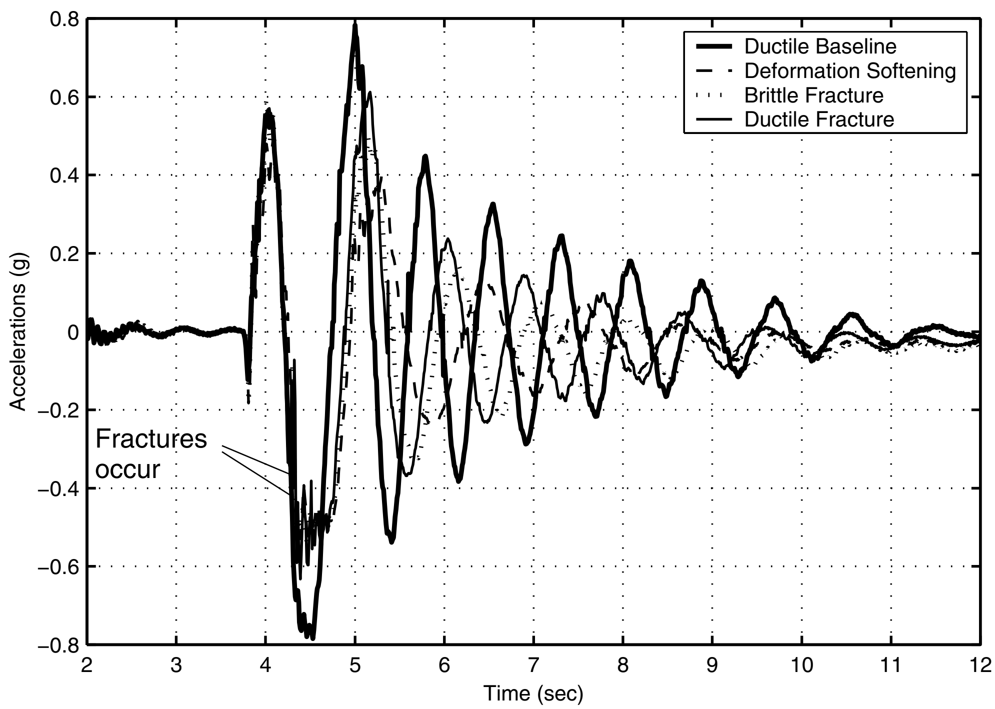

Figure 6-15. Comparison of second-floor absolute accelerations, B patterns, 1.2 sec cosine pulse

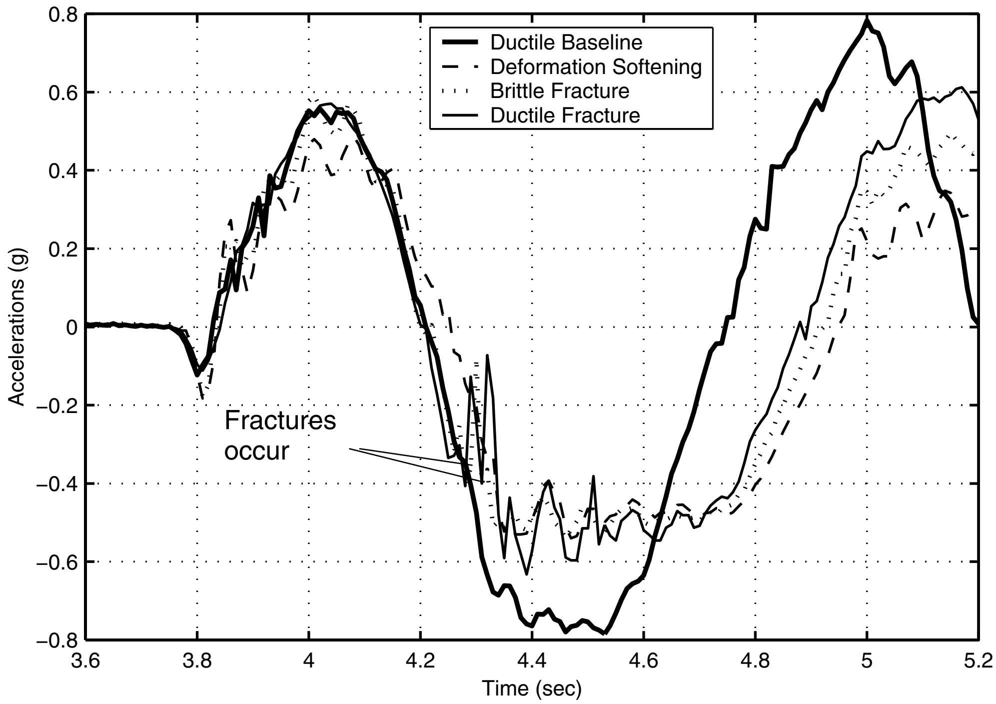

Figure 6-16. Close-up of second-floor absolute accelerations, B patterns, 1.2 sec cosine pulse

Relative acceleration time histories at the first and second floors are shown in Figures 6-17 through 6-20. The first observation is that the acceleration response is similar for all the patterns, with significant differences in maximum amplitude only for very short periods at the beginning of the excitation and in the middle of the negative portion of the pulse. The exception is the second-story accelerations for the ductile baseline case, which diverges after degradation begins in the other patterns. The close-ups in Figures 6-18 and 6-20 show that bursts of high-frequency activity occur in a sine pulse-like waveform after the fractures occur. These high frequencies do not seem to be caused by the fractures, however, because they are seen for the deformation softening case as well. The amplitude of this activity is about 0.4g for both stories, though degradation occurs only in the first story.

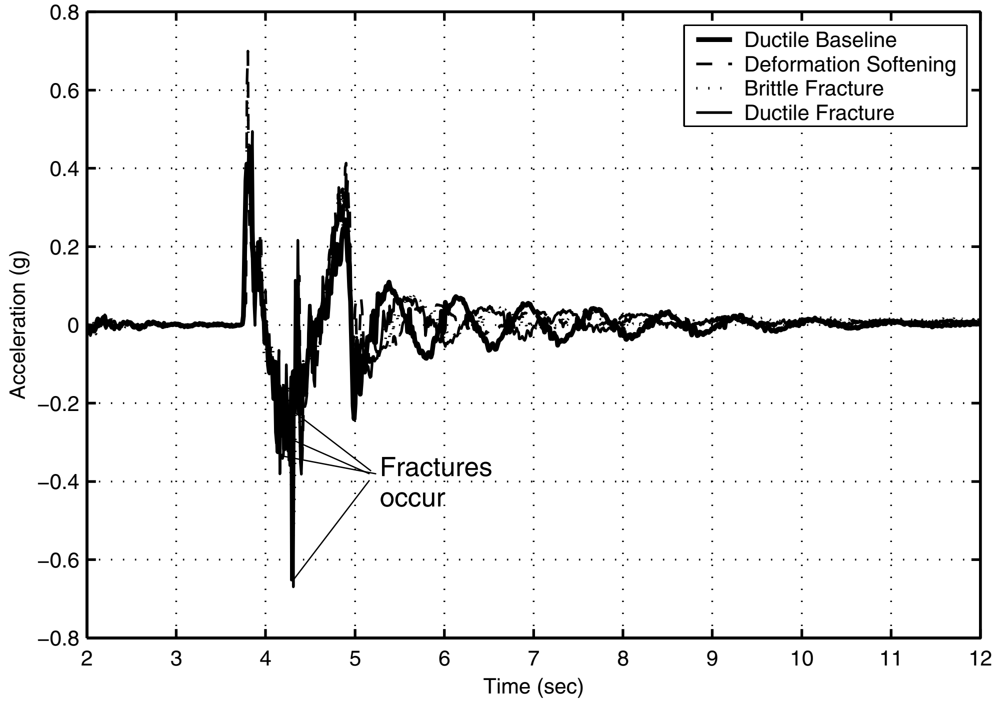

Figure 6-17. Comparison of first-floor relative accelerations, B patterns, 1.2 sec cosine pulse

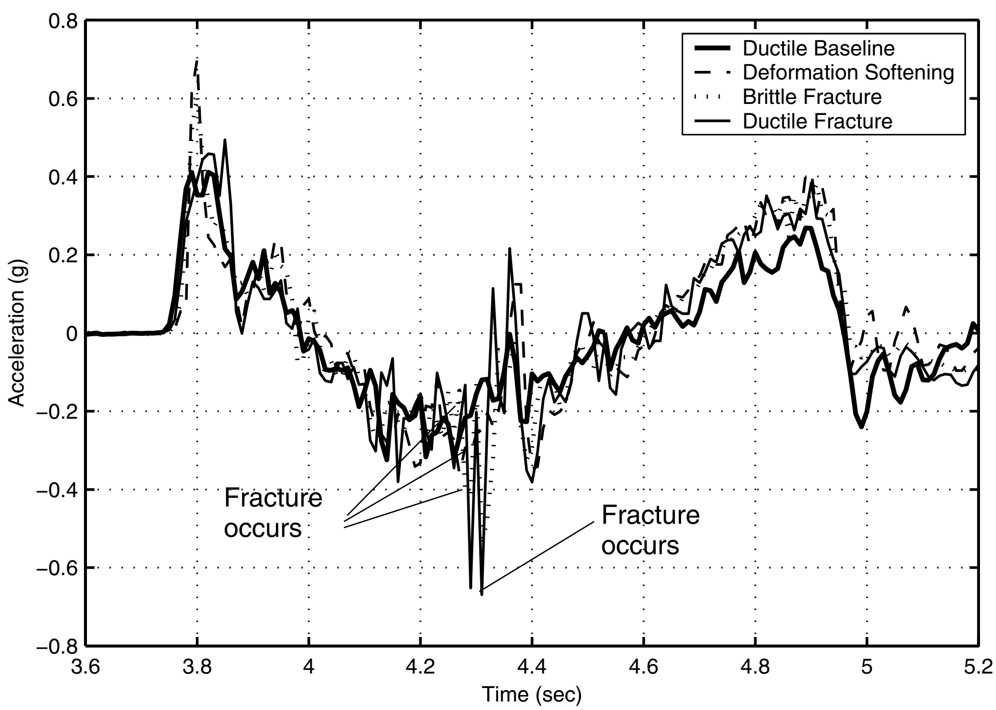

Figure 6-18. Close-up of first-floor relative accelerations, B patterns, 1.2 sec cosine pulse

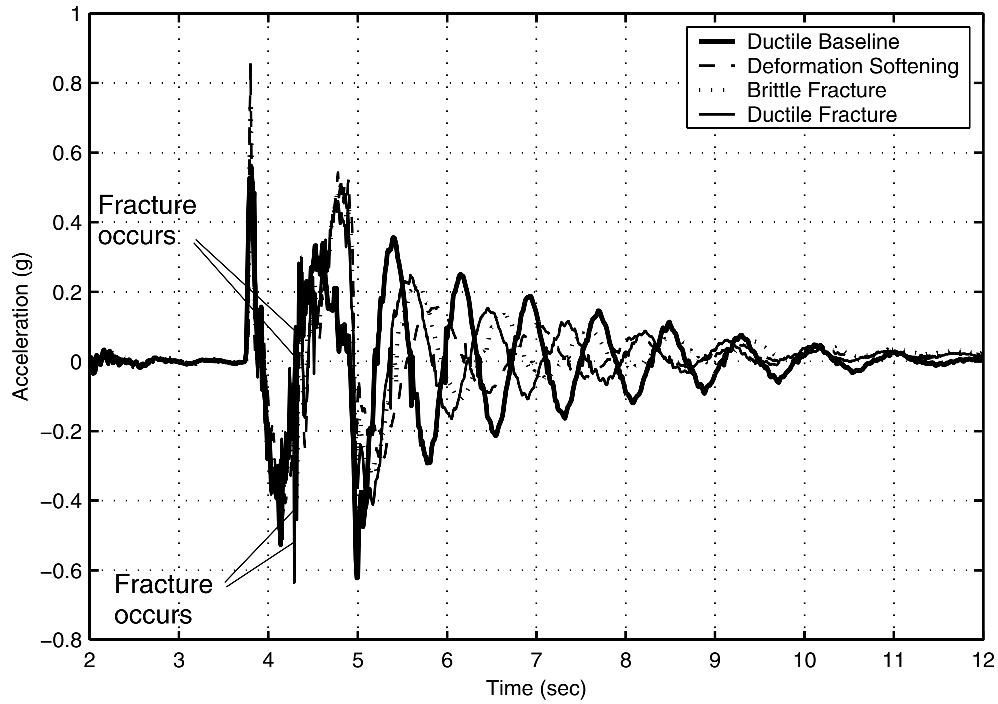

Figure 6-19. Comparison of second-floor relative accelerations, B patterns, 1.2 sec cosine pulse

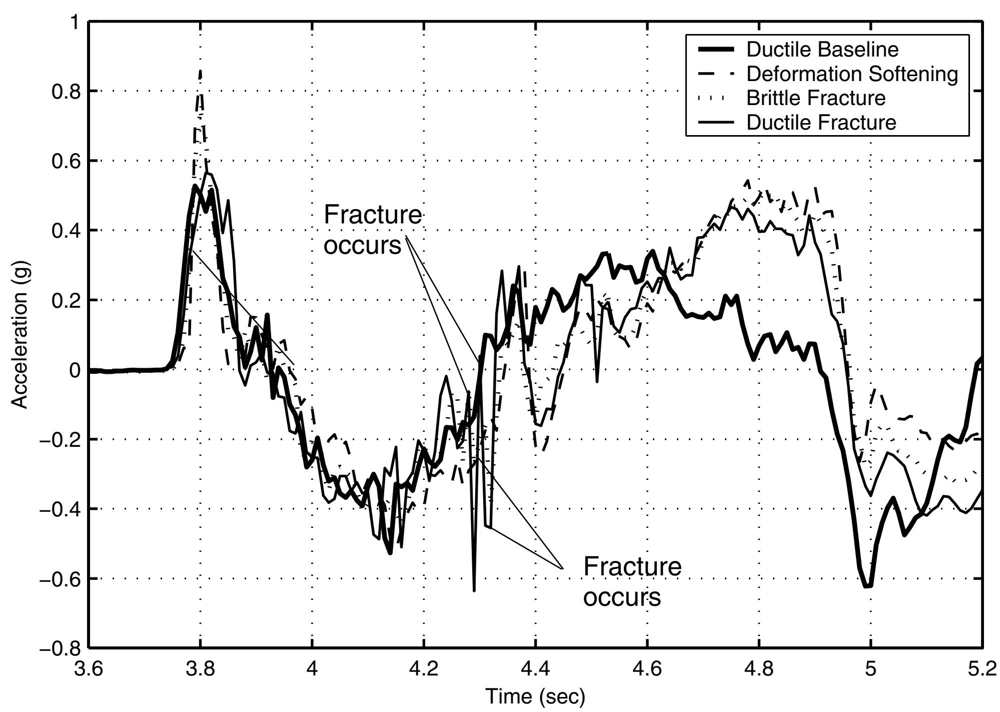

Figure 6-20. Close-up of second-floor relative accelerations, B patterns, 1.2 sec cosine pulse

Column axial force time histories for Main Column 1 (MC1) are compared in Figures 6-21 and 6-22. These forces are similar for the fracture and ductile baseline patterns until fracture occurs, at which point the forces in the fracturing system no longer increase in a smooth way. Only a small increase occurs prior to the response entering a long, essentially flat plateau which persists until the specimen unloads. The flatness of the plateau contrasts with the steady decrease seen previously in the base shear time histories. The axial force in MC1 is maintained because the decreases due to a reduction in beam shear are balanced by increases due to larger overturning moments as deformations increase. Since the bases of the columns are pinned, the frame overturning moment must be resisted by a tension-compression force couple composed of axial forces in MC1 and MC2.

The deformation softening case deviates from the ductile baseline and fracture cases during the first negative excursion due to plastic deformation, as discussed previously. However, the maximum value of base shear, which occurs after yielding, is very similar to that observed for the fracturing cases, which is roughly 75% of that observed for the ductile baseline case.

The column axial forces do not return to zero (as the base shear does) at the end of the excitation if there is residual displacement. By statics, the large residual displacement in combination with the weight of the structure creates a permanent overturning moment at the base, which is resisted by axial forces in the columns.

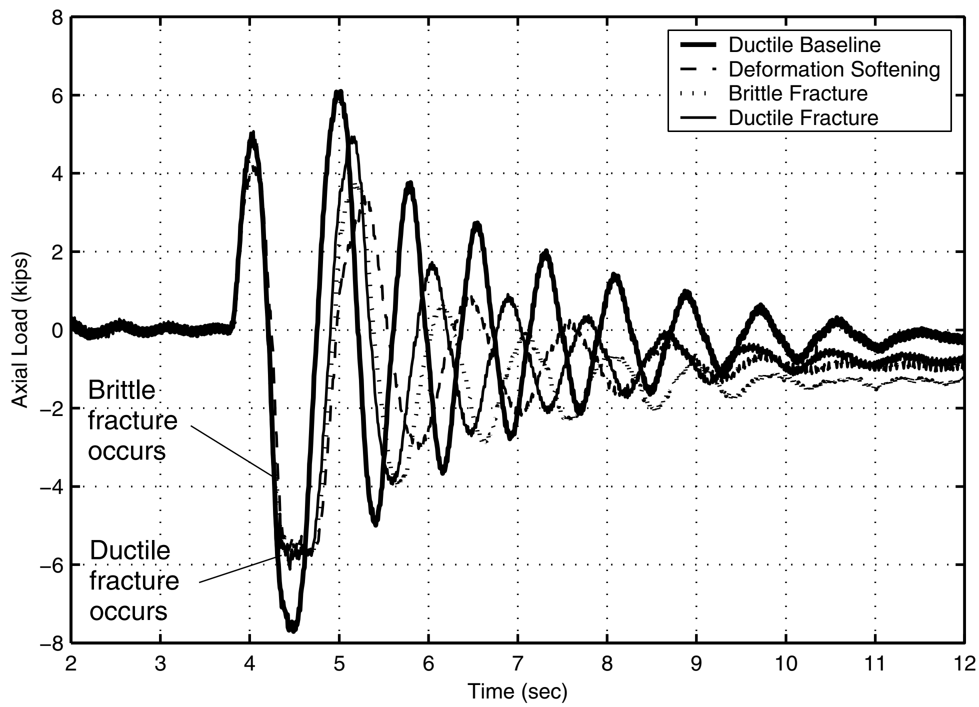

Figure 6-21. Comparison of MC1 axial force time histories, B patterns, 1.2 sec cosine pulse

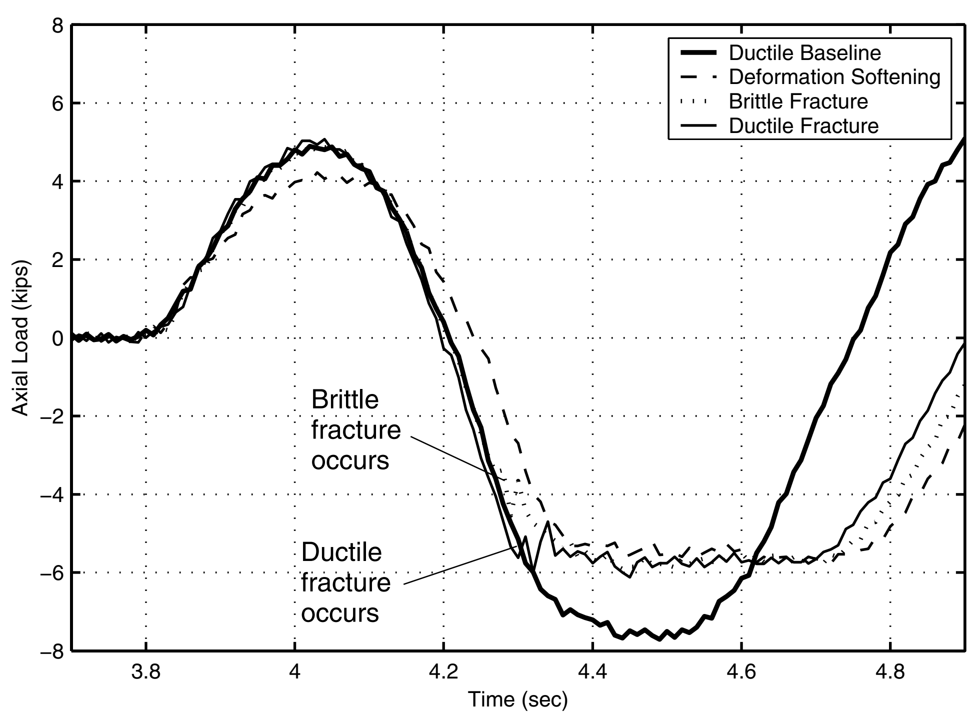

Figure 6-22. Close-up of MC1 axial force time histories, B patterns, 1.2 sec cosine pulse

The ductile fracture pattern had significant differences in response from the brittle fracture pattern, and the fractures seemed more spread out over time, so it is possible that some more yielding occurred prior to fracture than for the 0.6 second cosine pulse, which was discussed in Section 4.4.3. Due to the longer excitation and lower accelerations, the imposed strain rate is not as great for this excitation as for the 0.6 second cosine pulse, and this may play a role in making the connection slightly more ductile for this case.

The most important conclusion from this comparison set is that hysteretic degradation, regardless of whether it is fracture or deformation softening, has significant effects on most of the response parameters considered in this study. Maximum and residual displacements are increased, while base shear capacity is decreased, as are other force measures and accelerations.

6.2.2 Comparison Set 2 — C Patterns, 1.2 Second Cosine Pulse

As in Comparison Set 1, the key variable examined is the effect of hysteretic type. This set contains the ductile baseline case, CP brittle and ductile fracture patterns, and the deformation softening C pattern. These patterns have hysteretic degradation in all connections (except for the ductile baseline case, or course). The excitation for all tests is the 1.2 second cosine pulse at 100% amplitude. The catch cables were engaged for all tests except the ductile baseline case, so the maximum and residual values of the response quantities are in many cases determined by the level of interstory drift (approximately 16%) allowed by the catch cables. Percent differences are therefore not discussed, since they are determined from these values.

The complete displacement time history, with the point of catch cable engagement noted, is shown in Figure 6-23. All patterns except ductile baseline collapse during the first positive displacement excursion. In all of the cases, the impact was significant when the catch cables engaged, particularly for the DFS C case, which bounced off the cables back to vertical before coming to rest again, resulting in the odd-looking time history in Figure 6-23.

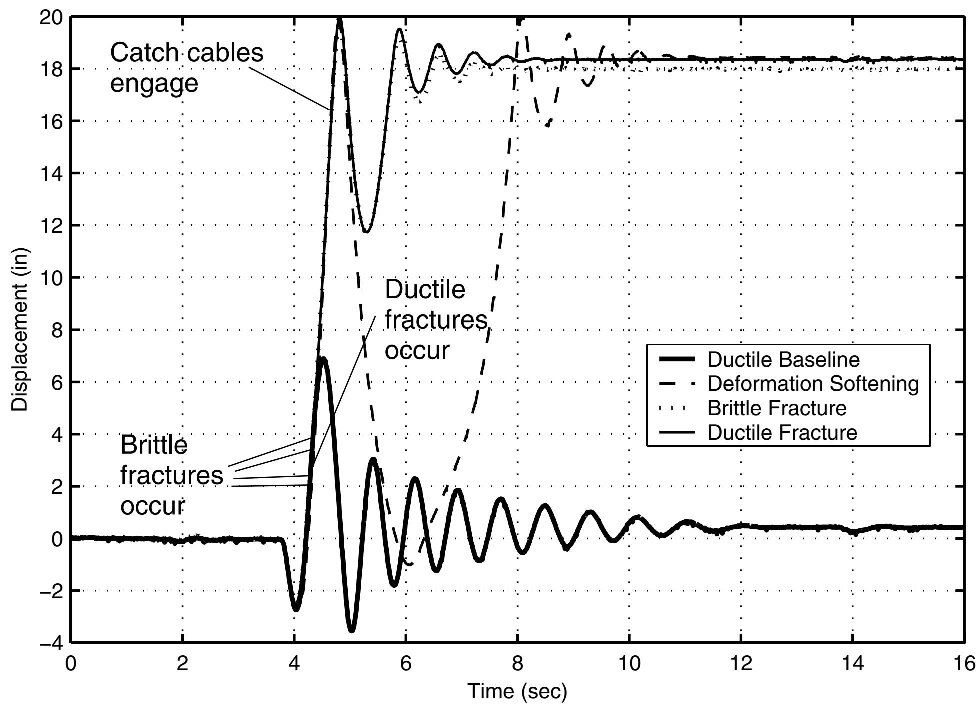

Figure 6-23. Comparison of relative displacements at top, selected C patterns, 1.2 sec cosine pulse

The pre-collapse interstory drift response of the various cases is shown in Figure 6-24. The response of the two fracture cases is identical to the ductile case until midway through the first negative excursion. The period of the fracture cases is slightly shorter than that of the ductile baseline case, but the response is similar until about 4% drift, when the ductile case response begins to slow. The deformation softening pattern shows some period elongation in the first negative excursion, followed by a rapid increase in drift and collapse. The slope of the displacement response is steeper, indicating greater velocity, which is evidenced by the larger impact of the cable catch shown in Figure 6-23. Second-story drifts are very similar to first-story drifts, so they are not discussed here.

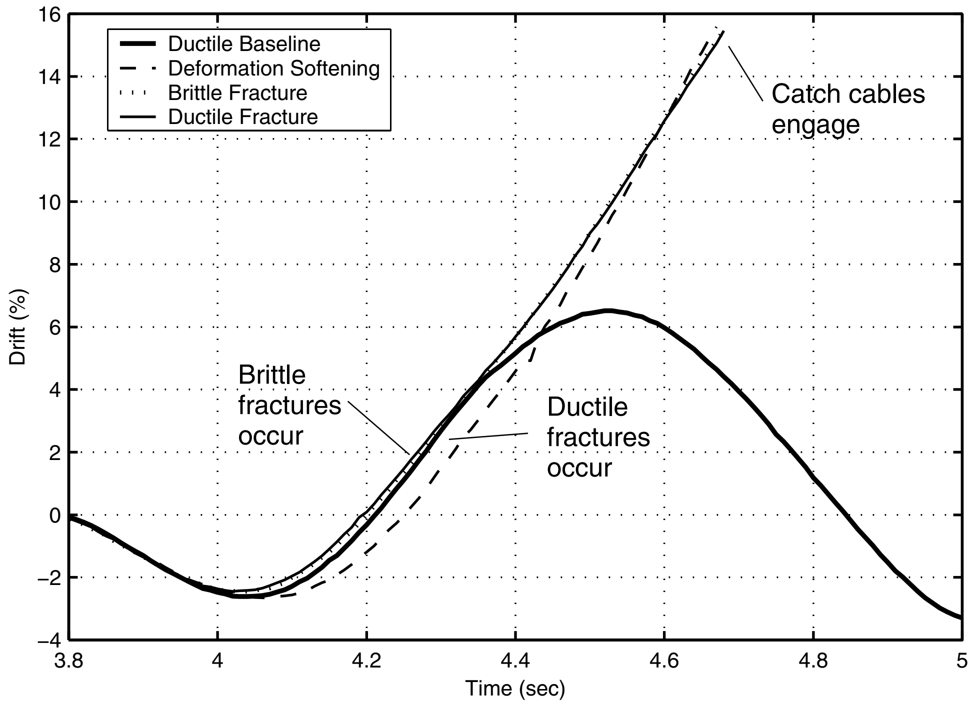

Figure 6-24. Comparison of first-story interstory drifts, C patterns, 1.2 sec cosine pulse

Base shear time histories are shown in Figures 6-25 and 6-26. All of the cases with degradation diverge suddenly from the ductile baseline case at the onset of degradation. This occurs at an approximately 50% larger base shear for the fracture cases than for the deformation softening case. However, after the initial transient effects due to fracture shown in Figure 6-26 subside, the remaining base shear capacity is only about 25% less for the deformation softening case.

In contrast to the B patterns examined in Comparison Set 1, there is no plateau of strength and the base shear begins to decrease at a fairly constant rate almost immediately for all of the degrading patterns. This is due to the presence of the degrading behavior at all of the connections, and the effects of degradation are not mitigated by the presence of ductile connections as they are for the B patterns. The rate at which the base shear decreases is very similar for all of the degrading cases, which can be explained by the similarity in post-yield and post-fracture stiffness shown in Figure 6-28.

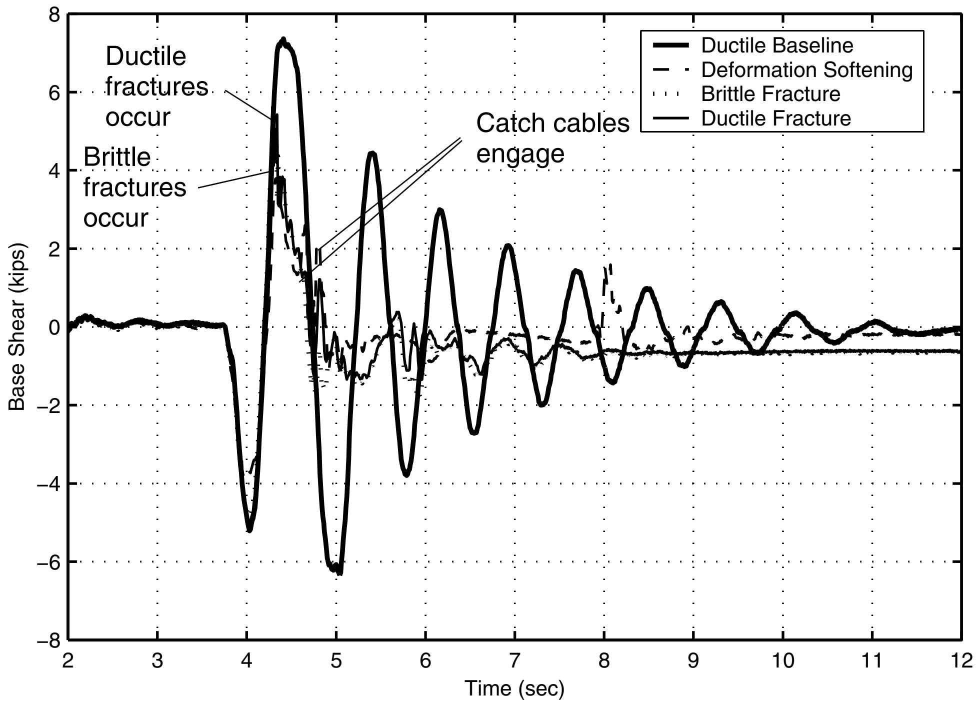

Figure 6-25. Comparison of base shear time histories, C patterns, 1.2 sec cosine pulse

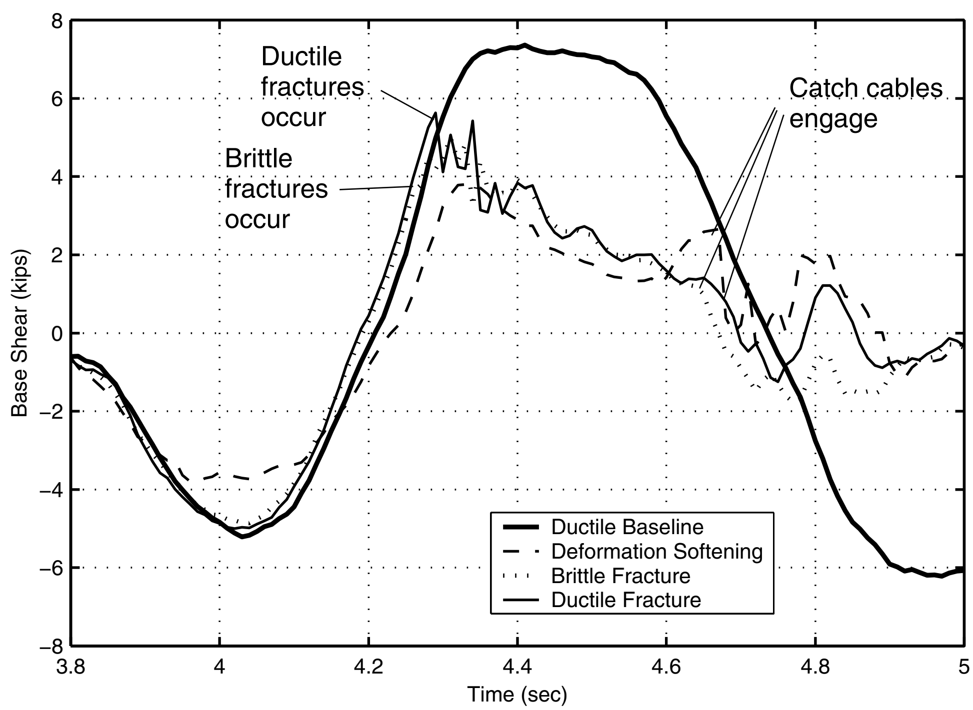

Figure 6-26. Close-up of base shear time histories, C patterns, 1.2 sec cosine pulse

The base shear and interstory drift time histories are next plotted together in Figure 6-27 to provide additional insight into the system behavior. The effects of the degradation are drastic for both fracture and deformation softening. The post-yield and post-fracture tangent stiffnesses of the system are both strongly negative, and the system strength is reduced by more than half from the time fracture or yielding occurs to the time the catch cables engage.

In addition, higher modes are clearly evident in the post-fracture response, particularly for the ductile fracture case. The participation of these modes is significantly less noticeable for the deformation softening and ductile baseline cases.

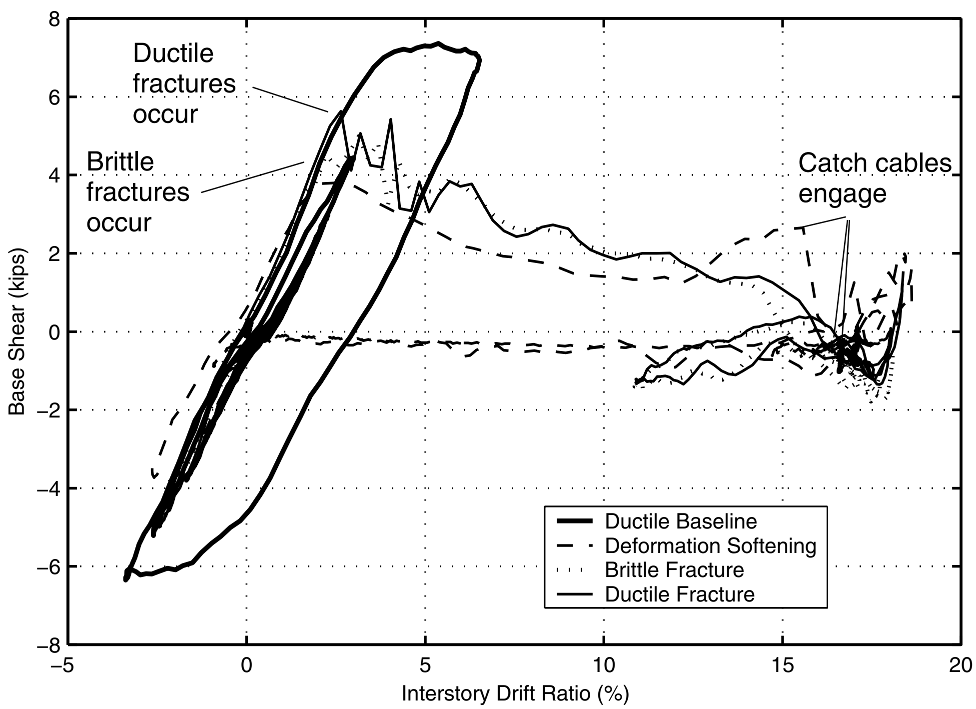

Figure 6-27. Comparison of base shear first-story drift hysteresis for 1.2 sec cosine pulse, C patterns

Similar trends are present in the connection moment-rotation hysteresis shown in Figure 6-28, except that there is no noticeable higher-mode response for any of the patterns. The occurrence of fracture is particularly evident in the ductile fracture case, and it appears that a small amount of yielding occurs just prior to fracture. The connection has clearly not reached its full plastic capacity, however. After fracture occurs, the tangent stiffness is virtually identical for the two fracture patterns, and is very similar to that of the deformation softening connection after buckling begins.

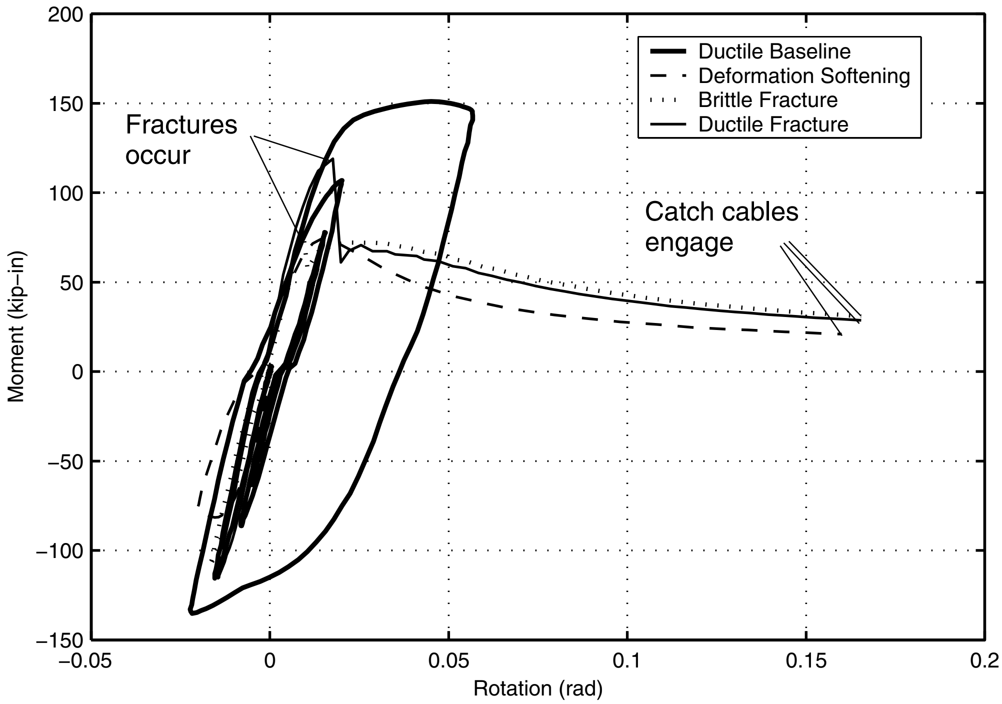

Figure 6-28. Comparison of C2 moment-rotation hysteresis, C patterns, 1.2 sec cosine pulse

Absolute acceleration time histories at the top of the frame are compared in Figure 6-29. The accelerations for the fracture cases are virtually identical to the ductile baseline case until fracture occurs, when the fracture-case accelerations suddenly become quite jagged. This high-frequency response decays significantly within about 0.2 seconds. The deformation softening case shows relatively little high-frequency response from the time when buckling begins to just before the catch cables engage.

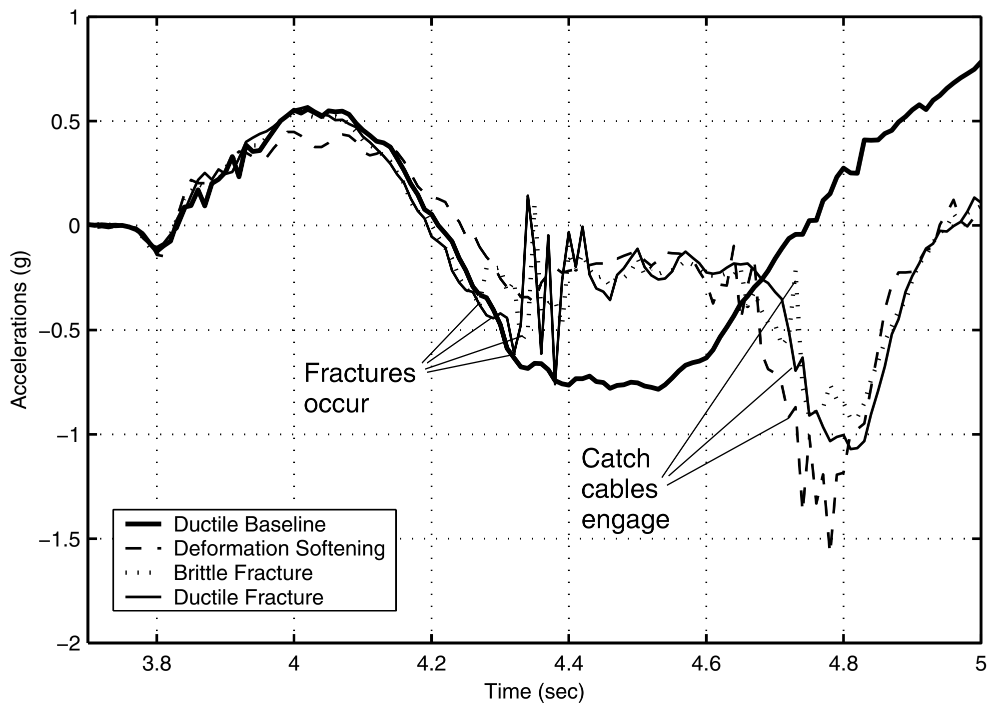

Figure 6-29. Close-up of second-story absolute accelerations, C patterns, 1.2 sec cosine pulse

The effects of hysteretic degradation on the overall system behavior are similar for the three types of degradation in this comparison set. The occurrence of degradation at all of the connections causes collapse for both fracturing and deformation softening cases for this excitation. In all cases, the strength loss caused by degradation lead to very large displacements, which cause geometric instability and collapse.

6.2.3 Comparison Set 3 — B Patterns, 0.6 Second Cosine Pulse

In Comparison Set 3, the BF BP, DF BP, and DFS B patterns are compared both with each other and with the DB C pattern for the 0.6 second cosine pulse excitation at 100% amplitude. The B and BP patterns have hysteretic degradation in the first-story connections only; the second-story connections are ductile baseline connections. In this set, as with the previous set, the key variable examined is hysteretic type. The percent differences for this set are found in Tables E-7 through E-9. It is possible that there was some interference from the catch cables in the three B pattern tests, but evidence is mixed and the catch cables certainly did not all engage fully. Relative displacements at the top of the structure and interstory drifts are compared in Figures 6-30 through 6-32.

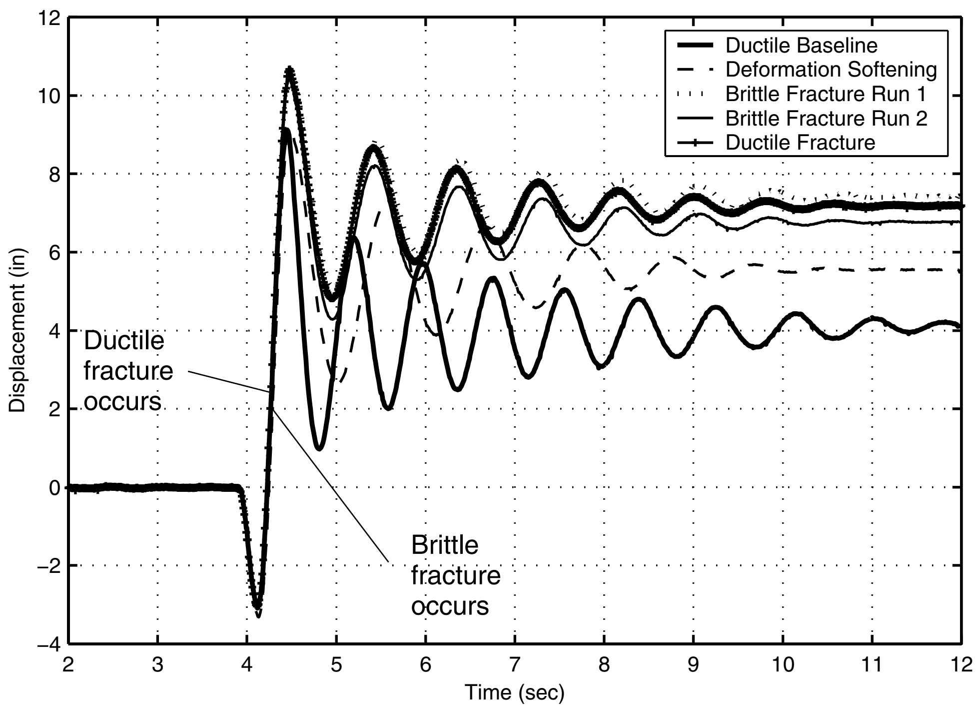

Figure 6-30. Comparison of relative displacements at top, B patterns, 0.6 sec cosine pulse

Next, in Figures 6-31 and 6-32, the portion of the response including the largest displacement excursion is examined. These plots show the critical region during and immediately following the pulse. The interstory drift ratio time histories are very similar for the first and second stories, with the first-story drifts being slightly larger; therefore only the first-story drifts are shown and discussed.

It is apparent from these interstory drift time histories that the fractures and the other types of deterioration studied do not cause any noticeable transient behavior or sudden changes in the global displacement response, which is very smooth in this region. The fractures also occur early in the pulse, with the brittle fractures and ductile fractures occurring at roughly the same time. Up until the point of fracture, the ductile baseline and fracturing cases have very similar responses as shown in Figure 6-31. After this point, the drift increases more rapidly for the fracturing cases than the ductile case, leading to larger maximum drifts for the fracture cases. There is also noticeable period elongation for the fracturing cases.

As shown in Figure 6-32, the deformation softening pattern diverges from the other patterns early on with the apparent period being elongated. This period lengthening is most likely due to coupon buckling and the ensuing loss of stiffness during the first negative incursion — the other patterns do not show the same degree of nonlinearity in this excursion (see Figures 6-36 and 6-37). The period elongation continues in the first positive incursion, and is significantly more than for either the ductile baseline or the “average” of the fracture cases (the ductile fracture case, which is almost the exact average). The maximum drift for the DFS case is about the same as the ductile baseline case, however.

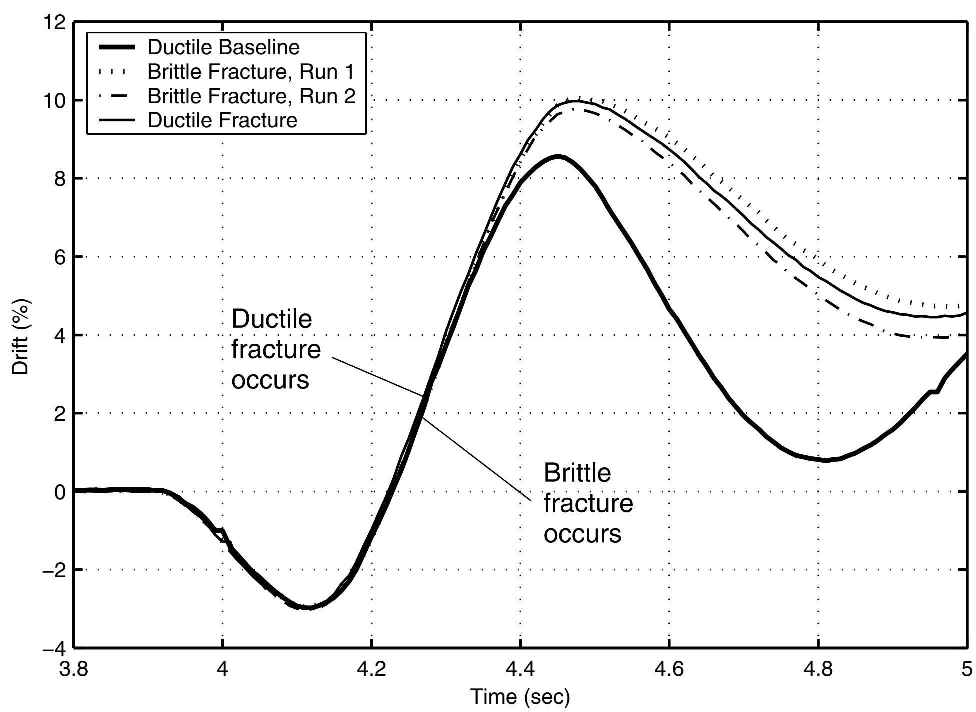

Figure 6-31. Close-up comparison of first-story interstory drifts, Fracture and DB patterns

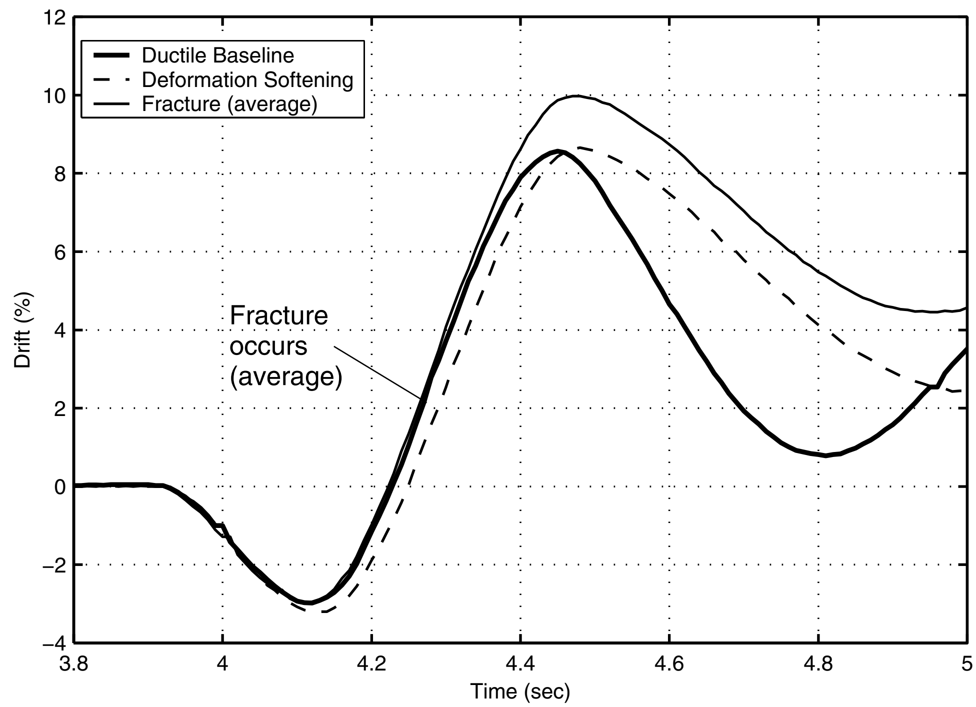

Figure 6-32. Comparison of first-story interstory drifts, deformation softening pattern added

As mentioned previously in Section 4.4.3, the percent differences between the DF BP and BF BP patterns were less than the global error bounds for all displacement measures. Thus, only differences between the BF BP pattern, the DB pattern and the DFS B pattern will be discussed. Maximum displacements and drifts were approximately 16% greater for the BF BP pattern than the DB pattern, while residual displacements and drifts were about 72% greater. The differences between the DFS B and DB pattern were less than the global error bounds for the maximum displacements and drifts, while the DFS B pattern showed residual displacements and drifts that were approximately 35% greater than for the DB pattern. Finally, the maximum displacements and drifts were approximately 15% greater for the BF BP pattern than the DFS B pattern, while the residual displacements and drifts were 28% greater.

In all of these cases, the maximum displacement values were much more similar than the residual displacement values. This indicates that multiple factors contribute to displacement values, and similar maximum displacements do not necessarily correspond to similar residual displacements.

Base shear time histories are shown in Figures 6-33 and 6-34. All of the types of hysteretic degradation caused significant reductions in base shear. In contrast to all of the other measures examined, there were significant differences—about 16%—between ductile and brittle fracture. Brittle fracture caused a decrease in maximum base shear of about 40% from the DB pattern and an increase of about 7% over the DFS B pattern.

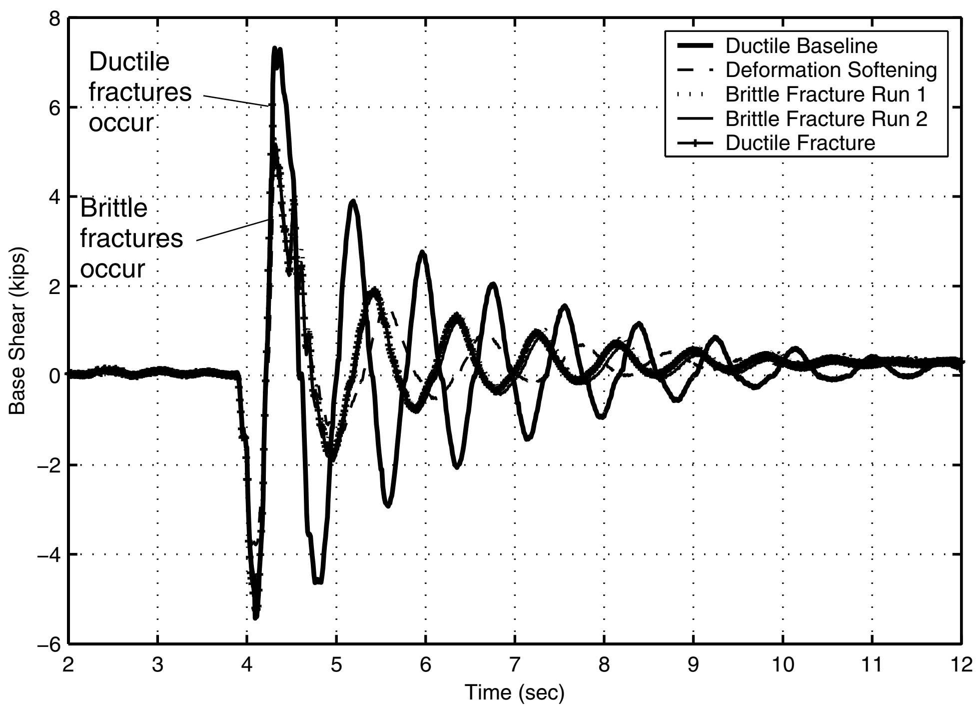

Figure 6-33. Comparison of base shear time histories, B patterns, 0.6 sec cosine pulse

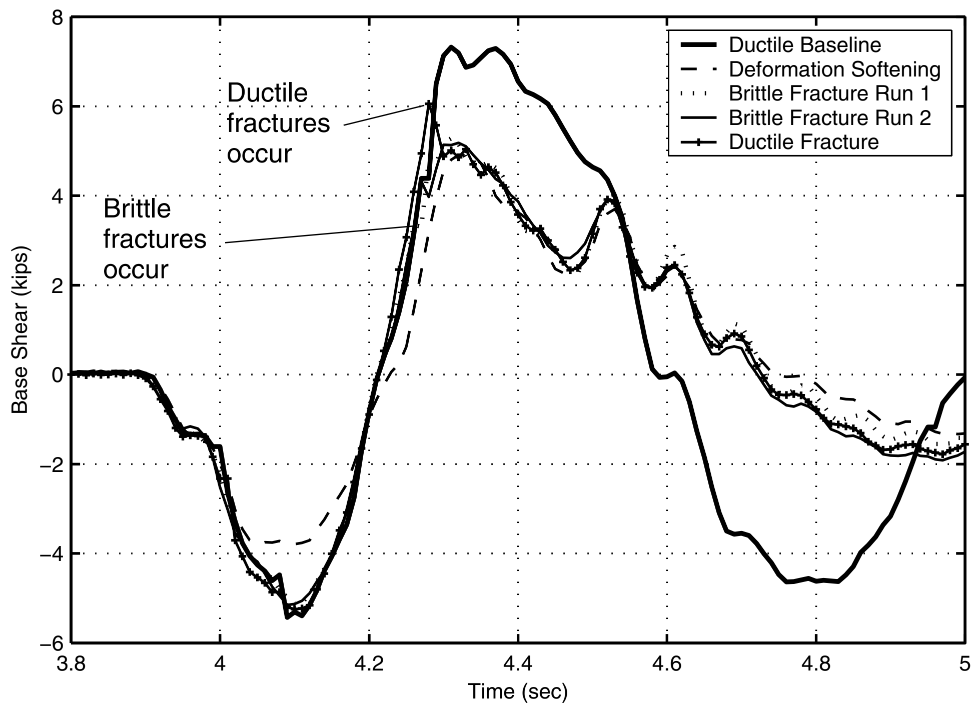

Figure 6-34. Close-up of base shear time histories, B patterns, 0.6 sec cosine pulse

A comparison of Figures 6-34 and 6-44 provides the primary indication that the catch cables may have interfered in the BF BP1, DF BP, and DFS B plots due to the presence of a similar waveform in Figure 6-34 as that which occurs at the cable catch for the C patterns. The potential interference occurs at about 4.45 seconds.

Base shear time histories are compared next in Figure 6-35. The three fracturing patterns show very similar behavior, though there is some ambiguity in the location of the fractures due to the coarseness of the data. All three of the cases show significant increases in displacement over the ductile baseline case, and the amount of increased displacement is similar to that which would be expected in Newmark’s energy preserved region of the response spectrum.

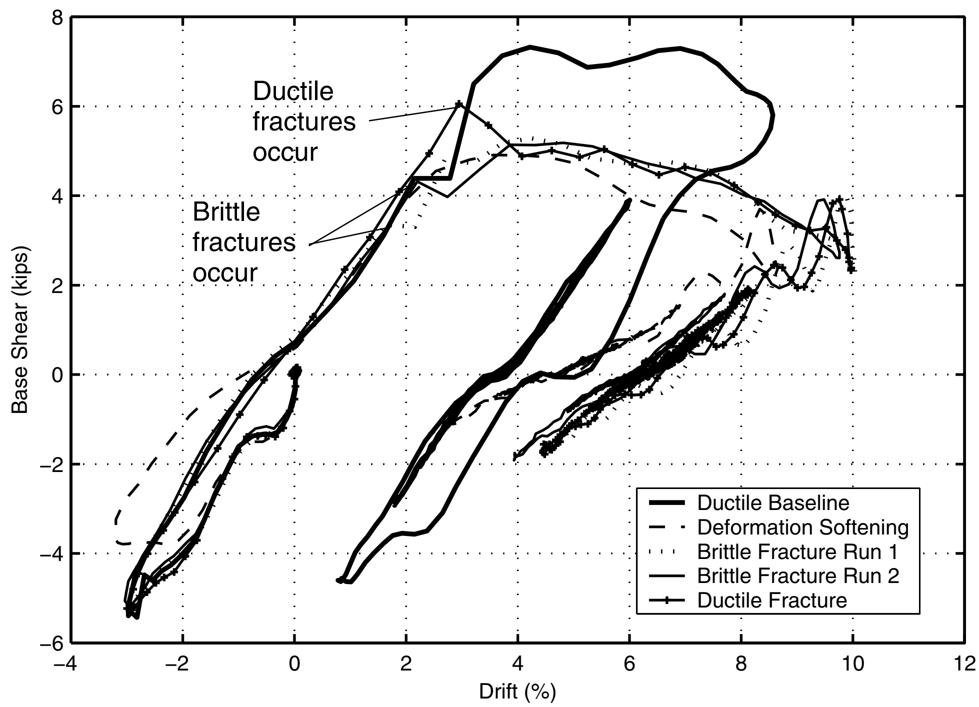

Figure 6-35. Comparison of base shear first-story drift hysteresis for 0.6 sec cosine pulse, B patterns

Likewise, the loss of strength in the deformation softening pattern leads to greater displacments. In contrast to the observations from Comparison Set 1, the system post-yield tangent stiffness of the deformation softening pattern is more negative than the system post-fracture tangent stiffness in the fracture pattern. The reasons for this difference are unclear, since the post-yield and post-fracture stiffnesses in the connection hysteresis are very similar, as shown in Figure 6-36.

Connection behavior of C2 is examined next, with moment-rotation hysteresis shown in Figure 6-36, and moment and rotation time histories plotted in Figures 6-37 through 6-39. As shown in Figure 6-36, maximum connection moments are significantly less (approximately half to two thirds) and maximum connection moments are significantly greater (by roughly one third) for the fracturing cases than for the ductile baseline case. Similar observations can be made for the deformation softening case relative to the ductile baseline case, though both maximum moments and rotations are smaller than for the fracture cases, making the differences from the ductile baseline case larger. The fracturing and deformation softening cases had very similar values of post-yield and post-fracture tangent stiffness.

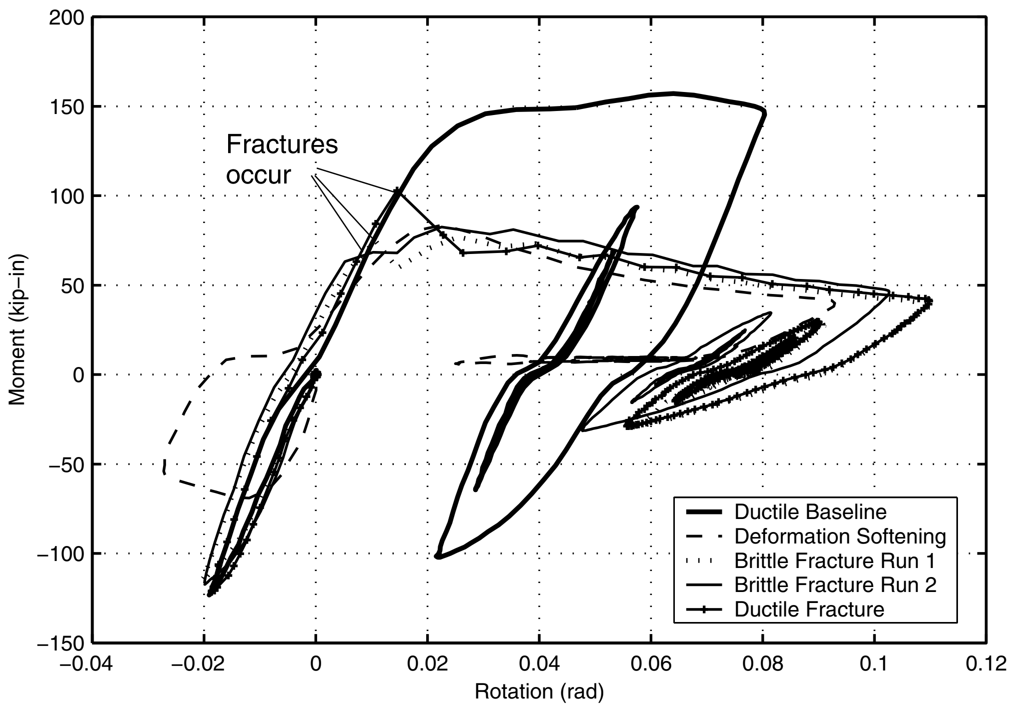

Figure 6-36. Comparison of C2 moment-rotation hysteresis, B patterns, 0.6 sec cosine pulse

Close-ups of the moment and rotation time histories in Figures 6-37 and 6-39, respectively, show that the fracture causes sudden and notable changes in both quantities, albeit in different ways. Connection moments are sharply reduced when fracture occurs, while the slope of the rotation curve changes significantly though there is no jump discontinuity. Deformation softening also quickly reduces connection moment, though in a smooth manner. Also, the slope of the rotation curve does not change suddenly.

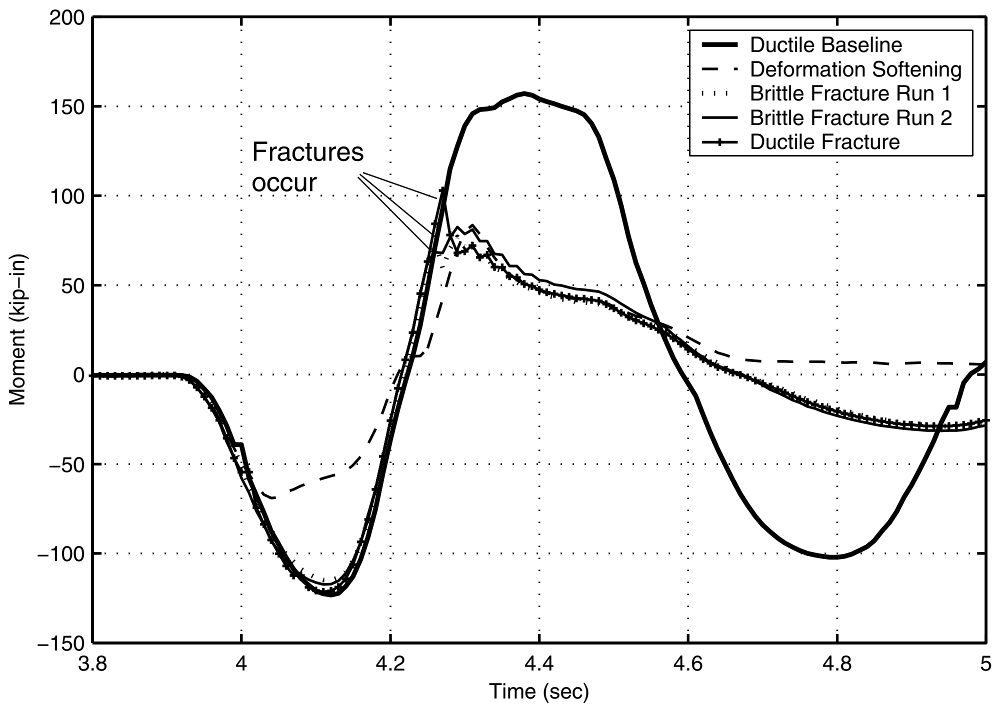

Figure 6-37. Close-up of C2 moments, B patterns, 0.6 sec cosine pulse

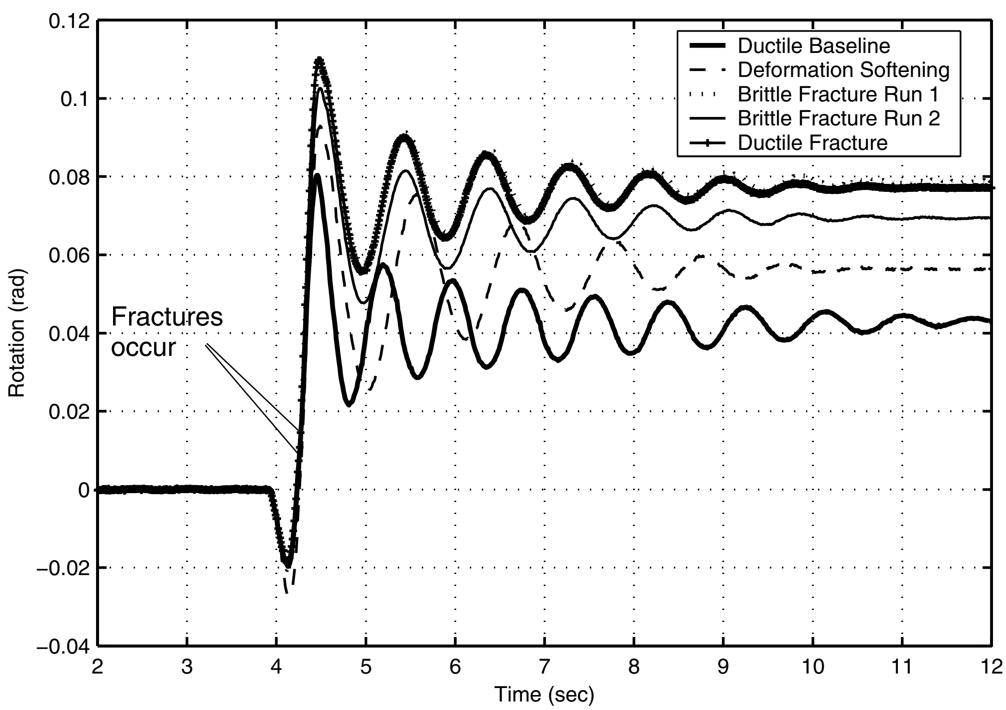

Figure 6-38. Comparison of C2 rotations, B patterns, 0.6 sec cosine pulse

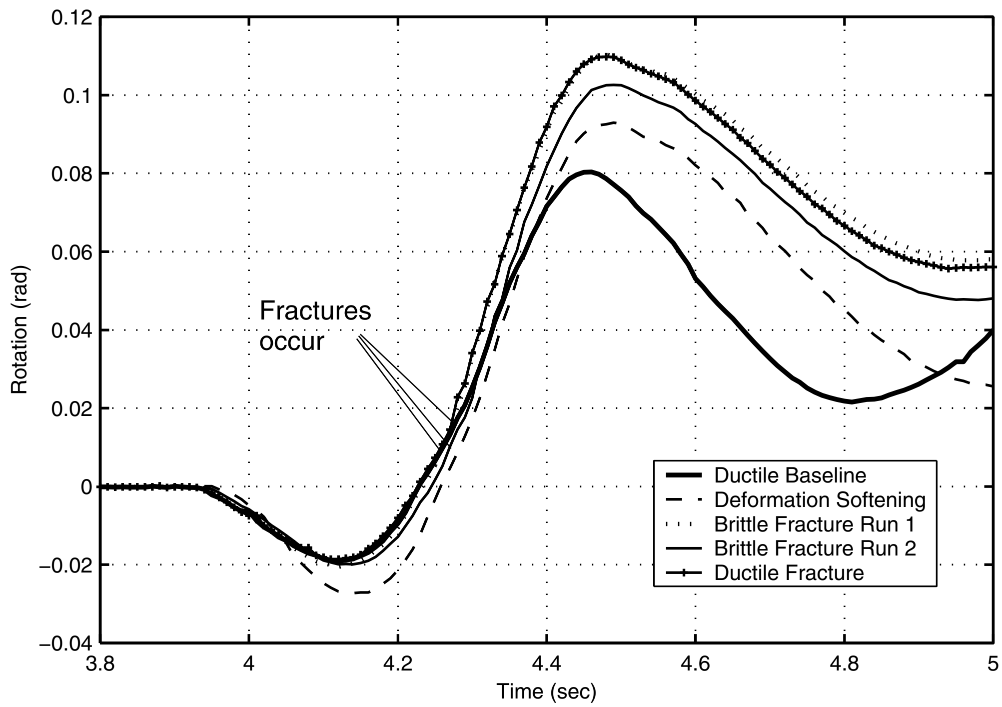

Figure 6-39. Close-up of C2 rotations, B patterns, 0.6 sec cosine pulse

A close-up of the absolute accelerations at the top of the frame is shown in Figure 6-40. Accelerations for all patterns except the deformation softening case are very similar until fracture occurs. Accelerations for the deformation softening case during this time frame are about 80% of those for the other patterns. After fracture occurs, the deformation softening and fracture patterns have very similar accelerations for the remainder of the time history. This similarity is primarily due to the similar force capacities for the two cases after degradation occurs, since total accelerations are related to forces.

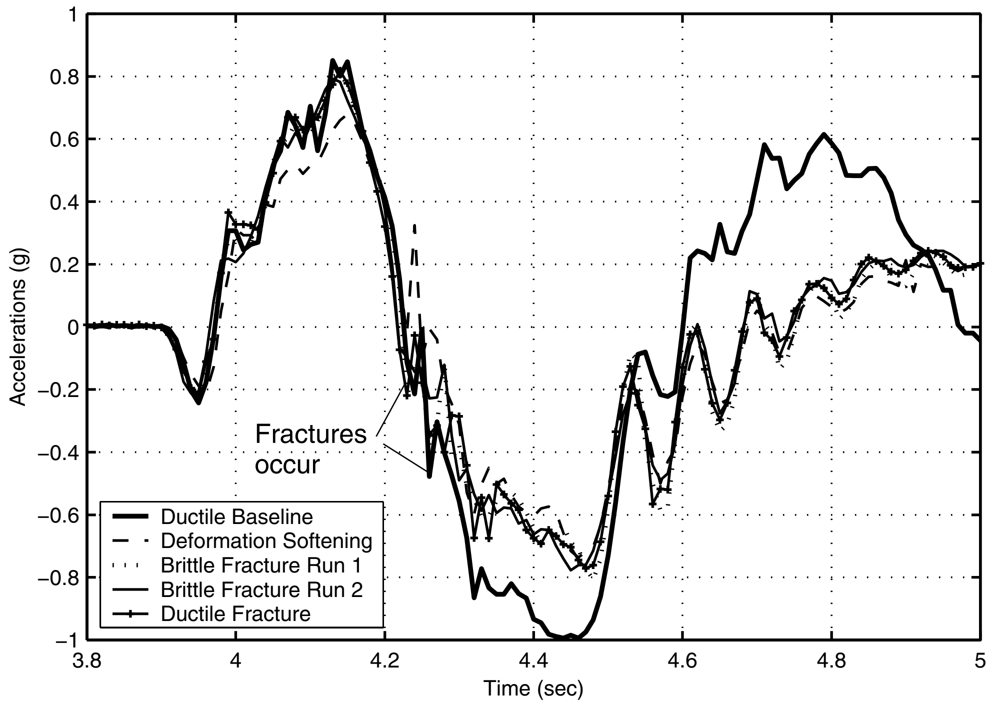

Figure 6-40. Close-up of second-story absolute accelerations, B patterns, 0.6 sec cosine pulse

Several observations can be drawn from this comparison set. The first is that the percent differences in residual displacement between degrading patterns and the ductile baseline case are much larger than the differences in maximum displacement, and in all cases both the maximum and residual drifts were larger for the degrading cases. Also, none of the types of deterioration cause any type of discontinuity in the global displacement response. As for the other comparison sets, first- and second-story drifts are very similar for all cases, despite the types of degradation occurring in the first story.

The system hysteresis (base shear-interstory drift ratio) shows that displacements are not preserved for this excitation, though it is on the descending branch of the response spectrum, and that the observed behavior is much more consistent with the energy-preserved range. This can be explained by noting that the specimen is at the top rather than the bottom of the descending branch, where the boundary (which is not clearly defined) between period ranges is located.

Deformation softening causes smaller maximum and residual drifts than fracture for this excitation, though the response is still significantly larger than that of the ductile baseline case.

However, displacement maxima for all of the degrading cases should be viewed with suspicion, since it is possible that there was some small amount of interference of the catch cables in these cases, which would affect the maximum values. Maximum force values are not affected by this, since the maximum occurs prior to the onset of degradation, which happens long before the catch cables could have interfered with specimen response.

6.2.4 Comparison Set 4 — C Patterns, 0.6 Second Cosine Pulse

This set contains the ductile baseline case, CP brittle and ductile fracture patterns, and the deformation softening C pattern, all excited with the 0.6 second cosine pulse at 100% amplitude. As in the previous sets, the key variable examined is the effect of hysteretic type. In this set, the catch cables were engaged on all of the tests except the ductile baseline. In the case of the DFS C pattern, one catch cable engaged early, and it is possible that the specimen may not have collapsed if the cable had not interfered. Percent differences are not discussed, since they were determined from maximum and residual values dependent on the prescribed cable-catch drift level, which was approximately 12%.

The relative displacement time history, with the point of catch cable engagement noted, is shown in Figure 6-41. All patterns except ductile baseline collapse during the first positive displacement excursion.

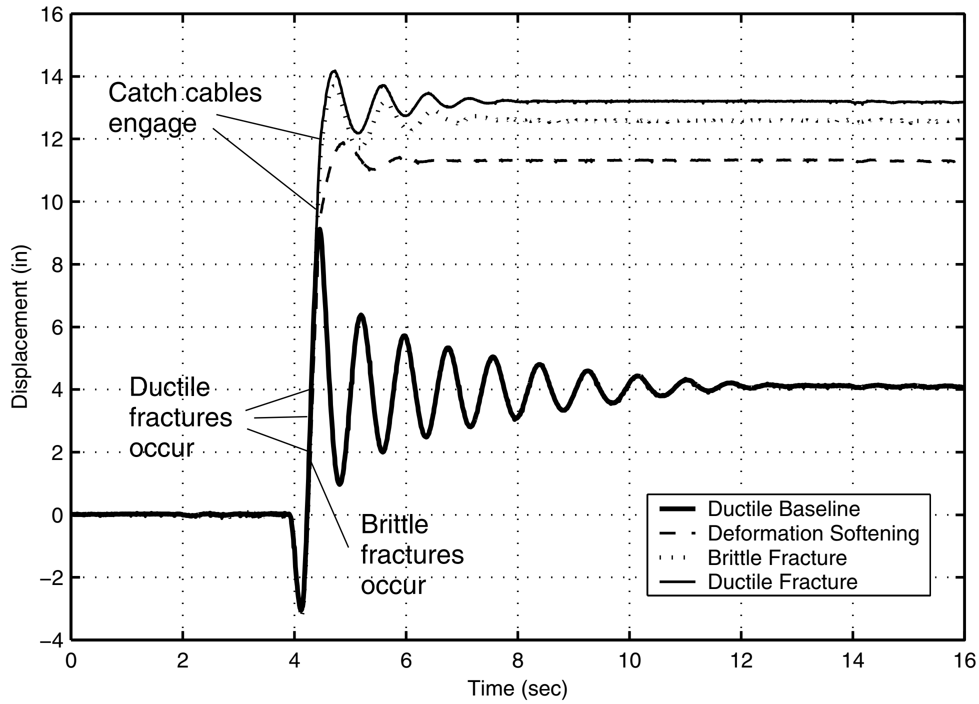

Figure 6-41. Comparison of relative displacements at top, C patterns, 0.6 sec cosine pulse

In the interest of space, the interstory drift time histories are shown only for the pre-collapse portion of the response, and only for the first story since the second-story drifts are very similar. Figure 6-42 shows that there is some period elongation for the deformation softening case due to yielding during the first negative displacement excursion (Figure 6-46). The fracture patterns show very similar response to the ductile baseline case, until the ductile case displacement curve begins to flatten out. It is notable that for the fracturing cases, where there are four closely spaced fractures, these fractures do not cause any sort of discontinuity of the response.

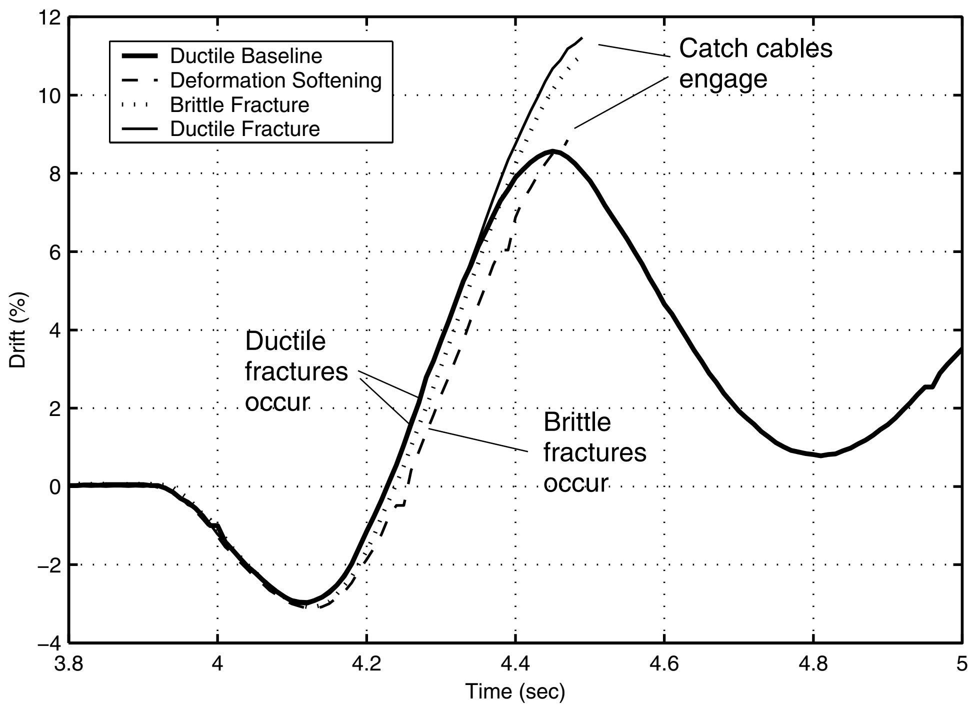

Figure 6-42. Comparison of first-story interstory drifts, C patterns, 0.6 sec cosine pulse

The base shear response is compared next in Figures 6-43 and 6-44. Both fracture and deformation softening cause very severe reductions in the base shear capacity, reducing it to near zero before the catch cables engage. This reduction begins as soon as degradation initiates; there is no plateau in the response. For the fracture cases, about half of the pre-fracture base shear capacity is lost due to the fractures, with the remaining loss due to a relatively steady reduction in the base shear.

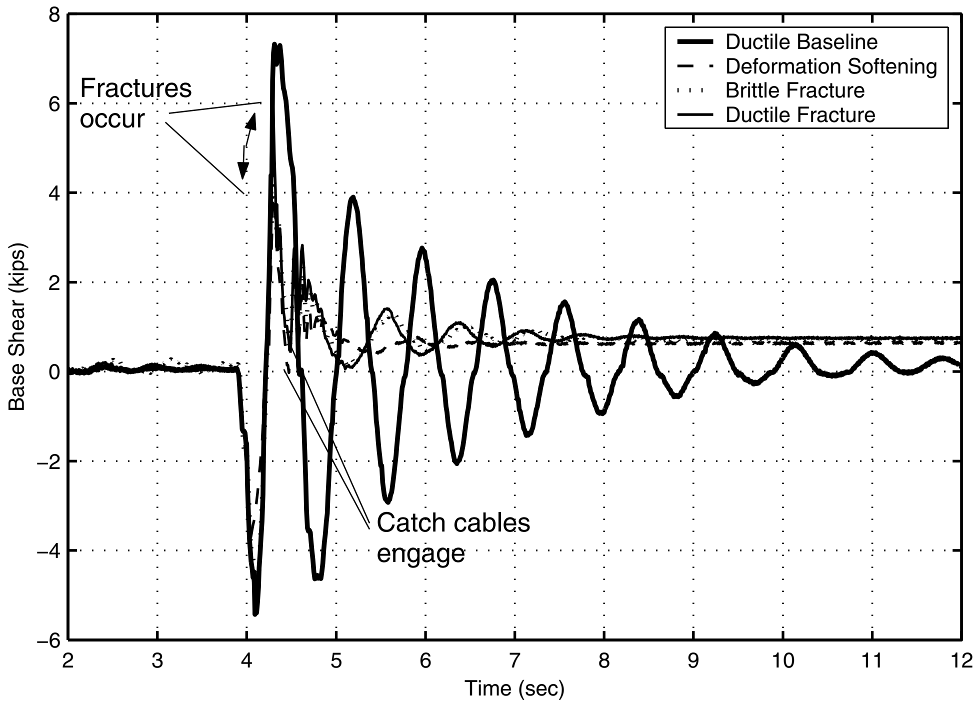

Figure 6-43. Comparison of base shear time histories, C patterns, 0.6 sec cosine pulse

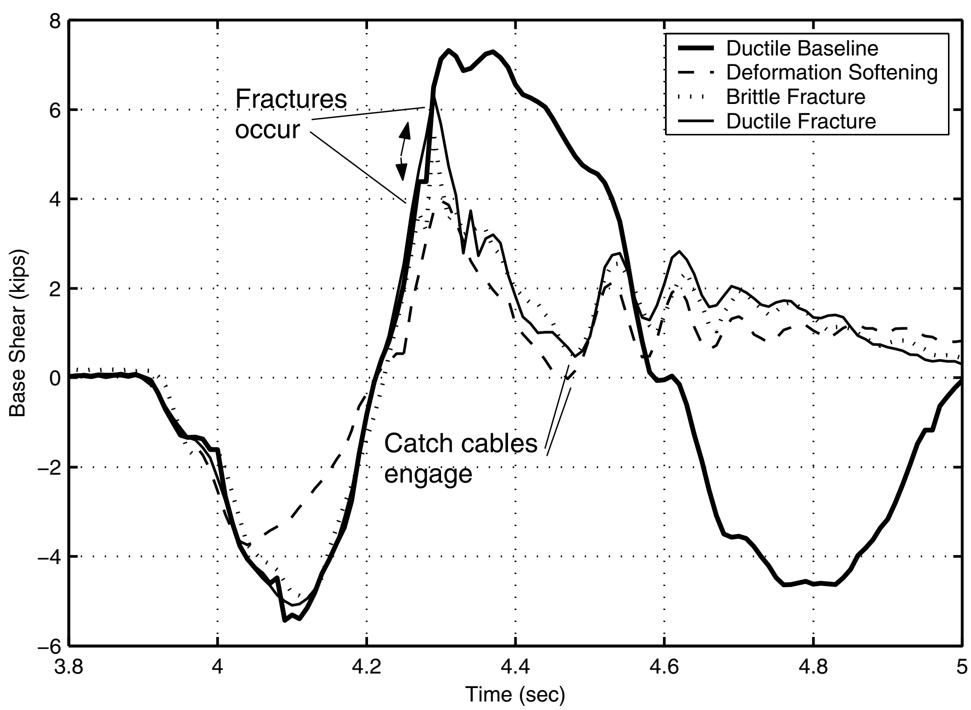

Figure 6-44. Close-up of base shear time histories, C patterns, 0.6 sec cosine pulse

System base shear-interstory drift ratio hysteresis is shown in Figure 6-45. The effects of strength degradation on response are very significant, and all of the degrading cases show very large negative system tangent stiffnesses after degradation has begun. This behavior is most pronounced for the deformation softening pattern, as the system strength drops all the way to zero before the catch cables engage. Both fracture patterns show similar post-fracture stiffnesses, which, while not as large as that of the deformation softening case, nevertheless lead to reduction of system strength to less than one kip before the catch cables engage.

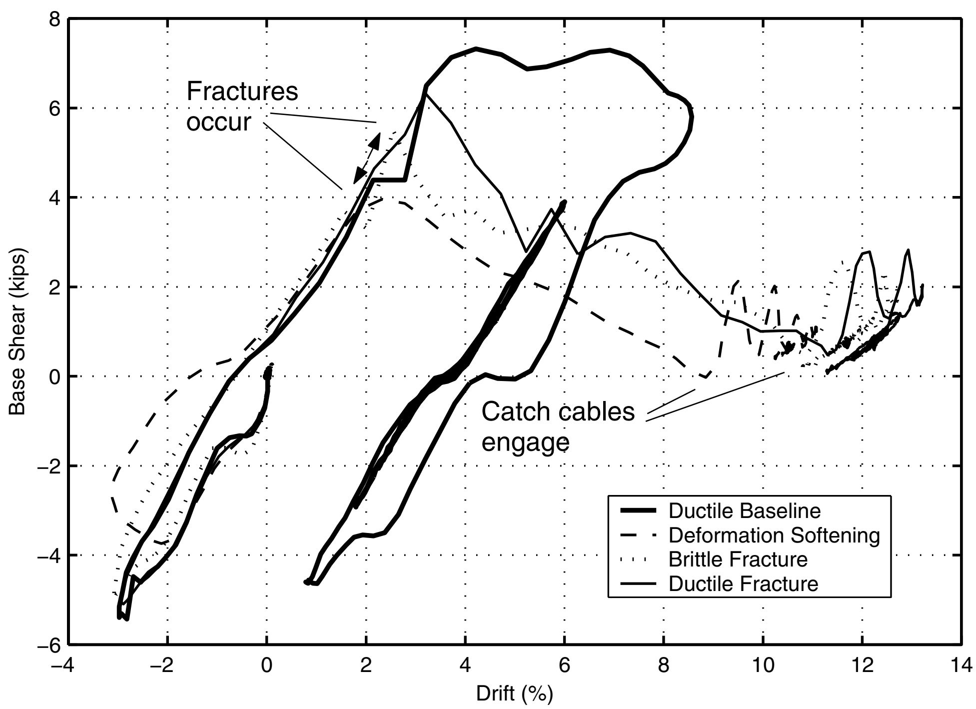

Figure 6-45. Comparison of base shear first-story drift hysteresis for 0.6 sec cosine pulse, C patterns

The degradation patterns also have negative tangent stiffness in the connection moment-rotation hysteresis, as shown in Figure 6-46. The slope of these stiffnesses is much less severe than the global tangent stiffness and seems to begin to flatten out as the rotations increase. Also, the significant plastic deformation in the deformation softening case in the first negative excursion is apparent. The brittle fracture case shows a small amount of yielding in this excursion as well, and it should be noted that this connection would have fractured had the top coupon been notched as well.

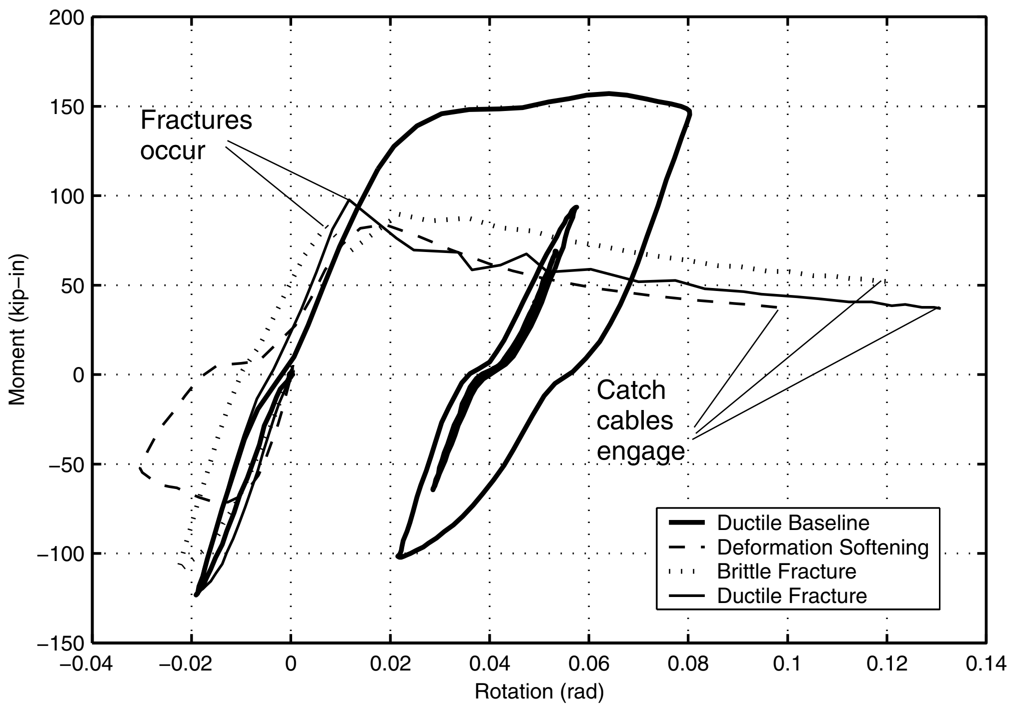

Figure 6-46. Comparison of C2 moment-rotation hysteresis, C patterns, 0.6 sec cosine pulse

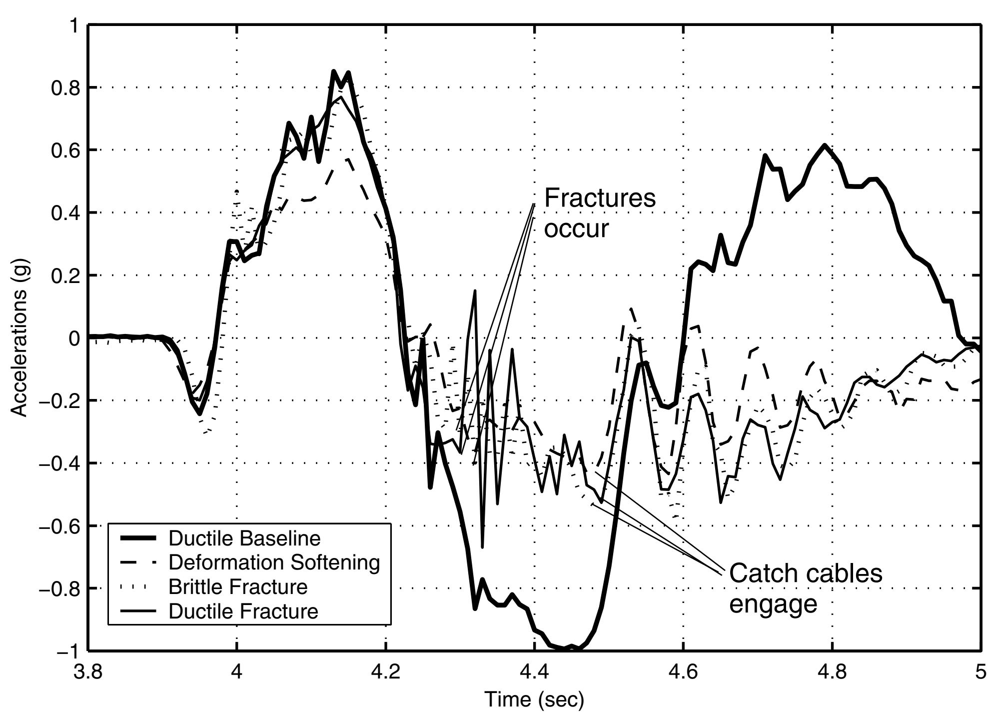

Figure 6-47. Close-up of second-story absolute accelerations, C patterns, 0.6 sec cosine pulse

The conclusions that can be drawn from this comparison set are similar to those for Comparison Set 2, which examined the same connection configurations patterns for the 1.2 second cosine pulse excitation. All of the patterns except the ductile baseline suffered collapse, with the caveat that the catch cables may have engaged early for the DFS C pattern. The behavior of all of the degrading cases was similar, with the deformation softening case losing strength earlier and at a slightly more rapid rate than the fracturing cases.

6.2.5 Comparison Sets 5a and 5b — JNF01 (Tabas-Based) Motion

In Comparison Set 5, the key variable examined is the effect of hysteretic type. This set is divided into two subsets, 5a and 5b. Set 5a contains the ductile baseline case, CB brittle and ductile fracture patterns, and the deformation softening C pattern. Set 5b contains the ductile baseline case and the brittle fracture BB and CB patterns. The CB patterns have fracture-capable bottom flanges only in all connections in both stories, while the BB pattern has fracture-capable bottom flanges only in the first-story connections. The excitation for all tests in both subsets is the JNF01 motion at 100% amplitude.

The percent differences for this set are found in Tables E-13 through E-15. In this case, some of the percent differences (most notably residual displacements) between the DF BP and BF BP patterns are larger than the global error bounds, so results will be discussed for the ductile and brittle fracture cases individually. The catch cables did not engage for any of the tests, so the response was unhindered.

6.2.5.1 Set 5a

Relative displacements at the top of the structure are plotted in Figure 6-48, and a close-up of the first-story interstory drifts during the strongest portion of the excitation is shown in Figure 6-49. The deformation softening C pattern for the JNF01 motion had residual drifts about three times those of the other patterns for JNF01. The unusual-looking response of this case shown in Figure 6-48 occurred because the connection hysteresis contains severe pinching (Figure 6-52), and this behavior, rather than negative post-yield stiffness, controlled the response. Therefore, the response does not provide any meaningful information about the effects of the deformation softening (negative post-yield stiffness) hysteretic type on the displacement response.

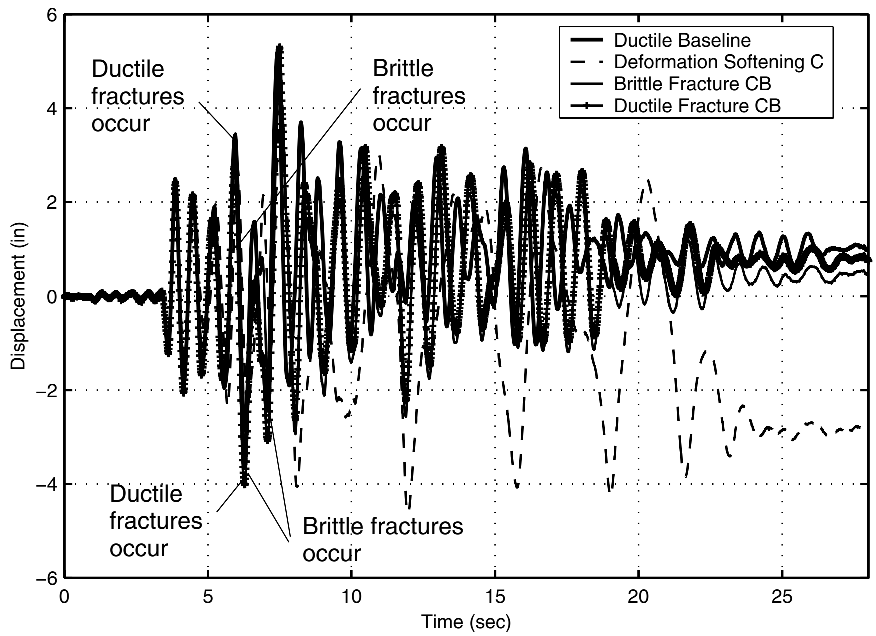

Figure 6-48. Comparison of relative displacements, Set 5a, JNF01 (Tabas-based) motion

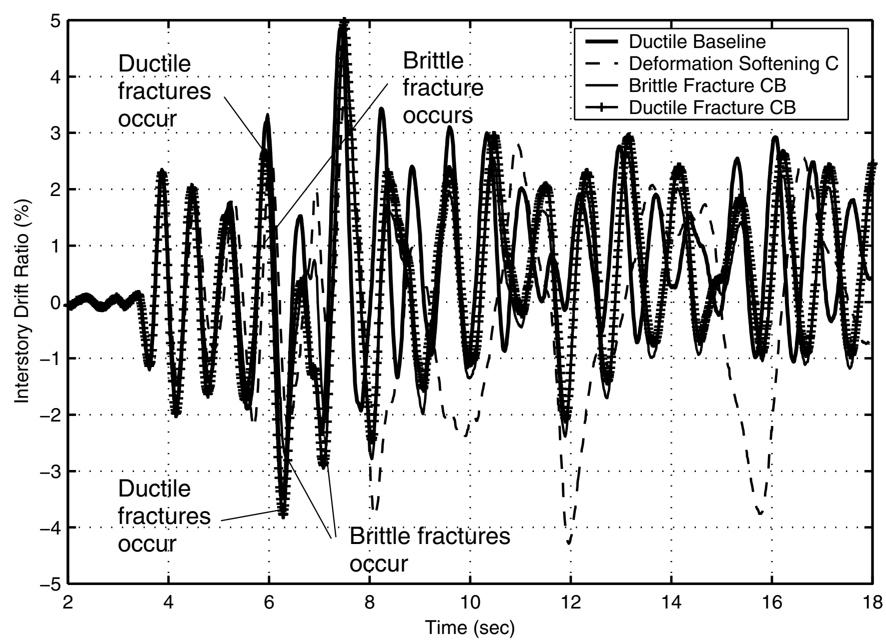

Figure 6-49. Close-up of first-story interstory drifts, Set 5a, JNF01 (Tabas-based) motion

The maximum displacements and drifts of the BF CB pattern were not significantly different from the DB pattern, while the residual displacements and drifts were about 130% greater for the DB pattern. This is expected, because the specimen is less stiff with the damaged BF CB pattern, and should “come back” farther from the same displacement when unloading.

The differences between DF CB and DB are also not significant for the maximum displacements and drifts, but the differences for residual displacements and drifts are significant, and are about 23% greater for DB C. The differences between BF CB and DF CB follow the same general pattern as the other comparisons made so far, with differences in the maximum values insignificant, and differences in the residual values of about 70%, with DF CB having larger values. For this ground motion, the percent differences alone do not provide evidence that there is no significant difference in behavior for the ductile and brittle fracture patterns.

Base shear time histories for Set 5a are shown in Figure 6-50. Maximum values of base shear are significantly greater for the ductile baseline case, by 35% for the brittle fracture case, about 27% for the ductile fracture case, and by about 250% for the deformation softening case. Due to high-frequency components in the base shear time history even for the ductile baseline case, it is difficult to determine the transient effects of fracture. However, the most important effect of fracture is the reduction in the base shear capacity of the specimen.

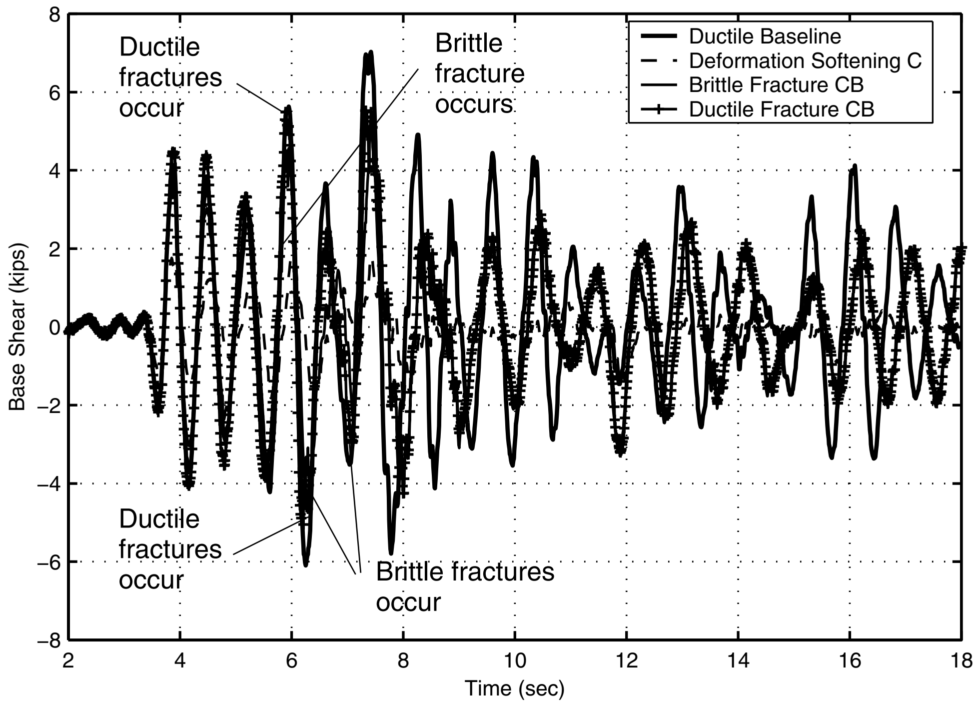

Figure 6-50. Close-up of base shear time histories, Set 5a, JNF01 (Tabas-based) motion

The base shear first-story interstory drift hysteresis is shown in Figure 6-51. The maximum drifts are preserved as the base shear capacity of the specimen decreases from the ductile baseline case to the patterns with hysteretic degradation. For this excitation, the structure is on the global descending branch of the pseudo-acceleration response spectrum (Figure 4-6), but is located at the base of a smaller, local ascending branch. This local ascending branch does not appear to have the capability to define a local “energy-preserved” or “short-period” range. However, this conclusion cannot be applied to other local ascending branches without further study.

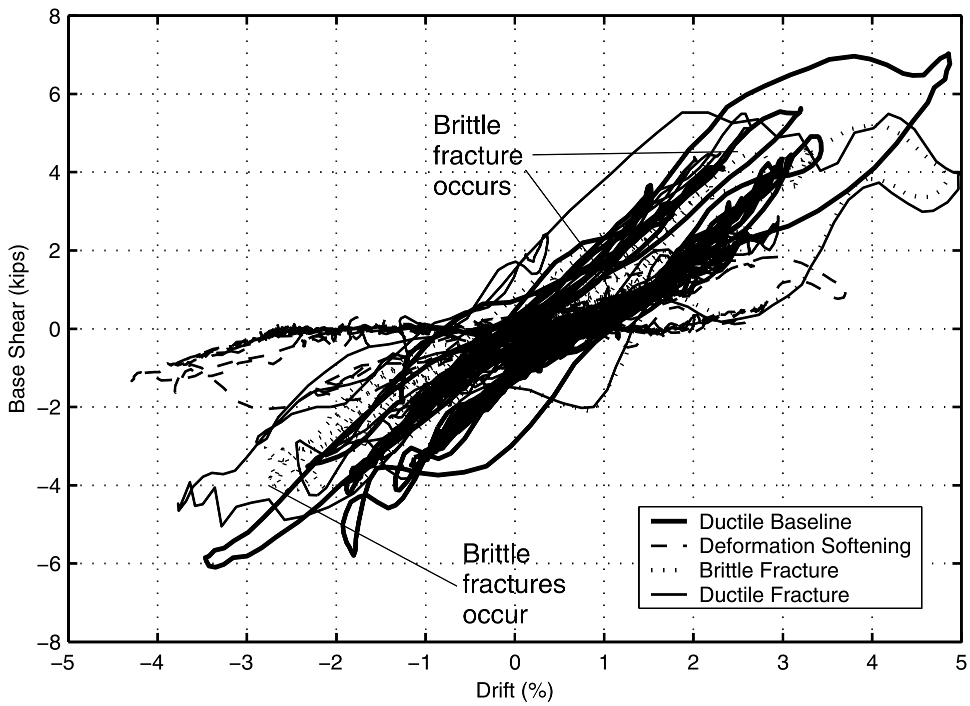

Figure 6-51. Comparison of base shear first-story drift hysteresis, Set 5a, JNF01 (Tabas-based) motion

Higher mode contributions can be clearly seen for all of the patterns. The severe pinching in the global hysteresis for the deformation softening pattern shows that the response is governed by connection slip rather than by connection degradation. The connection behavior is shown in Figure 6-52, and it is evident that the deformation softening loops contain a great deal of severe pinching.

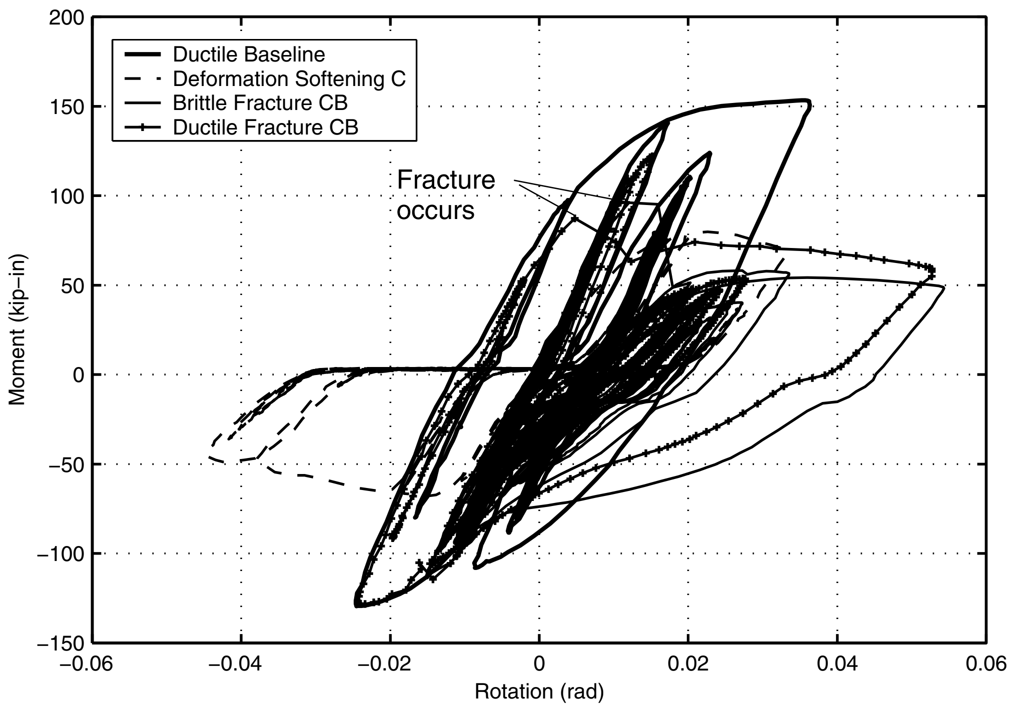

Figure 6-52. Comparison of C2 moment-rotation hysteresis, Set 5a, JNF01 (Tabas-based) motion

Ductile and brittle fracture patterns show similar hysteretic behavior, with maximum rotations that are very similar. The ductile fracture case has a distinctly negative post-fracture tangent stiffness, however, while the brittle fracture case shows only a very slight negative post-fracture stiffness.

Several observations can be made overall for Set 5a. The first of these is that the response of the deformation softening case was governed by pinching rather than negative post-yield stiffness, so valid comparisons cannot be made between the effects of fracture and negative post-yield stiffness.

The second observation was that brittle fracture caused less residual displacement than the ductile baseline case, while ductile fracture caused more. Percent differences for maximum displacements for the three patterns were less than the global error bounds, however. Differences in maximum base shear were considerably greater between the ductile baseline case and all of the patterns with hysteretic degradation. There was no significant difference between the brittle and ductile fracture cases for maximum base shear, however.

6.2.5.2 Set 5b

Relative displacements are compared for the ductile baseline, brittle fracture BB, and brittle fracture CB patterns in Figure 6-53. A close-up of interstory drift is shown for the portion of the response with the strongest shaking is shown in Figure 6-54. Like the other fracture patterns discussed previously, the maximum displacements and drifts were not significantly different between BF BB and DB C. In this case, the residual displacements and drifts had differences of less than 13%, which is only slightly above the global error bound. Therefore, there is an obvious gradient in residual displacement from the pattern with least stiffness (BF CB) and smallest residual displacements, and those patterns with the most stiffness (DB C) and largest residual displacements. The effect of fractures at all connections is apparent in the residual displacements, with the BF CB pattern having about 100% greater values than the BF BB pattern. Again, maximum displacements and drifts were not significantly different.

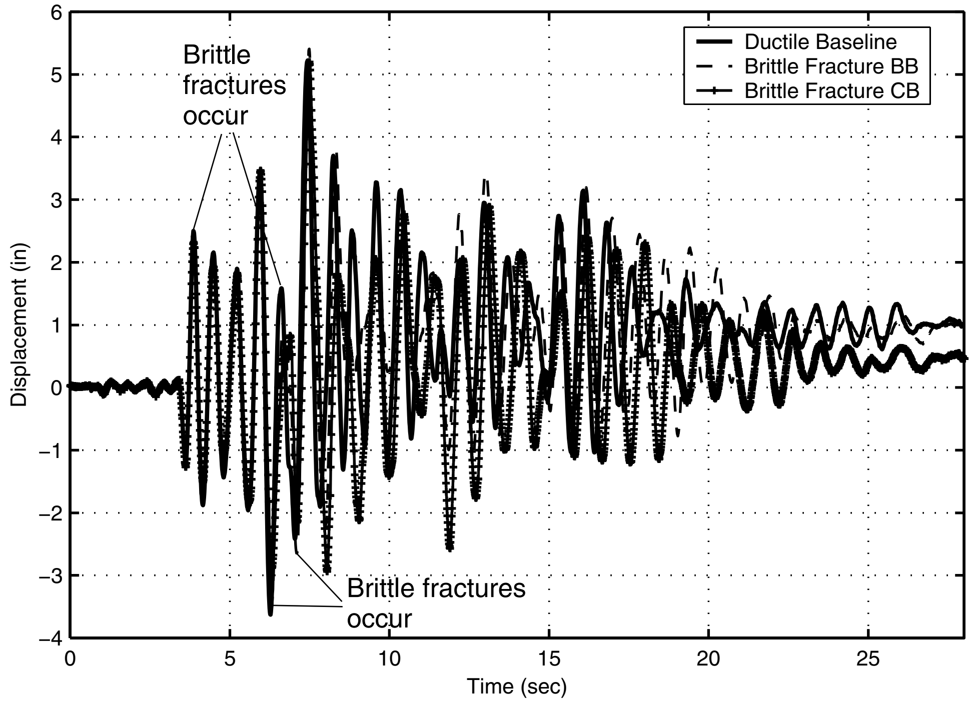

Figure 6-53. Comparison of relative displacements, Set 5b, JNF01 (Tabas-based) motion

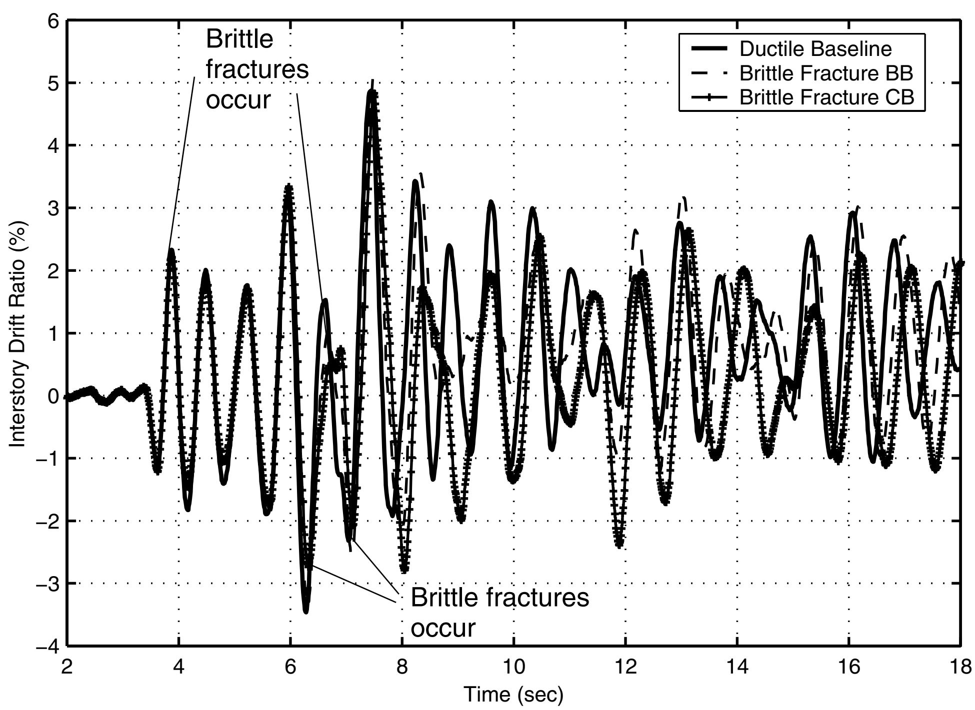

Figure 6-54. Close-up of first-story interstory drifts, Set 5b, JNF01 (Tabas-based) motion

Similar observations to those for Set 5a can be made for base shear response, which is shown in Figure 6-55. Maximum base shear values are significantly lower for the two fracturing cases, by about 15% in the BB case and about 35% in the CB case. The response of the three cases is in phase until about 6 seconds, when enough fractures have occurred to cause period elongation.

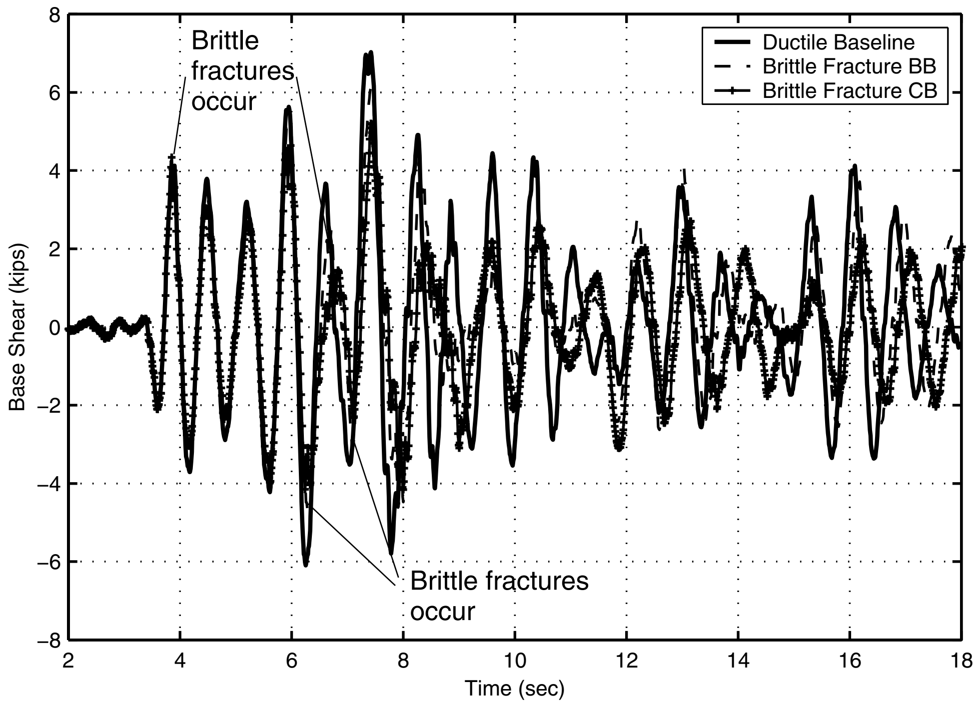

Figure 6-55. Close-up of base shear time histories, Set 5b, JNF01 (Tabas-based) motion

The base shear first-story interstory drift ratio hysteresis is shown for approximately the first half of the response only in Figure 6-56 in order to make the portion of the response with the strongest shaking easier to see. As for Set 5a, the maximum drifts are preserved as the base shear capacity of the specimen decreases from the DBC to the BF BB to BF CB pattern. Significant higher mode contributions are also present for all of the patterns.

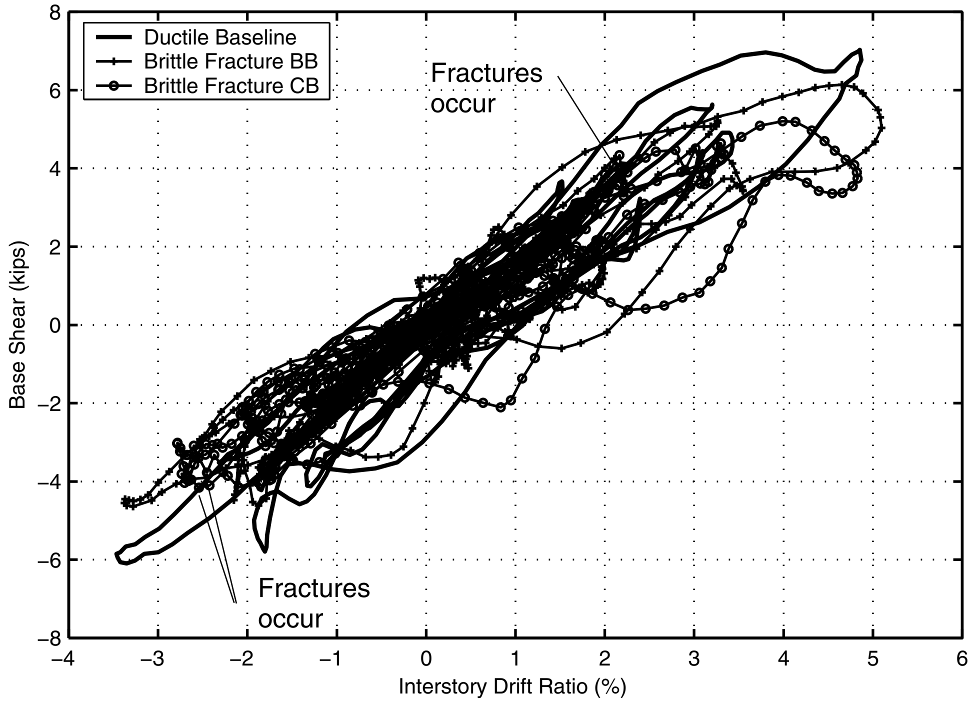

Figure 6-56. Comparison of base shear first-story drift hysteresis for JNF01 (Tabas-based) motion, Set 5a

Connection C2 moment-rotation hysteresis is shown in Figure 6-57. Maximum rotations are slightly larger for the brittle fracture CB case than the BB case, though the amount is within the global error estimate. The rotations are significantly larger than those of the ductile baseline case. The fractures appear to occur in the same excursion in the time history, and both cases experience significant post-fracture rotation. However, the post-fracture tangent stiffness for the two cases, which are virtually identical, is almost zero.

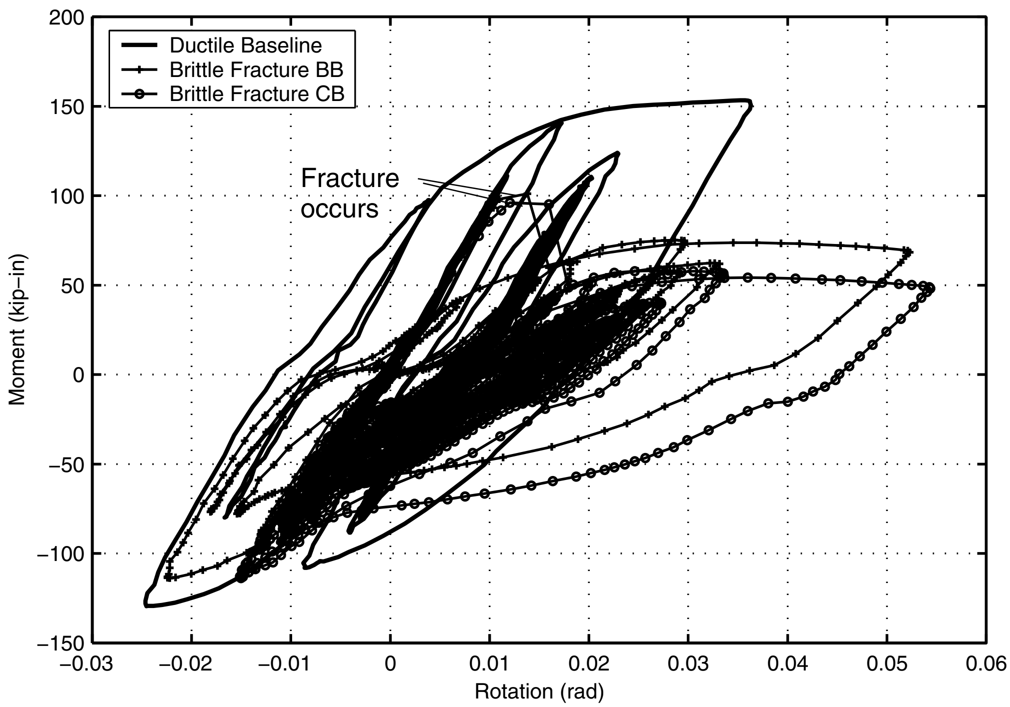

Figure 6-57. Comparison of C2 moment-rotation hysteresis, Set 5b, JNF01 (Tabas-based) motion

Overall, Set 5b shows that the number of fractures has only minor ramifications for system behavior for this excitation. These ramifications are confined primarily to reductions in base shear capacity. As shown previously, displacements are preserved for this excitation, so the reduction in strength has little effect on the maximum displacement response. For residual displacements, however, there are significant differences between the BB and CB patterns, with brittle fracture actually reducing the residual displacements over both the BB and ductile baseline cases, which have very similar values. Differences in period elongation are also significant. With the brittle fracture CB pattern having the most, followed by the BB pattern and the ductile baseline case.

6.2.6 Comparison Set 6 — JSE17 (Llolleo-Based) Motion

In Comparison Set 6, the key variable, as in the previous sets, is the effect of hysteretic type. The connection configuration patterns in this set are the ductile baseline case, CB brittle fracture pattern, and the strength-degrading C pattern. The CB patterns have fracture-capable bottom flanges only in all connections in both stories. The excitation for all tests is the JSE17 motion at 100% amplitude. The percent differences for this set are found in Tables E-16 through E-18. The catch cables did not engage for any of the tests, so the response was unhindered.

Relative displacements at the top of the frame are shown in Figure 6-58, with first-story interstory drifts shown in Figure 6-59. A close-up comparison of first-story interstory drifts is shown in Figure 6-60, and this shows the location of the fractures in pattern BF CB.

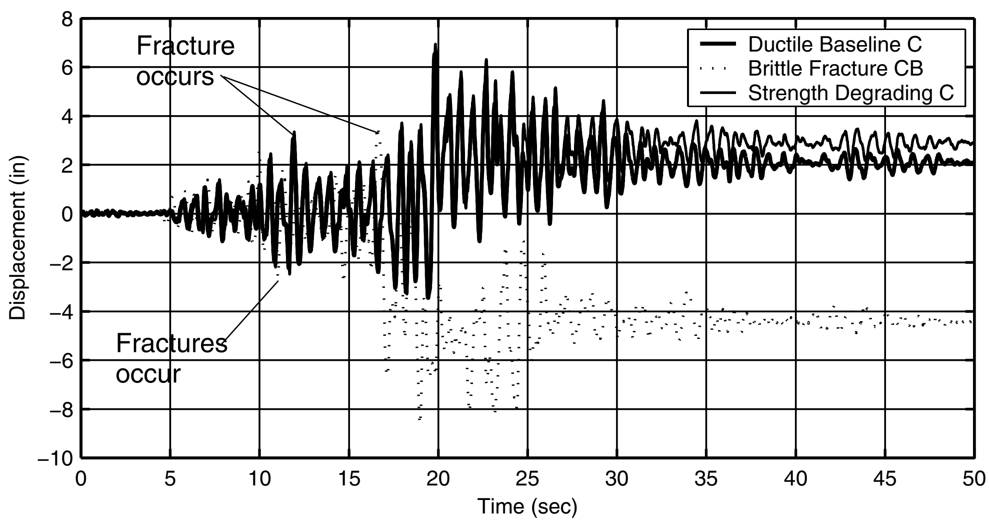

Figure 6-58. Comparison of relative displacements, all patterns, JSE17 (Llolleo-based) motion

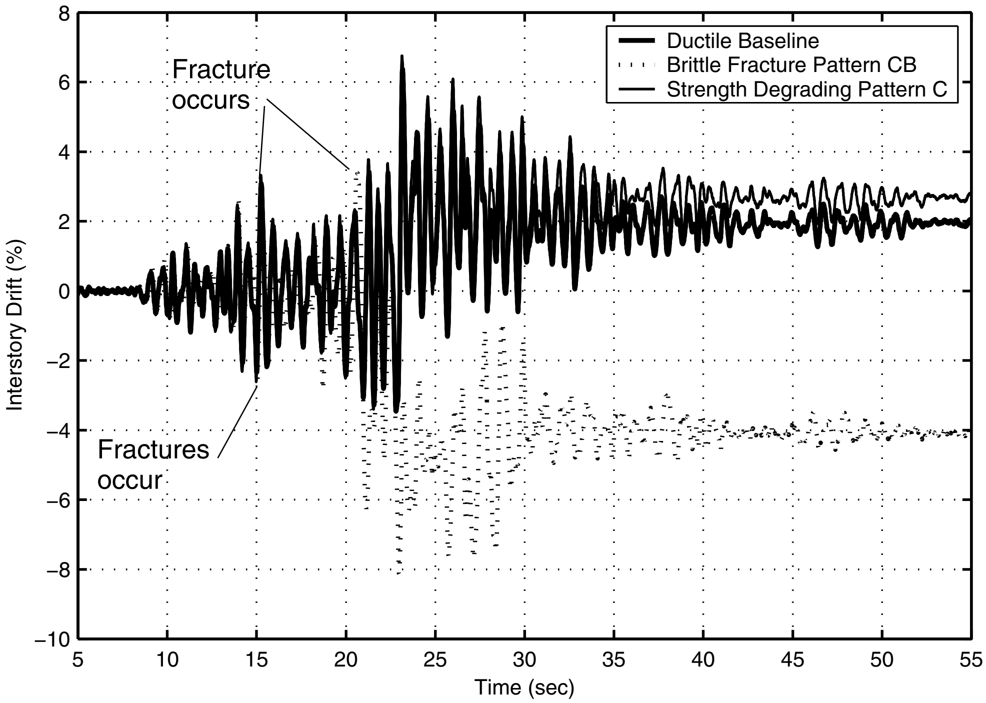

Figure 6-59. Comparison of first-story interstory drifts, JSE17 (Llolleo-based) motion

The strength-degrading (SD C) pattern had a response similar to the DB pattern, with maximum displacements and drifts slightly higher for the SD C pattern, and with residual displacements and drifts about 32% higher. It should be noted that the rate of strength degradation for the SD C pattern connections was relatively slow, as shown in Figure 3-8. The BF CB pattern had maximum displacements and drifts about 30% larger than the DB pattern, and residual drifts about 100% larger. The most likely cause of the much larger relative displacements for the BF CB pattern was some characteristic of the ground motion that affected the structure as the final fracture occurred, or immediately thereafter. This hypothesis is supported by the fact that the last fracture occurs just before the large displacement excursion that causes most of the permanent offset.

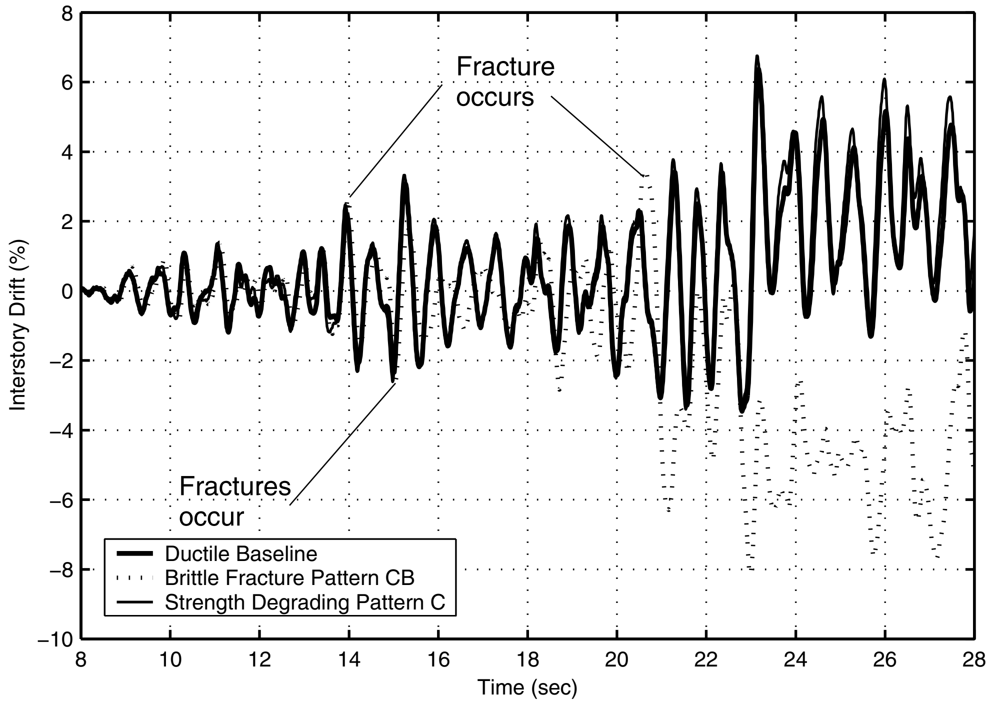

Figure 6-60. Close-up of first-story interstory drifts, JSE17 (Llolleo-based) motion

The base shear time histories for all patterns are compared in Figure 6-61. Base shear response for the ductile baseline and strength-degrading patterns is very similar, with the strength-degrading case actually achieving slightly larger maximum values, though the percent difference between them is less than the global error bound. In contrast, the maximum base shear for the fracturing case is significantly reduced, and is about 27% and 37% different from the ductile baseline and strength-degrading patterns.

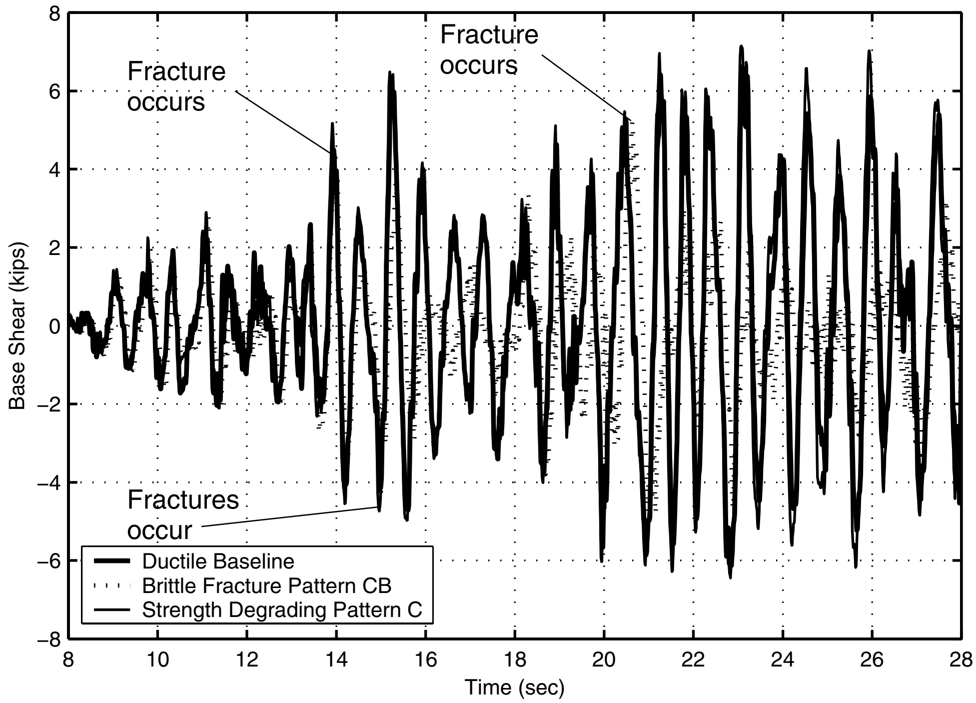

Figure 6-61. Close-up of base shear time histories, JSE17 (Llolleo-based) ground motion

A comparison of the global hysteresis in Figures 6-62 and 6-63 shows that displacements are not preserved for this case, since for the fracturing case strength loss leads to a large increase in displacement over the ductile baseline and strength-degrading cases. The behavior of the latter two cases is very similar, with little degradation evident for the strength-degrading case.

The structure is on the global descending branch of the pseudo-acceleration response spectrum (Figure 4-8) but is at the base of a local ascending branch. It is unclear whether the increase in displacement for the fracturing case is due to the influence of this local branch, but the possibility warrants further study.

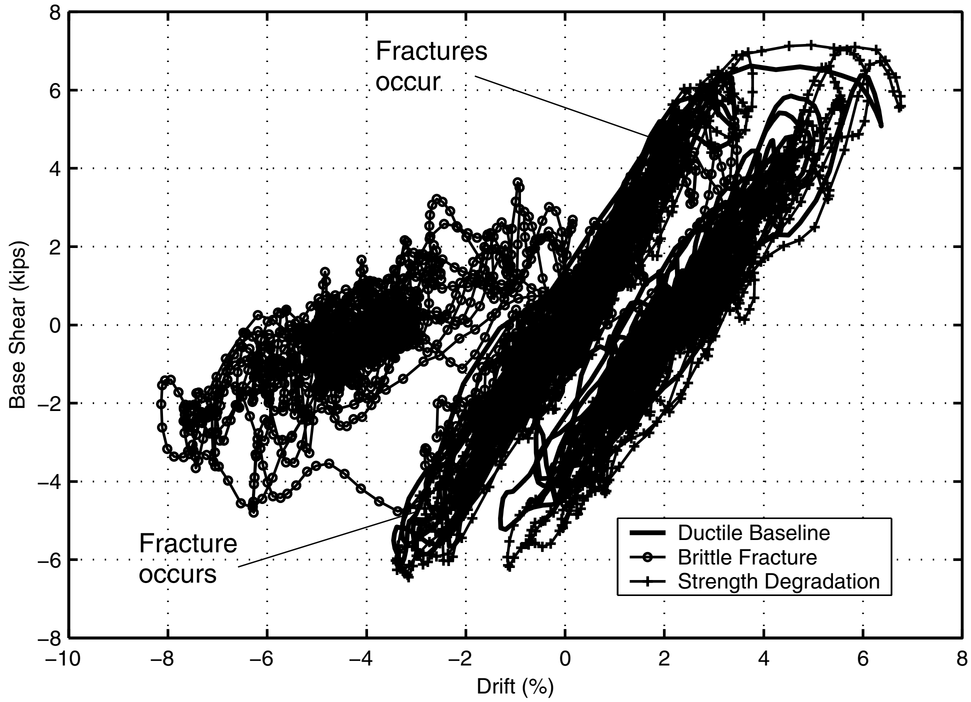

Figure 6-62. Comparison of base shear first-story drift hysteresis, JSE17 (Llolleo-based) motion

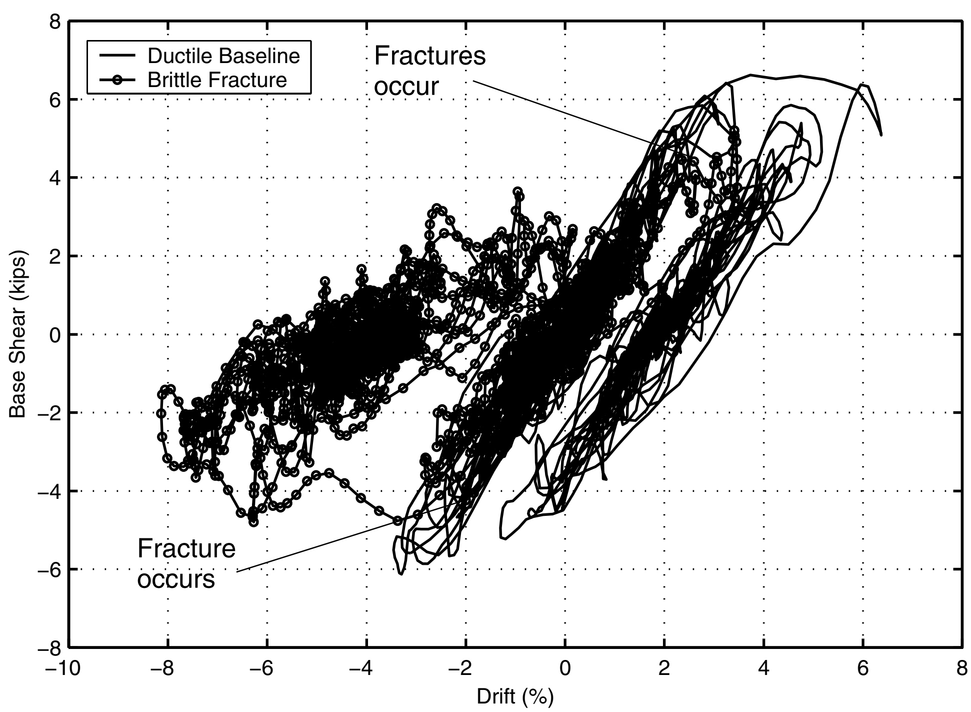

Figure 6-63. Comparison of base shear first-story drift hysteresis, DB and BF CB only

Comparisons of moment-rotation hysteresis for connection 2 (C2) are shown separately for ease of viewing for the ductile baseline and brittle fracture case in Figure 6-64 and the ductile baseline and strength-degrading case in Figure 6-65. The fracture is clearly indicated. As shown in Figure 6-65, the hysteretic behavior of the strength-degrading and ductile baseline connections was very similar for this excitation, and little degradation can be observed. This is primarily due to the fact that there was only one large yield cycle, and the strength-degrading connections were designed to degrade significantly over several large inelastic cycles.

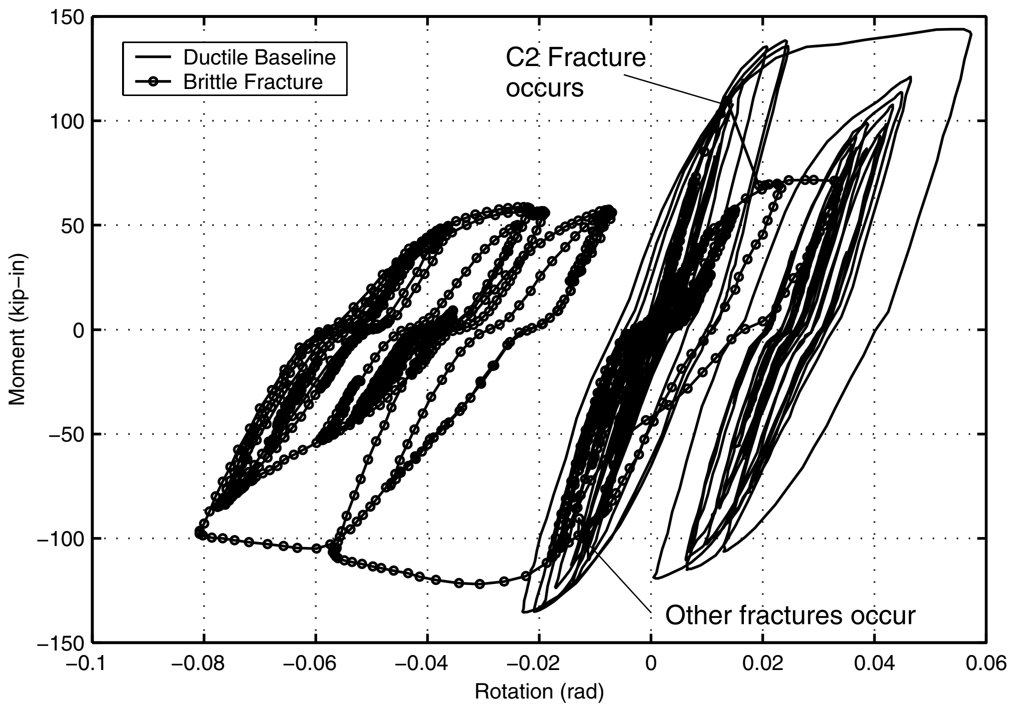

Figure 6-64. Comparison of C2 moment-rotation hysteresis, DB and BF CB, JSE17 (Llolleo-based) motion

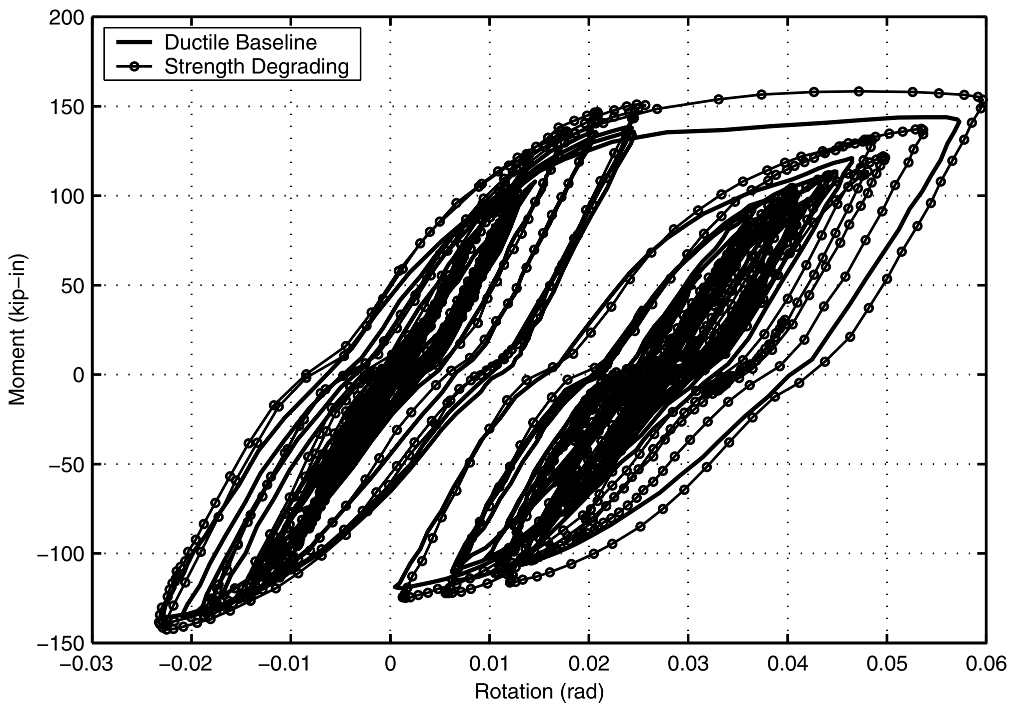

Figure 6-65. Comparison of C2 moment-rotation hysteresis, DB and SDC, JSE17 (Llolleo-based) motion

The first conclusion that can be drawn from this comparison set is that the response of the ductile baseline and strength-degrading connections was very similar, and little degradation occurs. Also, displacements were not preserved for this excitation, as brittle fracture caused a large increase in maximum and residual displacement over the ductile baseline and strength-degrading cases. The reason for this large increase is unclear, but is most likely due to the timely (or untimely) occurrence of the final fractures at the beginning of a large displacement excursion.

6.2.7 Comparison Set 7—DB C Pattern, All Excitations

In contrast to the previous comparison sets, the primary variable under consideration in Set 7 is excitation. The response of the ductile baseline case is compared for all four excitations. Because the durations of these excitations are very different, plotting time history results for each excitation together is not particularly useful. However, percent differences between maximum and residual values can be used to make meaningful comparisons. These differences are located in Tables E-19 through E-21.

The maximum displacements and drifts were largest for the 0.6 second pulse, followed by the 1.2 second pulse, and then the JSE17 and JNF01 motions. The residual displacements were slightly different, with the 0.6 second pulse again having the largest values, followed by the JSE17, JNF01, and 1.2 second pulse excitations. As expected, there were significant differences in the displacement response for the various excitations. The only instance in which there were not significant differences was the 1.2 second cosine pulse/ JSE17 comparison for the maximum values of displacement and interstory drift ratio. Displacements and interstory drifts were larger for the 1.2 second pulse than the 0.6 second pulse, by about 33% for maximum values and 840% for residual values. It should be noted here that the residual displacements and drifts for the 1.2 second pulse were very small, leading to the very large percent differences.

The differences between the 1.2 second pulse and the JNF01 motion were larger than expected, since the JNF01 motion contains a pulse with a period close to 1.2 seconds. However, there were other pulses in that record which evidently caused the pulse of interest to have less effect than anticipated. The maximum values of displacement and interstory drift ratio were larger by about 30% for the 1.2 second pulse, while the residual values were larger by about 130% for the JNF01 motion.

The maximum values of base shear are all within 12% of each other, and most are within the 10% error estimate for the test setup. This indicates that the connections yield strengths, which govern the maximum base shear, were consistent across the tests. Base shear-interstory drift hysteresis is compared in Figure 6-66. The maximum base shear values are similar for all excitations, though the maximum drifts are quite different, with the 0.6 second pulse having significantly larger drift. The response of the two earthquake motions is approximately bounded by the response of the 1.2 second cosine pulse.

The loops show varying amounts of high-frequency response, with the 1.2 second pulse showing very small contributions, and the rest of the excitations having significantly larger contributions. The greater high-frequency content for the ground motions and the 0.6 second cosine pulse is expected, since for these cases the first elastic vibration mode is on the descending branch of the pseudo-acceleration response spectrum, causing some of the higher modes to be in the peak region of the spectrum.

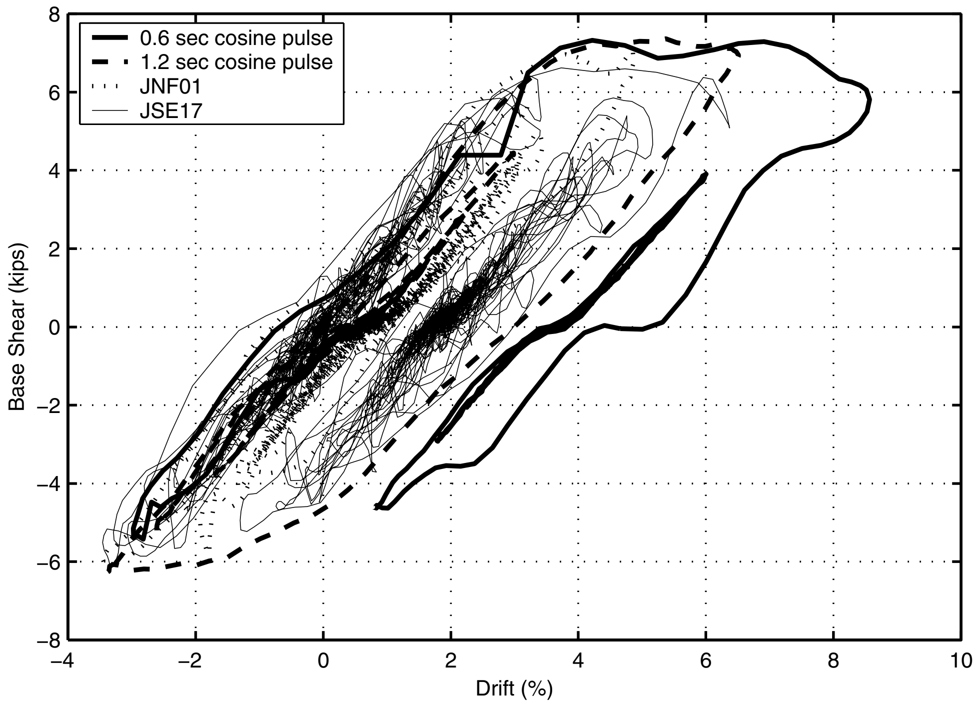

Figure 6-66. Comparison of DB patterns, all excitations

There was more variation in the strength degradation λ_{Vb} than base shear, which was expected due to the difference in duration of the excitations. Overall, only the 1.2 second pulse/JSE17 and JNF01/JSE17 comparisons were above the 20% significance level, though. As expected, the JSE17 motion caused the most degradation with 77% residual base shear. However, most of the degradation occurred during a single strong displacement excursion. The 0.6 second cosine pulse caused a similar amount of degradation with λ_{Vb} = 82%. The 1.2 second cosine pulse caused the least with 94% residual base shear. The JNF01 motion caused similar degradation to the 1.2 second cosine pulse with 92% residual base shear.

There were considerable differences in the amount of period elongation caused by the various excitations. For instance, there was a 68% difference in the period elongation caused by the shortest (0.6 second cosine pulse) and longest (JSE17) excitations. Only the 1.2 second cosine pulse/JNF01 and 0.6 second cosine pulse/JNF01 comparisons had percent differences less than the global error estimate of 20%.

Maximum absolute and relative accelerations were also highly variable among the excitations, with percent differences between 6% and 360%. This result was expected, since the accelerations are much more sensitive to high-frequency excitation than other response quantities.

6.2.8 Comparison Set 8 — BF CB Pattern, 1.2 Second Cosine Pulse, JNF01, JSE17

In this comparison set, the response of the BF CB pattern to the 1.2 second cosine pulse and the JNF01 motion are compared. This comparison is of interest due to the pulse of approximately 1.2 second duration present in the JNF01 motion. Due to the vastly differing durations of the two motions, plotting time history results together is not particularly helpful to understanding the similarities and differences of the effects of the pulses in the two excitations. However, percent differences are very helpful in this regard, and these are located in Tables E-22 through E-24.

The percent differences between the 1.2 second cosine pulse and the JNF01 motion are quite large for both maximum and residual displacements and drifts, despite both motions containing a pulse with approximately 1.2 second duration. These values are larger for the 1.2 second cosine pulse, by about 110% and 780% for maximum and residual values, respectively.

The percent differences for base shear, overturning moment, and absolute accelerations were less than the global error estimates. The base shear and period elongation ratios were slightly over the significance level with differences of about 26% each.

The base shear-interstory drift hysteresis for the two excitations is compared in Figure 6-67. The JNF01 response is approximately bounded by the 1.2 second cosine pulse, but the maximum interstory drift is much higher for the 1.2 second cosine pulse. The large deformations caused by the pulse waveform in the 1.2 second cosine excitation were not repeated for the 1.2 second pulse waveform within the JNF01 motion. A possible reason for this is the effect of earlier pulses in the JNF01 motion, which may have damaged the structure before the large pulse, causing the dynamic properties to change and the large pulse to have less effect.

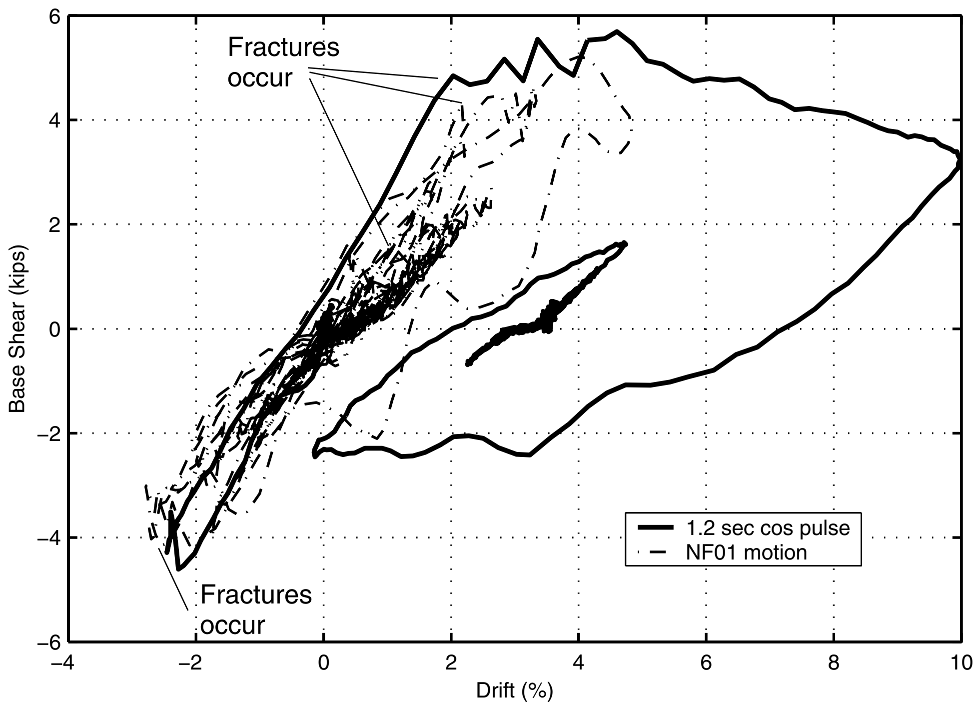

Figure 6-67. Comparison of base shear-drift hysteresis, BF CB patterns, JNF01 and 1.2 second cos pulse

6.2.9 Comparison Set 9 — All comparable B Patterns for Pulse Motions

The purpose of this comparison set is to examine the effects of the structure's response spectrum location on global behavior. This is accomplished by making comparisons between the base shear-interstory drift ratio hysteresis plots for selected connection configuration patterns that were tested with both the 0.6 and 1.2 second cosine pulses. The patterns used are the ductile baseline, brittle fracture BP, ductile fracture BP, and deformation softening B. The patterns are shown for the 0.6 second cosine pulse in Figure 6-68, and the 1.2 second cosine pulse in Figure 6-69.

The relative effects of strength loss are greater for the 1.2 second pulse than the 0.6 second pulse. The same amount of strength is lost between the ductile baseline case and the cases with various types of hysteretic degradation, but there is a much greater increase in displacement for the 1.2 second cosine pulse case. This result is expected, since for the 1.2 second case the specimen is in the short-period range, where strength is more important than in the intermediate, or Newmark's energy-preserved range, where the specimen is for the 0.6 second pulse. By visual examination of the two figures, energy is clearly not preserved for the 1.2 second pulse cases, while it is approximately preserved for the 0.6 second pulse cases.

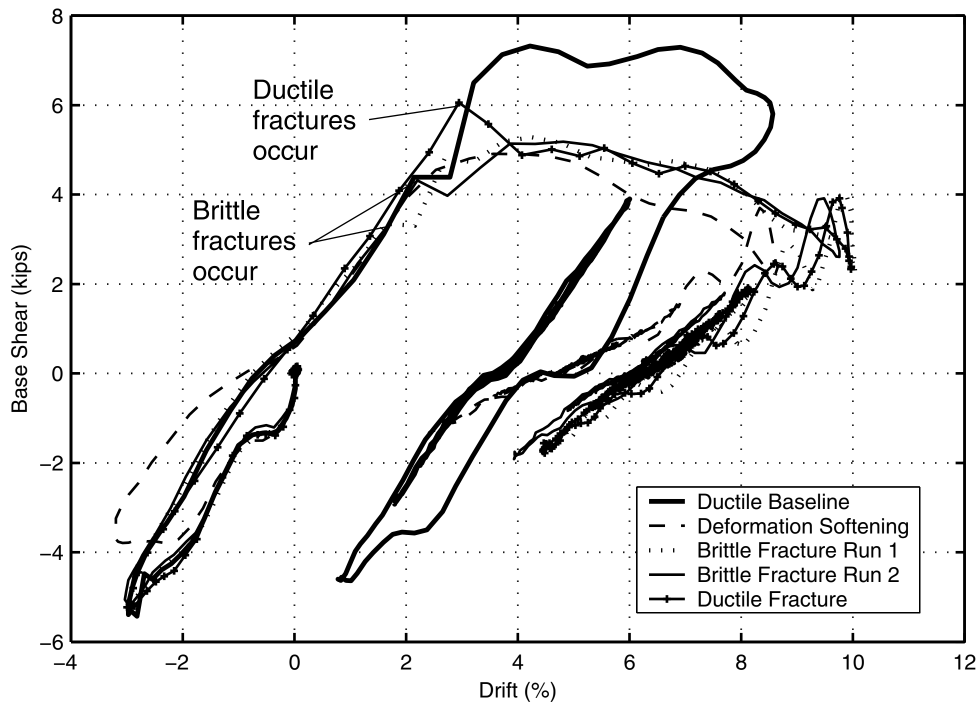

Figure 6-68. Comparison of base shear first-story drift hysteresis for 0.6 sec cosine pulse, B patterns

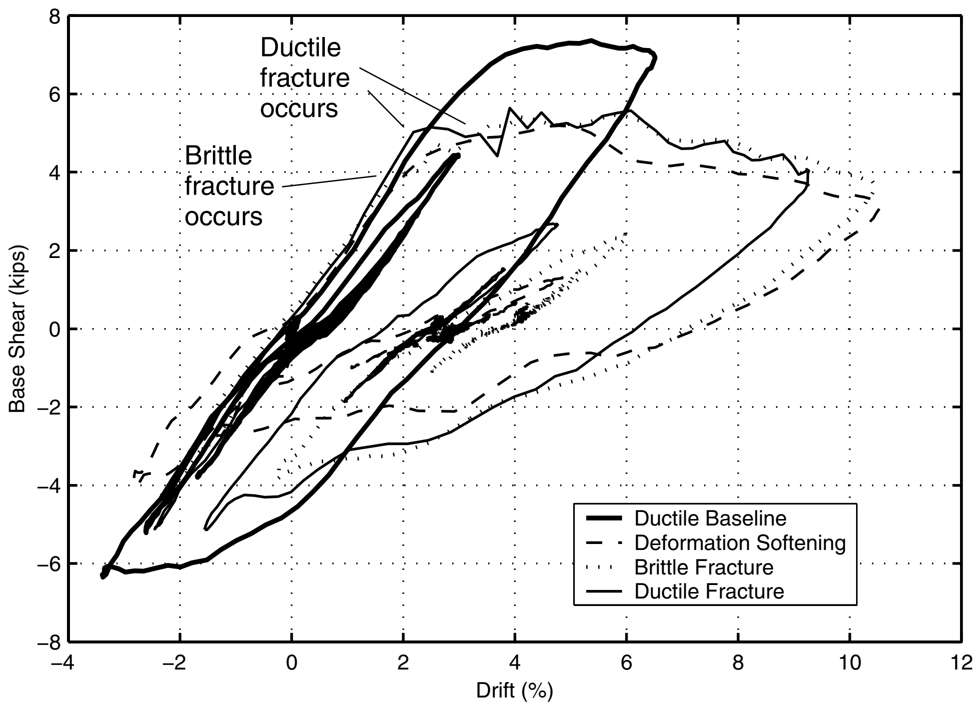

Figure 6-69. Comparison of base shear first-story drift hysteresis for 1.2 sec cosine pulse, B patterns

Percent differences for this case can be found in Tables E-25 through E-27.

6.2.10 Comparison Set 10 — Fracture Patterns, 0.6 Second Cosine Pulse

This set is divided into two subsets, 10a and 10b. Set 10a contains the ductile baseline case and the BP and CP brittle and ductile fracture patterns. In Comparison Set 10a, the key variable examined is the spatial distribution of the fracture hysteretic type. Since no significant differences between brittle and "ductile" fracture (which was not actually ductile) were found, data for both patterns are used in this set. The excitation for all of the tests in Set 10a is the 0.6 second cosine pulse at 100% amplitude. As discussed previously in Sets 3 and 4, the catch cables engaged fully for all of the CP patterns, and may have interfered in the BP pattern tests.

The key variable examined in Set 10b is the amplitude of the excitation. This subset contains the brittle fracture BP patterns. The excitation used is the 0.6 second cosine pulse at 50% and 100% amplitude. The catch cables may have interfered for the 100% amplitude tests. The percent differences for this set are found in Tables E-28 through E-30.

6.2.10.1 Set 10a

The displacement response of the specimen is shown in Figure 6-70. The effects of increasing the number of fractures from none to all of the tension flanges in the positive displacement direction is apparent. The maximum and residual drifts increase with the number of tension flanges lost, until collapse occurs when all tension flanges are lost for the CP patterns.

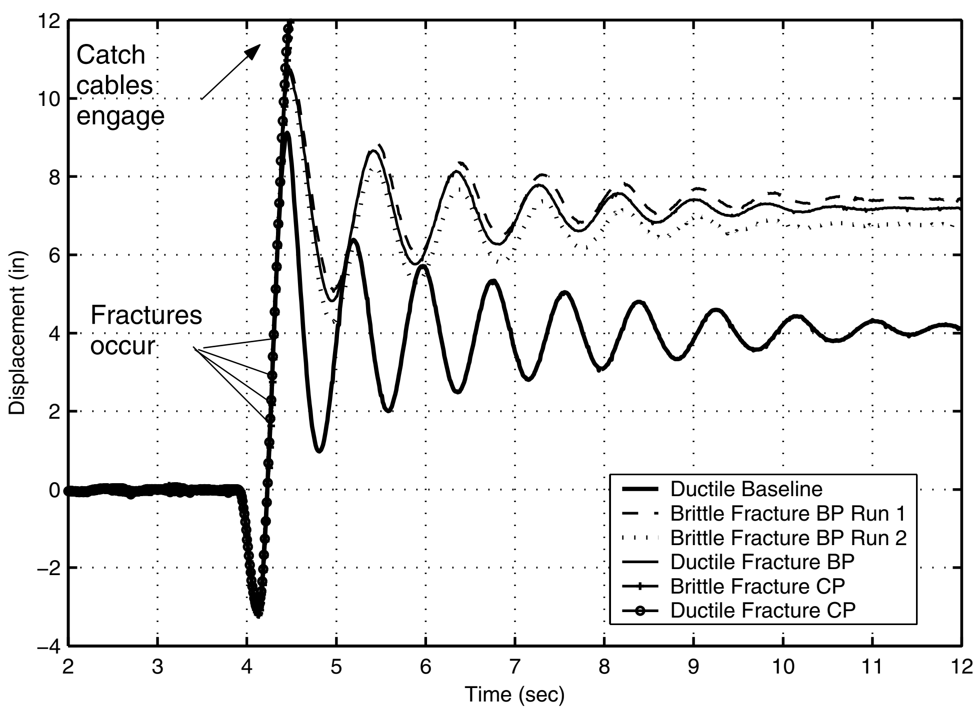

Figure 6-70. Comparison of relative displacements at top of frame, fracture patterns, 0.6 sec cosine pulse

The portion of the response during and just after the pulse is shown for first-story interstory drifts in Figure 6-71. The displacement time histories are similar for all of the cases, except that those with fractures simply go farther. The greater the number of fractures, the farther the specimen displaces.

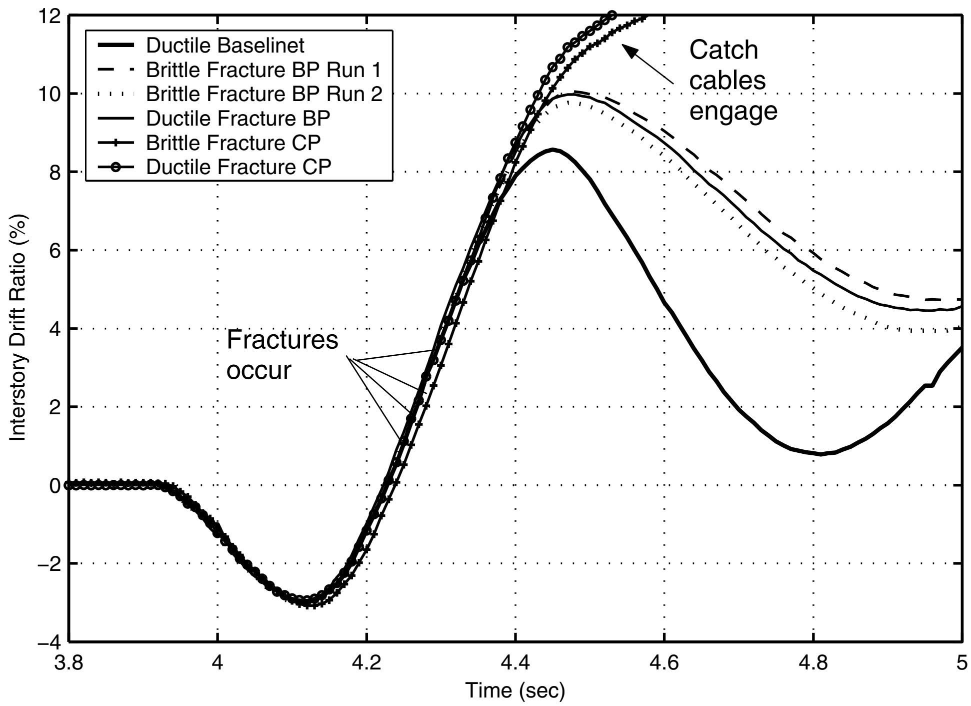

Figure 6-71. Comparison of first-story drift, fracture patterns, 0.6 sec cosine pulse

Base shear time histories are next compared for the various fracture patterns in Figure 6-72. The loss of strength when four fractures occur instead of two is significant, though the subsequent loss of strength due to negative post-fracture stiffness in the connection hysteresis (Figure 6-74) occurs at the same rate. The suspiciously similar waveforms for the BP and CP patterns at about 4.45 seconds indicated that the catch cable may have interfered for the BP patterns, as discussed in Set 3.

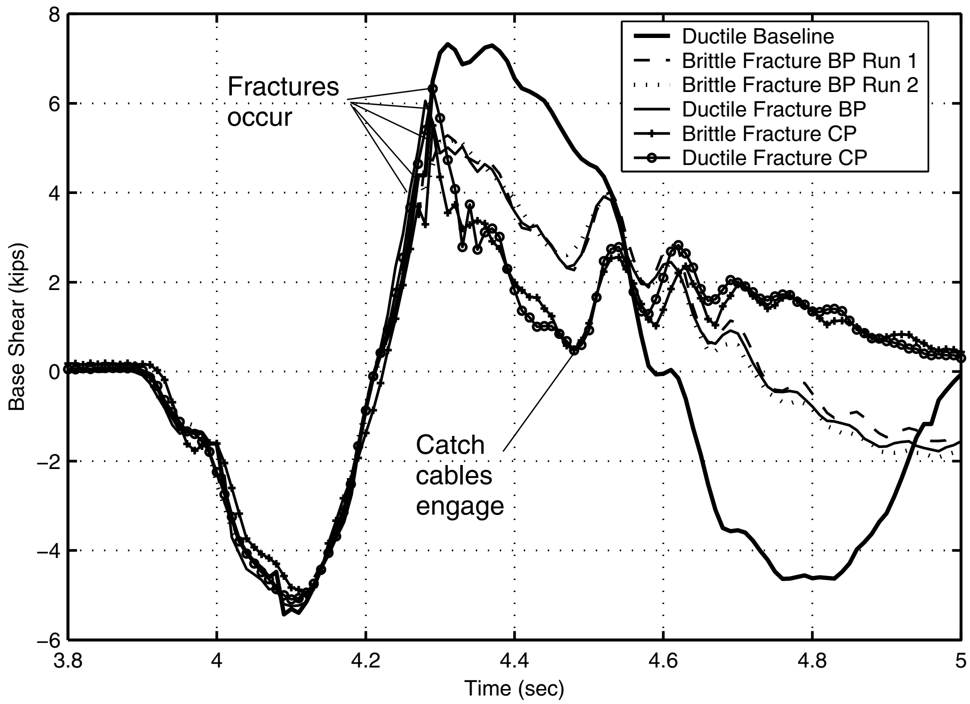

Figure 6-72. Comparison of base shear, fracture patterns, 0.6 sec cosine pulse

The base shear-interstory drift hysteresis loops in Figure 6-73 show similar post-fracture tangent stiffness for both BP and CP patterns, though the initial reduction in strength due to the fractures is much greater for the CP patterns. Consequently, because displacements are not preserved, this greater strength reduction leads to larger maximum drift.

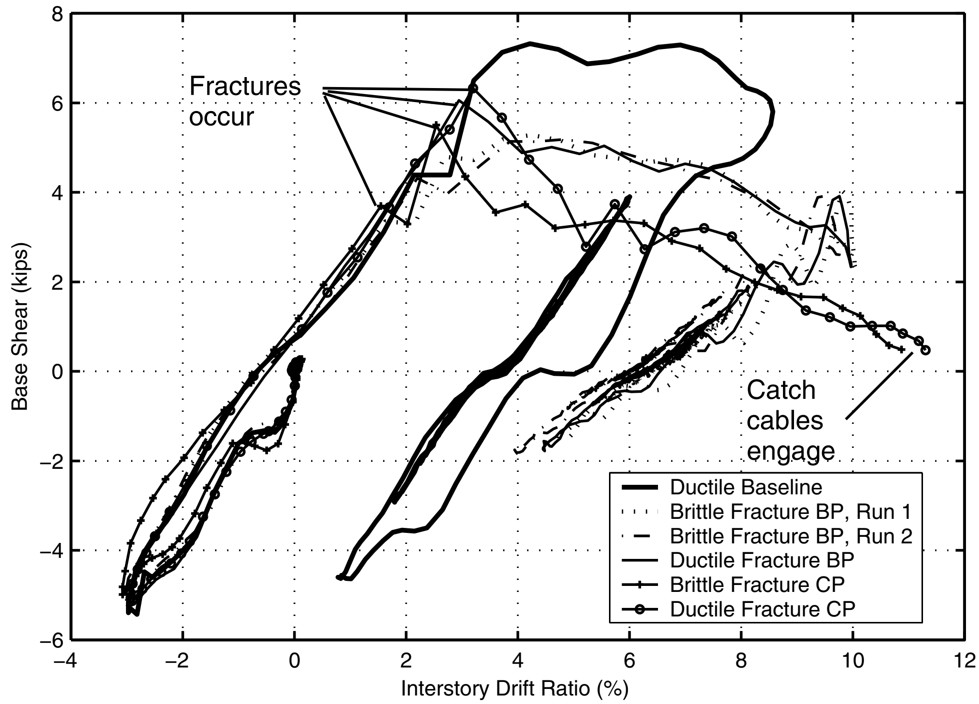

Figure 6-73. Comparison of base shear first-story drift hysteresis, fracture patterns, 0.6 sec cosine pulse

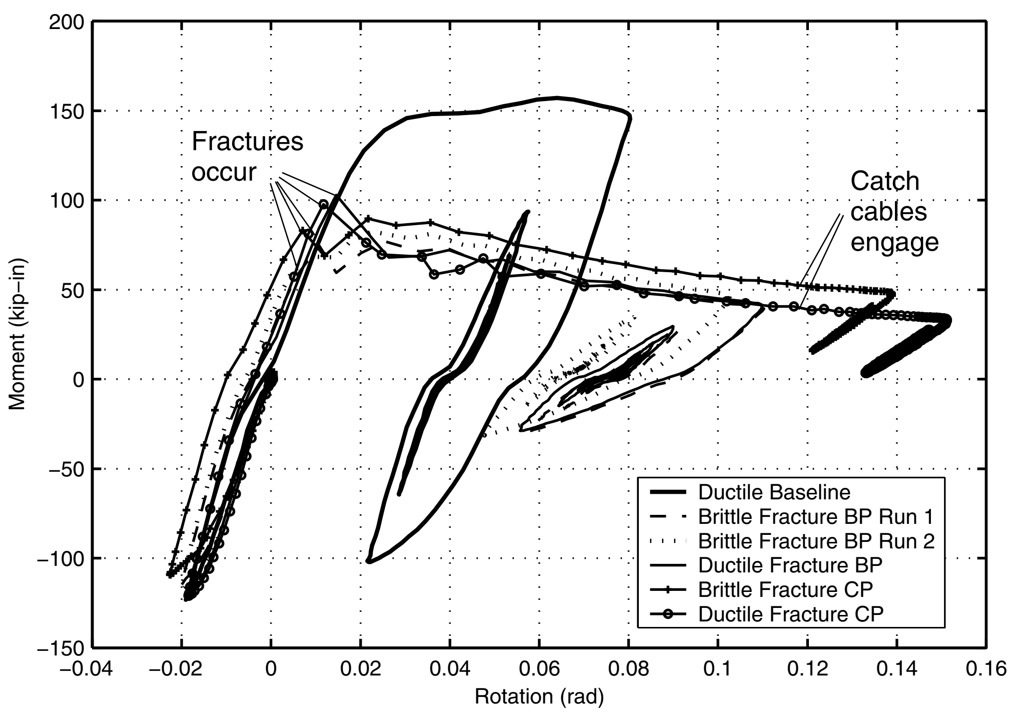

Figure 6-74. Comparison of connection C2 moment-rotation hysteresis, fracture patterns, 0.6 sec cosine pulse

This comparison set shows that fractures in all the tension flanges have much more adverse effects on the system response than fractures in tension flanges in one story only.

6.2.10.2 Set 10b

The effects of excitation amplitude on the displacement response, which are significant, are shown in Figure 6-75. The larger amplitude corresponds to a massive increase in both maximum and residual displacements. However, as shown in Figure 6-76, a corresponding increase in base shear does not occur since the maximum base shear is limited by the fracture moment of the connections, which is unchanged. There is significantly less degradation in base shear after fracture for the 50% amplitude case, though.

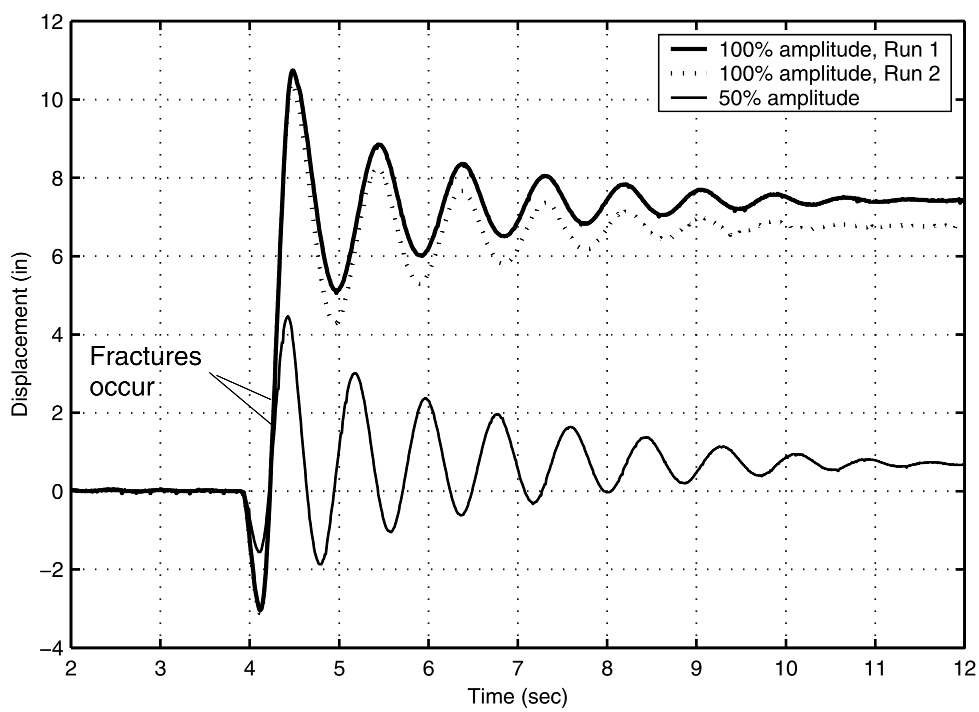

Figure 6-75. Effects of excitation amplitude on relative displacements at top of frame, BF BP pattern, 0.6 sec cosine pulse

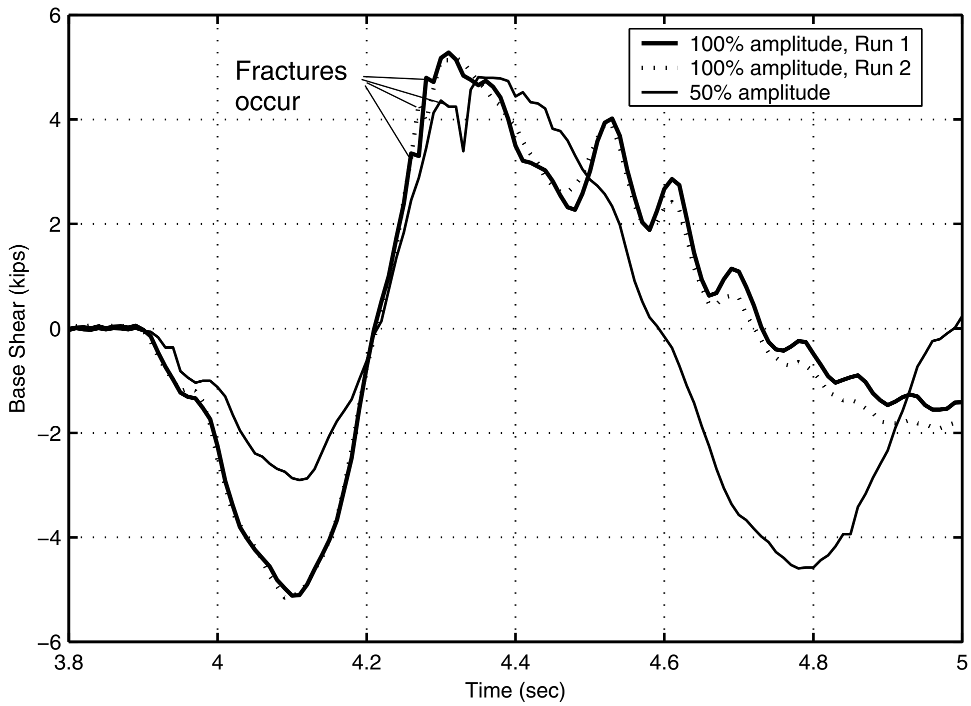

Figure 6-76. Effects of excitation amplitude on base shear, BF BP pattern

The base shear-interstory drift relations in Figure 6-77 and the connection moment-rotation relations in Figure 6-78 show that most of the increase in the deformations due to amplitude is due to plastic deformation after fracture occurs rather than due to the fracture itself. The larger the pulse amplitude, the further it continues to push the structure after fracture. Since these connections have a negative post-fracture tangent stiffness, as shown in Figure 6-78, pushing the structure further tends to exacerbate the increase in displacements.

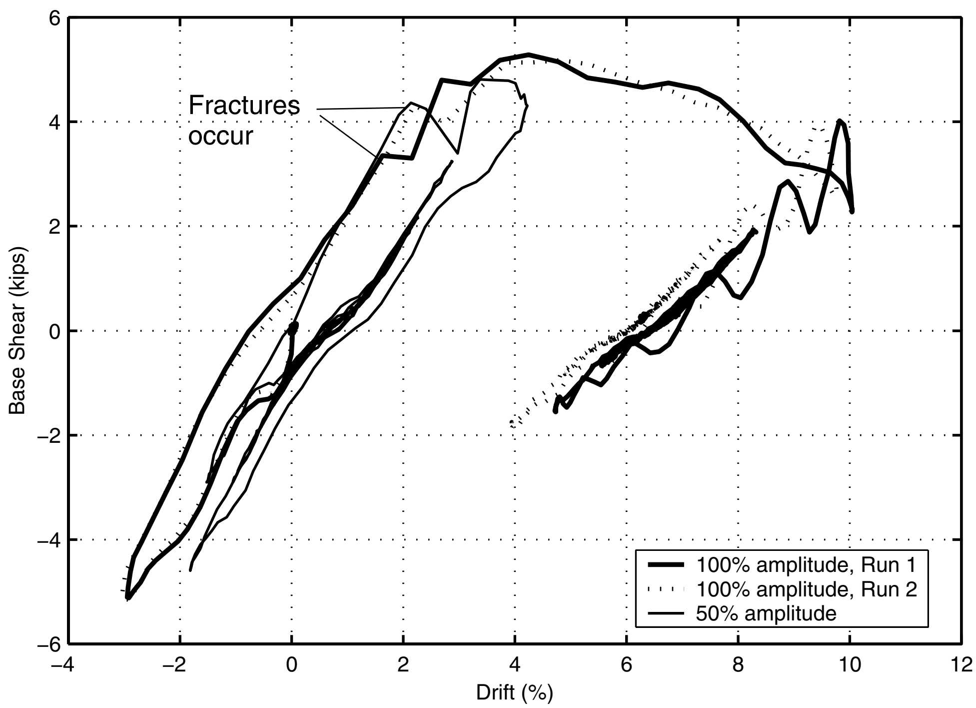

Figure 6-77. Effects of excitation amplitude on base shear first-story drift hysteresis, BF BP pattern

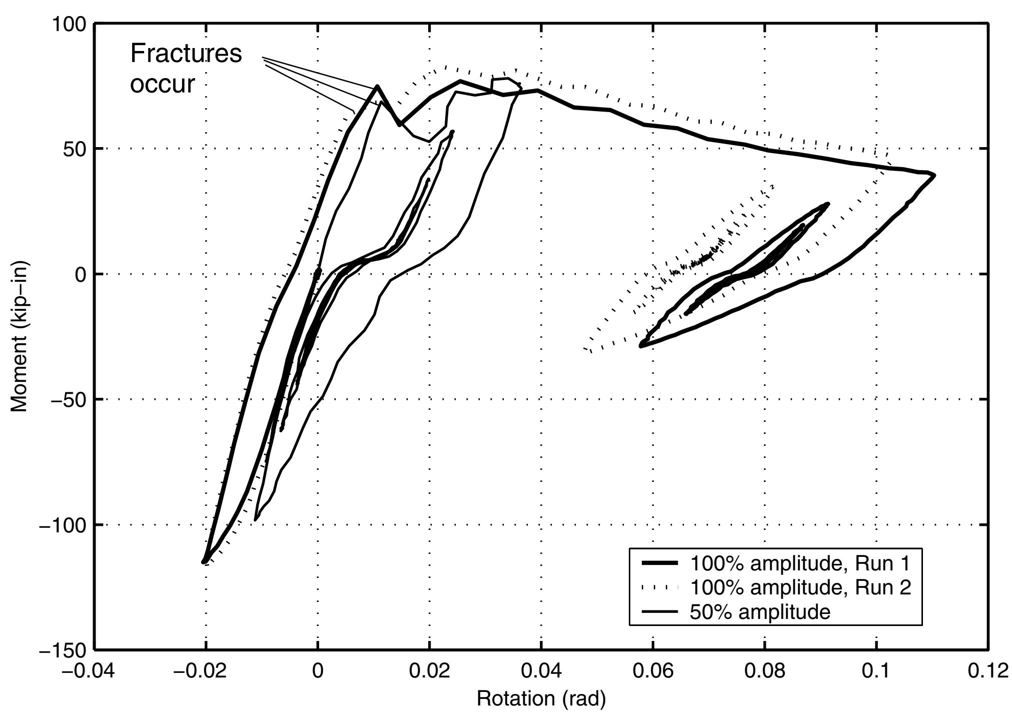

Figure 6-78. Effects of excitation amplitude on connection moment-rotation hysteresis, BF BP pattern

For this excitation, increasing the excitation amplitude for the BF BP pattern causes a large increase in maximum and residual displacements, as well as connection rotations. Maximum base shear and connection moment are relatively unchanged, since these values are limited by the capacity of the fracturing connections rather than the amplitude of the excitation.

6.2.11 Comparison Set 11 — Brittle Fracture Patterns, 1.2 Second Cosine Pulse

As was the case in Set 10, this set is divided into two subsets, 11a and 11b. Set 11a contains the ductile baseline case and the BP and CP brittle fracture patterns. In Comparison Set 10a, the key variable examined is the spatial distribution of the brittle fracture hysteretic type. The excitation for all of the tests in Set 11a is the 1.2 second cosine pulse at 100% amplitude. As discussed previously in Sets 1 and 2, the catch cables engaged fully for the BF CP pattern test, and did not interfere at all for the other patterns.

The key variable examined in Set 11b is the amplitude of the excitation. This subset contains the brittle fracture CP patterns. The excitation used is the 1.2 second cosine pulse at 50%, 75% and 100% amplitude. The 75% case has two prior fractures from the 50% case test, which was performed immediately prior to it. The catch cables did not engage or hinder the response for the 50% and 75% cases, and engaged fully for the 100% case.

The percent differences for both subsets are presented in Tables E-31 through E-33.

6.2.11.1 Set 11a

Relative displacements at the top of the frame are shown for the fracturing cases and the ductile baseline case in Figure 6-79. As shown, the number and spatial distribution of fractures have significant effects on the maximum and residual displacements. Comparing the DB, BP, and CP cases shows a progressive increase in displacements as more fractures occur. However, the maximum and residual displacements do not depend solely on the number of fractures, but are also dependent on their spatial distribution.

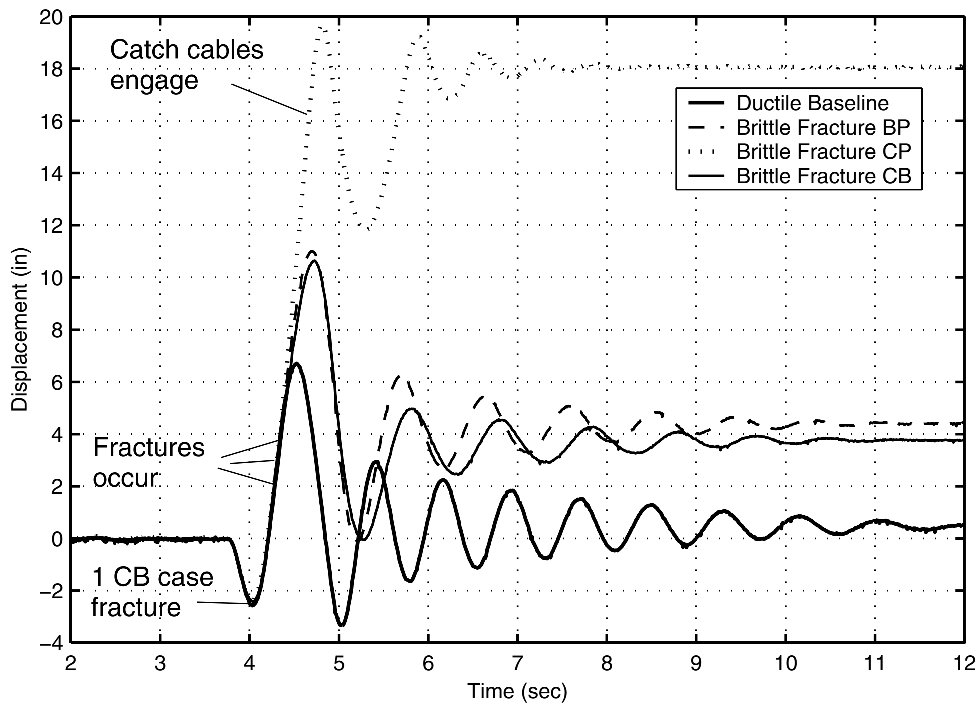

Figure 6-79. Effects of brittle fracture pattern on relative displacements at top, 1.2 sec cosine pulse

A comparison of the CB and CP patterns shows the effect of bottom flange-only fractures compared to top and bottom flange fractures. The CB pattern, which had only bottom flange fractures, had much smaller displacements than did the CP pattern, which had all tension flanges, both top and bottom, fracturing nearly simultaneously in the direction of the pulse. The CP pattern suffered collapse; the CB pattern did not. In fact, the response of the CB pattern was much closer to that of the BP pattern, which makes physical sense because both patterns had two connections with intact tension flanges, and therefore two connections with greater strength capacity to resist the pulse motion.

As shown in Figure 6-80, the response of the CB and BP patterns is similar in amplitude, but there are some subtle differences due to the location of the fractures. The CB pattern shows some period elongation due to a fracture in the first negative excursion, which causes its response to deviate from that of the ductile baseline case earlier. Also the maximum drift is less than for the BP pattern, possibly because the system is less stiff due to the prior fracture. The CB pattern still has very close to the full strength in the positive direction during the first positive drift excursion, since the fractured coupon is now in compression and can carry load through bearing. The fact that significant strength is not lost in the direction of interest is key to the response, since it has been demonstrated in earlier comparison sets that strength loss leads to increased displacement for this excitation.

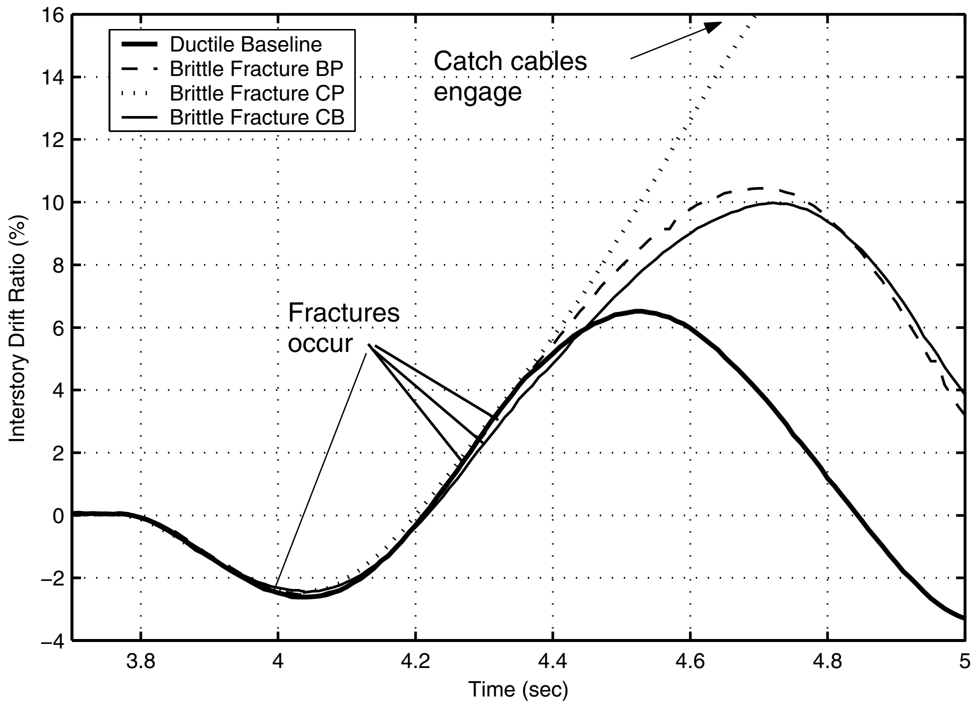

Figure 6-80. Close-up of effects of fracture pattern on first-story interstory drift ratio, 1.2 sec cosine pulse

The base shear-interstory drift hysteresis is compared in Figure 6-81. The CP pattern shows the largest effects due to fracture, as the system loses much more strength and thus displaces further, though the post-fracture tangent stiffness is roughly the same for all fracture patterns.

Similarities exist between the system hysteretic behavior of the BP and CB patterns for interstory drift during the major positive displacement excursion. During the second negative displacement excursion, which immediately follows the major positive excursion, the behavior of these two cases differs due to the loss of strength caused by the prior C1 fracture in the CB case. The BP case has no fracture capable flanges in tension during negative excursions, so fracture could not occur and lessen the capacity in that direction.

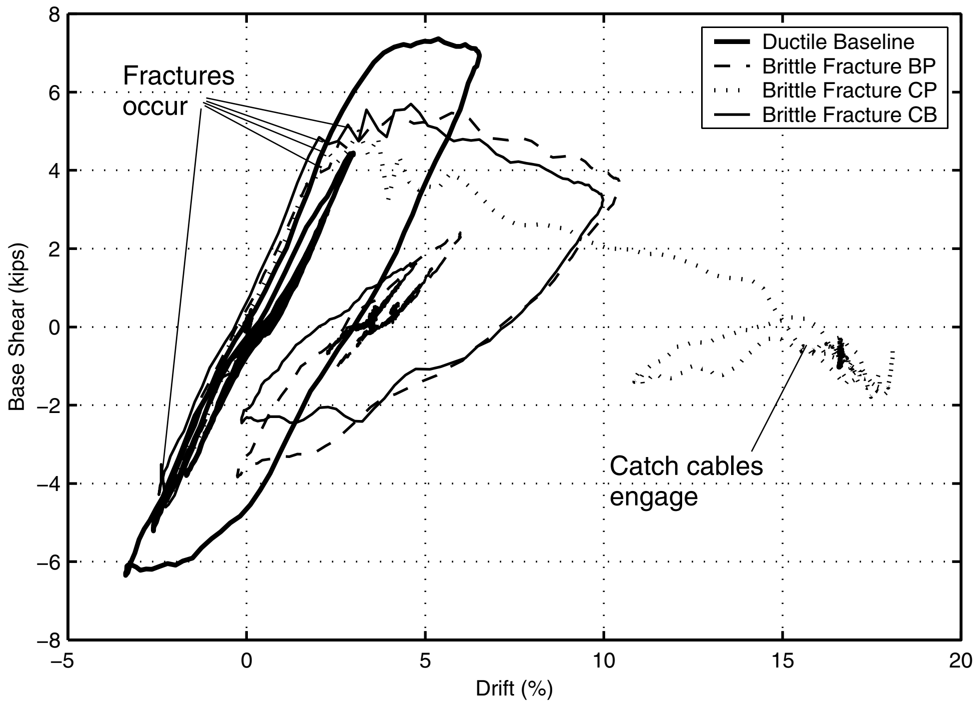

Figure 6-81. Comparison of base shear first-story drift hysteresis, fracture patterns, 1.2 sec cosine pulse

The major finding from Set 11a is that the spatial distribution of fractures can have significant effects on the system behavior. Fractures in the bottom flanges only have less effect than fractures of both top and bottom flanges in a particular direction, even if all of the connections can experience fracture. This is because at least half of the connections in the frame have nearly full strength at any one time (in both positive and negative directions), since fractured bottom flanges can bear in compression.

6.2.11.2 Set 11b

Figure 6-82 shows that the displacement response of systems with fracturing connections is dependent on the severity of the excitation, as measured by amplitude. In the case of the 50% case, fractures only occurred in the first story, though all connections were capable of fracture. In the 100% amplitude case, the excitation was strong enough to cause fracture as well as significant plastic deformation afterwards. The 75% amplitude case with two prior fractures shows that the increased amplitude of the excitation causes the remaining connections to fracture and significant plastic deformation as well.

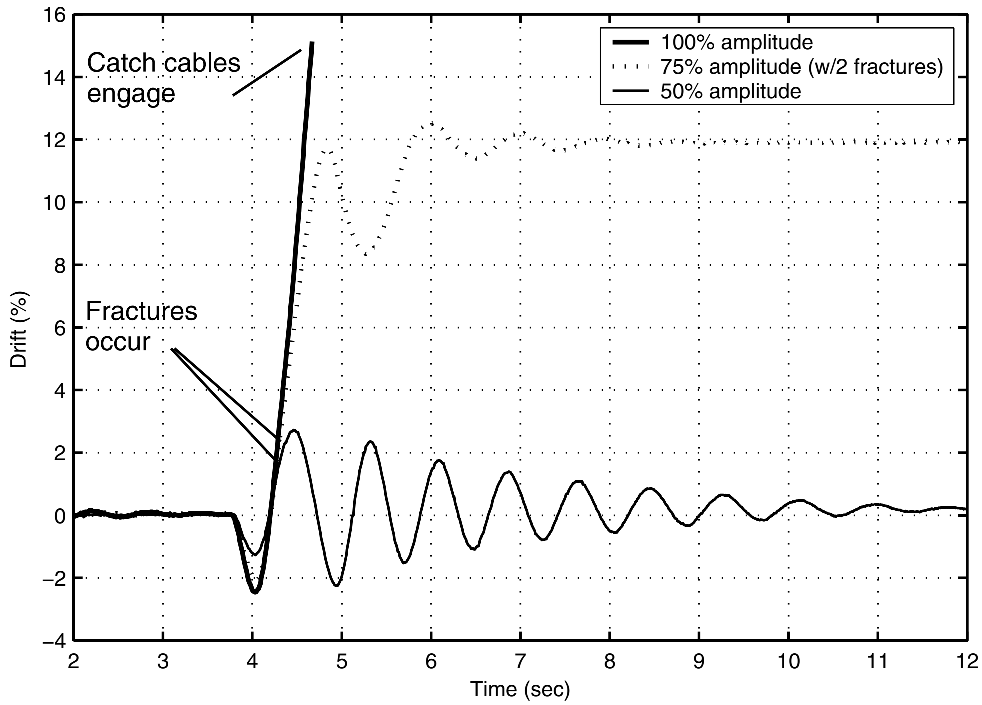

Figure 6-82. Effects of excitation amplitude on first-story interstory drifts, BF CP pattern

Figure 6-83 shows the region during the pulse in greater detail. The response is not discontinuous for any of the cases, though one might expect that the fracture could be seen more clearly for a lower-amplitude case, such as the 50% case.

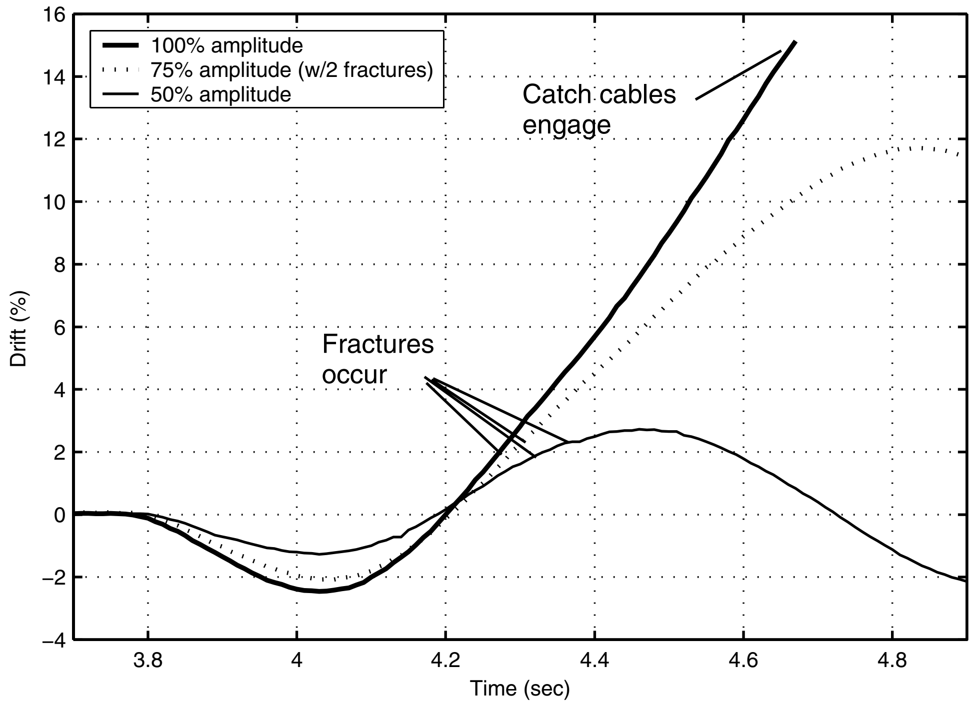

Figure 6-83. Close-up of effects of excitation amplitude on first-story interstory drifts, BF CP pattern

In Figure 6-84, the significant plastic deformation following fracture for the 100% and 75% cases can be clearly seen. The 50% case shows little plastic deformation; the structure has barely fractured when the specimen begins to unload. For the 75% case, the prior fracture damage causes the initial global stiffness to be reduced, compared to the other cases.

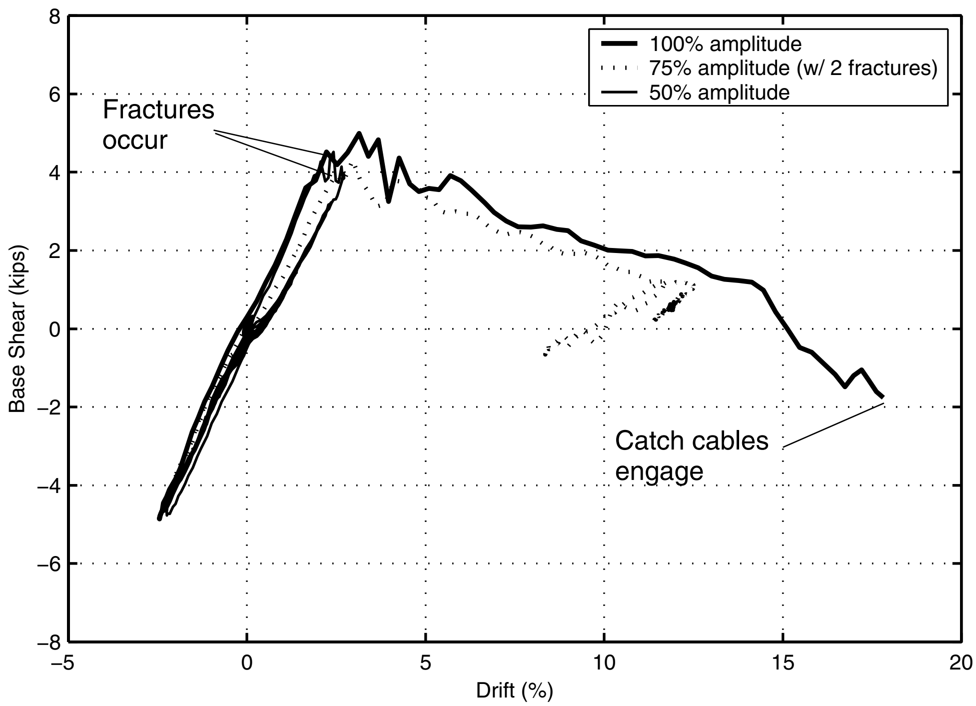

* BF CP 75% amplitude test was run with bottom story connections already fractured

Figure 6-84. Effects of excitation amplitude on base shear first-story drift hysteresis, BF CP pattern

This comparison set shows that the response of fracturing structures to pulse excitations depends largely on excitation amplitude. Large amplitude pulses cause fracture early in the pulse, and the continuing demands from the excitation cause buckling of the compression flange, leading to large amounts of plastic deformation. In contrast, a small amplitude pulse which barely causes fracture will not cause large deformations or significant additional strength loss due to buckling.

6.2.12 Comparison Set 12a & b — Brittle Fracture Patterns, 0.6 Second Cosine Pulse, 50% Amplitude

Comparison Set 12 is composed of tests from the wave propagation sequence of tests. All of the tests in this set were performed with the 0.6 second cosine pulse at 50% amplitude. The percent differences for this set are found in Tables E-34 through E-36. The catch cables did not interfere with the response in any way during any of the tests. Set 12 is divided into two subsets, 12a and

12b, which are described below. Set 12a contains the five brittle fracture A pattern tests, designated A–E. Test E has additional distributed mass along MB1 as described in Section 4.3 on page 79. In Comparison Set 12a, the key variable examined is the effect of this additional distributed mass on the beam. The key variable examined Set 12b is the spatial distribution of the brittle fracture hysteretic type. This subset contains the five brittle fracture A tests and the single BP pattern test.

6.2.12.1 Set 12a

As shown in Figure 6-85, the system behavior for all of the BF A pattern tests is remarkably similar. This demonstrates both the repeatability of the test and the small effects of additional beam mass on the overall system response. In most cases (except period elongation and acceleration) the percent differences in Tables E-34–E-36 between Test E and Tests A–D were smaller than between Tests A–D, showing that the effects of additional beam mass on global behavior were insignificant.

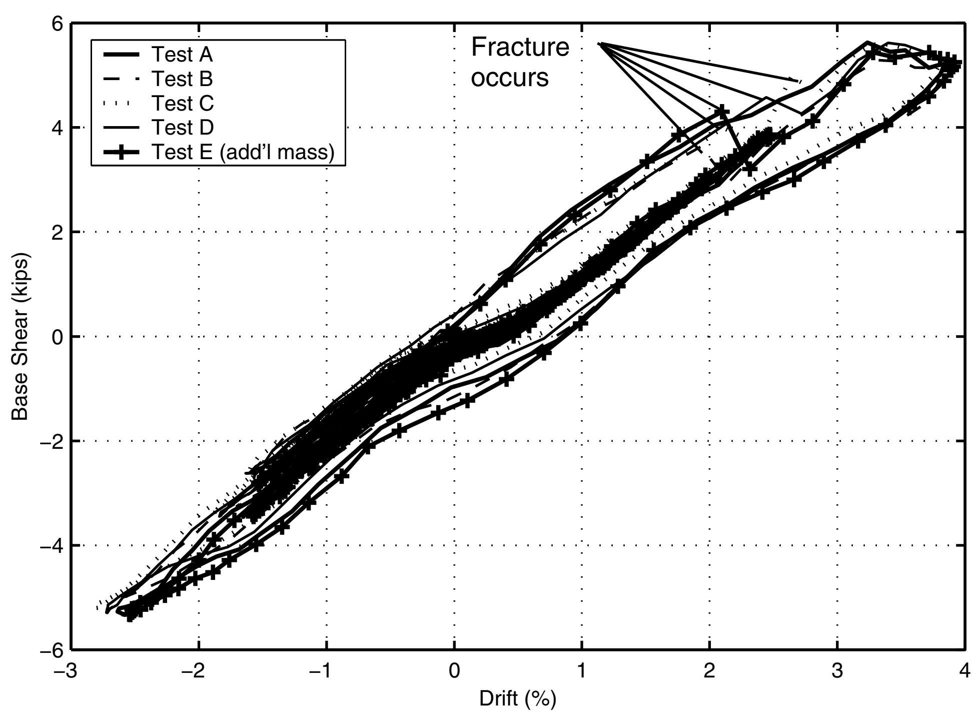

Figure 6-85. Comparison of base shear first-story drift hysteresis, BF A, 0.6 sec cosine pulse

Despite the small effects on global behavior, the additional beam mass has a significant effect on the dynamic properties of the beam itself. As discussed in Sections 5.4.2 and 5.4.4, both the change in beam deflected shape and the excitation of higher beam vibration modes caused by fracture can cause vertical accelerations of the beam. Vertical accelerations at midspan are shown in Figure 6-86, and the longer fundamental vibration mode of the beam with mass is apparent. The maximum accelerations are similar, but the vibration continues much longer for the case with mass, as evident in the portion of the time history from 4.3 to 4.5 seconds.

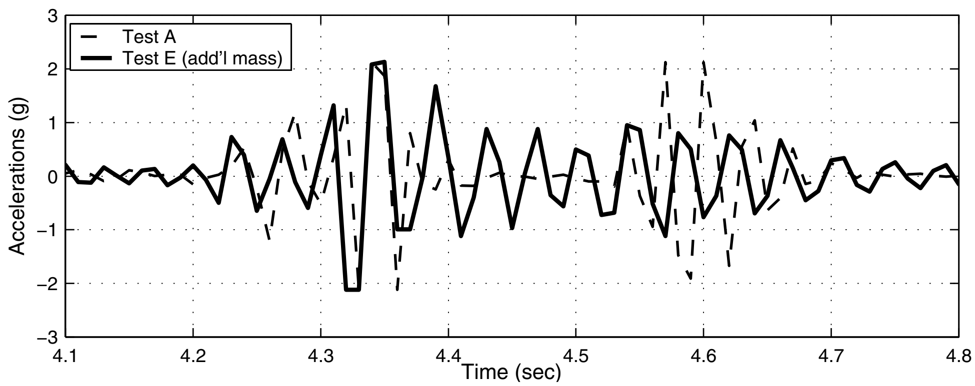

Figure 6-86. Comparison of MB1 midspan vertical accelerations, BF A pattern, 0.6 sec cosine pulse

The additional mass on the beam also affects another local fracture-induced phenomenon - the strain spike discussed in Section 5.4.3. High-speed strain time histories for Tests A and E are compared in Figure 6-87. As shown, the strain spike has a significantly lower amplitude for Test E. This indicates that additional mass along the beam may mitigate the strain spike. However, more study is needed to determine how much mass is needed and why adding mass seems to be helpful.

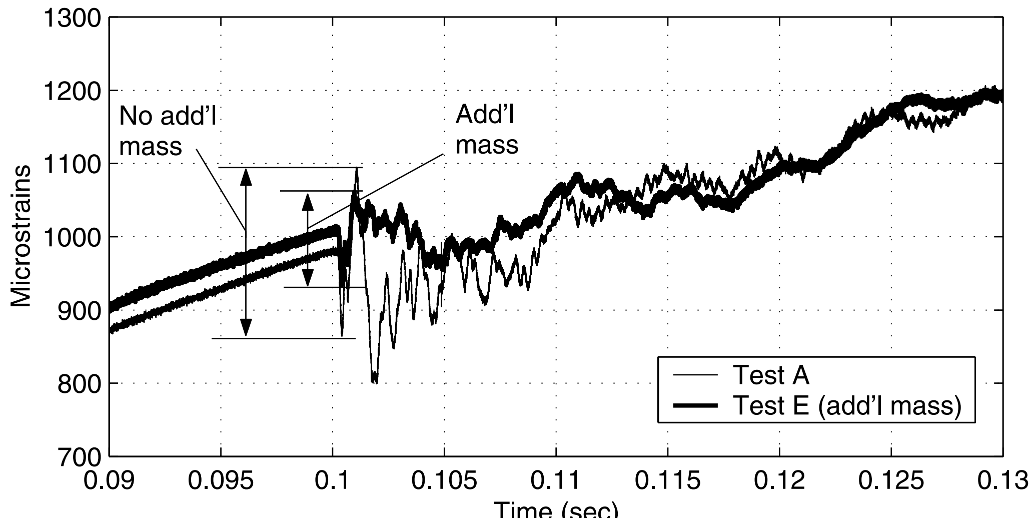

Figure 6-87. Effect of additional distributed mass on strain spike

6.2.12.2 Set 12b

The effects of the second brittle fracture in the first story can be seen in the interstory drift time history in Figure 6-88. The maximum interstory drifts increase by about 10%, and the BP pattern time history clearly deviates from the A patterns after the fractures occur. The residual drifts are also roughly triple for the BP pattern, to 0.65%. The effects of the fracture are also evident as a "shift" in the system hysteresis shown in Figures 6-89 and 6-90. The second fracture causes additional strength loss, though the amount is within the global error bounds.

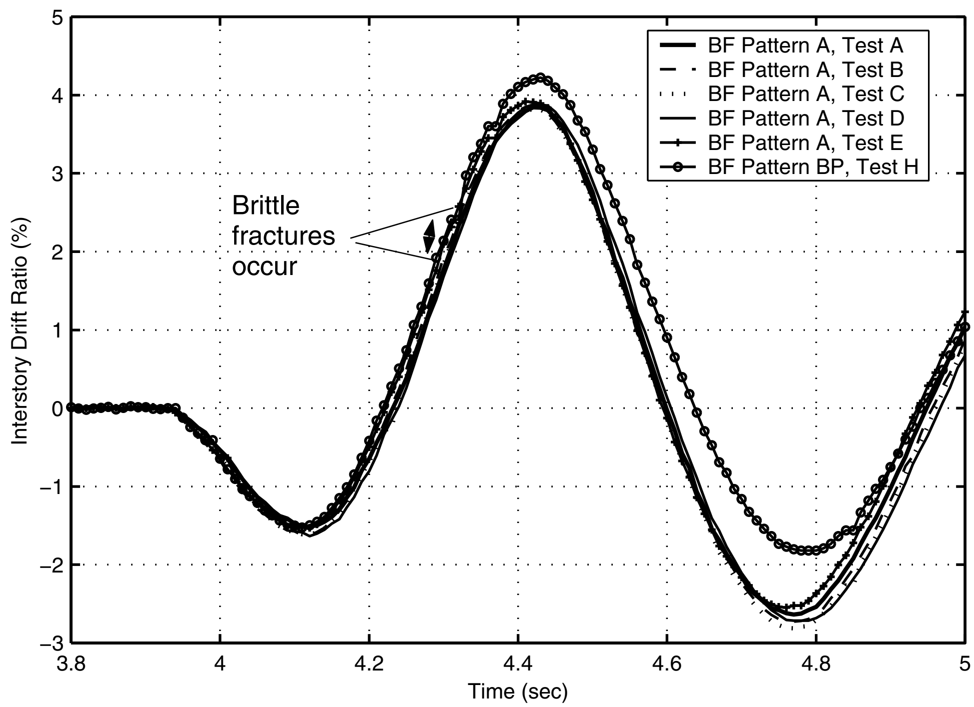

Figure 6-88. Comparison of first-story interstory drift ratio, BF A, BP patterns

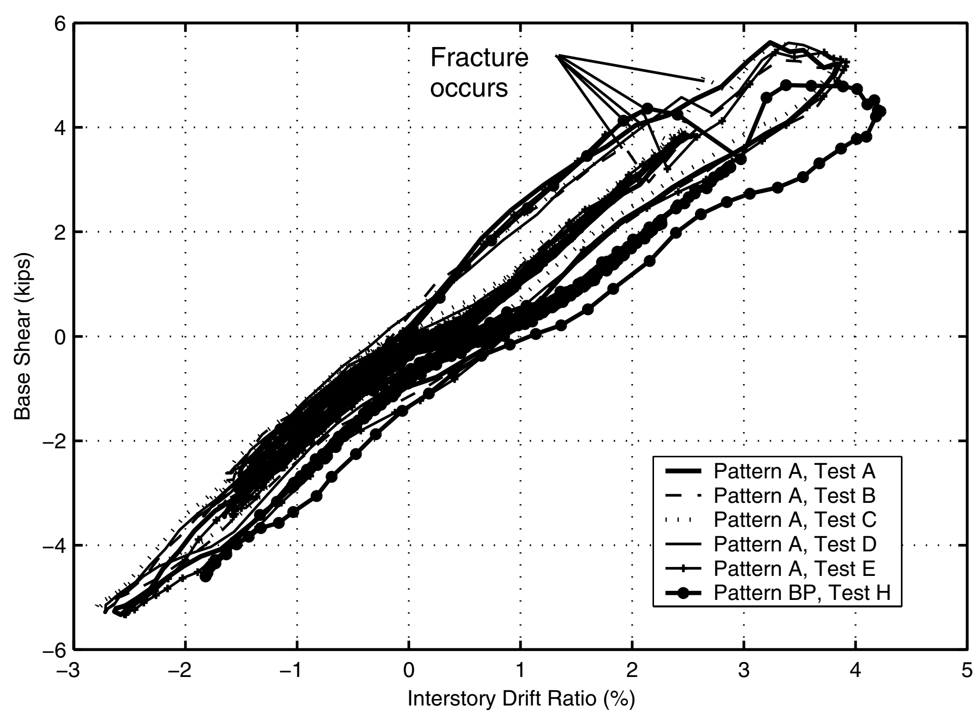

Figure 6-89. Comparison of base shear first-story drift hysteresis, BF A, BP patterns

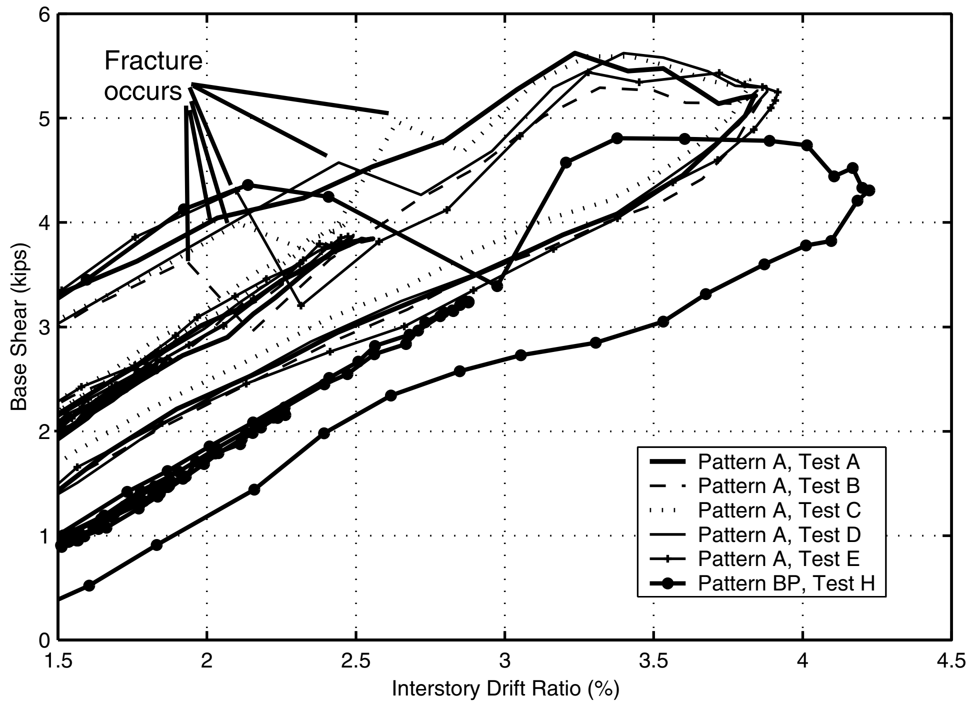

Figure 6-90. Close-up of base shear first-story drift hysteresis, brittle fracture A, BP patterns

6.3 SUMMARY AND CONCLUSIONS

Looking at the results of all of the comparison sets, several general observations can be made. For excitations where the structure is in a period range where strength affects the magnitude of the displacement response, hysteretic degradation that causes a substantial loss of strength will have significant effects on the response, regardless of the cause of the strength loss. Likewise, for excitations where the structure is in the long-period range where strength loss does not cause increases in displacements, the strength loss caused by hysteretic degradation will not adversely affect the response. However, depending on the type of degradation, results other than strength loss, such as negative tangent stiffness can affect the system behavior by different mechanisms.

6.3.1 Pulse Excitations

Both cosine pulse excitations caused large deformation responses in all of the cases, including the ductile baseline case. These responses were typically characterized by a single large displacement excursion, followed by decaying free vibration if collapse did not occur. No collapses were observed for the ductile baseline case or any of the B patterns for either of the pulses. The two ductile baseline connections present in the B patterns provided enough residual strength to prevent collapse.

Hysteretic degradation caused collapses to occur for most C patterns with the full-amplitude cosine pulse excitations. One very important exception was the BF CB pattern/1.2 second cosine pulse combination, where no collapse occurred, and a response very similar to that of the BF BP pattern was obtained instead. The BF CB and BF BP cases demonstrate that the number of intact tension flanges (and thus the number of connections with higher moment capacity) is more important that their spatial distribution for this frame geometry.

There were small but statistically significant (above the global error estimates for the tests) differences in the displacement response for ductile and brittle fracture for the 1.2 second cosine pulse and the JNF01 ground motion. Differences were not significant for the 0.6 second cosine pulse, as discussed in Section 4.4.3.

Comparisons with the ductile baseline case show that fracture causes increased maximum and residual displacements, loss of base shear capacity, and negative post-fracture tangent stiffness, both locally in the connection moment-rotation hysteresis and globally in the base shear-interstory drift hysteresis. The increase over the ductile baseline case in residual displacements is generally larger than the increase in maximum displacements. The severity of the effects of fracture are largely dependent on the number and spatial distribution of fractures. Fractures which caused the loss of full moment capacity in a particular response direction in 50% or less of the connections did not lead to collapse for the excitations studied. Loss of full moment capacity in a particular direction in 100% of the connections caused collapse for the pulse excitations.

A similar observation can be made for deformation softening, where the severity of the effects depend on the number of connections with negative post-yield stiffness. In the cases where deformation softening occurred in the first story only, collapse did not occur. If deformation softening occurred in all the connections; however, collapse occurred for both pulse excitations.

Deformation softening also has other effects on global behavior which are similar to fracture. These effects include increased maximum and residual drift and loss of global strength capacity. Fracture and deformation softening both reduce the base shear significantly when compared to the ductile baseline case. Interestingly, both fracture and deformation softening tend to reduce the base shear to about the same final value and the slopes of the post-degradation curves are similar. The effects of deformation softening are more severe than those of fracture in some cases, but less severe in others. More study is needed to determine why this is the case.

Fracture effects are also dependent on excitation amplitude. For large-amplitude pulses, the excitation continues to place large demands on the structure after fracture, driving it far into the inelastic range. A small-amplitude excitation may cause fracture, but will not continue to drive the structure in the inelastic range, limiting the permanent deformation. Most of the residual displacement in these tests was due to post-fracture plastic deformation rather than the fractures themselves.

6.3.2 Ground Motion Excitations

No collapses occurred for any of the patterns for either ground motion excitation. For the fracture patterns, this can be attributed to the fact that only the bottom flanges were allowed to fracture, and therefore two intact tension flanges were present at all times to resist the earthquake forces.

Displacement behavior of the fracturing cases, particularly residual displacements, appears to be sensitive to ground motion characteristics and possibly fracture timing with respect to those characteristics. For instance, the approximately 1.2 second pulse in the JNF01 motion had considerably less effect on the brittle fracture CB case than the 1.2 second cosine pulse. Therefore, the effects of pulses within motions may depend on the how the location of the pulse within the time history relates to the timing of fractures. The location of the structure on a local ascending branch (Figure 4-6) may also affect the response, since it is possible that some of these branches could define a local energy-preserved or short-period region. This is certainly not the case for all such branches, since the structure is located at the base of a local ascending branch for both ground motions, and displacements are preserved for the JNF01 motion but not for the JSE17 motion.

For the deformation softening pattern, the hysteretic loops were very pinched in addition to having negative post-yield stiffness, and this pinching behavior, rather than the negative post-yield stiffness, governed the response for the ground motion. Therefore, the test did not provide much useful information on the effects of negative post-yield stiffness for a ground motion record, and it was not possible to make comparisons with other hysteretic types.

The behavior of the strength-degrading pattern was very similar to that of the ductile base-line pattern, with greater period elongation and base shear degradation.

7 Analytical Model Development

This chapter describes the development and assessment of an analytical model that will be used in subsequent numerical simulations of dynamic response. The focus of the model development effort will be models for nonlinear dynamic analysis. As a first step in the model development process, modeling and analytical procedure options are discussed. By using a selection of these options, several trial models with varying degrees of complexity are proposed. These models are then used to reproduce data collected in several tests. The ability of these models to faithfully reproduce the data is then discussed, and a final model is chosen for use in further studies.

The priority of this chapter is to determine the model features needed to capture the specimen's system behavior as described by several response quantities of interest.

7.1 DESCRIPTION OF MODELING AND ANALYSIS OPTIONS

In this section, various available options for modeling and analysis are described in Sections 7.1.1 and 7.1.2, respectively. After review of the available options, selections are made for use in the trial models, which are discussed in Section 7.1.3.

In most analytical studies, there are trade-offs between accuracy and model complexity. Engineering judgment is used to determine a "reasonable" model, one sufficiently complex to capture the properties needed for acceptably accurate representation of the behavior of interest. For this reason, it is helpful to discuss the behavior of several models of varying levels of complexity, and identify the parameters and features that have a large impact on accuracy, as opposed to the those that have minor or negligible effects. This approach was followed in a number of the analytical studies discussed in Chapter 2, and it is the approach that will be followed here.

Consequently, three levels of model complexity are discussed: a simple two-dimensional model (2D), a moderately complex two-dimensional model, and a more complex three-dimensional (3D) model. It should be noted here that the complex 3D model considered is not a full finite element model. More refined finite element models might be necessary to capture details associated with local fracture-related phenomena. However, these phenomena are not the focus of these studies.

In addition to model complexity, there are also corresponding levels of complexity in the computational algorithms and procedures used to perform the analysis. For nonlinear analysis, there are trade-offs between accuracy and computational cost/algorithm complexity. Where possible (and appropriate), the same algorithms and procedures are used with all models. Because of sudden changes in force and stiffness associated with fracture and the negative post-yield (or post-fracture) stiffness observed in many of the tests, special attention to various aspects of the numerical solution may be needed. For this reason, and to satisfy the goal of using the same procedures for all trial models, some advanced methods are used. This does not present an undue burden, since the use of advanced methods does not necessarily create more work for the analyst [though the same can not be said for the computer!]] if the chosen software has implemented the methods and documented them in such a manner that they are user-friendly.

The advanced methods used are already in place in the chosen analysis software, the Open System for Earthquake Engineering Simulation (OpenSees), an open-source computational framework developed at UC Berkeley (McKenna, 2003). This software provides the analyst with a great degree of flexibility in choosing material models and computational algorithms and procedures, and is much more transparent than many other software packages.

7.1.1 Modeling Options

There are several major structural properties that must be modeled to provide an accurate analysis, including the specimen geometry, mass, damping, member cross-section properties, connection behavior, and geometric nonlinearity. It is also critical to properly model the locations and extent of material nonlinearity in the structure. The major options for modeling the key structural properties for the test specimen are shown below in Table 7-1. Only some of these options will be considered for use in the trial models.

Due to the test specimen's design, the modeling of nonlinearity can be greatly simplified. Since yielding was confined to the coupons within the clevis connection, the remainder of the members can be modeled as elastic. In addition, the confinement of nonlinearity to the small, discrete region of the clevis connections facilitates the use of a lumped plasticity model such as a zero-length rotational spring. A zero-length rotational spring defines the connection hysteretic behavior using a material model that describes the moment-rotation relationship for the connection. This approach is much simpler to implement than more complex options in which the coupons and clevis pieces are modeled individually. Therefore, connection hysteretic behavior will be modeled using zero-length springs. Offsets of the springs from centerline for models with clear-span dimensions are achieved by using rigid links.

Table 7-1. Modeling options for key test specimen structural properties

Property	Option	Description
Mass	Lumped	All mass lumped at nodes
	Lumped + distributed frame	Concrete block mass lumped at nodes, frame mass distributed along members
Mass moments of inertia	Not included	Mass moments of inertia set to zero
	Included	Mass moments of inertia included
Geometry	Centerline dimensions	Discrete member sizes not accounted for
	Clear-span dimensions	Column size, clevis attachment and end plates included
	Clear span w/panel zones	Column size included; panel zones modeled
Connection hysteretic behavior	Simple rotational spring	Nonlinear zero-length rotational spring with simple material models such as bilinear
	Realistic rotational spring	Nonlinear zero-length rotational spring with more complex material models such as a general hysteretic model or several materials in parallel or series
	Clevis connection modeled explicitly	Clevis modeled with elastic elements, coupons modeled with distributed plasticity elements
Damping	Rayleigh equivalent viscous	Equivalent viscous damping using Rayleigh's approach
Beam members	Elastic beam-column	Elastic beam-column elements with appropriate area, moment of inertia, and modulus of elasticity

Table 7-2. — *Continued*

Property	Option	Description
Truss members (needed only for 3D model)	Elastic truss	Elastic truss elements with appropriate area and modulus of elasticity
	Corotational truss	Truss elements formulated for use with corotational geometric transformation

Since the zero-length spring is the most promising modeling scheme for the connections, and there are many different types of material models that can be employed to model the different connection hysteretic behaviors, a separate discussion of these options is necessary. Five different hysteretic model types are being considered in this study, and the material model requirements for each type vary widely. The material models which are available in the OpenSees framework are shown for each hysteretic type in Table 7-2 below. The reader is referred to the OpenSees Command Language Manual (Mazzoni et al., 2003) for details.

Table 7-2. Material modeling options in OpenSees for zero-length rotational springs

Hysteretic Type	OpenSEES Material(s)	Description
Ductile Baseline	ElasticPP	Elastic-perfectly-plastic model
	Hysteretic	Modified Clough-type bilinear model
	Steel02	Minegatto-Pinto type model with Bauschinger effects
Brittle Fracture	ElasticPP in parallel with Elastic with strain limit	Contribution of Elastic w/strain limit material vanishes at fracture strain, leaving EPP
	Hysteretic	Modified Clough-type trilinear model with residual strength, negative branches
Ductile Facture	Same as brittle fracture	
Deformation Softening	Hysteretic	Modified Clough-type trilinear model with residual strength, pinching, negative branches
Strength Degrading	Hardening	Bilinear model with isotropic and kinematic hardening (or softening)
	Steel02	Minegatto-Pinto type model with Bauschinger effects and isotropic strain hardening (or softening)

Table 7-2. — *Continued*

Hysteretic Type	OpenSEES Material(s)	Description
Coupon slip (applies to all hysteretic types)	Hysteretic	Use of pinching parameters
	Two ElasticPPGap materials in parallel with an Elastic material, and this combination in series with material model for hysteretic type	Two elastic-perfectly-plastic gap materials (one for positive gap, one for negative gap) in parallel with an elastic material (to remove the zero slope) placed in series with the material model that represents the characteristics of the particular hysteretic type

The zero-length springs model elastic behavior, inelastic behavior, and slip. Elastic behavior is modeled in the zero-length spring as well as the beam because the goal is to accurately represent the behavior of clevis connection, which has a finite length, using the zero-length spring. The elastic contribution from the clevis connection is significant, since it is roughly half as stiff as the beam even though it has the same moment capacity.

In order to properly configure the zero-length springs, it is important to determine the relative contributions to the elastic rotation from the beam and clevis connection. To avoid "double counting" contributions to the member flexibility in the analytical model, only the elastic contribution from the clevis connection itself was included in the moment-rotation relation of the zero-length springs. The elastic contribution from the beam was removed from the moment-rotation relation used for the spring.

This was done empirically by determining how much elastic rotation needed to be incorporated into the clevis connections to match the total elastic end rotation measured during the selected test cases. The empirical selection of elastic stiffness was then checked by comparison with simple structural analysis theory and the clevis connection quasi-static test results (see Section 3.2.4). In most cases, the results were close. However, for the fracture cases, it was difficult to determine the precise rotation at fracture due to the sparseness of the data in the neighborhood of the fracture, so a larger difference between observed and theoretical elastic clevis rotation was permitted.

7.1.2 Analytical Procedure Options

There are a number of computational algorithms and analytical methods available for the different tasks performed during a nonlinear dynamic analysis. Only those algorithms and methods which are appropriate for the problem at hand *and* which have been implemented in OpenSees are discussed in this section. These options are presented in summary form in Table 7-3 below. Procedures used in the analysis of the trial models are chosen from this set of options. References are included for procedures that are not commonly implemented in structural analysis software. Additional information on all procedures can be found in the OpenSEES command language manual (Mazzoni et al., 2003).

Table 7-3. Applicable OpenSees analysis procedure options

Procedure	OpenSees Option	Description
Geometric transformation	Linear	Linear transformation (small displacement assumptions)
	PDelta	Linear transformation w/2nd order P-Δ effects
	Corotational	Exact transformation using the corotational formulation
Numerical integration	Newmark	Newmark's method with $\gamma = 0.5$, $\beta = 0.25$ (Average acceleration method)
	HHT	Hilbert-Hughes-Taylor method
Nonlinear solution algorithm	Newton	Standard Newton-Raphson algorithm
	KrylovNewton	Newton-Raphson algorithm with Krylov subspace acceleration (Scott and Fenves, 2003)
System of equations solver	SparseGeneral	Solves a general sparse system of equations using the SuperLU solver
	UmfPack	Solves a general sparse system of equations using the UMFPACK solver
Constraint handler	Penalty	Penalty method used to apply multipoint constraints
	Lagrange	Lagrange multipliers used to apply multipoint constraints

In many of the test cases, the specimen was subjected to displacements large enough to invalidate the small displacement assumption on which the standard linear geometric transformation is based. In these cases, geometric nonlinearity becomes very important, and the full nonlinear geometric theory implemented using the corotational formulation gives the most accurate results. However, in the cases where the simple 2D model is used, a linear transformation that includes second-order P-Δ effects is employed, since it is much more appropriate given the degree of accuracy of the model. In cases such as the wave propagation test sequence where displacements are relatively small, the linear transformation is adequate.

The numerical integration schemes available are the standard Newmark and Hilbert-Hughes-Taylor methods, both of which employ Rayleigh equivalent viscous damping. The solution algorithms available are the standard Newton-Raphson algorithm (with options available for no updating or reduced updating of the tangent stiffness matrix) and a new modification of this algorithm to incorporate Krylov subspace acceleration to improve convergence (Scott and Fenves, 2003). The latter algorithm is particularly useful in cases where the stiffness matrix is changing rapidly, such as when fracture occurs.

The appropriate constraint handlers are based on the standard penalty method and Lagrange multipliers. If Lagrange multipliers are used to handle constraints, it is necessary to use a sparse general solver for the system of equations, since zeros are placed on the diagonal and the stiffness matrix is no longer symmetric positive definite. Two sparse general solvers are available in OpenSees — the SuperLU and UMFPACK solvers. The reader is referred to the command language manual (Mazzoni et al., 2003) for discussion of all other procedures.

7.1.3 Selected Analytical Models

In the previous sections, the options for both the modeling and numerical analysis of the specimen were discussed. Based on both theoretical considerations and preliminary analyses, three models have been chosen for comparison and assessment with test data. Appropriate analytical procedures and algorithms have been paired with the models based on their complexity, with the goal of using the same procedures with all models where appropriate. The selected modeling and analytical procedure options for the trial models are shown below in Table 7-4.

Table 7-4. Parameters for chosen analytical models

Parameter	Model 1	Model 2	Model 3
Mass	Lumped at nodes	Lumped at nodes	Lumped at nodes
Mass moments of inertia	Not included	Included	Included
Model dimension	2D	2D	3D
Geometric dimensions	Centerline	Clear span	Clear span w/scissors type panel zone model
Frame elements	ElasticBeamColumn	ElasticBeamColumn	ElasticBeamColumn
Truss elements	N/A	N/A	Corotational Truss
Clevis connection models	Zero-length rotational springs	Zero-length rotational springs	Zero-length rotational springs
Ductile baseline (DB) hysteretic model	ElasticPP	Steel02 in series w/ElasticPPGap and Elastic	Steel02 in series w/ElasticPPGap and Elastic
Brittle fracture (BF) hysteretic model	Hysteretic w/negative post-yield stiffness	Hysteretic w/negative post-yield stiffness	Hysteretic w/negative post-yield stiffness
Deformation softening (DFS) hysteretic model	Hysteretic w/pinching	Hysteretic w/pinching	Hysteretic w/pinching
Strength degrading (SD) hysteretic model	Hardening	Steel02 w/strain hardening in series w/ElasticPPGap and Elastic	Steel02 w/strain hardening in series w/ElasticPPGap and Elastic
Damping	4% Rayleigh	4% Rayleigh	4% Rayleigh
Geometric transformation	PDelta	Corotational	Corotational
Constraint handler	Lagrange multipliers	Lagrange multipliers	Lagrange multipliers
Numerical integration	Newmark	Newmark	Newmark
Solution algorithm	KrylovNewton	KrylovNewton	KrylovNewton
SOE solver	Umfpack	Umfpack	Umfpack

7.2 ASSESSMENT WITH GLOBAL BEHAVIOR DATA

The results of nonlinear dynamic analyses using the three trial models described in the previous section are compared with test data in this section. Specifically, global behaviors such as interstory drift ratio and base shear are used to evaluate the quality of the results generated by analyses using the trial models. The models are compared to each other and to the data, and the best performing model is selected based on these comparisons.

7.2.1 Case Studies

Some of the representative case studies introduced in Chapter 5 will be utilized to evaluate the analytical models presented in Section 7.1.3. The performance of the analytical models can be most easily and reliably evaluated by using a selected set of key global response quantities, which include both normalized values, time histories, and hysteretic plots. Also examined was the first mode period T_1. Normalized values, which were defined in Section 4.4.2, provide a simple and portable means of comparing the system response. These normalized values are:

- Maximum interstory drift ratio
- Residual interstory drift ratio
- Elongation of first mode period

Time histories are invaluable for determining how well the model reproduces both the linear and nonlinear behavior of the test specimen. In particular, time histories provide information on the model's vibration properties and how well these follow the changes in the specimen's properties over the course of the excitation. Time histories were examined for the following global response quantities:

- Interstory drift ratio
- Base shear

Hysteretic plots serve a similar function to time histories, but contain information on local or global stiffness and nonlinear behavior that is not apparent from a time history. Hysteresis plots were examined for the following quantities:

- Connection moment-rotation
- Base shear-interstory drift ratio

Though all of the previously mentioned response quantities were examined, they were not weighted equally in the assessment. In terms of prioritization, the ability of the model to reproduce the maximum interstory drift ratio of the structure was deemed to be the most important criterion. The elastic vibration properties (evident in the displacement time history) and connection moment-rotation relationship were also very important, as was the maximum value of base shear. If all of these properties were equally well represented by the three trial models (an unlikely proposition), the next criterion used was the overall representation of the system behavior, as measured by the base shear-interstory drift ratio hysteresis. Other properties were used for further evaluation of the quality of the models, but were not critical criteria for model selection.

7.2.1.1 Ductile baseline case

The ductile baseline case used is the 1.2 second cosine pulse excitation, and the experimental results for this case are discussed in Section 5.2.1. Results from analyses using the three trial models are compared with the experimental data in Figures 7-1 through 7-5. Tabulated response quantities for the analyses and experimental data are compared in Table 7-5.

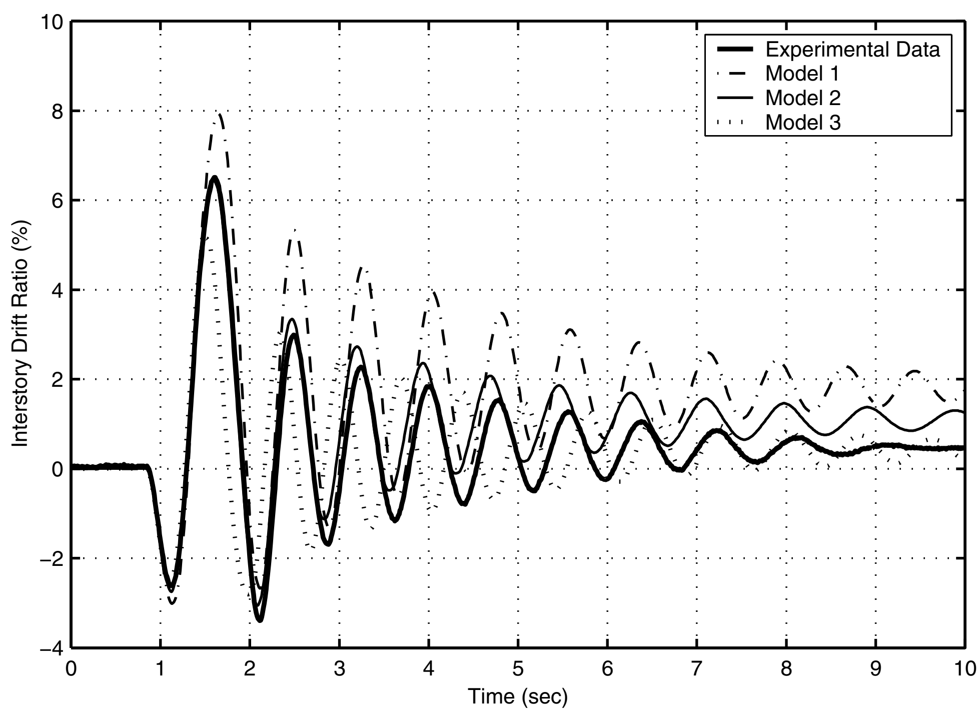

Figure 7-1. Comparison of first-story interstory drift for trial models and DBC test data

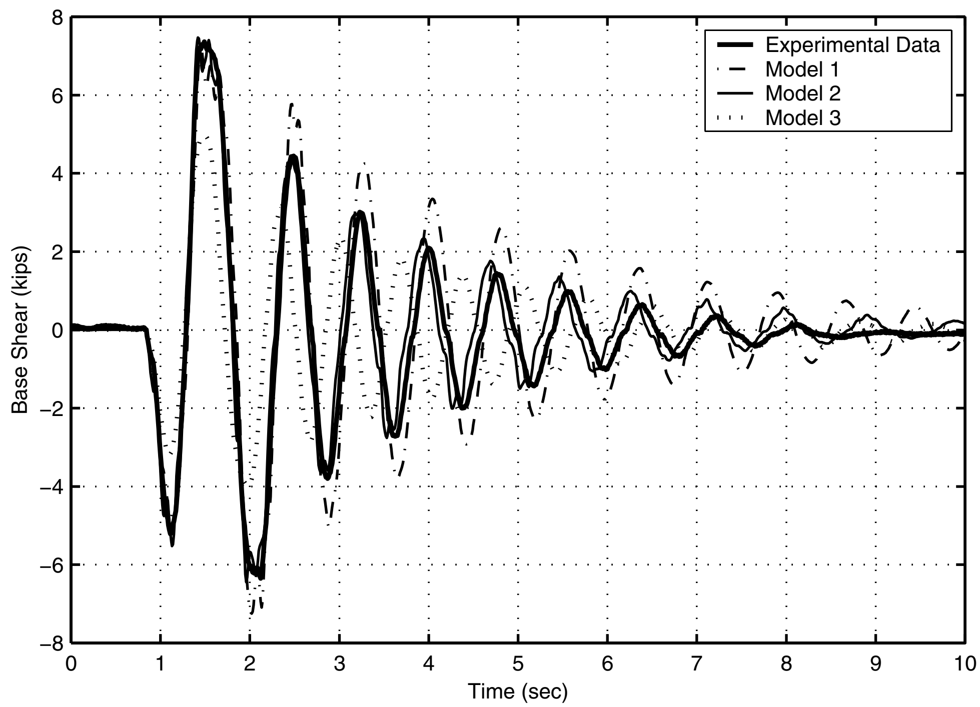

Figure 7-2. Comparison of base shear for trial models and DBC test data

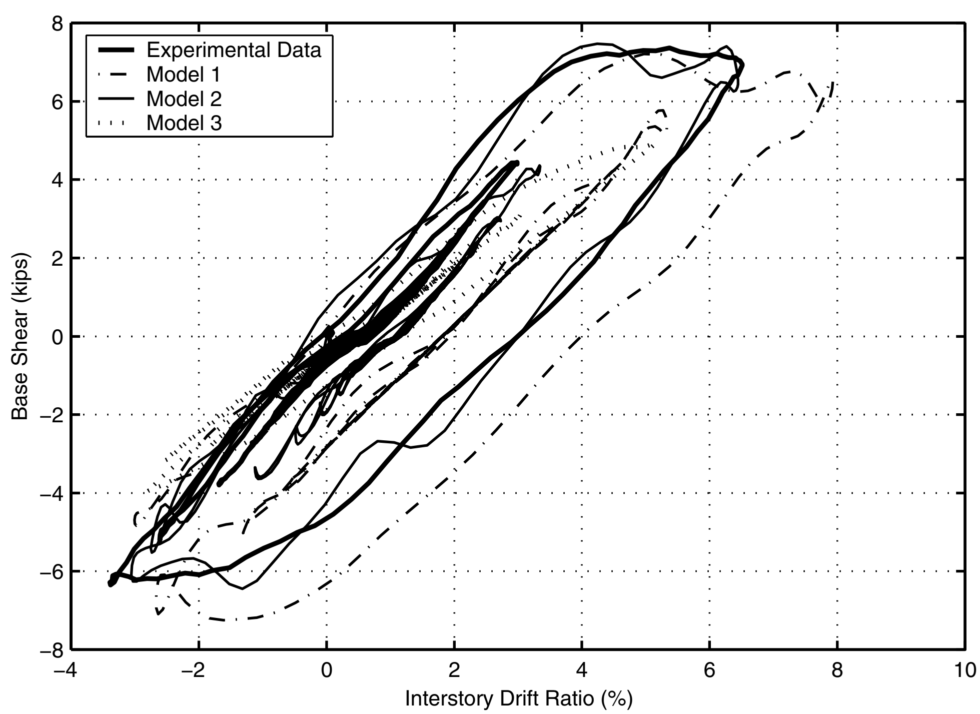

Figure 7-3. Comparison of base shear first-story interstory drift hysteresis for trial models and DBC test data

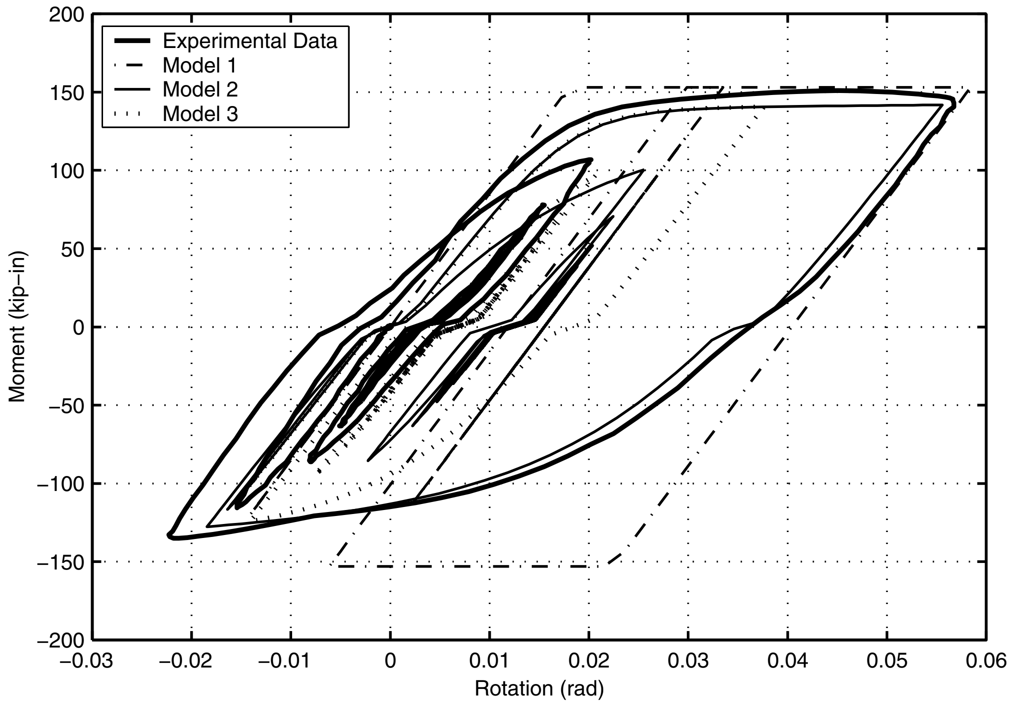

Figure 7-4. Comparison of C2 moment-rotation hysteresis for trial models and DBC test data

Numerical instability in the acceleration values was encountered with Model 3, as shown in Figure 7-5. The model seems to suffer from ringing, and many attempts to remove it from the response by adjusting the damping and other parameters failed.

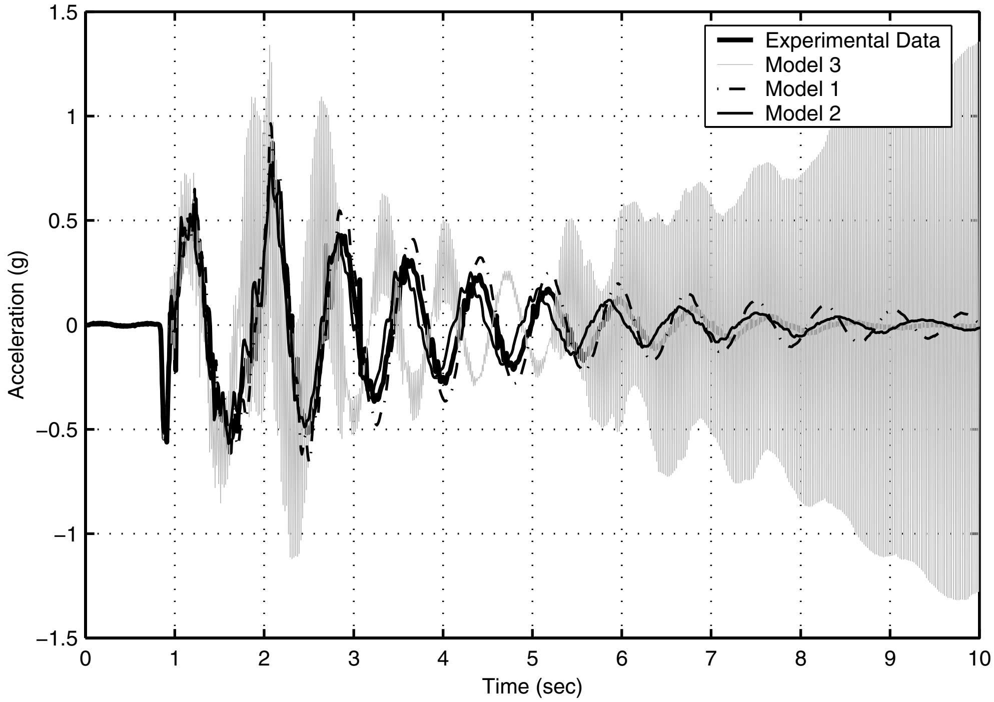

Figure 7-5. Numerical instability in acceleration for trial model 3

Table 7-5. Comparison of first-mode period and percent values of normalized response parameters for trial models and DBC test data

Parameter	Test case data	Model 1	Model 2	Model 3
$\Theta_{1\ \mathrm{Maximum}}$	6.5	7.9	6.4	5.2
$\Theta_{1\ \mathrm{Residual}}$	0.4	2.0	1.2	0.5
λ_{T1}	13	3.3	17*	0.02
T_1 undamaged (sec)	0.65	0.75	0.64*	1.64

* Gap element modeling slip in connections omitted for initial eigenvalue calculation

From the global base shear-interstory drift ratio hysteresis and time histories, Model 1 appears to be too flexible, which leads to excessive drifts. The connection hysteretic model for this case is also very simple, and the residual drifts are too large. Model 2 does a much better job of predicting drifts and forces, but is a bit on the stiff side after the pulse ends, as evidenced by the damaged period in the time history plots. Model 3 does not give improved accuracy in spite of its increased complexity. It is much too stiff and suffers from numerical instability problems in the accelerations. Thus, Model 2 appears to be the best choice for reproducing the behavior of the ductile baseline case.

7.2.1.2 Fracture case

Only one fracture case (the brittle case) is used for the assessment process. In many cases, as explained in Chapter 5, differences in major response quantities between ductile and brittle are not statistically significant. Also, since only a very small amount of plastic rotation was possibly obtained in the tests, it is not useful to try to define a hysteretic model to represent this behavior.

The fracture case used is the brittle fracture BP pattern with the 1.2 second cosine pulse excitation. The experimental results for this case are discussed in Section 5.2.2. Results from analyses using the three trial models are compared with the experimental data in Figures 7-6 through 7-9, and tabulated response quantities are compared in Table 7-6.

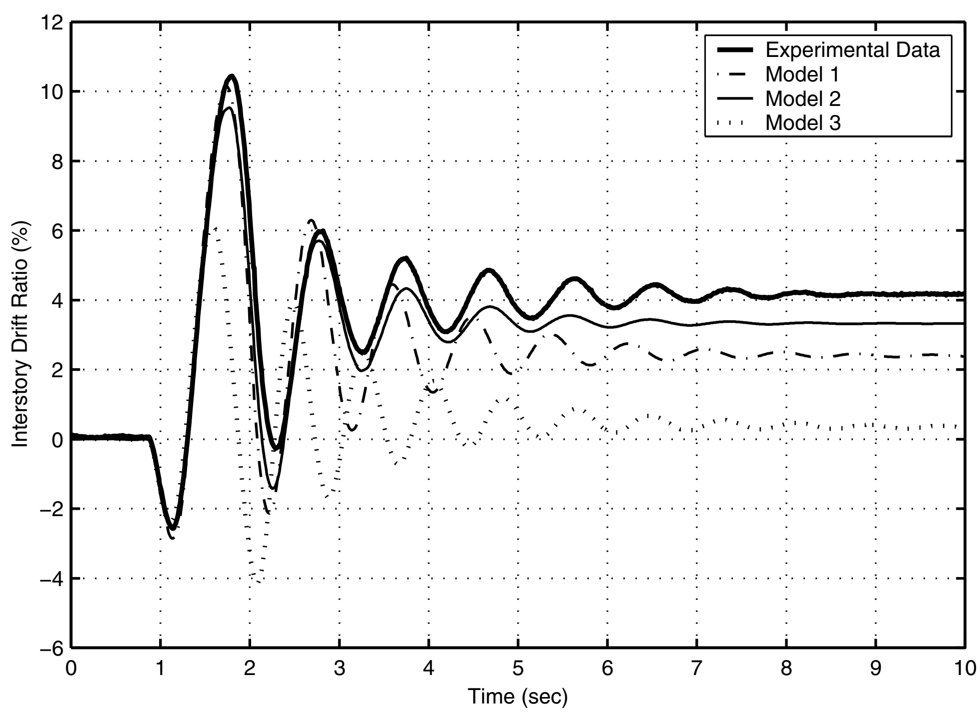

Figure 7-6. Comparison of first-story interstory drift for trial models and BF BP test data

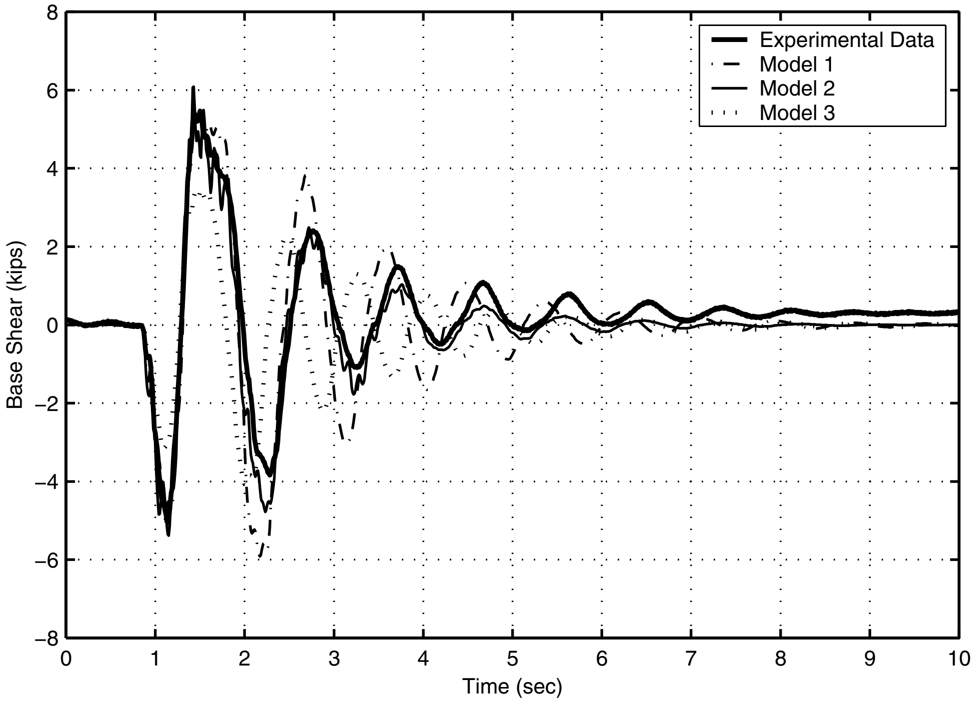

Figure 7-7. Comparison of base shear for trial models and BF BP test data

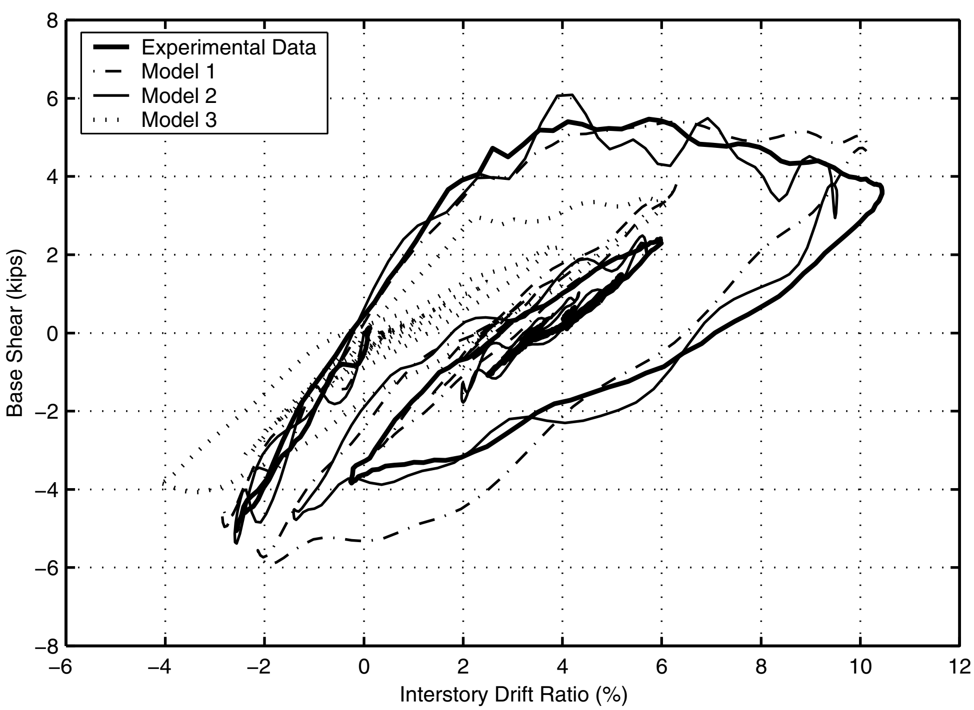

Figure 7-8. Comparison of base shear first-story interstory drift hysteresis for trial models and BF BP test data

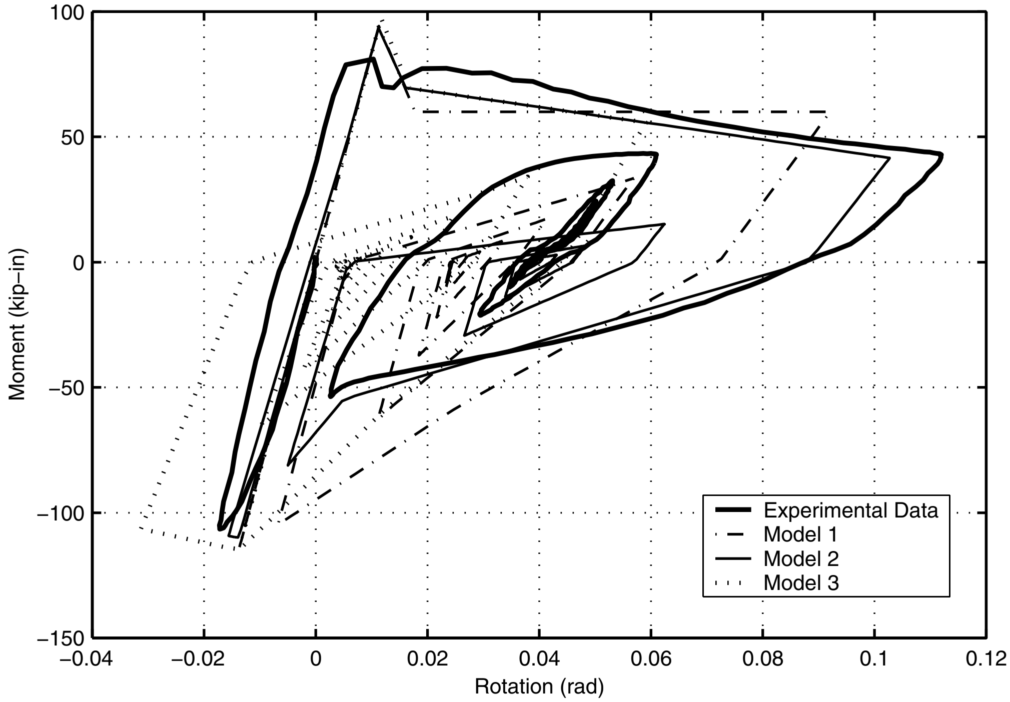

Figure 7-9. Comparison of C2 moment-rotation hysteresis for trial models and BF BP test data

Table 7-6. Comparison of first-mode period and percent values of normalized response parameters for trial models and BF BP test data

Normalized parameter	Test case data	Model 1	Model 2	Model 3
$\Theta_{1\ \text{Maximum}}$	10.4	10.2	9.5	6.1
$\Theta_{1\ \text{Residual}}$	4.1	2.4	3.3	0.4
λ_{T1}	36	35	18	0.01
T_1 undamaged (sec)	0.67	0.75	0.75	1.64

As was the case for the ductile baseline case, Model 2 best reproduces the behavior of the brittle fracture test case, though the reproduction of behavior is not as good. In particular, maximum deformations are underestimated, though the hysteretic model used shows very good agreement with the experimental data during the large displacement excursion. This is a consequence of the model being slightly stiffer than the real specimen. The hysteretic model does not represent the behavior after the large excursion nearly as well, however, leading to differences in the damaged period and residual displacement.

Models 1 and 3 show many of the same shortcomings that were discussed for the ductile baseline case. Also, as shown in Figure 7-9, the constant residual connection moment assumed after fracture for Model 1 causes the rotations to be underestimated because the negative post-fracture stiffness in the test data is not taken into account.

7.2.1.3 Deformation softening case

The deformation softening (negative post-yield stiffness) case used is the DFS B pattern with the 1.2 second cosine pulse excitation. The experimental results for this case are discussed in Section 5.2.4. Results from analyses using the three trial models are compared with the experimental data in Figures 7-10 through 7-13, while tabulated response quantities for the analyses and experimental data are compared in Table 7-7.

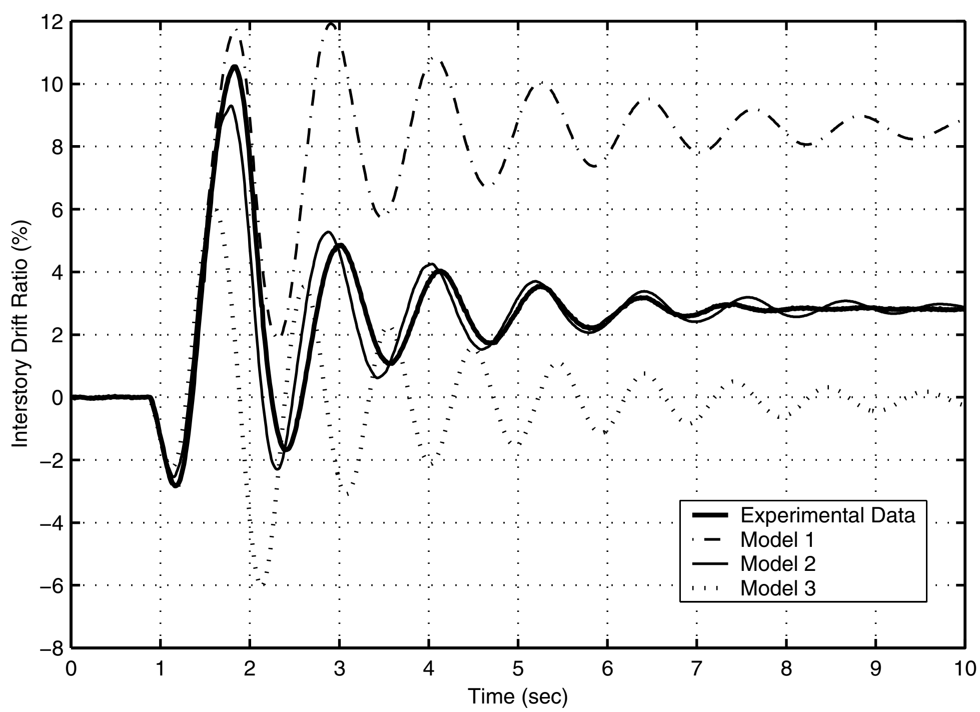

Figure 7-10. Comparison of first-story interstory drift for trial models and DFS B test data

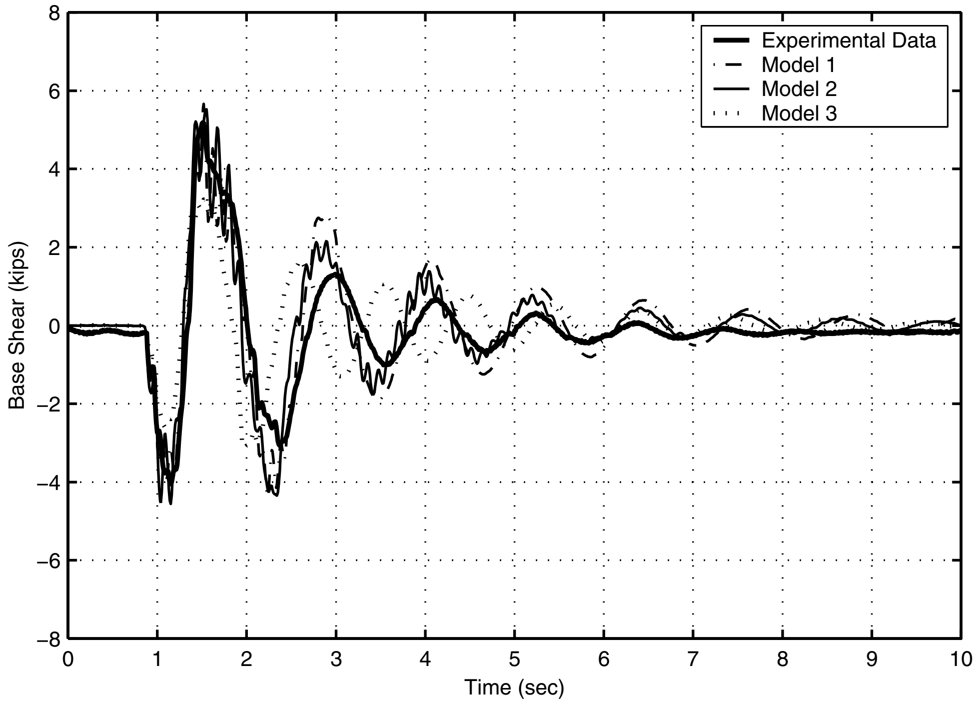

Figure 7-11. Comparison of base shear for trial models and DFS B test data

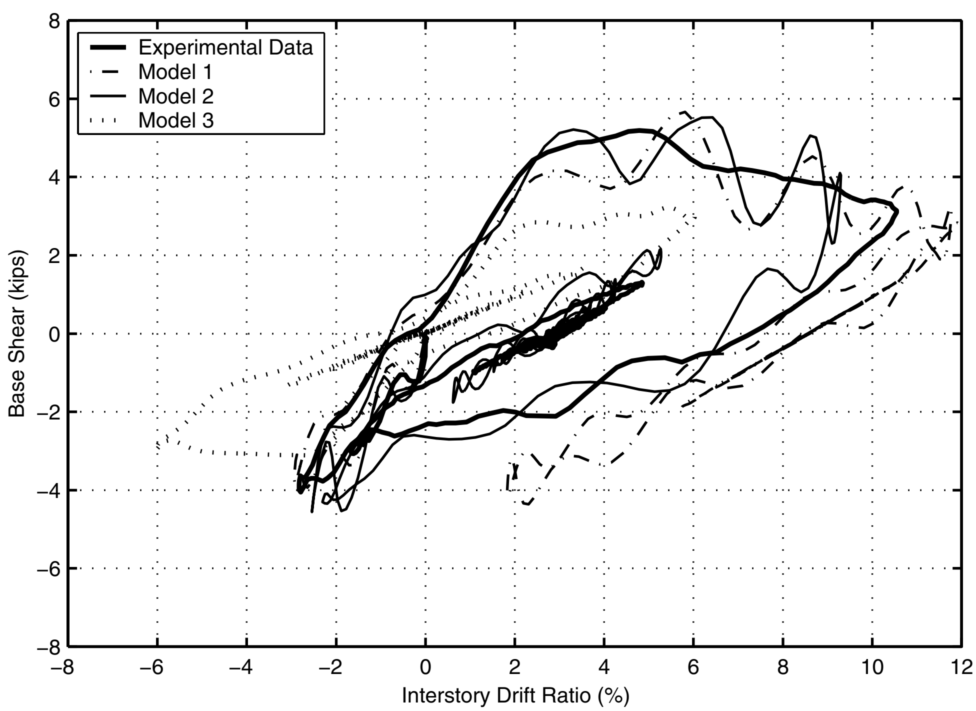

Figure 7-12. Comparison of base shear first-story interstory drift hysteresis for trial models and DFS B test data

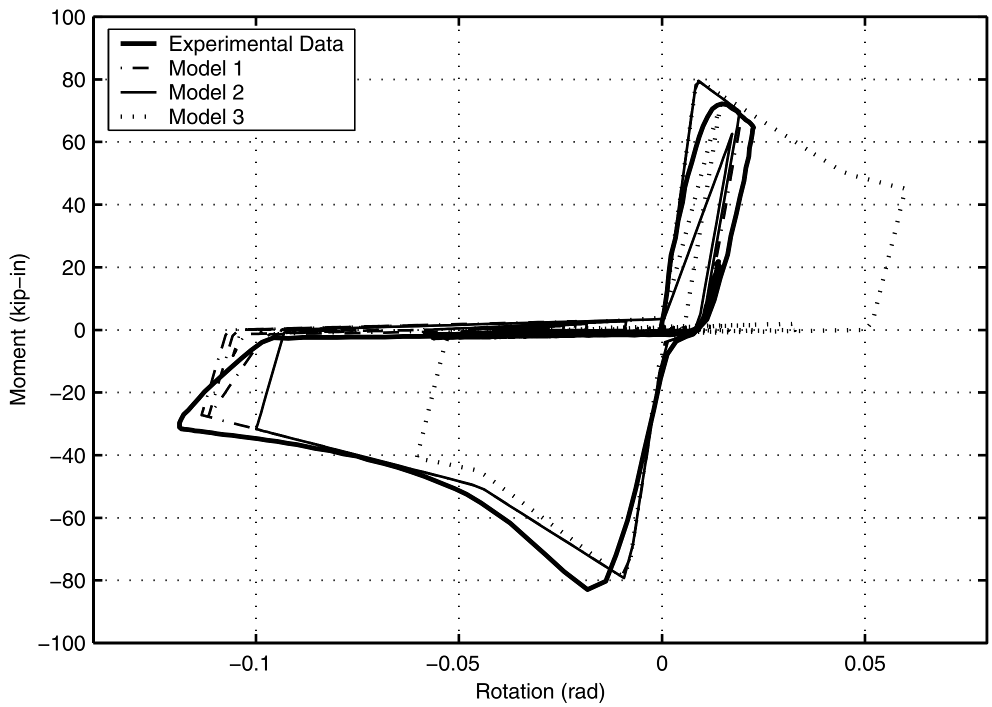

Figure 7-13. Comparison of C2 moment-rotation hysteresis for trial models and DFS B test data

Table 7-7. Comparison of first-mode period and percent values of normalized response parameters for trial models and DFS B test data

Normalized parameter	Test case data	Model 1	Model 2	Model 3
$\Theta_{1\ \mathrm{Maximum}}$	10.5	11.9	9.3	6.1
$\Theta_{1\ \mathrm{Residual}}$	2.8	8.6	2.7	0.1
λ_{T1}	76	61	42	0.0
T_1 undamaged (sec)	0.64	0.73	0.74	1.64

As shown in Figure 7-10, Model 2 is the only model capable of representing the displacement response of the specimen with any accuracy at all. The other cases either grossly overpredict (Model 1) or underpredict (Model 3) the interstory drift response over the entire time history. The maximum interstory drifts are underestimated by Model 2, but the residual drifts are predicted very well. Model 2 also predicts much more high-frequency response (Figure 7-12) than is actually present in the data. However, these shortcomings of Model 2 are relatively minor compared with the major flaws of the other models in the representation of the displacement response.

7.2.1.4 Strength-degrading case

The strength-degrading case used is the only one available — the SDC pattern with the JSE17 excitation. The experimental results for this case are discussed in Section 5.2.5. Results from analyses using the three trial models are compared with the experimental data in Figures 7-14 through 7-21. Since the excitation is lengthy, close-ups of key regions are provided for the time histories. Tabulated response quantities for the analyses and experimental data are compared in Table 7-8.

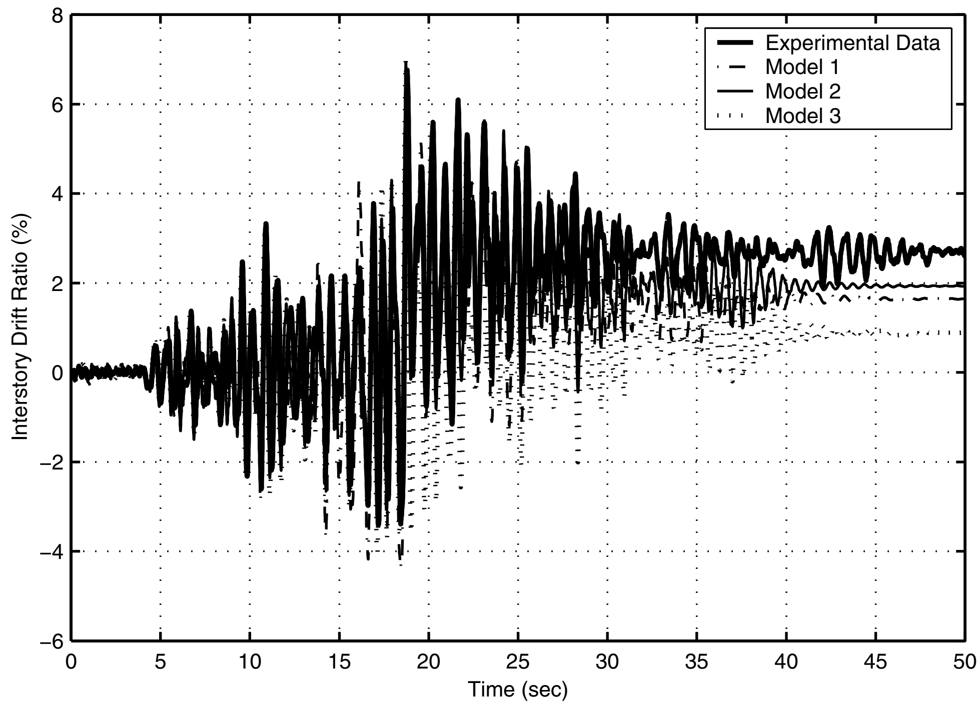

Figure 7-14. Comparison of first-story interstory drift for trial models and SDC test data

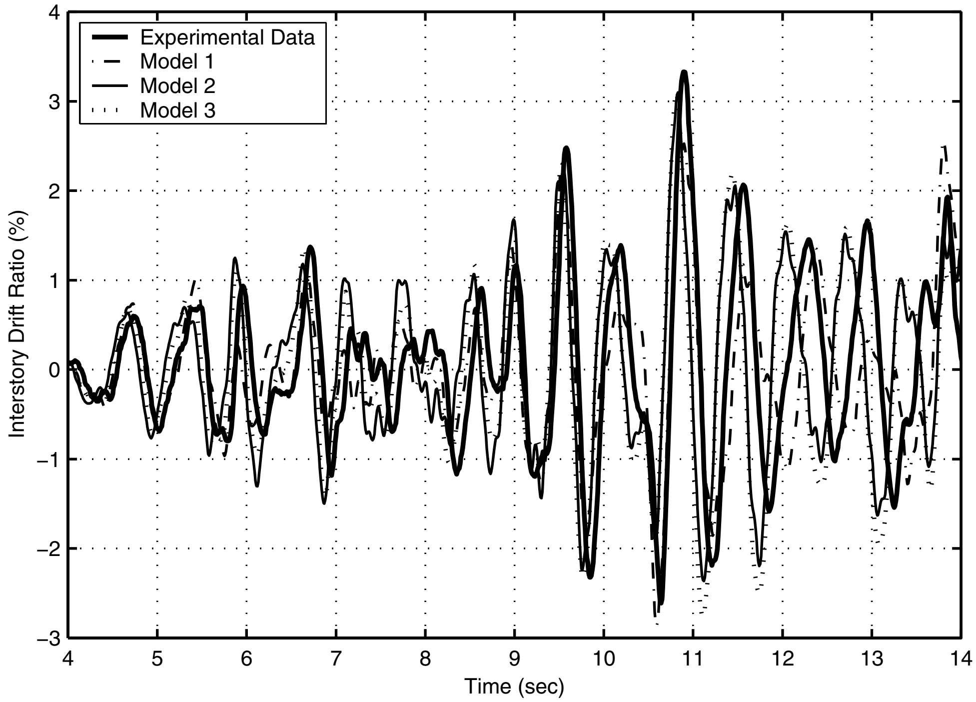

Figure 7-15. Close-up of first-story interstory drift for trial models and test data, 4–14 sec

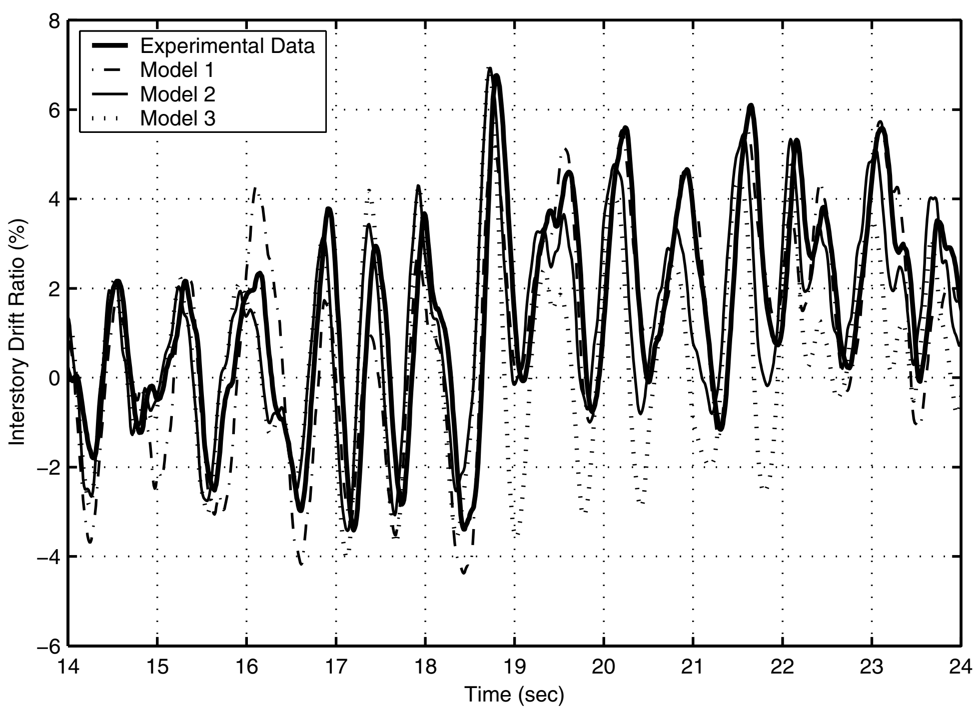

Figure 7-16. Close-up of first-story interstory drift for trial models and test data, 14–24 sec

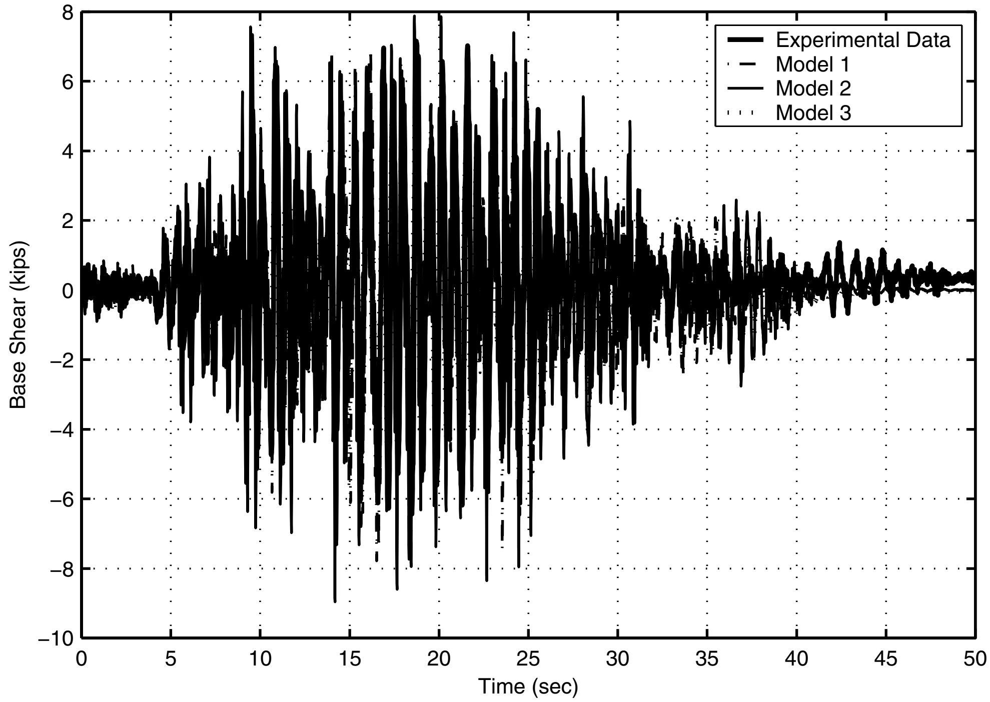

Figure 7-17. Comparison of base shear for trial models and SDC test data

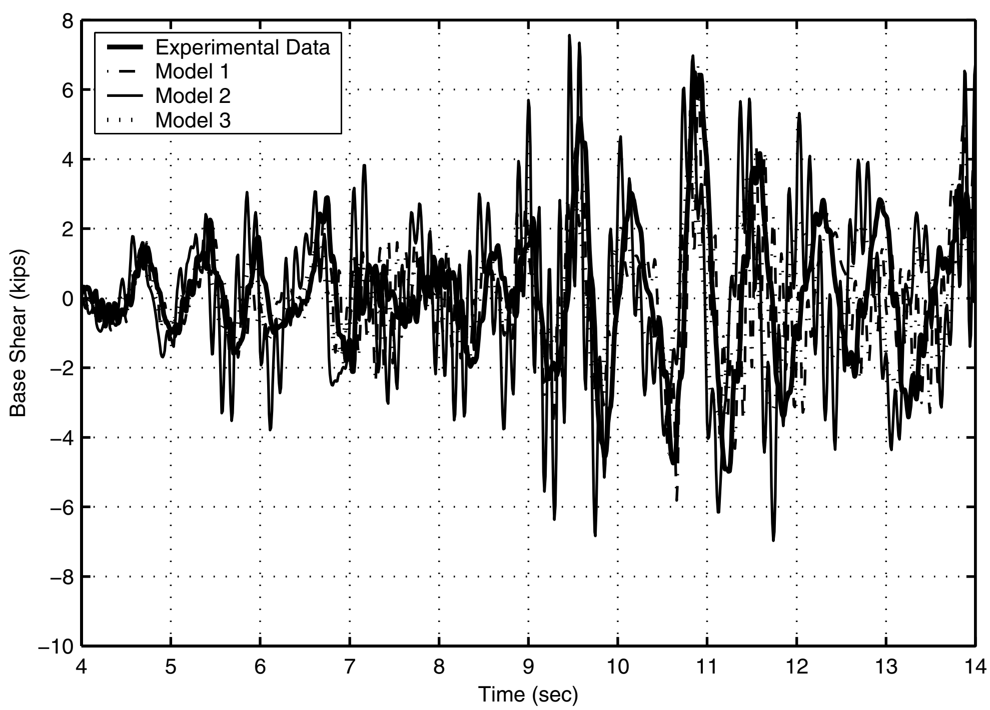

Figure 7-18. Close-up of base shear for trial models and SDC test data

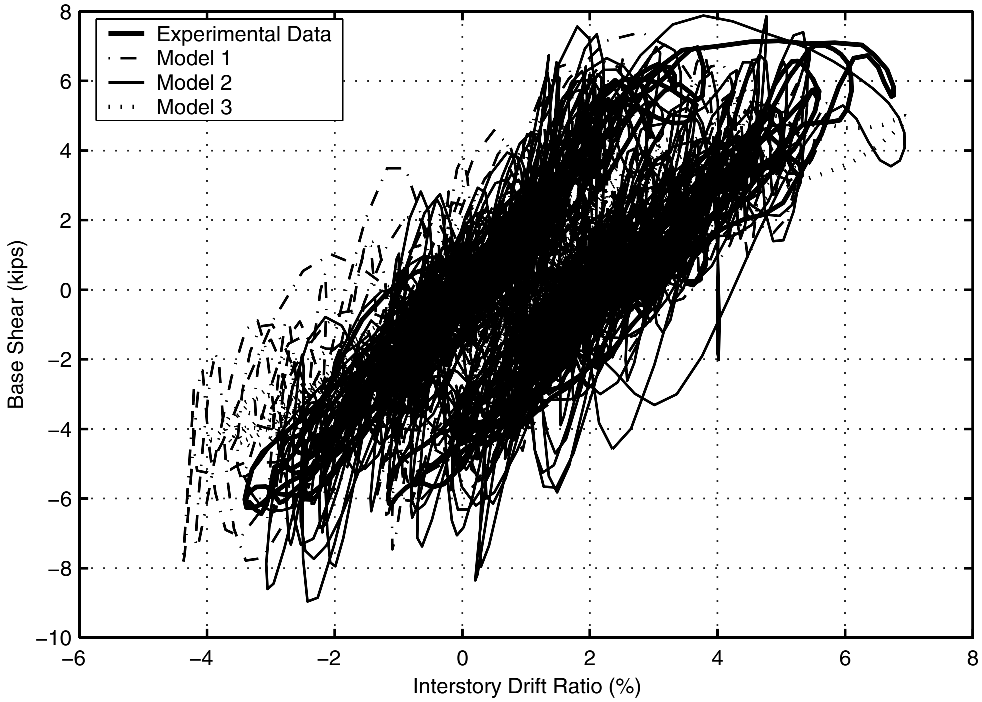

Figure 7-19. Comparison of base shear first-story interstory drift hysteresis for trial models and SDC test data

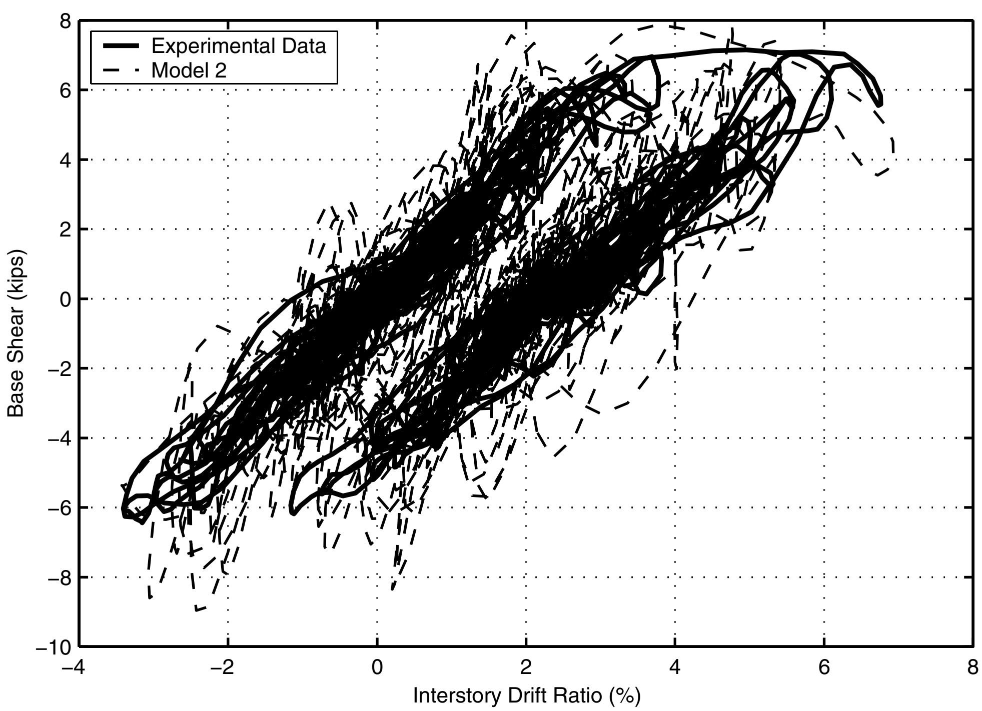

Figure 7-20. Comparison of base shear first-story interstory drift hysteresis for Model 2 and SDC test data

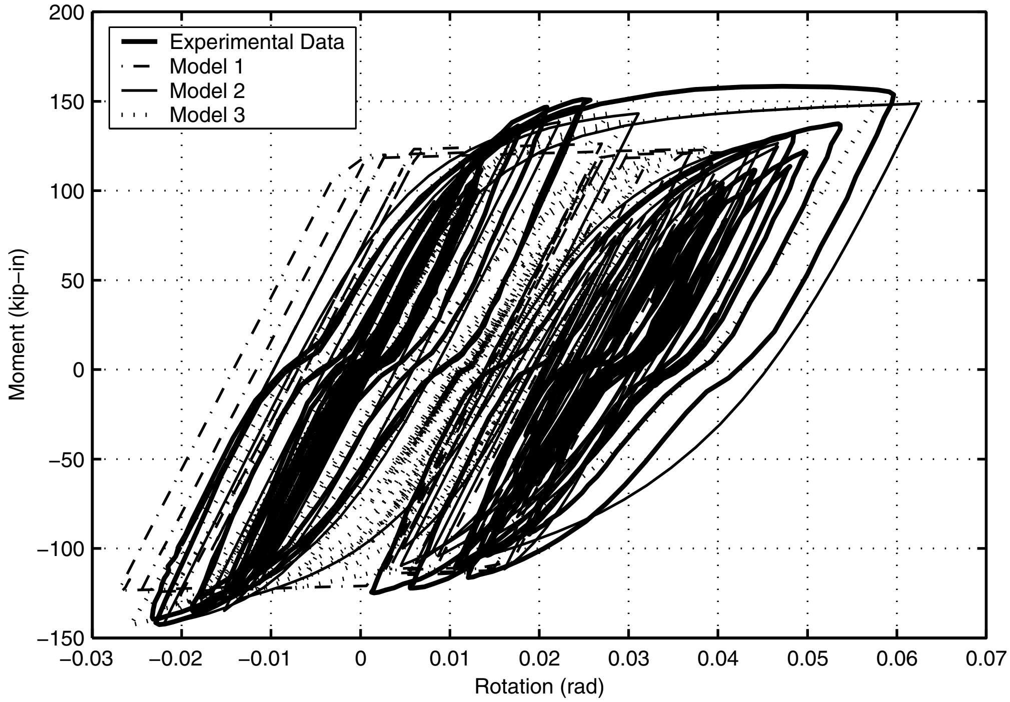

Figure 7-21. Comparison of C2 moment-rotation hysteresis for trial models and test data

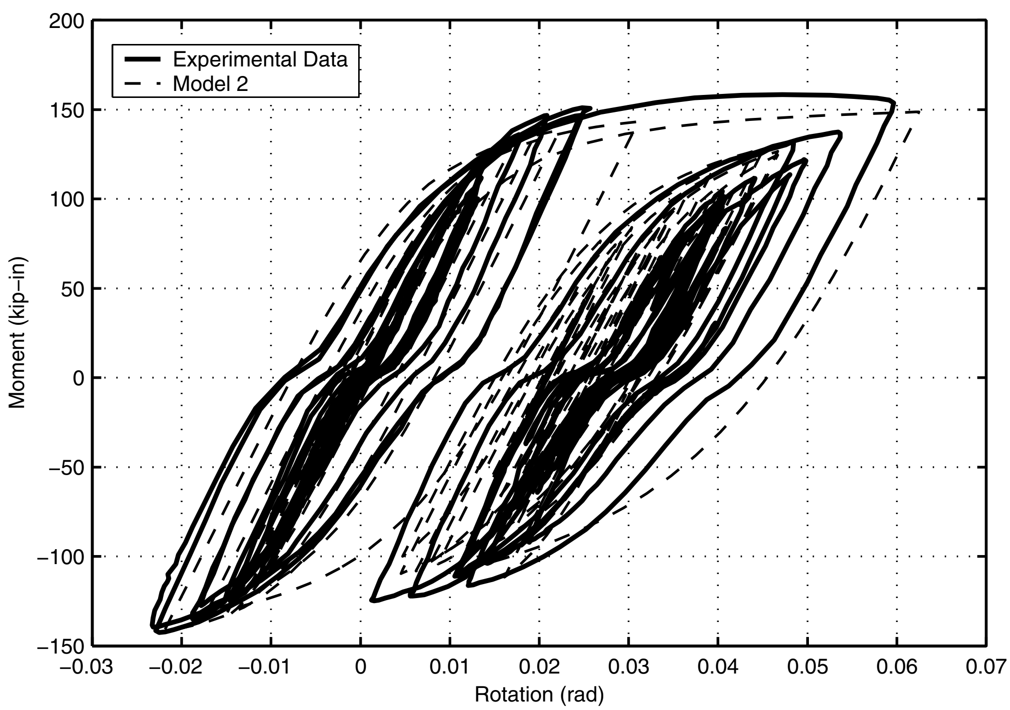

Figure 7-22. Comparison of C2 moment-rotation hysteresis for Model 2 and test data

Table 7-8. Comparison of first-mode period and percent values of normalized response parameters for trial models and SDC test case data

Normalized parameter	Test case data	Model 1	Model 2	Model 3
$\Theta_{1\ \text{Maximum}}$	6.8	5.7	6.9	7.0
$\Theta_{1\ \text{Residual}}$	2.7	1.6	1.9	0.9
λ_{T1}	36	3.1	2.3	0.1
T_1 undamaged (sec)	0.64	0.73	0.63	1.64

The strength-degrading case uses the same hysteretic model as the ductile baseline case, but with strain hardening (or softening, in this case) turned on. Similar issues are therefore expected when the trial models are compared to the experimental data, and this is what in fact happens. Maximum displacements/drifts and base shear are predicted well, while the residual displacements are underestimated by all models, with Model 3 being the worst. Overall, Model 2 shows the best agreement for this case.

7.2.1.5 Selected model based on global behavior

As shown in the comparisons of the trial models with the case studies, Model 2 is best able to reproduce the data. Model 1 is too simple and too flexible, and its accuracy suffers from not accounting for clear-span dimensions and realistic ductile connection behavior. On the other hand, Model 3 is overly complex and too stiff, which causes it to grossly underestimate drifts. In this case, a more complicated model does not lead to greater accuracy.

Thus, Model 2 is chosen for use in further studies.

7.3 SENSITIVITY TO MODEL PARAMETERS

During the course of the model assessment, sensitivity to various modeling and analysis parameters was examined as well. Several parameters were found to have significant sensitivities, and these will be discussed individually here.

7.3.1 Specimen Dimensions

The response of the specimen was determined to be quite sensitive to whether clear-span or centerline dimensions were used. The use of clear-span dimensions stiffens the structure significantly, and is the major reason for the difference in stiffness between Models 1 and 2. As is evident from the comparisons with data in previous sections, the stiffer Model 2 better reproduces the test results. Thus, the use of clear-span dimensions was found to be important for a correct representation of structure stiffness (and therefore dynamic properties), which was also a key finding of the analytical studies discussed in Section 2.3.6.

7.3.2 Mass and Mass Moment of Inertia

Inclusion of the correct total mass is of course critical for the correct determination of the structure's fundamental period, as well as for the determination of forces. In addition to the total mass, it was determined that the inclusion of mass moments of inertia was important for correctly reproducing the maximum displacement response. Displacements tend to be underpredicted to a much greater degree by Model 2 if the mass moments of inertia are not included.

7.3.3 Column Section Properties

Since the columns make a large contribution to the stiffness of the entire frame, the vibration properties of structure are sensitive to moderate changes in column stiffness. This sensitivity is not particularly pronounced for maximum displacements, since a great deal of the deformation is due to material nonlinearity, which is not affected by the section properties of the columns, which remain elastic. The column stiffness has a much greater effect on the fundamental period of the system.

7.3.4 Post-Yield and Post-Fracture Stiffness

It was determined that use of the correct post-yield or post-fracture stiffness was important for determining the maximum response in cases with large pulse excitations. In the fracturing and deformation softening cases, maximum and residual drifts could be significantly underestimated if negative post-yield or post-fracture stiffness was not included in the model. In addition, the degradation in system strength is not correctly modeled if the negative stiffness is not included. This becomes particularly important in the short- and intermediate-period ranges, where decreases in strength lead to increases in displacement.

7.3.5 Connection Unloading and Reloading Stiffness

The connection unloading and reloading stiffnesses were determined to have fairly large effects on the free vibration response of the structure after a pulse as well as the residual displacements. In particular, the general hysteretic material model (used in the zero-length rotational springs at the connections for the fracture and deformation softening cases) did not correctly represent these stiffnesses. This material model makes Clough-type assumptions (Mazzoni et al., 2003) about kinematic softening which do not represent the behavior observed in the tests. The use of this material model, which matches the moment-rotation envelope very well, leads to large inaccuracies in residual displacements and damaged-state vibration properties.

For the ductile baseline case, the residual displacements were found to be sensitive to the inclusion of Bauschinger-type effects in the connection moment-rotation relation. Models with this behavior were able to much better represent both the hysteretic behavior and the residual displacements.

7.3.6 Connection Slip

The modeling of the pinching that occurred in many connection hystereses as the moments passed through zero was determined to be important for the correct determination of the vibration properties after damage occurs. The damaged period was found to be quite sensitive to this parameter. However, since the damaged period was affected to a much greater degree by the assumptions about stiffness degradation discussed in Section 7.3.5, the effects of the sensitivity to connection slip modeling were minor.

7.3.7 Damping

Rayleigh damping is a convenient method for providing equivalent viscous damping. Since the damping matrix contains mass-proportional and stiffness-proportional portions, a choice as to which stiffness will be used is necessary in nonlinear problems, where the stiffness matrix is changing. If the tangent stiffness is chosen, any changes to the stiffness matrix will affect the damping matrix as well. For certain types of nonlinear problems encountered in this study, changes in the stiffness matrix may be both large and sudden, particularly in the case of fracture. This raises concerns about the time variance of the damping matrix if tangent stiffness-proportional Rayleigh damping is used. It may also be possible to get negative damping values if negative post-yield stiffness is severe. The choice of initial stiffness or tangent stiffness can lead to fairly large differences in the structural response, depending on the amount of change in the stiffness matrix. The sensitivity to the type of stiffness used can best be examined by looking at the test cases described previously, which use the 1.2 second cosine pulse excitation.

For instance, in the ductile baseline case, the structural response is virtually the same for both stiffnesses. In contrast, for the BF BP fracture pattern the response depends on the stiffness used to calculate the Rayleigh damping matrix. The sensitivity to damping is aggravated by the sensitivity to post-fracture stiffness discussed previously. Displacements and connection hysteresis for a hysteretic model with zero post-fracture stiffness are shown in Figures 7-23 and 7-24. Figures 7-25 and 7-26 show the results for a hysteretic model with a negative post-fracture stiffness, which is a better fit for the experimental data.

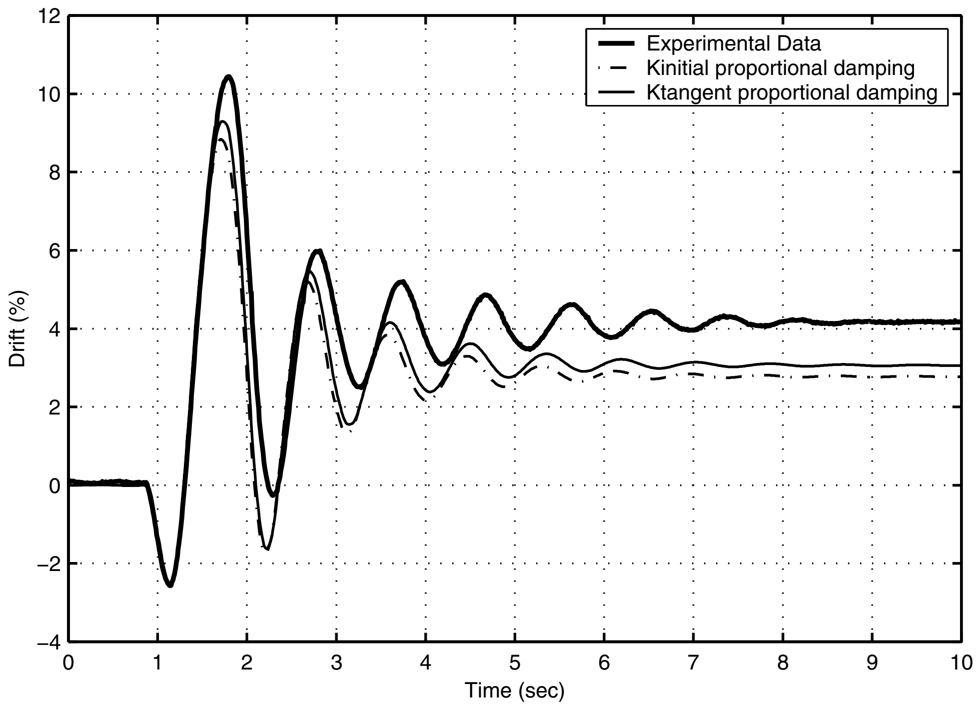

Figure 7-23. Comparison of first-story interstory drifts for hysteretic model with Kpf = 0

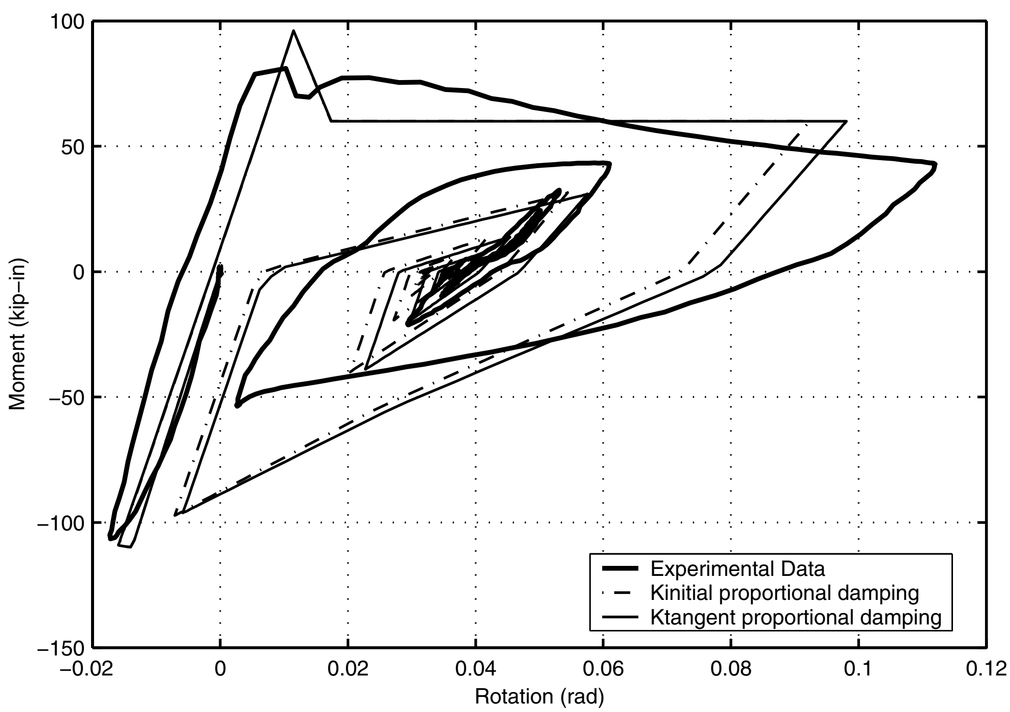

Figure 7-24. Comparison of connection hysteresis for hysteretic model with Kpf = 0

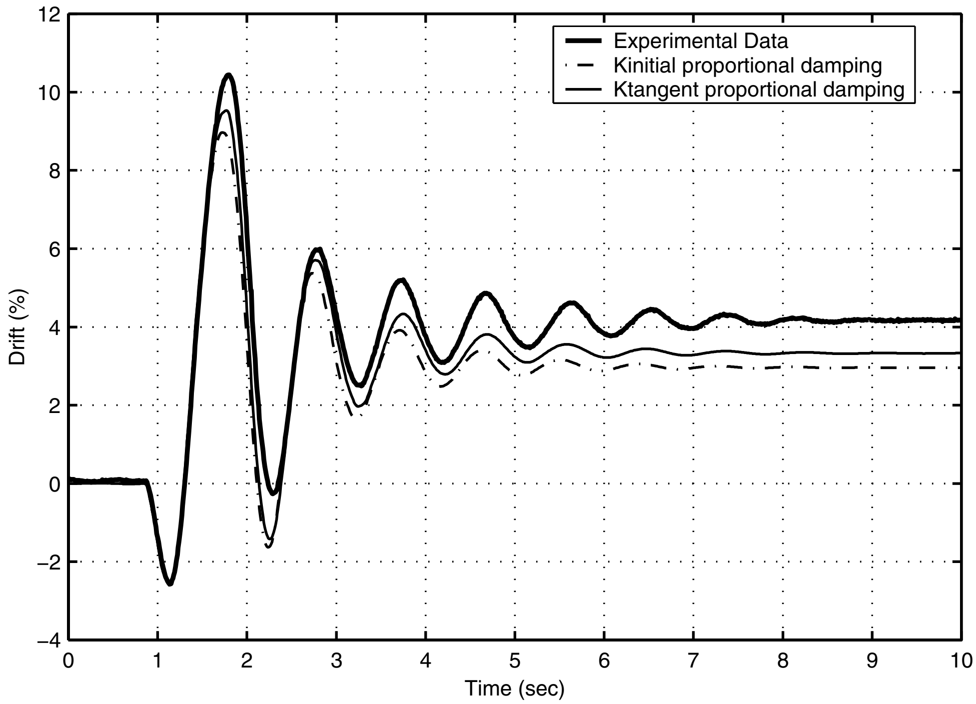

Figure 7-25. Comparison of first-story interstory drifts for hysteretic model with Kpf < 0

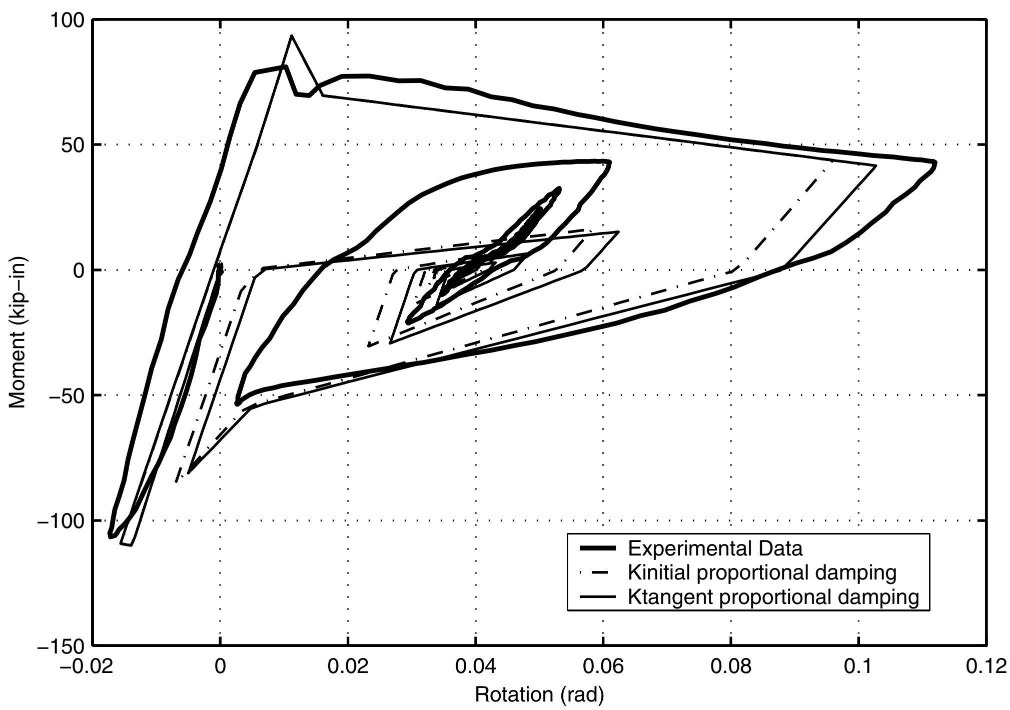

Figure 7-26. Comparison of connection hysteresis for hysteretic model with Kpf < 0

The difference in the displacement time histories caused by the use of different stiffnesses for the damping calculations is exacerbated by the addition of negative post-fracture stiffness to the connection hysteresis. Clearly, for problems where the stiffness matrix changes dramatically, it is important to consider which stiffness is being used in Rayleigh damping calculations, particularly if residual displacement is an important response quantity.

7.4 SUMMARY

Three trial models were assessed using test data from the case studies is Chapter 5. The model which was best able to reproduce the test results was determined for all cases to be Model 2, which is a two-dimensional model of intermediate complexity. The more complex three-dimensional model, Model 3, was found to have no advantages in accuracy, and in fact showed several disadvantages.

As a part of the model development process, critical properties that must be modeled correctly were identified. These include the specimen mass (including mass moments of inertia), geometry, member section properties, material properties, connection hysteretic behavior (strength, stiffnesses and degradation properties), and amount of equivalent viscous damping. In addition, it is very important to include the effects of geometric nonlinearity. Full nonlinear geometry theory is preferable to linearized P-Δ representations if large to collapse level drifts occur.

During the assessment of the trial models, several important sensitivities were observed. The most important of these included specimen dimensions, damping, and several parameters related to connection hysteretic modeling, such as stiffness values in the nonlinear range, Bauschinger effects, and kinematic softening parameters. In particular, the effects of negative post-yield and post-fracture stiffness are important, and should be included in connection hysteretic models if such behavior is anticipated in the connections being modeled.

8 Analytical Studies

This chapter contains the results of an analytical parametric study carried out using the model developed in the previous chapter. The objective of this study is three-fold: to investigate cases of interest which were not tested experimentally, to determine the sensitivity of structural response to hysteretic behavioral characteristics and frame properties, and to determine the response of the specimen to excitations different from those used for the shaking table tests. Model 2, which was presented in the previous chapter, is used for all of the analyses in this chapter. Since a model of the test specimen, which underwent very large drifts without collapse, was used for these analyses, it should not come as a surprise that the drifts reported here are large. Drifts of this magnitude are not expected in actual buildings.

8.1 ANALYTICAL STUDY PLAN

It is helpful for organizational purposes to divide this study into several substudies which are focused on the variation of one major parameter each. These substudies include effects of amplitude on the experimentally tested cases, effects of connection hysteretic properties, (particularly those measuring degradation), effects of frame parameters, and effects of excitation. The results of these substudies are presented in Sections 8.2 through 8.5, respectively. Parameters and analysis methods used in the substudies are defined in Section 8.1.1. Study organizational details are located in Section 8.1.2.

8.1.1 Definitions

Most of the parameters discussed in the remainder of this chapter have been defined previously, so the focus of this section is on those parameters which are being used for the first time. However, references to previously defined terms or quantities are provided in Section 8-1.

Table 8-1. References to previously defined terms and quantities

Term or Quantity	Reference Location	Page
Hysteretic behavior types	Table 3-1, Figure 3-8	42, 44
Tested connection configuration patterns	Figure 4-9	62
Shaking table excitations	Table 4-2	61
SAC Joint Venture ground motion suites	Section 4.1.1, Somerville, 1997	53, 308
Analytical model characteristics	Table 7-4	234

8.1.1.1 Parameters

Pattern CTB, Top and Bottom Flange Fractures

In the interest of time and cost efficiency, patterns where all flanges were fracture-capable were not tested experimentally. However, this pattern is of interest and can easily be examined analytically. This pattern is referred to as CTB, where C indicates all connections in the structure fracture, and TB indicates both the top and bottom flanges fracture. The hysteretic behavior of a connection with both top and bottom flange fractures can be justifiably assumed to be a combination of the response of the top and bottom-flange only combinations, due to the modular nature of the clevis connection design. Analytical studies using these patterns can be used to examine the response of structures with very brittle connections in all locations.

In the case of cosine pulse excitations, it is likely that the behavior will be similar to that seen for the CP patterns. However, in cases where the pulse amplitude is large, the behavior may be significantly different, since fracture will occur in the first negative excursion for CTB patterns, while it cannot occur for CP patterns.

Hysteretic Parameters for Fracturing Connections

In the subsequent analytical studies, brittle fracture and ductile fracture are clearly distinct hysteretic types, and some parameters are applicable for one type of fracture and not the other. Hysteretic parameters for each case are shown in Figures 8-1 and 8-2, respectively.

As fracture occurs, the moment capacity of the connection drops sharply, as shown in Figure 8-1. The post-fracture moment capacity is most easily defined as the ratio of the residual moment capacity M_r to the moment capacity immediately before fracture occurs, M_f. In the case of brittle fracture, the value of M_f used is less than the value of the plastic moment M_p. After fracture occurs and the moment capacity drops to M_r, the slope of the subsequent branch of the hysteretic loop is defined as the post-fracture tangent stiffness K_{pf}. This quantity is expressed in terms of a decimal fraction of the initial elastic stiffness K_i.

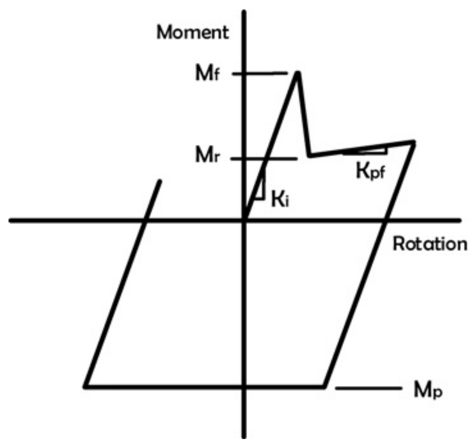

Figure 8-1. Definition of hysteretic parameters for a brittle fracturing connection

For a ductile fracturing connection, the fracture occurs after the plastic moment has been reached. The key parameter for ductile fracturing connections is the amount of plastic rotation θ_p which occurs prior to fracture as shown in Figure 8-2. Also, due to the limitations of the trilinear connection hysteretic model used, only zero post-fracture tangent stiffness is possible for ductile fracture.

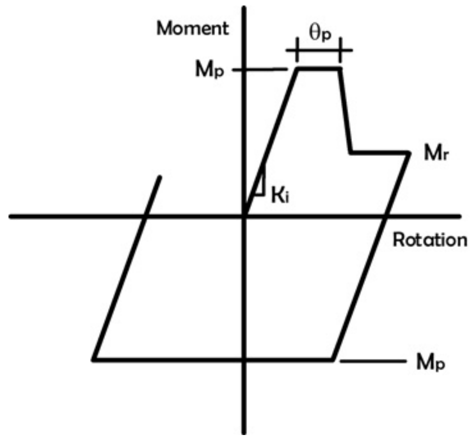

Figure 8-2. Definition of hysteretic parameters for a ductile fracturing connection

8.1.1.2 Analysis procedures

The incremental dynamic analysis (IDA) method was first suggested by Bertero (Bertero, 1977), though it has only recently become feasible to implement due to increases in computing capability. The IDA method has been recently applied in seismic response studies, most notably by Vamvatsikos and Cornell (Vamvatsikos and Cornell, 2002). This method has numerous applications, which vary from the simple investigation of the effects of excitation amplitude to the development of fragility curves for performance-based design. The method consists of a series of nonlinear dynamic analyses of a particular structural model, in which the same excitation is used at increasing amplitudes. The factor used for the amplitude scaling of earthquake excitations is defined as the scalar α, which obeys the relation

$$a_{amplified} = \alpha a_{original}$$

where $a_{amplified}$ is the amplitude-scaled acceleration time hi, and $a_{original}$ is the acceleration time hi in original form. The scale factor α varies linearly from the initial value of the scale factor α_o to the final value of the scale factor α_f in constant increments of $\Delta\alpha$. The first analysis is performed at a very low amplitude of the excitation, and α is increased until some criterion for the collapse of the structure is met. In each analysis, the state of the structure is reset to its original, undamaged state; damage is not cumulative across analyses.

The incremental dynamic analysis (IDA) method was used in this study to examine the effects of excitation amplitude. For a single excitation, the acceleration time hi was simply multiplied by α. In the cases where the SAC suites of ground motion records were used, the simple approach of applying a uniform amplification scale factor to all records in the suite was adopted. The use of a uniform scale factor preserves the variability in amplitude between individual ground motions that was intended by the creators of the suites.

It is important to remember when looking at plots of IDA results for the SAC motions that the abscissa contains the uniform scale factor used for the entire suite of motions, rather than a measure of ground motion amplitude. Because of this, individual ground motions may have different values of intensity measures such as peak ground acceleration. An amplitude scale factor of one indicates that all motions have the same scale as when downloaded from the SAC website.

8.1.2 Study Organization

As previously mentioned, the study discussed in this chapter has been divided into four substudies for organizational purposes. Major parameters and the associated excitation cases are shown in Table 8-2. Connection hysteretic properties examined are listed separately.

Table 8-2. Parametric study matrix

Parameter	Values of Parameter	Shaking Table Excitations	Additional Cosine Pulses	SAC LA 10/50	SAC LA 2/50
Amplitude	All tested DB, BF, DFS, SD patterns	x			
	Ductile fracture BP & CP w/θ_p = 0.01, 0.02 rad	x			

Table 8-2. — *Continued*

Parameter	Values of Parameter	Shaking Table Excitations	Additional Cosine Pulses	SAC LA 10/50	SAC LA 2/50
Excitation	Ductile baseline	x	x	x	x
	Brittle fracture CB w/ Kpf = 0, Mr = 60 and Kpf, Mr = best fit		x	x	
	Brittle fracture CTB w/ Kpf = 0, Mr = 60 and Kpf, Mr = best fit		x	x	x
	Ductile fracture CB w/ θ_p = 0.01, 0.02 rad		x	x	x
	Ductile fracture CTB w/ θ_p = 0.01, 0.02 rad		x		
Post-fracture moment Mr	Mr/Mp = 0.1, 0.2, 0.3, 0.4, 0.5, 0.6, 0.8	x			
Post-fracture tangent stiffness Kpf	Kpf/Ki = -0.07, -0.05, -0.02, 0, 0.02, 0.05	x			
Post-yield stiffness Kpy	Kpy/Ki = -0.07, -0.05, -0.03, -0.02, 0.01, 0	x			
Column stiffness	Ic/Ib = 0.5, 0.75, 1.0, 2.0, 3.0	x			
P-Δ effects	None, Full nonlinear theory for Kpf, Kpy cases above	x			

8.2 EFFECTS OF EXCITATION AMPLITUDE

The sensitivity of the results to the amplitude of excitation is examined in this section by the use of incremental dynamic analysis (IDA), which was defined in Section 8.1.1.2. The recorded shaking table accelerations for each selected test were used as the excitation for the appropriate connection pattern. IDAs for the brittle fracture, ductile fracture, and deformation softening patterns tested are shown in Figures 8-3 through 8-5, and 8-6 through 8-8, for the 1.2 and 0.6 second cosine pulses, respectively. Since fewer patterns were tested for the JNF01 and JSE17 motions, all cases are shown together for each motion in Figures 8-9 and 8-10, respectively. The ductile baseline case is included for reference in all plots.

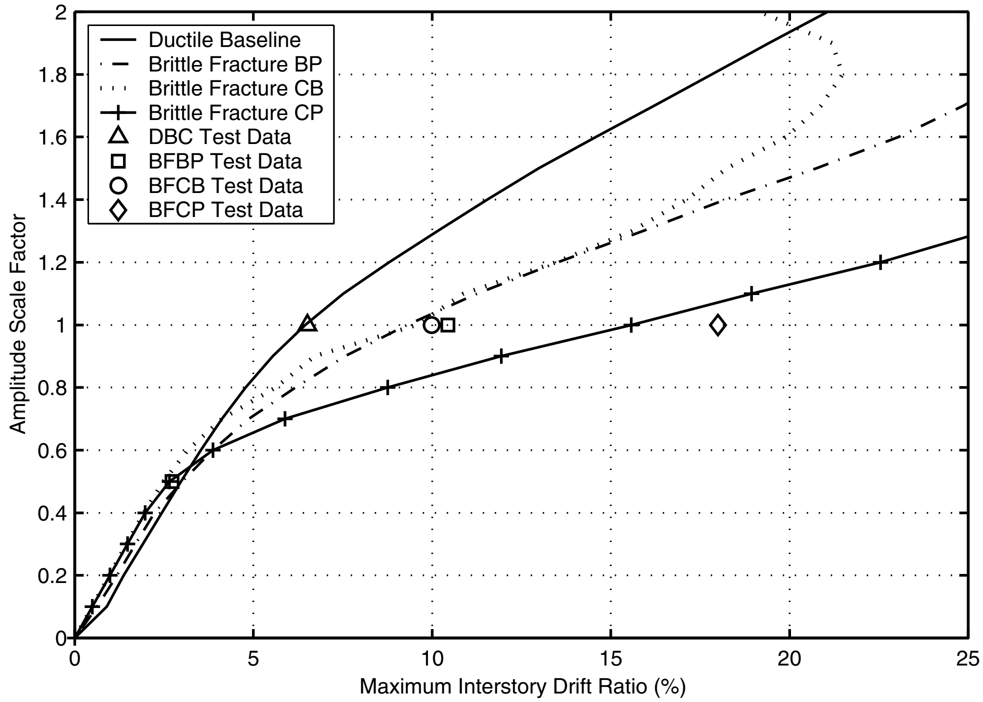

Figure 8-3. Comparison of IDAs corresponding to 1.2 sec cosine pulse tests, BF patterns

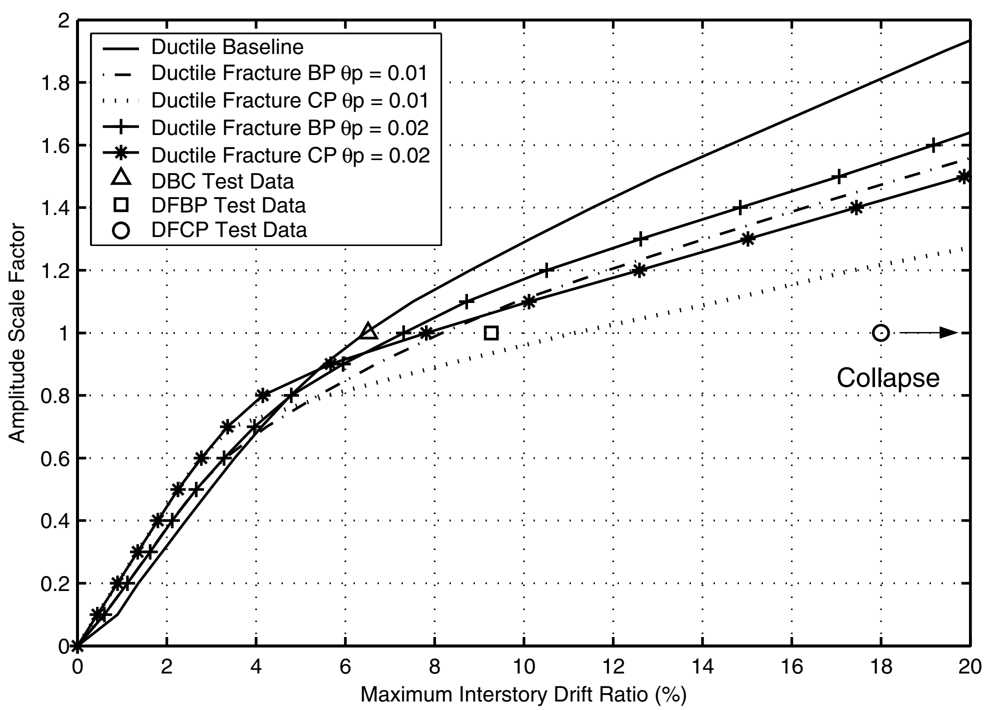

Figure 8-4. Comparison of IDAs corresponding to 1.2 sec cosine pulse tests, DF patterns

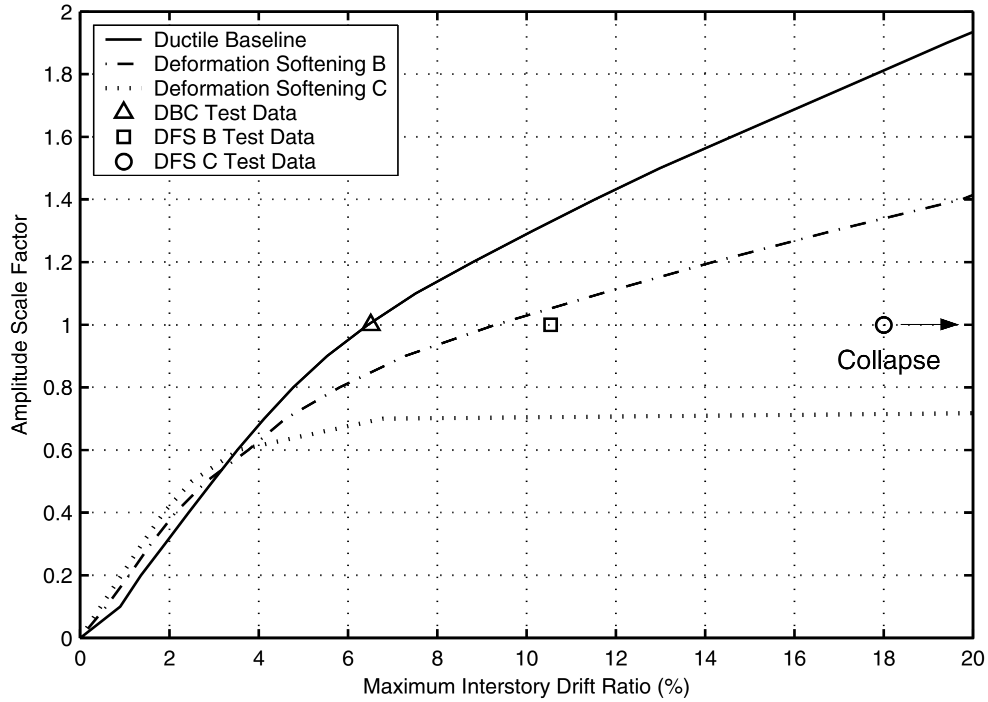

Figure 8-5. Comparison of IDAs corresponding to 1.2 sec cosine pulse tests, DFS patterns

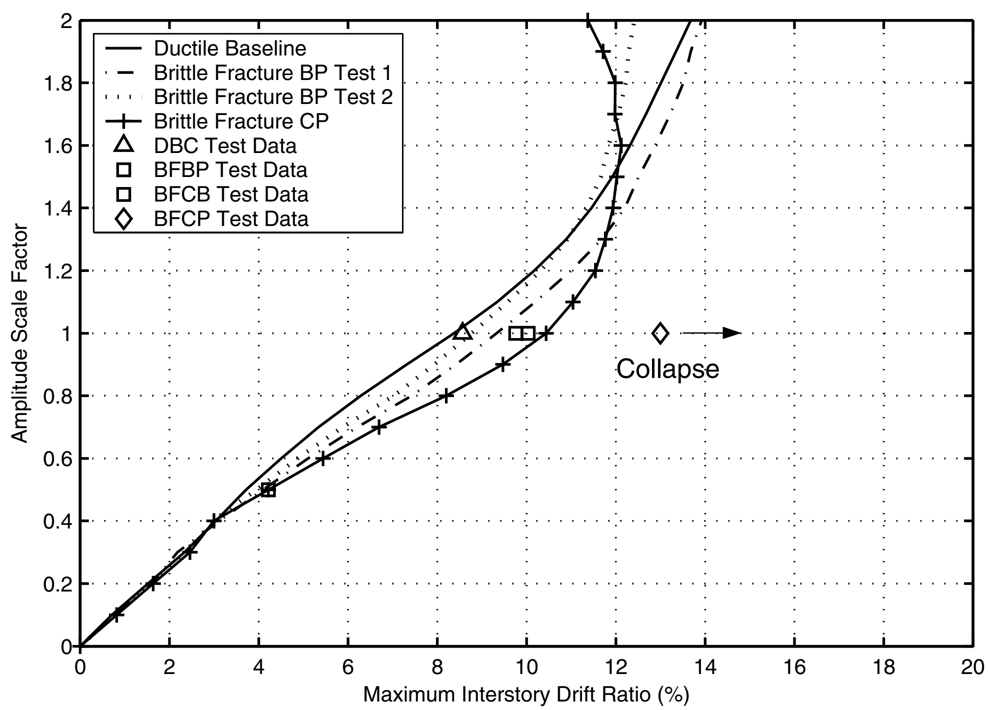

Figure 8-6. Comparison of IDAs corresponding to 0.6 sec cosine pulse tests, BF patterns

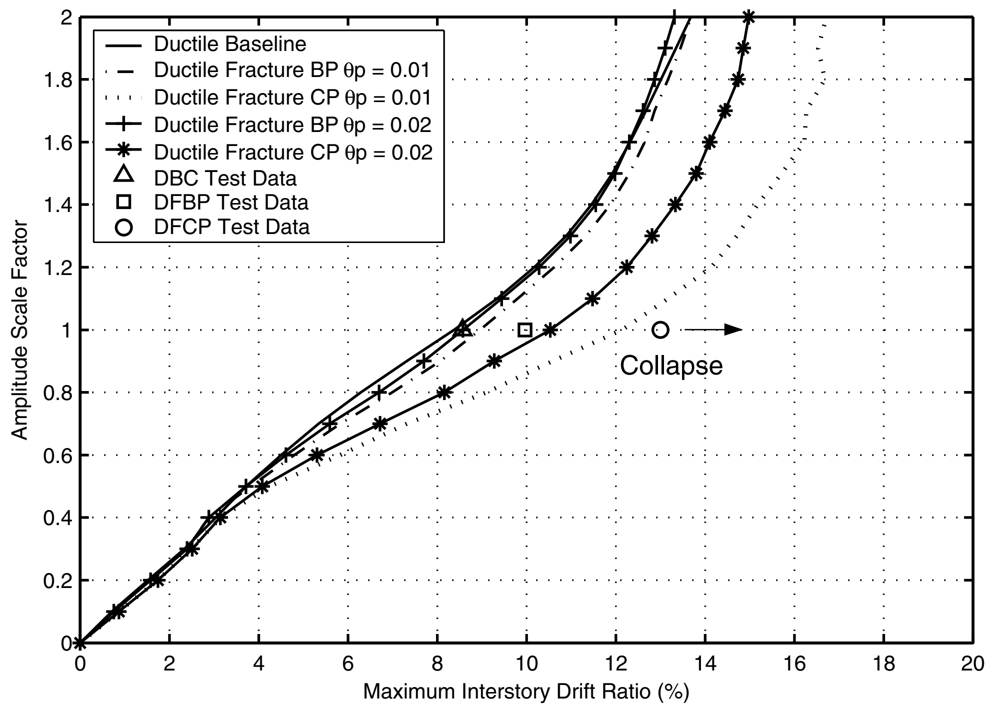

Figure 8-7. Comparison of IDAs corresponding to 0.6 sec cosine pulse tests, DF patterns

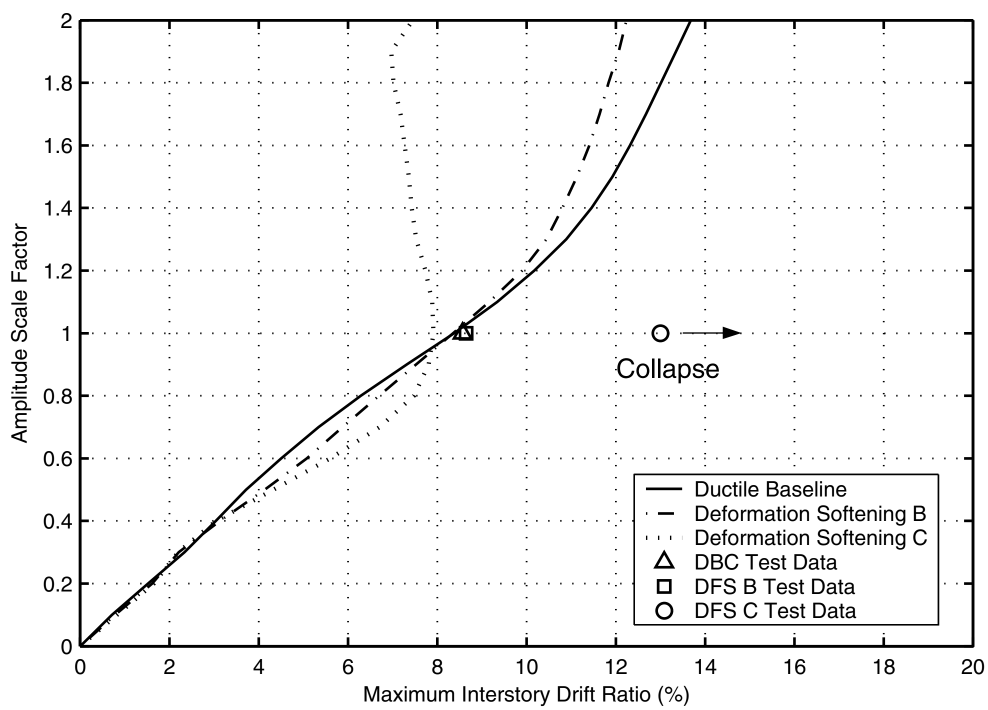

Figure 8-8. Comparison of IDAs corresponding to 0.6 sec cosine pulse tests, DFS patterns

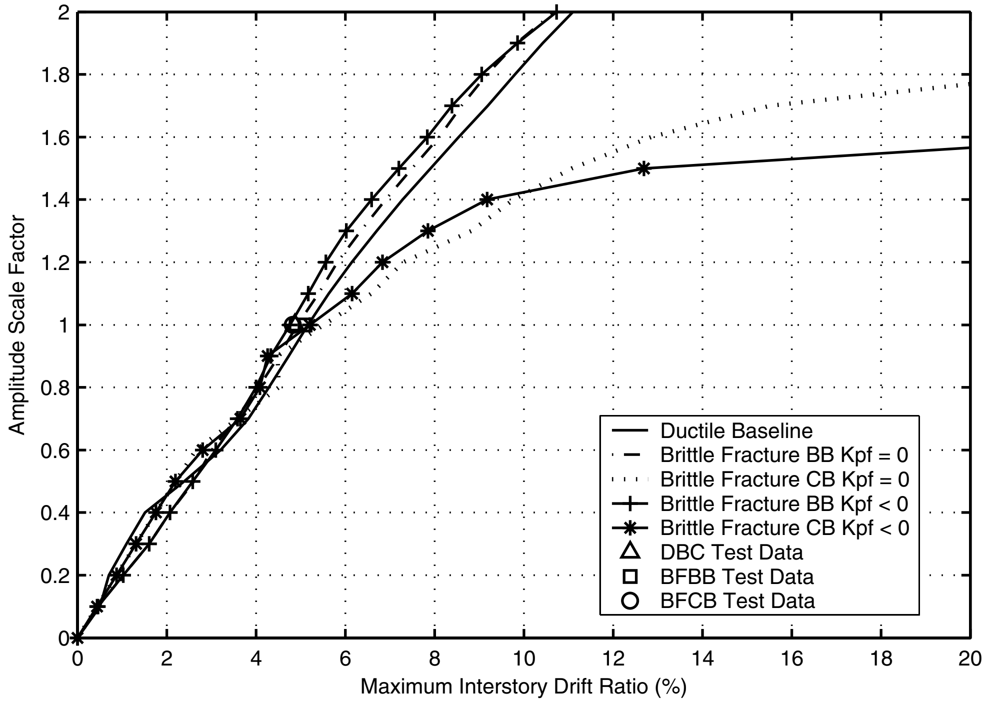

Figure 8-9. Comparison of IDAs corresponding to JNF01 tests

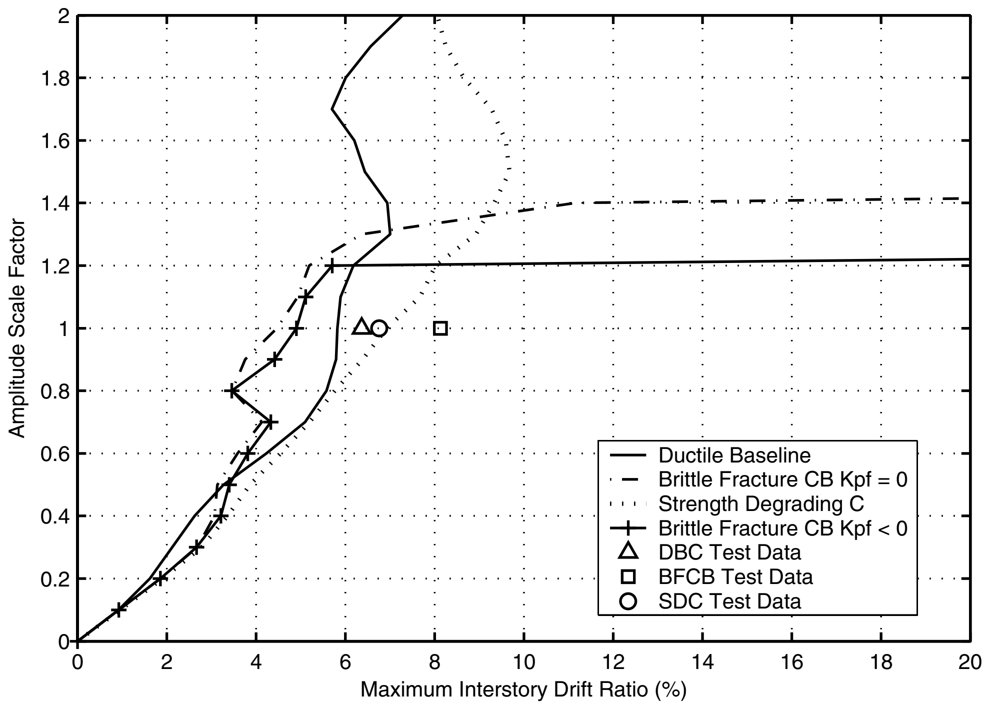

Figure 8-10. Comparison of IDAs corresponding to JSE17 tests

Relatively good agreement is obtained between the test results (point values) and the corresponding values of the IDA curve in most cases. The notable exceptions are the ductile fracture cases, which on the average show more discrepancy between the data and the analytical results than for other types of hysteretic degradation. This is most likely due to the "ductile" fracture cases having significantly less plastic rotation capacity than assumed in the analytical model. However, this result shows that ductile fracture may help behavior in some cases, though the results are a bit mixed. This issue will be discussed in greater detail in Section 8.3.4.

The other case where significant deviation occurs is the brittle fracture case for the JSE17 motion, where the analysis badly underpredicts the maximum drift. It is unclear why this occurs, but it is possible that small differences between the damaged-state vibration characteristics of the model and the specimen translate into larger differences in response to the particular pulse-like waveform contained in the JSE17 motion.

8.3 CONNECTION HYSTERETIC PARAMETERS

The major focus of this section is the effects of the severity of hysteretic deterioration on response. Modeling parameters that control the rate or amount of deterioration are:

- Post-fracture residual moment capacity
- Post-fracture stiffness
- Plastic rotation prior to fracture
- Number of flanges permitted to fracture
- Post-yield stiffness

Also included in the substudy of connection hysteretic parameters are studies of patterns which were not tested. Two ductile fracture cases with different amounts of plastic rotation prior to fracture initiation were examined. The use of these values also allows for a more thorough investigation into the role pre-fracture ductile behavior might play in reducing adverse system behavior.

In this section, the effects of various hysteretic degradation parameters on the displacement response of the test specimen are examined. These parameters are specific to the different types of hysteretic degradation and are related to the severity of the degradation. For instance, in the case of fracture, the residual moment capacity, post-fracture stiffness, and amount of plastic rotation prior to fracture all contribute in different ways to the severity of the effects of the fracture on the frame's behavior. The effects of the various hysteretic degradation parameters are examined for the tested connection configuration patterns and compared with test data.

8.3.1 Effects of Post-Fracture Residual Moment Capacity

A range of values of the M_r/M_f ratio (defined in Section 8.1.1.1) between 0.1 and 1.0 are examined in this section, with 0.1 indicating a very severe reduction of 90% in moment capacity and 1.0 indicating no reduction (ductile behavior). This wide range of residual capacities allows the examination of trends associated with residual moment capacity and number and location of fractures. These trends can be seen in Figures 8-11 and 8-12 for the case of the 1.2 second and 0.6 second cosine pulse shaking table test excitations. Trends with excitation amplitude for each level of residual moment are shown in Figures 8-13 through 8-17 for three fracturing connection patterns.

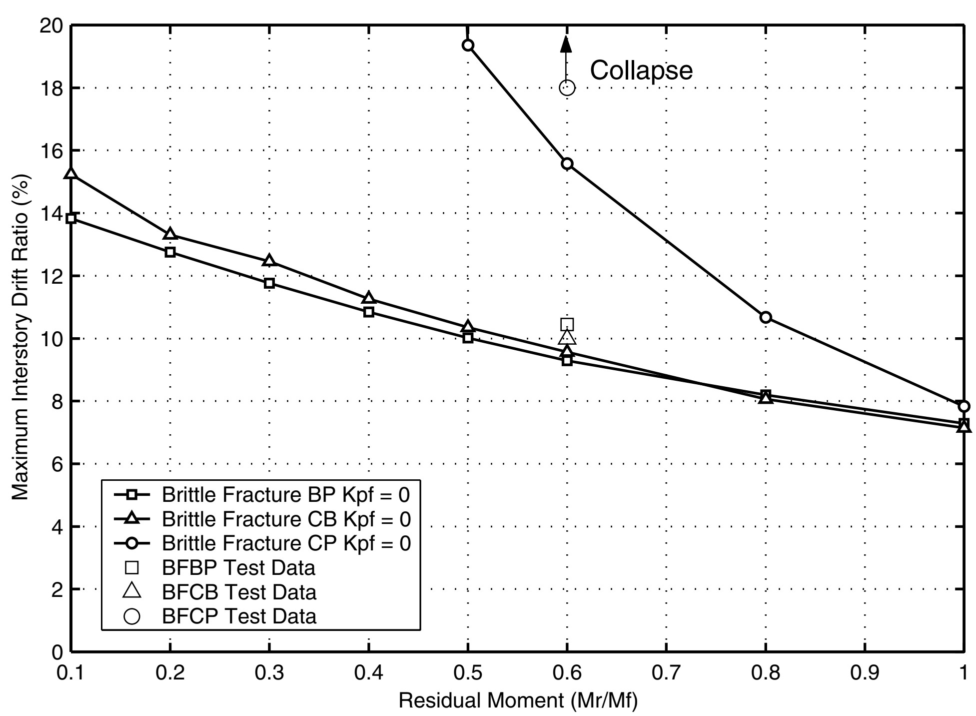

Figure 8-11. Post-fracture moment capacity vs. interstory drift ratio, 1.2 sec cosine pulse, test amplitude (1.0)

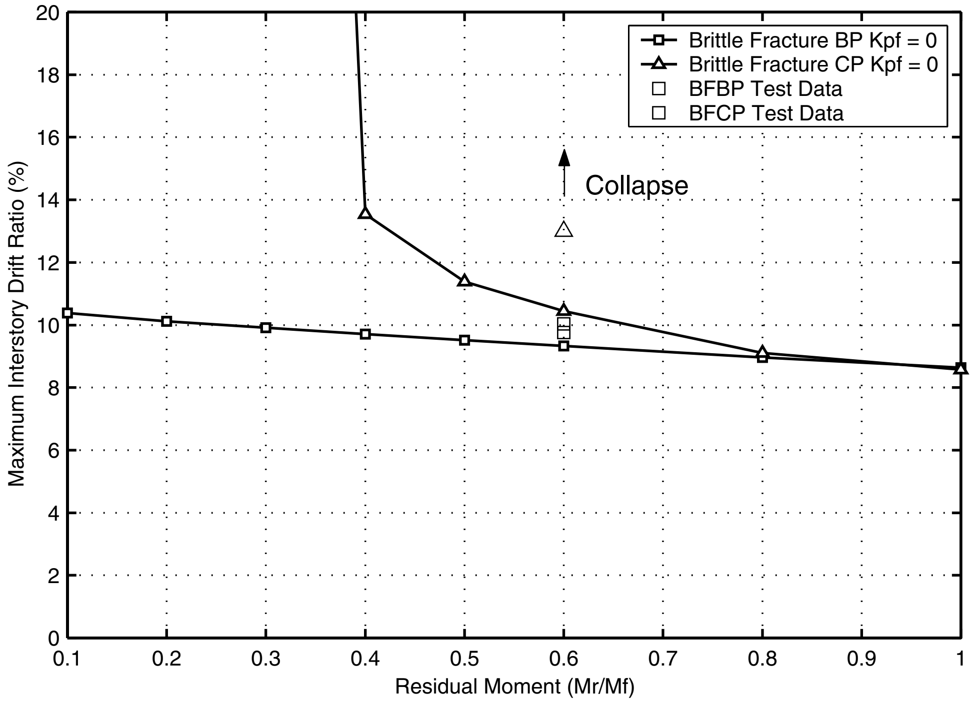

Figure 8-12. Post-fracture moment capacity vs. interstory drift ratio, 0.6 sec cosine pulse, test amplitude (1.0)

It is apparent from Figures 8-11 and 8-12 that the CP patterns (where all the tension flanges fracture nearly simultaneously during the pulse) are much more sensitive to residual moment capacity than the BP patterns, which have fractures in the first only. In fact, the sensitivity may be worse than indicated in the above plots, since comparison with the test data shows an underprediction of drifts. In the case of CP pattern fractures, it is clear that collapse can only be prevented for the level of excitation considered in Figure 8-12 if the level of strength reduction is small. However, as shown in the Figures 8-15 and 8-16, sufficient residual moment capacity can prevent collapse for low to moderate drift levels.

In the case of the BP pattern, the amount of sensitivity to residual moment capacity varies with excitation. The variation is much more dramatic for the 1.2 second cosine pulse than the 0.6 second cosine pulse, which is expected, since strength is more important in the 1.2 second case due to the response spectrum position of the structure.

Prior analytical studies (Hart in SAC, 1995, Luco and Cornell, 1999) have concluded that moderate variations in post-fracture residual moment capacity have little or no effect on the response of the system unless the reduction is very severe. However, these studies considered structures which were generally on the descending branch of the response spectrum for the selected excitations, where strength is less important. Figures 8-13 and 8-14 show the effects of post-fracture moment capacity for increasing amplitudes of two cosine pulse excitations. The structure is on the ascending branch for the 1.2 second pulse, and on the descending branch for the 0.6 second pulse. The shape of the IDA curves is quite different for the two cases, with reduction in post-fracture capacity leading to collapse at much lower amplitudes for the case where the structure is on the ascending branch.

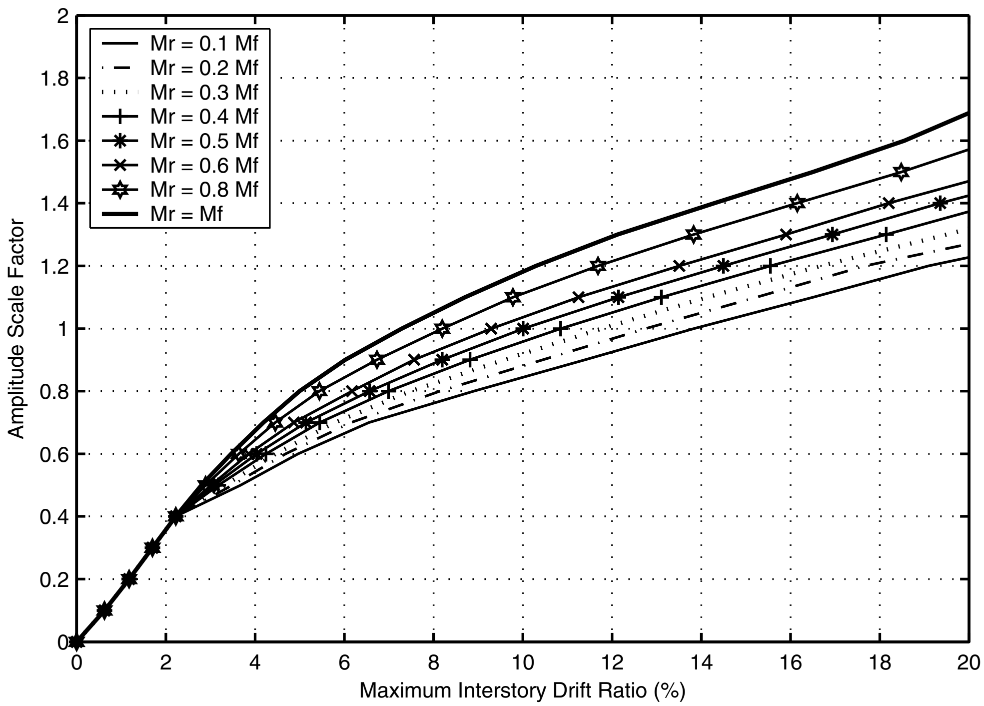

Figure 8-13. Comparison of IDAs for variable Mr, BF BP pattern, 1.2 second cosine pulse

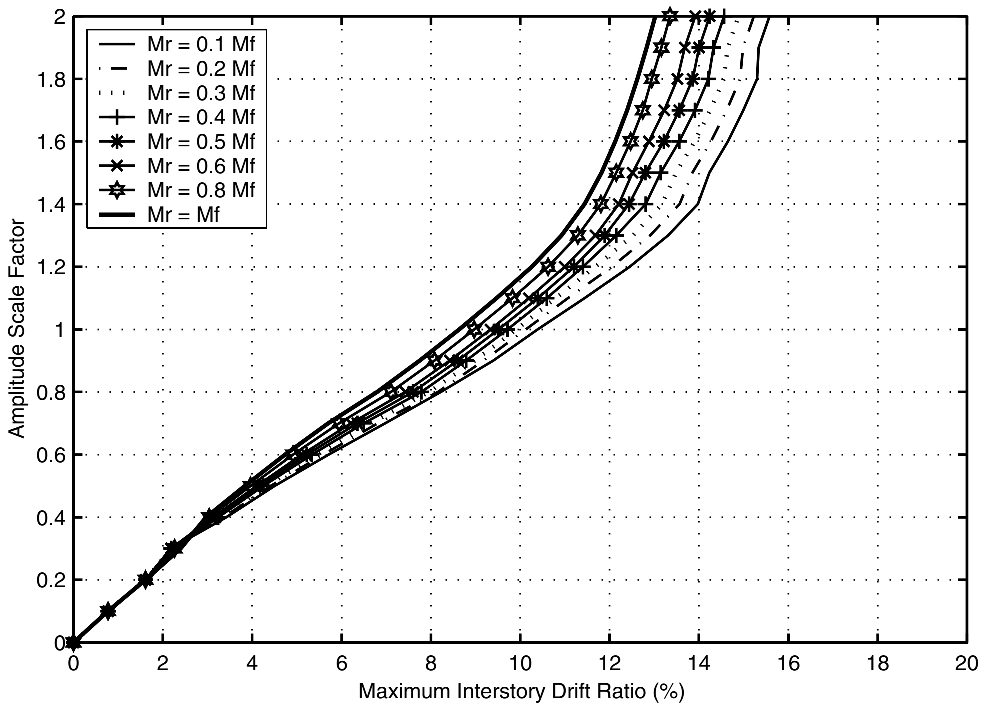

Figure 8-14. Comparison of IDAs for variable Mr, BF BP pattern, 0.6 sec cosine pulse

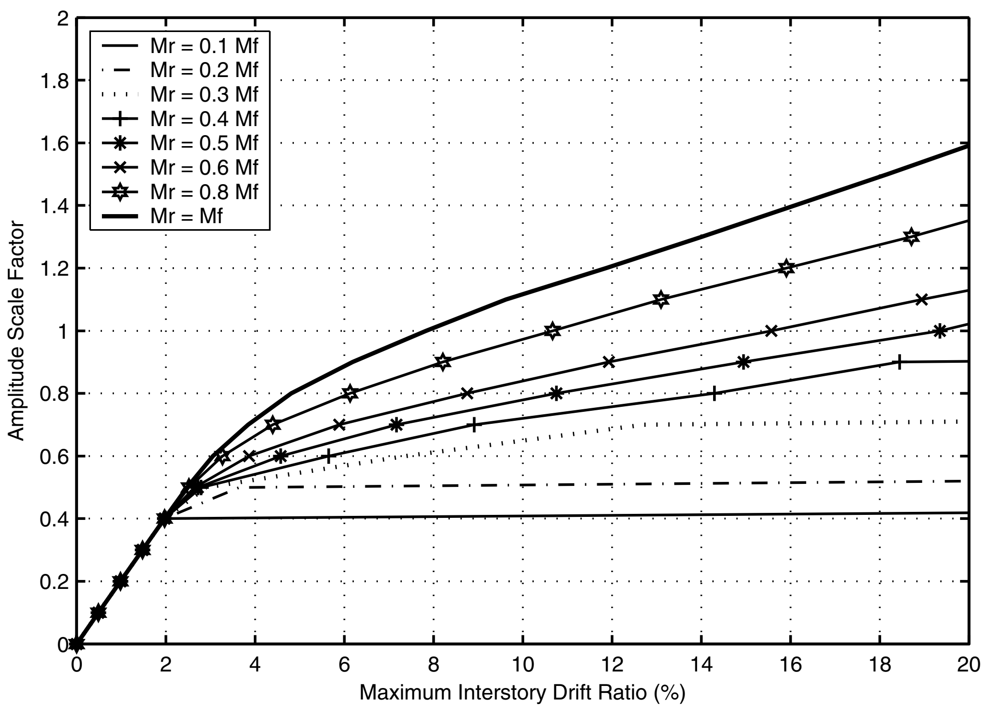

Figure 8-15. Comparison of IDAs for variable Mr, BF CP pattern, 1.2 sec cosine pulse

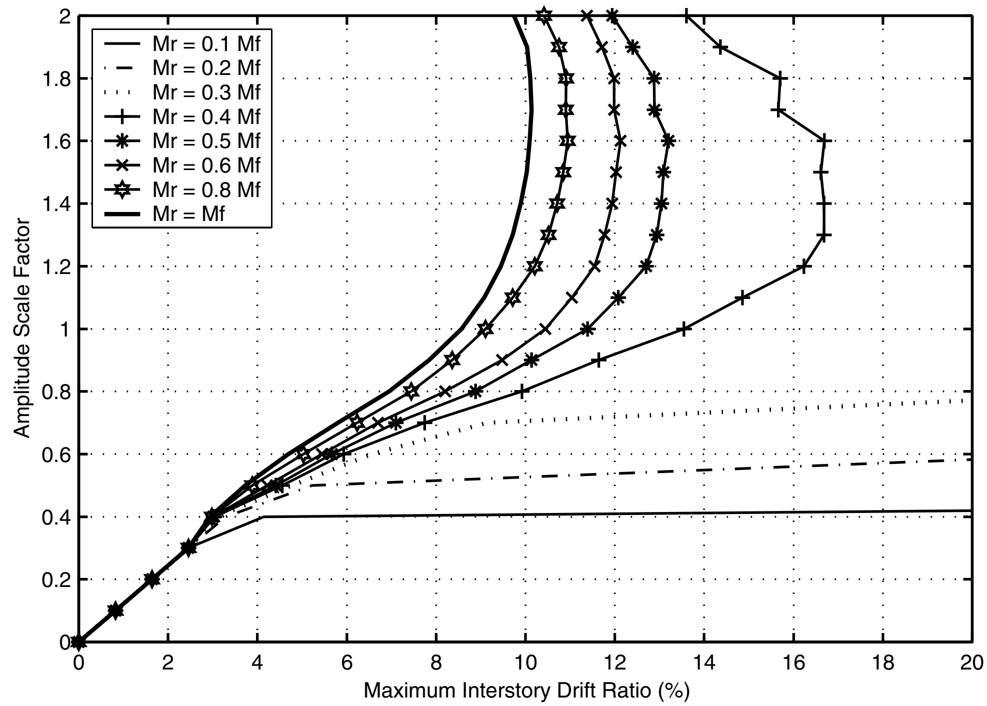

Figure 8-16. Comparison of IDAs for variable Mr, BF CP pattern, 0.6 sec cosine pulse

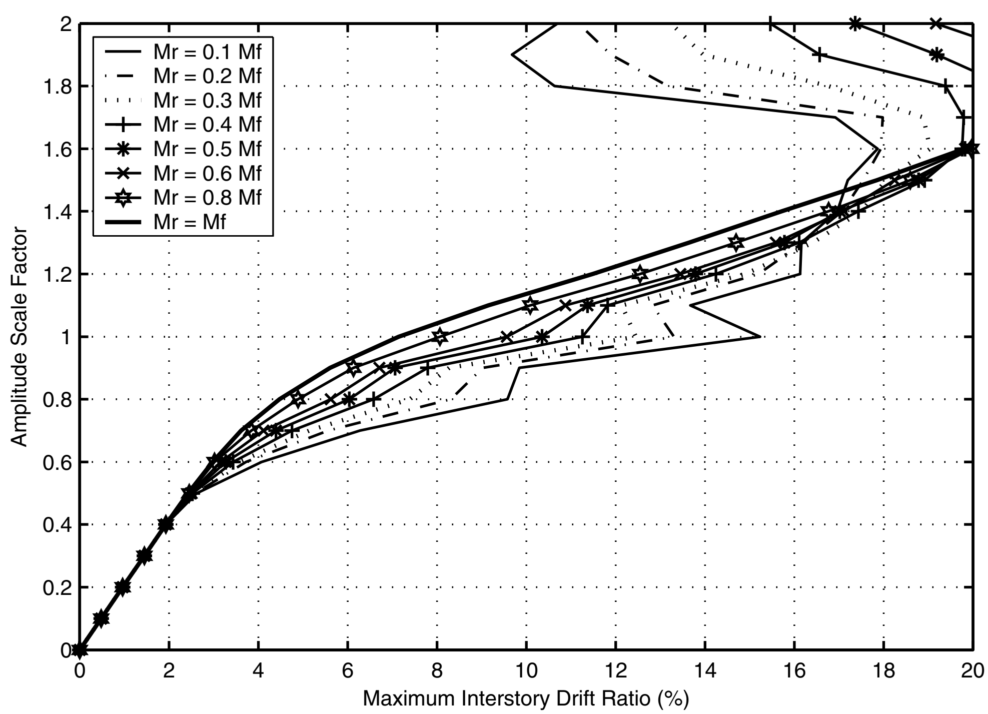

Figure 8-17. Comparison of IDAs for variable Mr, BF CB pattern, 1.2 sec cosine pulse

In general, the effects of post-fracture residual moment capacity depend largely on the number and spatial distribution of fractures. In the case of brittle fractures localized in one (pattern BP), even very severe loss of moment capacity in the fractured connections does not necessarily lead to collapse. Whether collapse occurs depends on the capacity of the intact connections relative to the severity of the excitation. Similar observations can be made for the case where fractures are confined to the bottom flanges only, except that collapse occurrence is determined by the capacity of the fractured connections when the fractured flange is in compression, rather than the capacity of the intact connections. On the other hand, if fractures cause loss of capacity in every connection in one direction of motion (pattern CP or CTB), less severe strength loss and lower amplitudes of excitation are needed to cause collapse.

8.3.2 Effects of Post-Fracture Tangent Stiffness

In this section, the effects of post-fracture tangent stiffness are explored. This parameter is particularly relevant in cases where the specimen continues to deform significantly in the same direction after fracture occurs. In the cases studied, this happens when the fracture occurs early in a large pulse excitation. The effects of the variation of post-fracture stiffness from strongly positive to strongly negative are shown in Figure 8-18.

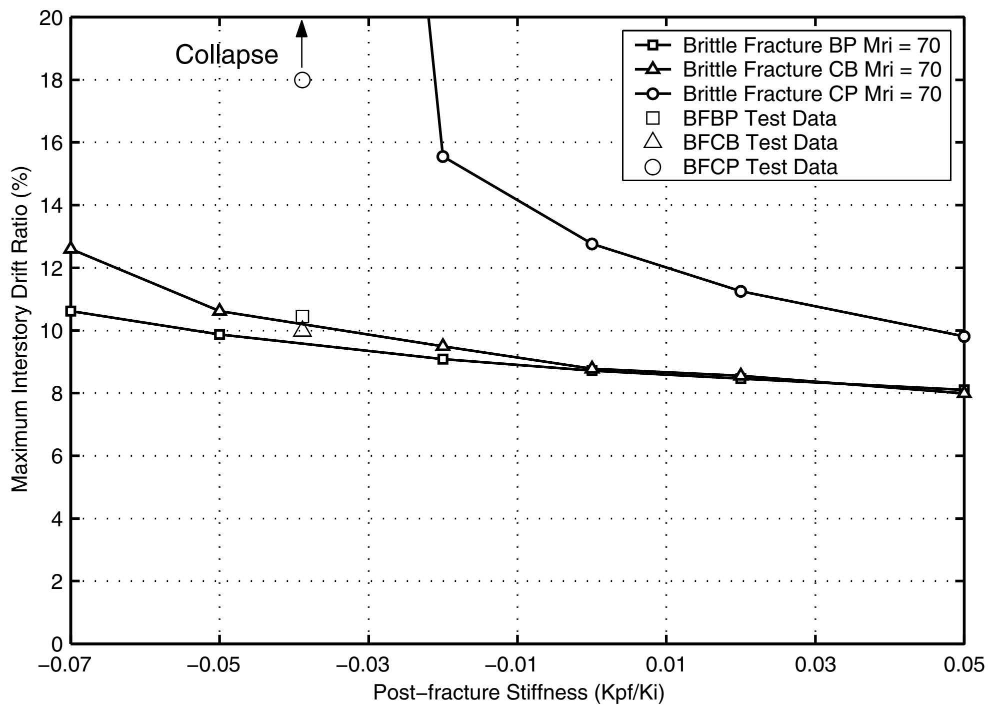

Figure 8-18. Post-fracture stiffness vs. interstory drift ratio, 1.2 second cosine pulse, test amplitude (1.0)

Pattern CP is most sensitive to changes in slope post-fracture stiffness. This is because all of the fractures occur at nearly the same time, and so the tangent stiffness of all connections is the post-fracture stiffness. For the other patterns, only two of the connections can fracture at any one time, so only two connections have the post-fracture tangent stiffness. This greatly reduces the sensitivity to post-fracture stiffness, and a significant increase in drift is observed only when K_{pf} becomes strongly negative.

It should also be remembered that at this amplitude of excitation geometric nonlinearities are important, and that a positive post-fracture tangent slope in the connection hysteresis counteracts the global P-Δ effects. For this reason, the curves flatten out for the larger positive values rather than decreasing rapidly. For the larger negative values, the P-Δ effects and negative post-fracture stiffness are additive, resulting in a larger combined effect on the displacement response. The relative contributions of geometric nonlinearity and connection behavior, which were obtained by running the analysis with and without geometric nonlinearities, are shown in Figure 8-19.

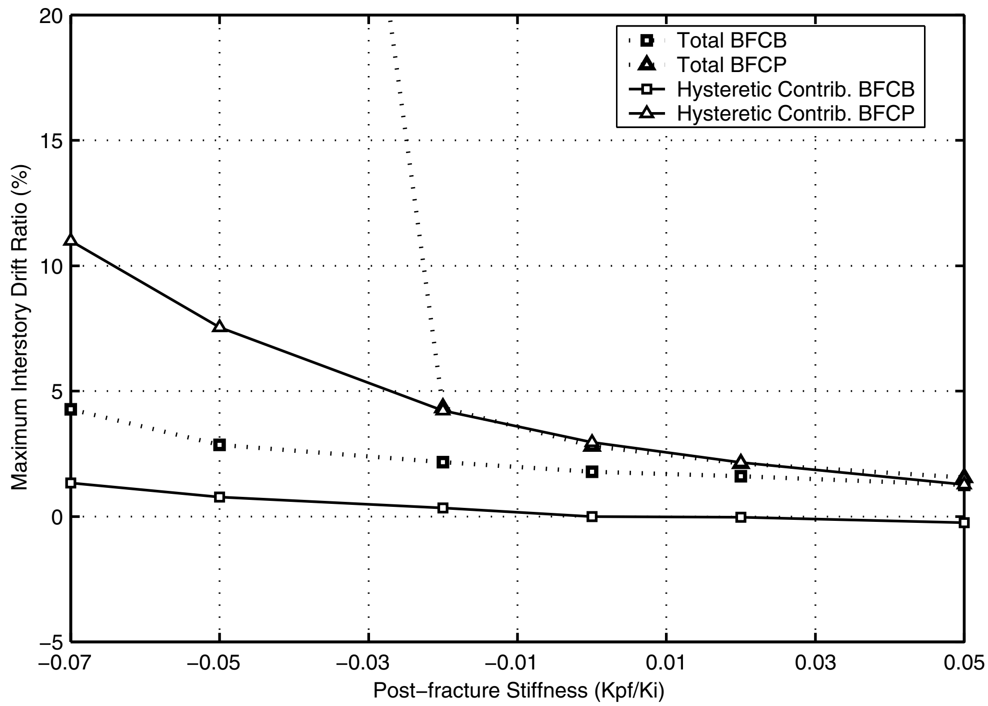

Figure 8-19. Relative contribution of geometric and hysteretic negative stiffnesses, 1.2 second cosine pulse, test amplitude (1.0)

The variation of the effects of post-fracture stiffness with amplitude are shown for the brittle fracture BP, CP, and CB patterns in Figures 8-20 through 8-22. For all of the patterns, the effect of post-fracture stiffness increases with amplitude. This is most likely due to the combined effects of geometric stiffness reduction (due to P-Δ), which increases with amplitude, and hysteretic stiffness reduction, which was discussed previously.

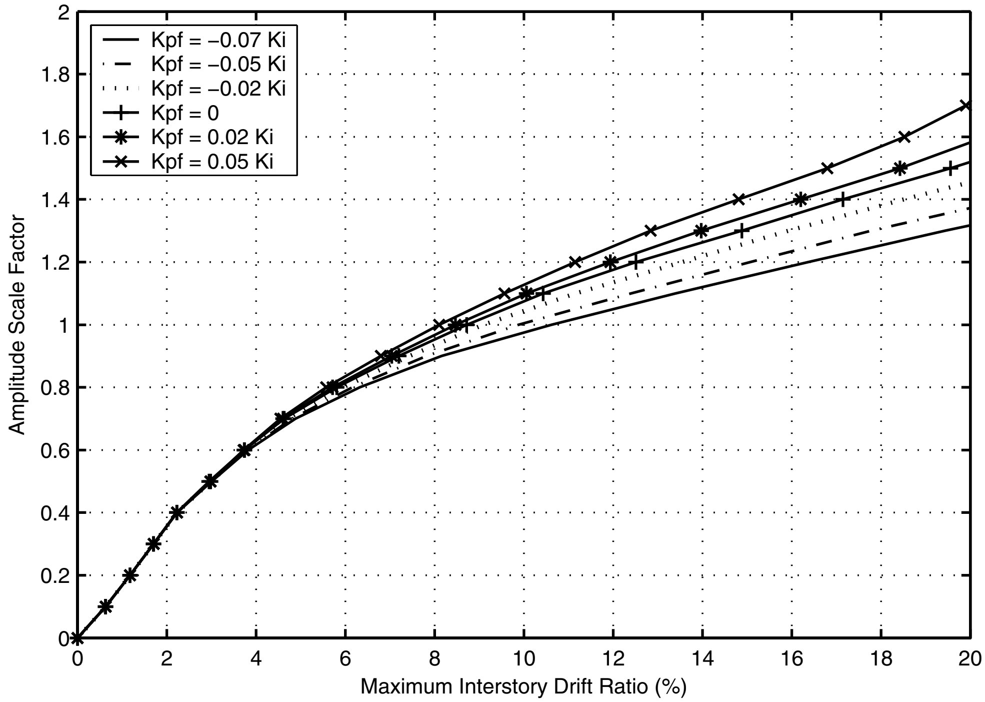

Figure 8-20. Comparison of IDAs for variable Kpf, BF BP pattern, 1.2 sec cosine pulse

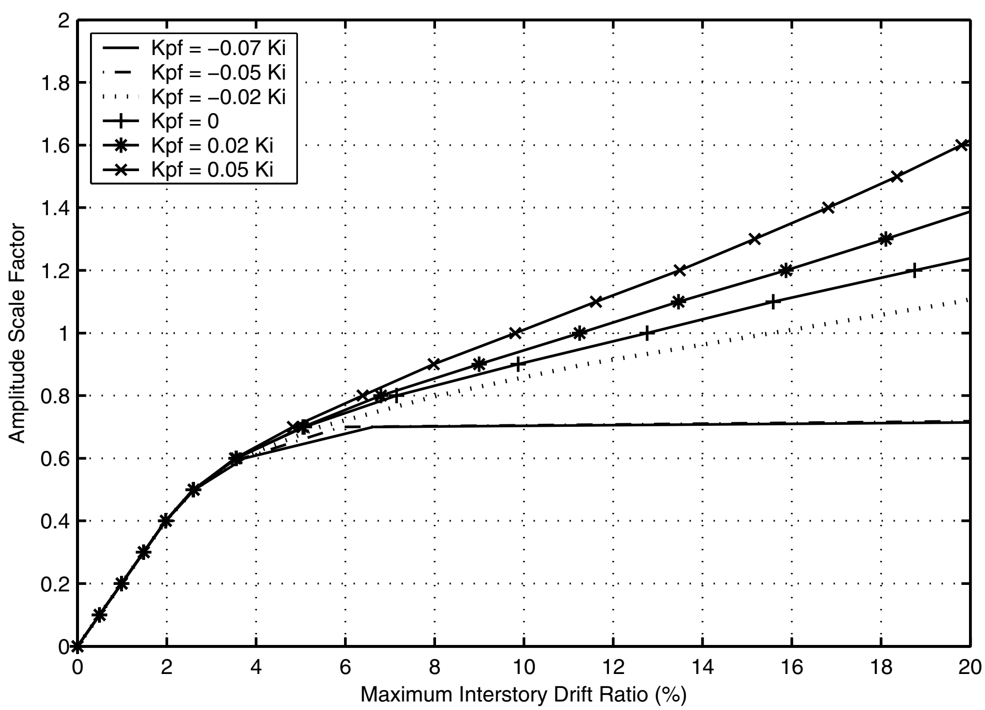

Figure 8-21. Comparison of IDAs for variable Kpf, BF CP pattern, 1.2 sec cosine pulse

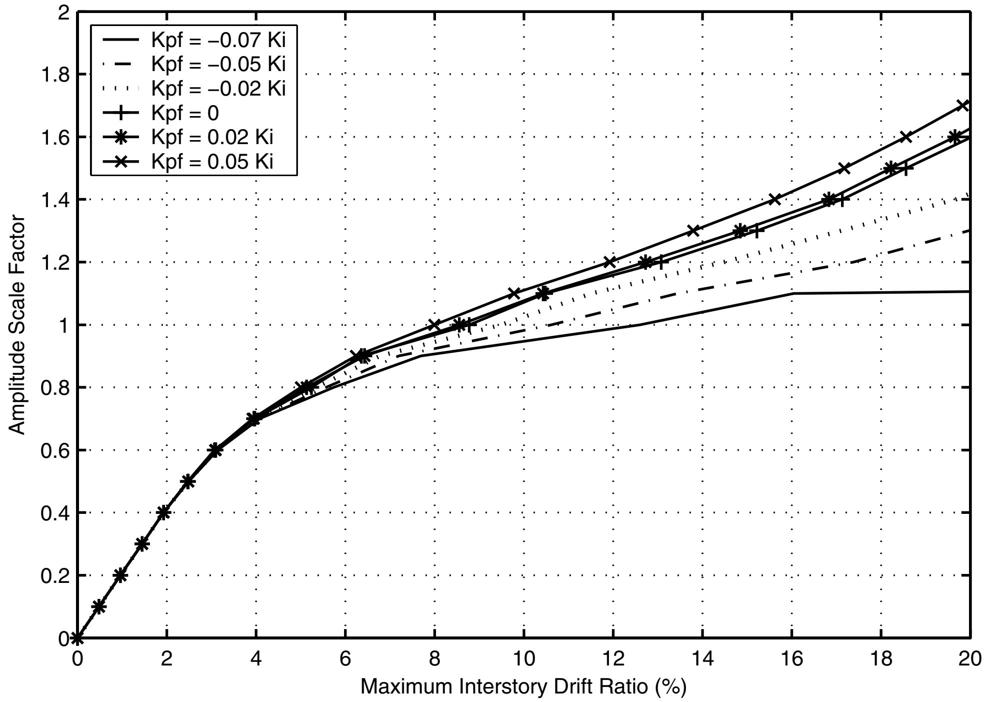

Figure 8-22. Comparison of IDAs for variable Kpf, BF CB pattern, 1.2 sec cosine pulse

8.3.3 Effects of Amount of Negative Post-Yield Tangent Stiffness

In this section, the effects of the amount of negative post-yield tangent stiffness are examined for the deformation softening patterns DFS B and DFS C. In Figure 8-23, the variance of interstory drift ratio with stiffness is shown. As expected, the C pattern is affected to a much greater extent than the B pattern because it has four connections suffering the negative post-yield stiffness. This figure also shows that there seems to be a critical level of post-yield stiffness where collapse occurs if all connections have that level of stiffness, as is the case for the C pattern. The ductile connections in the top in the B pattern prevent this global instability.

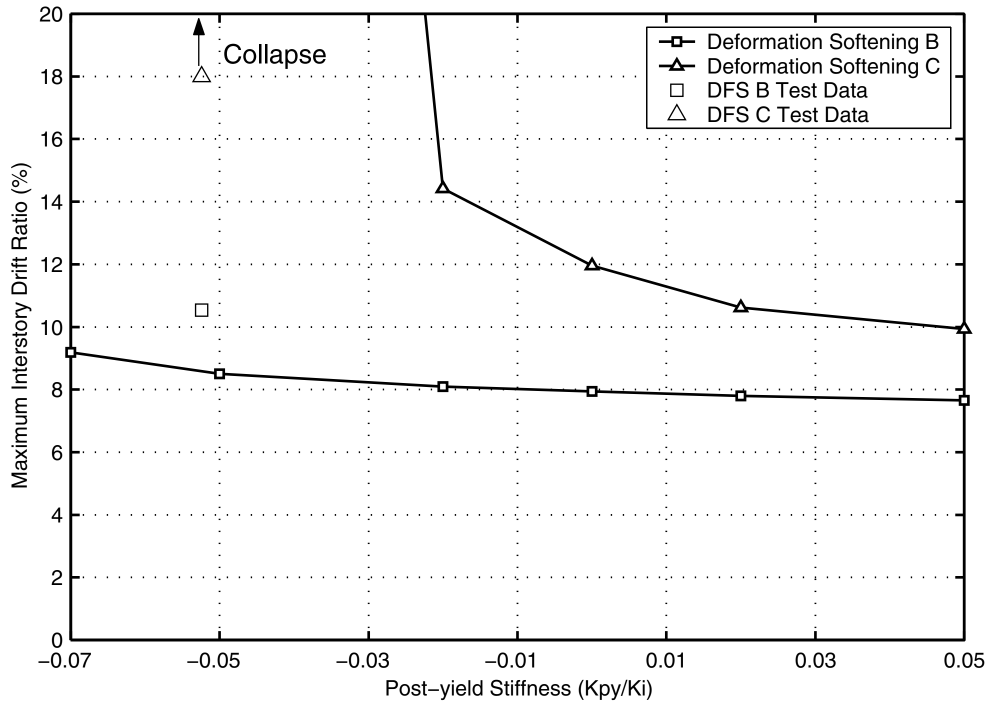

Figure 8-23. Post-yield stiffness vs. interstory drift ratio, 1.2 second cosine pulse, test amplitude (1.0)

In Figures 8-24 and 8-25, IDAs are plotted for the DFS B and DFS C patterns, respectively. The excitations used are the appropriate recorded shaking table excitations for the 1.2 second cosine pulse.

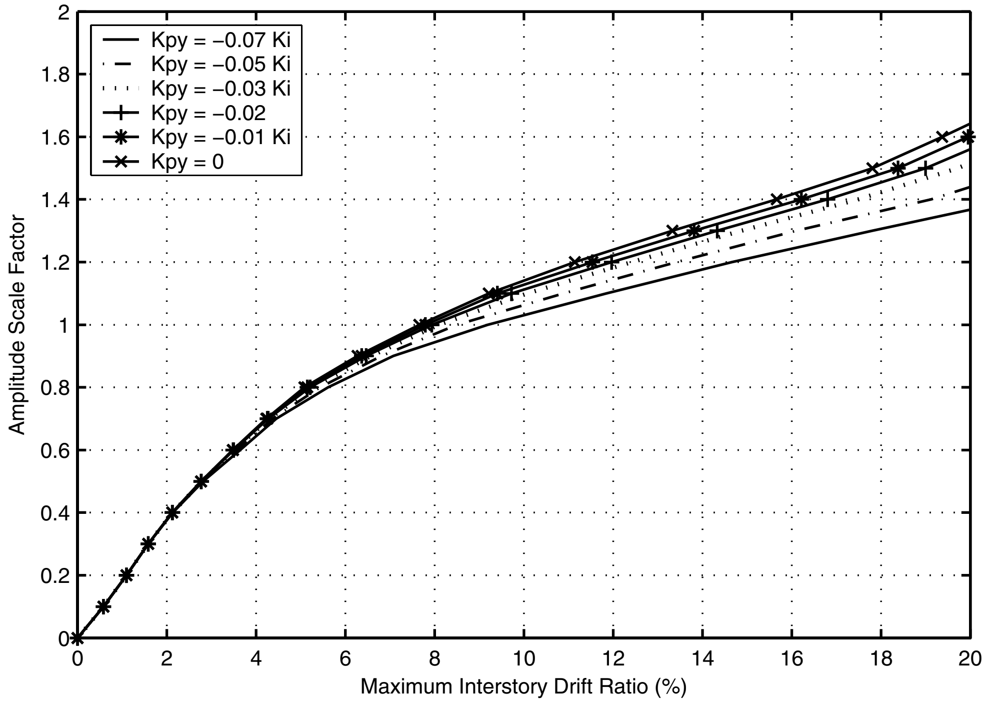

Figure 8-24. Comparison of IDAs for variable Kpy, DFS B pattern, 1.2 second cosine pulse

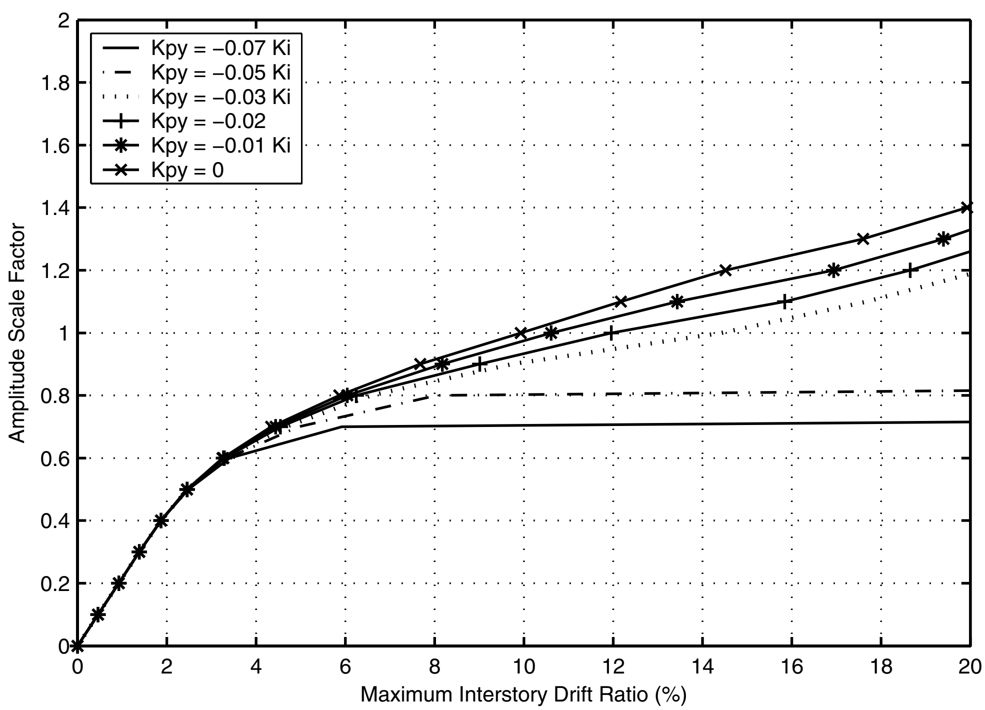

Figure 8-25. Comparison of IDAs for variable Kpy, DFS C pattern, 1.2 second cosine pulse

For the B pattern, the effects of the level of deformation softening are small until drifts become quite large (approximately 6%), as shown in Figure 8-24. In contrast, the effects begin to cause divergence in the responses at just over 3% drift for the C pattern. These results indicate that a large amount of negative post-yield stiffness can have very adverse effects on the system behavior, but the effects are pronounced only if a majority of the connections exhibit this behavior. Also, the same additive relationship between negative hysteretic stiffness and P-Δ effects that was seen for post-fracture stiffness occurs for post-yield stiffness as well. These combined effects tend to increase with amplitude, so the expected excitation is also a factor in determining whether deformation softening can lead to structural instability.

8.3.4 Effects of Plastic Rotation Prior to Fracture

In this section, the effects of pre-fracture plastic rotation are examined. Three values of plastic rotation prior to fracture are examined: zero, 0.01 radian, and 0.02 radian. The “zero” case corresponds to a brittle fracture, which would be expected from a pre-Northridge connection, while the other values are appropriate for post-Northridge connections that show limited plastic rotation capacity. IDAs for these cases are shown in Figures 8-26 and 8-27.

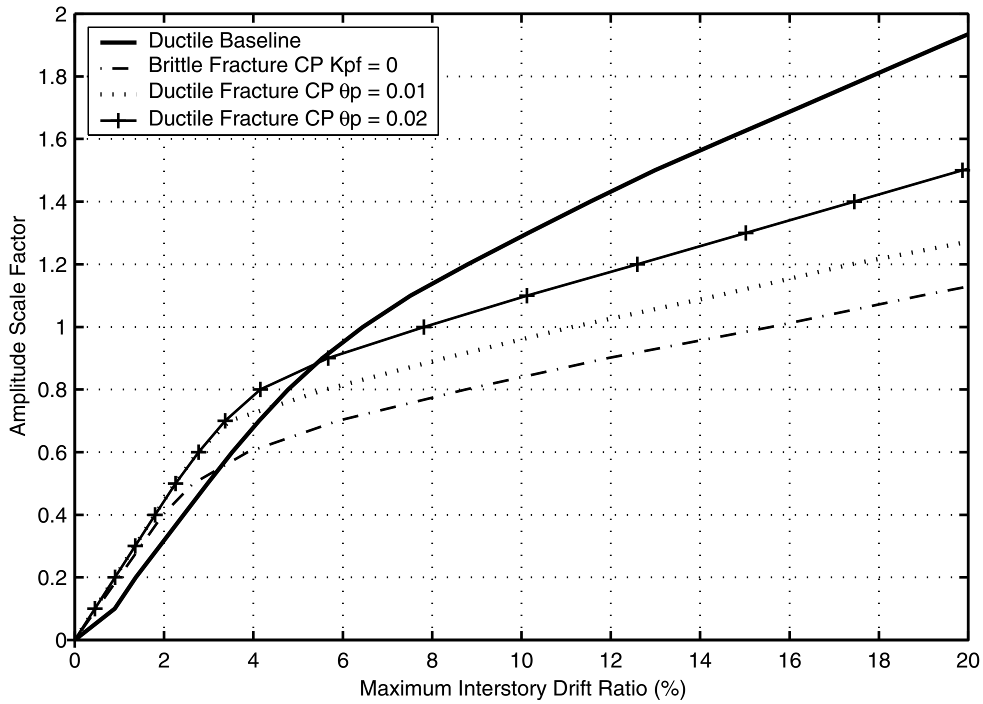

Figure 8-26. Comparison of IDAs for varying pre-fracture θp, 1.2 sec cosine pulse

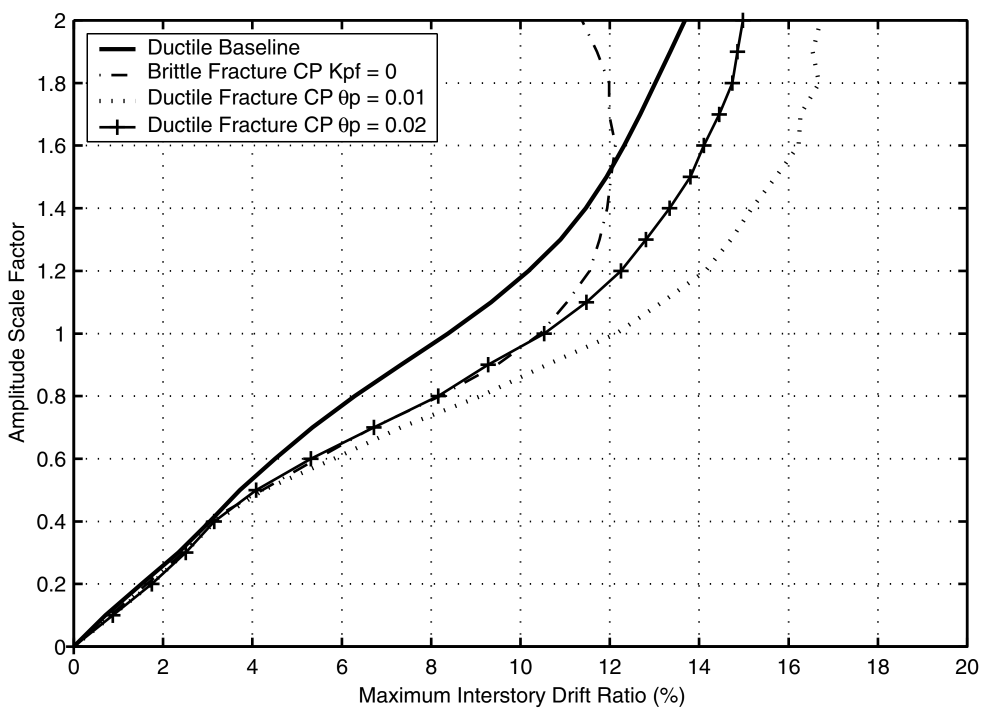

Figure 8-27. Comparison of IDAs for varying pre-fracture θp, 0.6 sec cosine pulse

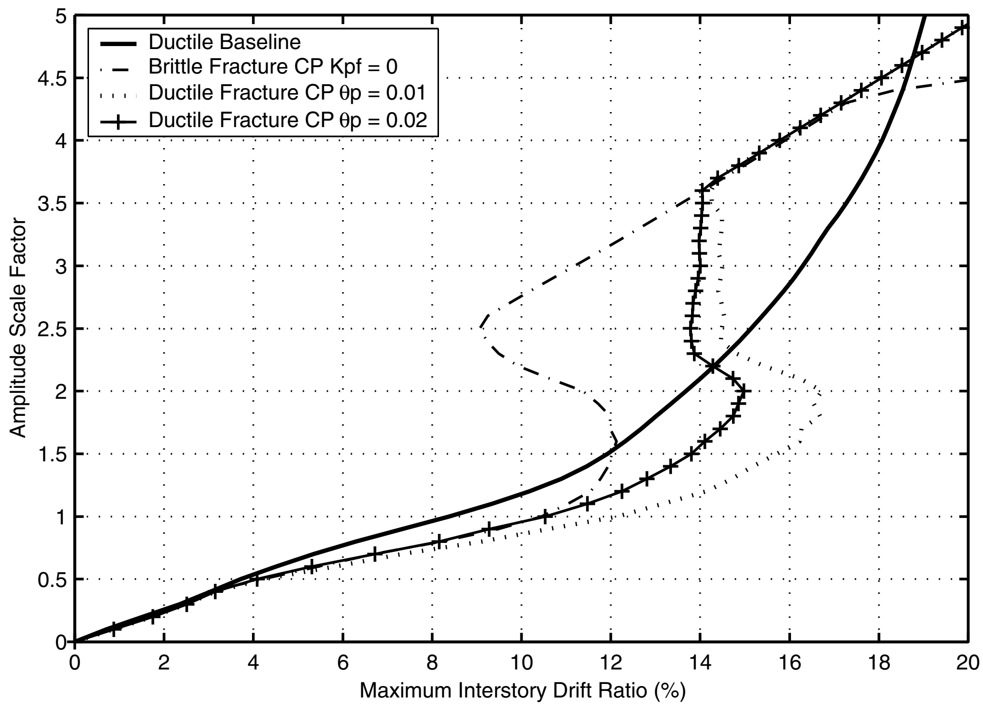

Figure 8-28. Comparison of IDAs for varying pre-fracture θp, 0.6 sec cosine pulse excitation, large amplitude scale factor values

In the case of the 1.2 second cosine pulse, the effects of plastic rotation prior to fracture are generally beneficial, decreasing the drift for a given amplitude, particularly for larger drifts. However, the opposite is true for the 0.6 second case, as the plastic rotation prior to fracture appears to make things worse for the lower amplitudes shown in Figure 8-27. This is counterintuitive, and more work is necessary to determine why this is the case. At very large amplitudes, as shown in Figure 8-28, the effects of plastic rotation can be beneficial.

8.4 EFFECTS OF FRAME PROPERTIES

The effects of variations in column stiffness are examined in this section by varying the ratio of the cross-section moments of inertia of the columns to the beams (Ic/Ib) and keeping the beam cross section constant. Interstory drifts are plotted versus the column-to-beam stiffness ratio for the test excitation amplitude in Figure 8-29. Interstory drifts are not particularly sensitive to column stiffness unless the columns section stiffness becomes less than that of the beam. Next, IDAs are compared for varying column stiffness for the ductile baseline and brittle fracture BP, CP, and CB in Figures 8-30 through 8-33.

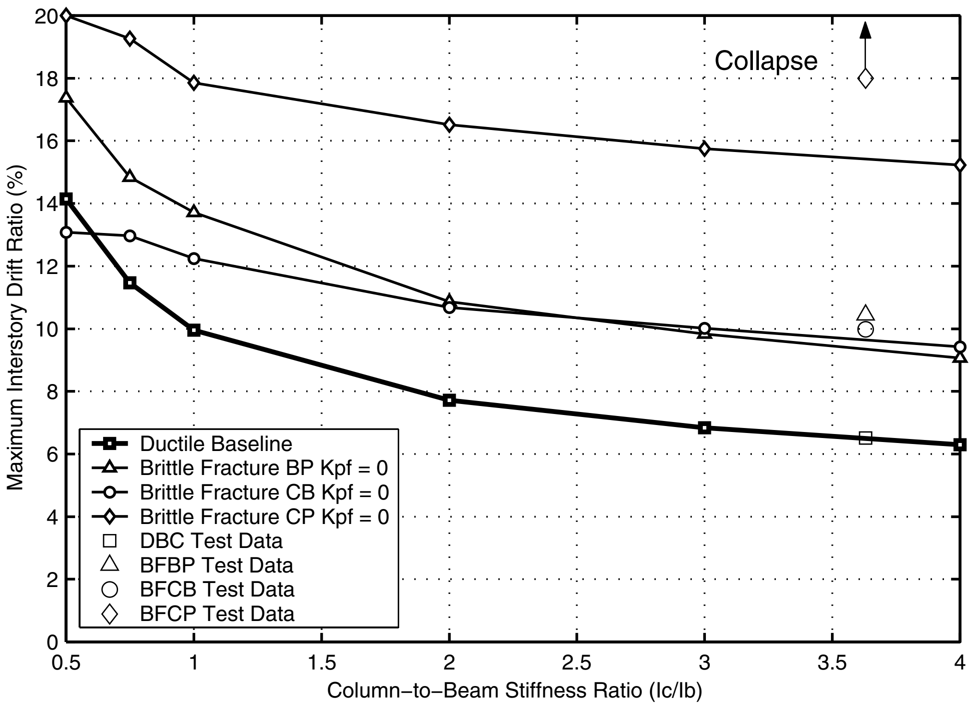

Figure 8-29. Column-to-beam section stiffness ratio vs. interstory drift ratio, 1.2 sec cosine pulse, test amplitude (1.0)

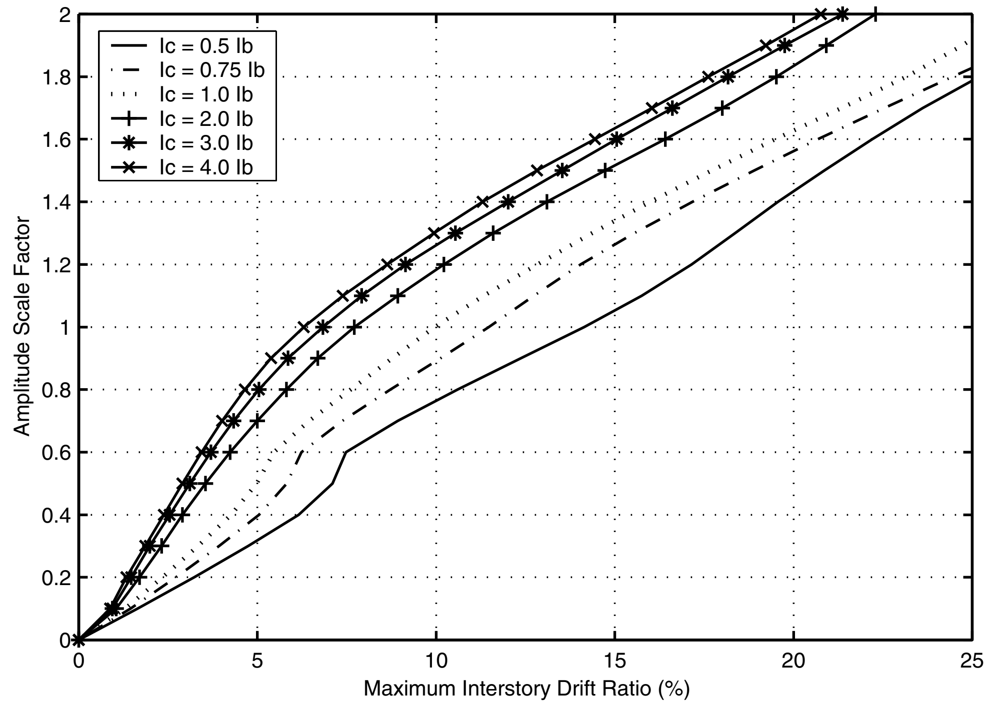

Figure 8-30. Comparison of IDAs for varying Ic, DB case, 1.2 sec cosine pulse

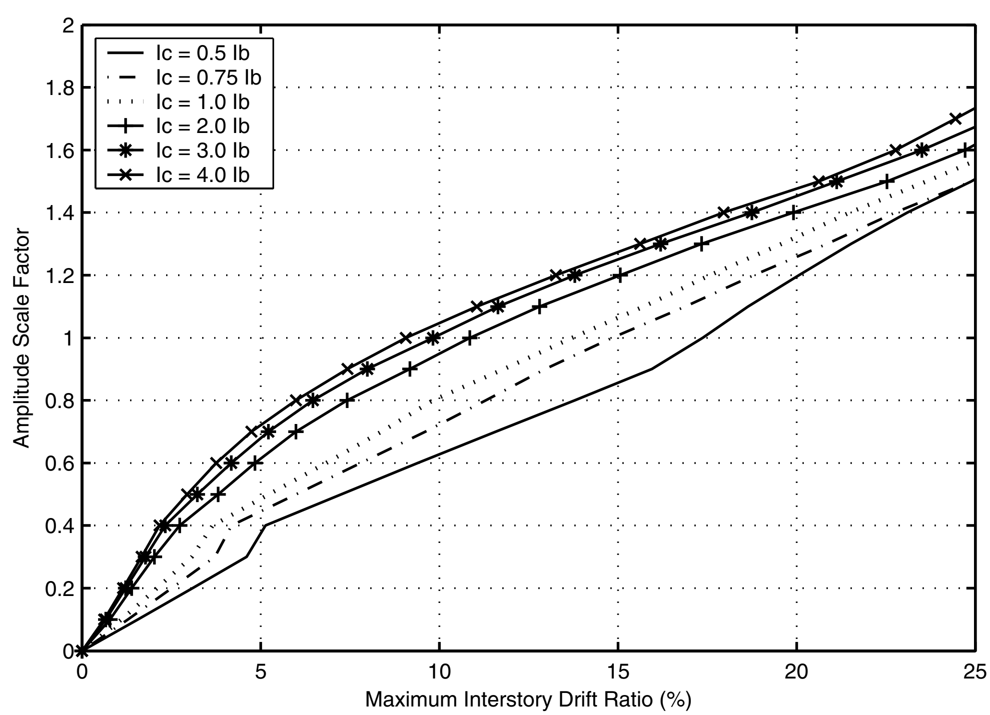

Figure 8-31. Comparison of IDAs for varying Ic, BF BP pattern, 1.2 sec cosine pulse

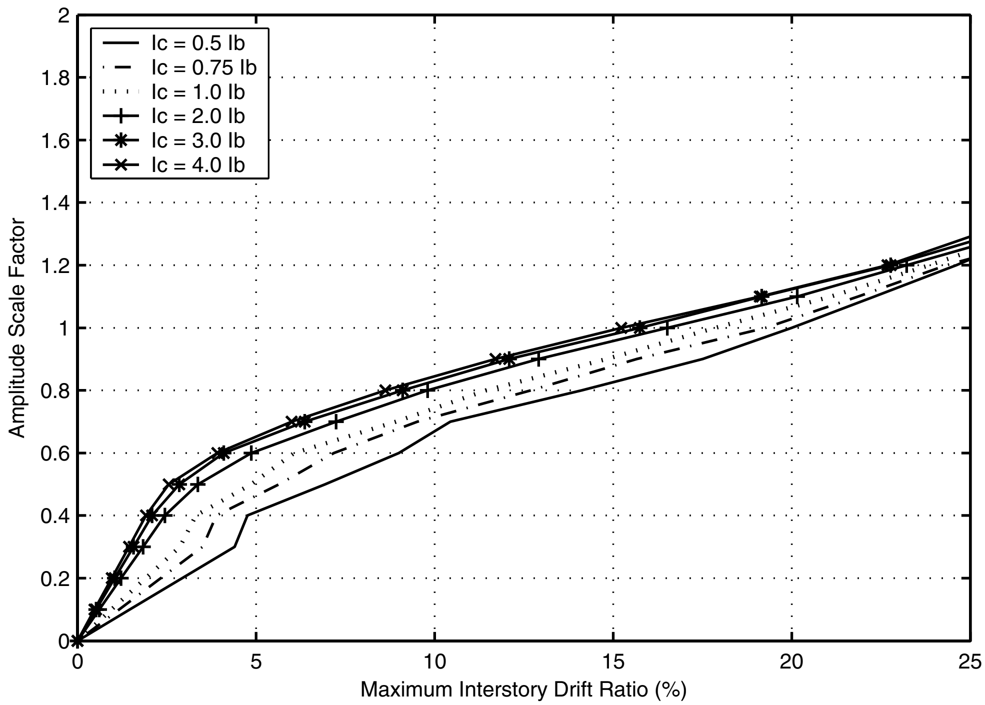

Figure 8-32. Comparison of IDAs for varying Ic, BF CP pattern, 1.2 second cosine pulse

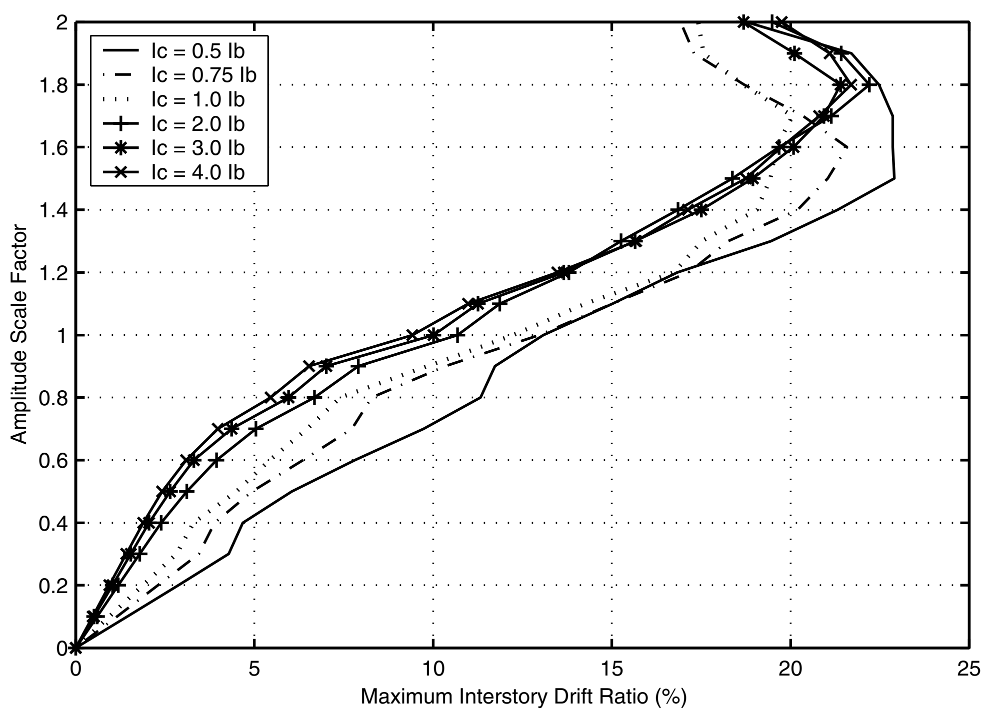

Figure 8-33. Comparison of IDAs for varying Ic, BF CB pattern, 1.2 second cosine pulse

For the connection configuration patterns shown above, the effects of column stiffness are not large unless the columns become much more flexible than the beams. Most cases seem to show similar rates of variation in drift with Ic/Ib ratio, with the exception of the brittle fracture CB pattern, which does not show a rapidly steepening slope as the columns become very flexible. This may have something to do with fractures in the other direction, which tends to “balance” the response and lead to moderate positive and negative displacement excursions as opposed to a small negative excursion and a large positive excursion. This may cause the response to be less sensitive to the column stiffness.

8.5 EFFECTS OF EARTHQUAKE EXCITATION

In this section, the response of the test specimen to earthquake excitations other than those used in the experimental series is examined. The selected excitations include a variety of trigonometric pulses and the SAC Joint Venture suites of ground motions for the Los Angeles area for the 10% in 50 year and 2% in 50 year earthquake hazard levels.

8.5.1 Pulse Excitations

In this section, the effect of structure period-to-pulse period ratio $T_{structure}/T_{pulse}$ on interstory drift is examined. This is done using shock spectra calculated for *the test specimen* with cosine pulse excitations of varying periods and constant peak velocities of 25 in./sec (the test excitation amplitude), 37.5 in./sec (1.5 times test amplitude), and 50 in./sec (2 times test amplitude). These spectra, which were created for both the CB (bottom flange only) and CTB (top and bottom flange) patterns, are shown in Figures 8-34 through 8-39.

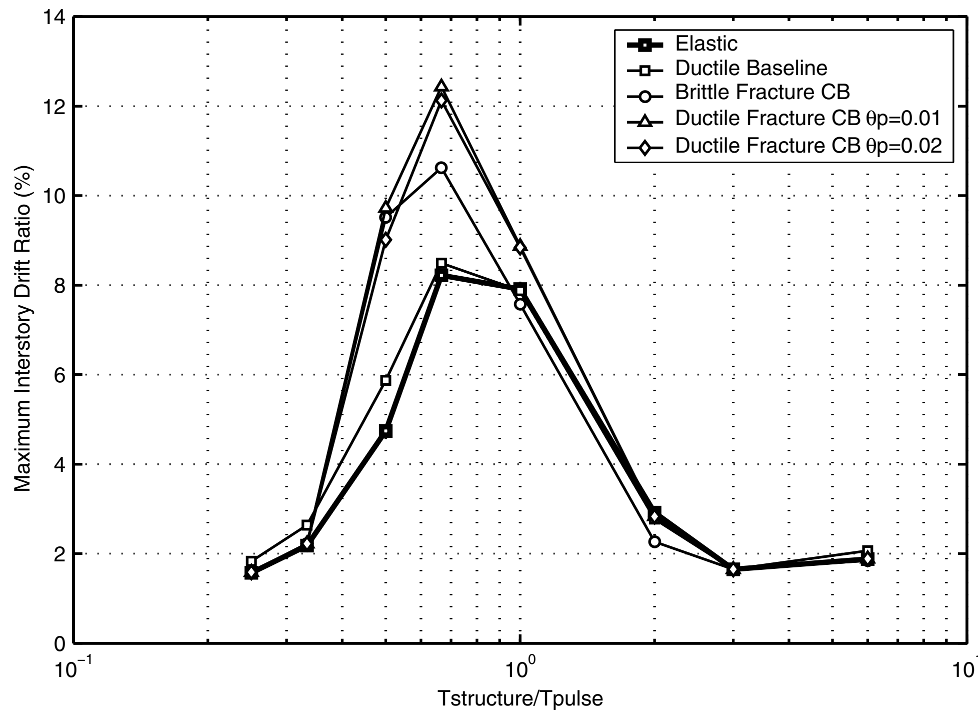

Figure 8-34. Variation of interstory drift w/cosine pulse period, Vp=25 in./sec, CB patterns

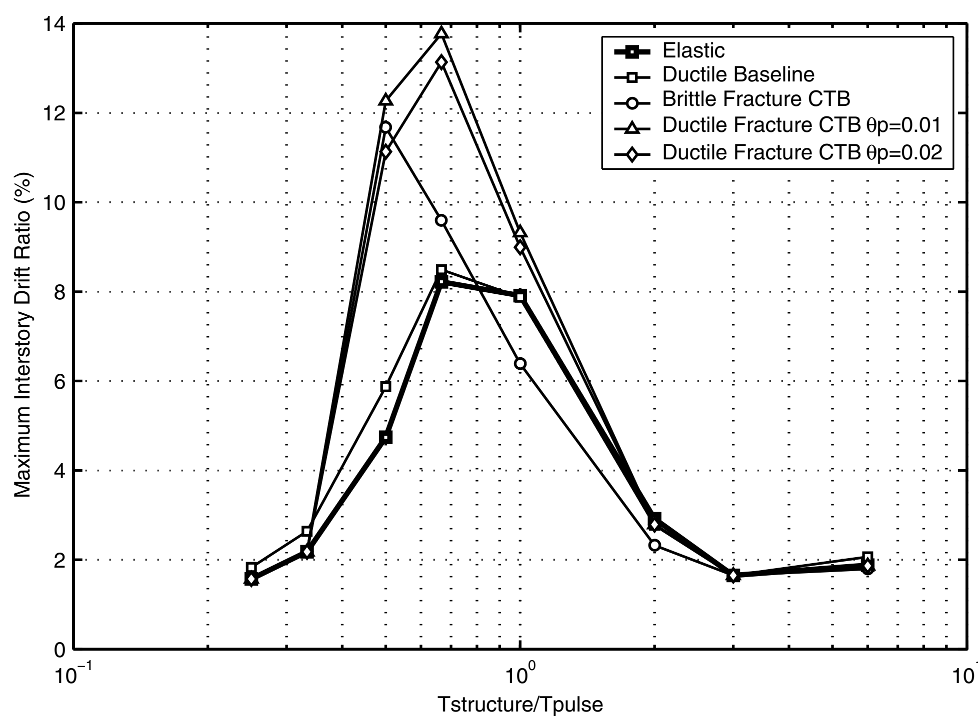

Figure 8-35. Variation of interstory drift w/cosine pulse period, Vp=25 in./sec, CTB patterns

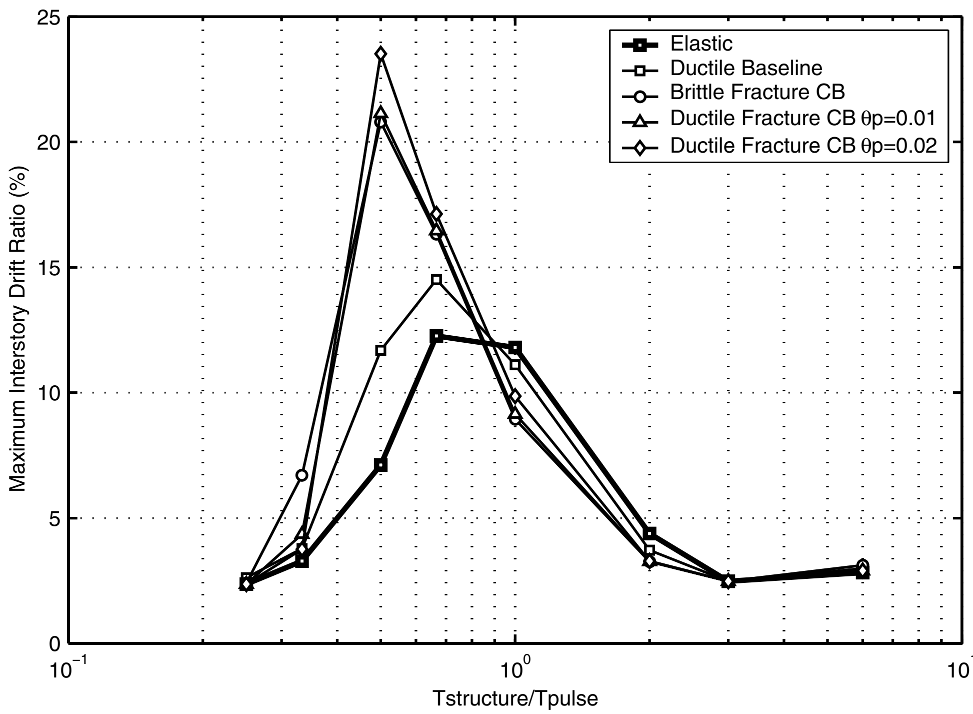

Figure 8-36. Variation of interstory drift w/cosine pulse period, Vp=37.5 in./sec, CB patterns

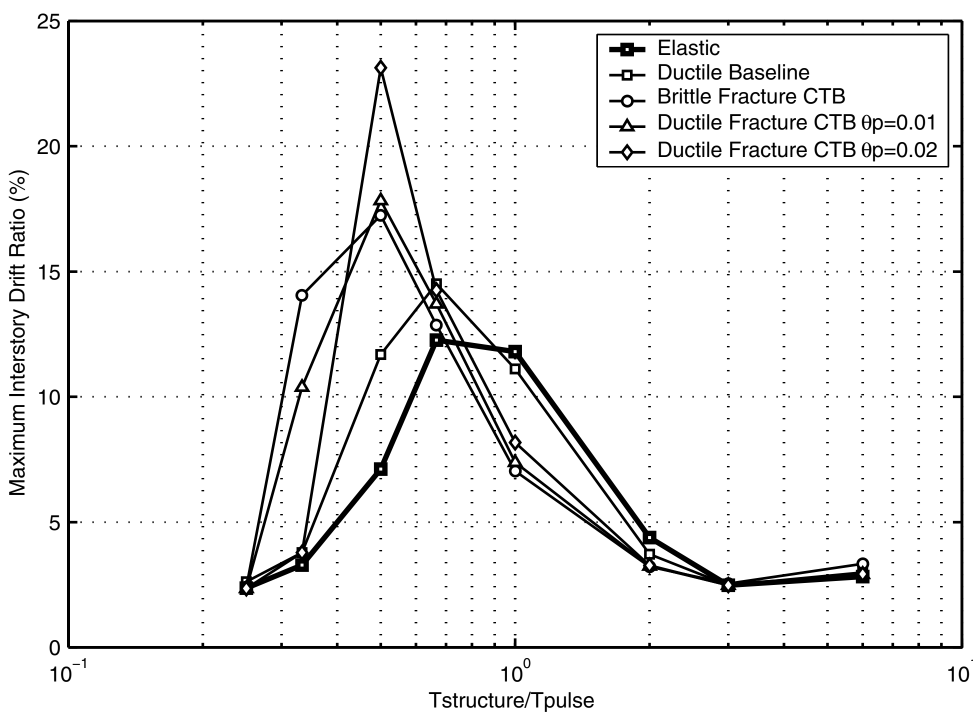

Figure 8-37. Variation of interstory drift w/cosine pulse period, Vp=37.5 in./sec, CTB patterns

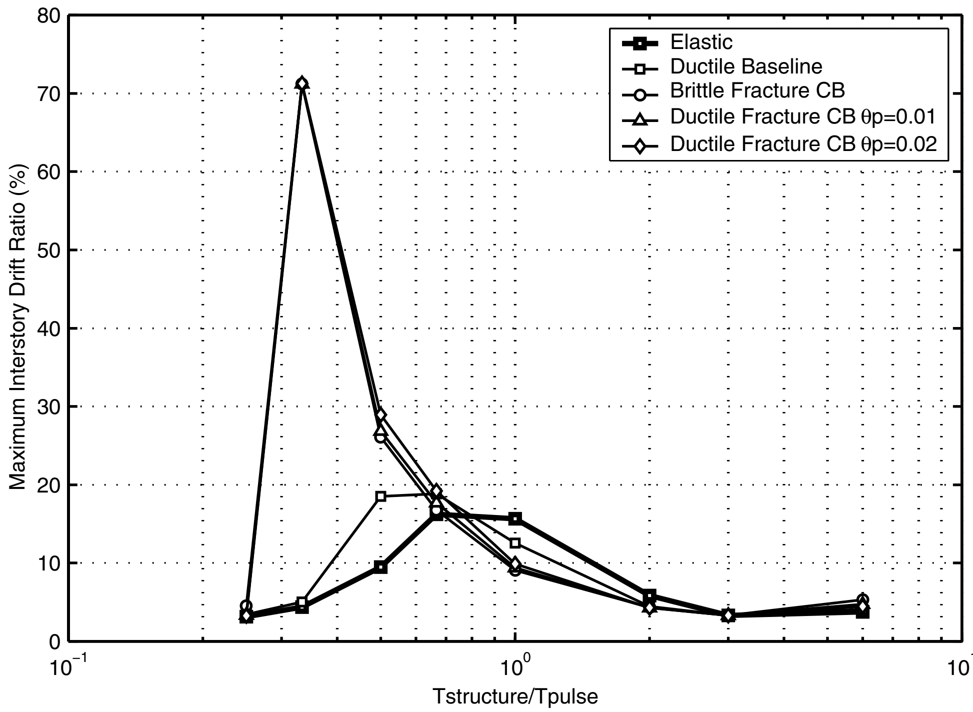

Figure 8-38. Variation of interstory drift w/cosine pulse period, Vp=50 in./sec, CB patterns

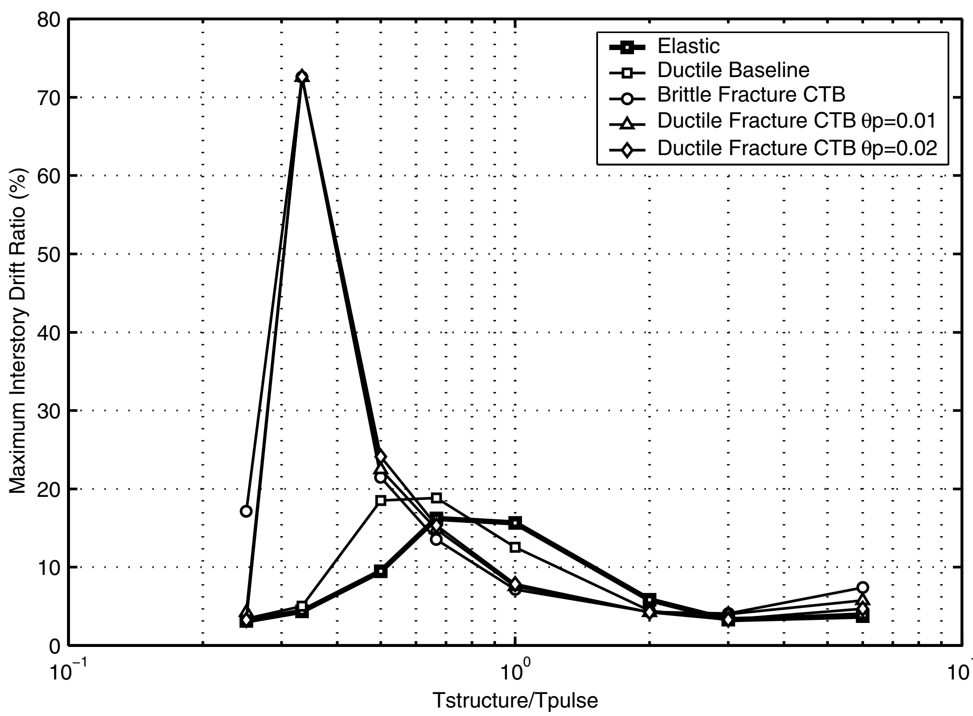

Figure 8-39. Variation of interstory drift w/cosine pulse period, Vp=50 in./sec, CTB patterns

In the case of the test amplitude (Vp = 25 in./sec), the pulse period which causes the largest response is 1.5 times the model's first mode period. As the peak pulse velocity increases, the location where the maximum response is obtained is shifted to the left for the fracturing cases and the pulse period becomes longer and longer with respect to the period of the specimen.

For all of the peak pulse velocities, the fracturing cases cause increased displacement in the region to the left of the peak where the T/T_{pulse} ratio is small. For very small values, however, the behavior of the specimen is elastic and there is no increase. For the 25 in./sec cases, ductile fracture causes larger responses outside this region to the right of the peak. As the peak pulse velocity increases, the region where ductile fracture causes larger response shrinks and becomes approximately the same as the region for brittle fracture.

For all of the peak pulse velocities, there is a region to the right of the peak where brittle fracture actually reduces the displacement response. For the larger peak pulse velocities 1.5 and 2.0 times the test velocity, ductile fractures reduce the response in this region as well. The beneficial effects of fracture appear to increase with severity, as the reduction is larger for the CTB cases than the CB cases.

8.5.2 Earthquake History Excitations

The model was subjected to two suites of earthquake histories which were developed by the SAC Joint Venture (Somerville, 1997) for the Los Angeles area. These two suites of motions were developed for the 10% probability of exceedance in 50 years and 2% probability of exceedance in 50 years seismic hazard levels. These suites of motions are referred to as the SAC LA 10/50 and SAC LA 2/50 suites, respectively.

Median values of IDAs are compared for the SAC LA 10/50 and 2/50 motions in Figures 8-40 and 8-41, respectively. These median values were determined by taking the natural logarithms of the interstory drift values, finding the median, and then taking the exponential of this value to convert back to interstory drift ratio. There was a great deal of scatter in the IDA results, which is shown for the ductile cases in Figures 8-43 and 8-44. Equal or greater amounts of scatter occurred for the fracturing cases as well. Because of this, only general trends will be discussed.

For the 10/50 suite of motions, all of the fracturing patterns cause larger interstory drifts for lower amplitude scale factors than the ductile baseline case. All of the fracture cases except for the brittle fracture cases with best-fit negative post-fracture stiffness have similar IDA curves. This indicates that the response is relatively insensitive to the location and type of fracture unless negative post-fracture stiffness is present.

For the SAC LA 2/50 suite, the ground motions are more severe, and this is reflected in the much earlier onset of collapse for the median values shown in Figure 8-41. Because of this, a set of IDAs with a much finer scale factor discretization is shown for the lower portion of the curve in Figure 8-42.

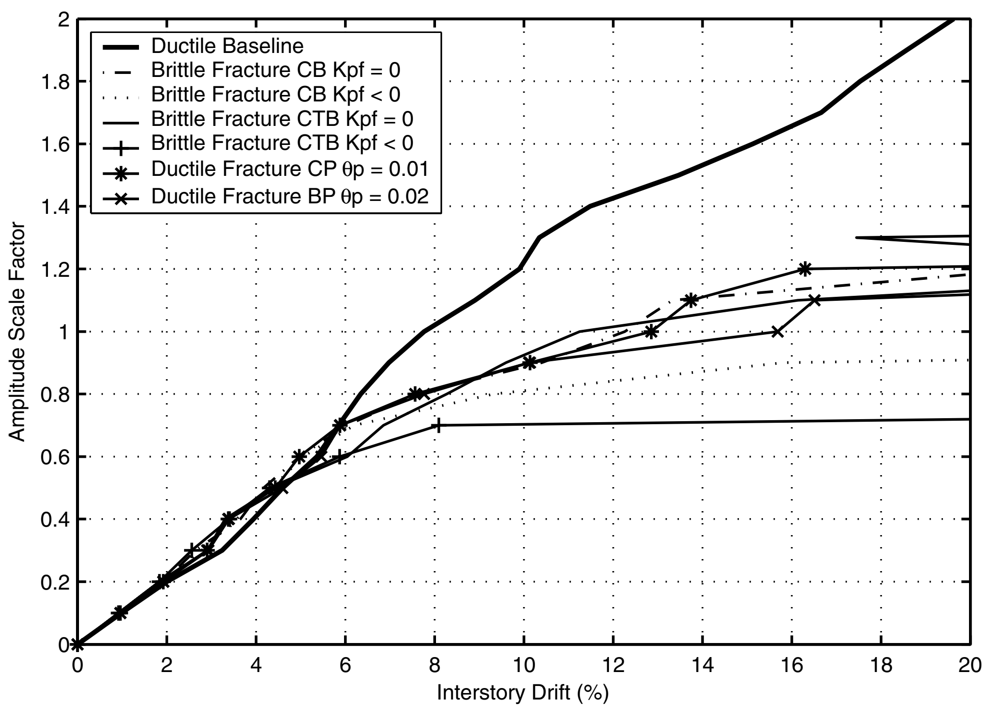

Figure 8-40. Comparison of median IDA values for SAC LA 10/50 suite of motions

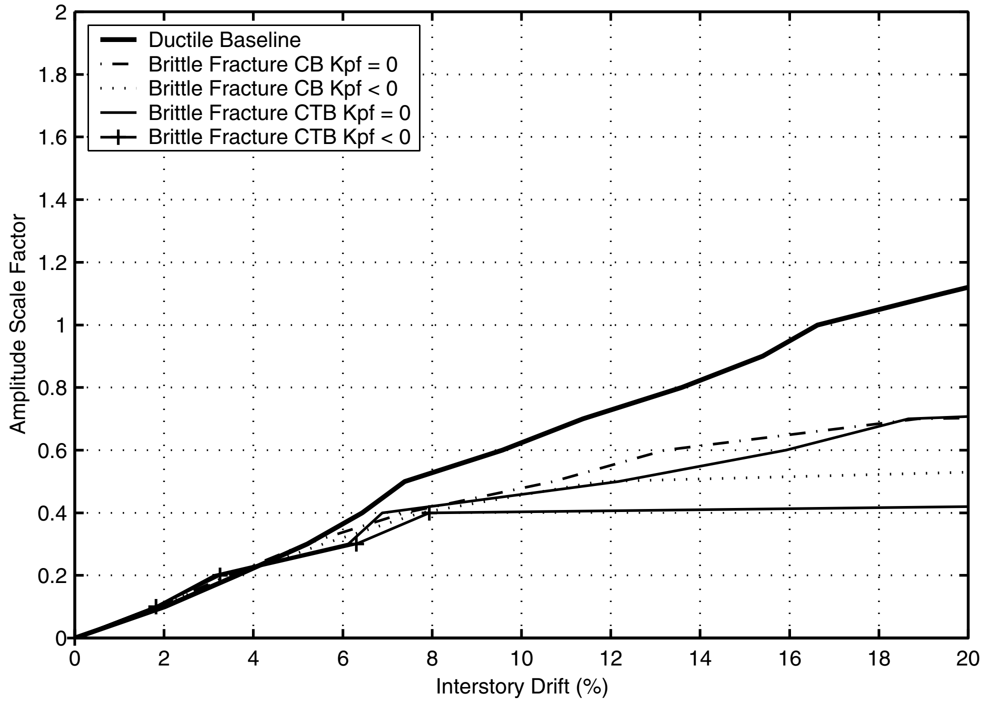

Figure 8-41. Comparison of median IDA values for SAC LA 2/50 suite of motions

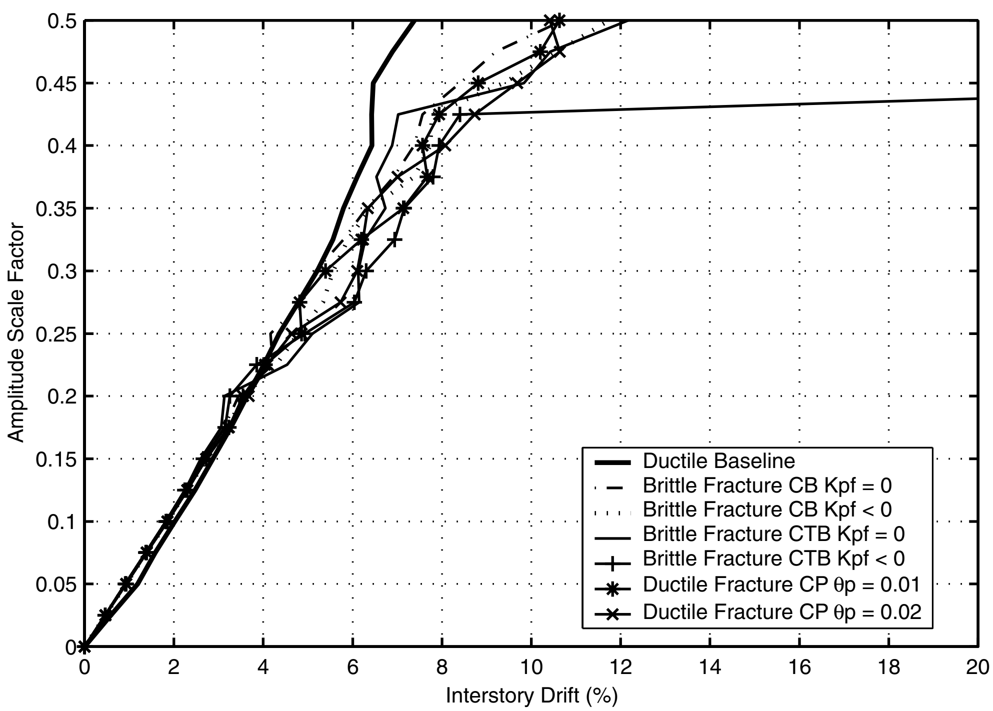

Figure 8-42. Comparison of median IDA values for SAC LA 2/50 suite of motions, high resolution

As shown in Figure 8-42, fractures cause larger drifts than the ductile baseline case for the same amplitude. There is little difference in the shape of the curves, except that the brittle fracture CTB case becomes unstable at lower amplitude than the other fracturing cases do.

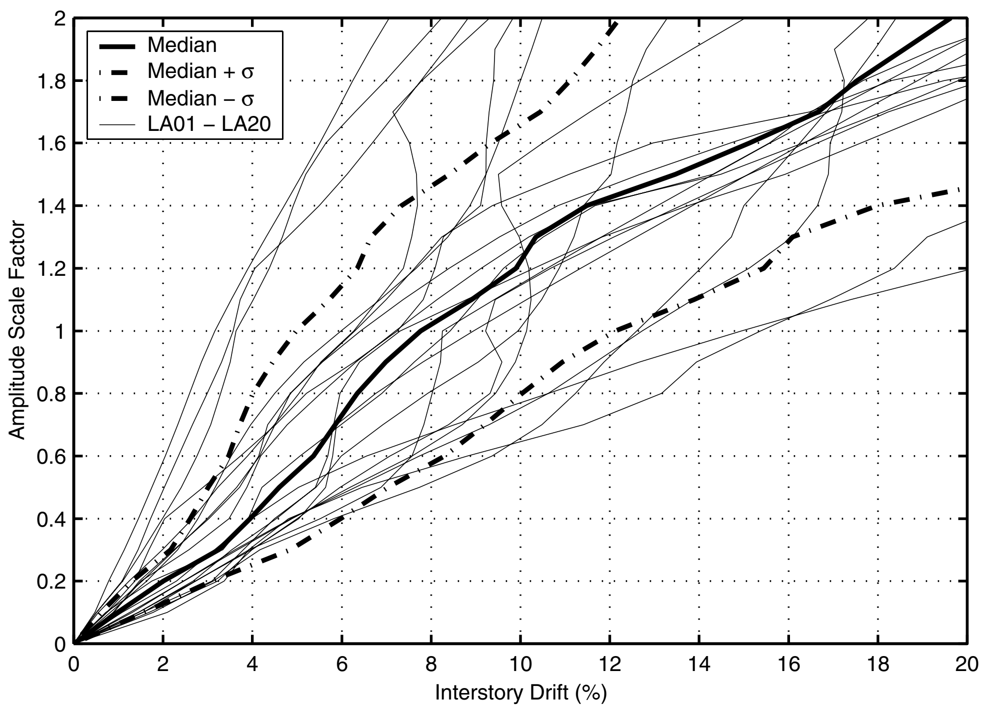

Figure 8-43. IDAs for SAC LA 10/50 suite of motions, ductile baseline case

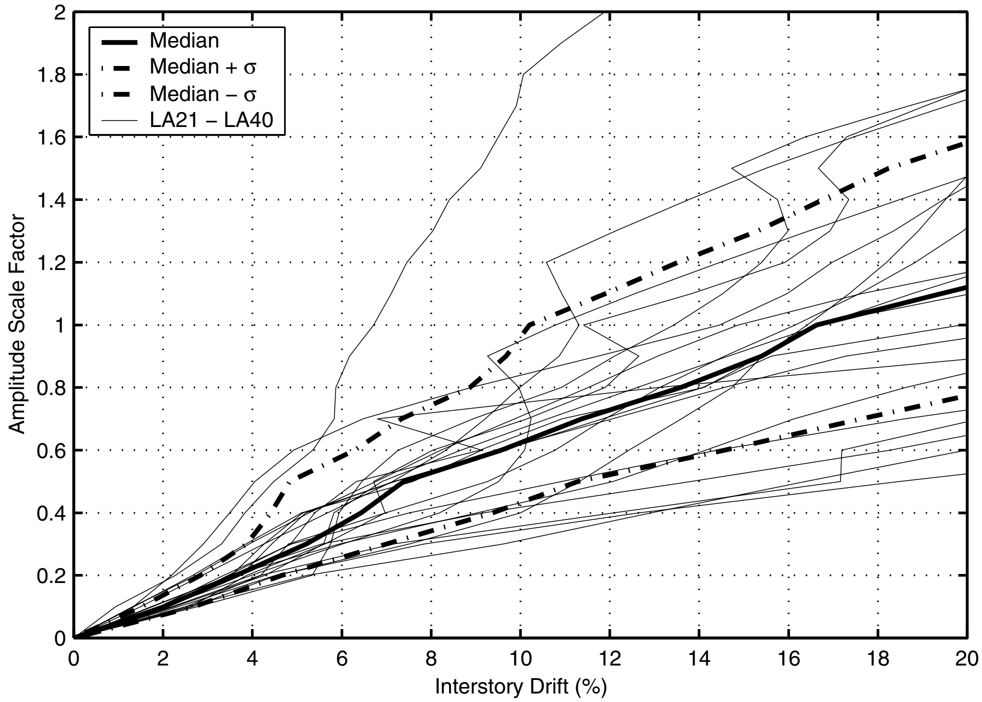

Figure 8-44. IDAs for SAC LA 2/50 suite of motions, ductile baseline case

It should be mentioned here that the test specimen was not designed to conform to the interstory drift requirements set forth in FEMA 273 (FEMA, 1997). Simple interstory drift predictions made using the provisions in FEMA 273 (but neglecting P-Δ effects by setting $C_3 = 1$) indicate that drifts of approximately 5.5% and 11% can be expected for the ductile case for this specimen at the 10% in 50 year and 2% in 50 year earthquake hazard levels, respectively. Since these estimates do not include P-Δ effects, it is not surprising that they are a bit lower than the median values shown in Figures 8-43 and 8-44.

The FEMA evaluation also places the structure in the constant acceleration portion of the elastic pseudo-acceleration spectrum for both 10/50 and 2/50 hazard levels, which corresponds to Newmark's energy-preserved range for an inelastic spectrum. This indicates that strength loss should lead to larger displacements for the patterns with strength degradation, and this is in fact what was observed.

8.6 SUMMARY

Several hysteretic parameters related to the severity of fracture were examined, including post-fracture residual moment capacity, post-fracture tangent stiffness, and amount of plastic rotation prior to fracture. These parameters were all shown to affect the deformation response of the model, but the severity of the effects of these parameters were found to be dependent on number and spatial distribution of fractures as well as excitation amplitude, in addition to the values of the parameters themselves.

Hysteretic degradation parameters that affect system strength, such as residual post-fracture moment capacity, have significant effects on the response in situations where system strength is important to behavior. This occurs in Newmark's short-period and energy-preserved ranges of the response spectrum. These regions of the response spectrum may encompass a larger range of periods for near-field motions than for far-field motions, causing strength to be important for larger numbers of structures.

The effects of strength loss due to fracture as well as ductile forms of degradation are exacerbated if the number of connections with fracture is increased, and the effects can be acute if the strength loss occurs in one direction during a pulse.

The effects of plastic rotation before fracture are mixed. In the case of the 1.2 second cosine pulse, behavior improves with increased plastic rotation prior to fracture. The opposite is true for the 0.6 second pulse, however. Response spectrum position, along with pulse amplitude, may play a role in causing the difference.

For large drifts, the effects of negative post-yield or post-fracture tangent stiffness in the connection hysteresis combine with geometric nonlinearity (P-Δ) effects to force the structure to extreme drifts or collapse. In the cases where there is positive post-yield or post-fracture tangent stiffness in the connection hysteresis, this positive stiffness tends to counteract the effects of geometric nonlinearity, resulting in reduced drift. Therefore, if drifts are to be predicted accurately via analysis, the analytical model must make realistic assumptions about post-yield or post-fracture stiffness, particularly if negative tangent stiffness is likely to occur. The likelihood of this can be estimated using experimental data from beam-column connection tests.

Frame parameters related to stiffness, such as column section stiffness and height, contribute to the elastic flexibility of the frame. Decreases in member stiffness can cause increases in elastic drift demand (depending on period range), thereby potentially increasing the overall maximum drifts for the structure.

The “shock spectra” for the specimen showing the effect of pulse duration indicate that the region where the most adverse effects on the displacement response due to hysteretic degradation occur is dependent on the peak velocity of the pulse. For increasing peak velocity, the most adverse T-structure/T-pulse ratio migrates to shorter and shorter periods. As the aspect ratio of the structure changes, higher-mode effects may also affect the critical value of this ratio. However, this is a topic for further study.

The deformation response is not highly sensitive to amplitude for the test excitations, but instead increases gradually in most cases. The notable exception is the BFCB pattern with the JSE17 excitation, which displays sudden instability with little warning. It is unclear why this is the case.

9 Conclusions and Recommendations for Future Work

9.1 CONCLUSIONS

The objective of this study was to examine the effects of connection hysteretic behavior on the seismic behavior of steel moment frames. This was accomplished by dynamic testing of a frame specimen and analytical simulations. Five types of hysteretic behavior, defined in Section 1.1, were examined. Both the experimental and analytical portions of this study produced results which show that the effects of degradation in connection hysteretic behavior on system response are dependent on several factors. These factors include the region of the response spectrum where the system is located, the type of degradation, the severity of that degradation, and the amplitude of the earthquake excitation.

Based on both the experimental and analytical portions of this study, the following general observations can be made on the effects of brittle fracture on system behavior for the short and intermediate structure period-to-pulse period ($T_{structure}/T_{pulse}$) ranges for pulse excitations:

- global displacements are increased over ductile baseline behavior
- system strength capacity is reduced from pre-fracture levels
- the severity of the effects of fracture is dependent on the number and spatial distribution of fractures as well as the amplitude of the excitation
- the severity of the effects of fracture also depends on various hysteretic characteristics including post-fracture residual moment capacity and post-fracture tangent stiffness
- four local dynamic phenomena caused by fracture were observed experimentally: change of beam deflected shape, propagation of elastic waves, excitation of higher vibration modes in the beam, and local area moment redistribution
- these local fracture-induced phenomena were found to have small effects on the global response in most cases
- analytical models that did not account for these local phenomena were still able to reproduce the system response reasonably well

The following observations can be made from the analytical studies on the effects of structure period-to-pulse period ($T_{structure}/T_{pulse}$) range on behavior of systems with brittle fracture at the top and bottom flanges and bottom flanges only of the connections:

- Brittle fracture adversely affects the system behavior in both cases (top and bottom flange fractures and bottom flange fractures only) by increasing the maximum and residual drifts and causing substantial strength loss, as well as a loss of stiffness which causes period elongation, in the shorter-period “ascending branch” ($T_{structure}/T_{pulse} < 2/3$) of the response spectrum for pulse excitations
- Brittle fracture also matters for both cases in the intermediate period range ($2/3 < T_{structure}/T_{pulse} < 3$) or upper “descending branch” for pulse excitations for the same reasons
- Top and bottom flange fractures cause greater drifts in the short and short-intermediate regions of the spectrum (together $0.25 < T_{structure}/T_{pulse} < 1$) than bottom flanges only
- Neither fracture distribution adversely affects the response in the long-period range ($T_{structure}/T_{pulse} > 3$) for pulse excitations

Based on analytical studies, the effects of ductile fracture (meaning significant plastic rotation occurs prior to fracture) versus brittle fracture are as follows:

- ductile fracture does not provide any advantages or disadvantages over brittle fracture in the long-period range for pulse excitations
- the difference between plastic rotation values of 0.01 and 0.02 radians before fracture has a small effect on the results in the intermediate period range for pulse excitations
- these amounts of plastic rotation (0.01 and 0.02 radians) can cause larger interstory drifts than those for brittle fracture (zero plastic rotation) at low to moderate amplitudes of excitation
- at very large amplitudes of excitation, some amount of plastic rotation, on the order of 0.01 to 0.02 radians, may be beneficial

For deformation softening (i.e., negative post-yield stiffness) in the connection hysteresis, the following observations can be made for the short and intermediate $T_{structure}/T_{pulse}$ ranges:

- global displacements are increased over ductile baseline behavior
- system strength capacity is reduced continually as the specimen becomes nonlinear under loading
- the severity of the effects of deformation softening is dependent on the number of deformation-softening connections as well as the amplitude of the excitation
- the severity of the effect of deformation softening also depends on the post-yield tangent stiffness

- deformation softening can combine with P-Δ effects at large deformations and produce unstable system response

The above findings suggest that attention during the development and acceptance of connections needs to be placed on the tangent slope of the hysteretic curve after yielding as well as on the deformation capacity.

Since the forms of hysteretic degradation examined here all cause strength loss, they were found to have larger effects on the response in the period ranges where strength is important. The reasons for the strength loss were found to be less important than the severity of the strength loss.

Overall, the effects of fracture and other forms of hysteretic degradation range from severe to negligible, depending primarily on period range, severity of degradation, and amplitude of excitation.

9.2 FUTURE WORK

A great deal of potential remains for work in the area of system behavior of moment frames. The series of experiments performed in this study could be extended to consider several other interesting cases:

- allowing both top and bottom flange fractures for ground motion excitations
- varying amounts of negative post-yield stiffness
- varying post-fracture stiffness, particularly negative post-fracture stiffness
- varying plastic rotation capacity prior to fracture
- different rates of strength degradation, particularly increased rates
- additional ground motions

These cases were investigated analytically, but experimental verification of the analytical results is highly desirable.

Also, high-speed data could be collected for more tests, and these data would facilitate understanding of immediate post-fracture phenomena. In addition, the effects of degrading connection behavior for other specimen configurations, particularly taller specimens, should be examined, as should structures with more degrees of freedom (for the purposes of investigating higher mode effects). Efforts should also be made to test full-scale specimens.

The test frame incorporating the idealized mechanical connections has proven to be quite useful and additional studies related to effects of hysteretic shape should be considered, including those associated with partially restrained connections and shape memory alloys. Special details with post-tensioning applied that would tend to reduce residual displacements could also be considered. The frame may also provide a useful repeatable test bed for development of hybrid simulation and active control methods.

Future analytical work includes further investigations on how to define Newmark-esque period ranges for near-fault ground motions and structures with various types of degradation, and finite element analysis to study post-fracture wave propagation and energy dissipation by fracture-induced phenomena.

Understanding the effects of connection hysteretic behavior on system performance is key to developing performance-based engineering methods and practices for steel moment-resisting frame structures. At present, knowledge of the relationship between connection behavior and system behavior is still limited, and thus great potential exists for significant future research in this area.

REFERENCES

AIJ (1995). *Preliminary reconnaissance report of the 1995 Hyogoken-Nanbu earthquake*, English edition, Architectural Institute of Japan, Tokyo, Japan.

AIJ (1995). *Reconnaissance report on damage to steel building structures observed from the 1995 Hyogoken-Nanbu earthquake*, Kinki Branch, Architectural Institute of Japan, Osaka, Japan (in Japanese with attached abridged English version).

AIJ (1997). *Full-scale test on plastic rotation capacity of steel wide-flange beams connected with square tube steel columns*, Kinki Branch, Architectural Institute of Japan, Osaka, Japan (in Japanese with attached abridged English version).

Astaneh-Asl, A., J.-H. Shen, K.M. McMullin, D. Modjtahedi, and E. D'Amore (1998). Stability of damaged steel frames in Los Angeles, *Engineering Structures*, 20(4-6), 433-446.

Barsom, J.M. (1975). Development of the AASHTO fracture-toughness requirements for bridge steels, *Engineering Fracture Mechanics*, 7, 605-618.

Bertero, V. V., et al. (1995). Seismological and engineering aspects of the 1995 Hyogoken-Nanbu (Kobe) earthquake, *Report No. UCB/EERC-95/10*, Earthquake Engineering Research Center, University of California at Berkeley.

Bertero, V.V. (1977). Strength and deformation capacities of buildings under extreme environments, *Structural Engineering and Structural Mechanics*, Prentice-Hall, Englewood Cliffs, New Jersey, 211-215.

Bertero, V.V., J.C. Anderson, and H. Krawinkler (1994). Performance of steel building structures during the Northridge earthquake, *Report No. UCB/EERC-94/09*, Earthquake Engineering Research Center, University of California at Berkeley.

Bonowitz, D. and B.F. Maison (1998). Are steel frames safe? Probabilistic seismic evaluation of existing WSMF buildings, *Proceedings, Sixth U.S. National Conference on Earthquake Engineering, Seattle, Washington*, Earthquake Engineering Research Institute, Oakland, California.

Chopra, A. K. (1995). *Dynamics of structures, theory and applications to earthquake engineering*, Prentice Hall, New Jersey.

Clough, R. and J. Penzien (1993). *Dynamics of structures*, McGraw-Hill, New York.

Engelhardt, M.D. and T.A. Sabol (1994). Testing of welded steel moment connections in response to the Northridge earthquake: progress report to the AISC advisory sub-committee on special moment resisting frame research, *Northridge Steel Update I*, AISC, Chicago, Illinois.

FEMA (1997). NEHRP guidelines for the seismic rehabilitation of buildings, *FEMA-273*, prepared by the SAC Joint Venture for the Federal Emergency Management Agency, Washington, DC.

FEMA (2000). Recommended seismic design criteria for new steel moment frame buildings, *FEMA-350*, prepared by the SAC Joint Venture for the Federal Emergency Management Agency, Washington, DC.

FEMA (2000). State of the art report on connection performance, *FEMA-355D*, prepared by the SAC Joint Venture for the Federal Emergency Management Agency, Washington, DC.

FEMA (2000). State of the art report on past performance of steel moment-frame buildings in earthquakes, *FEMA-355E*, prepared by the SAC Joint Venture for the Federal Emergency Management Agency, Washington, DC.

Foutch, D. A., and S. Shi (1998). Effects of hysteresis types on the seismic response of buildings, *Proceedings, 6th U.S. National Conference on Earthquake Engineering, Seattle, Washington*, Earthquake Engineering Research Institute, Oakland, California.

Foutch, D.A. and S. Shi (1996). *Connection element (type 10) for DRAIN-2DX*, Department of Civil Engineering, University of Illinois, Urbana-Champaign.

Foutch, D.A., and S.-Y. Yun (2002). Modeling of steel moment frames for seismic loads, *Journal of Constructional Steel Research*, 58(5-8), 529-564.

Graff, K. F. (1975). *Wave motion in elastic solids*, Ohio State University Press, Ohio.

Gupta, A. and H. Krawinkler (1999). Prediction of seismic demands for SMRFs with ductile connections and elements, *SAC/BD-99/06*, SAC Joint Venture, Sacramento, California.

Gupta, A. and H. Krawinkler (2000). Seismic demands for performance evaluation of steel moment resisting frame structures (SAC Task 5.4.3), *BLUME-132*, John A. Blume Earthquake Engineering Center, Stanford University, Palo Alto, California.

Hachem, M. (2000). *BiSpec*, Computer program available from NiSEE, University of California at Berkeley.

Hasegawa, T. (2000). Shaking table test on earthquake response behavior of steel moment resisting frames with yielding joint panel, *Journal of Structural and Construction Engineering (Transactions of AIJ)*, 528, 143-149 (in Japanese).

Holmes, W.T. and P. Somers ed. (1995). Northridge earthquake of January 17, 1994 reconnaissance report, volume 2, *Earthquake Spectra*, 11, Supplement C, Earthquake Engineering Research Institute, Oakland, California.

International Conference of Building Officials (1997). *Uniform Building Code*, Los Angeles, California.

Kolsky, H. (1976). The waves generated by brittle fracture in glass, *Transactions of the Society of Rheology*, 20(3), 441-454.

Krawinkler, H. and B. Alavi (1998). Development of improved design procedures for near fault ground motions, *Proceedings, SMIP98 Seminar on Utilization of Strong Motion Data, Oakland, California*, California Strong Motion Instrumentation Program, Sacramento, California.

Krawinkler, H., A. Gupta, R. Medina and N. Luco (2000). Loading histories for seismic performance testing of SMRF components and assemblies, *SAC/BD-00/10*, SAC Joint Venture, Sacramento, California.

Kuwamura, H. and K. Yamamoto (1997). Ductile crack as trigger of brittle fracture in steel, *Journal of Structural Engineering*, 123(6), 729-735.

Lee, K. and D.A. Foutch (2000). Performance prediction and evaluation of special moment frame buildings for seismic loads, *SAC/BD-00/25*, SAC Joint Venture, Sacramento, California.

Lee, K. and D.A. Foutch (2002). Seismic performance evaluation of pre-Northridge steel frame buildings with brittle connections, *Journal of Structural Engineering*, 128(4), 546-555.

Lee, K.-H., B. Stojadinovic, S.C. Goel, A.G. Margarian, J. Choi, A. Wongkaew, B.P. Reyher, and D.-Y. Lee (2000). Parametric tests on unreinforced connections, Vol. I and II, *SAC/BD-00/01 and 01A*, SAC Joint Venture, Sacramento, California.

Lee, S.-J. and L.-W. Lu (1989). Quasi-static tests of scaled model building, *Journal of Structural Engineering*, 115(8), 1895-1916.

Lide, D. R., ed. (1992). *CRC handbook of chemistry and physics*, CRC Press, Boca Raton, Florida.

Luco, N. and C.A. Cornell (1999). The effects of connection fractures on steel moment resisting frame seismic demands and safety: A report on SAC Phase II Task 5.4.6, *SAC-BD/99-03*, SAC Joint Venture, Sacramento, California.

Luco, N. and C.A. Cornell (2000). Effects of connection fractures on SMRF seismic drift demands, *Journal of Structural Engineering*, 126(1), 127-136.

Mahin, S. A. and K. Morishita, (1998). The effect of strength deterioration on the dynamic response of simple systems subjected to impulsive loading, *Proceedings, U.S.-Japan Workshop on Near-field Earthquake Damage in Urban Areas, Honolulu, Hawaii*, published as *EERL 98-01*, Earthquake Engineering Research Laboratory, California Institute of Technology, Pasadena, California.

Maison, B.F. (1992). *PC-ANSR: A computer program for nonlinear structural analysis*, Available from National Information Service for Earthquake Engineering - NISEE/Computer Applications, University of California, Berkeley.

Maison, B.F., and D. Bonowitz (1999). How safe are pre-Northridge WSMFs? A case study of the SAC Los Angeles nine-story building, *Earthquake Spectra*, 15(4), 765-789.

Maison, B.F., and K. Kasai (1997). Analysis of Northridge damaged thirteen-story WSMF building, *Earthquake Spectra*, 13(3), 451-473.

Makris, N. and S.-P. Chang (2000). Effect of viscous, viscoplastic, and friction damping on the response of seismic isolated structures, *Earthquake Engineering and Structural Dynamics*, 29.

Manjoine, M.J. (1944). Influence of rate of strain and temperature on yield stresses of mild steel, *Transactions, ASME*, 66, A211-218.

Mazzoni, et al. (2003). *Open system for earthquake engineering simulation (OpenSees) command language manual*, published online at www.opensees.berkeley.edu.

McKenna, Frank (2003). *OpenSees: Open system for earthquake engineering simulation*, Computer program, available from worldwide web site: www.opensees.berkeley.edu, University of California, Berkeley.

Molina, F. J.; et al. (1999). Bi-directional pseudodynamic test of a full-size three-storey building, *Earthquake Engineering & Structural Dynamics*, 28 (12), 1541-1566.

Naeim, F., K. Skliros, A. M. Reinhorn, and M. V. Sivaselvan, (2000). Effects of hysteretic deterioration characteristics on seismic response of moment resisting steel structures, *SAC/BD-99/18*, SAC Joint Venture, Sacramento, California.

Naeim, F., R.M. Lobo, K. Skliros, and M. Sgambelluri, (1999). Seismic performance of four instrumented steel moment resisting buildings during the January 17, 1994 Northridge earthquake, *Proceedings, SMIP98 Seminar on Utilization of Strong Motion Data, Oakland, California*, California Strong Motion Instrumentation Program, Sacramento, California.

Nakashima, M., C.W Roeder, and Y. Maruoka (2000). Steel moment frames for earthquakes in United States and Japan, *Journal of Structural Engineering*, 126(8), 861-868.

Nakashima, M., K. Inoue, and M. Tada (1998). Classification of damage to steel buildings observed in the 1995 Hyogoken-Nanbu earthquake, *Engineering Structures*, 20(4-6), 271-281.

Nakashima, M., T. Minami, and I. Mitani, (2000). Moment redistribution caused by beam fracture in steel moment frames, *Journal of Structural Engineering*, 126(1), 137-144.

Newmark, N.M. and J.W. Hall (1982). *Earthquake spectra and design*, Earthquake Engineering Research Institute, Oakland, California.

Powell, G.H. (1992). *DRAIN-2DX*, Computer program, available from National Information Service for Earthquake Engineering - NISEE/Computer Applications, University of California, Berkeley.

Rahnama, M. and H. Krawinkler, (1993). Effects of soft soil and hysteresis model on seismic demands, *BLUME-108*, John A. Blume Earthquake Engineering Center, Stanford University, Palo Alto, California.

Ricles, J.M., et al. (2002). Inelastic cyclic testing of welded unreinforced moment connections, *Journal of Structural Engineering*, 128(4), 429-440.

SAC (1995). Technical report: analytical and field investigations of buildings affected by the Northridge earthquake of January 17, 1994, *SAC 95-04*, SAC Joint Venture, Sacramento, California.

SAC (1995). Technical report: surveys and assessment of damage to buildings affected by the Northridge earthquake of January 17, 1994, *SAC 95-06*, SAC Joint Venture, Sacramento, California.

Scott, M.H. and G.L. Fenves (2003). A Krylov subspace accelerated Newton algorithm, *Proceedings, 2003 ASCE Structures Congress, Seattle, Washington*, American Society of Civil Engineers.

Somerville, P. (1997). Development of ground motion time histories for phase 2 of the FEMA/SAC steel project, *SAC-BD/97-04*, SAC Joint Venture, Sacramento, California.

Somerville, P. (1998). Development of an improved ground motion representation for near fault ground motions, *Proceedings, SMIP98 Seminar on Utilization of Strong Motion Data, Oakland, California*, California Strong Motion Instrumentation Program, Sacramento, California.

The Mathworks, Inc. (1999). *MATLAB*, Computer program, available from The Mathworks, Inc., Natick, Massachusetts.

Uetani, K. and H. Tagawa, (2000). Seismic response of steel building frames considering brittle fractures: effects of fracture models and ground motion properties, *Confronting Urban Earthquakes: Report of Fundamental Research on the Mitigation of Urban Disasters Caused by Near-Field Earthquakes*, Kyoto University, 470-473.

Vamvatsikos, D. and C.A. Cornell (2002). Incremental dynamic analysis, *Earthquake Engineering & Structural Dynamics*, 31 (3), 491-514.

Van Dam, M. (2000). Effect of hysteretic degradation on seismic response of steel structures, *M.Eng. Thesis*, University of California at Berkeley.

Youssef, N. F., D. Bonowitz, and J. L. Gross, A survey of steel moment resisting frame buildings affected by the 1994 Northridge earthquake, *NISTIR 5625*, National Institute of Standards and Technology, Gaithersburg, Maryland.

Appendix A: Drawings of Specimen

A complete set of shop drawings were prepared for the steel fabricator, RBJ, Incorporated, by Peter dePavloff. This set of drawings is presented in this appendix. The safety catch cables are not shown in the shop drawings, since they use standard rigging details selected and provided by the fabricator.

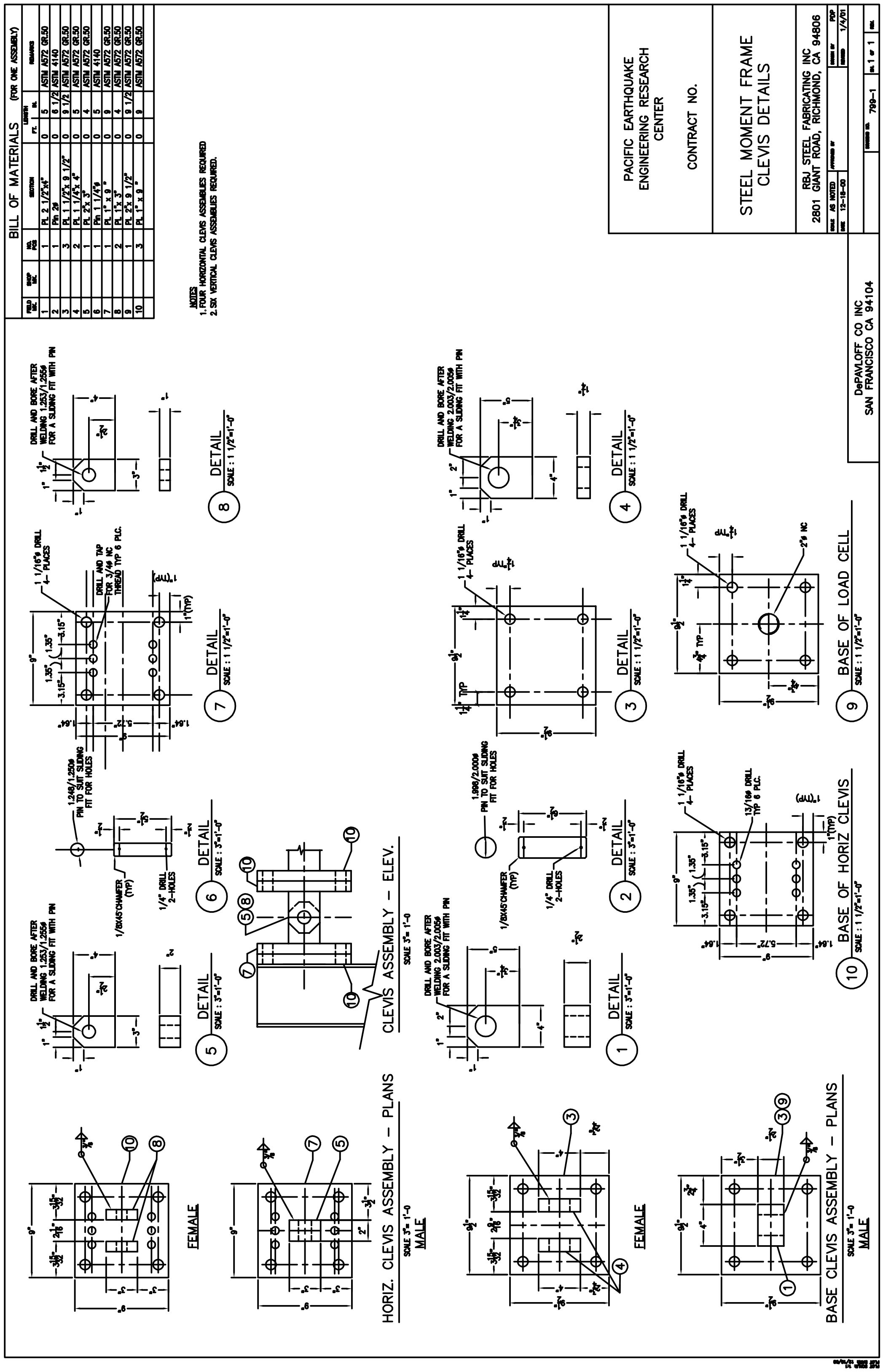
BILL OF MATERIALS (FOR ONE ASSEMBLY)
NOTES
1. FOUR HORIZONTAL CLEVIS ASSEMBLIES REQUIRED
2. SIX VERTICAL CLEVIS ASSEMBLIES REQUIRED.
PACIFIC EARTHQUAKE ENGINEERING RESEARCH CENTER
CONTRACT NO.
STEEL MOMENT FRAME CLEVIS DETAILS
RBJ STEEL FABRICATING INC 2801 GIANT ROAD, RICHMOND, CA 94806
DePAVLOFF CO INC SAN FRANCISCO CA 94104
799-1
HORIZ. CLEVIS ASSEMBLY – PLANS
FEMALE
MALE
CLEVIS ASSEMBLY – ELEV.
BASE CLEVIS ASSEMBLY – PLANS
FEMALE
MALE
DETAIL 1
DETAIL 2
DETAIL 3
DETAIL 4
DETAIL 5
DETAIL 6
DETAIL 7
DETAIL 8
BASE OF LOAD CELL 9
BASE OF HORIZ CLEVIS 10

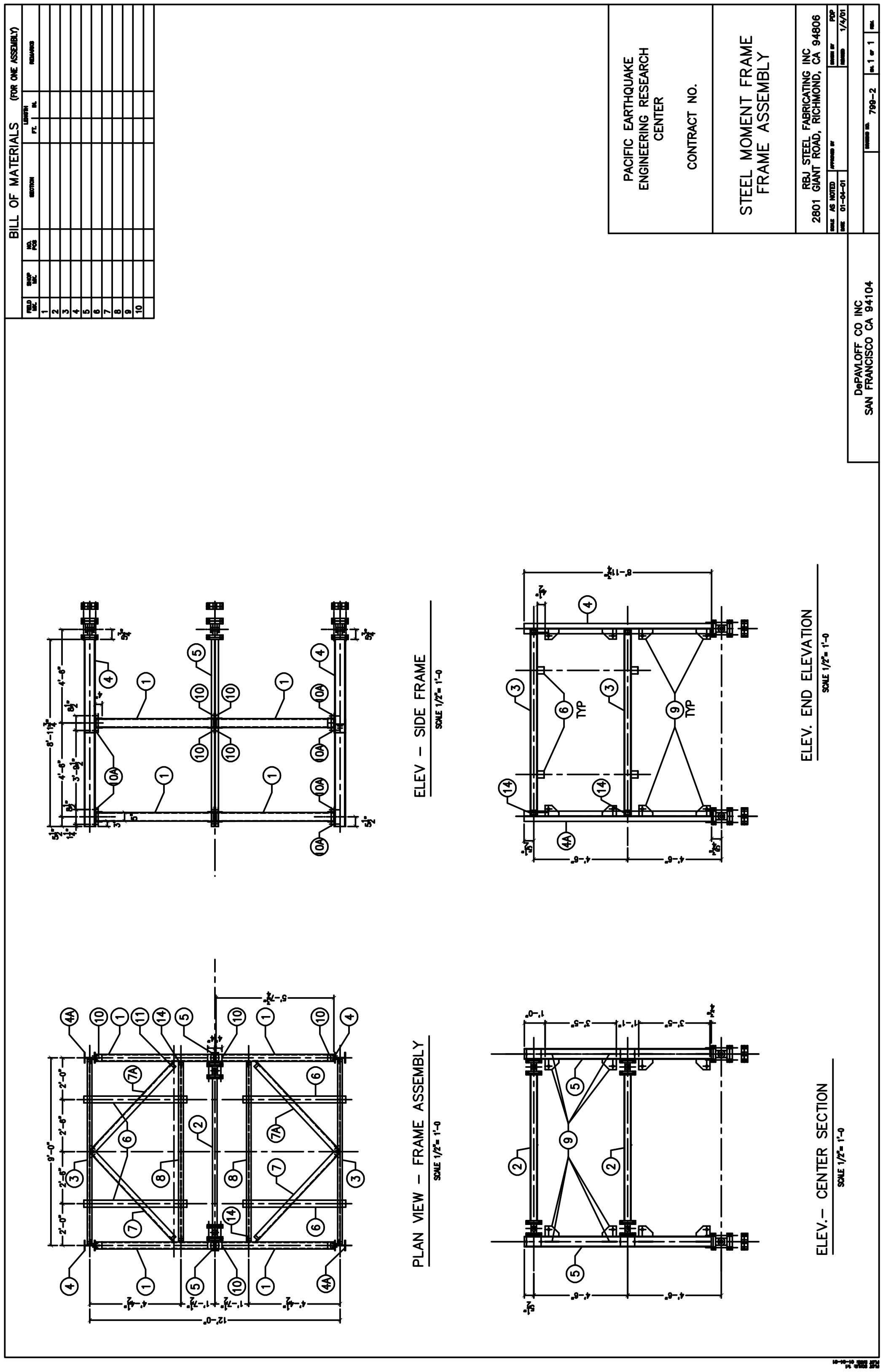
BILL OF MATERIALS (FOR ONE ASSEMBLY)
PLAN VIEW – FRAME ASSEMBLY
SCALE 1/2"= 1'-0
ELEV – SIDE FRAME
SCALE 1/2"= 1'-0
ELEV.– CENTER SECTION
SCALE 1/2"= 1'-0
ELEV. END ELEVATION
SCALE 1/2"= 1'-0
PACIFIC EARTHQUAKE ENGINEERING RESEARCH CENTER
CONTRACT NO.
STEEL MOMENT FRAME
FRAME ASSEMBLY
RBJ STEEL FABRICATING INC
2801 GIANT ROAD, RICHMOND, CA 94806
DePAVLOFF CO INC
SAN FRANCISCO CA 94104
799-2

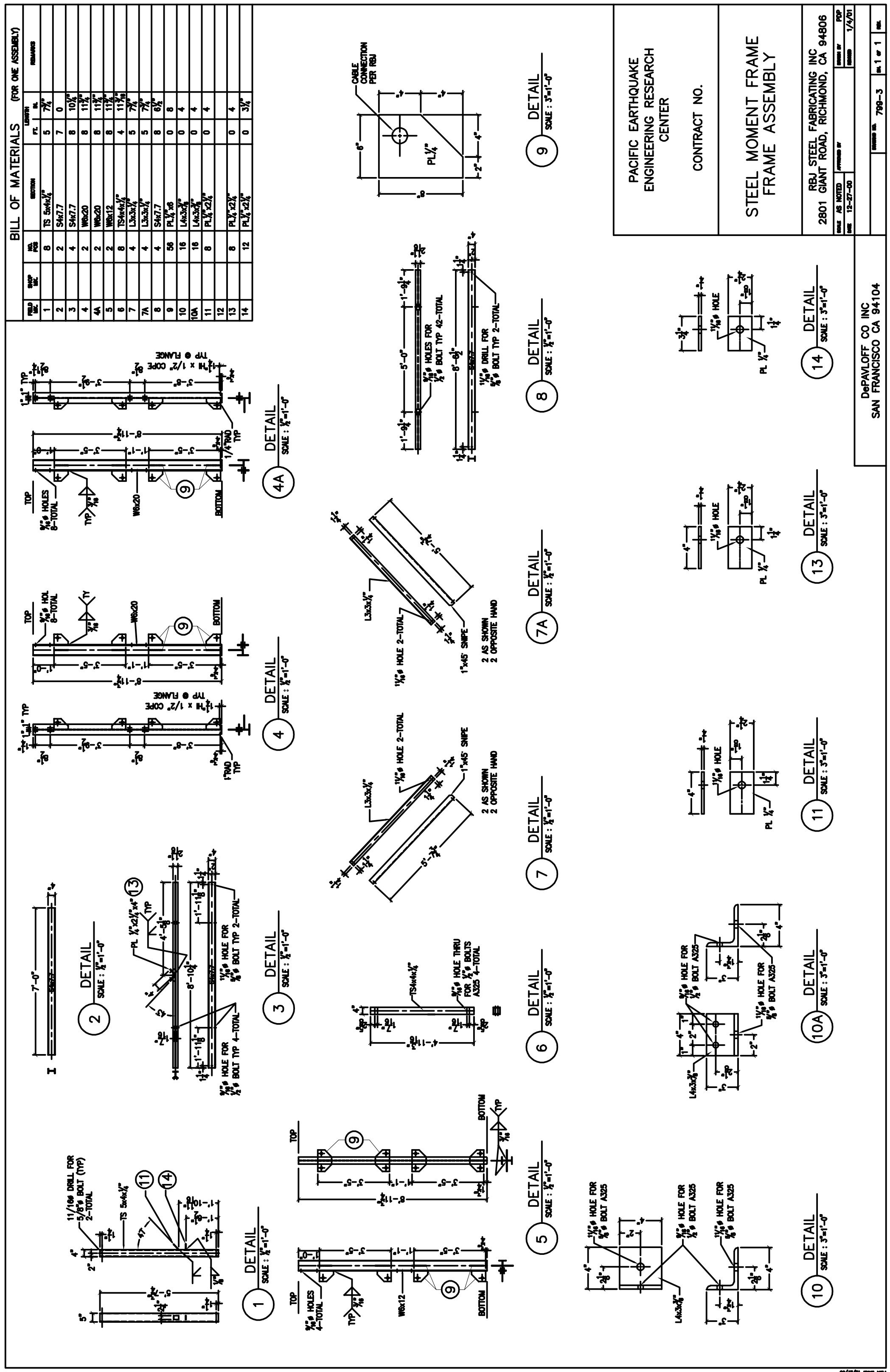
BILL OF MATERIALS (FOR ONE ASSEMBLY)
PACIFIC EARTHQUAKE ENGINEERING RESEARCH CENTER
CONTRACT NO.
STEEL MOMENT FRAME FRAME ASSEMBLY
RBJ STEEL FABRICATING INC
2801 GIANT ROAD, RICHMOND, CA 94806
DePAVLOFF CO INC
SAN FRANCISCO CA 94104
799-3
DETAIL 1
DETAIL 2
DETAIL 3
DETAIL 4
DETAIL 4A
DETAIL 5
DETAIL 6
DETAIL 7
DETAIL 7A
DETAIL 8
DETAIL 9
DETAIL 10
DETAIL 10A
DETAIL 11
DETAIL 13
DETAIL 14

Appendix B: Instrumentation Details

This appendix consists of a list of channels with instrument type and location shown in Table B-1.

Table B-1. List of channels

Channel Number	Transducer Type	Response Quantity	Coord. System and Orientation	Transducer Location
ph 1	-	date	-	-
ph 2	-	time	-	-
1	LVDT	table disp.	global Y	table: H1o stroke
2	LVDT	table disp.	global X	table: H2o stroke
3	LVDT	table disp.	global Y	table: H3o stroke
4	LVDT	table disp.	global X	table: H4o stroke
5	LVDT	table disp.	global Z	table: V1o stroke
6	LVDT	table disp.	global Z	table: V2o stroke
7	LVDT	table disp.	global Z	table: V3o stroke
8	LVDT	table disp.	global Z	table: V4o stroke
9	A	table accel.	global Y	table: H1-2 acc
10	A	table accel.	global X	table: H3-4 acc
11	A	table accel.	global Y	table: H4-1 acc
12	A	table accel.	global X	table: H2-3 acc
13	A	table accel.	global Z	table: 1v acc
14	A	table accel.	global Z	table: 2v acc
15	A	table accel.	global Z	table: 3v acc
16	A	table accel.	global Z	table: 4v acc
17	LC 1	shear	local x	perimeter column 1
18	LC 1	moment	local x	perimeter column 1
19	LC 1	shear	local y	perimeter column 1
20	LC 1	moment	local y	perimeter column 1
21	LC 1	axial load	global Z	perimeter column 1
22	LC2	shear	local x	perimeter column 2

Table B-1. — *Continued*

Channel Number	Transducer Type	Response Quantity	Coord. System and Orientation	Transducer Location
23	LC2	moment	local x	perimeter column 2
24	LC2	shear	local y	perimeter column 2
25	LC2	moment	local y	perimeter column 2
26	LC2	axial load	global Z	perimeter column 2
27	LC4	shear	local x	main column 1
28	LC4	moment	local x	main column 1
29	LC4	shear	local y	main column 1
30	LC4	moment	local y	main column 1
31	LC4	axial load	global Z	main column 1
32	LC 5	shear	local x	main column 2
33	LC 5	moment	local x	main column 2
34	LC 5	shear	local y	main column 2
35	LC 5	moment	local y	main column 2
36	LC 5	axial load	global Z	main column 2
37	LC 6	shear	local x	perimeter column 3
38	LC 6	moment	local x	perimeter column 3
39	LC 6	shear	local y	perimeter column 3
40	LC 6	moment	local y	perimeter column 3
41	LC 6	axial load	global Z	perimeter column 3
42	LC 7	shear	local x	perimeter column 4
43	LC 7	moment	local x	perimeter column 4
44	LC 7	shear	local y	perimeter column 4
45	LC 7	moment	local y	perimeter column 4
46	LC 7	axial load	global Z	perimeter column 4
47	A	frame accel	global X	perimeter column 2 base
48	A	frame accel	global X	main column 2 base
49	A	frame accel	global X	perimeter column 4 base
50	A	frame accel	global X	perimeter column 2 midheight
51	A	frame accel	global X	main column 2 midheight
52	A	frame accel	global X	perimeter column 4 midheight
53	A	frame accel	global X	perimeter column 2 top
54	A	frame accel	global X	main column 2 top
55	A	frame accel	global X	perimeter column 4 top
56	A	frame accel	global Y	perimeter column 1 base

Table B-1. — *Continued*

Channel Number	Transducer Type	Response Quantity	Coord. System and Orientation	Transducer Location
57	A	frame accel	global Y	perimeter column 2 base
58	A	frame accel	global Y	perimeter column 1 midheight
59	A	frame accel	global Y	midspan 1st story perimeter beam
60	A	frame accel	global Y	perimeter column 2 midheight
61	A	frame accel	global Y	perimeter column 1 top
62	A	frame accel	global Y	midspan 2nd story perimeter beam
63	A	frame accel	global Y	perimeter column 2 top
64	A	frame accel	global Z	midspan 1st story main beam (MB1)
65	A	frame accel	global Z	midspan 2nd story main beam (MB2)
66	SG	beam strain	local x	L (East) end story 1 main beam T flange
67	SG	beam strain	local x	L (East) end story 1 main beam T flange
68	SG	beam strain	local x	L (East) end story 1 main beam B flange
69	SG	beam strain	local x	L (East) end story 1 main beam B flange
70	SG	beam strain	local x	R (West) end story 1 main beam T flange
71	SG	beam strain	local x	R (West) end story 1 main beam T flange
72	SG	beam strain	local x	R (West) end story 1 main beam B flange
73	SG	beam strain	local x	R (West) end story 1 main beam B flange
74	SG	beam strain	local x	L (East) end story 2 main beam T flange
75	SG	beam strain	local x	L (East) end story 2 main beam T flange
76	SG	beam strain	local x	L (East) end story 2 main beam B flange
77	SG	beam strain	local x	L (East) end story 2 main beam B flange
78	SG	beam strain	local x	R (West) end story 2 main beam T flange
79	SG	beam strain	local x	R (West) end story 2 main beam T flange
80	SG	beam strain	local x	R (West) end story 2 main beam B flange
81	SG	beam strain	local x	R (West) end story 2 main beam B flange
82	SG	column strain	local x	bottom main column 1 outside flange
83	SG	column strain	local x	bottom main column 1 inside flange
84	SG	column strain	local x	lower mid main column 1 outside flange
85	SG	column strain	local x	lower mid main column 1 inside flange
86	SG	column strain	local x	upper mid main column 1 outside flange
87	SG	column strain	local x	upper mid main column 1 inside flange
88	SG	column strain	local x	top main column 1 outside flange
89	SG	column strain	local x	top main column 1 inside flange
90	SG	column strain	local x	bottom main column 2 outside flange

Table B-1. — *Continued*

Channel Number	Transducer Type	Response Quantity	Coord. System and Orientation	Transducer Location
91	SG	column strain	local x	bottom main column 2 inside flange
92	SG	column strain	local x	lower mid main column 2 outside flange
93	SG	column strain	local x	lower mid main column 2 inside flange
94	SG	column strain	local x	upper mid main column 2 outside flange
95	SG	column strain	local x	upper mid main column 2 inside flange
96	SG	column strain	local x	top main column 2 outside flange
97	SG	column strain	local x	top main column 2 inside flange
98	SG	column strain	local x	bottom perimeter column 2 outside flange
99	SG	column strain	local x	bottom perimeter column 2 inside flange
100	SG	column strain	local x	lower mid perimeter col. 2 outside flange
101	SG	column strain	local x	lower mid perimeter column 2 inside flange
102	SG	column strain	local x	upper mid perimeter col. 2 outside flange
103	SG	column strain	local x	upper mid perimeter column 2 inside flange
104	SG	column strain	local x	top perimeter column 2 outside flange
105	SG	column strain	local x	top perimeter column 2 inside flange
106	SR	beam strain	local x’	L (East) end story 1 main beam web
107	SR	beam strain	local y’	L (East) end story 1 main beam web
108	SR	beam strain	local x’	R (West) end story 1 main beam web
109	SR	beam strain	local y’	R (West) end story 1 main beam web
110	SR	beam strain	local x’	L (East) end story 2 main beam web
111	SR	beam strain	local y’	L (East) end story 2 main beam web
112	SR	beam strain	local x’	R (West) end story 2 main beam web
113	SR	beam strain	local y’	R (West) end story 2 main beam web
114	SR	column strain	avg of local x’, y’	bottom main column 1 web
115	SR	column strain	avg of local x’, y’	lower mid main column 1 web
116	SR	column strain	avg of local x’, y’	upper mid main column 1 web
117	SR	column strain	avg of local x’, y’	top main column 1 web
118	SR	column strain	avg of local x’, y’	bottom main column 2 web
119	SR	column strain	avg of local x’, y’	lower mid main column 2 web
120	SR	column strain	avg of local x’, y’	upper mid main column 2 web
121	SR	column strain	avg of local x’, y’	top main column 2 web
122	SR	column strain	avg of local x’, y’	bottom perimeter column 2 web
123	SR	column strain	avg of local x’, y’	lower mid perimeter column 2 web
124	SR	column strain	avg of local x’, y’	upper mid perimeter column 2 web

Table B-1. — *Continued*

Channel Number	Transducer Type	Response Quantity	Coord. System and Orientation	Transducer Location
125	SR	column strain	avg of local x’, y’	top perimeter column 2 web
126	open	-	-	-
127	open	-	-	-
128	open	-	-	-
129	30" LP	frame disp	global X	perimeter column 2 base
130	30" LP	frame disp	global X	main column 2 base
131	30" LP	frame disp	global X	perimeter column 4 base
132	30" LP	frame disp	global X	perimeter column 2 midheight
133	30" LP	frame disp	global X	main column 2 lower midheight
134	30" LP	frame disp	global X	main column 2 upper midheight
135	30" LP	frame disp	global X	perimeter column 4 midheight
136	30" LP	frame disp	global X	perimeter column 2 top
137	30" LP	frame disp	global X	main column 2 top
138	30" LP	frame disp	global X	perimeter column 4 top
139	15" LP	frame disp	global Y	perimeter column 1 base
140	15" LP	frame disp	global Y	perimeter column 2 base
141	15" LP	frame disp	global Y	perimeter column 1 midheight
142	15" LP	frame disp	global Y	midspan 1st story perimeter beam
143	15" LP	frame disp	global Y	perimeter column 2 midheight
144	30" LP	frame disp	global Y	perimeter column 1 top
145	30" LP	frame disp	global Y	midspan 2nd story perimeter beam
146	30" LP	frame disp	global Y	perimeter column 2 top
147	2" DCDT	clevis disp	local x	top of clevis 1 (E end story 1)
148	2" DCDT	clevis disp	local x	bottom of clevis 1 (E end story 1)
149	2" DCDT	clevis disp	local x	top of clevis 2 (W end story 1)
150	2" DCDT	clevis disp	local x	bottom of clevis 2 (W end story 1)
151	2" DCDT	clevis disp	local x	top of clevis 3 (E end story 2)
152	2" DCDT	clevis disp	local x	bottom of clevis 3 (E end story 2)
153	2" DCDT	clevis disp	local x	top of clevis 4 (W end story 2)
154	2" DCDT	clevis disp	local x	bottom of clevis 4 (W end story 2)
155	60" LP	frame disp	global X	perimeter column 2 top
156	60" LP	frame disp	global X	perimeter column 4 top

Appendix C: Testing Program Details

A listing of the tests performed, together with span settings, file names, and other test run information is provided in this appendix.

Table C-1. Test log

Date	Data file name	Configuration	Signal/Test type	Span	a_{gmax} (g)
22-May	010522160413	-	Load cell	-	-
	010522162415	-	Load cell	-	-
	010523085146	-	Load cell	-	-
	010523092620	-	Load cell	-	-
	010523093601	-	Load cell	-	-
23-May	010523155612	DB C	Stiffness pull	-	-
	010523161034	DB C	Snapback	-	-
	010523162601	DB C	Stiffness pull	-	-
	010523162853	DB C	Snapback	-	-
24-May	010524102127	DB C	Stiffness pull	-	-
	010524102352	DB C	Snapback	-	-
	010524103223	DB C	Stiffness pull	-	-
	010524103520	DB C	Snapback	-	-
	010524140833	DB C	Stiffness pull	-	-
	010524141034	DB C	Snapback	-	-
	010524142831	DB C	Stiffness pull	-	-
	010524143151	DB C	Snapback	-	-
	010524160237	DB C	White noise	5	0.06
	010524162648	DB C	JPULSE06	25	0.034
	010524163714	DB C	JPULSE06	500	0.678
25-May	010525084643	BF B P	Stiffness pull	-	-
	010525084955	BF B P	Snapback	-	-
	010525090057	BF B P	Stiffness pull	-	-

Table C-1. — *Continued*

Date	Data file name	Configuration	Signal/Test type	Span	a_{gmax} (g)
	010525090427	BF B P	Snapback	-	-
	010525092932	BF B P	Stiffness pull	-	-
	010525093227	BF B P	Snapback	-	-
	010525102543	BF B P	White noise	5	0.06
	010525103705	BF B P	JPULSE06	500	0.678
	010525144701	BF B P	White noise	5	0.06
	010525150159	BF B P	JPULSE06	500	0.678
	010525171435	BF C P	Stiffness pull	-	-
	010525171659	BF C P	Snapback	-	-
	010525172442	BF C P	Stiffness pull	-	-
	010525172838	BF C P	Snapback	-	-
	010525175636	BF C P	White noise	5	0.06
	010525183200	BF C P	JPULSE06	500	0.678
29-May	010529103823	DF B P	Stiffness pull	-	-
	010529104105	DF B P	Snapback	-	-
	010529104827	DF B P	Stiffness pull	-	-
	010529105019	DF B P	Snapback	-	-
	010529111320	DF B P	White noise	5	0.06
	010529112558	DF B P	JPULSE06	500	0.678
	010529144224	DF C P	Stiffness pull	-	-
	010529144544	DF C P	Snapback	-	-
	010529145024	DF C P	Stiffness pull	-	-
	010529145436	DF C P	Snapback	-	-
	010529151343	DF C P	White noise	5	0.06
	010529152221	DF C P	JPULSE06	500	0.678
	010529174551	DFS B	Stiffness pull	-	-
	010529174846	DFS B	Snapback	-	-
	010529180210	DFS B	Stiffness pull	-	-
	010529180445	DFS B	Snapback	-	-
	010529181913	DFS B	White noise	5	0.06
	010529182334	DFS B	JPULSE06	500	0.678
30-May	010530093524	DFS C	Stiffness pull	-	-
	010530093800	DFS C	Snapback	-	-
	010530094303	DFS C	Stiffness pull	-	-
	010530094531	DFS C	Snapback	-	-

Table C-1. — *Continued*

Date	Data file name	Configuration	Signal/Test type	Span	a_{gmax} (g)
	010530100023	DFS C	White noise	5	0.06
	010530101108	DFS C	JPULSE06	500	0.678
	010530130952	DB C	Stiffness pull	-	-
	010530131228	DB C	Snapback	-	-
	010530133520	DB C	White noise	5	0.06
	010530134158	DB C	JPULSE12	1000	0.339
	010530155357	BF B P	White noise	5	0.06
	010530160557	BF B P	JPULSE12	1000	0.339
	010530180004	BF C P	White noise	5	0.06
	010530181413	BF C P	JPULSE12	1000	0.339
31-May	010531100257	DF B P	White noise	5	0.06
	010531101731	DF B P	JPULSE12	1000	0.339
	010531131645	DF C P	White noise	5	0.06
	010531132607	DF C P	JPULSE12	1000	0.339
	010531155243	DFS B	White noise	5	0.06
	010531170616	DFS B	JPULSE12	1000	0.339
1-June	010601090926	DFS C	White noise	5	0.06
	010601091124	DFS C	White noise	5	0.06
	010601092502	DFS C	JPULSE12	1000	0.339
	010601115325	BF C B	White noise	5	0.06
	010601120814	BF C B	JNF01	954	0.836
	010601132702	BF C B	White noise	5	0.06
	010601144554	BF C B	White noise	5	0.06
	010601145503	BF C B	JPULSE12	1000	0.339
	010601163012	BF B B	White noise	5	0.06
	010601164220	BF B B	JNF01	954	0.836
	010601174432	DF C B	White noise	5	0.06
	010601175543	DF C B	JNF01	954	0.836
	010604151508	DFS C	White noise	5	0.06
	010604153825	DFS C	JNF01	954	0.836
	010604171729	DB C	White noise	5	0.06
	010604172829	DB C	JNF01	954	0.836
5-June	010605090747	SD C	Stiffness pull	-	-
	010605091024	SD C	Snapback	-	-
	010605091700	SD C	Stiffness pull	-	-

Table C-1. — *Continued*

Date	Data file name	Configuration	Signal/Test type	Span	a_{gmax} (g)
	010605091903	SD C	Snapback	-	-
	010605095840	SD C	White noise	5	0.06
	010605100730	SD C	JSE17	685	1.77
	010605114457	BF C P	White noise	5	0.06
	010605120625	BF C P	JPULSE12	500	0.170
	010605120901	BF C P	JPULSE12	750	0.254
	010605132324	BF C B	White noise	5	0.06
	010605133243	BF C B	JSE17	685	1.77
	010605160701	DB C	White noise	5	0.06
	010605162243	DB C	JSE17	685	1.77
	010605174843	BF A	White noise	5	0.06
	010605180155	BF A	JPULSE6	250	0.339
6-June	010606094756	BF A	White noise	5	0.06
	010606102635	BF A	JPULSE6	250	0.339
	010606120248	BF A	White noise	5	0.06
	010606121220	BF A	JPULSE6	250	0.339
	010606143434	BF A	White noise	5	0.06
	010606144314	BF A	JPULSE6	250	0.339
	010606172348	BF A	White noise	5	0.06
	010606173249	BF A	JPULSE6	250	0.339
	010606180837	BF B P	White noise	5	0.06
	010606181206	BF B P	JPULSE6	250	0.339

Appendix D: Data Summary Tables

A tabular summary of the data obtained from the 32 high-level shaking table tests is presented in this appendix. This summary consists of maximum values of all response quantities of interest, and residual values of selected response quantities such as interstory drift and connection rotation. The tables are organized by response quantity.

Table D-1. Summary of in-plane displacements

Excitation	Pattern	Maximum D_{Table} (in)	Maximum $D_{Rel\ base}$ (in)	Maximum $D_{Rel\ Story1}$ (in)	Maximum $D_{Rel\ Story2}$ (in)	Residual $D_{Rel\ Story1}$ (in)	Residual $D_{Rel\ Story2}$ (in)
0.6 sec cosine pulse	DB C	2.45	0.73	4.69	9.12	2.08	4.12
	BF BP 1	2.45	0.84	5.47	10.74	3.78	7.44
	BF BP 2	2.45	0.82	5.33	10.42	3.43	6.77
	DF BP	2.44	0.82	5.43	10.66	3.65	7.20
	DFS B	2.44	0.72	4.71	9.20	2.81	5.56
	BF CP *	2.43	1.14	7.01	13.69	6.40	12.62
	DF CP *	2.46	1.11	7.23	14.18	6.70	13.22
	DFS C *	2.44	0.92	6.03	11.89	5.76	11.35
	BF A A	1.22	0.33	2.10	4.04	0.13	0.26
	BF A B	1.20	0.33	2.12	4.08	0.12	0.24
	BF A C	1.21	0.34	2.11	4.03	0.08	0.14
	BF A D	1.21	0.34	2.14	4.10	0.09	0.19
	BF A E	1.23	0.33	2.13	4.11	0.10	0.21
	BF BP H	1.21	0.37	2.32	4.46	0.35	0.70

Table D-1. — *Continued*

Excitation	Pattern	Maximum D_{Table} (in)	Maximum $D_{Rel\ base}$ (in)	Maximum $D_{Rel\ Story1}$ (in)	Maximum $D_{Rel\ Story2}$ (in)	Residual $D_{Rel\ Story1}$ (in)	Residual $D_{Rel\ Story2}$ (in)
1.2 sec cosine pulse	DB C	4.98	0.63	3.59	6.89	0.22	0.44
	BF BP	4.97	0.90	5.73	11.16	2.25	4.43
	DF BP	4.96	0.84	5.11	9.92	1.43	2.80
	DFS B	4.97	0.87	5.75	11.25	1.50	3.01
	BF CP 1 *	4.95	1.62	10.00	19.59	9.12	17.98
	BF CP 2	2.46	0.29	1.53	2.89	0.09	0.18
	BF CP 3	3.73	1.06	6.86	13.50	6.50	12.88
	BF CB	4.98	0.89	5.50	10.79	1.89	3.76
	DF CP *	4.97	1.63	10.13	19.98	9.28	18.34
	DFS C *	4.97	1.62	10.20	20.02	9.36	18.46
JNF01 (Tabas)	DB C	4.69	0.44	2.69	5.22	0.50	1.01
	BF BB	4.70	0.44	2.79	5.41	0.44	0.90
	BF CB	4.69	0.45	2.68	5.20	0.21	0.43
	DF CB	4.72	0.42	2.72	5.31	0.37	0.75
	DFS C	4.71	0.38	2.36	4.65	-1.48	-2.89
JSE17 (Llolleo)	DB C	3.31	0.54	3.47	6.82	1.07	2.17
	BF CB	3.33	0.65	4.37	8.75	-2.23	-4.43
	SD C	3.30	0.57	3.67	7.22	1.45	2.90
Statistical values:							
Maximum *		4.98	1.63	10.20	20.02	9.36	18.46
Minimum		1.20	0.29	1.53	2.89	0.08	0.14
Mean *		3.32	0.73	4.62	9.04	2.42	4.79
Median *		3.31	0.69	4.53	8.94	1.44	2.85
Standard deviation *		1.45	0.39	2.44	4.82	3.14	6.20

* Catch cables engaged — values compromised

Table D-2. Summary of maximum in-plane displacement differences

Excita-tion	Pattern	Table	Base			Top of Story 1			Top of Story 2		
			MC2-PC2	PC4-MC2	PC4-PC2	MC2-PC2	PC4-MC2	PC4-PC2	MC2-PC2	PC4-MC2	PC4-PC2
		(in)	(in)	(in)	(in)	(in)	(in)	(in)	(in)	(in)	(in)
0.6 sec cosine pulse	DB C	0.28	0.12	0.09	0.18	0.15	0.21	0.35	0.46	0.65	0.65
	BF BP 1	0.23	0.12	0.10	0.15	0.13	0.12	0.24	0.33	0.45	0.43
	BF BP 2	0.25	0.11	0.10	0.14	0.14	0.15	0.20	0.35	0.38	0.34
	DF BP	0.26	0.13	0.09	0.17	0.18	0.13	0.23	0.31	0.43	0.37
	DFS B	0.29	0.11	0.11	0.15	0.16	0.13	0.22	0.29	0.37	0.40
	BF CP *	0.29	0.09	0.10	0.16	0.12	0.18	0.18	0.31	0.25	0.25
	DF CP *	0.25	0.10	0.11	0.17	0.13	0.14	0.14	0.21	0.43	0.35
	DFS C *	0.28	0.12	0.09	0.17	0.19	0.09	0.25	0.23	0.37	0.45
	BF A A	0.17	0.08	0.09	0.13	0.08	0.11	0.18	0.25	0.23	0.12
	BF A B	0.16	0.06	0.13	0.16	0.11	0.14	0.24	0.34	0.27	0.15
	BF A C	0.23	0.11	0.10	0.18	0.09	0.11	0.17	0.42	0.35	0.27
	BF A D	0.19	0.09	0.10	0.15	0.10	0.10	0.18	0.43	0.33	0.27
	BF A E	0.15	0.11	0.12	0.17	0.12	0.12	0.23	0.45	0.35	0.28
	BF BP H	0.19	0.09	0.08	0.16	0.09	0.09	0.17	0.41	0.32	0.23
1.2 sec cosine pulse	DB C	0.39	0.19	0.19	0.31	0.22	0.15	0.35	0.54	0.55	0.49
	BF BP	0.41	0.19	0.21	0.33	0.18	0.21	0.34	0.41	0.52	0.47
	DF BP	0.49	0.21	0.23	0.37	0.27	0.27	0.53	0.53	0.58	0.72
	DFS B	0.49	0.23	0.21	0.42	0.16	0.27	0.39	0.47	0.45	0.50
	BF CP 1*	0.45	0.24	0.18	0.35	0.64	0.27	0.89	1.05	0.71	1.74
	BF CP 2	0.31	0.18	0.18	0.32	0.14	0.13	0.26	0.25	0.13	0.17
	BF CP 3	0.30	0.12	0.12	0.17	0.14	0.15	0.19	0.25	0.13	0.20
	BF CB	0.37	0.14	0.23	0.32	0.16	0.24	0.36	0.39	0.27	0.27
	DF CP *	0.35	0.18	0.20	0.25	0.53	0.24	0.65	0.72	0.53	1.24
	DFS C *	0.39	0.19	0.19	0.33	0.31	0.39	0.48	0.36	0.59	0.93
NF01 (Tabas)	DB C	0.36	0.17	0.15	0.28	0.19	0.16	0.34	0.49	0.24	0.32
	BF BB	0.34	0.11	0.17	0.21	0.17	0.20	0.30	0.38	0.27	0.19
	BF CB	0.35	0.18	0.16	0.27	0.22	0.18	0.32	0.46	0.30	0.19
	DF CB	0.27	0.13	0.18	0.23	0.19	0.16	0.30	0.46	0.28	0.25
	DFS C	0.36	0.16	0.14	0.27	0.19	0.16	0.31	0.36	0.21	0.19

Table D-2. — *Continued*

Excitation	Pattern	Table	Base			Top of Story 1			Top of Story 2		
			MC2-PC2	PC4-MC2	PC4-PC2	MC2-PC2	PC4-MC2	PC4-PC2	MC2-PC2	PC4-MC2	PC4-PC2
		(in)	(in)	(in)	(in)	(in)	(in)	(in)	(in)	(in)	(in)
SE17 (Llolleo)	DB C	0.18	0.11	0.14	0.18	0.13	0.10	0.21	0.39	0.31	0.19
	BF CB	0.21	0.09	0.13	0.22	0.14	0.18	0.29	0.47	0.32	0.22
	SD C	0.24	0.11	0.16	0.18	0.12	0.17	0.27	0.44	0.31	0.25
Statistical values:											
Maximum		0.49	0.24	0.23	0.42	0.64	0.39	0.89	1.05	0.71	1.74
Minimum		0.15	0.06	0.08	0.13	0.08	0.09	0.14	0.21	0.13	0.12
Mean		0.30	0.14	0.14	0.23	0.18	0.17	0.30	0.41	0.37	0.41
Median		0.28	0.12	0.14	0.18	0.16	0.16	0.26	0.40	0.34	0.27
Standard deviation		0.09	0.05	0.05	0.08	0.12	0.07	0.16	0.16	0.14	0.34

* Catch cables engaged

Table D-3. Summary of interstory drifts

Excitation	Pattern	Maximum Story1 Drift	Maximum Story2 Drift	Residual Story1 Drift	Residual Story2 Drift
		(%)	(%)	(%)	(%)
0.6 sec cosine pulse	DB C	8.56	8.20	3.82	3.78
	BF BP 1	10.04	9.75	6.89	6.78
	BF BP 2	9.76	9.43	6.28	6.19
	DF BP	9.97	9.69	6.67	6.57
	DFS B	8.66	8.34	5.14	5.08
	BF CP *	12.70	12.41	11.70	11.53
	DF CP *	13.22	12.91	12.23	12.07
	DFS C *	11.09	10.87	10.50	10.35
	BF A A	3.84	3.58	0.26	0.24
	BF A B	3.88	3.63	0.21	0.22
	BF A C	3.82	3.57	0.12	0.12
	BF A D	3.88	3.64	0.17	0.20
	BF A E	3.92	3.65	0.23	0.21
	BF BP H	4.22	3.97	0.65	0.64

Table D-3. — *Continued*

Excitation	Pattern	Maximum Story1 Drift (%)	Maximum Story2 Drift (%)	Residual Story1 Drift (%)	Residual Story2 Drift (%)
1.2 sec cosine pulse	DB C	6.51	6.10	0.44	0.40
	BF BP	10.44	10.05	4.10	4.04
	DF BP	9.27	8.90	2.56	2.54
	DFS B	10.54	10.19	2.80	2.79
	BF CP 1 *	18.09	17.78	16.60	16.42
	BF CP 2	2.72	2.52	0.16	0.16
	BF CP 3	12.52	12.35	11.86	11.80
	BF CB	9.98	9.79	3.49	3.46
	DF CP *	18.37	18.24	16.96	16.78
	DFS C *	18.62	18.21	17.07	16.85
JNF01 (Tabas)	DB C	4.87	4.70	0.89	0.94
	BF BB	5.10	4.84	0.83	0.85
	BF CB	4.83	4.66	0.37	0.40
	DF CB	4.98	4.80	0.71	0.71
	DFS C	4.29	4.23	-2.68	-2.62
JSE17 (Llolleo)	DB C	6.37	6.20	1.98	2.03
	BF CB	8.13	8.12	-4.09	-4.07
	SD C	6.76	6.58	2.66	2.68
Statistical values:					
Maximum *		18.6	18.2	17.1	16.9
Minimum		2.72	2.52	0.12	0.12
Mean *		8.44	8.19	4.42	4.38
Median *		8.35	8.16	2.61	2.61
Standard deviation *		4.44	4.41	5.73	5.66

* Catch cables engaged — values compromised

Table D-4. Summary of out-of-plane displacements without large deformation geometric correction

Excitation	Pattern	Maximum D_{Table} (in)	Maximum $D_{Rel\ base}$ (in)	Maximum $D_{Rel\ Story1}$ (in)	Maximum $D_{Rel\ Story2}$ (in)	Residual $D_{Rel\ Story1}$ (in)	Residual $D_{Rel\ Story2}$ (in)
0.6 sec cosine pulse	DB C	0.039	0.089	0.155	0.356	0.054	0.129
	BF BP 1	0.023	0.068	0.107	0.539	0.079	0.451
	BF BP 2	0.024	0.068	0.132	0.419	0.111	0.312
	DF BP	0.049	0.124	0.215	0.572	0.171	0.454
	DFS B	0.034	0.087	0.148	0.416	0.125	0.305
	BF CP *	0.187	0.370	0.578	1.387	0.411	1.303
	DF CP *	0.022	0.063	0.455	1.459	0.435	1.434
	DFS C *	0.030	0.079	0.380	1.195	0.367	1.183
	BF A A	0.022	0.040	0.072	0.141	0.000	-0.001
	BF A B	0.055	0.089	0.113	0.119	-0.025	-0.027
	BF A C	0.031	0.067	0.065	0.149	0.001	0.001
	BF A D	0.040	0.071	0.101	0.198	0.026	0.022
	BF A E	0.026	0.066	0.066	0.122	-0.024	-0.020
	BF BP H	0.062	0.119	0.115	0.196	-0.001	0.015
1.2 sec cosine pulse	DB C	0.037	0.284	0.609	1.014	0.017	0.010
	BF BP	0.036	0.262	0.666	1.355	0.121	0.266
	DF BP	0.089	0.333	0.586	1.032	-0.023	-0.004
	DFS B	0.174	0.319	0.478	0.945	0.040	0.060
	BF CP 1 *	0.024	0.258	0.664	2.274	0.624	2.217
	BF CP 2	0.081	0.172	0.240	0.327	0.109	0.097
	BF CP 3	0.053	0.102	0.376	1.323	0.335	1.275
	BF CB	0.074	0.204	0.530	1.047	-0.053	0.027
	DF CP *	0.028	0.219	0.689	2.467	0.665	2.444
	DFS C *	0.034	0.243	0.779	2.644	0.759	2.627
JNF01 (Tabas)	DB C	0.034	0.206	0.441	0.703	0.038	0.057
	BF BB	0.054	0.182	0.313	0.455	0.011	0.014
	BF CB	0.056	0.172	0.264	0.358	-0.071	-0.071
	DF CB	0.070	0.162	0.312	0.495	-0.076	-0.063
	DFS C	0.039	0.206	0.269	0.491	0.046	0.101

Table D-4. — *Continued*

Excitation	Pattern	Maximum D_{Table} (in)	Maximum $D_{Rel\ base}$ (in)	Maximum $D_{Rel\ Story1}$ (in)	Maximum $D_{Rel\ Story2}$ (in)	Residual $D_{Rel\ Story1}$ (in)	Residual $D_{Rel\ Story2}$ (in)
JSE17 (Llolleo)	DB C	0.038	0.110	0.156	0.300	0.039	0.056
	BF CB	0.053	0.105	0.206	0.673	0.076	0.202
	SD C	0.063	0.131	0.258	0.493	0.040	0.097
Statistical values:							
Maximum		0.19	0.37	0.78	2.64	0.76	2.63
Minimum		0.02	0.04	0.06	0.12	0.0001	0.001
Mean		0.05	0.16	0.33	0.80	0.14	0.47
Median		0.04	0.13	0.27	0.52	0.04	0.10
Standard deviation		0.04	0.09	0.22	0.68	0.22	0.77

* Catch cables engaged

Table D-5. Summary of out-of-plane displacements with large deformation geometric correction

Excitation	Pattern	Maximum D_{Table} (in)	Maximum $D_{Rel\ base}$ (in)	Maximum $D_{Rel\ Story1}$ (in)	Maximum $D_{Rel\ Story2}$ (in)	Residual $D_{Rel\ Story1}$ (in)	Residual $D_{Rel\ Story2}$ (in)
0.6 sec cosine pulse	DB C	0.039	0.050	0.071	0.008	0.024	0.010
	BF BP 1	0.023	0.029	0.006	0.045	0.021	0.063
	BF BP 2	0.024	0.029	0.048	0.041	0.029	0.010
	DF BP	0.049	0.084	0.120	0.086	0.077	0.090
	DFS B	0.034	0.047	0.092	0.084	0.069	0.088
	BF CP *	0.187	0.330	0.288	0.269	0.123	0.190
	DF CP *	0.022	0.023	0.137	0.231	0.120	0.213
	DFS C *	0.030	0.038	0.145	0.288	0.134	0.281
	BF A A	0.022	0.026	0.023	0.042	0.000	0.002
	BF A B	0.055	0.074	0.063	0.014	0.025	0.028
	BF A C	0.031	0.053	0.013	0.030	0.001	0.001
	BF A D	0.040	0.056	0.051	0.084	0.026	0.022
	BF A E	0.026	0.052	0.020	0.020	0.024	0.020
	BF BP H	0.062	0.107	0.081	0.101	0.002	0.012

Table D-5. — *Continued*

Excitation	Pattern	Maximum D_{Table} (in)	Maximum $D_{Rel\ base}$ (in)	Maximum $D_{Rel\ Story1}$ (in)	Maximum $D_{Rel\ Story2}$ (in)	Residual $D_{Rel\ Story1}$ (in)	Residual $D_{Rel\ Story2}$ (in)
1.2 sec cosine pulse	DB C	0.037	0.083	0.192	0.221	0.017	0.008
	BF BP	0.036	0.061	0.209	0.323	0.085	0.129
	DF BP	0.089	0.131	0.141	0.085	0.037	0.059
	DFS B	0.174	0.129	0.073	0.008	0.024	0.003
	BF CP 1 *	0.024	0.061	0.076	0.011	0.041	0.026
	BF CP 2	0.081	0.123	0.140	0.158	0.109	0.097
	BF CP 3	0.053	0.011	0.072	0.146	0.038	0.117
	BF CB	0.074	0.008	0.123	0.174	0.078	0.072
	DF CP *	0.028	0.020	0.075	0.110	0.061	0.113
	DFS C *	0.034	0.047	0.157	0.265	0.145	0.266
JNF01 (Tabas)	DB C	0.034	0.040	0.169	0.242	0.036	0.050
	BF BB	0.054	0.026	0.096	0.072	0.010	0.008
	BF CB	0.056	0.018	0.080	0.034	0.072	0.073
	DF CB	0.070	0.006	0.104	0.136	0.077	0.067
	DFS C	0.039	0.052	0.036	0.051	0.031	0.042
JSE17 (Llolleo)	DB C	0.038	0.035	0.032	0.060	0.031	0.023
	BF CB	0.053	0.037	0.005	0.117	0.041	0.064
	SD C	0.063	0.054	0.133	0.175	0.025	0.038
Statistical values:							
Maximum		0.19	0.33	0.29	0.32	0.15	0.28
Minimum		0.02	0.01	0.00	0.01	0.00	0.00
Mean		0.05	0.06	0.10	0.12	0.05	0.07
Median		0.04	0.05	0.08	0.09	0.04	0.05
Standard deviation		0.04	0.06	0.06	0.09	0.04	0.07

* Catch cables engaged

Table D-6. Summary of maximum out-of-plane displacement differences

Excitation	Pattern	Table	Base	Top of Story 1			Top of Story 2		
				PC1-PB1	PB1-PC2	PC1-PC2	PC1-PB2	PB2-PC2	PC1-PC2
		(in)	(in)	(in)	(in)	(in)	(in)	(in)	(in)
0.6 sec cosine pulse	DB C	0.06	0.19	0.16	0.15	0.27	0.24	0.12	0.37
	BF BP 1	0.07	0.11	0.23	0.25	0.22	0.13	0.12	0.23
	BF BP 2	0.07	0.12	0.11	0.08	0.18	0.15	0.11	0.21
	DF BP	0.12	0.12	0.11	0.07	0.18	0.12	0.12	0.20
	DFS B	0.09	0.14	0.11	0.09	0.18	0.16	0.09	0.23
	BF CP *	0.23	0.21	0.10	0.08	0.14	0.14	0.10	0.17
	DF CP *	0.07	0.11	0.09	0.07	0.12	0.12	0.10	0.19
	DFS C *	0.10	0.16	0.12	0.10	0.22	0.15	0.09	0.23
	BF A A	0.10	0.11	0.07	0.08	0.11	0.07	0.12	0.19
	BF A B	0.11	0.16	0.08	0.09	0.15	0.09	0.13	0.22
	BF A C	0.12	0.18	0.08	0.09	0.14	0.09	0.10	0.18
	BF A D	0.09	0.12	0.08	0.08	0.12	0.10	0.11	0.19
	BF A E	0.09	0.18	0.09	0.08	0.14	0.11	0.12	0.21
	BF BP H	0.14	0.15	0.07	0.07	0.12	0.08	0.10	0.16
1.2 sec cosine pulse	DB C	0.11	0.32	0.17	0.17	0.31	0.17	0.16	0.31
	BF BP	0.12	0.33	0.16	0.18	0.30	0.17	0.18	0.31
	DF BP	0.29	0.39	0.20	0.19	0.38	0.21	0.24	0.45
	DFS B	0.30	0.37	0.15	0.15	0.28	0.17	0.22	0.38
	BF CP 1 *	0.11	0.31	0.32	0.34	0.66	0.52	0.38	0.88
	BF CP 2	0.25	0.27	0.12	0.11	0.20	0.10	0.10	0.20
	BF CP 3	0.09	0.17	0.10	0.09	0.18	0.09	0.12	0.20
	BF CB	0.35	0.30	0.14	0.15	0.25	0.14	0.18	0.32
	DF CP *	0.17	0.29	0.23	0.25	0.47	0.36	0.26	0.61
	DFS C *	0.12	0.35	0.19	0.15	0.28	0.27	0.28	0.55
JNF01 (Tabas)	DB C	0.13	0.25	0.14	0.14	0.27	0.18	0.16	0.30
	BF BB	0.13	0.20	0.11	0.13	0.22	0.17	0.20	0.27
	BF CB	0.14	0.31	0.16	0.15	0.29	0.20	0.18	0.31
	DF CB	0.13	0.21	0.14	0.14	0.26	0.18	0.16	0.30
	DFS C	0.12	0.28	0.13	0.14	0.25	0.18	0.16	0.30

Table D-6. — *Continued*

Excitation	Pattern	Table	Base	Top of Story 1			Top of Story 2		
				PC1-PB1	PB1-PC2	PC1-PC2	PC1-PB2	PB2-PC2	PC1-PC2
		(in)	(in)	(in)	(in)	(in)	(in)	(in)	(in)
JSE17 (Llolleo)	DB C	0.13	0.16	0.08	0.08	0.15	0.13	0.16	0.23
	BF CB	0.12	0.23	0.12	0.11	0.20	0.20	0.17	0.31
	SD C	0.20	0.19	0.11	0.09	0.17	0.14	0.18	0.29
Statistical values:									
Maximum		0.35	0.39	0.32	0.34	0.66	0.52	0.38	0.88
Minimum		0.06	0.11	0.07	0.07	0.11	0.07	0.09	0.16
Mean		0.14	0.22	0.13	0.13	0.23	0.17	0.16	0.30
Median		0.12	0.20	0.12	0.11	0.21	0.15	0.14	0.25
Standard deviation		0.07	0.08	0.06	0.06	0.11	0.09	0.06	0.15

* Catch cables engaged

Table D-7. Summary of maximum in-plane accelerations

Excitation	Pattern	A_{Table}	Relative			Absolute		
			A_{Base}	A_{Story1}	A_{Story2}	A_{Base}	A_{Story1}	A_{Story2}
		(g)	(g)	(g)	(g)	(g)	(g)	(g)
0.6 sec cosine pulse	DB C	1.01	0.28	1.04	1.50	0.85	0.74	0.99
	BF BP 1	1.12	0.35	1.06	1.55	0.90	0.74	0.81
	BF BP 2	0.99	0.31	0.93	1.40	0.82	0.55	0.79
	DF BP	1.03	0.40	0.98	1.48	0.87	0.65	0.82
	DFS B	1.05	0.24	0.96	1.42	0.84	0.56	0.74
	BF CP *	1.07	0.48	0.93	1.54	1.07	0.66	0.83
	DF CP *	1.23	1.17	1.48	1.41	0.87	0.54	0.77
	DFS C *	0.98	0.26	0.96	1.32	0.82	0.25	0.57
	BF A A	0.57	0.63	0.51	0.84	0.64	0.24	0.73
	BF A B	0.57	0.59	0.49	0.85	0.54	0.27	0.73
	BF A C	0.51	0.59	0.46	0.91	0.56	0.17	0.74
	BF A D	0.49	0.72	0.45	0.81	0.61	0.16	0.74
	BF A E	0.52	0.52	0.44	0.85	0.57	0.18	0.76
	BF BP H	0.55	0.43	0.48	0.80	0.57	0.15	0.71

Table D-7. — *Continued*

Excitation	Pattern	A_{Table}	Relative			Absolute		
			A_{Base}	A_{Story1}	A_{Story2}	A_{Base}	A_{Story1}	A_{Story2}
		(g)	(g)	(g)	(g)	(g)	(g)	(g)
1.2 sec cosine pulse	DB C	0.48	0.14	0.41	0.62	0.50	0.24	0.78
	BF BP	0.68	0.65	0.61	0.74	0.81	0.24	0.59
	DF BP	0.72	0.97	0.67	0.64	1.01	0.29	0.63
	DFS B	0.78	0.19	0.70	0.86	0.65	0.25	0.54
	BF CP 1 *	0.79	0.73	0.79	1.02	0.80	0.46	0.93
	BF CP 2	0.46	0.71	0.51	0.49	0.72	0.25	0.54
	BF CP 3	0.50	0.42	0.51	0.50	0.44	0.34	0.74
	BF CB	0.63	0.72	0.73	0.71	0.78	0.36	0.78
	DF CP *	0.60	0.85	0.92	1.08	0.58	0.41	1.07
	DFS C *	0.65	0.54	0.64	1.26	0.55	0.58	1.58
JNF01 (Tabas)	DB C	0.73	0.22	0.68	1.11	0.69	0.27	0.83
	BF BB	0.75	0.48	0.71	1.18	0.75	0.22	0.80
	BF CB	0.74	0.89	0.77	1.12	0.73	0.32	0.95
	DF CB	0.72	0.93	0.83	1.32	0.94	0.42	0.96
	DFS C	0.70	0.21	0.62	1.03	0.67	0.19	0.62
JSE17 (Llolleo)	DB C	1.91	0.54	1.90	2.48	1.76	0.33	1.22
	BF CB	1.84	1.08	1.85	2.18	1.67	0.39	0.97
	SD C	1.83	0.53	1.92	2.44	1.61	0.33	1.31
Statistical values:								
Maximum		1.91	1.17 *	1.92	2.48	1.76	0.74	1.58 *
Minimum		0.46	0.14	0.41	0.49	0.44	0.15	0.54
Mean		0.85	0.55	0.84	1.17	0.82	0.37	0.83
Median		0.73	0.54	0.72	1.09	0.77	0.32	0.78
Standard deviation		0.39	0.27	0.42	0.50	0.32	0.17	0.22

* Catch cables engaged — values compromised

Table D-8. Summary of maximum out-of-plane accelerations

Excitation	Pattern	A_{Table}	Relative			Absolute		
			A_{Base}	A_{Story1}	A_{Story2}	A_{Base}	A_{Story1}	A_{Story2}
		(g)	(g)	(g)	(g)	(g)	(g)	(g)
0.6 sec cosine pulse	DB C	0.05	0.41**	0.13	0.12	0.41**	0.09	0.11
	BF BP 1	0.09	0.98**	0.21	0.18	0.96**	0.20	0.17
	BF BP 2	0.08	0.14**	0.13	0.10	0.22**	0.12	0.09
	DF BP	0.12	0.17	0.18	0.18	0.12	0.13	0.18
	DFS B	0.05	0.42	0.16	0.12	0.38	0.12	0.10
	BF CP *	0.22	0.18	0.40	0.16	0.10	0.27	0.16
	DF CP *	0.34	0.36	0.35	0.61	0.21	0.32	0.27
	DFS C *	0.05	0.11	0.10	0.14	0.08	0.07	0.10
	BF A A	0.04	0.13	0.13	0.18	0.09	0.14	0.18
	BF A B	0.05	0.34	0.17	0.08	0.35	0.15	0.09
	BF A C	0.04	0.16	0.17	0.27	0.20	0.15	0.26
	BF A D	0.06	0.11	0.30	0.21	0.16	0.28	0.23
	BF A E	0.06	0.16	0.16	0.16	0.13	0.17	0.14
	BF BP H	0.06	0.13	0.22	0.20	0.11	0.20	0.18
1.2 sec cosine pulse	DB C	0.03	0.07	0.20	0.15	0.06	0.20	0.15
	BF BP	0.10	0.13	0.16	0.14	0.07	0.11	0.13
	DF BP	0.21	0.45	0.18	0.22	0.24	0.15	0.23
	DFS B	0.08	0.17	0.13	0.11	0.09	0.10	0.06
	BF CP 1 *	0.14	0.69	0.37	0.25	0.70	0.37	0.25
	BF CP 2	0.18	0.26	0.32	0.22	0.17	0.27	0.23
	BF CP 3	0.11	0.15	0.15	0.22	0.10	0.16	0.17
	BF CB	0.16	0.19	0.23	0.17	0.16	0.17	0.15
	DF CP *	0.10	0.36	0.25	0.21	0.27	0.27	0.25
	DFS C *	0.09	0.31	0.19	0.16	0.31	0.18	0.12
JNF01 (Tabas)	DB C	0.08	0.13	0.16	0.13	0.08	0.16	0.13
	BF BB	0.08	0.15	0.23	0.19	0.15	0.24	0.20
	BF CB	0.16	0.25	0.25	0.28	0.25	0.25	0.16
	DF CB	0.22	0.31	0.30	0.32	0.22	0.23	0.24
	DFS C	0.06	0.12	0.10	0.10	0.08	0.09	0.11
JSE17 (Llolleo)	DB C	0.10	0.26	0.26	0.23	0.22	0.22	0.29
	BF CB	0.11	0.23	0.26	0.26	0.27	0.31	0.24
	SD C	0.11	0.37	0.23	0.45	0.28	0.20	0.47

Table D-8. — *Continued*

Excitation	Pattern	A_{Table} (g)	Relative A_{Base} (g)	Relative A_{Story1} (g)	Relative A_{Story2} (g)	Absolute A_{Base} (g)	Absolute A_{Story1} (g)	Absolute A_{Story2} (g)
Statistical values:								
Maximum		0.34	0.98	0.40	0.61	0.96	0.37	0.47
Minimum		0.03	0.07	0.10	0.08	0.06	0.07	0.06
Mean		0.11	0.26	0.21	0.20	0.23	0.19	0.18
Median		0.09	0.19	0.19	0.18	0.19	0.18	0.17
Standard deviation		0.07	0.19	0.08	0.11	0.19	0.07	0.08

* Catch cables engaged
** Value from fewer instruments than normal due to PC1 base accelerometer malfunction

Table D-9. Summary of maximum global forces

Excitation	Pattern	In-Plane at Base Shear (kips)	In-Plane at Base OTM (kip-in)	In-Plane at Base Moment from LC (kip-in)	Out-of-Plane at Base Shear (kips)	Out-of-Plane at Base Moment from LC (kip-in)	Total Axial (kips)
0.6 sec cosine pulse	DB C	7.3	740	104	0.5	10	2.4
	BF BP 1	5.3	554	80	0.6	8	2.4
	BF BP 2	5.2	553	77	0.6	7	2.3
	DF BP	6.1	553	95	0.6	9	2.7
	DFS B	4.9	494	73	0.7	10	2.3
	BF CP *	5.5	541	75	0.6	12	2.7
	DF CP *	6.3	547	91	0.8	7	2.2
	DFS C *	4.0	401	62	0.6	9	2.0
	BF A A	5.6	557	75	0.5	10	1.9
	BF A B	5.3	558	71	0.5	10	1.6
	BF A C	5.6	568	75	0.4	9	1.7
	BF A D	5.6	555	73	0.5	10	1.4
	BF A E	5.4	573	73	0.4	13	2.2
	BF BP H	4.8	510	66	0.3	11	1.8

Table D-9. — *Continued*

Excitation	Pattern	In-Plane at Base			Out-of-Plane at Base		Total Axial
		Shear	OTM	Moment from LC	Shear	Moment from LC	
		(kips)	(kip-in)	(kip-in)	(kips)	(kip-in)	(kips)
1.2 sec cosine pulse	DB C	7.4	694	101	0.8	10	1.8
	BF BP	5.5	504	78	0.6	9	2.5
	DF BP	5.6	541	84	0.8	11	3.6
	DFS B	5.2	505	79	1.0	13	2.1
	BF CP 1 *	5.0	607	74	2.3	40	6.0
	BF CP 2	4.8	465	64	0.5	11	1.8
	BF CP 3	4.3	406	59	0.5	9	1.8
	BF CB	5.7	505	78	0.7	12	2.2
	DF CP *	5.6	715	88	1.8	30	5.5
	DFS C *	3.8	900	111	1.0	22	5.2
NF01 (Tabas)	DB C	7.0	650	95	0.8	10	2.3
	BF BB	6.1	579	84	0.7	10	1.9
	BF CB	5.2	495	75	0.6	10	2.8
	DF CB	5.5	535	79	0.8	10	2.5
	DFS C	2.0	381	63	0.5	8	2.0
SE17 (Llolleo)	DB C	6.6	692	101	0.8	16	3.7
	BF CB	5.2	466	83	0.8	12	3.1
	SD C	7.2	750	105	1.4	16	3.9
Statistical values:							
Maximum		7.4	900	111	2.3	40	6.0
Minimum		2.0	381	59	0.3	7	1.4
Mean		5.5	565	81	0.8	12	2.6
Median		5.5	553	78	0.6	10	2.3
Standard deviation		1.1	110	13	0.4	7	1.1

* Catch cables engaged

Table D-10. Summary of connection rotations

Excitation	Pattern	Maximum				Residual			
		C1 (rad)	C2 (rad)	C3 (rad)	C4 (rad)	C1 (rad)	C2 (rad)	C3 (rad)	C4 (rad)
0.6 sec cosine pulse	DB C	0.082	0.080	0.072	0.071	-0.043	0.043	-0.042	0.042
	BF BP 1	0.117**	0.110	0.096	0.093	-0.041	0.079	-0.077	0.074
	BF BP 2	0.106	0.103	0.088	0.090	-0.072	0.069	-0.068	0.069
	DF BP	0.116**	0.110	0.096	0.088	-0.260	0.077	-0.076	0.070
	DFS B	0.095	0.093**	0.077	0.079	-0.060	0.028	-0.056	0.057
	BF CP *	0.145	0.139	0.141	0.141	-0.136	0.130	-0.133	0.132
	DF CP *	0.151**	0.151	0.149	0.145	-0.294	0.143	-0.140	0.137
	DFS C *	0.126	0.123	0.122	0.124	-0.121	0.118	-0.117	0.119
	BF A A	0.023	0.039	0.020	0.020	-0.003	0.002	-0.003	0.002
	BF A B	0.023	0.040	0.020	0.020	-0.002	0.002	-0.002	0.001
	BF A C	0.024	0.037	0.020	0.020	-0.001	0.001	-0.001	0.001
	BF A D	0.024	0.038	0.020	0.021	-0.002	0.001	-0.002	0.002
	BF A E	0.024	0.040	0.021	0.021	-0.002	0.003	-0.002	0.002
	BF BP H	0.041	0.036	0.025	0.025	-0.008	0.006	-0.007	0.007
1.2 sec cosine pulse	DB C	0.058	0.057	0.049	0.049	-0.006	0.004	-0.006	0.005
	BF BP	0.114	0.112	0.096	0.096	-0.048	0.045	-0.044	0.045
	DF BP	0.100	0.098	0.081	0.082	-0.029	0.028	-0.028	0.027
	DFS B	0.119	0.113	0.099	0.100	-0.034	0.030	-0.032	0.032
	BF CP 1 *	0.205	0.207**	0.207	0.208	-0.190	0.096	-0.192	0.193
	BF CP 2	0.022	0.023	0.012	0.015	-0.001	0.003	-0.002	0.001
	BF CP 3	0.143	0.142	0.141	0.136	-0.137	0.136	-0.135	0.130
	BF CB	0.099	0.113	0.093	0.108	-0.037	0.041	-0.039	0.037
	DF CP *	0.220	0.213	0.216	0.212	-0.201	0.198	-0.200	0.197
	DFS C *	0.220	0.219	0.216	0.215	-0.202	0.202	-0.200	0.200
NF01 (Tabas)	DB C	0.045	0.036	0.030	0.034	-0.011	0.008	-0.009	0.012
	BF BB	0.040	0.052	0.033	0.034	-0.010	0.008	-0.009	0.010
	BF CB	0.035	0.054	0.032	0.044	-0.002	0.008	-0.005	0.004
	DF CB	0.040	0.053	0.034	0.048	-0.009	0.007	-0.007	0.007
	DFS C	0.045	0.045	0.041	0.040	0.030	-0.031	0.029	-0.028
SE17 (Llolleo)	DB C	0.055	0.057	0.048	0.050	-0.019	0.024	-0.022	0.022
	BF CB	0.094	0.081	0.090	0.075	0.047	-0.046	0.046	-0.045

Table D-10. ***Continued***

Excitation	Pattern	Maximum				Residual			
		C1	C2	C3	C4	C1	C2	C3	C4
		(rad)	(rad)	(rad)	(rad)	(rad)	(rad)	(rad)	(rad)
	SD C	0.061	0.060	0.054	0.047	-0.033	0.030	-0.032	0.026
Statistical values:									
Maximum *		0.220	0.219	0.216	0.215	0.047	0.202	0.046	0.200
Minimum		0.022	0.023	0.012	0.015	0.001	0.001	0.001	0.001
Mean *		0.088	0.090	0.079	0.080	-0.061	0.047	-0.050	0.050
Median *		0.088	0.081	0.075	0.073	-0.031	0.028	-0.030	0.027
Standard deviation *		0.058	0.054	0.059	0.058	0.086	0.062	0.066	0.066

* Catch cables engaged — values compromised
** Rotation calculated from one displacement transducer only due to malfunction of 2nd transducer

Table D-11. Summary of maximum connection moments (projected to the clevis pin)

Excitation	Pattern	C1	C2	C3	C4
		(kip-in)	(kip-in)	(kip-in)	(kip-in)
0.6 sec cosine pulse	DB C	151.4	157.1	150.7	155.8
	BF BP 1	119.1	114.9	143.6	147.9
	BF BP 2	120.4	117.2	150.4	145.1
	DF BP	119.8	121.4	140.8	157.2
	DFS B	78.4	83.5	140.9	133.6
	BF CP *	118.6	109.3	104.0	108.8
	DF CP *	128.0	120.8	112.2	109.4
	DFS C *	84.8	84.0	74.7	80.9
	BF A A	136.0	114.8	142.8	134.4
	BF A B	137.1	110.8	143.9	134.4
	BF A C	133.9	111.8	136.8	131.5
	BF A D	133.7	115.8	143.7	133.5
	BF A E	135.7	116.5	145.1	135.4
	BF BP H	109.1	98.2	130.3	133.0
1.2 sec cosine pulse	DB C	145.6	150.9	142.8	145.2
	BF BP	111.4	106.5	146.5	147.6
	DF BP	115.4	112.9	149.0	152.6
	DFS B	82.9	95.7	138.9	138.5
	BF CP 1 *	109.4	108.6	105.8	105.4

Table D-11. — *Continued*

Excitation	Pattern	C1	C2	C3	C4
		(kip-in)	(kip-in)	(kip-in)	(kip-in)
	BF CP 2	105.1	100.1	101.8	97.4
	BF CP 3	90.6	82.0	94.0	87.6
	BF CB	127.9	103.5	129.6	93.5
	DF CP *	119.2	119.0	113.2	111.3
	DFS C *	78.8	81.5	80.4	76.5
JNF01 (Tabas)	DB C	132.8	153.4	136.0	128.6
	BF BB	130.2	113.7	145.0	137.6
	BF CB	137.4	113.7	126.3	106.0
	DF CB	121.2	128.2	132.6	114.3
	DFS C	80.0	79.9	74.8	77.8
JSE17 (Llolleo)	DB C	155.3	143.9	149.0	139.9
	BF CB	124.0	121.9	115.6	126.3
	SD C	151.0	158.3	155.3	175.2
Statistical values:					
Maximum		155.3	158.3	155.3	175.2
Minimum		78.4	79.9	74.7	76.5
Mean		119.5	114.1	128.0	125.1
Median		120.8	113.7	137.8	133.2
Standard deviation		21.8	21.3	23.3	25.0

* Catch cables engaged

Table D-12. Summary of maximum

Excitation	Pattern	Main Column 1 (kip-in)				Main Column 2 (kip-in)				Perim. Column 2 (kip-in)			
		Base	At Midheight Connection		Top	Base	At Midheight Connection		Top	Base	At Midheight Connection		Top
			Below	Above			Below	Above			Below	Above	
0.6 sec cosine pulse	DB C	3	205	47	173	6	198	25	180	21	42	21	2
	BF BP 1	2	141	74	164	4	141	75	176	--	--	24	3
	BF BP 2	3	142	71	174	4	140	47	176	--	--	22	2
	DF BP	4	149	81	162	--	--	49	188	11	27	24	3
	DFS B	2	120	65	163	3	126	48	162	9	26	23	2
	BF CP *	5	143	35	117	--	--	26	128	11	23	22	2

Table D-12. — *Continued*

Excitation	Pattern	Main Column 1 (kip-in) Base	Main Column 1 At Midheight Connection Below	Main Column 1 At Midheight Connection Above	Main Column 1 Top	Main Column 2 (kip-in) Base	Main Column 2 At Midheight Connection Below	Main Column 2 At Midheight Connection Above	Main Column 2 Top	Perim. Column 2 (kip-in) Base	Perim. Column 2 At Midheight Connection Below	Perim. Column 2 At Midheight Connection Above	Perim. Column 2 Top
	DF CP *	4	148	23	126	7	143	36	129	15	23	33	2
	DFS C *	2	99	28	84	5	105	29	93	8	19	18	4
	BF A A	3	164	25	150	4	133	34	157	61	121	14	1
	BF A B	2	166	25	152	4	130	34	160	66	115	12	1
	BF A C	2	164	27	152	4	132	30	156	70	114	13	2
	BF A D	3	164	30	153	4	134	31	158	68	118	10	1
	BF A E	3	168	28	154	5	139	33	159	69	119	15	3
	BF BP H	2	134	57	150	3	123	27	158	53	101	17	18
1.2 sec cosine pulse	DB C	3	190	29	165	5	191	17	173	11	19	18	2
	BF BP	31	152	74	170	5	136	47	178	13	18	17	2
	DF BP	4	151	88	175	5	144	44	186	13	20	19	2
	DFS B	2	130	76	159	10	140	42	167	11	19	17	2
	BF CP 1*	21	137	41	130	4	123	32	124	42	24	43	4
	BF CP 2	2	125	38	112	3	119	13	114	45	101	11	5
	BF CP 3	3	115	31	104	4	105	17	100	15	85	12	2
	BF CB	4	146	32	143	23-	160-	40	116	9	15	13	2
	DF CP *	4	142	48	129	15	137	39	140	32	17	20	3
	DFS C *	1	97	38	89	14	97	45	90	49	33	19	3
JNF01 (Tabas)	DB C	3	179	34	160	7	193	22	151	--	--	24	2
	BF BB	2	174	49	161	26	171	51	162	34	31	23	2
	BF CB	3	147	46	141	8	124	52	118	12	20	21	4
	DF CB	3	148	43	144	25	173	--	152	--	--	20	2
	DFS C	2	101	33	82	8	100	19	90	25	73	21	1
JSE17 (Llolleo)	DB C	3	192	44	161	6	180	36	165	33	143	35	18
	BF CB	3	141	67	131	6	126	53	139	59	103	37	34
	SD C	3	202	56	177	--	--	40	205	--	--	39	28
Statistical values:													
Maximum		31	205	88	177	26	198	75	205	70	143	43	34
Minimum		1.3	97	23	82	3	97	13	90	8	15	10	1
Mean		4	149	46	144	8	140	38	148	32	58	21	5
Median		3	147	42	152	5	136	36	158	25	31	20	2
Standard deviation		6	27	19	27	7	27	14	30	22	44	8	8

* Catch cables engaged

--Strain gage malfunction; no data available

Table D-13. Summary of maximum column axial loads

Excitation	Pattern	PC1 (kips)	PC2 (kips)	MC1 (kips)	MC2 (kips)	PC3 (kips)	PC4 (kips)
0.6 sec cosine pulse	DB C	1.2	1.4	8.5	7.4	0.8	1.2
	BF BP 1	1.1	1.6	6.1	5.9	1.0	1.7
	BF BP 2	1.1	1.5	6.3	5.8	1.1	1.8
	DF BP	1.0	1.5	6.4	5.5	1.0	1.8
	DFS B	1.1	1.4	5.7	5.0	1.0	1.5
	BF CP *	1.5	1.7	5.6	5.3	0.7	0.8
	DF CP *	1.2	1.7	5.4	5.3	0.9	1.2
	DFS C *	1.3	1.5	4.0	3.7	0.9	1.7
	BF A A	0.7	0.6	6.0	5.0	0.4	0.5
	BF A B	0.6	0.6	6.1	5.0	0.4	0.6
	BF A C	0.7	0.7	6.1	5.2	0.4	0.6
	BF A D	0.7	0.6	6.1	5.1	0.6	0.6
	BF A E	0.7	0.6	6.3	5.1	0.4	0.7
	BF BP H	0.7	0.7	5.7	5.1	0.4	0.6
1.2 sec cosine pulse	DB C	0.9	0.8	7.7	6.8	0.6	0.7
	BF BP	1.2	1.2	5.9	5.4	0.8	1.0
	DF BP	0.9	1.0	6.1	5.6	0.9	1.3
	DFS B	1.0	1.0	5.8	5.4	1.1	1.6
	BF CP 1 *	4.6	1.6	4.9	4.6	1.3	4.3
	BF CP 2	0.5	0.4	4.6	4.4	0.4	0.4
	BF CP 3	1.2	1.0	4.1	4.1	1.0	1.2
	BF CB	1.2	1.2	5.6	5.1	0.8	1.0
	DF CP *	3.2	1.3	5.0	4.8	1.3	2.8
	DFS C *	2.4	1.5	5.6	4.5	2.9	2.8
JNF01 (Tabas)	DB C	0.8	0.7	7.1	6.0	0.6	0.9
	BF BB	0.9	0.8	6.3	5.6	0.6	0.7
	BF CB	0.8	0.8	5.5	5.7	0.5	1.0
	DF CB	0.8	1.0	6.1	5.5	0.6	1.1
	DFS C	0.8	0.6	4.0	3.5	0.5	0.7

Table D-13. — *Continued*

Excitation	Pattern	PC1 (kips)	PC2 (kips)	MC1 (kips)	MC2 (kips)	PC3 (kips)	PC4 (kips)
JSE17 (Llolleo)	DB C	1.1	1.3	8.3	6.5	0.9	1.3
	BF CB	1.7	1.3	5.5	5.2	1.2	1.2
	SD C	1.0	1.3	8.9	6.8	0.8	1.3
Statistical values:							
Maximum		4.6	1.7	8.9	7.4	2.9	4.3
Minimum		0.5	0.4	4.0	3.5	0.4	0.4
Mean		1.2	1.1	6.0	5.3	0.8	1.3
Median		1.0	1.1	6.0	5.3	0.8	1.1
Standard deviation		0.8	0.4	1.2	0.8	0.5	0.8

* Catch cables engaged

Appendix E: Data Comparison Tables

In this appendix, comparisons are made for response quantities of interest between tests using percent differences. The comparisons are organized by the comparison sets defined in Section 6.1. Comparison Set 3 contains two BF BP pattern/0.6 second cosine pulse (100% amplitude) tests, and these repeated tests are used along with the set of repeated BF A tests (Comparison Set 12) to determine error bounds for the experimental program. These error bounds are located in Table 4-9. Tables E-7 through E-9 contain percent differences between the two repeated BF BP tests which are then compared to percent differences between these tests and the others in the comparison set.

The repeated BF A tests are found in Set 12, which contains four BF A pattern/0.6 second cosine pulse (50% amplitude) tests. Percent differences for this set are found in Tables E-34 through E-36. Percent differences for the remaining comparison sets are found in Tables E-10 through E-33.

It should be noted that for determining whether the difference in quantities is less than the global error bound, in some cases the absolute error bounds in Table 4-9 control, rather than the percentage error bounds. In these cases, large percent differences that are indicated as being less than the global error bounds actually have small absolute differences.

E.1 COMPARISON SET 1— B PATTERNS, 1.2 SECOND COSINE PULSE

Table E-1. Percent differences in in-plane displacements and interstory drifts, Set 1

Percent differences between		Max Relative Displacement (in)			Residual Dis-placement (in)		Max Interstory Drift (%)		Residual Inter-story Drift (%)	
		Base	Story 1	Story 2	Story 1	Story 2	Story 1	Story 2	Story 1	Story 2
BF BP	DB C	42.5	59.6	62.1	909	907	60.3	64.7	831	904
DF BP	DB C	32.3	42.3	44.0	542	537	42.3	45.9	481	532
DFS B	DB C	37.2	60.2	63.4	573	583	61.9	66.9	536	594
BF BP	DF BP	7.8	12.2	12.5	57.2	58.0	12.7	12.9	60.1	58.8
BF BP	DFS B	3.9*	0.3*	0.8*	50.0	47.3	1.0*	1.4*	46.4	44.7
DF BP	DFS B	3.7*	12.5	13.4	4.8*	7.2*	13.8	14.4	9.3*	9.8*

* Percent difference is less than or equal to error bounds

Table E-2. Percent differences in major response quantities, Set 1

Percent differ-ences between		Max Relative Accel		Max Absolute Accel		Max Vb	Max OTM	λ_{Vb}	λ_{T1}
		Story 1	Story 2	Story 1	Story 2				
BF BP	DB C	47.6	19.6	0.0*	32.2	34.7	37.6	44.5	182
DF BP	DB C	63.0	2.1*	20.8	23.8*	30.7	28.2	35.0	216
DFS B	DB C	70.4	37.7	4.2*	44.4	41.8	37.3	58.1	487
BF BP	DF BP	10.4*	17.1	20.8	6.8*	3.1*	7.3*	7.0*	11.9*
BF BP	DFS B	15.4	15.1	4.2*	9.3*	5.2*	0.3*	9.4*	107.9
DF BP	DFS B	4.5*	34.8	16.0*	16.7*	8.5*	7.1*	17.1*	85.9

* Percent difference is less than or equal to error bounds

Table E-3. Percent differences in maximum values of connection response quantities, Set 1

Percent differences between		Maximum θ_{conn}				Maximum M_{conn}			
		C1	C2	C3	C4	C1	C2	C3	C4
BF BP	DB C	95.5	97.4	95.4	96.8	30.7	41.7	2.6*	1.7*
DF BP	DB C	71.2	72.2	63.7	67.3	26.2	33.7	4.4*	5.1*
DFS B	DB C	104.4	98.5	101.4	104.1	75.6	57.8	2.8*	4.8*
BF BP	DF BP	14.2	14.7	19.4	17.6	3.6*	5.9*	1.7*	3.3*
BF BP	DFS B	4.6*	0.5*	3.0*	3.7*	34.3	11.4	5.5*	6.6*
DF BP	DFS B	19.4	15.2	23.0	22.0	39.2	18.0	7.3	10.2

* Percent difference is less than or equal to error bounds

E.2 COMPARISON SET 2—C PATTERNS, 1.2 SECOND COSINE PULSE

Table E-4. Percent differences in in-plane displacements and interstory drifts, Set 2

Percent differences between		Max Relative Displacement (in)			Residual Displacement (in)		Max Interstory Drift (%)		Residual Interstory Drift (%)	
		Base	Story 1	Story 2	Story 1	Story 2	Story 1	Story 2	Story 1	Story 2
BF CP**	DB C	156	178	185	3990	3990	178	191	3668	3980
BF CB	DB C	40.0	53.1	56.7	748	755	53.3	60.4	692	761
DF CP**	DB C	53.2	47.7	47.9	42.7	42.5	46.7	47.7	43.1	42.2
DFS C**	DB C	155	184	191	4100	4098	186	198	3770	4090
BF CP**	BF CB	82.7	81.8	81.6	383	379	81.2	81.6	376	374
BF CP**	DF CP**	0.2*	1.3*	2.0*	1.8*	2.0*	1.5*	2.6*	2.2*	2.2*
BF CP**	DFS C**	0.4*	2.0*	2.2*	2.7*	2.6*	2.9*	2.4*	2.8*	2.6*
DF CP**	DFS C**	0.6*	0.7*	0.2*	0.8*	0.6*	1.4*	0.2*	0.6*	0.4*

* Percent difference is less than or equal to error bounds

** Catch cables engaged—values compromised

Table E-5. Percent differences in major response quantities, Set 2

Percent differences between		Max Relative Accel		Max Absolute Accel		Max Vb	Max OTM	λ_{Vb}	λ_{T1}
		Story 1	Story 2	Story 1	Story 2				
BF CP**	DB C	92.5	64.4	91.7	19.2*	47.6	14.3	371	n/a
BF CB	DB C	77.9	13.8	50.0*	0.0*	29.3	37.2	65.9	301
DF CP**	DB C	79.7	114	20.6*	44.6	30.8	76.1	96.2	n/a
DFS C**	DB C	55.9	103	142	103	93.0	29.7	193	n/a
BF CP**	BF CB	8.2*	44.5	27.8*	19.2*	14.1	20.1	184	n/a
BF CP**	DF CP**	16.3	5.1*	12.2*	15.1*	12.9	17.8	41.1	n/a
BF CP**	DFS C**	23.4	23.5	26.1*	69.9	30.8	48.2	60.9	n/a
DF CP**	DFS C**	43.5	17.5	41.5*	47.7	47.7	25.8	127	n/a

* Percent difference is less than or equal to error bounds

** Catch cables engaged

Table E-6. Percent differences in maximum values of connection response quantities, Set 2

Percent differences between		Maximum θ_{conn} C1	C2	C3	C4	Maximum M_{conn} C1	C2	C3	C4
BF CP**	DB C	253	264	319	326	33.1	39.0	34.9	37.7
BF CB	DB C	70.4	98.7	88.0	120	13.8	45.9	10.1	55.3
DF CP**	DB C	53.7	50.0	52.8	56.7	31.5	45.1	20.5	27.0
DFS C**	DB C	279	286	338	340	84.7	85.1	77.6	89.8
BF CP**	BF CB	107	83.4	123	93.4	17.0	5.0*	22.5	12.8
BF CP**	DF CP**	7.4*	3.1*	4.3*	2.1*	9.0*	9.5*	7.0*	5.6*
BF CP**	DFS C**	7.5*	5.8*	4.5*	3.4*	38.8	33.2	31.7	37.8
DF CP**	DFS C**	0.1*	2.6*	0.2*	1.3*	51.3	45.9	40.9	45.5

* Percent difference is less than or equal to error bounds

** Catch cables engaged

E.3 COMPARISON SET 3—B PATTERNS, 0.6 SECOND COSINE PULSE

Table E-7. Percent differences in in-plane displacements and interstory drifts, Set 3

Percent differences between		Max Relative Displacement			Residual Displacement		Max Interstory Drift		Residual Interstory Drift	
		Base	Story 1	Story 2	Story 1	Story 2	Story 1	Story 2	Story 1	Story 2
BF BP 1	**BF BP 2**	**2.7**	**2.7**	**3.0**	**10.2**	**9.9**	**2.9**	**3.4**	**9.7**	**9.5**
BF BP 1	DB C	15.1	16.6	17.7	81.8	80.6	17.3	18.9	80.3	79.5
BF BP 2	DB C	12.0	13.5	14.2	64.9	64.4	14.0	15.0	64.3	64.0
Average of above 2		13.6	15.1	16.0	73.3	72.5	15.6	17.0	72.3	71.7
BF BP 1	DF BP	2.7*	0.8*	0.7*	3.5*	3.3*	0.7*	0.6*	3.3*	3.1*
BF BP 2	DF BP	0.0*	1.9*	2.3*	6.6*	6.4*	2.2*	2.7*	6.2	6.2*
Average of above 2		1.4*	1.4*	1.5*	5.0*	4.8*	1.4*	1.7*	4.8*	4.6*
BF BP 1	DFS B	15.6	16.3	16.7	34.3	33.9	16.0	16.9	34.0	33.5
BF BP 2	DFS B	12.6	13.2	13.3	21.8	21.9	12.8	13.1	22.2	22.0
Average of above 2		14.1	14.7	15.0	28.0	27.9	14.4	15.0	28.1	27.7
DF BP	DB C	12.1	15.7	16.9	75.7	74.9	16.4	18.1	74.5	74.1
DFS B	DB C	0.5*	0.3*	0.8*	35.4	34.9	1.1*	1.7*	34.5	34.4

* Percent difference is less than or equal to that between BF BP 1 and BF BP 2

Table E-8. Percent differences in major response quantities, Set 3

Percent differences between		Max Relative Accel Story 1	Max Relative Accel Story 2	Max Absolute Accel Story 1	Max Absolute Accel Story 2	Max Vb	Max OTM	λ_{Vb}	λ_{T1}
BF BP 1	**BF BP 2**	**14.4**	**11.0**	**34.5**	**2.5**	**2.0**	**0.2**	**17.3**	**17.1**
BF BP 1	DB C	2.3*	3.3*	0.0*	22.2	38.5	33.6	90.8	107
BF BP 2	DB C	11.9*	7.5*	34.5*	25.3	41.3	33.8	62.7	142
BF BP 1	DF BP	8.0*	5.1*	13.8*	1.2*	14.7	0.2*	11.7*	31.6
BF BP 2	DF BP	6.0*	5.6*	18.2**	3.8	16.9	0.1*	31.0	12.3*
BF BP 1	DFS B	9.9*	9.2*	32.1*	9.5	7.7	12.2	5.8*	49.6
BF BP 1	DFS B	4.2*	1.6*	1.8*	6.8	5.6	12.1	10.9*	27.7
DF BP	DB C	5.6*	1.7*	13.8*	20.7	20.8	33.9	113	172
DFS B	DB C	7.4*	5.8*	32.1*	33.8	49.1	50.0	80.4	209

* Percent difference is less than or equal to that between BF BP 1 and BF BP 2

Table E-9. Percent differences in maximum values of connection response quantities, Set 3

Percent differences between		Maximum θ_{conn} C1	C2	C3	C4	Maximum M_{conn} C1	C2	C3	C4
BF BP 1	**BF BP 2**	**10.4**	**7.5**	**9.1**	**3.8**	**1.1**	**2.0**	**4.7**	**1.9**
BF BP 1	DB C	43.0	37.3	33.0	31.3	27.1	36.7	4.9	5.4
BF BP 2	DB C	29.5	27.7	22.0	26.5	25.8	34.0	0.2*	7.4
BF BP 1	DF BP	0.4*	0.5*	0.1*	5.9	0.6*	5.6	2.0*	6.3
BF BP 2	DF BP	10.0*	7.0*	8.9*	2.0*	0.5*	3.6	6.8	8.4
BF BP 1	DFS B	23.0	18.9	24.8	19.0	51.9	37.7	1.9*	10.7
BF BP 1	DFS B	11.4	10.6	14.5	14.7	53.6	40.4	6.7	8.6
DF BP	DB C	42.4	36.7	32.8	24.0	26.4	29.4	7.1	0.9
DFS B	DB C	16.2	15.5	6.6	10.3	93.2	88.1	7.0	16.6

* Percent difference is less than or equal to that between BF BP 1 and BF BP 2

E.4 COMPARISON SET 4—C PATTERNS, 0.6 SECOND COSINE PULSE

Table E-10. Percent differences in in-plane displacements and interstory drifts, Set 4

Percent differences between		Max Relative Displacement (in)			Residual Displacement (in)		Max Interstory Drift (%)		Residual Interstory Drift (%)	
		Base	Story 1	Story 2	Story 1	Story 2	Story 1	Story 2	Story 1	Story 2
BF CP**	DB C	56.2	49.2	50.0	208	207	48.3	51.3	206	205
DF CP**	DB C	53.0	54.0	55.4	223	221	54.4	57.3	220	220
DFS C**	DB C	25.8	28.5	30.3	177	176	29.4	32.5	175	174
BF CP**	DF CP**	2.0*	3.2*	3.6*	4.8*	4.7*	4.1*	4.0*	4.5*	4.7*
BF CP**	DFS C**	24.1	16.1	15.1	11.0	11.2	14.6	14.2	11.4	11.4
DF CP**	DFS C**	21.6	19.8	19.2	16.3	16.5	19.3	18.8	16.5	16.6

* Percent difference is less than or equal to error bounds

** Catch cables engaged—values compromised

Table E-11. Percent differences in major response quantities, Set 4

Percent differences between		Max Relative Accel		Max Absolute Accel		Max Vb	Max OTM	λ_{Vb}	λ_{T1}
		Story 1	Story 2	Story 1	Story 2				
BF CP**	DB C	11.4*	2.5*	12.1*	19.3*	32.9	36.8	821	n/a
DF CP**	DB C	43.1	6.3*	37.0	28.6	15.7	35.2	980	n/a
DFS C**	DB C	7.9*	14.3*	196	74	85.0	84.8	100	n/a
BF CP**	DF CP**	59.4	8.9*	22.2*	7.8*	14.9	1.2*	17.3*	n/a
BF CP**	DFS C**	3.2*	17.1	164	45.6	39.1	35.0	100	n/a
DF CP**	DFS C**	54.4	7.5*	116	35	59.8	36.6	100	n/a

* Percent difference is less than or equal to error bounds
** Catch cables engaged

Table E-12. Percent differences in maximum values of connection response quantities, Set 4

Percent differences between		Maximum θ_{conn}				Maximum M_{conn}			
		C1	C2	C3	C4	C1	C2	C3	C4
BF CP**	DB C	76.5	72.9	94.7	97.6	27.6	43.8	45.0	43.2
DF CP**	DB C	83.8	88.2	105.6	103.1	18.3	30.0	34.4	42.4
DFS C**	DB C	53.6	53.5	68.8	73.9	78.5	87.1	101.8	92.5
BF CP**	DF CP**	4.1*	8.8*	5.6*	2.8*	7.9*	10.6	7.9*	0.6*
BF CP**	DFS C**	14.9	12.7	15.4	13.6	39.9	30.1	39.2	34.4
DF CP**	DFS C**	19.6	22.6	21.8	16.8	50.9	43.9	50.2	35.2

* Percent difference is less than or equal to error bounds
** Catch cables engaged

E.5 COMPARISON SET 5A & B—JNF01 (TABAS-BASED) MOTION

Table E-13. Percent differences in in-plane displacements and interstory drifts, Set 5

Percent differences between		Max Relative Displacement (in)			Residual Displacement (in)		Max Interstory Drift (%)		Residual Interstory Drift (%)	
		Base	Story 1	Story 2	Story 1	Story 2	Story 1	Story 2	Story 1	Story 2
BF CB	DB C	2.0*	0.1*	0.5*	138	138	0.8*	1.0*	139	138
DF CB	DB C	5.4	1.1*	1.6*	37.3	34.9	2.2*	2.1*	25.3	32.6
DFS C	DB C	16.1	13.6	12.4	194	186	13.5	11.1	202	177
BF CB	DF CB	7.5	1.2*	2.1*	73.0	76.2	3.0*	3.1*	90.6	79.4
BF CB	DFS C	18.4	13.5	11.8	598	579	12.5	10.0	622	559
DF CB	DFS C	10.2	14.9	14.2	304	285	15.9	13.5	279	268
BF BB	DB C	0.6*	4.0*	3.5*	13.5	12.0	4.7*	3.0*	7.3*	10.6
BF CB	BF BB	1.4*	4.1*	4.0*	109	112	5.5	4.0*	123	115

* Percent difference is less than or equal to error bounds

Table E-14. Percent differences in major response quantities, Set 5

Percent differences between		Max Relative Accel		Max Absolute Accel		Max Vb	Max OTM	λ_{Vb}	λ_{T1}
		Story 1	Story 2	Story 1	Story 2				
BF CB	DB C	14.5	0.5*	22.7*	3.7*	35.0	31.4	28.4	175
DF CB	DB C	22.2	18.5	18.5*	14.5*	27.2	21.5	28.4	246
DFS C	DB C	9.3	8.3	55.6*	15.7*	243	70.8	81.8	769
BF CB	DF CB	6.7	17.9	42.1*	33.9	6.1*	8.2*	0.0*	25.7
BF CB	DFS C	25.2	8.9	45.5*	18.8*	154	30.0	41.6	216
DF CB	DFS C	33.5	28.3	31.3*	1.1*	170	40.6	41.6	151
BF BB	DB C	4.7*	5.8	68.4*	53.2	14.5	12.3	12.1*	79.5
BF CB	BF BB	9.4	5.2	121	54.8	17.9	17.0	14.6*	53.3

* Percent difference is less than or equal to error bounds

Table E-15. Percent differences in maximum values of connection response quantities, Set 5

Percent differences between		Maximum θ_{conn}				Maximum M_{conn}			
		C1	C2	C3	C4	C1	C2	C3	C4
BF CB	DB C	28.2	49.7	9.0*	29.9	3.4*	34.9	7.7*	21.3
DF CB	DB C	10.9	45.1	13.4	40.3	9.6*	19.6	2.6*	12.5
DFS C	DB C	0.9*	23.2	39.8	16.9	66.1	92.0	82.0	65.2
BF CB	DF CB	15.5	3.2*	4.0*	8.0*	13.4	12.8	5.0*	7.8*
BF CB	DFS C	29.3	21.5	28.3	11.1	71.8	42.4	69.0	36.2
DF CB	DFS C	12.0	17.7	23.3	20.0	51.5	60.6	77.4	46.8
BF BB	DB C	11.1	44.0	11.8	0.1*	2.0*	34.9	6.6*	7.0*
BF CB	BF BB	15.3	3.9*	2.6*	30.1	5.5*	0.0*	14.8	29.8

* Percent difference is less than or equal to error bounds

E.6 COMPARISON SET 6—JSE17 (LLOLLEO-BASED) MOTION

Table E-16. Percent differences in in-plane displacements and interstory drifts, Set 6

Percent differences between		Max Relative Displacement (in)			Residual Displacement (in)		Max Interstory Drift (%)		Residual Interstory Drift (%)	
		Base	Story 1	Story 2	Story 1	Story 2	Story 1	Story 2	Story 1	Story 2
BF CB	DB C	20.6	26.0	28.4	107	104	27.7	31.0	106	100
SD C	DB C	6.7	5.7	5.9	35.0	33.3	6.1	6.1	34.1	31.6
BF CB	SD C	13.0	19.2	21.2	53.5	52.7	20.3	23.4	53.7	52.0

* Percent difference is less than or equal to error bounds

Table E-17. Percent differences in major response quantities, Set 6

Percent differences between		Max Relative Accel		Max Absolute Accel		Max Vb	Max OTM	λ_{Vb}	λ_{T1}
		Story 1	Story 2	Story 1	Story 2				
BF CB	DB C	2.9*	13.9*	18.2*	25.8	27.2	48.7	53.6	27.6
SD C	DB C	1.0*	1.9*	0.0*	7.4*	8.0*	8.4*	1.3*	25.8
BF CB	SD C	4.0*	11.9*	18.2*	35.1	37.4	61.2	55.7	60.5

* Percent difference is less than or equal to error bounds

Table E-18. Percent differences in maximum values of connection response quantities, Set 6

Percent differences between		Maximum θ_{conn}				Maximum M_{conn}			
		C1	C2	C3	C4	C1	C2	C3	C4
BF CB	DB C	70.5	41.1	86.5	50.0	25.3	18.0	28.9	10.8
SD C	DB C	10.4	4.1*	11.4	6.7*	2.8*	10.1	4.2*	25.2
BF CB	SD C	54.4	35.5	67.4	60.0	21.8	29.9	34.3	38.7

* Percent difference is less than or equal to error bounds

E.7 COMPARISON SET 7—DB C PATTERN, ALL EXCITATIONS

Table E-19. Percent differences in in-plane displacements and interstory drifts, Set 7

Percent differences between		Max Relative Displacement (in)			Residual Dis-placement (in)		Max Interstory Drift (%)		Residual Inter-story Drift (%)	
		Base	Story 1	Story 2	Story 1	Story 2	Story 1	Story 2	Story 1	Story 2
0.6 s pulse	1.2 s pul.	14.8	30.7	32.5	833	836	31.5	34.4	767	839
0.6 s pulse	JNF01	66.2	74.8	74.7	313	306	75.9	74.5	331	300
0.6 s pulse	JSE17	35.2	35.3	33.8	93.4	89.4	34.5	32.3	92.6	85.5
1.2 s pulse	JNF01	44.7	33.7	31.8	126	130	33.7	29.8	101	135
1.2 s pulse	JSE17	17.7	3.5*	1.0*	383	394	2.2*	1.6*	350	406
JNF01	JSE17	22.9	29.2	30.5	113	115	30.8	31.9	124	116

* Percent difference is less than or equal to error bounds

Table E-20. Percent differences in major response quantities, Set 7

Percent differences between		Max Relative Accel		Max Absolute Accel		Max Vb	Max OTM	λ_{Vb}	λ_{T1}
		Story 1	Story 2	Story 1	Story 2				
0.6 s pulse	1.2 s pulse	152	141	208	26.9	0.6*	6.7*	15*	32.2
0.6 s pulse	JNF01	53.3	35.1	174	19.3*	4.1*	13.8	12.5*	15.2*
0.6 s pulse	JSE17	83.6	65.1	124	23.2	10.5	6.9*	6.9*	68.1
1.2 s pulse	JNF01	64.5	78.7	12.5*	6.4*	4.8*	6.7*	2.4*	14.8*
1.2 s pulse	JSE17	363	298	37.5*	56.4	11.2	0.2*	23.1	122
JNF01	JSE17	181	123	22.2*	47.0	6.1*	6.5*	20.2	93.5

* Percent difference is less than or equal to error bounds

Table E-21. Percent differences in maximum values of connection response quantities, Set 7

Percent differences between		Maximum θ_{conn}				Maximum M_{conn}			
		C1	C2	C3	C4	C1	C2	C3	C4
0.6 s pulse	1.2 s pulse	41.3	41.6	46.7	45.7	4.0*	4.1*	5.6*	7.3*
0.6 s pulse	JNF01	84.4	121	145	109	14.0	2.4*	10.8	21.2
0.6 s pulse	JSE17	48.6	40.2	49.3	41.5	2.6*	9.2*	1.1*	11.3
1.2 s pulse	JNF01	30.5	56.2	66.9	43.5	9.6*	1.6*	4.9*	12.9
1.2 s pulse	JSE17	5.2	1.0	1.8	2.9	6.6*	4.9*	4.4*	3.8*
JNF01	JSE17	24.1	57.8	63.9	47.7	16.9	6.6*	9.5*	8.8*

* Percent difference is less than or equal to error bounds

E.8 COMPARISON SET 8—BF CB PATTERN, 1.2 SEC COSINE PULSE AND JNF01

Table E-22. Percent differences in in-plane displacements and interstory drifts, Set 8

Percent differences between		Max Relative Displacement (in)			Residual Displacement (in)		Max Interstory Drift (%)		Residual Interstory Drift (%)	
		Base	Story 1	Story 2	Story 1	Story 2	Story 1	Story 2	Story 1	Story 2
1.2 s pulse	JNF01	98.7	105	108	791	782	107	110	841	773

* Percent difference is less than or equal to error bounds

Table E-23. Percent differences in major response quantities, Set 8

Percent differences between		Max Relative Accel		Max Absolute Accel		Max Vb	Max OTM	λ_{Vb}	λ_{T1}
		Story 1	Story 2	Story 1	Story 2				
1.2 s pulse	JNF01	5.9*	57.8	12.5*	21.8*	9.3*	2.2*	26.2	26.9

* Percent difference is less than or equal to error bounds

Table E-24. Percent differences in maximum values of connection response quantities, Set 8

Percent differences between		Maximum θ_{conn}				Maximum M_{conn}			
		C1	C2	C3	C4	C1	C2	C3	C4
1.2 s pulse	JNF01	185	107	188	143	7.4*	9.9*	2.6*	13.4

* Percent difference is less than or equal to error bounds

E.9 COMPARISON SET 9—COMPARABLE B & C PATTERNS, 0.6 & 1.2 SECOND COSINE PULSES

Table E-25. Percent differences in in-plane displacements and interstory drifts, Set 9

% difference between pulses for pattern	Max Relative Displacement (in)			Residual Displacement (in)		Max Interstory Drift (%)		Residual Interstory Drift (%)	
	Base	Story 1	Story 2	Story 1	Story 2	Story 1	Story 2	Story 1	Story 2
DB C	14.8	30.7	32.5	833	836	31.5	34.4	767	839
BF BP 1	7.8	4.8*	3.9*	68.1	68.0	4.0*	3.1*	67.9	67.9
BF BP 2	10.8	7.6	7.1	52.5	52.9	7.0	6.6	53.0	53.4
DF BP	2.8*	6.2	7.5	155	157	7.6	8.8	160	159
DFS B	20.1	22.2	22.3	87.8	84.9	21.8	22.2	83.4	81.9
BF CP**	42.7	42.7	43.1	42.5	42.5	42.4	43.3	41.9	42.4
DF CP**	45.9	40.2	40.9	38.4	38.7	38.9	41.3	38.7	39.0
DFS C**	76.4	69.1	68.4	62.4	62.6	67.9	67.5	62.5	62.8

* Percent difference is less than or equal to error bounds

** Catch cables engaged—values compromised

Table E-26. Percent differences in major response quantities, Set 9

% difference between pulses for pattern	Max Relative Accel		Max Absolute Accel		Max Vb	Max OTM	λ_{Vb}	λ_{T1}
	Story 1	Story 2	Story 1	Story 2				
DB C	152	141	208	26.9	0.6*	6.7*	15.2*	31.1
BF BP 1	74.7	108	208	37.3	3.4*	10.0*	52.1	4.3*
BF BP 2	52.6	87.8	129	33.9	5.5*	9.8*	29.7	12.3*
DF BP	46.6	132	124	30.2*	7.5*	2.2*	81.8	12.8*
DFS B	37.7	65.7	124	37.0	5.8*	2.3*	31.4	45.0
BF CP**	17.7	50.5	43.5	12.0*	10.4	12.2	125	n/a
DF CP**	61.3	31.4	31.7*	39.0	12.3	30.7	87.2	n/a
DFS C**	49.9	4.1*	132	177	3.7*	124.6	100.0	n/a

* Percent difference is less than or equal to error bounds

** Catch cables engaged

Table E-27. Percent differences in maximum values of connection response quantities, Set 9

% difference between pulses for pattern	Maximum θ_{conn}				Maximum M_{conn}			
	C1	C2	C3	C4	C1	C2	C3	C4
DB C	41.3	41.6	46.7	45.7	4.0*	4.1*	5.6*	7.3*
BF BP 1	3.3*	1.5*	0.2*	2.8*	6.9*	7.9*	2.0*	0.2*
BF BP 2	6.9*	9.2*	9.3*	6.7*	8.1*	10.0*	2.7*	1.7*
DF BP	17.6	12.4	19.0	8.0*	3.8*	7.6*	5.8*	3.1*
DFS B	24.5	21.4	28.9	27.0	5.8*	14.6	1.5*	3.7*
BF CP**	41.4	48.8	46.8	47.8	8.5*	0.6*	1.8*	3.1*
DF CP**	45.9	41.0	45.0	46.9	7.3*	1.5*	1.0*	1.8*
DFS C**	74.6	77.4	77.0	73.8	7.6*	3.0*	7.6*	5.8*

* Percent difference is less than or equal to error bounds

** Catch cables engaged

E.10 COMPARISON SET 10—FRACTURE PATTERNS, 0.6 SECOND COSINE PULSE

Table E-28. Percent differences in in-plane displacements and interstory drifts, Set 10

Percent differences between		Max Relative Displacement (in)			Residual Displacement (in)		Max Interstory Drift (%)		Residual Interstory Drift (%)	
		Base	Story 1	Story 2	Story 1	Story 2	Story 1	Story 2	Story 1	Story 2
BF A A	BF BP H	13.7	10.1	10.5	168	169	9.9	11.0	152	171
BF BP H	BF BP 1	127	136	141	976	968	138	146	962	960
BF BP H	BF BP 2	121	130	134	876	872	131	138	868	868
BF BP H	DF BP	121	134	139	940	934	136	144	928	928
BF BP 1	BF CP**	35.7	28.0	27.4	69.3	69.7	26.5	27.2	69.9	70.2
BF BP 2	BF CP**	39.4	31.4	31.3	86.6	86.5	30.2	31.5	86.4	86.3
BF BP 1	DF CP**	33.0	32.0	32.0	77.5	77.8	31.6	32.3	77.6	78.1
BF BP 2	DF CP**	36.6	35.6	36.0	95.6	95.3	35.5	36.8	94.9	95.0
DF BP	DF CP**	36.5	33.1	32.9	83.6	83.6	32.6	33.2	83.5	83.6

* Percent difference is less than or equal to error bounds

** Catch cables engaged—values compromised

Table E-29. Percent differences in major response quantities, Set 10

Percent differences between		Max Relative Accel		Max Absolute Accel		Max Vb	Max OTM	λ_{Vb}	λ_{T1}
		Story 1	Story 2	Story 1	Story 2				
BF A A	BF BP H	5.6*	4.9*	60.0*	2.8*	17.0	9.3*	3.5*	32.8
BF BP H	BF BP 1	120	94.0	393	14.1*	9.9*	8.7*	109	50.5
BF BP H	BF BP 2	92.0	74.9	267	11.3*	7.7*	8.5*	77.9	76.3
BF BP H	DF BP	104	84.7	333	15.5*	26.0	8.4*	133	98.1
BF BP 1	BF CP**	13.9*	0.7*	12.1*	2.5*	4.2*	2.4*	383	n/a
BF BP 2	BF CP**	0.5*	10.1*	20.0*	5.1*	6.3*	2.3*	466	n/a
BF BP 1	DF CP**	39.9	9.7*	37.0	5.2*	19.7	1.2*	466	n/a
BF BP 2	DF CP**	60.1	1.1*	1.9*	2.6*	22.1	1.1*	564	n/a
DF BP	DF CP**	51.1	4.4*	20.4*	6.5*	4.4*	1.0*	407	n/a

* Percent difference is less than or equal to error bounds

Table E-30. Percent differences in maximum values of connection response quantities, Set 10

Percent differences between		Maximum θ_{conn}				Maximum M_{conn}			
		C1	C2	C3	C4	C1	C2	C3	C4
BF A A	BF BP H	82.7	6.3*	23.6	24.3	24.7	16.9	9.5*	1.0*
BF BP H	BF BP 1	183	203	281	277	9.2*	17.1	10.2	11.2
BF BP H	BF BP 2	156	181	249	263	10.3	19.3	15.4	9.1*
BF BP H	DF BP	182	201	280	256	9.8*	23.6	8.0*	18.2
BF BP 1	BF CP**	23.5	25.9	46.4	50.5	0.4*	5.2*	38.2	35.9
BF BP 2	BF CP**	36.3	35.4	59.7	56.2	1.4*	7.3*	44.7	33.4
BF BP 1	DF CP**	28.6	37.0	54.6	54.7	7.5*	5.1*	28.1	35.2
BF BP 2	DF CP**	42.0	47.3	68.6	60.6	6.3*	3.1*	34.1	32.7
DF BP	DF CP**	29.1	37.7	54.8	63.8	6.9*	0.5*	25.5	43.8

* Percent difference is less than or equal to error bounds

** Catch cables engaged

E.11 COMPARISON SET 11—FRACTURE PATTERNS, 1.2 SECOND COSINE PULSE

Table E-31. Percent differences in in-plane displacements and interstory drifts, Set 11

Percent differences between		Max Relative Displacement (in)			Residual Displacement (in)		Max Interstory Drift (%)		Residual Interstory Drift (%)	
		Base	Story 1	Story 2	Story 1	Story 2	Story 1	Story 2	Story 1	Story 2
BF BP	DF BP	7.8	12.2	12.5	57.2	58.0	12.7	12.9	60.1	58.8
BF BP	BF CP 1**	79.5	74.3	75.5	306	306	73.2	76.8	305	307
BF BP	BF CB	1.8*	4.3*	3.5*	19.1	17.8	4.6*	2.7*	17.5	16.6
BF BP	DF CP**	79.9	76.7	79.0	313	314	75.9	81.4	314	316
DF BP	BF CP 1**	93.5	95.5	97.5	538	542	95.2	99.7	548	546
DF BP	BF CB	5.9	7.6	8.8	32.1	34.1	7.7	9.9	36.2	36.2
DF BP	DF CP**	93.8	98.2	101	549	555	98.2	105	562	560
BF CP 1**	BF CP 2	464	555	579	9626	9867	565	605	9999	10127
BF CP 1**	BF CP 3	52.9	45.7	45.1	40.2	39.7	44.4	44.0	40.0	39.1
BF CP 2	BF CP 3	269	350	368	6838	7036	360	390	7111	7251

* Percent difference is less than or equal to error bounds

** Catch cables engaged

Table E-32. Percent differences in major response quantities, Set 11

Percent differences between		Max Relative Accel		Max Absolute Accel		Max Vb	Max OTM	λ_{Vb}	λ_{T1}
		Story 1	Story 2	Story 1	Story 2				
BF BP	DF BP	10.4*	17.1	20.8*	6.8*	3.1*	7.3*	7.0*	11.9*
BF BP	BF CP 1**	30.4	37.5	91.7	57.6	9.5*	20.5	226	n/a
BF BP	BF CB	20.5	5.1*	50.0*	32.2*	4.2*	0.3*	14.8*	42.0
BF BP	DF CP**	51.6	44.5	70.8*	81.4	3.1*	42.0	360	n/a
DF BP	BF CP 1**	18.1	61.0	58.6*	47.6	12.9	12.2	249	n/a
DF BP	BF CB	9.2*	11.4*	24.1*	23.8*	1.0*	7.0*	22.9	26.9
DF BP	DF CP**	37.3	69.2	41.1*	69.8	0.0*	32.3	392	n/a
BF CP 1**	BF CP 2	55.7	108	84.0	72.2	4.6*	30.6	300	n/a
BF CP 1**	BF CP 3	54.5	103	35.3*	25.7*	15.9	49.4	39.0	n/a
BF CP 2	BF CP 3	0.8*	2.1*	36.0*	37.0*	10.7	14.5	188	128

* Percent difference is less than or equal to error bounds

** Catch cables engaged

Table E-33. Percent differences in maximum values of connection response quantities, Set 11

Percent differences between		Maximum θ_{conn}				Maximum M_{conn}			
		C1	C2	C3	C4	C1	C2	C3	C4
BF BP	DF BP	14.2	14.7	19.4	17.6	3.6*	5.9*	1.7*	3.3*
BF BP	BF CP 1**	80.5	84.6	114	116	1.8*	2.0*	38.4	40.0
BF BP	BF CB	14.7	0.7*	3.9*	11.8	14.9	3.0*	13.0	57.9
BF BP	DF CP**	93.8	90.3	124	121	7.0*	11.7	29.3	32.6
DF BP	BF CP 1**	106	112	156	154	5.5*	3.9*	40.7	44.7
DF BP	BF CB	0.5*	15.4	14.9	31.5	10.9	9.1*	14.9	63.2
DF BP	DF CP**	121	118	167	160	3.3*	5.4*	31.5	37.0
BF CP 1**	BF CP 2	832	813	1561	1296	4.1*	8.5*	3.9*	8.3*
BF CP 1**	BF CP 3	43.1	45.4	46.5	53.4	20.7	32.5	12.6	20.3
BF CP 2	BF CP 3	551	528	1034	810	16.0	22.0	8.4*	11.1

* Percent difference is less than or equal to error bounds

** Catch cables engaged

E.12 COMPARISON SET 12—BF A, BP PATTERNS, 0.6 SEC COS PULSE, 50% AMP.

Table E-34. Percent differences in in-plane displacements and interstory drifts, Set 12

Percent differences between		Max Relative Displacement (in)			Residual Displacement (in)		Max Interstory Drift (%)		Residual Interstory Drift (%)	
		Base	Story 1	Story 2	Story 1	Story 2	Story 1	Story 2	Story 1	Story 2
Max/ min BF A A-D		5.6	1.5*	1.7*	66.6	82.1	1.6*	2.1*	120	101
BF A A	BF A E	1.1*	1.3*	1.7*	28.8	21.4	1.9*	2.2*	13.1	14.7
BF A B	BF A E	0.2*	0.8*	0.7*	15.7	10.7	1.0*	0.6*	5.9*	6.2*
BF A C	BF A E	4.4*	1.0*	1.8*	29.4	50.0	2.5*	2.4*	94.8	75.5
BF A D	BF A E	3.1*	0.1*	0.1*	19.3	11.7	0.9*	0.3*	30.2	5.6*
Max/ min BF A A-E		5.6	1.5*	1.8*	66.6	82.1	2.5*	2.4*	120	101
BF BP	BF A A	13.7	10.1	10.5	168	169	9.9	11.0	152	171
BF BP	BF A B	12.2	9.5	9.4	198	195	9.0	9.3	202	192
BF BP	BF A C	7.7	9.7	10.6	346	390	10.5	11.2	456	445
BF BP	BF A D	9.1	8.5	8.7	311	265	8.8	9.0	272	228
BF BP	BF A E	12.5	8.7	8.7	245	227	7.8	8.6	185	210
Avg. of above 5 diffs		10.6	9.5	9.8	256	255	9.6	10.1	271	259

* Percent difference is less than or equal to error bounds

Table E-35. Percent differences in major response quantities, Set 12

Percent differences between		Max Relative Accel Story 1	Max Relative Accel Story 2	Max Absolute Accel Story 1	Max Absolute Accel Story 2	Max Vb	Max OTM	λ_{Vb}	λ_{T1}
Max/ min BF A A-D		12.2*	12.7*	68.8*	1.4*	6.2*	2.4*	4.6*	28.3
BF A A	BF A E	17.0	1.8*	33.3*	4.1*	3.4*	2.8*	4.0*	27.8
BF A B	BF A E	13.6*	0.2*	50.0*	4.1*	2.7*	2.7*	0.6*	36.1
BF A C	BF A E	5.6*	7.1*	5.9*	2.7*	2.8*	0.9*	1.5*	61.1
BF A D	BF A E	4.2*	5.2*	12.5*	2.7*	3.4*	3.3*	2.4*	63.9
Max/ min BF A A-E		17.0	12.7*	68.8*	4.1*	6.2*	3.3*	4.6*	63.9
BF BP	BF A A	5.6*	4.9*	60.0*	2.8*	17.0	9.3*	3.5*	32.8
BF BP	BF A B	2.6*	6.5*	80.0*	2.8*	10.1	9.4*	8.3*	24.6
BF BP	BF A C	4.8*	14.3*	13.3*	4.2*	16.3	11.4	6.1*	5.3*
BF BP	BF A D	6.3*	1.5*	6.7*	4.2*	16.9	8.8*	5.2*	3.5*
BF BP	BF A E	10.7*	6.8*	20.0*	7.0*	13.1	12.4	7.7*	69.7
Avg. of above 5 diffs		4.8*	6.8*	40.0*	3.5*	15.1	9.7*	5.8*	16.6

* Percent difference is less than or equal to error bounds

Table E-36. Percent differences in max.imum values of connection response quantities, Set 12

Percent differences between		Maximum θ_{conn} C1	Maximum θ_{conn} C2	Maximum θ_{conn} C3	Maximum θ_{conn} C4	Maximum M_{conn} C1	Maximum M_{conn} C2	Maximum M_{conn} C3	Maximum M_{conn} C4
Max/ min BF A A-D		7.4*	6.3*	3.8*	5.9*	2.5*	4.5*	5.2*	2.2*
BF A A	BF A E	4.0*	4.5*	3.0*	4.0*	0.2*	1.4*	1.7*	0.7*
BF A B	BF A E	3.2*	2.1*	4.5*	3.6*	1.0*	5.1*	0.9*	0.7*
BF A C	BF A E	0.4*	8.5*	6.8*	2.6*	1.3*	4.2*	6.1*	3.0*
BF A D	BF A E	3.2*	7.2*	4.2*	1.9*	1.5*	0.6*	1.0*	1.4*
Max/ min BF A A-E		7.4*	8.5*	6.8*	5.9*	2.5*	5.1*	6.1*	3.0*
BF BP	BF A A	82.7	6.3*	23.6	24.3	24.7	16.9	9.5*	1.0*
BF BP	BF A B	81.4	8.8*	25.4	23.9	25.7	12.8	10.4	1.1*
BF BP	BF A C	75.0	2.4*	28.3	22.7	22.8	13.8	5.0*	1.2*
BF BP	BF A D	70.2	3.6*	25.1	17.4	22.6	17.9	10.3	0.4*
BF BP	BF A E	75.7	11.1	20.0	19.6	24.4	18.6	11.4	1.8*
Avg. of above 5 diffs		77.3	5.3*	25.6	22.1	23.9	15.4	8.8*	0.9*

* Percent difference is less than or equal to error bounds

PEER REPORTS

PEER reports are available from the National Information Service for Earthquake Engineering (NISEE). To order PEER reports, please contact the Pacific Earthquake Engineering Research Center, 1301 South 46th Street, Richmond, California 94804-4698. Tel.: (510) 231-9468; Fax: (510) 231-9461.

PEER 2003/13 *Effects of Connection Hysteretic Degradation on the Seismic Behavior of Steel Moment-Resisting Frames.* Janise E. Rodgers and Stephen A. Mahin. March 2004.

PEER 2003/10 *A Beam-Column Joint Model for Simulating the Earthquake Response of Reinforced Concrete Frames.* Laura N. Lowes, Nilanjan Mitra, and Arash Altoontash. February 2004.

PEER 2003/08 *A Technical Framework for Probability-Based Demand and Capacity Factor Design (DCFD) Seismic Formats*. Fatemeh Jalayer and C. Allin Cornell. November 2003.

PEER 2003/06 *Performance of Circular Reinforced Concrete Bridge Columns under Bidirectional Earthquake Loading*. Mahmoud M. Hachem, Stephen A. Mahin, and Jack P. Moehle. February 2003.

PEER 2003/05 *Response Assessment for Building-Specific Loss Estimation.* Eduardo Miranda and Hesameddin Aslani. September 2003.

PEER 2003/04 *Experimental Assessment of Columns with Short Lap Splices Subjected to Cyclic Loads*. Murat Melek, John W. Wallace, and Joel Conte. April 2003.

PEER 2003/03 *Probabilistic Response Assessment for Building-Specific Loss Estimation.* Eduardo Miranda and Hesameddin Aslani. September 2003.

PEER 2003/02 *Software Framework for Collaborative Development of Nonlinear Dynamic Analysis Program.* Jun Peng and Kincho H. Law. September 2003.

PEER 2003/01 *Shake Table Tests and Analytical Studies on the Gravity Load Collapse of Reinforced Concrete Frames.* Kenneth John Elwood and Jack P. Moehle. November 2003

PEER 2002/24 *Performance of Beam to Column Bridge Joints Subjected to a Large Velocity Pulse.* Natalie Gibson, André Filiatrault, and Scott A. Ashford. April 2002.

PEER 2002/23 *Effects of Large Velocity Pulses on Reinforced Concrete Bridge Columns.* Greg L. Orozco and Scott A. Ashford. April 2002.

PEER 2002/22 *Characterization of Large Velocity Pulses for Laboratory Testing.* Kenneth E. Cox and Scott A. Ashford. April 2002.

PEER 2002/21 *Fourth U.S.-Japan Workshop on Performance-Based Earthquake Engineering Methodology for Reinforced Concrete Building Structures*. December 2002.

PEER 2002/20 *Barriers to Adoption and Implementation of PBEE Innovations.* Peter J. May. August 2002.

PEER 2002/19 *Economic-Engineered Integrated Models for Earthquakes: Socioeconomic Impacts.* Peter Gordon, James E. Moore II, and Harry W. Richardson. July 2002.

PEER 2002/18 *Assessment of Reinforced Concrete Building Exterior Joints with Substandard Details.* Chris P. Pantelides, Jon Hansen, Justin Nadauld, and Lawrence D. Reaveley. May 2002.

PEER 2002/17 *Structural Characterization and Seismic Response Analysis of a Highway Overcrossing Equipped with Elastomeric Bearings and Fluid Dampers: A Case Study.* Nicos Makris and Jian Zhang. November 2002.

PEER 2002/16 *Estimation of Uncertainty in Geotechnical Properties for Performance-Based Earthquake Engineering.* Allen L. Jones, Steven L. Kramer, and Pedro Arduino. December 2002.

PEER 2002/15 *Seismic Behavior of Bridge Columns Subjected to Various Loading Patterns.* Asadollah Esmaeily-Gh. and Yan Xiao. December 2002.

PEER 2002/14 *Inelastic Seismic Response of Extended Pile Shaft Supported Bridge Structures.* T.C. Hutchinson, R.W. Boulanger, Y.H. Chai, and I.M. Idriss. December 2002.

PEER 2002/13 *Probabilistic Models and Fragility Estimates for Bridge Components and Systems.* Paolo Gardoni, Armen Der Kiureghian, and Khalid M. Mosalam. June 2002.

PEER 2002/12 *Effects of Fault Dip and Slip Rake on Near-Source Ground Motions: Why Chi-Chi Was a Relatively Mild M7.6 Earthquake.* Brad T. Aagaard, John F. Hall, and Thomas H. Heaton. December 2002.

PEER 2002/11 *Analytical and Experimental Study of Fiber-Reinforced Strip Isolators*. James M. Kelly and Shakhzod M. Takhirov. September 2002.

PEER 2002/10 *Centrifuge Modeling of Settlement and Lateral Spreading with Comparisons to Numerical Analyses***.** Sivapalan Gajan and Bruce L. Kutter. January 2003.

PEER 2002/09 *Documentation and Analysis of Field Case Histories of Seismic Compression during the 1994 Northridge, California, Earthquake.* Jonathan P. Stewart, Patrick M. Smith, Daniel H. Whang, and Jonathan D. Bray. October 2002.

PEER 2002/08 *Component Testing, Stability Analysis and Characterization of Buckling-Restrained Unbonded Braces™.* Cameron Black, Nicos Makris, and Ian Aiken. September 2002.

PEER 2002/07 *Seismic Performance of Pile-Wharf Connections.* Charles W. Roeder, Robert Graff, Jennifer Soderstrom, and Jun Han Yoo. December 2001.

PEER 2002/06 *The Use of Benefit-Cost Analysis for Evaluation of Performance-Based Earthquake Engineering Decisions*. Richard O. Zerbe and Anthony Falit-Baiamonte. September 2001.

PEER 2002/05 *Guidelines, Specifications, and Seismic Performance Characterization of Nonstructural Building Components and Equipment*. André Filiatrault, Constantin Christopoulos, and Christopher Stearns. September 2001.

PEER 2002/04 *Consortium of Organizations for Strong-Motion Observation Systems and the Pacific Earthquake Engineering Research Center Lifelines Program: Invited Workshop on Archiving and Web Dissemination of Geotechnical Data, 4–5 October 2001*. September 2002.

PEER 2002/03 *Investigation of Sensitivity of Building Loss Estimates to Major Uncertain Variables for the Van Nuys Testbed.* Keith A. Porter, James L. Beck, and Rustem V. Shaikhutdinov. August 2002.

PEER 2002/02 *The Third U.S.-Japan Workshop on Performance-Based Earthquake Engineering Methodology for Reinforced Concrete Building Structures*. July 2002.

PEER 2002/01 *Nonstructural Loss Estimation: The UC Berkeley Case Study. Mary C. Comerio and John C. Stallmeyer.* December 2001.

PEER 2001/16 *Statistics of SDF-System Estimate of Roof Displacement for Pushover Analysis of Buildings.* Anil K. Chopra, Rakesh K. Goel, and Chatpan Chintanapakdee. December 2001.

PEER 2001/15 *Damage to Bridges during the 2001 Nisqually Earthquake.* R. Tyler Ranf, Marc O. Eberhard, and Michael P. Berry. November 2001.

PEER 2001/14 *Rocking Response of Equipment Anchored to a Base Foundation.* Nicos Makris and Cameron J. Black. September 2001.

PEER 2001/13 *Modeling Soil Liquefaction Hazards for Performance-Based Earthquake Engineering.* Steven L. Kramer and Ahmed-W. Elgamal. February 2001.

PEER 2001/12 *Development of Geotechnical Capabilities in OpenSees.* Boris Jeremic. September 2001.

PEER 2001/11 *Analytical and Experimental Study of Fiber-Reinforced Elastomeric Isolators*. James M. Kelly and Shakhzod M. Takhirov. September 2001.

PEER 2001/10 *Amplification Factors for Spectral Acceleration in Active Regions.* Jonathan P. Stewart, Andrew H. Liu, Yoojoong Choi, and Mehmet B. Baturay. December 2001.

PEER 2001/09 *Ground Motion Evaluation Procedures for Performance-Based Design.* Jonathan P. Stewart, Shyh-Jeng Chiou, Jonathan D. Bray, Robert W. Graves, Paul G. Somerville, and Norman A. Abrahamson. September 2001.

PEER 2001/08 *Experimental and Computational Evaluation of Reinforced Concrete Bridge Beam-Column Connections for Seismic Performance*. Clay J. Naito, Jack P. Moehle, and Khalid M. Mosalam. November 2001.

PEER 2001/07 *The Rocking Spectrum and the Shortcomings of Design Guidelines.* Nicos Makris and Dimitrios Konstantinidis. August 2001.

PEER 2001/06 *Development of an Electrical Substation Equipment Performance Database for Evaluation of Equipment Fragilities*. Thalia Agnanos. April 1999.

PEER 2001/05 *Stiffness Analysis of Fiber-Reinforced Elastomeric Isolators.* Hsiang-Chuan Tsai and James M. Kelly. May 2001.

PEER 2001/04 *Organizational and Societal Considerations for Performance-Based Earthquake Engineering.* Peter J. May. April 2001.

PEER 2001/03 *A Modal Pushover Analysis Procedure to Estimate Seismic Demands for Buildings: Theory and Preliminary Evaluation.* Anil K. Chopra and Rakesh K. Goel. January 2001.

PEER 2001/02 *Seismic Response Analysis of Highway Overcrossings Including Soil-Structure Interaction.* Jian Zhang and Nicos Makris. March 2001.

PEER 2001/01 *Experimental Study of Large Seismic Steel Beam-to-Column Connections.* Egor P. Popov and Shakhzod M. Takhirov. November 2000.

PEER 2000/10 *The Second U.S.-Japan Workshop on Performance-Based Earthquake Engineering Methodology for Reinforced Concrete Building Structures.* March 2000.

PEER 2000/09 *Structural Engineering Reconnaissance of the August 17, 1999 Earthquake: Kocaeli (Izmit), Turkey.* Halil Sezen, Kenneth J. Elwood, Andrew S. Whittaker, Khalid Mosalam, John J. Wallace, and John F. Stanton. December 2000.

PEER 2000/08 *Behavior of Reinforced Concrete Bridge Columns Having Varying Aspect Ratios and Varying Lengths of Confinement.* Anthony J. Calderone, Dawn E. Lehman, and Jack P. Moehle. January 2001.

PEER 2000/07 *Cover-Plate and Flange-Plate Reinforced Steel Moment-Resisting Connections.* Taejin Kim, Andrew S. Whittaker, Amir S. Gilani, Vitelmo V. Bertero, and Shakhzod M. Takhirov. September 2000.

PEER 2000/06 *Seismic Evaluation and Analysis of 230-kV Disconnect Switches.* Amir S. J. Gilani, Andrew S. Whittaker, Gregory L. Fenves, Chun-Hao Chen, Henry Ho, and Eric Fujisaki. July 2000.

PEER 2000/05 *Performance-Based Evaluation of Exterior Reinforced Concrete Building Joints for Seismic Excitation.* Chandra Clyde, Chris P. Pantelides, and Lawrence D. Reaveley. July 2000.

PEER 2000/04 *An Evaluation of Seismic Energy Demand: An Attenuation Approach.* Chung-Che Chou and Chia-Ming Uang. July 1999.

PEER 2000/03 *Framing Earthquake Retrofitting Decisions: The Case of Hillside Homes in Los Angeles.* Detlof von Winterfeldt, Nels Roselund, and Alicia Kitsuse. March 2000.

PEER 2000/02 *U.S.-Japan Workshop on the Effects of Near-Field Earthquake Shaking.* Andrew Whittaker, ed. July 2000.

PEER 2000/01 *Further Studies on Seismic Interaction in Interconnected Electrical Substation Equipment.* Armen Der Kiureghian, Kee-Jeung Hong, and Jerome L. Sackman. November 1999.

PEER 1999/14 *Seismic Evaluation and Retrofit of 230-kV Porcelain Transformer Bushings*. Amir S. Gilani, Andrew S. Whittaker, Gregory L. Fenves, and Eric Fujisaki. December 1999.

PEER 1999/13 *Building Vulnerability Studies: Modeling and Evaluation of Tilt-up and Steel Reinforced Concrete Buildings.* John W. Wallace, Jonathan P. Stewart, and Andrew S. Whittaker, editors. December 1999.

PEER 1999/12 *Rehabilitation of Nonductile RC Frame Building Using Encasement Plates and Energy-Dissipating Devices.* Mehrdad Sasani, Vitelmo V. Bertero, James C. Anderson. December 1999.

PEER 1999/11 *Performance Evaluation Database for Concrete Bridge Components and Systems under Simulated Seismic Loads.* Yael D. Hose and Frieder Seible. November 1999.

PEER 1999/10 *U.S.-Japan Workshop on Performance-Based Earthquake Engineering Methodology for Reinforced Concrete Building Structures.* December 1999.

PEER 1999/09 *Performance Improvement of Long Period Building Structures Subjected to Severe Pulse-Type Ground Motions*. James C. Anderson, Vitelmo V. Bertero, and Raul Bertero. October 1999.

PEER 1999/08 *Envelopes for Seismic Response Vectors.* Charles Menun and Armen Der Kiureghian. July 1999.

PEER 1999/07 *Documentation of Strengths and Weaknesses of Current Computer Analysis Methods for Seismic Performance of Reinforced Concrete Members.* William F. Cofer. November 1999.

PEER 1999/06 *Rocking Response and Overturning of Anchored Equipment under Seismic Excitations.* Nicos Makris and Jian Zhang. November 1999.

PEER 1999/05 *Seismic Evaluation of 550 kV Porcelain Transformer Bushings.* Amir S. Gilani, Andrew S. Whittaker, Gregory L. Fenves, and Eric Fujisaki. October 1999.

PEER 1999/04 *Adoption and Enforcement of Earthquake Risk-Reduction Measures.* Peter J. May, Raymond J. Burby, T. Jens Feeley, and Robert Wood.

PEER 1999/03 *Task 3 Characterization of Site Response General Site Categories*. Adrian Rodriguez-Marek, Jonathan D. Bray, and Norman Abrahamson. February 1999.

PEER 1999/02 *Capacity-Demand-Diagram Methods for Estimating Seismic Deformation of Inelastic Structures: SDF Systems*. Anil K. Chopra and Rakesh Goel. April 1999.

PEER 1999/01 *Interaction in Interconnected Electrical Substation Equipment Subjected to Earthquake Ground Motions.* Armen Der Kiureghian, Jerome L. Sackman, and Kee-Jeung Hong. February 1999.

PEER 1998/08 *Behavior and Failure Analysis of a Multiple-Frame Highway Bridge in the 1994 Northridge Earthquake.* Gregory L. Fenves and Michael Ellery. December 1998.

PEER 1998/07 *Empirical Evaluation of Inertial Soil-Structure Interaction Effects.* Jonathan P. Stewart, Raymond B. Seed, and Gregory L. Fenves. November 1998.

PEER 1998/06 *Effect of Damping Mechanisms on the Response of Seismic Isolated Structures.* Nicos Makris and Shih-Po Chang. November 1998.

PEER 1998/05 *Rocking Response and Overturning of Equipment under Horizontal Pulse-Type Motions.* Nicos Makris and Yiannis Roussos. October 1998.

PEER 1998/04 *Pacific Earthquake Engineering Research Invitational Workshop Proceedings, May 14–15, 1998: Defining the Links between Planning, Policy Analysis, Economics and Earthquake Engineering.* Mary Comerio and Peter Gordon. September 1998.

PEER 1998/03 *Repair/Upgrade Procedures for Welded Beam to Column Connections.* James C. Anderson and Xiaojing Duan. May 1998.

PEER 1998/02 *Seismic Evaluation of 196 kV Porcelain Transformer Bushings.* Amir S. Gilani, Juan W. Chavez, Gregory L. Fenves, and Andrew S. Whittaker. May 1998.

PEER 1998/01 *Seismic Performance of Well-Confined Concrete Bridge Columns.* Dawn E. Lehman and Jack P. Moehle. December 2000.